Real-time investigation of temporal and spatial correlations in fast neutron assay from spontaneous and stimulated fission

Submitted in accordance with the requirements
of Lancaster University for the degree of
Doctor of Philosophy

by

Rashed Sarwar

May 23, 2019

Commenced November 2014; Submitted: September 2018; Examined: February 2019; Accepted May 2019.

For my parents, sister and Farah,
with love.

Acknowledgements

William Blake, an 18th - 19th century English poet, painter and printmaker once said: No bird soars too high if he soars with his own wings. The achievement that makes up this thesis is quite minor in comparison to the seminal poetries and visual arts of Blake, but it goes without saying that reaching thus far could hardly have been realized without the affection, direction and support of my family, friends and colleagues.

The guidance, time and support provided to me by Professor Malcolm Joyce were unquestionably crucial to see me through both the highs and the hair-pulling moments over the better part of the last three years. He has been the dream supervisor that anyone could hope for and has been the Alpha Ursae Minoris to help me sail through the unknowns that accompany researching towards a PhD qualification. The patience he has shown my sometimes naive and impatient approach was the major driving force towards the completion of this work.

I would also like to thank Dr Colin H Zimmerman, Dr Paul Little and Dr Robert Mills from the National Nuclear Laboratory, and Dr Robert Grover and Dr Barrie Greenhalgh from the Sellafield Ltd for their support towards achieving this goal.

Special thanks to Dr Steven Croft from the Oak Ridge National Laboratory for hosting me in their laboratory and for allowing me to pick his brain for his vast seemingly limitless knowledge on everything nuclear safeguard related. I am also grateful to the supporting team of experts and researchers at the nuclear safeguard group at the Oak Ridge National Laboratory, especially thankful to Dr G. Nutter and Angela Simone.

I would also like to show huge appreciation to all my colleagues at Lancaster University and Culham Centre for Fusion Energy; especial to Dr Stephen Adams, Dr Michael Aspinall, Dr Richard Wilbraham, and Dr Ashley Jones for their guidance regarding the write-up period. Thanks also to my colleagues, in no particular order, Alex, Helen, Chris, Johnny and Vytas for the assists given to me at some stage over the last three years of my work.

I acknowledge the Engineering and Physical Sciences Research Council (EPSRC), DISTINCTIVE consortium, UK Nuclear Data Network and Faculty of Science and Engineering at the Lancaster University for funding the research, and the support of an EPSRC ADRIANA award granted to the Department of Engineering at Lancaster University which allowed me access to all the toys.

I would like to thank my parents. I appreciate the support provided by them throughout my lifetime. If they had not made the sacrifices that they made I would not have made it half as far as I have. I would also like to thank my sister, Sayma, and my sisters-in-law, Sarah and Naima.

A special and final thank you to my wife, partner-in-crime, soul-mate, best friend and my better-half, Farah. She has tolerated for the better part of the last three years of me drifting in my own world of research leading to countless missed anniversaries, dates, movies and weekends. She has been the constant support in all my endeavours and after years of proof-reading my work, she deserves a recognition far greater than a mention in the acknowledgement section. Thank you very much.

Abstract

A study of the use of digital techniques for the real-time, fast neutron coincidence analysis of time- and space-correlated radiations emitted by californium-252 and uranium-235 is described. These radiations have been measured with detectors based on the organic liquid scintillant, EJ-309. Time-synchronized neutron and γ-ray event-trains, separated with pulse shape discrimination, have been sampled with a field-programmable gate array programmed with an algorithm developed in this research. This approach has been used to extract the interval time distribution of this event-train, with a time resolution of 5 ns, to investigate the temporal correlation between the neutrons and/or γ rays emitted in the spontaneous fission of californium-252. The established model for the characterization of the interval-time distributions of correlated thermal neutron events, used widely in thermal neutron coincidence assay, has been extended to fast neutrons. The influence of geometry and the surroundings on these distributions has been investigated and quantified: the temporal coefficients for the die-away of the distributions for neutrons and γ rays are 3.18 ± 0.09 ns and 1.49 ± 0.06 ns, respectively. It has been observed that 99.7% of the correlated neutrons and γ rays are detected within 27 ns and 21 ns of each other, respectively, when a low-scatter geometry is examined. The spatial distribution of fast neutrons emitted in spontaneous fission (californium-252) has also been investigated to yield the evidence for the angular distribution of higher-order, correlated neutrons presented in this thesis; this infers a dipolar trend for third (triplet) and fourth (quadruplet) neutrons consistent with that known for second (doublet) neutrons. The γ-ray emission has been used to provide time-of-flight information and hence the neutron spectrum for fission neutrons from californium-252. A technique for the determination of the foreground and background coincidence distribution of the emitted fast neutrons and/or γ rays for passive and active neutron coincidence counting methods has been developed. Finally, two models have been developed to correct for erroneous coincidence events which might otherwise limit the use of organic scintillators in coincident assay: one for photon breakthrough and one for detector crosstalk. These models have been validated using californium-252 indicating that photon-breakthrough constitutes a 20% increase in the neutron count rates whilst crosstalk can result in increases of 10% and 35% on first-and second-order coincident events, respectively, for the investigated geometries. The instrumentation, techniques and results reported in this thesis extend our understanding of the fundamental temporal characteristics of nuclear fission, and are of direct relevance to the application of organic scintillators with pulse shape discrimination to nuclear safeguards and non-proliferation verification.

Declaration

I, Rashed Sarwar, hereby certify that this thesis and the research described in it is all my own work unless otherwise indicated and has not been submitted in any previous application for a higher degree. The work presented here was carried out at Lancaster University between November 2014 and April 2018. I, as the author and candidate, acknowledge Dr Paul Little of UK National Nuclear Laboratory (NNL) for executing the FISPIN simulations, the results of which are included in this thesis. I also acknowledge Dr Stephen Croft of Oak Ridge National Laboratory (ORNL) for accommodating us in his laboratory and participating in scientific discussions which was helpful towards developing a method of validating the crosstalk model. Additionally, I acknowledge Dr G Nutter and Ms Angela Simone of ORNL and Dr Vytautas Astromskas of Lancaster University for assisting in the experiments conducted at the ORNL. I also acknowledge Dr Olivier Litaizem of De la recherche à l'industrie (CEA) and Dr Patrick Talou of Los Alamos National Laboratory (LANL), and their respective research groups, for providing data and helpful suggestions for the simulation works. Finally, I also acknowledge the support of Lancaster University and the Engineering and Physical Sciences Research Council (EPSRC), the UK 'DISTINCTIVE' university consortium, (www.distinctiveconsortium.org) and the support of the Science and Technology Facilities Council (STFC) via the UK Nuclear Data Network (http://www.ukndn.ac.uk/). The apparatus used in this research is part of the UK National Nuclear Users Facility (www.nnuf.ac.uk), supported under EPSRC grant 'ADRIANA', EP/L025671/1.

Date..... Signature of candidate.....

Rashed Sarwar

Contents

List of tables

List of figures

List of symbols

α	Alpha particle constituent of a helium nucleus, radiation particle
β^+	Positron particle, radiation particle
β^-	Electron particle, radiation particle
$\chi(E)$	Isotropic fission spectrum
δS	Elementary surface
ΔT	Gate-width for coincidence measurements, nanosecond (ns)
δT	Smallest time-bin in a distribution, nanosecond (ns)
ϵ	Detection efficiency
γ	Gamma ray or photon particle, radiation particle
$\mathbf{r}$	Vector coordinate of space
μ_l	Linear Attenuation Coefficient, meter^{-1} (m^{-1})
ν	Order of multiplicity
$\nu(r)$	Reduced factorial moment of rth order
ν_{in}	Reduced factorial moment of nth order for induced fission
ν_{sn}	Reduced factorial moment of nth order for spontaneous fission
Ω	Solid angle
$\Phi(\mathbf{r}, \Omega, E, t)$	Scalar neutron flux per unit volume, solid angle, and energy
$\Psi(\mathbf{r}, \Omega, E, t)$	Angular neutron flux per unit volume, solid angle, and energy
Σ_x	Microscopic cross section for x type nuclear reaction, per unit length
σ_x	microscopic cross section for x type nuclear reaction, barn (b)
τ	Detector die-away, nanosecond (ns)
Θ	Scattering angle in centre-of-mass frame of reference
θ	Scattering angle in laboratory frame of reference
A	Mass Number, i.e. total number of protons and neutrons
b_k or $b(k)$	Background (accidental) coincidence distribution of kth order
B_x	Breakthrough factor for particle type x
E'_γ	Energy of a scattered γ-ray, kiloelectron volt (keV)
E'_n	Energy of a scattered neutron, kiloelectron volt (keV)
E_γ	Incident energy of a γ-ray, kiloelectron volt (keV)

E_b	Binding energy, kiloelectron volt (keV)
E_e	Energy of an ejected electron, kiloelectron volt (keV)
E_n	Incident energy of a neutron, kiloelectron volt (keV)
E_r	Recoil energy, kiloelectron volt (keV)
$E_{e,max}$	Maximum energy with which an electron may be ejected with, kiloelectron volt (keV)
F	Fission rate, second^{-1} (s^{-1})
f_d	Doubles gate fraction
F_i	Induced fission rate, second^{-1} (s^{-1})
f_k or $f(k)$	Foreground (real) coincidence distribution of kth order
F_s	Spontaneous fission rate, second^{-1} (s^{-1})
f_t	Triples gate fraction
$G(\nu)$	γ-ray multiplicity distribution, i.e. γ-ray number distribution
g_k or $g(k)$	Mixed (real + accidental) coincidence distribution of kth order
I	Intensity
$J(\mathbf{r}, E, t)$	Neutron current density vector per unit area, energy, and time
L	Linear length, metre (m)
m_e	Resting mass of an electron, kilogram (kg)
m_n	Resting mass of a neutron, kilogram (kg)
M_L	Leakage multiplication
$n(\mathbf{r}, \Omega, E, t)$	Neutron density, or the number of neutrons per unit volume, solid angle, and energy
$P(\nu)$	Neutron multiplicity distribution, i.e. neutron number distribution
$P_i(\nu)$	Neutron multiplicity distribution from induced fission, i.e. neutron number distribution
$P_s(\nu)$	Neutron multiplicity distribution from spontaneous fission, i.e. neutron number distribution
t	Time, nanosecond (ns)
t_g	Size of coincidence window or gate, nanosecond (ns)
t_{pd}	Size of pre-delay gate, nanosecond (ns)
XT_x	Crosstalk factor for particle type x
Z	Atomic Number, i.e. number of proton in an element

List of elements & compounds

Al Aluminium.

Am Americium.

AmBe Americium Beryllium.

AmLi Americium Lithium.

B Boron.

Be Beryllium.

C Carbon.

Cf Californium.

Cl Chlorine.

Cm Curium.

Co Cobalt.

Cs Caesium.

Ge Germanium.

H Hydrogen.

He Helium.

I Iodine.

K Potassium.

Li Lithium.

N Nitrogen.

O Oxygen.

Pb Lead.

Pu Plutonium.

Ra Radium.

Tc Technetium.

Th Thorium.

U Uranium.

List of abbreviations

ADC analogue-to-digital converter.

AFNCC active fast neutron coincidence counting.

ANCC active neutron coincidence counting.

ASCII American Standard Code for Information Interchange.

BNC Bayonet Neill-Concelman.

BWR boiling water reactor.

CCM charge comparision method.

CEF Cascade Evaporation Fission.

CERN Conseil Européen pour la Recherche Nucléaire.

ENDF/B-VII Evaluated Nuclear Data Library.

EPSRC Engineering and Physical Sciences Research Council.

FIFO first in, first out.

FIR finite impulse response.

FoM figure-of-merit.

FPGA field-programable gate array.

FREYA Fission Reaction Event Yield Algorithm.

GPIO general purpose input/output.

GUI graphical user interface.

GWd/MTU gigawatt day per metric tonne of uranium.

HEC High-End Cluster.

HEU highly-enriched uranium.

HLW high-level waste.

HT high-tension.

ITD interval-time distribution.

JANIS Java-based Nuclear Data Information System.

LAN local area network.

LLNL Lawrence Livermore National Laboratory.

LLW low-level waste.

LXDE Lightweight X11 Desktop Environment.

MCA Multi-Channel Analyser.

MCNP Monte Carlo N-Particle.

MFA Mixed-Field Analysers.

MOX mixed-oxide.

NDA nondestructive analysis.

NNL National Nuclear Laboratory.

NPL National Physical Laboratory.

ORNL Oak Ridge National Laboratory.

PCB printed circuit board.

PDF probability distribution function.

PFNCC passive fast neutron coincidence counting.

PGA pulse gradient analysis.

PLL phase-locked loops.

PMT photo-multiplier tube.

PNCC passive neutron coincidence counting.

PoP proof-of-principle.

PSD pulse shape discrimination.

PWR pressurized water reactor.

RAM random access memory.

RISC reduced instruction set computing.

RMSE root mean squared error.

SNF spent nuclear fuel.

SNM special nuclear material.

SNR signal-to-noise ratio.

SSE sum of squares due to error.

TCP/IP Transmission Control Protocol/Internet Protocol.

ToF time-of-flight.

TTL transistor-transistor logic.

UART Universal Asynchronous Receiver/Transmitter.

UOX uranium oxide.

USB universal serial bus.

VHDL VHSIC Hardware Description Language.

VHSIC Very High Speed Integrated Circuit.

ZCM zero-crossing method.

Glossary

accidental event is a detected event from uncorrelated processes from different fission chains, (α, n) reactions and random sources of background.

active neutron coincidence counting refers to a technique of analysing correlated neutrons from induced fission (upon interrogation with external neutron source) usually within a short time window.

angular distribution corresponds to a distribution that provides information about the spatial correlation of particles. The distribution consists of normalised coincident fast neutron response as a function of the angle of the detector position relative to that of a reference detector, the latter being the detector that triggers the coincidence trigger window.

background coincidence count represents the number of events detected in the delayed-gate corresponding to uncorrelated processes (i.e. accidental counts).

background coincidence distribution represents a particle number distribution, similar to the probability density function, of the recorded coincident events from an experiment based on the background coincidence count consisting of accidental events only.

background factorial moment distribution represents the factorial moment distribution of the coincidence distribution from the delayed-gate corresponding to uncorrelated processes (i.e. accidental counts).

BARE8 describes the arrangement consisting of 8 EJ-309 based liquid scintillation detectors arranged in a 20.5 cm ring with a radioactive source at the centre.

BARE15 describes the arrangement consisting of 15 EJ-309 based liquid scintillation detectors arranged in a 26.75 cm ring with a radioactive source at the centre.

CASTLE12 describes the arrangement consisting of 12 EJ-309 based liquid scintillation detectors arranged in three 4 by 4 blocks which make up three faces of a square.

centre-of-mass frame of reference is a frame of reference where the centre of mass is at rest, but it is not necessarily at the origin of the coordinate system.

Cherenkov radiation is electromagnetic radiation emitted when a charged particle (such as an electron) passes through a dielectric medium at a speed greater than the phase velocity of light in that medium emitting a characteristic blue glow.

coincidence distribution represents a particle number distribution, similar to the probability density function, of the recorded coincident events from an experiment. It is constructed by making a tally of the number of times a specific order of coincidence occurred.

coincidence-gate represents a time-interval over which events are scanned for.

coincident event events or particles which are correlated in time and/or space.

crosstalk describes a phenomenon by which a single incident particle triggers multiple detectors and thereby appears as a multiplet within an acquisition window when measuring coincident events.

crosstalk-factor is defined as a distribution of the ratio of the number of *crosstalk* events to the total number of events detected as a function of order of crosstalk.

DE1-SoC is a development kit by Terasic designed around an Altera System-on-Chip FPGA, which combines a dual-core Cortex-A9 embedded subsystem with programmable logic for flexibility.

delayed-gate represents the gate opened to measure the background coincident count.

doubles gate-fraction represents the proportion of doubles events that are detected after correction for detection efficiencies was made.

event-train corresponds to a series of tightly placed events (in time) that can be assumed to be correlated events from the same fission event.

foreground coincidence count represents the number of events detected in the prompt-gate corresponding to fission and uncorrelated processes (i.e. real + accidental counts).

foreground coincidence distribution represents a particle number distribution, similar to the probability density function, of the recorded coincident events from an experiment based on the foreground coincidence count consisting of both real and accidental events.

foreground factorial moment distribution represents the factorial moment distribution of the coincidence distribution from the prompt-gate corresponding to fission and uncorrelated processes (i.e. real + accidental counts).

gate-fraction represents the proportion of emitted particles from a fission event that are detected after correction for detection efficiencies was made.

gate-width an acquisition window in time, ΔT, within which coincident events are measured.

idle-gate represents the period of time allowed between the prompt- and delayed-gates.

interval-time distribution a time histogram reflecting the time escaped between the detection of tightly placed events (in time) that can be assumed to be correlated events from the same fission event - a probability distribution if normalized.

joint represents combined neutron and γ-ray events from the Mixed-Field Analyser (MFA), i.e. the same TTL lead is used per channel to transmit the signals to implicate arrival of both neutron and γ-ray events.

K-electrons are the electrons belonging to the closest shell to the nucleus called the "s shell", also known as the "K shell".

laboratory frame of reference is a frame of reference centred on the laboratory and is at rest when measurements are taken.

level-shifter a custom PCB board using two SN74CBTD3861 chips designed to convert 5V-TTL signals from the MFA to 3.3 V in order to be compatible with the DE1-SoC board.

Lightweight X Desktop Environment a free desktop environment with comparatively low resource requirements.

linear energy transfer describes how much energy a charged particle transfers to the material traversed per unit distance.

liquid drop model describes the fluid like behaviour of the atomic nucleus. The fluid is comprised of nucleons (protons and neutrons) held together by the strong nuclear force taking into account the position of each nucleon on the surface or in the interior of the nucleus.

multiplet the size of a detected event cluster/burst, i.e. event-train.

multiplicity register represents the complete set of instrumentation developed in this thesis: DE1-SoC development board with the proposed algorithm along with the level-shifter.

neutron spectroscopy is the measure of neutron energy.

non-Poissonian deviation in the Poissonian approximation of a given number of events occurring in a fixed interval of time or space if these events occur with a known constant rate *but* are correlated in time, contrary to the Poisson approximation of the binomial distribution.

number distribution describes the *probability distribution functions* outlining the likelihood of a given number of neutrons, n, that may be emitted following fission.

optical photon is a photon with a wavelength much greater than the typical atomic spacing. Such a particle is produced when a charged particle, e.g. an electron or proton, traverses through a dielectric material with velocity above the Cherenkov threshold or through a scintillation material.

order-of-coincidence the size of a detected event cluster/burst, i.e. event-train.

passive neutron coincidence counting refers to a technique of analysing correlated neutrons from spontaneous fission within a short time window.

photon-breakthrough refers to the phenomenon by which a γ-ray event from a scatter based detector is misclassified as a neutron event due to limitations in the pulse shape discrimination technique. It primarily occurs for low energy γ rays where the small response from the interaction exposes the limitation of the mathematical algorithm.

Poissonian describes probability of a given number of events occurring in a fixed interval of time or space in accord with the Poisson approximation of the binomial distribution if these events occur with a known constant rate and independently of the time.

predelay-gate represents the period of time allowed to escape before the prompt-gate is opened to allow the detectors to recover from the initial detection.

prompt-gate represents the gate opened to measure the foreground coincident count.

Q-value in nuclear physics refers to the amount of energy released or absorbed by a reaction.

radioactive materials describes materials which emit radiation such as protons, neutrons, electrons, etc., due to change in their nuclear state.

real correlated coincidence distribution represents a particle number distribution, similar to the probability density function, consisting of real events only.

real event represents an event made up of particles from a fission process correlated to each other.

real factorial moment distribution represents the factorial moment distribution of the coincidence distribution from the prompt-gate corresponding to correlated processes (i.e. real counts).

reduced factorial moment distribution is a statistical quantity representing the expectation or average of falling factorial of a particle number distribution or a coincidence distribution.

REFL15 describes an arrangement consisting of 15 EJ-309 based liquid scintillation detectors arranged around the face of a tank from which a ^{252}Cf source is exposed.

satellite event corresponds to the event that cannot issue gates but will count towards the coincidence distribution count.

trigger event corresponds to the event that issues new coincidence window, i.e. the first event in an event-train.

Total describes the total number of events detected, equivalent to the first factorial moment, i.e. singles.

Chapter 1

Introduction

With the end of the Second World War and the start of the Cold War between the United States of America and the then Soviet Union, the world saw a rapid growth in the scope of both civilian and military nuclear power. The development and use of the first atomic bombs, a response so strong compared to anything the world has previously seen, prompted the Bulletin of the Atomic Scientists' Science and Security Board to create the iconic Doomsday Clock [1], a measure of the likelihood of a man-made nuclear catastrophe. This fear of self-annihilation eventually led to the formation of the International Atomic Energy Agency (IAEA) whose aim is to encourage peaceful use of nuclear technology; as stated by President D Eisenhower in his "Atoms for peace" speech at the UN General Assembly in December 1953 [2]. Eventually, almost every nation signed the Treaty of Non-Proliferation of Nuclear Weapons on 1st July 1968. In order to ensure that the signatories remain true to this philosophy, considerable focus has been devoted to research related to nuclear safeguards. Such research has focused on both the ability to trace *special nuclear material (SNM)* and other *radioactive materials* to enforce the treaty towards non-proliferation of SNM.

The existence of *radioactive materials* (i.e. materials which emit particles such as neutrons, electrons, etc., due to change in their atomic state) is quite common as they are widely used in daily life. For example, the material used for 'glow-in-the-dark' dials of watches and clocks in the early 20th century was a radium isotope that gave the clocks a green glow. *Radioactive materials* are also used in various industries (e.g. ^{60}Co, ^{137}Cs, ^{226}Ra, etc.) and for medicinal treatments (e.g. ^{99m}Tc, ^{57}Co, ^{125}I, etc.). Some of these materials are also naturally occurring (e,g. ^{40}K, ^{226}Ra, ^{238}U, etc.). This thesis is primarily concerned with a group of *radioactive materials* sometimes referred to as *special nuclear materials* and includes any plutonium isotopes

and uranium enriched with ^{233}U or ^{235}U [3]. These materials form naturally in stars but are not readily available for mining on earth as they have, for the most part, decayed away since the formation of the planet (with the exception of ^{235}U which only constitutes ≈0.7 wt. % of natural uranium ore). However, these materials can be made inside commercial and research nuclear reactors. The Generation III reactors frequently require a special type of uranium based fuel which contains a higher fraction of fissile material which is either achieved via enrichment (i.e. increasing the proportion of ^{235}U compared to ^{238}U) or via extraction of fissile material (i.e. ^{239}Pu and ^{241}Pu) from *spent nuclear fuel (SNF)* and mixing it with fresh *uranium oxide (UOX)* to form a *mixed-oxide (MOX)* fuel. The concern of nuclear safeguards is to ensure that none of the enriched uranium content and the various plutonium isotopes is diverted to produce weapons. Additionally, not all SNF from civilian or research nuclear reactors may be repurposed and there is a need to decommission old reactors after the end of their lifespan. These spent fuels and activated structures from decommissioned reactors also need to be accounted for as they can be hazardous to the environment if not properly stored. However, this storage process can be very expensive, for example, the Swedish *Spent Fuel Repository (SFR)*, as well as their long- and short-lived waste repositories, are expected to cost an additional £9.2 billion, starting 2018, for completion [4]. Thus it is important to identify initially the constituents of the waste materials before disposal, to be able to classify them as either low-level or high-level waste, with low-level wastes easily taken care of using minimal expense instead of combining all waste into one high-level, high maintenance, and more expensive (due to higher storage costs) waste package. Further, should the technology become available on an industrial process scale to transmute long-lived radioactive isotopes to shorter-lived species, knowledge of projected lifespans at an isotopic level will be essential to assess the suitability of the different permanent disposal options. Since SNF disposal will always be the subject of extensive public debate, this knowledge of the projected life of radioactive substances is usually a requirement to support policy decisions despite the vast timescales involved.

From a complementary and equally significant perspective, whilst the ability to retrieve the SNF from deep disposal at some point in the future is often deemed desirable in most disposal option studies, the ease with which a remedial assessment of the isotopic content of these materials might be achieved once the SNF is consigned is nonetheless likely to be heavily constrained. Thus, there is a significant imperative to be able to carry out accurate assessments, particularly of fissile content, prior to long-term disposal. This supports the need to ensure that end-of-life safeguards accounts are prepared with confidence; the isotopes typically at the focus of such assessments being the various plutonium isotopes, ^{235}U and to a lesser extent ^{237}Np isotopes.

1.1 The current status of quantification and its inherent challenges

To quantify the composition of nuclear materials for storage or tamper-identification purposes, several *non-destructive analysis (NDA)* techniques (i.e. processes by which the sample being studied is not destroyed as a result of examination) can be employed, including: (i) γ tomography methods to reconstruct the spatial distribution of the emitted γ-ray radiation from various isotopes which constitute the sample [5, 6], (ii) thermal neutron detectors, such as fork detectors with a fission chamber to determine the presence and quantity of neutron emitting isotopes [7], (iii) *passive neutron coincidence counting (PNCC)* and *active neutron coincidence counting (ANCC)* with thermal neutron detectors, such as ^{3}He-filled detectors, to measure the temporal correlation of the neutron field [8], and (iv) *Cherenkov radiation* measurements using Cherenkov detectors [9].

A variety of analytical techniques have been developed [7, 8, 26] to measure the neutron emission rates to ascertain the plutonium and uranium content in nuclear materials experimentally. Some of these methods rely on the detection of correlated neutrons emitted during the spontaneous fission of the different major actinides, either via passive or active means. Given the emission of spontaneous fission neutrons, which are correlated in the temporal domain, these techniques measure the deviation from the correlated characteristics of the correlated neutron field to determine the total mass of fissile materials.

Each of the above mentioned methods has its own advantages and disadvantages. For example, γ rays have high penetration but its use is complicated by the fact that many fission fragments (e.g. ^{90}Sr, ^{137}Cs, etc.) present in SNF give rise to large amounts of γ-ray radiation making the determination of fissile material very complex [10]. Further to this, the use of a fission chamber to count neutrons requires *highly-enriched uranium (HEU)*, which renders it necessary to control the detectors themselves. Additionally, the detection of neutrons from a material does not necessarily imply the presence of fissile materials, as neutrons can be emitted by other mechanisms, such as (α, n) reactions. These are to be discussed in detail in Chapter 2. To determine that the detected neutrons are indeed from fissile materials, a further temporal analysis of the neutron field emitted from the test sample usually needs to be undertaken. As such materials undergo spontaneous and induced fission, during which they disintegrate into two smaller fragments emitting multiple correlated neutrons (and γ rays) in the time domain, a temporal analysis can provide a means for the quantification of fissile materials. There are two popular methods of carrying out such an analysis: (i) the Rossi-α method [11] and (ii) the Feynman-Y [12] method. These methods, although used initially in reactor analysis [13, 14], have been adopted widely with thermal neutron detectors, such as ^{3}He-filled detectors, for the

detection of time-correlated thermal neutrons that are emitted from spontaneous fission and the induced fission of fissile materials. Furthermore, such statistical methods can indicate the fluctuation of the neutron population in time, inferring the *non-Poissonian* characteristic of the neutron die-away characteristic in a fission chain. In this thesis, the primary focus is on the Rossi-α technique which provides the foundation for the PNCC and ANCC techniques.

Whilst essentially blind to γ-ray radiation with high detection efficiency, very desirable properties when trying to detect neutron properties, ^{3}He-filled thermal neutron counters have a major drawback pertaining to the energy levels of the particles they are sensitive to, i.e. they can only detect thermal neutrons. As a consequence of this, the fast neutron fields originating from fissile materials, due to spontaneous or induced fission have to be thermalized. As such, these thermal neutrons lose some of their salient properties, such as temporal and spatial information, along with information regarding the incident energy of the neutrons. As a result of thermalisation, the coincidence window needed for the PNCC and ANCC is substantially wider (to the order of 40-50 μs) [15, 16] than the typical time taken for the fission-correlated fast neutron field to die away (typically less than 100 ns). Thus, the proportion of chance-correlated counts (i.e. *accidental events*) increases. ^{3}He also suffers from an additional limitation. As ^{3}He is a by-product of nuclear weapons production, the global ^{3}He inventory has reduced significantly with the decline of the nuclear arms race leading to ^{3}He being "supply constrained", a challenge compounded by its relatively short half-life of 12.3 years [17, 18].

Finally, an alternative process of achieving these characterizations could be the use of depletion codes. However, this again will be limiting, this time by the quality of the burn-up history as an incomplete history will exacerbate uncertainties in record-keeping. In addition, there will be potential errors introduced by uncertainties in the nuclear data used in such codes.

1.2 The objectives and novelty of this research

The research in this thesis describes a comprehensive investigation to see if it is theoretically possible to obtain ageing information of spent fuel and to develop new instrumentation that can carry out the required analysis in real-time in order to investigate the temporal and spatial properties of radiation fields from fissile materials. The results of the simulated isotropic inventory in SNF presented in section 4.1 of this thesis illustrate that the impact of changing composition, due to ageing, on the emission of correlated events from SNF is a subtle, but nonetheless a distinct difference in the spontaneous fission multiplicity distribution between plutonium and curium isotopes that exists mostly for *high-order coincidence distributions*. Successfully measuring such higher-order coincident events is difficult utilising the thermal PNCC and ANCC techniques in the nuclear industry due to the limitation discussed above; i.e. long gate-widths increasing the

proportion of accidental counts, thereby reducing the statistics of the measurements.

To avoid the thermalisation process, PNCC and ANCC utilize an array of detectors which are sensitive to fast neutrons, such as organic liquid scintillation detectors. One of the earliest reports of fast neutron-multiplicity counting based on the use of organic scintillators in an unmoderated environment is from Wachter *et al.* [19] in the late 1980s. This study used analogue instrumentation and highlighted the key benefits of organic scintillators, such as sensitivity to high-order coincident events and significantly-reduced levels of *accidentals* over thermal assays. The main reasons for these detectors not being in mainstream use after almost half a century of research are: (i) the need to have fast electronics to process the rapid signals generated by these detectors (i.e. the pulse width from these detectors is typically between 50 to 200 ns) [20], (ii) their sensitivity to γ-ray fields requiring implementation of *pulse shape discrimination (PSD)* analysis, (iii) their reliance on scatter reactions in order to detect radiation which often leads to partial energy deposition and therefore detector *crosstalk* [19], and (iv) the scintillant materials being toxic and flammable substances.

However, since the start of the 21st century, xylene based scintillants have been developed which have reduced dramatically toxicity and flammability. Furthermore, increases in the speed of electronics means instruments are now commercially available which can process the pulses from organic scintillation detectors and can distinguish the neutron events from γ-ray events, e.g. *Mixed-Field Analysers (MFA)* from Hybrid Instruments Ltd [21] and the 7xx digitizer families from CAEN [22, 23]. These advancements in processing capability have led to a resurgence in fast research assays over the last decade, resulting in the development of several prototypes implemented for special nuclear material assays [24, 25, 26, 27, 28, 29, 30, 31]. However, despite these improvements, a small fraction of low-energy γ rays can be misclassified as neutrons (i.e. *photon-breakthrough* [19]) using such techniques. Additionally, fast neutron assay systems (for investigating temporal properties) are still not properly able to carry out the required analysis in real-time and are often based on the mathematical techniques developed for previous generation thermal neutron detectors. Therefore, fast neutron assay does not address the problems of *photon-breakthrough* and detector *crosstalk*, as neither of these are a significant hindrance to thermal neutron assay. Moreover, these methods often do not include real-time PSD to reduce the effect of *photon-breakthrough*. As a consequence of these limitations, most prototype assays usually need the detector signals to be post-processed by skilled analysts.

1.2.1 This thesis

First, fundamental background information related to the topic is presented in Chapter 2. The development and implementation of an algorithm/technique, referred to as the *multiplicity*

register, to carry out real-time analysis of temporal and spatial distortion of the *non-Poissonian* properties of emitted, correlated particles from both spontaneous and induced fission is presented in Section 3.2. This section also reports on a technique for PNCC and ANCC using arrays of fast neutron organic scintillation detectors, sometimes referred to as *passive fast neutron coincidence counting (PFNCC)* and *active fast neutron coincidence counting (AFNCC)*. The algorithm produces a particle number distribution based on the coincidence events recorded from a sample undergoing spontaneous and induced fission. The digital sampling of analogue signals from the detectors was obtained in real-time using MFAs from Hybrid Instruments Ltd., UK. These devices process the events arising from the scintillators and discriminate them to identify the type of event (i.e. γ-ray or neutron event) using the *Pulse Gradient Analysis (PGA)* technique [32]. Using this instrumentation, several experiments were conducted to validate algorithms and also to investigate the temporal and spatial properties of the particles emitted by spontaneous and stimulated fission. Sections 3.3 and 3.4 outline the experimental rigs, and the different experiments and analyses that were carried out, respectively. A Geant4 model, reported in section 3.7, was also developed as part of this research which simulates the detailed physical interactions which occur inside organic scintillation detectors to help validate the results.

The proposed techniques are applied in various experiments, the results of which are presented in Chapter 4. Section 4.2 then presents the results from a temporal analysis of ^{252}Cf sources using two experimental arrangements designed to investigate the influence of scattered particles. Based on the results, this section also proposes an extension to the standard Rossi-α model in order to quantify the impact of neutron scattering on the *interval-time distribution* (i.e. temporal distribution). Section 4.3 describes attempts to determine the neutron spectrum of a ^{252}Cf source, using the same instrumentation, with several experimental arrangements designed to augment the hardness of the neutron flux to investigate if the proposed techniques can discern the change in neutron energy spectrum. The experimentally-obtained *angular distribution* of individual neutrons from the recorded coincident events are presented in section 4.4 illustrating the first evidence for the higher-order angular distributions from spontaneous fission. The results from PFNCC and AFNCC, using fast organic scintillation detectors, of ^{252}Cf and of fresh UOX fuel of various different enrichments are presented using multiple detector arrangements in section 4.5. This section also includes several correlated and uncorrelated γ-ray sources. Finally, section 4.6 presents the results that were obtained based on the investigations that were carried out regarding detector *crosstalk* and *photon-breakthrough*. Chapter 5 discusses the results obtained during the course of this research and compares them to relevant prior-art by other research institutes. In section 5.6, the understanding gained from the analysis of detector *crosstalk* and *photon-breakthrough* when using organic scintillation detectors is detailed. This section also proposes two models for quantifying the bias in numerical analysis as a consequence of detector *crosstalk*

and *photon-breakthrough*, and subsequently correcting the bias empirically. Finally, chapter 6 outlines some of the investigations that could be done in the future, while chapter 7 concludes the thesis and its findings.

In summary, this thesis reports investigations into temporal and spatial correlation of the neutron field emitted during spontaneous and induced fission. There are still many challenges that need to be solved, but, the findings of this research will help guide future investigations towards improving the effectiveness of these systems. The following publications have resulted from the research detailed within this thesis at the time of submission:

- R. Sarwar, V. Astromskas, C.H. Zimmerman, G. Nutter, A.T. Simone, S. Croft, M.J. Joyce, An event-triggered coincidence algorithm for fast-neutron multiplicity assay corrected for cross-talk and photon breakthrough, *Nuclear Instruments and Methods in Physics Research Section A: Accelerators, Spectrometers, Detectors and Associated Equipment*, In press - 23 June 2018, DOI: 10.1016/j.nima.2018.06.056.
- [1] R. Sarwar, V. Astromskas, C. H. Zimmerman, S. Croft, M. J. Joyce, High-order angular correlation of californium-252 fission neutrons and the effect of detector crosstalk, *2018 Symposium on Radiation Measurements and Application*, 11-14 June 2018, Michigan, USA.
- R. Sarwar, V. Astromskas, C. H. Zimmerman, S. Croft, M. J. Joyce, Real-time determination of Rossi-α distribution, active fast neutron multiplicity, neutron angular distribution and neutron spectrum using organic liquid scintillators, *IEEE Nuclear Science Symposium 2017*, 21-28 Oct 2017, Atlanta, USA.
- R. Sarwar, M. J. Joyce and C. H. Zimmerman, A prototype system for real-time fast neutron multiplicity using liquid scintillation detectors, *IEEE Nuclear Science Symposium 2016*, France.
- R. Sarwar, M. J. Joyce and C. H. Zimmerman, Fast neutron multiplicity counting with zero accidentals, *Plutonium Futures - The Science 2016*, Baden-Baden, Germany.

[1] Due to requirements imposed by the organizers, the conference record will be included upon successful completion of the review process, with M. J. Joyce as the lead author; full author list: M. J. Joyce, R. Sarwar, V. Astromskas, A. Chebboubi, S. Croft, O. Litaize, P. Talou, R. Vogt and C. H. Zimmerman.

Chapter 2

Background

Radiation is defined as the transmission of energy in the form of particles or waves in matter or space. Radiation may be classified into two groups: ionising radiation (alpha, beta, protons, neutrons, X-ray, γ ray, etc.) or non-ionising radiation (radio waves, TV, microwave, infrared, visible light and ultraviolet). This chapter presents some fundamental information about two forms of ionising radiation, γ rays and neutrons, and the various techniques used in industry to scrutinise and model radiation fields.

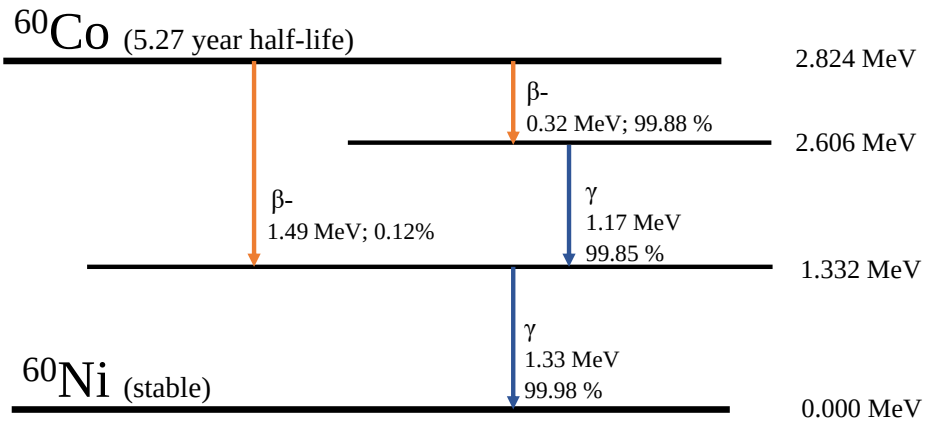

Figure 2.1 | Decay scheme of ^{60}Co. Illustration of the various energy bands in the decay of ^{60}Co, indicating that 99.9% of its decay results in the production of two γ lines of 1.173 MeV and 1.332 MeV along with a 318 keV β- particle. The data were extracted using the *Java-based Nuclear Data Information System (JANIS)* toolkit [33].

2.1 Gamma radiation

Gamma rays are high energy electromagnetic waves emitted during the de-excitation of an atomic nucleus [34]. Such waves are composed of massless particles known as photons in their highest energy range and hence traverse through a vacuum at the speed of light. Despite being part of the electromagnetic spectrum, it is common practice to use energy to express γ-ray strength rather than frequency or wavelength.

2.1.1 Origin

The emission of γ rays takes place due to a change between states at the nuclear level. During the γ-ray emission process, no change in the nuclear configuration takes place, i.e. the number of protons and neutrons remains unchanged. Such emissions can be associated with an alpha/beta/fission decay which leaves the parent isotope in an excited state. The energies of the emitted γ rays are characteristic of the radiating nuclide, and hence are sometimes used for characterisation of different radioactive isotopes and nuclear phenomena. As an example, figure 2.1 shows the different paths and their corresponding energy steps by which two γ rays are emitted following beta decay from cobalt-60, ^{60}Co, with respective energies of 1.172 MeV and 1.332 MeV.

The number of γ rays emitted from a fissioning isotope that is undergoing spontaneous or induced fission is also dependent on the type of fissile material [34, 35, 36, 37, 38] and can be exploited as a means to characterise the sample by determining the number of correlated γ rays. This is discussed in more detail in section 2.3.

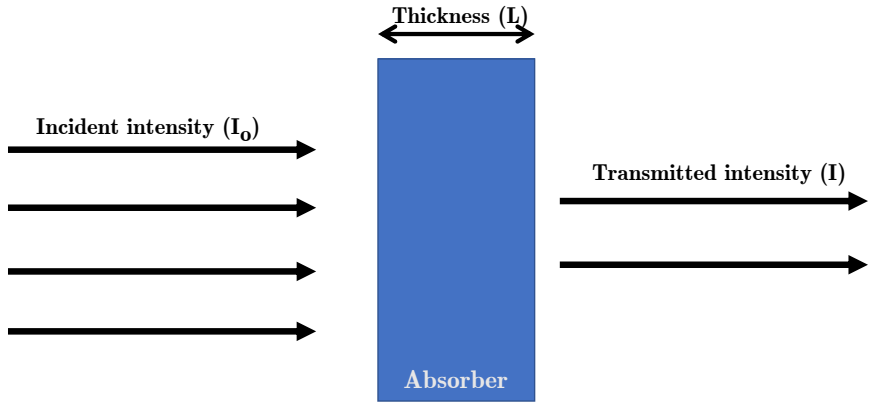

Figure 2.2 | γ-ray transmission and attenuation. Fundamental law of transmission of γ rays. (Redrawn from Passive Nondestructive Assay of Nuclear Materials [39]).

2.1.2 Interaction with matter

Despite having a unique energy spectrum and characteristic rate of emission, the detected γ-ray intensity measured from a given sample is always attenuated due to interactions within the sample and its surroundings [39]. As shown in figure 2.2, a γ-ray radiation field with an intensity of I_0 traversing through a medium of thickness L in cm, will only register an intensity I as given by equation 2.1, where μ_l is the attenuation coefficient and has units of cm^{-1}. The energy of the incident γ rays must be constant during the transmission process. The value of μ_l is dependent on the composition of the material and the energy of the incident γ ray. Additionally, different materials have different values for this coefficient.

$$I = I_0 e^{-\mu_l L} \tag{2.1}$$

As a consequence of this attenuation, it is difficult to construct appropriate calibration standards as the size and shape of the radiation sample will have an influence. Although accurate mapping of detector efficiency as a function of source position and energy can be made, uncertainties in the value of the measured activity will still exist.

Here, the main focus is the detection of γ-ray radiation from 1 keV to 3000 keV. At these energies, the primary mode of interaction with matter can be classified into three processes: (i) photoelectric absorption, (ii) Compton scattering and (iii) pair production. As can be observed in figure 2.3, the energy of the incident γ-ray and the composition of the medium dictates which process is going to prevail [39, 40]. In the following subsections, these three mechanisms are explained briefly along with reference to how such interactions may facilitate their detection.

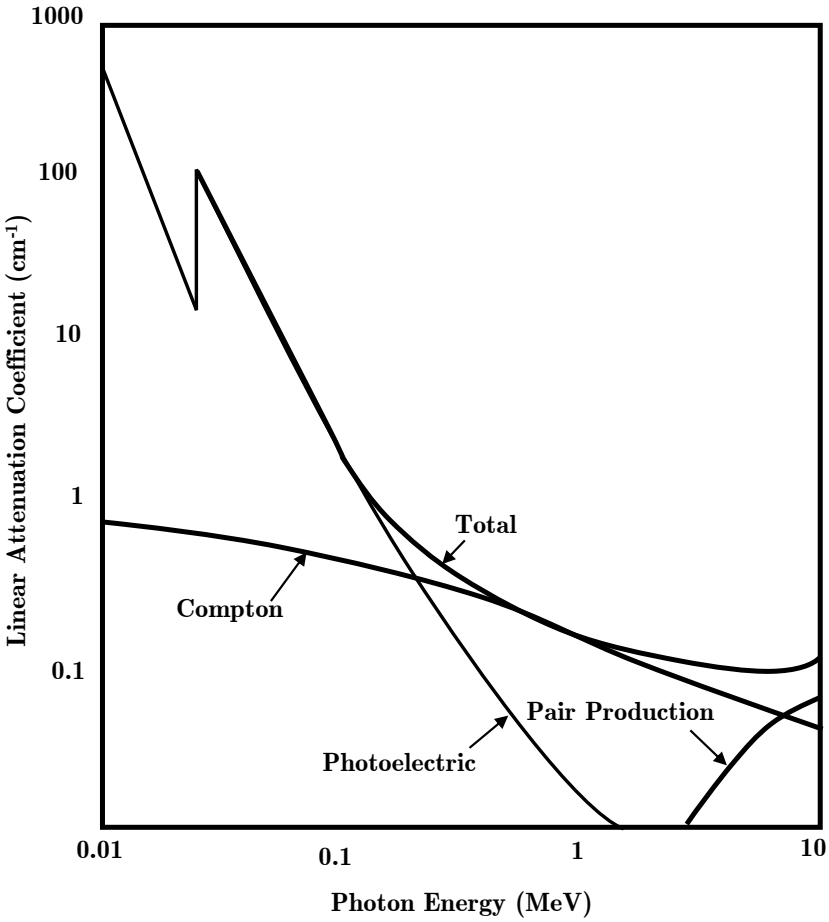

Figure 2.3 | Energy dependence of γ-ray interaction. Energy dependence of the various γ-ray interaction processes in sodium iodide. Schematic description of the main processes by which γ rays interact with matter. (Schematically redrawn based on the original illustration from Atomic Nucleus by R. D. Evans [41]).

Photoelectric absorption

During the photoelectric absorption process, the incident γ ray passes all of its energy to the inner-most electrons of the target atom. Specifically, a γ ray of a given energy, E_γ, is absorbed by target atom which overcomes the binding energy of an electron, E_b, resulting in the ejection of the electron with a kinetic energy, E_e, as shown in equation 2.2. Some energy is converted to recoil energy of the atom to maintain conservation of momentum, but this is of little consequence observationally given the ejected electron has a negligible mass compared to the target atom. This process is schematically illustrated in figure 2.4(a). Given that the magnitude of E_b is very small relative to the incident energy of the γ ray, the energy associated with one photoelectric absorption reflects closely to the incident γ-ray energy.

$$E_e = E_\gamma - E_b \tag{2.2}$$

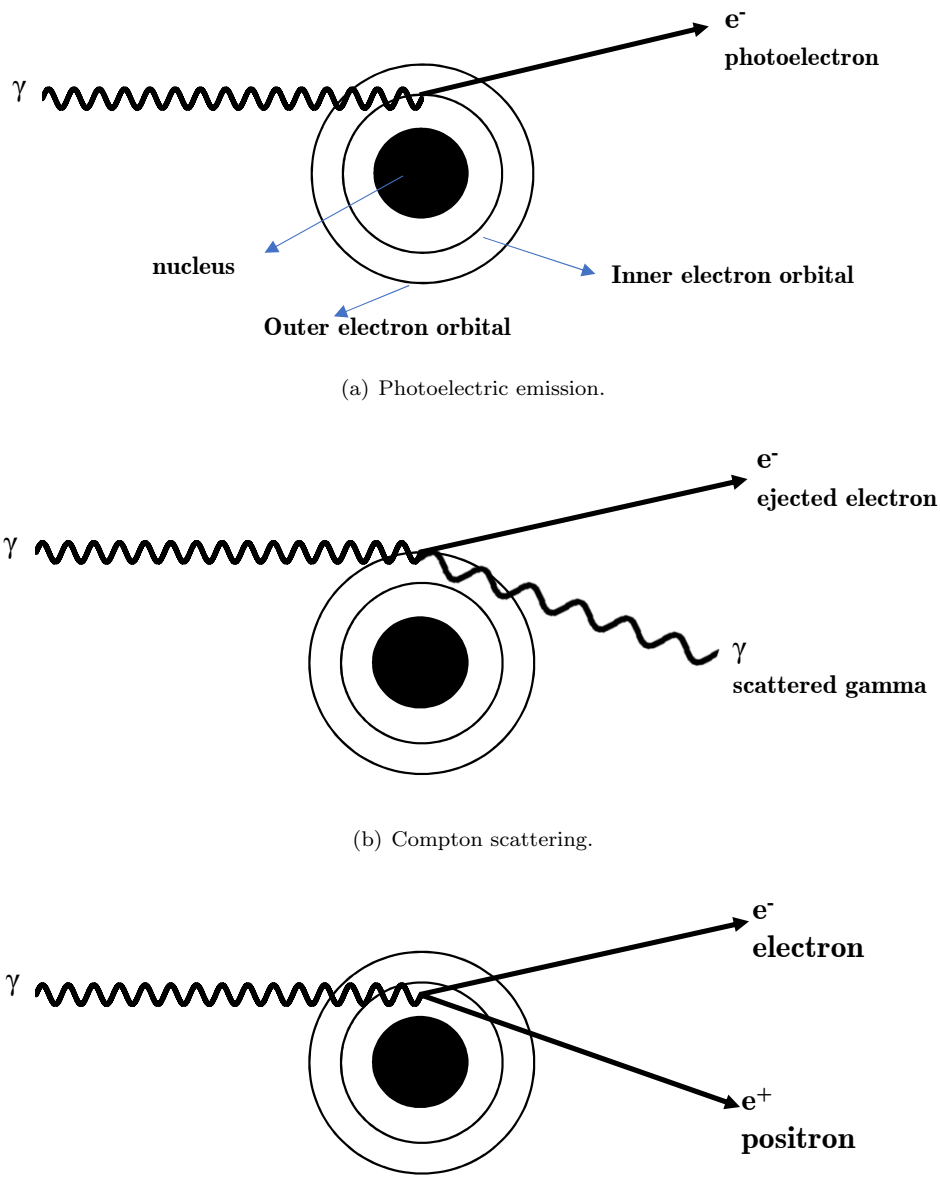

(a) Photoelectric emission.

(b) Compton scattering.

(c) Pair production.

Figure 2.4 | γ-ray interactions. Schematic of the main processes by which γ rays interact with matter: **(a)** photoelectric absorption **(b)** Compton scattering and **(c)** pair production. (Redrawn based on the illustration in the Radiochemistry and Nuclear Chemistry by Gregory Choppin, *et al.* [40]).

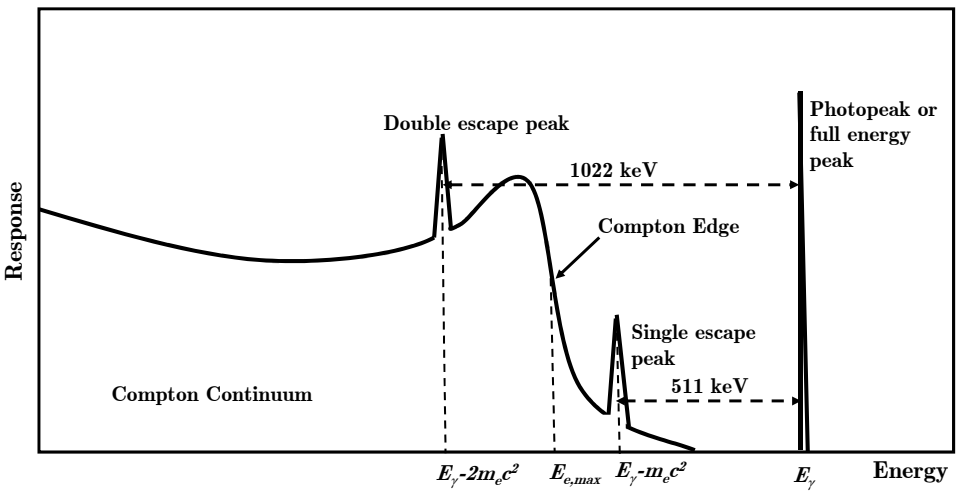

Figure 2.5 | Detector response to γ-ray radiation. Schematic of a high-resolution spectrum of γ-ray radiation due to different interaction processes [42].

The probability that the γ ray will undergo such a collision depends on the atomic number of the absorber, i.e. heavier atoms have a larger number of *K-electrons*, which refers to the inner atomic electrons. Thus the probability of interaction via photoelectric absorption is much greater in materials with large atomic numbers. This interaction probability decreases rapidly as the energy of the photon radiation increases, as shown in figure 2.3. There is, however, an abrupt discontinuity in probability of photoelectric reaction, sometimes referred to as the "k-edge". This occurs when the incident γ ray has slightly higher energy compared to the binding energies of k-electrons due to resonance, which allows for more electrons to be emitted.

Figure 2.5 shows the response from a hypothetical, high-resolution γ-ray detector which undergoes various types of interaction to enable detection of an incoming γ ray of energy E_γ. A detector system exploiting photoelectric absorption would ideally only have a sharp peak in its response, referred to as the photopeak, as shown in figure 2.5 at E_γ, due to the complete transfer of energy that takes place between the two particles.

Compton scattering

Compton scattering refers to the inelastic scattering of a γ ray on a free or weakly bound outer electron, as illustrated in figure 2.4(b), partially transferring a portion of its energy to the electron due to the law of conservation of momentum. This electron is then ejected with a kinetic energy, E_e, equal to the difference between the energy of the incident γ ray (E_γ), the energy of the scattered γ ray (E'_γ) and the binding energy of the electron (E_b); as denoted by equation 2.3, where θ is the scattering angle of the γ ray. The energy of the scattered γ ray is dependent on the angle between the incident and the scattered γ ray, θ, and is expressed in equation 2.4 (ignoring the binding energy, E_b), where m_ec^2 is the energy equivalent of the resting mass of the

electron, 511 keV.

$$E_e = E_\gamma - E'_\gamma - E_b \tag{2.3}$$

$$E'_\gamma \approx \frac{E_\gamma m_e c^2}{E_\gamma(1-\cos\theta) + m_e c^2} \tag{2.4}$$

$$E_{e,max} = \frac{2E_\gamma^2}{2E_\gamma + m_e c^2} \tag{2.5}$$

A complete deposition of energy is not possible in this case, and hence the energy of the ejected electron, E_e, will range from approximately 0 (for $\theta \approx 0°$) to $E_{e,max}$ (for $\theta = 180°$ scatter). The $E_{e,max}$ is expressed in equation 2.5 (ignoring the binding energy of the electrons).

A Compton scatter spectrum from a mono-energetic γ-ray source is illustrated in figure 2.5, labelled as the "Compton continuum" between zero and the "Compton edge" at $E_{e,max}$.

Pair production

Here a γ ray with an energy of at least 1.022 MeV, equivalent to twice the rest mass energy of an electron (i.e. 511 keV), can create an electron-positron pair, as shown in figure 2.4(c), with the excess energy above 1.022 MeV transferred to the electron and positron pair as kinetic energy. Once the electron-positron pair loses its kinetic energy, it may undergo an annihilation reaction (i.e. collision of an electron and a positron whereby both particles are destroyed), emitting two 511 keV γ rays with opposing directional vectors.

From the detection point of view, if both the emitted 511 keV γ rays are absorbed within the detector, a full energy peak will be registered in the measured spectrum. Similarly, if one escapes, then a count will be registered at the position 511 keV below the peak corresponding to that of the associated photopeak, as shown in figure 2.5.

2.2 Neutron radiation

The primary focus of the research presented here is neutrons and their detection. This section is divided into three parts: section 2.2.1 reviews some basic concepts and terminologies used to express different properties in neutron physics, section 2.2.2 outlines the sources of neutron radiation; and section 2.2.3 briefly reviews the process by which neutrons interact with matter.

2.2.1 Some fundamental concepts

Relationship between incident energy and time-of-flight

Using the non-relativistic annotation of kinetic energy, $E = 0.5mv^2$, the relationship between neutron *time-of-flight (ToF)* (i.e. time taken for a neutron to traverse from its point of origin to a given destination) and the kinetic energy of a neutron can be expressed by equation 2.6, where E_n is the energy of the detected neutron in MeV, m_n is the rest mass of the neutron (1.675×10^{-27}) kg, d is the distance between the source and the detector in metres (including the detector's thickness) and $c = 6.242 \times 10^{12}$ as the conversion factor from joules to MeV.

$$E_n = \frac{1}{2} m_n \left(\frac{d}{\Delta T}\right)^2 c \tag{2.6}$$

Cross-section

In general, the *microscopic cross-section* of a reaction, σ, for a thin target or single nucleus case, is an effective area that expresses the probability that a nuclear reaction will occur between the nucleus and an incident particle [43]. It has a dimension in area, and is sometimes expressed by the unit barn (b), where 1 b = 10^{-28} m^2. The value of the microscopic cross-section varies from isotope to isotope as a function of energy of the incident particle. Using the microscopic cross-section, the *reaction rate*, R, of a nuclear reaction between the nucleus and an incident particle can be expressed. This is shown in equation 2.7, where N is the number of available atoms, ϕ is the mono-energetic neutron flux, v is the neutron speed and n is the neutron density.

$$R = N\sigma\phi_0 = N\sigma n v \tag{2.7}$$

In the case of a thick target, this is split into thinner dimensions, dx, allowing the above equation to be expanded to equation 2.8 where, Σ is referred to as the *macroscopic cross-section* and has a unit of cm^{-1} [43], ρ is the density of the medium, N_a is the Avogadro's constant, and M is the mass number. The *macroscopic cross-section* thus represents the probability of

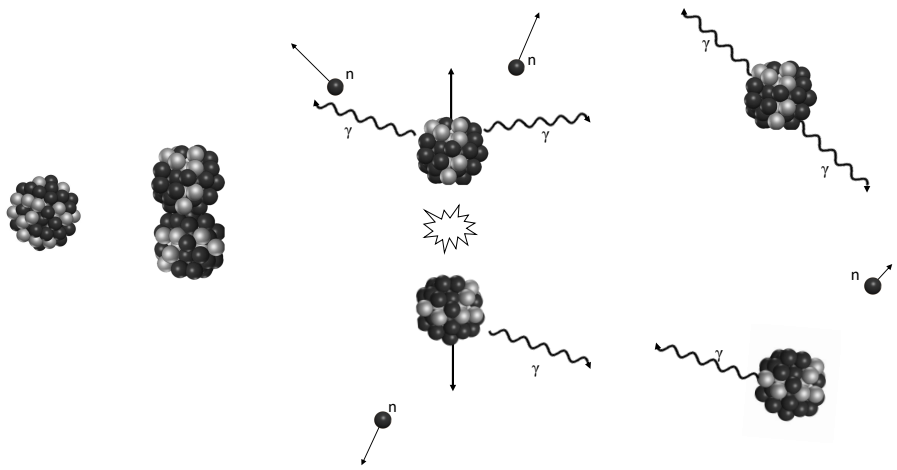

(a) Nucleus. (b) Saddle point. (c) Scission. (d) Delayed emission.

Figure 2.6 | Spontaneous fission using the liquid-drop model. Different stages of spontaneous fission of a nucleus represented through the *liquid drop model* [45, 46] where **(a)** unstable nucleus, **(b.)** saddle point, **(c)** scission, and **(d.)** emission of delayed particles. (Redrawn from an illustration in Passive Nondestructive Assay of Nuclear Material [44]).

interaction per unit path length.

$$R = \Sigma\phi \quad \text{where, } \Sigma = n\sigma = \frac{\rho N_a}{M}\sigma \tag{2.8}$$

2.2.2 Origin

Neutron radiation is an exotic form of radiation in comparison to the number of γ-ray sources available in nature and from cosmic radiation. A primary source of neutron radiation are man-made isotopes, usually produced inside nuclear fission and fusion reactors. Such sources have a high neutron emission rate which may be emitted due to several different nuclear processes [44], as detailed below.

Spontaneous fission

The physics behind this type of nuclear process is derived from the *liquid drop model* [45], illustrated in figure 2.6. In any atomic nucleus containing multiple protons, there is a constant competition between the strong short-ranged nuclear forces trying to hold the nucleus together and the repulsive electrostatic forces from the protons trying to push it apart [44, 47]. In most isotopes, the short-ranged strong nuclear forces are strong enough to subdue the repulsive forces. However, the additional protons in the heavy elements such as in figure 2.6(a) result in a strong repulsive force. Despite the increase in the number of nucleons, the probability of the nucleus being deformed increases, in extreme cases leading to a “saddle point”, as illustrated in

figure 2.6(b), where the two halves of the nucleus are connected by a narrow "neck". At this stage, if the isotope is able to overcome the *potential barrier*[1] due to *quantum tunnelling*[2], the two pieces may undergo scission and break into two separate fragments, called *primary fission fragments*. These fragments, usually of unequal mass, are accelerated in opposing directions emitting a varying number of neutrons and γ rays, as illustrated in figure 2.6(c). It is accepted that 95% of the prompt particles that are emitted during a fission process are from the fully-accelerated fragments, while the rest are emitted after some time [48], as shown in figure 2.6(d). The probability of whether an isotope will undergo such a process, referred to as *fission yield*, is related to the number of protons and neutrons the isotope has, with heavier isotopes generally having higher probability of undergoing such reactions. Additionally, the fission yield for even-even isotopes is typically higher than that of odd-even and odd-odd isotopes. This is because an even-even nucleus has a total ground-state spin of zero and hence the outermost pairs of neutrons and protons can simultaneously couple their spins to zero, thereby lowering the *potential barrier*. Some of the most commonly-found spontaneously fissile materials built up during irradiation of nuclear fuel in a fission reactor include plutonium-239 (^{239}Pu), ^{240}Pu, ^{242}Pu, curium-242 (^{242}Cm), ^{244}Cm and californium-252 (^{252}Cf).

Induced fission

Fission events that are induced by the bombardment of the target nucleus by another particle, usually a neutron (which in itself may have been produced by prior fission events) [44], are known as *induced fission* events. If the gain in excitation energy from neutron absorption is larger than the binding energy of the target nucleus, it splits into two fragments and emits a number of neutrons, γ rays, β- particles, etc.

(α, n) reaction

Most heavy nuclei, due to the strong repulsive electrostatic force from the large number of protons, are able to overcome the Coulomb barrier through quantum tunnelling and undergo α decay. As energetic α particles have a short range of interaction in matter, it is possible for an α-particle to lead to an (α, n) reaction provided that (i) it interacts with a target nucleus with a low atomic number (i.e. oxygen or fluorine) which is in close vicinity [44], and (ii) the incident α particle has enough energy to overcome the Coulomb barrier. This is a common phenomenon in *spent nuclear fuel (SNF)*, where α emitting sources are readily available (e.g. americium-241 (^{241}Am), ^{238}Pu, ^{242}Cm, ^{244}Cm, etc.) along with suitable low-Z atoms (e.g. oxygen-17 (^{17}O), ^{18}O, etc.). Table 2.1 illustrates the yield of some of the common isotopes found in SNF showing significantly larger yield when the α particles are of higher energies. However, the probability

[1] The activation energy required for a nucleus of an atom to undergo spontaneous fission.

[2] A quantum mechanical phenomenon where a particle tunnels through a barrier that it classically could not surmount.

Table 2.1 | (α, n) reaction yield. The table lists the (α, n) reaction yield for some of the common isotopes found in spent nuclear fuel [44].

Isotope	***Total half-life [years]***	***Avg. α energy [MeV]***	***(α, n) yield [n·s^{-1}·g^{-1}]***	
			Oxide	*Fluoride*
^{235}U	7.04×10^8	4.76	7.1×10^{-4}	8.0×10^{-2}
^{238}U	4.49×10^9	4.19	8.3×10^{-5}	2.8×10^{-2}
^{238}Pu	8.77×10^1	5.49	1.3×10^4	2.2×10^6
^{239}Pu	2.41×10^4	5.15	3.8×10^1	5.6×10^3
^{240}Pu	6.56×10^3	5.15	1.4×10^2	2.1×10^4
^{241}Pu	1.44×10^1	4.89	1.3×10^0	1.7×10^2
^{242}Pu	3.76×10^5	4.90	2.0×10^0	2.7×10^2
^{241}Am	4.33×10^2	5.48	2.7×10^3	
^{242}Cm	163 days	6.10	3.8×10^6	
^{244}Cm	1.81×10^1	5.80	7.4×10^4	
^{252}Cf	2.65×10^0	6.11	6.0×10^5	

of such reactions falls dramatically as the target nucleus mass increases, due to the increased repulsive electrostatic force between the target nucleus and the α particle. This may be observed when comparing the (α, n) yields between oxides and fluorides in table 2.1. It should be noted that these reactions also emit multiple γ rays which are correlated to each other in the temporal domain.

Photo fission

These reactions are based on supplying sufficient excitation energy to a nucleus by absorption of a γ ray leading to the disintegration of the nuclei via nuclear fission. The probability of such reactions occurring is very small and as such experiments and simulations presented in this thesis do not take them into account.

Other nuclear reactions

There are several other minor processes that may be used for the production of neutrons, including (i) (p, xn) emission of x number of neutron(s) following bombardment of a target by a proton, (ii) (γ, n) emission of a neutron following absorption of high-energy a γ ray and (iii) (n, xn) reaction with the emission of x number of neutron(s) when a target is bombarded with an external neutron source. The energy required for the emission of a higher number of protons or neutrons is larger and hence high order events have a smaller cross-section.

2.2.3 Interaction with matter

There are several ways by which neutrons may interact with matter based on the microscopic cross-section (σ_x) of the target nucleus, where x is the type of reaction. These can be categorised into two broad groups [44], as detailed in the following subsections.

Scattering reactions

Scattering is a type of nuclear reaction where a neutron is "scattered" by a target nucleus; the speed and direction of the incident neutron changes but the nucleus is left with the same number of protons and neutrons it had before the interaction. As a consequence, the target nucleus will have some recoil velocity and may be left in an excited state, leading to the eventual release of radiation. These reactions can be further subdivided into two groups; (i) elastic scattering and (ii) inelastic scattering. This thesis is primarily concerned with the first process and as such it is discussed in further detail below.

Elastic scattering is when a neutron collides with a target nucleus, as is illustrated in figure 2.7, transferring part of its kinetic energy to the nucleus. The total momentum and the total kinetic energy of the neutron and nucleus remains unchanged by the interaction [43]. Therefore, the *Q-value*, i.e. the difference between the initial and the final energy of the two-body system, remains zero. Only a fraction of the kinetic energy may be transferred to the nucleus. To analyse the kinematics of this process, both *centre-of-mass frame of reference* (illustrated in figure 2.7(a), annotated by the subscripts c in the equations below) and *laboratory frame of reference* (illustrated in figure 2.7(b), annotated by the subscripts l in the equations below) need to be utilised. In the *centre-of-mass frame of reference*, the total momentum is zero for the two body system consisting of the neutron, denoted by n, and nucleus, denoted by N, hence

$$v_{n,c}m_n = v_{N,c}m_N \quad \text{where, } m_n = 1 \text{ and } m_N = A \tag{2.9}$$

Transformation between the two frames of reference can be done by adding or subtracting a velocity component, v_0. Since the target nucleus is at rest prior to the collision, the velocity of the neutron prior to the collision can be expressed per equation 2.11.

$$v_0 = v_{N,c} - v_{N,l} = v_{N,c} - 0 = \frac{v_{n,c}}{A} \tag{2.10}$$

$$v_{n,l} = v_{n,c} + v_0 = v_{n,c}\frac{A+1}{A} \tag{2.11}$$

Hence, the total energy of the system in both frames of reference can be related to each other

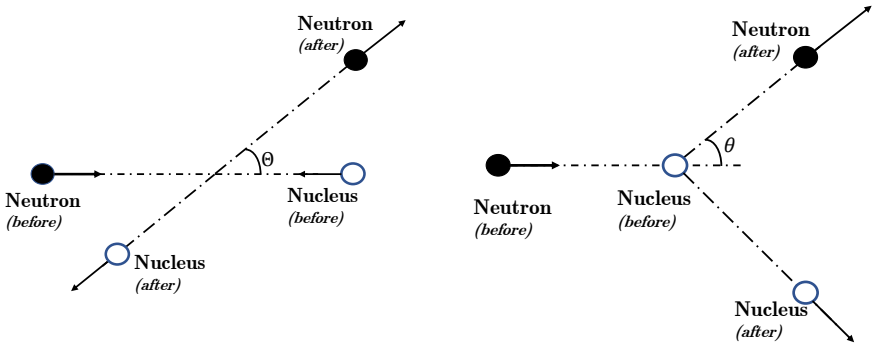

(a) Centre-of-mass frame. (b) Laboratory frame.

Figure 2.7 | Elastic scatter reaction. Elastic scattering of a neutron by a nucleus, as observed in the **(a)** centre-of-mass and **(b)** laboratory reference systems, based on original drawing by Lamarsh [43].

using equation 2.12.

$$E_c = \frac{A}{1+A} E_l \tag{2.12}$$

Preserving the conservation of energy and considering that the collision between the two bodies occurs at some angle, the recoil energy of the non-relativistic nucleus in the *laboratory frame of reference*, E'_r, may therefore be expressed as [49]:

$$E'_r = \frac{2A}{(1+A)^2}(1-\cos\Theta)E_n \tag{2.13}$$

where, Θ is the scattering angle in the *centre-of-mass frame of reference* and E_n is the initial kinetic energy of the neutron in the *laboratory frame of reference*. Finally, equation 2.15 can be obtained by inserting equation 2.14 in equation 2.13, where θ is the scattering angle in the *laboratory frame of reference*.

$$\cos\theta = \sqrt{\frac{1-\cos\Theta}{2}} \tag{2.14}$$

$$E'_r = \frac{4A}{(1+A)^2}\cos^2\theta E_n \tag{2.15}$$

The maximum possible recoil energy occurs when $\cos^2\theta = 1$, i.e. $\theta = 180°$, leading to the neutron being scattered with energy of E'_n. Hence, it is evident that smaller targets will be able to reduce neutron speed more effectively, especially in the event of a head-on collision, and that the fractional energy per collision is independent of incident neutron energy. Finally, using the law of conservation of energy, the average energy of a neutron scattered off a light nucleus can

be expressed by equation 2.16 [43], assuming isotropic scatter.

$$\bar{E'_n} = \frac{E_n}{2}\left[1 - \left(\frac{A-1}{A+1}\right)^2\right] \tag{2.16}$$

Inelastic scattering is similar to elastic scattering, except that the target nucleus is excited to a higher energy state, which it eventually decays by releasing some forms of radiation. Due to this excitation process, the kinetic energies of the two particles are not conserved.

Absorption reactions

Absorption is a type of nuclear reaction where a neutron is "absorbed" by a nucleus thereby gaining some excitation energy. A wide range of processes can follow this absorption in order for the excited nucleus to return to the ground state:

Capture radiation associated with the release one or more γ rays, i.e. (n, γ) reaction, in order to release the energy gained by the absorption of the neutron. Hence, the target nucleus gains an extra neutron.

Charged particles (i.e. proton, α, etc.) are released as a result of the excitation energy gained during the neutron absorption process via (n, p), (n, α), (n, d) reactions, etc. Note that the cross-section for removing additional protons is smaller than that for removing a single proton.

Non-charged particles such as two or more neutrons may be released as a result of the excitation energy gained during the absorption of the neutron via (n, xn) reaction, where x is greater than one. Again, the cross-section for removing additional neutrons is smaller than that for removing a single neutron.

Fission, as discussed earlier in section 2.2.2, the gain in the excitation energy due to the absorption reaction may lead to the formation of two or more fission fragments along with multiple neutrons and γ rays. This happens if the excitation energy gained by the nucleus from absorbing the neutron is larger than the *potential barrier* of the nucleons.

Total cross-section

The cross-sections associated with the various interactions with matter described above can be designated by the following notations:

$$\sigma_t = \text{total cross section} = \sigma_s + \sigma_a \tag{2.17}$$
$$\sigma_s = \text{scattering cross section} = \sigma_{n,n} + \sigma_{n,n'} \tag{2.18}$$
$$\sigma_a = \text{absorption cross section} = \sigma_{n,\gamma} + \sigma_{n,f} + \sigma_{n,xn} + \sigma_{n,xp} \tag{2.19}$$

where, $\sigma_{n,n}$ = elastic scattering cross section, $\sigma_{n,n'}$ = inelastic scattering cross section, $\sigma_{n,\gamma}$ = capture cross section, $\sigma_{n,f}$ = fission cross section, $\sigma_{n,xn}$ = *(n, xn)* cross section, and $\sigma_{n,xp}$ = *(n, xp)* cross section.

Table 2.2 | Multiplicity of neutrons and γ ray from spontaneous fission. The neutron *number distributions* and Watt spectrum coefficients (see equation 2.22) for spontaneous fission of various actinides [44].

(a) Neutron number distributions for spontaneous fission.

	Order of multiplicity									
Isotope	*0*	*1*	*2*	*3*	*4*	*5*	*6*	*7*	*8*	*9*
^{252}Cf	0.0021	0.0247	0.1229	0.2714	0.3076	0.1877	0.0677	0.0141	0.0017	0.0001
^{242}Cm	0.0213	0.1467	0.3268	0.3268	0.1375	0.0374	0.0026	0.0008	0.0002	0.0000
^{244}Cm	0.0150	0.1162	0.2998	0.3332	0.1838	0.0430	0.0088	0.0003	0.0000	0.0000
^{248}Cm	0.0067	0.0596	0.2206	0.3509	0.2544	0.0894	0.0167	0.0017	0.0000	0.0000
^{238}Pu	0.0563	0.2107	0.3797	0.2224	0.1047	0.0262	0.0000	0.0000	0.0000	0.0000
^{240}Pu	0.0632	0.2320	0.3333	0.2528	0.0986	0.0180	0.0020	0.0000	0.0000	0.0000
^{242}Pu	0.0679	0.2293	0.3341	0.2476	0.0997	0.0182	0.0031	0.0000	0.0000	0.0000
^{238}U	0.0482	0.2485	0.4253	0.2284	0.0423	0.0073	0.0000	0.0000	0.0000	0.0000

(b) Watt spectrum parameters for spontaneous fission.

	Watt spectrum	
Isotope	a *[/MeV]*	*b [/MeV]*
^{252}Cf	0.847	1.034
^{242}Cm	1.108	3.720
^{244}Cm	1.126	3.891
^{238}Pu	1.179	4.169
^{240}Pu	1.257	4.689
^{242}Pu	1.220	4.366
^{238}U	1.542	6.810

2.3 Correlation between particles from fission

As described in the previous sections, following spontaneous and induced fission, a number of prompt neutrons and γ rays are emitted [34, 35, 50, 51, 52]. All particles released during a fission event are correlated[3] to each other in four domains: i) number of particles released; ii) temporal separation between the released particles; iii) spatial separation between the released particles; and iv) the energies at which the particles are emitted. Such correlations have been studied widely [36, 37, 38].

The neutron *number distributions* (i.e. *probability distribution functions* outlining the likelihood of a given number of neutrons, n, that may be emitted following fission) of some common spontaneously fissile isotopes are illustrated in figure 2.8(a) and table 2.2(a). These *number distributions* depend on the mass of the fission fragments that are created during the fission process [54], which in turn is dependent on the mass of the parent isotope and the excitation energy of the inducing neutron (latter is valid for induced fission only). Such correlation may also be noticed in the prompt γ rays that are emitted during spontaneous fission [55], as shown in figure 2.8(b).

Further to this, each of the prompt neutrons and γ rays expelled from the parent nucleus have different times of emission but are clustered together in the sub-nanosecond region (i.e. $< 10^{-13}$ second [44]). Additionally, as the fission fragments break away, the energies with which they escape are correlated to one another [56]. As the subsequent particles that are emitted share among themselves the energy that the fission fragments gained during the fission process, this gives rise to the energy correlation between them. This is not to be confused with the Maxwellian statistical distribution, which is widely used for the energy distribution of the average or individual neutrons that are emitted from a fission isotope. Here, correlation refers to the fact that the energy of the first neutron, which itself has a Maxwellian statistical distribution, will impact the energy of subsequent neutrons, i.e. their position in the Maxwellian distribution.

A significant proportion of the neutrons expelled during spontaneous and induced fission are emitted from two fission fragments which usually have unequal mass. These fragments move away from each other due to the kinetic energy gained during the fission process. Since 95% of all the particles emitted during the fission process are from fully accelerated fragments [48], the released particles contain part of that momentum in accordance with conservation law. As a consequence, neutrons emitted from a single fission fragment will be polarized in the same direction (i.e. the emitted neutrons will have a small angular separation); whereas neutrons emitted from two complementary fragments will be focused in opposing directions (i.e. the emitted neutrons will

[3] A mutual relationship or connection, i.e. interdependence, between two or more things, e.g. the energy of the first emitted neutron will impact the energy of subsequent neutrons.

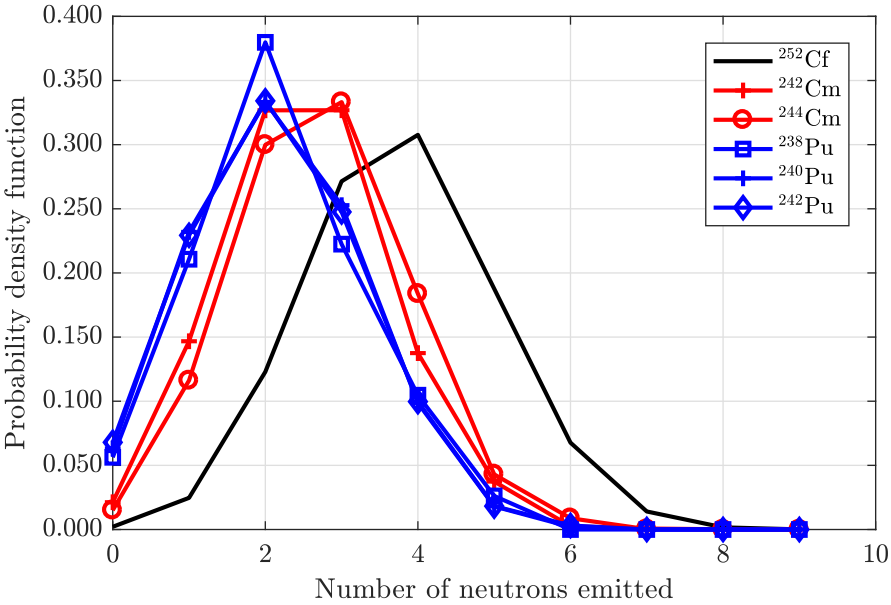

(a) Neutron number distribution for spontaneous fission of various isotopes.

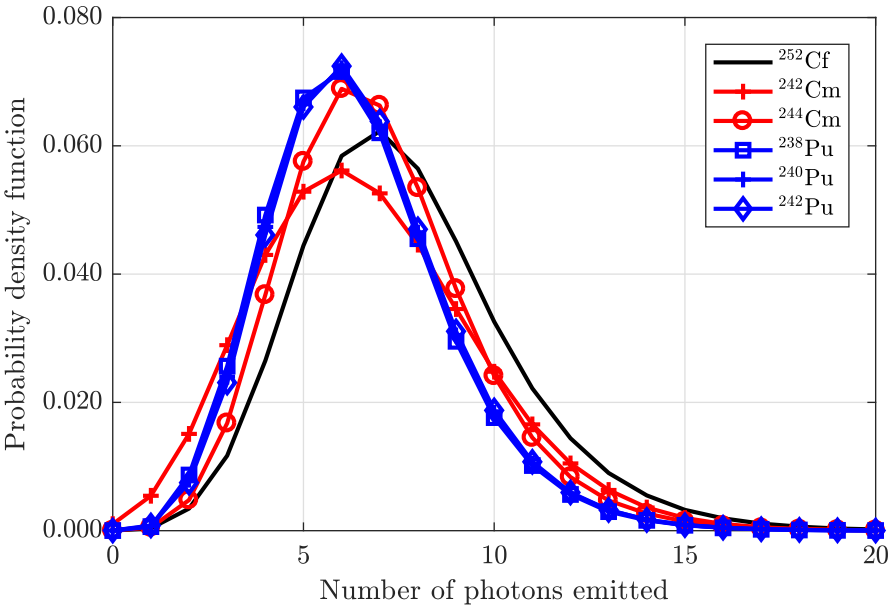

(b) γ-ray number distribution for spontaneous fission of various isotopes.

Figure 2.8 | Neutron and γ-ray number distributions following spontaneous fission of various isotopes. Illustration of the **(a)** neutron and **(b)** γ-ray *number distributions* following spontaneous fission of various isotopes. These data points are discrete distributions and the straight-line fit was added to guide the eye only. The distributions were obtained from the FREYA libraries [53] using a C++ script (see appendix D.1).

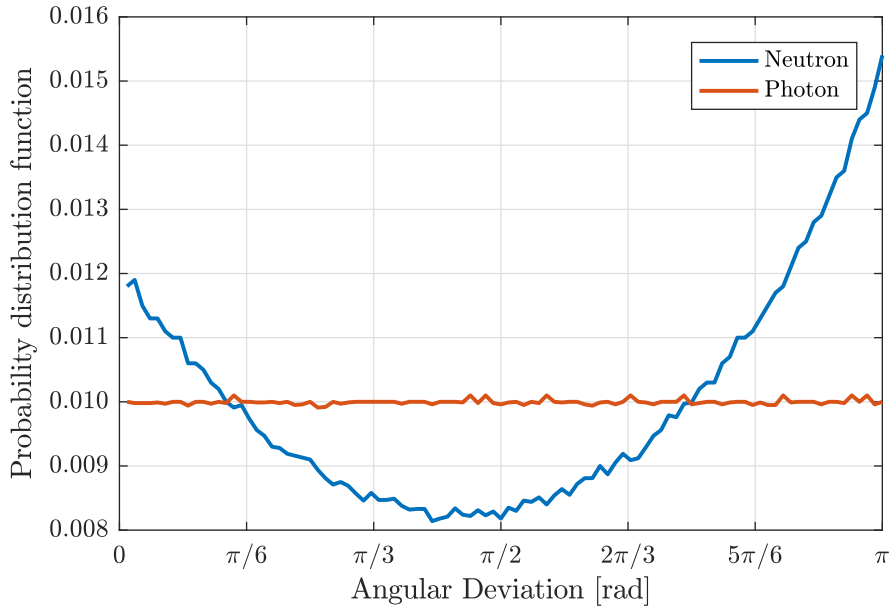

Figure 2.9 | Angular correlation of neutron and γ-ray particles from spontaneous fission of ^{252}Cf. Angular separations between the particles emitted from the spontaneous fission of ^{252}Cf isotope extracted from the FREYA library [53] using a C++ script (see appendix D.2).

have a large angular separation). Thus, the neutrons originating from fissioning isotopes will have an anisotropic spatial correlation, i.e. they are emitted preferentially near 0 and π rad relative to each other. Additionally, the rotation of the fission fragments is also documented to have a small influence on the anisotropy of the distribution [48, 57]. The number of neutrons that are emitted during the descent from saddle to scission and during the acceleration of the fragments is limited, as only 5% of the emitted neutrons fall in this category, but may still have a discernible contribution towards the spatial anisotropy. These trends in spatial distribution are illustrated in figure 2.9 for ^{252}Cf.

2.3.1 Fission models for correlated particles

There are several models that have evolved over the past decades which can be used to predict the characteristics of neutrons and γ rays that are emitted from fission events [48, 59]. These include, but are not limited to:

1. *CGMF* which is an implementation of the statistical Hauser-Feshbach nuclear reaction theory [60] applied to the de-excitation of the primary fission fragments which are described as compound nuclei with an initial excitation energy, spin and parity. Each emitted neutron and γ-ray particle removes its kinetic energy from the fragment's intrinsic excitation energy, while doing little to change the fragment's angular momentum [61, 62].

2. *Fission Reaction Event Yield Algorithm (FREYA)* which generates complete fission events

providing the full kinematic information on the fission products, and all the subsequently emitted neutrons and photons, by relying on experimental data; and is supplemented using a simple physics-based model when no experimental data are available [53, 57].

3. *FIFRELIN* which is based on empirical models associated with macroscopic or microscopic ingredients or both with the fission fragment de-excitation being performed within Weisskopf (for uncoupled neutron and γ-ray emission) or Hauser-Feshbach (for coupled neutron and γ-ray emission) statistical theory [63].

To complete this thesis, the FREYA model [53, 57, 64] was used for modelling correlated particles. It uses experimental data for neutron and γ-ray[4] number distributions (i.e. P_ν for neutron and G for γ ray) from spontaneous fission (see table 2.2(a) on page 24). If no data exist, it uses Terrell's approximation [65] in equation 2.20 for neutron and Valentine's approximation [66] in equation 2.21 for γ-ray emissions, with parameters taken from Ensslin [34].

$$\sum_{n=0}^{\nu} P_n = \frac{1}{\sqrt{2\pi}} \int_{-\infty}^{\frac{\nu-\bar{\nu}+0.05+b}{\sigma}} \exp^{-\frac{t^2}{2}} dt \tag{2.20}$$

$$\prod(G) = \binom{a+G+1}{G} \left(\frac{a}{a+\bar{G}}\right)^G \left(1 - \frac{a}{a+\bar{G}}\right), \text{ where } a \approx 26 \tag{2.21}$$

$$E_n = \sqrt{\frac{\pi b}{4a}} \frac{\exp^{\frac{b}{4a}}}{a} \exp^{-cE'} \sinh(\sqrt{bE'}) \tag{2.22}$$

The energy distributions of neutrons (E_n) from spontaneous fission events are defined using the Watt spectrum equation (see equation 2.22). The values of the coefficients of the Watt spectrum equation are taken from Ensslin [34] (see table 2.2(a) on page 24). For neutron-induced fission, FREYA uses TART's implementation [67]. The energy correlation is then computed by the FREYA model by imposing a constraint on the total event energy of all emitted particles using a technique whereby the average outgoing prompt γ-ray energy and prompt neutron energy are expressed by an actinide-dependent quadratic expression. In this method, the description of γ-ray spectra is limited to ^{232}U, ^{235}U, ^{238}U, ^{239}Pu and ^{252}Cf, whilst the neutron energy spectra is available for 73 different actinides based on Evaluated Nuclear Data Library 2008.

[4]Experimental data for γ number distributions are only available for spontaneous fission of ^{252}Cf. Others are only estimates and are not measured data.

2.4 Radiation detection

Since the primary focus of this thesis is the detection of neutrons with respect to neutron coincidence counting, this section will only briefly address γ-ray detection techniques.

2.4.1 Gamma detectors

Gamma rays interact with the electrons in matter through ionisation, using which, it is often possible to characterise γ-ray radiation. This ionisation process produces free charge carriers which can then be collected to register the incident particle. Some of the widely used γ-ray detectors in the field of *non-destructive analysis (NDA)* of radioactive materials are detailed in the sub-sections below.

Gas-filled detectors

These detectors contain a sensitive region filled with pressurised gas which is placed between two electrodes [68], as depicted in figure 2.10(a). The gas is usually noble/inert gas like argon, krypton or xenon. The voltage across the electrodes is operated either in the "ionisation region" or "proportional region" [69]. The former is commonly referred to as *ionization chamber*, whilst the latter as *proportional counters*. The latter is operated such that only the primary ionisation charge can attain enough kinetic energy to cause further ionisation to produce a signal which is proportional to the energy of the incident particle, although greatly amplified. Since the energy of the incident γ ray dictates how many molecules are ionised, it is possible to determine the energy of the incident particle by analysing the output signals from these detectors [68]. The efficiency of these detectors is modest and can be used for spectroscopy when the energies of the incident particles are within a few tens of keV. Increasing the voltage can improve the efficiency, however, the primary ionisation charge particles produce further secondary ionisation, and the output pulse is no longer related to the incident energy of the interacting radiation. These particular kinds of detectors are also referred to as Geiger-Müller (GM) detectors [69, 70].

Semiconductor detectors

These detectors make use of semiconductor diodes composing of p-type and n-type semiconductor materials [68, 71]. The electrons in the valence band of these materials only require a relatively small amount of excitation energy to move to the conduction band where they can freely move thereby producing an electron-hole pair compared to an insulator. This gap between the valence band and the conduction band, also referred to as the bandgap, is typically about 1 eV for semiconductors compared to the 5-eV gap in insulators. This excitation energy is provided to the valence electrons when the electron interacts with incoming γ ray. The number of electron-hole pairs produced is proportional to the energy deposited by the incident particle.

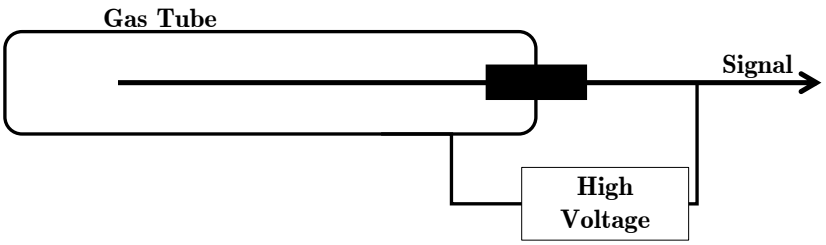

(a) Typical construction of a gas-filled counter.

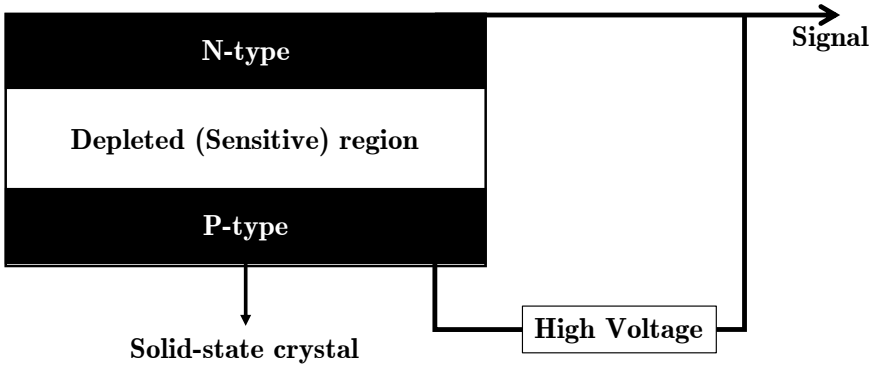

(b) Typical schematic of a solid state based detector.

Figure 2.10 | Schematic of a gas-filled and solid state detector. (a) The gas confined in the tube makes up the active region of the detector which is ionised when radiation interacts with it. The electric field due to the strong potential difference accelerates the ions on to the wire. (Redrawn based on Passive Nondestructive Assay of Nuclear Material [68]). **(b)** A p-n junction collects the charge produced due to ionisation from the incident radiation in the sensitive region. (Redrawn based on Passive Nondestructive Assay of Nuclear Material [68]).

When exposed to an electric field from the electrodes, as illustrated in figure 2.10(b), these pairs drift parallel to the field towards the oppositely-charged electrodes, where the magnitude of the pulse is measured. Since the energy required to produce a single electron-hole pair is very low, which also negates the need of using a *photo-multiplier tube (PMT)*, these detectors have very good energy resolution. One of the most commonly-used detectors using semiconductors are the hyperpure germanium crystals (HPGe) detectors. However, the crystals used in these detectors are easily damaged when exposed to neutron radiation, resulting in reduced amplitude leading to a tailing effect in the spectra.

Scintillation detectors

The active region of these detectors constitutes either organic or inorganic materials in solid or liquid state. When exposed to radiation, they produce a flash of luminescence which can be amplified by PMT [68, 72]. These materials can be sensitive to α, β, γ-ray and neutron radiation, and usually require some kind of *pulse shape discrimination (PSD)* to be able to detect the incoming particles. These detectors will be discussed in more detail in section 2.6.

Table 2.3 | Common materials used in neutron detectors. Typical values of the efficiency of neutron detectors when neutrons enter the detector perpendicular to the detector face [73]. The γ-ray sensitivity outlines the maximum strength of a γ-ray field, as a ratio of the neutron field, which permits the detectors to function properly.

Detector Type	***Active Material***	***Incident Energy***	***Efficiency [%]***	***γ-ray sensitivity***
Plastic Scintillators	^{1}H	1 MeV	78	0.01
Liquid Scintillators	^{1}H	1 MeV	78	0.1
Loaded Scintillators	^{6}Li	1 MeV	50	1
^{4}*He*	^{4}He	1 MeV	1	1
^{3}*He*	^{3}He	Thermal	77	1
BF_3	^{10}B	Thermal	46	10
^{10}*B-chamber*	^{10}B	Thermal	10	1000
Fission chamber	^{235}U	Thermal	0.5	10^6

2.4.2 Neutron detectors

Unlike γ-ray radiation, it is extremely difficult to detect neutrons directly as they are charge neutral. Instead, they can only be detected via one of the interaction methods discussed in section 2.2.3, i.e. by relying on neutron scatter or absorption reactions and subsequently detecting the secondary charged particles (i.e. protons, α particles or fission fragments) that are produced. Three of the most common types of neutron detectors are discussed in the following subsections.

Gas-filled detectors

These detectors, which have historically been the most commonly used detectors in non-destructive neutron assays, typically use helium-3 (^{3}He), boron-10 (^{10}B) or BF_3 as the primary active material. As these isotopes have very high cross-sections for absorption of thermal neutrons (as illustrated in figure 2.11(a)), such detectors have relatively high efficiencies. These interactions produce charged particles (i.e. ^{3}He(n, p) and ^{10}B(n, α)), which is indicative of a neutron being detected.

$$^{3}\text{He} + \text{n} = {}^{3}\text{H} + {}^{1}\text{H} + 765 \text{ keV}$$

$$^{10}\text{B} + \text{n} = {}^{7}\text{Li} + {}^{4}\text{He} + 2310 \text{ keV} + 480 \text{ keV } \gamma \text{ ray; with a reaction intensity of } 94\%$$

At 4 atm, as demonstrated in table 2.3, ^{3}He has a 77% intrinsic efficiency for thermal neutrons, which drops to 0.2% for 1 MeV and 0.002% for 2 MeV neutrons [73] due to its reduced cross-section for fast neutrons. These materials, as shown in table 2.3 [73], have very limited sensitivity to γ-ray radiation, thereby eliminating the need for any requirement for event discrimination. Boron-loaded detectors have even stronger immunity to γ-ray fields compared to ^{3}He-based detectors, however this advantage comes at the expense of reduced efficiency in detecting thermal

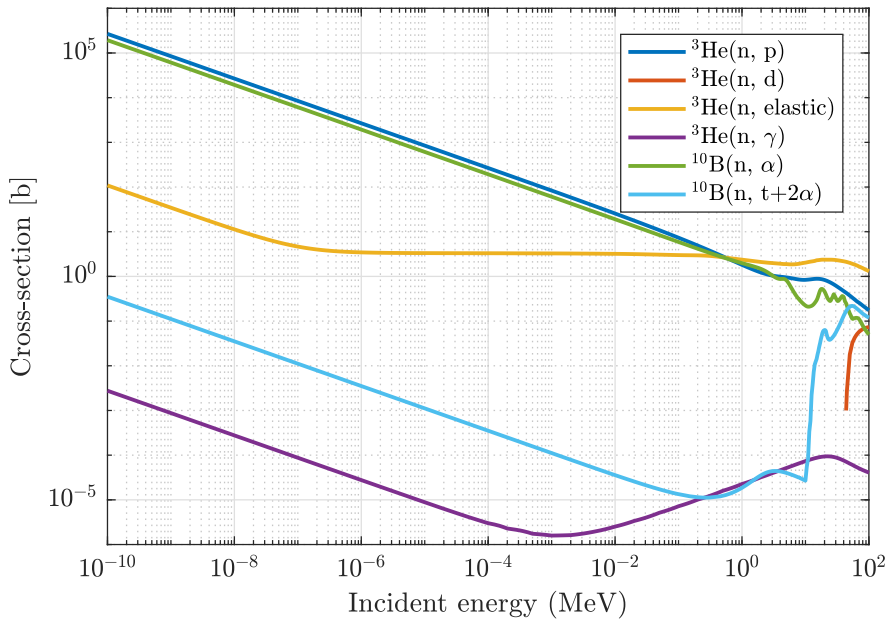

(a) Absorption and scattering cross-sections of ^{3}He and ^{10}B.

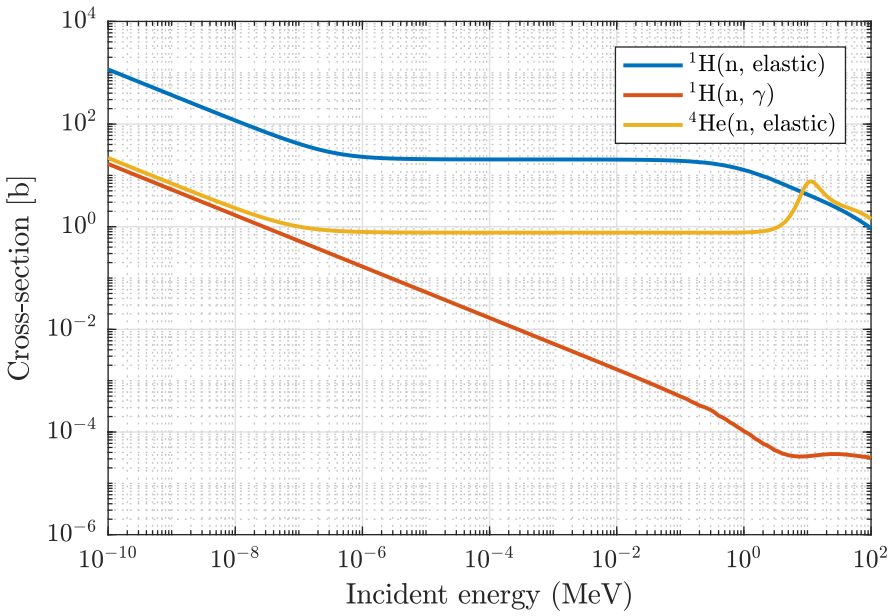

(b) Elastic and inelastic scattering cross-sections of ^{1}H and ^{4}He.

Figure 2.11 | Cross-sections for neutron interaction with ^{1}H, ^{10}B, ^{3}He and ^{4}He. (a) ^{3}He has the highest cross-section for (n, p) reaction compared to that of other isotopes with negligible cross-section for scattering reactions. ^{10}B has slightly smaller cross-section for thermal neutrons compared to ^{3}He. **(b)** The neutron elastic scattering cross-section of ^{1}H is higher compared to that of ^{4}He, however, ^{4}He has higher cross-section for neutrons of 10 MeV or above, making them sensitive to neutrons from both energy groups. The plots were extracted using the JANIS toolkit [33] using the ENDF/B-VII.I library [74].

neutrons. Despite being immune to γ rays and having high efficiency for thermal neutrons, ^{3}He detectors have a major drawback, i.e. they are only sensitive to thermal neutrons. Therefore, a stage is required dedicated to the thermalisation of the fast neutrons that are emitted from spontaneous fission, for example.

^{6}Lithium-based thermal neutron detectors

Based on the high cross-section for the ^{6}Li(n, α) reaction of 940 barns for thermal neutrons [75], lithium doped materials are an alternative to ^{3}He for the detection of thermal neutrons. There have been several implementations in such detectors, like those using lithium glass which is a Ce^{3+} activated amorphous material (i.e. SiO_2 (75.6%), Li_2O (11.3%), Al_2O_3 (4.9%), and Ce_2O_3 (7.8%)) with high ^{6}Li content, and this is reported to have a response time of approximately 75 ns [76, 77].

Europium doped crystalline lithium iodide, ^{6}LiI(Eu), is sensitive to both γ-ray and neutron radiation with relatively long signal die-away characteristics of 1.4 μs, but has poorly defined broad peaks corresponding to fast mono-energetic neutrons [78]. However, they are reported to perform adequately well for thermal neutrons [75].

Cerium and europium doped scintillators, such as the $LiCaAlF_6$ and $LiSrAlF_6$ have decay times of $\approx$ 40 ns and $\approx$ 1.5μs, respectively; and are sensitive to both neutron and γ-ray radiation [79]. These materials are effective thermal and epithermal neutron detectors with pulse height discrimination. Although, these detectors are sensitive to fast neutrons as well, their performance is not very good [80].

Cs_2LiYCl_6(Ce) detectors are sensitive to both γ rays and neutrons (thermal and fast). Thermal neutrons are detected as a result of ^{6}Li(n, α) reaction, while fast neutrons are detected via ^{35}Cl(n, p) and ^{35}Cl(n, α) [81].

Organic Scintillation detectors

Some organic scintillators are sensitive to neutrons as well as γ-radiation [72]. The physics involved in these detectors originates with the elastic scattering of neutrons on either hydrogen or carbon atoms, with an intrinsic efficiency of 78% for 1 MeV incident neutrons, as illustrated in table 2.3 [73]. This relatively high efficiency for fast neutrons compared to helium-based materials is due to hydrogen's higher cross-section for undergoing elastic scattering when exposed to neutron radiation compared to the *(n, n')* cross-section for ^{3}He, as can be observed in figure 2.11(b). While pressurised ^{4}He scintillation are sensitive to both fast and thermal neutrons (see figure 2.11(b)), its efficiency for fast neutrons is very low at only 1% despite having higher cross-section for neutron with more than 10 MeV kinetic energy compared to ^{1}H.

2.5 Neutron multiplicity analysis

Non-destructive assay of fissile material is often based on the measurement of correlated penetrating radiations emitted from fissioning isotopes [15, 82]; principally neutrons, but also γ rays. This correlation of radiation in time with the parent fission event can be analysed for characterization purposes. The most widespread approaches by which such analysis is carried out are the Rossi-α [11, 13, 15] and the Feynman-Y [12, 14, 83] methods. In this thesis, only the Rossi-α method is investigated.

2.5.1 Rossi-α method

The Rossi-α method enables a direct observation of prompt neutron emissions that share a common ancestor. However, since it is not possible to correlate detected neutrons to their specific parent fission event, this trend is extracted by recording the time at which events arise across a range of time bins of width ΔT relative to the stimulus of a preceding trigger event to yield the characteristic time interval distribution. In the most common scenario, this is the time elapsed between subsequent neutron detections which is measured and is plotted in a histogram referred to as the *interval-time distribution* in this thesis, as shown in figure 2.12(a). The correlation of radiation in time with the parent fission event is evidenced by a peak in intensity near to the point of fission which declines as time $\rightarrow \infty$; a trend known as the die-away. This *interval-time distribution* comprises of two groups of events: (i) neutrons correlated directly with a corresponding fission (i.e. *real events*) and (ii) those from uncorrelated processes from different fission chains, (α, n) reactions, scattering and random sources of background (i.e. *accidental events*). This distribution may be modelled using an exponential function in equation 2.23, where ε is the detector efficiency, F is the fission rate, ν_1 & ν_2 are the factorial moments[5] and τ is the detector die-away. This model corresponds to the probability of a random event being the detector count rate multiplied by the *gate-width*, ΔT, which is an acquisition window in time within which the *coincident events* are measured. If the second event is indeed from the same fission event, the probability $P(\delta t)$ decreases exponentially in time characterised by the detector die-away, τ. The accidental events will manifest itself as a time-independent (i.e. constant) term.

$$P(\delta t)\Delta T = \Big[\underbrace{\varepsilon\nu_1\Big(\frac{\nu_2}{2\nu_1^2}\Big)\frac{\exp^{-\frac{t}{\tau}}}{\tau}}_{\text{reals}} + \underbrace{F\varepsilon\nu_1}_{\text{accidentals}}\Big]dt \tag{2.23}$$

The *interval-time distribution* derived from the Rossi-α method, sometimes referred to as the Rossi-α distribution, is illustrated schematically in figure 2.12(a) for the assay of thermalised neutrons (using for instance ^{3}He detectors) with the red curve and for that without thermalisation

[5] See section 2.8.1 for definition of factorial moment.

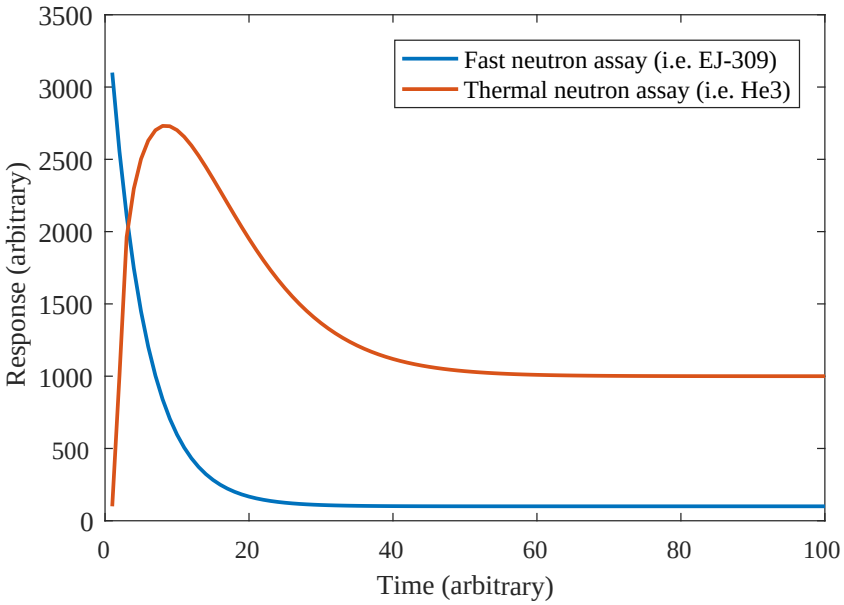

(a) A schematic representation of the Rossi-α time interval distribution in terms of count rate versus the time.

(b) The time and the placement of the coincidence windows for typical thermal and fast neutron assays.

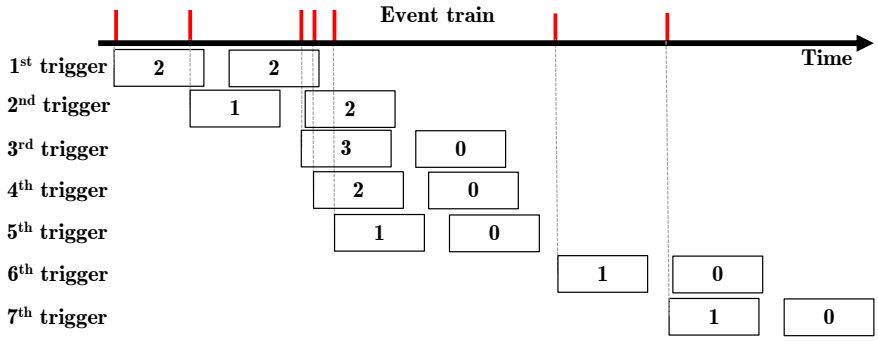

(c) Overview of the data processing for the construction of the multiplicity histogram.

Figure 2.12 | Rossi-α distribution and histogram construction. **(a)** A schematic representation of the Rossi-α time interval distribution in terms of count rate versus the time that has elapsed after fission (not illustrated to scale in the figure). Neutron events as a function of time following an arbitrary start event for both thermal (red line) and fast neutrons (blue line). **(b)** The *coincidence-gates* required for the thermal assay is much longer due to longer detector die-away arising because of the need to moderate the neutrons to optimise detection efficiency. Compared to thermal detectors, liquid scintillators enable a narrower coincidence window to be used by three orders of magnitude. **(c)** Overview of the data processing needed; each unique trigger (highlighted in grey) initiates a prompt and delayed gate and the number of *coincident events* is recorded.

(using for instance organic liquid scintillators) with the blue curve. The different trends of the two curves will be further discussed in section 2.5.2. To derive *interval-time distribution*, every detected neutron starts a sweep and records the arrival times of the subsequent neutrons which are binned in a time-series histogram over a preselected interval where the bin-width (δt, the time-period of the clock driving the electronics, usually 20 ns to 50 ns for thermal assays) is much smaller than the detector die-away and the *gate-width*. The most widely used method of carrying out such analysis uses a method called the "Updating One-shot Circuit" [84], which is commonly known as the shift-register method [85].

Reduced factorial moment distribution from shift-register algorithm

For the purpose of neutron multiplicity analysis, the Rossi-α curve is not usually constructed explicitly from experimental data but rather the correlation in time is exploited by counting the number of neutrons detected within two separate small time intervals (or *coincidence-gates*) [84, 85]: (i) *foreground coincidence counts* made up of events either from correlated fission or uncorrelated processes (i.e. *real* + *accidental events*) and (ii) *background coincidence counts* made up of events from uncorrelated processes (*accidental events*) from different fission chains, (α, n) reactions, and random sources of background. The first *coincidence-gate* is called the *prompt-gate*, while the second *coincidence-gate* is called *delayed-gate*. These two gates are separated by a period, referred to in this thesis as the *idle-gate*, during which no measurements are taken. This *idle-gate* is added to ensure that the accidental *coincidence-gate* is positioned sufficiently long after the exponential die-away component of the curve has passed. Additionally, there may be a third gate prior to the start of the two *coincidence-gates* already mentioned, referred to as the *predelay-gate*, which is assigned in order to allow the detectors to have sufficient time to recover after the trigger.

The placement of the two *coincidence-gates* is depicted in figure 2.12(b). The gates are placed such that every event initiates acquisition windows, leading to a periodical overlap of *coincidence-gates*, as shown in figure 2.12(c). The neutrons detected within the *prompt-gate* and *delayed-gate* are binned into two separate histograms, which mathematically correspond to the reduced factorial moment distribution of the neutron *coincidence distribution*. Hence, in this thesis, the histograms are referred to as the *foreground factorial moment distribution* and the *background factorial moment distribution*, from which it is common practice to determine mean detection rate (singles), correlated pair rates (doubles) and higher-order correlation rates (i.e. triples, etc.). This method of determining the *reduced factorial moment distributions* is often referred to as the *shift-register method* as its electronic implementation, discussed in the following subsection, is based on the use of shift-registers.

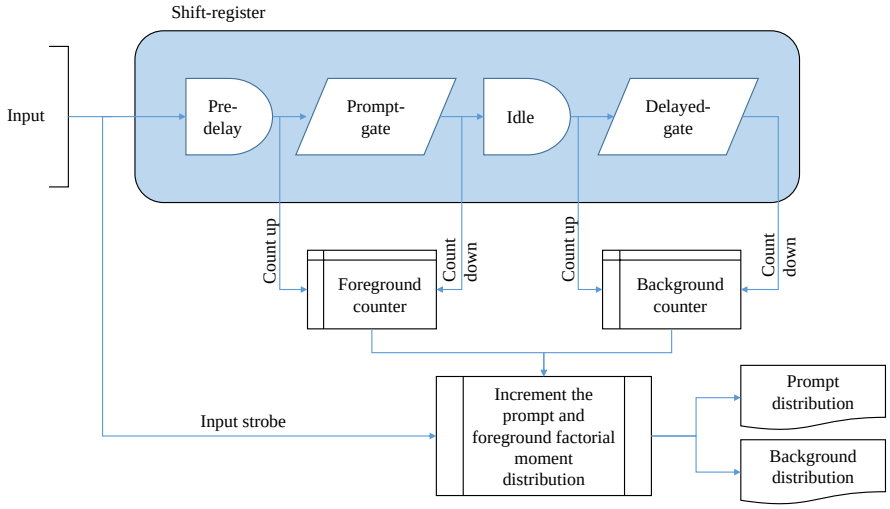

Figure 2.13 | Shift register based algorithm for computing multiplicity histogram. (Redrawn based on the original illustration in Passive Nondestructive Assay of Nuclear Materials [84]).

Electronics of Updating One-shot Circuit

Figure 2.13 shows a sketch of the different components involved in the circuit [84] that is used in such analysis. In the first stage, the signals from the detectors are passed through an OR gate and connected to a multistage shift-register. The shift register is divided into four segments, representing *predelay-gate*, *prompt-gate*, *idle-gate* and *delayed-gate* segments. These gates are schematically illustrated in figure 2.12(b). Input from the detector (one representing an event and zero representing no event) is shifted through the shift-register from left to right, with each clock cycle. To keep count of the number of active events in a shift register representing the *prompt-gate* and *delayed-gate* segments, strobes from the start and end of each gate are used to drive an adder and subtracter towards two individual counters representing the *foreground coincidence count* and *background coincidence count*. These counters are equivalent to the order of the *reduced factorial moment distribution*. Finally, the input entering the shift register is strobed to drive a process which increments the *foreground factorial moment distribution* and the *background factorial moment distribution* using the two counters, previously mentioned, to represent the order of coincidence. To be able to process data at high count rates and to prevent signal pileup, a derandomiser circuit may be placed in between the detector signals and the pre-delay segment, since it is not possible to represent more than one detected particle in a serial bus. This circuit acts as a time-shifted multiplexer by serialising any overlapping signals in a sequence.

Mathematical Analysis

The mathematical formulation described in this section is based on ^{3}He assay using a spontaneous fission source and is hinged on the following assumptions [15]: (i) all induced fission neutrons are emitted simultaneously with the original spontaneous fission or (α, n) reaction; (ii) neutron detector efficiency and the probability of fission have no spatial dependency; (iii) (α, n) and spontaneous fission neutrons have the same energy spectrum, so that the detection efficiency, the fission probability p_s, and the induced fission multiplicity ν_i are the same for both neutron sources; (iv) neutron capture without fission is negligible; and (v) distributions of neutron multiplicity and neutron energy emitted in each fission are not correlated.

The experimentally *measured reduced factorial moment distribution* (f_k), where k is the order of coincidence, is actually a mixture of the *foreground factorial moment distribution* (g_k) and the *background coincidence distribution* (b_k) as expressed in equation 2.24.

$$f_k = \frac{F\varepsilon\nu_1}{S} g_k + (1 - \frac{F\varepsilon\nu_1}{S}) b_k \tag{2.24}$$

Since g_k is also a convolution of the *real factorial moment distribution* (r_k) and b_k, equation 2.25 is combined with equation 2.24 to form equation 2.26.

$$g_k = \sum_{j=0}^{k} \binom{k}{j} r_k b_{k-j} \tag{2.25}$$

$$f_k - b_k = \frac{F\varepsilon\nu_1}{S} \Big[\sum_{j=0}^{k} \binom{k}{j} r_k b_{k-j} - b_k \Big] \tag{2.26}$$

Using these formulations, it is possible to define the singles, doubles and triples rates as the product of r_k and the trigger rate ($S - S_{\text{bkg}}$) [15].

$$\text{Singles} = (S - S_{\text{bkg}}) r_0 = S \tag{2.27}$$

$$\text{Doubles} = (S - S_{\text{bkg}}) r_1 = S(f_1 - b_1) \tag{2.28}$$

$$\text{Triples} = \frac{S - S_{\text{bkg}} r_2}{2!} \tag{2.29}$$

Now, given that (α, n) reactions always produce one neutron, equation 2.30 represents the probability of number of neutrons emitted during spontaneous fission [15].

$$P_s(\nu) = \frac{\alpha\nu_s \delta_{1,\nu} + p_s(\nu)}{1 + \alpha\nu_s} \tag{2.30}$$

where, $\delta_{1,\nu} = 0$ for spontaneous fission event and 1 otherwise, α is the ratio between (α, n) reaction neutrons to the spontaneous fission neutrons, ν_s is the multiplicity of spontaneous fission,

and $p_s(\nu)$ is the probability of the ν order multiplicity for spontaneous fission. Using equation 2.30, equations 2.31, 2.32 and 2.33 can be derived to define the first three factorial moments of the emitted neutron distribution as shown by Boehnel [86] using a point model.

$$\nu_1 = M\nu_{s1}(1+\alpha) \tag{2.31}$$

$$\nu_2 = M^2\Big[\nu_{s2} + \Big(\frac{M-1}{\nu_{i1}-1}\Big)\nu_{s1}\nu_{i2}(1+\alpha)\Big] \tag{2.32}$$

$$\begin{aligned}\nu_3 = M^3\Bigg\{&\nu_3 + \Big(\frac{M-1}{\nu_{i1}-1}\Big)\Big[3\nu_{s2}\nu_{i2} + \nu_{s1}\nu_{i3}(\alpha+1)\Big] \\ &+3\Big(\frac{M-1}{\nu_{i1}-1}\Big)^2\nu_{s1}\nu_{i2}^2(\alpha+1)\Bigg\}\end{aligned} \tag{2.33}$$

where, M is the self-multiplication, where the neutrons emitted from a fission process subsequently induces further fission within the material, and ν_i is the multiplicity of induced fission of the ith order. Taking into account the efficiency of the detectors and the *gate-fraction* (i.e. f_d is the fraction of emitted neutrons that were detected due to the finite size of the *gate-width* and is expressed in equation 2.34), it is possible to cast equations 2.31, 2.32 & 2.33 to equations 2.35, 2.36 & 2.37 in order to reflect experimental conditions, using the formulations expressed in equations 2.27, 2.28 & 2.29 [15].

$$f_d = \exp^{-\frac{t_{pd}}{\tau}}\left(1-\exp^{-\frac{t_g}{\tau}}\right) \tag{2.34}$$

$$\nu_1 = F\varepsilon M\nu_{s1}(1+\alpha) \tag{2.35}$$

$$\nu_2 = \frac{F\varepsilon^2 f_d M^2}{2!}\Big[\nu_{s2} + \Big(\frac{M-1}{\nu_{i1}-1}\Big)\nu_{s1}\nu_{i2}(1+\alpha)\Big] \tag{2.36}$$

$$\begin{aligned}\nu_3 = \frac{F\varepsilon^3 f_t M^3}{3!}\Bigg\{&\nu_3 + \Big(\frac{M-1}{\nu_{i1}-1}\Big)\Big[3\nu_{s2}\nu_{i2} + \nu_{s1}\nu_{i3}(\alpha+1)\Big] \\ &+3\Big(\frac{M-1}{\nu_{i1}-1}\Big)^2\nu_{s1}\nu_{i2}^2(\alpha+1)\Bigg\}\end{aligned} \tag{2.37}$$

where, τ is the detector die-away, f_d is the doubles gate fraction, f_t is the triples gate fraction, t_{pd} is the size of the *predelay-gate* and t_g is the size of the *coincidence-gate*. In this thesis, it is assumed that there is no self-multiplication and no (α, n) reaction contribution, and hence the values of M and α are taken to be 1 and 0, respectively.

2.5.2 Thermal and fast neutron assays

The methods described in the previous section have been adopted widely with ^{3}He based thermal neutron detectors for the detection of time-correlated neutrons emitted from both stimulated and spontaneously-fissile isotopes to determine the multiplication factor of an arrangement of fissile material under study. Systems based on ^{3}He have been favoured to date because of their

high detection efficiencies for thermal neutrons, stability in use, strong immunity to γ-ray interference and extensive knowledge base, as discussed previously in section 2.4.2. These ^{3}He-based assays have been studied extensively for decades and depend on well-established relationships that were discussed in the section 2.5.1 to interpret *passive neutron coincidence counting (PNCC)* and *active neutron coincidence counting (ANCC)* measurements, which were developed based on the physics involved in ^{3}He-based thermal assay.

As was discussed in section 2.3, the time taken for the fission radiation to be emitted from a fragmenting nucleus is in the sub-picosecond domain. Neutrons that are emitted from fission have to traverse the distance between the site of fission and a detection system, and this introduces a delay between the time taken for the radiation to be evolved and its detection. Minimising the source-detector distance to below $\approx$ 10 cm, corresponding to a time interval of $\approx$ 5 ns, is often constrained by the geometrical arrangement of the detector system and the position of the sample under scrutiny. There is also often a requirement for there to be a finite detector volume to achieve adequate detection efficiency. Thus, the limiting range in time between the evolution of fission radiation and its arrival at a detector system is of the order of tens of nanoseconds. This interval results in unavoidable dispersion of the arrival times of fission neutrons at the detector system due to their energy spectrum (i.e. speed distribution), and this is manifested as a broadening of the statistical fluctuation in arrival times at the detector, relative to the hypothetical distribution of emission times.

However, the majority of the neutrons that are emitted from a fissioning isotope are fast. For example, the mean energy of the neutrons emitted from the spontaneous fission of ^{252}Cf is $\approx$ 2.13 MeV, while the most probable energy is $\approx$ 0.7 MeV. Therefore, a thermalisation stage is usually necessary to exploit the optimum neutron absorption cross-section of the ^{3}He-based detector assay, which has a very low cross-section for fast neutrons, as can be observed in figure 2.11(a). Insofar as multiplicity and ToF analysis are concerned, the implication of using ^{3}He-based thermal neutron detectors, as a consequence of this thermalisation stage, is two-fold: (i) the detector die-away and therefore the *gate-width* needed is substantially longer (i.e. to the order of 40 μs to 70 μs) compared to that of a system sensitive to fast neutron detectors (i.e. between 20 ns to 25 ns, as depicted schematically in figure 2.12(b) on page 35) [26]; and (ii) information about incident energy is lost in this process thereby eliminating the prospect of exploiting the energy information to derive additional benefits of the assay. Since the rise and fall of the neutron population (i.e. the prompt neutron die-away characteristic) in a fission chain can be due to either spontaneous fission, (α, n) reactions or scattering, the various aspects of the change in the neutron population cannot be fully determined when using such thermal detectors. Additionally, the relatively long *gate-width* also results in a substantially larger number of *accidental events* which hampers the statistical performance of the numerical analysis of

data from these assays, thereby preventing them from effectively detecting potentially useful, high-order coincidence events. Furthermore, as the production of ^{3}He and ^{4}He is linked to the manufacture process of nuclear weapons and due to increased demand for homeland security application, these helium products are becoming increasingly more expensive to acquire with a decline in their stock over the last few years [17, 18].

2.6 Scintillation detectors

Scintillation detectors have briefly been discussed in section 2.4. In this section, a more in-depth description is given regarding the physics involved in such detectors, and their advantages and disadvantages are highlighted.

The material that is used in the active region of the detectors must [72] (i) produce detectable light when subjected to radiation, (ii) have a linear or well-defined light yield (i.e. the amount of light produced for an incident radiation with a given energy), (iii) induce light with a short die-away/decay time and (iv) have good optical properties and reflective index to enable coupling of the light to a sensor (e.g. a PMT). While inorganic scintillants (e.g. NaI(Tl), CsI(Tl), LiI(Eu), etc.) have the best linear light yield, they are insensitive to fast neutron radiation and have a slow response time which is not ideal for ToF applications. Organic scintillants, such as xylene-based compounds have good efficiency for fast neutrons due to the large scattering cross-section of hydrogen with neutrons and have a very fast response time.

There are several kinds of organic scintillators that are commercially available which were considered for this project. Pure organic crystal based scintillators like anthracene have very good efficiency, but are not ideal for the PSD techniques needed to distinguish between different event types. Stilbene is a good alternative given that it has the best PSD performance compared to other types of scintillants, however it is very fragile and the light response from this material is known to vary depending on the angle between the crystal and the incident particle [72]. Plastic scintillators such as polymerised styrene (e.g. EJ-299) are very popular given that they can be moulded into different shapes and sizes and are relatively inexpensive, however they suffer from poor neutron and γ-ray discrimination performance. Liquid scintillators (e.g. EJ-309) are often the cheapest option, have very small attenuation lengths and can be used in large volumes. Although these materials have limited efficiency, they have adequate PSD performance [72].

2.6.1 Physics of organic scintillants

The physics of the organic scintillants based on organic molecules arises from certain symmetric properties which allow for a π-electron structure to exist within the electronic band [72, 87], as illustrated in figure 2.14. This makes the molecules prone to excitation by incident radiation. When an incident particle interacts with the molecules, energy is transferred to the molecules by exciting the electrons from the ground state (S_0) to one of the excited singlet states (S_1, S_2, etc). The energy required for a transition from S_0 to S_1 is between 3 eV and 4 eV, whereas the vibrational states are usually separated by 0.15 eV. This excitation process for a γ ray is different from a neutron interaction, illustrated in figure 2.15:

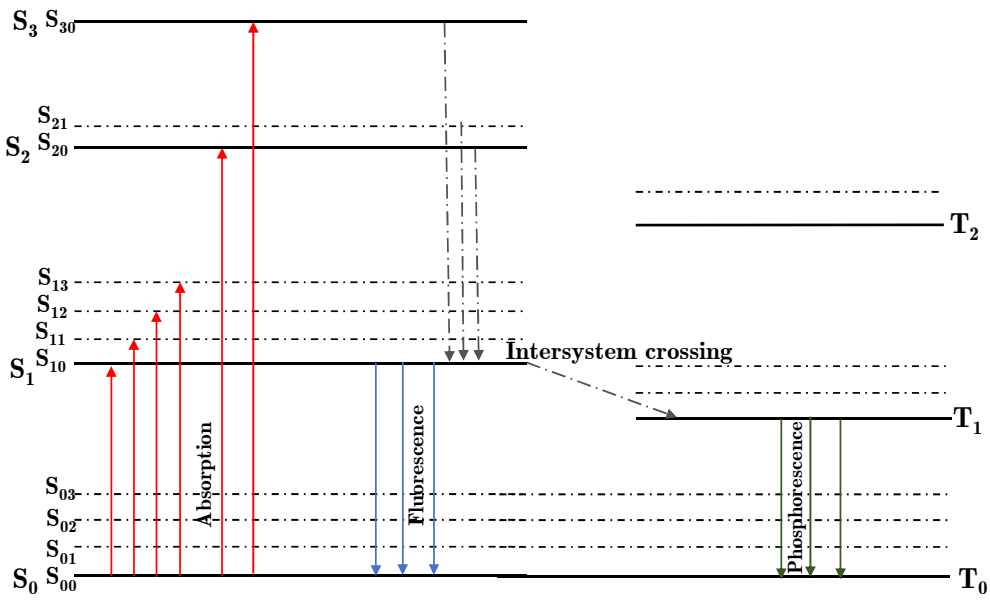

Figure 2.14 | π-electron model. Energy levels of an organic molecule with π-electron structure. The image was reproduced based on the original illustration by J. B. Birks in The Theory and Practice of Scintillation Counting [87].

1. *γ-ray radiation:* The γ rays interact with the valence electrons in the scintillation material through Compton scattering thereby liberating a stream of free electrons. Not all of the energy in the incident γ ray is deposited, and the scattered γ ray may undergo further Compton scattering in the medium or escape the active volume altogether. The excited electron then falls back to ground state by exciting the organic scintillation molecules.

2. *Neutron:* The mechanism by which neutrons interact with the active volume is very similar to γ-ray interactions, except that the initial charged particle is produced by elastic collisions between the incident neutron and the protons in the hydrogen or carbon atoms, hence passing some of its kinetic energy to the proton. At this stage, the incident neutron is scattered to a slower energy band, and may undergo further scattering reactions within the active region or escape the volume altogether. The energy which was transferred to the proton allows it to excite the scintillation molecules.

Due to the excitation by the proxy particles, i.e. electrons and protons, it is possible to excite the organic scintillation molecules to occupy one of the higher order singlet states (i.e. S_1, S_2, S_3, etc.) or one of the vibrational states (i.e. S_{11}, S_{12}, S_{13}, etc.). However, they eventually fall back to the S_0 state through internal conversion. For this de-excitation process, one of several paths may be taken to produce the *optical photons* [72, 87]:

1. *Prompt fluorescence:* This is the most probable process via which the molecule will transit

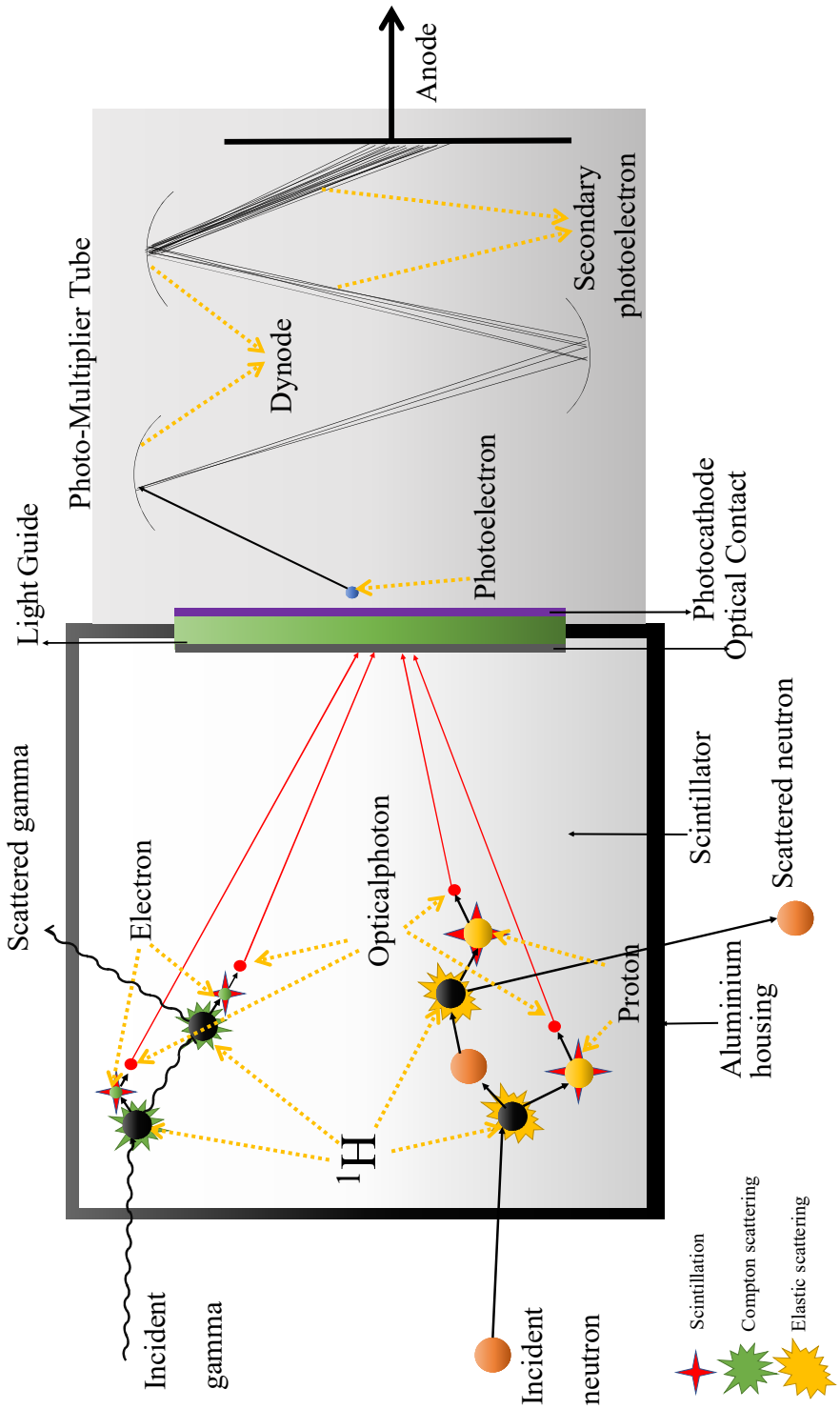

Figure 2.15 | Schematic of an EJ-309 based liquid scintillator. Illustration of an EJ-309 based scintillation detector (not to scale) used in this research showing the process by which an incoming neutron (and γ ray) produces a proton (or electron) which acts as a proxy towards the production of *optical photons*. These *optical photons* travel to the photocathode where they generate photoelectrons which are then multiplied by the cascade of dynodes inside the PMT.

to one of the vibrational states of the ground state within a few nanoseconds resulting in the production of scintillation light via *optical photons* (labelled as *fluorescence* in figure 2.14).

2. *Phosphorescence:* Some excited singlet states may be converted into the lowest triplet state (T_1) through intersystem crossing (labelled as *intersystem crossing* in figure 2.14), from where the molecule will drop to the S_0 state via emission of radiation ($<$ 1 millisecond), releasing *optical photons*. This process is referred to as phosphorescence.

3. *Delayed fluorescence:* While in T_1 state, some molecules will be excited back to S_{10} through thermal excitation, from where the molecule will drop to the S_0 state via the normal fluorescence process. This transition delays the production of the *optical photons* and hence is called the delayed fluorescence; this may have a die-away of several hundred nanoseconds.

4. *Quenching:* Other de-excitation modes are available to the excited molecules which do not involve the emission of *optical photons* but heat or chemical reactions instead.

The light produced during the downward transitions have longer wavelengths compared to the absorption wavelength of the scintillation medium with little overlap between the optical absorption and emission spectra. Hence, the self-quenching of the fluorescence is very small, thereby preserving the energy information of the incident radiation.

The proportion of delayed fluorescence is related to the delayed fluorescence density. This delayed fluorescence density is primarily determined by the *linear energy transfer (LET)* of the incoming particles' proxies (i.e. electrons and protons), or the amount of energy transferred to the material per unit distance traversed. The heavier the particle, for instance protons compared to electrons, the larger the *linear energy transfer* and hence the higher production of delayed fluorescence. Therefore, the tail of the pulse arising from a proton (which is the proxy for a neutron) will be longer (i.e. have a longer die-away) compared to that of an electron (which is a proxy for a γ ray), as depicted schematically in figure 2.16. This difference between the shape of the pulse can be exploited by PSD techniques which allow the incident radiation type to be determined.

2.6.2 Pulse shape discrimination

The signals from these detectors therefore carry information in their shape, or more precisely, in their rise and decay times. These signals are typically 30 ns to 200 ns long [20] and comprise of at least two exponential components with a decay constant. The information needed for successful discrimination of incident particles lies in the decay time of emitted light which is prolonged when produced by particles with larger LET. There are several digital analytical methods, known as *pulse shape discrimination (PSD)*, that can exploit this difference to identify the type of incident

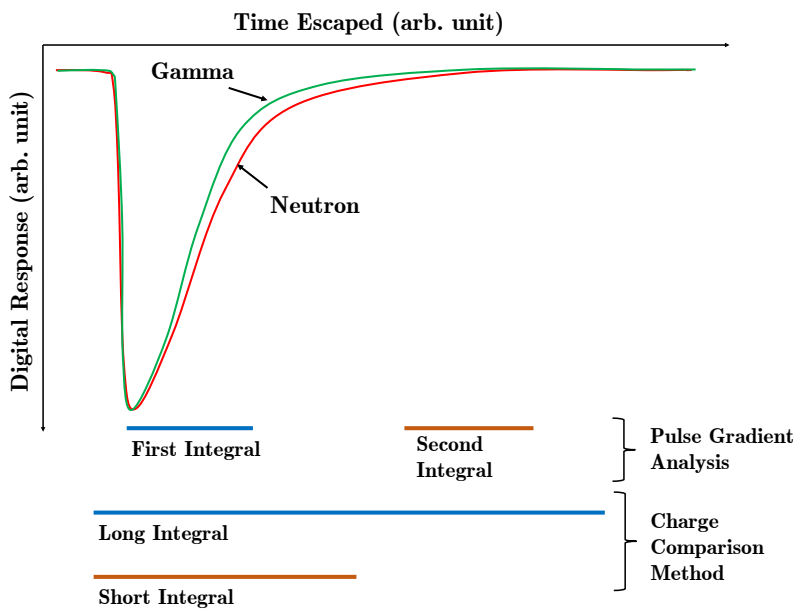

Figure 2.16 | Light response from scintillant due to electron and proton detection. Due to the larger LET of the proton, the tail of the signal from a proton (which acts as a proxy to incident neutron particles) contains more charge. By calculating the ratio between the amount of charge accumulated under the peak to that in the tail of this plot would allow for the identification of the incident particles. The positioning of the charge integrating gates for PGA and CCM are also included below the plot.

particles. Typically, these algorithms may have an uncertainty of between 3% to 5%.

Since the late-1950s [88] until the mid-2000, analogue systems were used for carrying out pulse shape discrimination usually using one of the two dominating algorithms: (i) the *zero-crossing method (ZCM)* [89] or (ii) the *charge comparison method (CCM)* [88] method. With the advancement in digital signal processing techniques using modern high speed electronics, it became possible to implement real-time pulse shape discrimination algorithms to carry out the functions of their analogue counterparts, often with better performance in terms of *figure-of-merit (FoM)* [90]. Recently, a new high-speed method was implemented to carry out PSD by analysing the gradient of the signal die-away, a process referred to as the *Pulse Gradient Analysis (PGA)* [32]. These three popular methods for PSD are briefly described below:

1. *Charge Comparison Method (CCM):* This method determines the charge accumulated under a pulse over two different intervals (i.e. the long integral from the start of the trigger until the end of the pulse and the short integral from the start of the trigger for a shorter period, $\approx 10\%$ of the long integral, so as to omit the tail end of the pulse) [88]. The ratio between the two integrals is used to identify the particle type. Figure 2.16 illustrates the two integrals on the pulse.

2. *Pulse Gradient Analysis (PGA):* This method is based on a comparison of the peak amplitude and the amplitude of a sample occurring a defined time interval after the peak amplitude, known as the first and second integral, respectively, using two moving average filters [32, 91]. Figure 2.16 illustrates the two integrals on the pulse.

3. *Zero-crossing method (ZCM):* This method transforms the analogue signal into bipolar signals to determine the time elapsed between the trigger and the zero-crossing point to assert whether an incident event is a photon or a neutron. This is achieved by implementing a digital constant fraction discriminator, which is an electronic circuit designed to find the maxima of a pulse by finding the zero gradient of its slope, to determine the time elapsed between the maxima and the time at which the shaped signal crosses the zero line. This difference in timing is used for event discrimination [92].

2.6.3 Photon-breakthrough

Any mischaracterisation of event is referred to as breakthrough in this thesis, therefore, photon-breakthrough refers to a γ-ray event which has been misclassified as a neutron event.

The emission of neutrons is almost always associated with the emission of γ rays, and often the rate of photon emission is significantly greater than that of neutron emission, e.g. in the case of ^{252}Cf source, the γ-ray flux may be up to 10 times the neutron flux. Depending on the type of PSD algorithm (see section 2.6.2) and the assigned detector threshold, only a small proportion of events might be misclassified. However, even a small degree of misclassification of γ-ray events can impact the neutron count significantly, which can have an adverse effect on the outcome of the numerical analysis [93]. This is a common occurrence as the analogue signal induced by the low-energy particles, which therefore produce low-amplitude pulses, do not have sufficient amplitude to provide enough resolution for the PSD technique to be applied effectively, thereby making this region the most prominent in relation to misclassified events (see figure 4.21 on page 134).

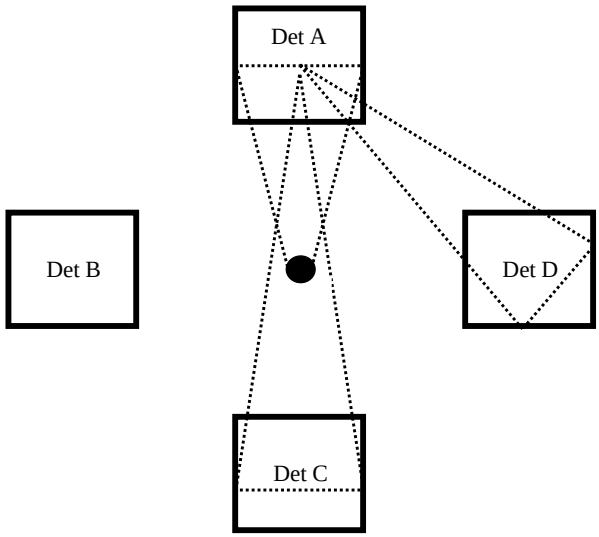

Figure 2.17 | Schematic illustration of detector crosstalk. The detectors A, B, C and D in a simplistic arrangement equidistant around a source, together with schematic representations of a solid angle between the source and detector A. There is a small but finite probability that a neutron which triggered detector A will escape the detector with sufficient energy to migrate to the neighbouring detectors and trigger a second scatter event that may manifest as a double event provided it does so within the *gate-width*. Redrawn based on original artwork presented in reference [94].

2.6.4 Crosstalk

Due to the dependence of organic scintillators on scattering reactions to detect radiation, these detectors are vulnerable to detector crosstalk. This is a phenomenon by which a single incident particle triggers multiple detectors and thereby appears as a multiplet, as illustrated in figure 2.17. If a proper correction model is not taken into account while carrying out numerical analysis, it may lead to mischaracterisation of the assay. It is common practice to deactivate adjacent detectors under the assumption that crosstalk is most likely to take place between neighbouring detectors. Whilst it is true that crosstalk is mostly likely in adjacent detectors, the angular distribution of the emitted neutrons from fission events (see figure 2.9 on page 27) implies neutrons emitted from the same fission fragment will be more tightly spaced and so detection by adjacent detectors will not be entirely due to crosstalk, and so deactivating adjacent detectors is not an optimal solution and may over-compensate. Alternatively, it is also possible to tackle such erroneous measurements analytically by using correction models, such as the one proposed in this thesis in section 5.6.1 on page 174.

2.7 Modelling in nuclear safeguards

In the nuclear field, being able to model various scenarios using a well optimised code is vital for designing prototype systems and validating experimental results. Previously, in section 2.3, brief descriptions of various fission models were presented. This section describes techniques and codes to model various radiation fields and detectors.

2.7.1 Evaluating nuclear inventory

For the analysis of inventories of different isotopes in a sample of SNF there are several computer codes based on neutron activation analysis techniques that can be used. The fundamentals of this analysis [95] depend on the fact that inventory of any isotope, i, changes due to (i) other materials with fixed half-lives decaying into that isotope via radioactive decay, fission process or neutron absorption, increasing the density of the isotope i; and (ii) the isotope i undergoing neutron absorption or fission reaction due to neutron irradiation, or undergoing radioactive decay. This is further complicated by multiple different competing nuclear reactions and decay paths, and the dependence of the nuclear reaction rate on the neutron flux; the latter in turn is also dependent on the neutron flux and spectrum of the entire sample. As a consequence, the calculation has to be carried out in a time-iterative loop. The basic dynamics of this analysis can be illustrated using equation 2.38 [95], where λ_i is the decay constant of isotope i, $\lambda_{i,j}$ is the decay constant of isotope j producing isotope i, σ_i is the absorption cross-section of isotope i, ϕ is the neutron flux, σ_{ij} cross-section of a reaction converting isotope j to i, σ_f is the fission cross-section and Y_{ki} is the yield of fission product i from the fission of k.

$$\frac{dN_i}{dt} = -N_i(\lambda_i + \sigma_i\phi) + \Sigma_j N_j(\lambda_{ij} + \sigma_{ij}\phi) + \Sigma_k N_k \sigma_{fk}\phi Y_{ki} \tag{2.38}$$

FISPIN is one of the many computer codes that is able to carry out such a calculation using a point model [96]. It calculates the changes in the numbers of atoms of various heavy isotopes (i.e. actinides) and fission products within a sample of nuclear fuel element, as it is subjected to periods of irradiation and cooling (i.e. storage in spent fuel pool for example). Based on number densities, the code is also able to calculate the isotope-wise neutron emission rates from a sample fuel due to spontaneous fission and (α, n) reactions. Additionally, it also provides information regarding the neutron and γ spectrum, and the contribution of α, β ad γ decay towards heat generation. Since it is a point model, there are certain limitations to this code, namely that it can only model homogeneous samples. The required radioactive decay constant, modes of decay and branching ratio for various isotopes are taken from the Joint Evaluated Fission and Fusion (JEFF) Nuclear Data Library, version 2.2 [97]. Extensive validation of the code has been carried out illustrating its effectiveness. The results for the curium inventory, which is of interest in this

thesis, shows that FISPIN consistently under-predicts the trends by a negligible margin [98, 99].

2.7.2 Modelling the transportation of neutron

A major part of modelling how the neutron population evolves with time involves solving the neutron transport equation [100], which infers the neutron density (i.e. $n(\mathbf{r}, \bar{\Omega}, E, t)$ or the number of neutrons per unit volume, solid angle, and energy, where $\mathbf{r}$ is a vector representation of space, Ω is solid angle, E is energy and t is time). The neutron density is dependent on the angular neutron flux (i.e. $\Psi(\mathbf{r}, \bar{\Omega}, E, t)$ having a dimension of neutrons per unit area, solid angle, energy, and time), the scalar neutron flux (i.e. $\Phi(\mathbf{r}, E, t)$ having a dimension of neutrons per unit area, energy, and time) and the neutron current density vector (i.e. $\mathbf{J}(\mathbf{r}, E, t)$ which is a vector quantity with a dimension of neutrons per unit area, energy, and time). These parameters are defined in equations 2.39, 2.40 and 2.41, respectively.

$$\Psi(\mathbf{r}, \bar{\Omega}, E, t) = v(E)n(\mathbf{r}, \bar{\Omega}, E, t) \tag{2.39}$$

$$\Phi(\mathbf{r}, E, t) = \int_{4\pi} \Psi(\mathbf{r}, \bar{\Omega}, E, t)d\omega = \int_{4\pi} v(E)n(\mathbf{r}, \bar{\Omega}, E, t)d\omega \tag{2.40}$$

$$\mathbf{J}(\mathbf{r}, E, t) = \int_{4\pi} \bar{\Omega}\Psi(\mathbf{r}, \bar{\Omega}, E, t)d\omega = \int_{4\pi} \bar{\Omega}v(E)n(\mathbf{r}, \bar{\Omega}, E, t)d\omega \tag{2.41}$$

Considering an elementary surface of dS, it can be shown that $v(E)dS\cos\theta n(\mathbf{r}, \bar{\Omega}, E, t)$ neutrons per solid angle, energy and time may pass through a surface dS representing a cylindrical volume $v(E)dS\cos\theta$. Since $\bar{\Omega} \cdot \mathbf{x} = \cos\phi$, where $\mathbf{x}$ is the unit elementary vector defined in the x-axis, one can show that

$$v(E)dS\cos\theta n(\mathbf{r}, \bar{\Omega}, E, t) = \mathbf{dS}\bar{\Omega}\Psi(\mathbf{r}, \bar{\Omega}, E, t) \tag{2.42}$$

which represents the number of neutrons at $\mathbf{r}$, having a direction of $\bar{\Omega}$ and energy E, flowing through a surface dS per unit time, solid angle and energy.

$$\int_V \frac{\delta}{\delta t} n(\mathbf{r}, \bar{\Omega}, E, t)dVdt \tag{2.43}$$

The number of neutrons contained inside a volume V, bound by surface S, within a given time interval dt (i.e. equation 2.43) can be determined by finding the balance between the (i) injection of new neutrons due to scattering and production of new neutrons from fission, etc; (ii) loss of neutrons due to scattering and absorption; and (iii) transport of neutron through S.

The injection of new neutrons into the volume V has two sources; neutrons contained in any energy bin and having any direction that are scattered into the energy bin dE around E and direction $\bar{\Omega}$ contained in the solid angle $d\omega$, and neutrons produced by fission reactions.

Therefore, the production of new neutrons within the volume can be expressed as

$$\begin{aligned}\int_V \int_{4\pi} \int_0^\infty \Sigma_s(\mathbf{r}, \bar{\Omega}' \to \Omega, E' \to E, t)\Psi(\mathbf{r}, \bar{\Omega}', E', t) dV d\omega' dE' dt \\ + \frac{\chi(E)}{4\pi} \int_V \int_0^\infty \nu\Sigma_f(\mathbf{r}, E', t)\Phi(\mathbf{r}, E', t) dV dE' dt\end{aligned} \tag{2.44}$$

where, $\Sigma_s(\mathbf{r}, \bar{\Omega}' \to \Omega, E' \to E, t)$ represents the macroscopic cross-section for scatter from $\bar{\Omega}'$ and E' to $\bar{\Omega}$ and E, $\chi(E)$ is the isotropic fission spectrum and $\Sigma_f(\mathbf{r}, E', t)$ is the macroscopic fission cross-section.

Similarly, the disappearance of neutrons from V can be expressed using the total macroscopic cross-section, $\Sigma_T(\mathbf{r}, E', t)$, as shown in equation 2.45.

$$\int_V \Sigma_T(\mathbf{r}, E, t)\Psi(\mathbf{r}, \bar{\Omega}, E, t) dV dt \tag{2.45}$$

The transport of neutrons to and from the volume V with surface S per unit solid angle and energy can be expressed by equation 2.46. Using the divergence theorem[6], one can rewrite this equation as equation 2.47.

$$dt \int_S \mathbf{dS} \cdot \bar{\Omega}\Psi(\mathbf{r}, \bar{\Omega}, E, t) \tag{2.46}$$

$$\int_V \bar{\Omega} \cdot \bar{\nabla}\Psi(\mathbf{r}, \bar{\Omega}, E, t) dV dt \tag{2.47}$$

Hence, combining the above equations, one can obtain the Boltzmann equation (also known as the transport equation) as expressed in equation 2.48.

$$\begin{aligned}\underbrace{\frac{\delta}{v(E)\delta t}\Psi(\mathbf{r}, \bar{\Omega}, E, t)}_{\text{neutron density}} \\ + \underbrace{\bar{\Omega} \cdot \bar{\nabla}\Psi(\mathbf{r}, \bar{\Omega}, E, t) dt}_{\text{transport}} + \underbrace{\Sigma_T(\mathbf{r}, E, t)\Psi(\mathbf{r}, \bar{\Omega}, E, t) dt}_{\text{removal through capture or scatter}} \\ = \underbrace{\frac{\chi(E)}{4\pi} \int_0^\infty \nu\Sigma_f(\mathbf{r}, E', t)\Phi(\mathbf{r}, E', t) dE' dt}_{\text{production through fission}} \\ \underbrace{+ \int_{4\pi} \int_0^\infty \Sigma_s(\mathbf{r}, \bar{\Omega}' \to \Omega, E' \to E, t)\Psi(\mathbf{r}, \bar{\Omega}', E', t) d\omega' dE' dt}_{\text{production through scattering}}\end{aligned} \tag{2.48}$$

There are several *Monte Carlo N-Particle (MCNP)* based codes, e.g. MCNP [101], TART [102], Geant4 [103], etc. that may be used to solve the transport equation, i.e. equation 2.48. In most cases, they use an average fission model, i.e. using uncorrelated fission neutrons and γ rays

[6] Also referred to as the Gauss's theorem, it relates to the flux of a vector field passing though a surface to the behaviour of the flux inside the volume represented by the surface.

sampled from the same probability density function rather than those derived from a collection of individual fission processes [48]. This is satisfactory for the calculation of average quantities such as flux, energy deposition, mean-free-path, etc., however is not ideal for event-by-event stochastic analysis of correlated particles that are emitted from materials in the assay. Over the past decades, several codes are available that can use correlated fission models, such as the MCNPX-PoliMi [104] extension to MCNPX which includes the angular correlations of fission neutrons based on the assumption that the ^{252}Cf spontaneous fission distribution can be employed for all fissionable nuclides. A newer option introduced for the treatment of fission events, utilising the *Lawrence Livermore National Laboratory (LLNL)* fission library version 1.8 [64] in MCNPX2.7.0 [105] and MCNP6 [106], features a time-correlated sampling of γ rays from neutron-induced fission, photo-fission and spontaneous fission. However, MCNP6 is still sampling outgoing neutron particles from average fission model. The fission models FREYA and *CGMF* mentioned in section 2.3 are also to be included with MCNP6.2 [53], which was yet to be released at the time of writing this thesis.

2.7.3 Modelling the optical physics of liquid scintillants

There are several approaches to solving the non-linear response of scintillation detectors, with the most common practice involving a post-processing script to convert the deposited neutron or γ-ray energy to light output using an empirical formula [107]. However, this method does not take into account some of the optical properties of the detector and does not simulate the effect of light readout devices on the detector response. There are several codes that are able to simulate light output from scintillants, e.g. SCINFUL [108],‘ PHPESR [109] and EGS4/PRESTA [110], etc. However, they are limited in the type of geometry that can be modelled [111]. PHOTRACK [112], which is an optical transport solver, can be used to post-process MCNP6 PTRAC output to achieve the desired goal. However, this involves using two different codes to achieve a solution. Alternatively, Geant4, developed by *Conseil Européen pour la Recherche Nucléaire (CERN)*, can simulate the optical process that takes place inside a scintillator, using the G4OpticalPhysics model, and has been widely studied and validated [111, 113].

2.8 Additional fundamental concepts

In this section, some additional information regarding the methodology of determining error propagation and goodness-of-fit are discussed briefly.

2.8.1 Factorial moments

Factorial moment is a mathematical quantity defined as the expectation value of a random variable, or the long-run average value of repetitions of the experiment it represents. It is defined by equation 2.49, where $\nu(r)$ is the rth factorial moment and $p(n)$ is the probability of the nth order *number distribution*.

$$\nu(r) = \sum_{n=k}^{\infty} \frac{n!}{(n-r)!} p(n) \tag{2.49}$$

In order to take into account the experimental efficiencies while converting the *number distribution* to a factorial moment distribution, equation 2.49 can further be modified to equation 2.50.

$$\nu(r) = \sum_{n=k}^{\infty} \frac{n!}{(n-r)!} \left(\frac{1}{\varepsilon}\right)^r p(n) \tag{2.50}$$

2.8.2 Error propagation

The statistical analysis of the nature of radioactive processes and activities has a very broad scope. As neutron and γ-ray counts from experiments and simulations are used for further calculations, the errors in the datum are propagated to the final results [114]. In this section, some rudimentary methods for determining the magnitude of error that are present in the results due to the errors in the variables are detailed.

$$r1 = a + b + c \tag{2.51}$$

$$r2 = \frac{ab}{c} \tag{2.52}$$

Equations 2.51 and 2.52 show two simple mathematical expressions involving three variables (i.e. a, b and c), with each variable having corresponding uncertainties of σ_a, σ_b and σ_c, respectively. Here, σ_x is the standard deviation (i.e. spread of values from a set of repeated measurements) of the variable x, e.g. total count, and is determined by equation 2.53, assuming that the measurements were taken over t second(s), and that the spread follows a Poisson

distribution.

$$\sigma_x = \frac{\sqrt{x}}{t} \tag{2.53}$$

The uncertainties of the results of equations 2.51 and 2.52, i.e. the propagated errors of $r1$ and $r2$ due to the calculus, are given in equations 2.54 and 2.55, respectively; assuming the errors of the individual variables are uncorrelated to each other.

$$\sigma_{r1} = \sqrt{\sigma_a^2 + \sigma_b^2 + \sigma_c^2} \tag{2.54}$$

$$\sigma_{r2} = r2\sqrt{\left(\frac{\sigma_a}{a}\right)^2 + \left(\frac{\sigma_b}{b}\right)^2 + \left(\frac{\sigma_c}{c}\right)^2} \tag{2.55}$$

2.8.3 Goodness-of-fit

This thesis attempts to fit different mathematical models into distributions which were measured based on the results from various experiments and simulations. It is imperative to analyse how accurately fitted models are able to accommodate the measured dataset. This measure of accuracy is sometimes referred to as the goodness-of-fit. There are several techniques which were used in this thesis to calculate this parameter, which are mentioned below.

Sum of squares due to error

The *sum of squares due to error (SSE)* statistic, also referred to as the Chi-squared statistic, is a measure of the total deviation between values from a fitted response and the dataset that was used to construct the fit. Hence, if there is no deviation between the fitted response and the dataset, the SSE would be equal to 0. Equation 2.56 expresses the formulation of measuring such statistics, where $y(i)$ and $y_f(i)$ are the ith term of measured and fitted responses, respectively, and $w(i)$ is the weighting factor which, in this thesis, was assigned to be $1/(\sigma_i)^2$.

$$SSE = \sum_{i=0}^{n} w(i)\big(y(i) - y_f(i)\big)^2 \tag{2.56}$$

Dividing the *SSE* statistic by the number of independent pieces of data, v, leads to a parameter referred to as the *reduced Chi-squared* or χ_v^2.

Root mean squared error

Also known as the fit standard error or the standard error of the regression, *Root Mean Squared Error (RMSE)* statistic is the square root of the total deviation between values from a fitted response and mean of the dataset that was used to construct the fit. For a perfect fit, the RMSE would be equal to 0. Equation 2.57 expresses the formulation of measuring such

statistics, where $y(i)$ and $y_f(i)$ are the ith term of measured and fitted responses, respectively, v is the number of independent pieces of data and $w(i)$ is the weighting factor which, in this thesis, was assigned to be $1/(\sigma_i)^2$.

$$RMSE = \sqrt{\frac{1}{v}\sum_{i=0}^{n} w(i)\big(y(i) - y_f(i)\big)^2} \tag{2.57}$$

R-Square statistics

Similar to the other statistics mentioned earlier in this section, this parameter determines the robustness of a plot by finding the deviation from unity to the ratio between the SSE and sum of squares about the mean, and is expressed in equation 2.58.

$$R\text{-}Square = 1 - \frac{SSE}{\sum_{i=0}^{n} w(i)\big(y(i) - \bar{y}\big)^2} \tag{2.58}$$

Chapter 3

Experimental and Simulation Methods

This chapter defines the experimental and simulation methods employed in this research. Section 3.1 focuses on the instrumentation used to acquire and discriminate events from EJ-309 based liquid scintillation detectors in real-time. Section 3.2 addresses the design and implementation of the *multiplicity register* developed in the course of this research. Section 3.3 describes the implementation of experimental setups, while section 3.4 details the type of experiments that were conducted. The method of calibration the detector arrays uses is detailed in section 3.5.

Finally, sections 3.6 and 3.7 describe the FISPIN and Geant4 simulation models that were used in this research.

3.1 Digital data acquisition from mixed radiation fields

The radiation field arising from spontaneous fission and induced fission consists of various types of radiation including, but not limited to neutrons, γ rays, α and β^-. The EJ-309 scintillation detector, described in detail in section 3.1.1, is however only sensitive to the neutron and γ-ray radiation due to its aluminium housing which absorbs the α and β particles. The acquisition and the real-time *pulse shape discrimination (PSD)* were carried out using the four-channel *Mixed-Field Analysers (MFA)* produced by Hybrid Instruments Ltd. as described in section 3.1.2. The output from the MFA was then fed into the *multiplicity register* to carry out coincidence analysis, which is described in section 3.2.

3.1.1 Scintillation detectors

The detectors used for the experiments of this research were the VS-1105-21 (Scionix, Netherlands) detectors, which are schematically illustrated in figure 3.1. The detectors each comprise a scintillant volume of 100 mm $\times$ 100 mm $\times$ 120 mm which is filled with EJ-309 (Eljen Technology, Sweetwater, TX) (see appendix A.1 for information on the EJ-309 compound). The optical signals are converted to an electric signal using a photomultiplier tube of type 9821 FLB (ADIT Electron Tubes, Sweetwater, TX) which is coupled to the scintillant via a photocathode (see appendix A.2 for information on the scintillator and *photo-multiplier tube (PMT)*). This scintillator exhibits excellent PSD properties, which is particularly useful for fast neutron counting and spectrometry in the presence of γ-ray radiation [115]. When interacting with γ-ray radiation, *optical photons* are produced with a linear response of 12,300 *optical photons* per MeV per incident electron [116]. The light output due to interaction with neutrons, which are generated through a proton proxy, is non-linear in nature and is well documented [117, 118]. The light output from both neutron and γ-ray interactions are presented in figure 3.2. When compared to light output due to γ-ray interaction in other common organic scintillants like NE-213, BC-501 and EJ-301, the EJ-309 performance is similar, however, the light output of EJ-309 due to neutron interaction is lower compared to that of others.

The PMTs were operated with a *high-tension (HT)* supply voltage ranging from -1500 V to -1900 V DC to correct for inherent inconsistencies between PMT performance. The output signals from the PMTs were connected to individual channels on the MFAs for PSD, via a 3 m length of 50 Ω (RG58) coaxial cable. This cable preserved the pulse shape sufficiently to allow successful pulse-shape analysis.

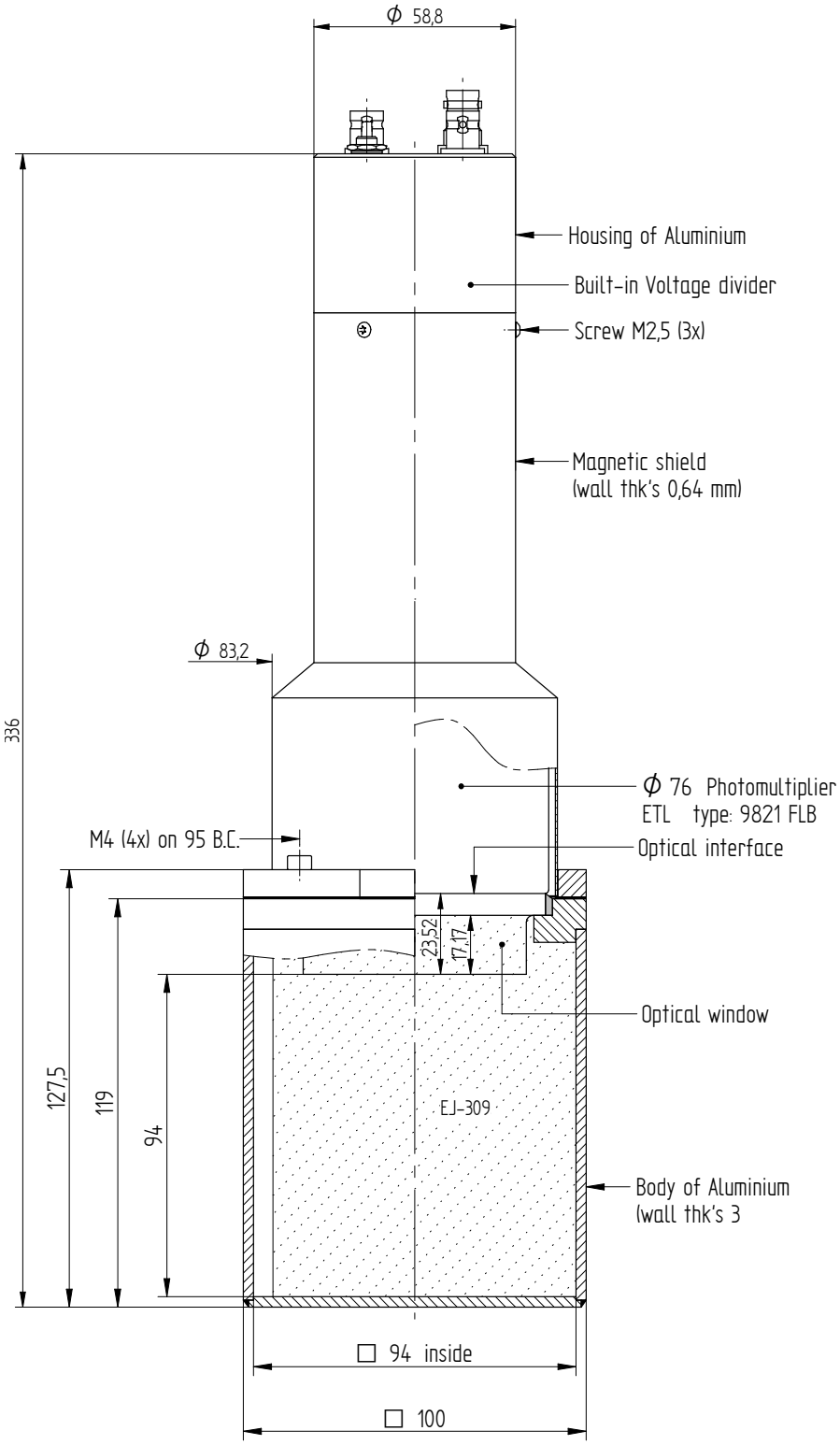

Figure 3.1 | Schematic of VS-1105-21, EJ-309 based organic liquid scintillation detector. Engineering drawing of the EJ-309 based scintillation detectors that were used in the experiments conducted during the course of this research. The drawing was obtained via private communication with the manufacturer.

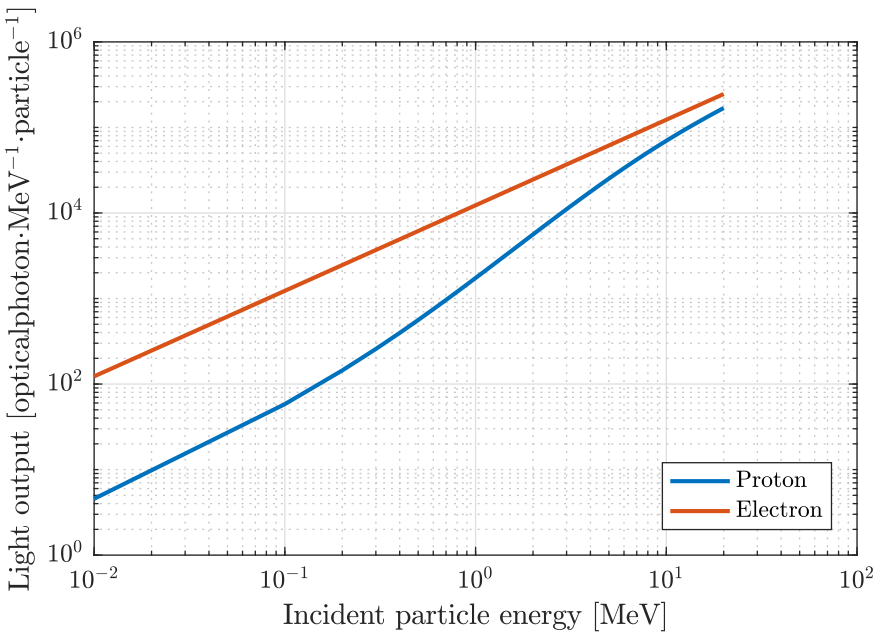

Figure 3.2 | Light output from EJ-309 based organic scintillator. The number of *optical photons* released from the EJ-309 organic scintillant as a function of energy deposited by electrons and protons. While electrons normally generate an essentially linear response, the light yields from protons are nonlinear. Data for electrons were from the datasheet of the liquid [116], while data for protons was taken from previous works in reference [118].

3.1.2 Mixed-Field Analysers

In this section, the design and commissioning of the MFA, pictured and detailed by means of a block diagram shown in figure 3.3, are briefly described. This device can digitise and analyse analogue signals arising from fast organic liquid scintillators, including but not limited to legacy fast liquid scintillation detectors (BC-510, NE-213 and EJ-301, plastic scintillators (EJ-299) and low-hazard scintillators (EJ-309). It continuously samples at 500 million samples-per-second (MS/s) using a 12-bit bipolar *analogue-to-digital converter (ADC)* and carries out digital PSD in real-time [21, 94]. The unit incorporates a HT power supply to achieve a self-contained portable design. The unit used in this research, MFA4.3, comprises of four channels, each with its own HT power supply. The principal processing is carried out by a Xilinx Virtex 5 *field-programable gate array (FPGA)* which is loaded with the MFA4.3-Aug15 firmware. The firmware contains four modules of PSD offering the independent data processing pathways for each channel (see section 2.6.2 on page 45 and figure 2.16 on page 46 for the methodology for PSD). The PSD algorithm includes baseline correction, *finite impulse response (FIR)* filtering, identification of distinguishing parameters, and the determination of event type. At the rising and falling edge of a 250 MHz clock, the ADC is read and if the difference between this sample and the preceding sample is more than a predefined threshold, an event is triggered. Once the trigger is invoked, the subsequent ADC samples are read into a continuously filling, fixed-size, *first in, first out (FIFO)* buffer which is used to carry out PSD analysis using the *Pulse Gradient Analysis (PGA)*

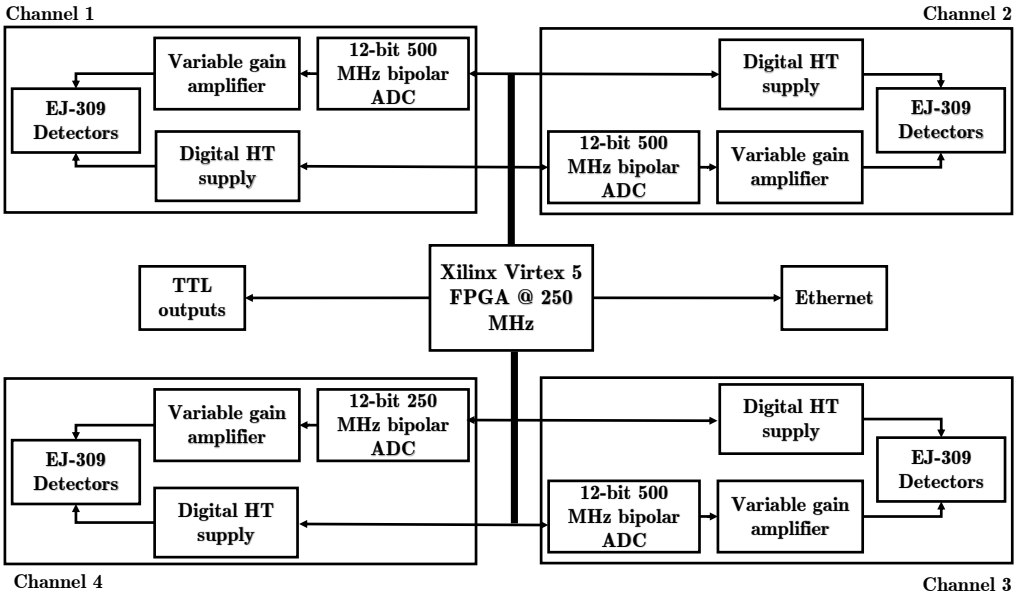

(a) Schematic representation of the different components that make up the Mixed-Field Analysers.

(b) Four MFAx4.3 Mixed-Field Analysers by Hybrid Instruments, Ltd., UK.

Figure 3.3 | Mixed-Field Analysers.(a) Schematic diagram of the main components that make up the mixed field analysers which were used for the discrimination of incoming events. Each channel consists of its own variable gain amplifier, analogue-to-digital converter and high tension power supply. **(b)** The analysers are transported in crates as shown in the picture [119].

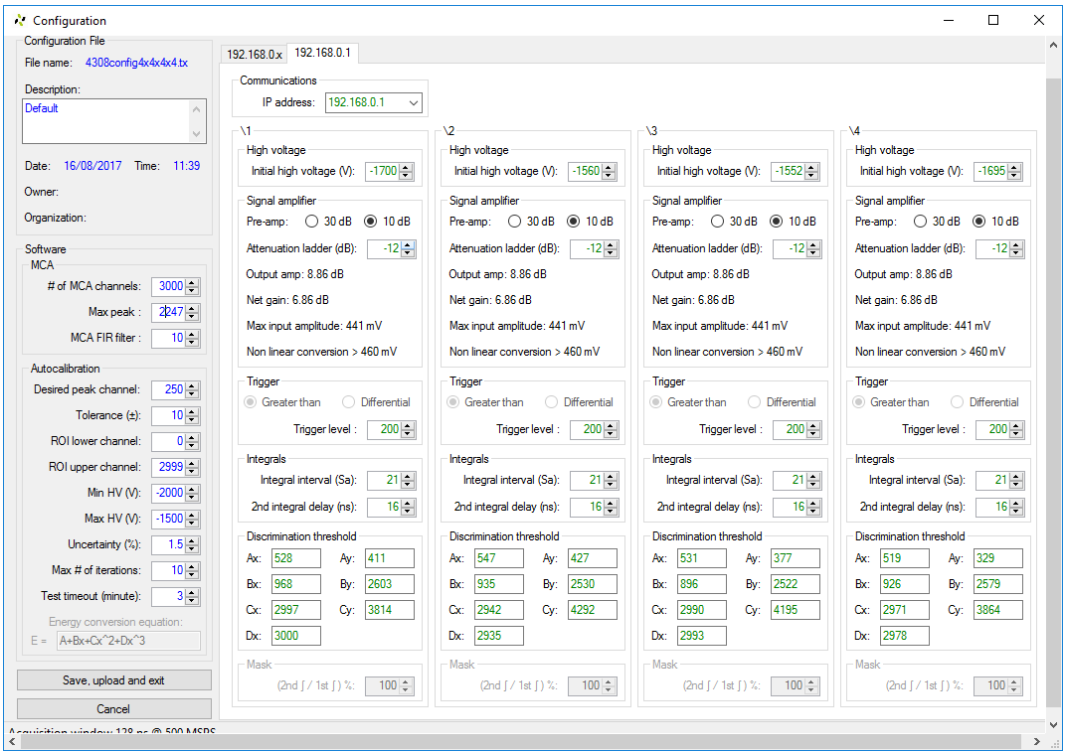

Figure 3.4 | GUI Screenshot of the configuration page. Configuration page of the 4-channel MFA GUI. Each channel can be configured to have its own HT supply, amplifier gain, trigger type, trigger threshold, and co-ordinates of a 3-point line for determining event type.

technique mentioned in section 2.6.2 on page 45. The entire process of discrimination takes 345 ns and, since the algorithm has an individual PSD module for each channel, the device can process concurrent signals in multiple channels. At the end of the processing, the firmware fills a buffer with the pulse height information and PSD integrals information (i.e. the average charge under two fixed-size gates, as detailed in section 2.6.2) and sends it over an ethernet connection to a remote computer. Additionally, each channel is in control of two synchronised *transistor-transistor logic (TTL)* signals, where one of two (neutron or γ ray) 50 ns output pulses are triggered. The TTL signals are only fired after a predefined number of cycles has escaped since the trigger, and therefore they are synchronised in time making it ideal for multiplicity and time-of-flight applications. The TTL outputs have a maximum timing jitter of less than 6 ns (or 2 ns assuming a Gaussian spread) which is thought to originate from the summation of the random clock jitter according to reference [94].

The MFA hardware is supplied with a GUI which allows for configuration of detector HT parameters for all detectors on an individual basis as well as other PSD and trigger parameters. It also presents the output data in plots or as *American Standard Code for Information Interchange (ASCII)* dumps. Figure 3.4 shows the configuration menu of GUI.

The following list summarises the features [94] of the MFA manufactured by Hybrid Instru-

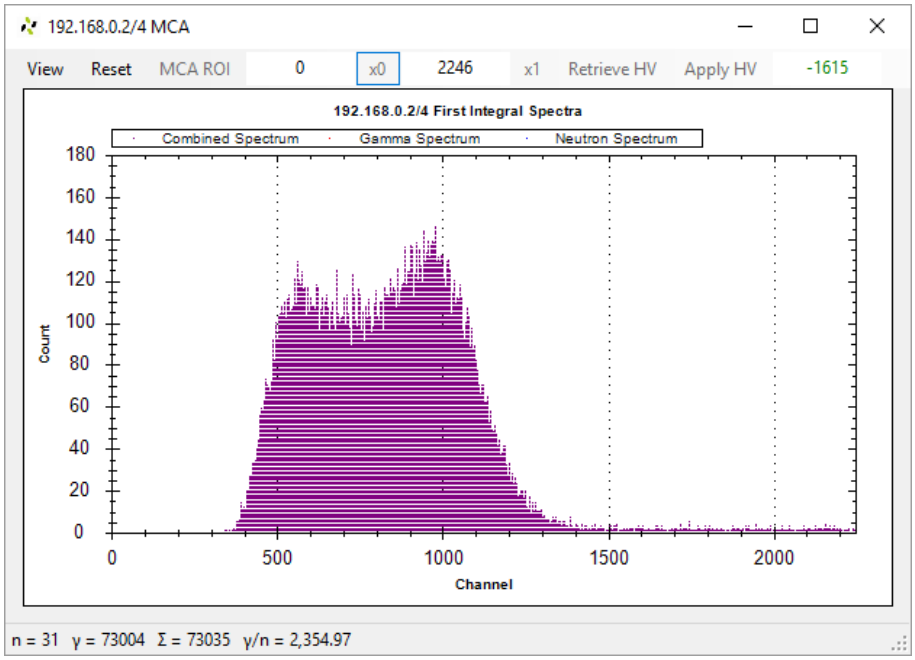

(a) MCA Plot using ^{137}Cs source.

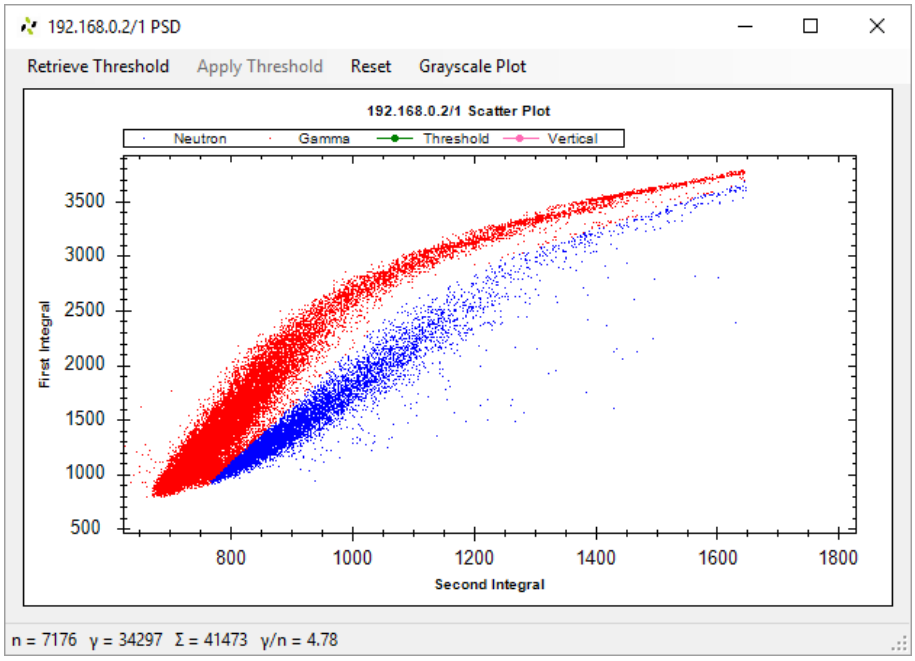

(b) PSD Plot using ^{252}Cf source.

Figure 3.5 | GUI Screenshots: MCA and PSD plots. (a) MFA *graphical user interface (GUI)* illustrating the MCA plot using a EJ-309 based liquid scintillation detector when exposed to a caesium-137 (^{137}Cs) source. The x-axis corresponds to the digitised pulse height, referred to as channel while the y-axis corresponds the intensity of the response. Calibration may be done by changing the HT voltage in the top-right corner of the window. **(b)** PSD window where a scatter plot between the first and second integral of the detected pulse from a EJ-309 based detector is plotted. By changing a 3-point based straight line, the MFA is instructed to consider the red plume to be γ-ray events while the rest of the events in blue are considered as neutrons.

ments Ltd.:

1. Separate time synchronised TTL signals to indicate the detection of a neutron or γ ray.
2. Integrated *Multi-Channel Analyser (MCA)* in one self-contained, portable unit.
3. Throughput of 3 million pulses per second per channel.
4. Compatibility with legacy fast liquid scintillation detectors (BC-510, NE-213 and EJ-301), low-hazard scintillators (EJ-309), and plastic scintillators (EJ-299).
5. A GUI supporting the user configurable parameters for all detectors (i.e. voltage levels from the system's integrated supplies and threshold settings to separate neutron and γ ray) on an individual basis and the output data arising from them.

Figure 3.5(a) illustrates the pulse height spectrum from a ^{137}Cs and figure 3.5(b) demonstrates the PSD plots of the radiation field from californium-252 (^{252}Cf) for a single detector using the *BARE15* setup, which will be detailed in section 3.3.4 on page 82.

3.2 Digital data processing for coincidence analysis

Following spontaneous fission or induced fission, various radiations including neutrons and γ rays are expelled from the fission fragments. Assays designed to work with helium-3 (^{3}He) detectors have historically used the shift-register based technique as depicted in figure 2.12(a) in section 2.5.1 on page 34. The output of this algorithm are two *reduced factorial moment distributions*, commonly referred to as a multiplicity histograms. The popularity of this method is due to the well-established methods for mathematical analysis as well as the fact that this method allows for the assay to be used in a very strong radiation field. However, the correction terms needed to account for the different physics involved in scintillation detectors (due to *crosstalk* and *photon-breakthrough*) when using this method make it inappropriate for these detectors.

In section 3.2.1, the algorithm proposed in this thesis to carry out multiplicity analysis is detailed and compared to the shift-register method. Section 3.2.2 outlines how this algorithm was used to construct the *interval-time distribution (ITD)*. The algorithm has been implemented in a development kit which is discussed in sections 3.2.3 and 3.2.4. This device is referred to in this work as the *multiplicity register*.

3.2.1 Cluster-size method

The schematic of the algorithm is illustrated in figure 3.6. In this method, a neutron is first detected by the "noise dampening circuit" by sampling the TTL outputs from the MFA at 200 MHz . The noise dampening technique involves asserting that the TTL line has to be active for 30 ns before it can be considered as a valid signal. Assuming that there are no prior events detected (i.e. it is the first event detected), the "TriggerGenerator" module will issue a trigger opening the *prompt-gate* for measuring the *foreground coincidence count* and disable itself. The size of this gate is user-defined via dip-switches. During this window, the "TriggerGenerator" module will scan for incoming γ-ray or neutron events or both, and count them. The duration of this gate as defined by the user is asserted by incrementing a counter (i.e the *GateCounter* inside the "TimerModule"). Following the end of the *prompt-gate*, the system is idled for 150 ns (in accordance to the *idle-gate* in section 2.5.1 on page 34) after which which the *delayed-gate* (of the same size as the *prompt-gate*) is issued to assess the *background coincidence count*. At the end of the two *coincidence-gates*, a reset signal is issued, which increments the corresponding *foreground coincidence distribution* and *background coincidence distribution*, resets "TimerModule", and re-activates the trigger mechanism of the "TriggerGenerator" module. At a fixed interval, a subsystem reads the two distributions periodically using a 256-bit bus through multiplexing and transmits them to the remote computer. The two *coincidence distributions* (i.e. *foreground coincidence distribution* and *background coincidence distribution*) are constructed to function

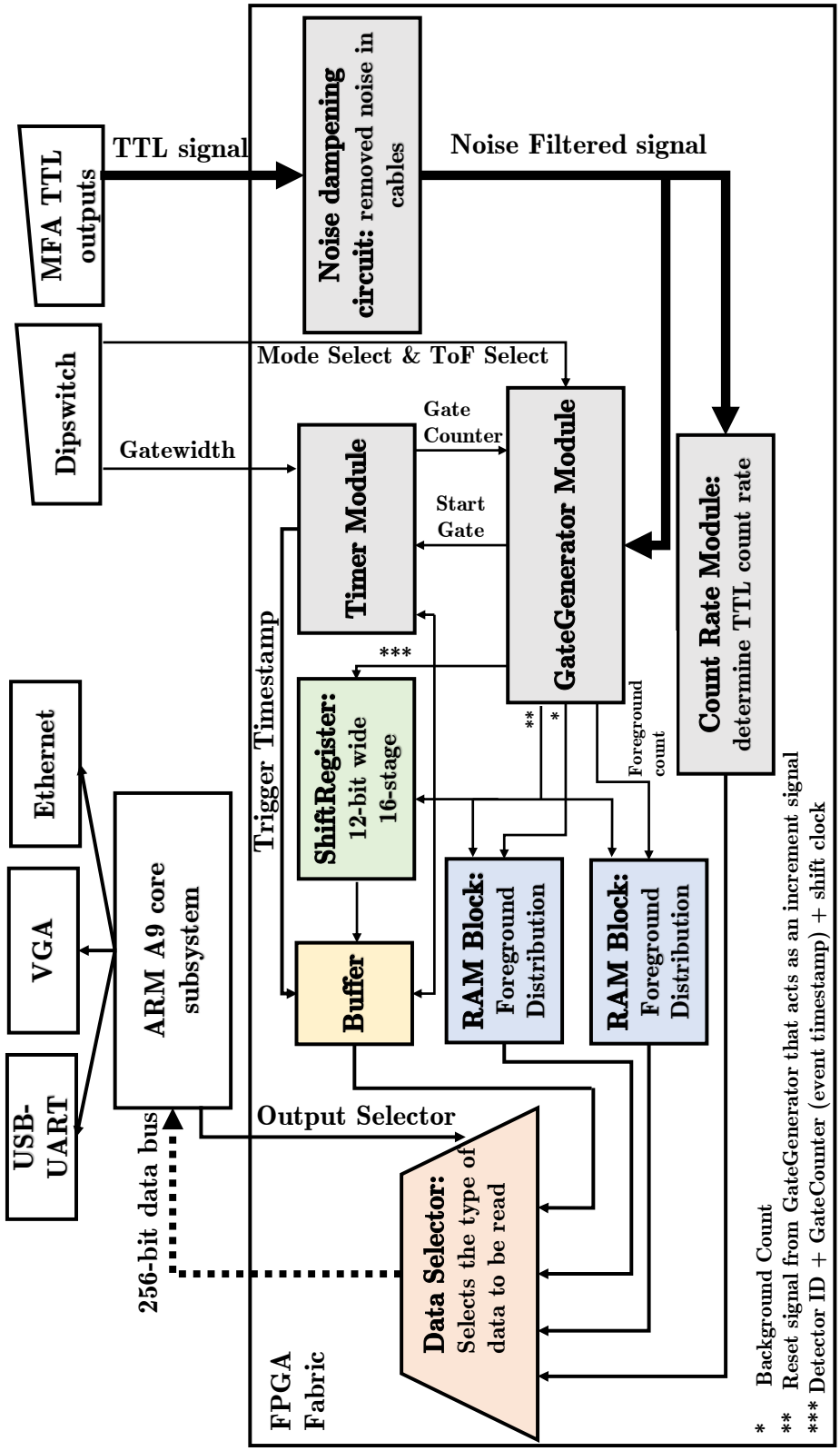

Figure 3.6 | **Schematic diagram of the multiplicity register.** Schematic representation of the different components of the algorithm used to carry out multiplicity and timing analysis of incoming events.

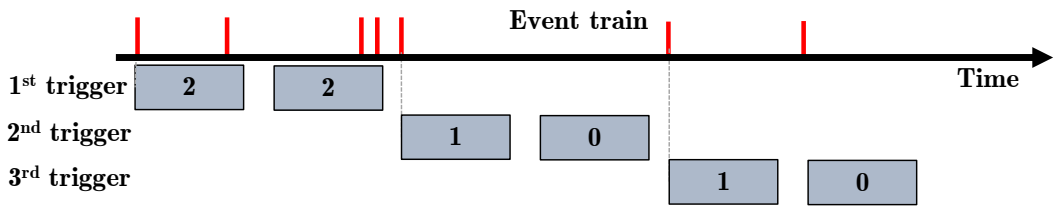

Figure 3.7 | Placement of the coincidence-gates. Illustration of the placement of the two *coincidence-gates* with respect to incoming events demonstrated in the *event-train*. The proposed cluster-size algorithm only issues *coincidence-gates* for unique events thereby creating a distribution corresponding to the size of the incoming clusters.

like a dual-channel asynchronous 512-bit *random access memory (RAM)* block corresponding to 16 *multiplets*, each having a 32-bit counter. The placement of the *coincidence-gates* by this method are shown in figure 3.7, and the resulting distribution reflects the size of the cluster of coincidence events with the different order of *multiplets* referred to as singlets, doublets, triplets, quadruplets, etc. Since the TTL inputs from the MFA are sampled by a 200 MHz clock on the *multiplicity register*, each clock cycle is equivalent to a 5-ns bin.

The algorithm is designed to take 16 TTL inputs from the MFA which can correspond to 16 neutron or γ ray TTLs from 16 detectors, or 8 neutron and 8 γ-ray TTLs originating from 8 detectors. These inputs are classified into two categories: (i) *trigger-events* which correspond to the inputs that can issue new *prompt-gate* or the first event in an *event-train* and (ii) *satellite-events* which cannot issue gates but will count towards the coincidence count. The device can operate in either of the two modes: (i) *Mode 1*, where all 16 TTL inputs can issue *trigger-events* and *satellite-events*, or (ii) *Mode 2*, where 8 TTL inputs are used as *trigger-events* while the remaining 8 TTL inputs act as *satellite-events*. The mode in which the device is to operate is manually set by the user using a dip-switch.

Comparison with shift register method

This proposed method is different from what has traditionally been used in the industry, i.e. the shift-register method detailed in section 2.5.1. The advantage of this method is that it allows for determining the *multiplets* as opposed to the *reduced factorial moment distribution*. However, the resulting *coincidence distributions* can easily be converted to *reduced factorial moment distributions*, thereby allowing the familiarity of the shift-registered method. Such event triggered methods have not had traction in the scientific community, as the *coincidence-gates* in assays using thermal detectors are wide which prevents suchs method from being used in strong radiation fields. However, mixed field analysers using liquid scintillators require significantly narrower *coincidence-gates*, therefore negating such issues.

The proposed method of analysis will allow for the extraction of the *number distributions* of

the emitted radiation, which is a low-level data stream compared to the *reduced factorial moment distributions* produced by the shift-register based method. Therefore, using the proposed method, one may obtain a more in-depth picture of the assay, which would allow new correction models to be developed.

3.2.2 Interval time distribution

The system's "TimerModule" has two counters which can be used for time-stamping purposes. The first is a 32-bit wide counter used for time-stamping the trigger (referred to as *TriggerStamp*) by counting the number of cycles elapsed between subsequent triggers, while the second counter (referred to as *GateCounter* in section 3.2.1) can be used as an analogue to the number of cycles elapsed between the trigger and the detection of subsequent events. Hence, this counter was used for time-stamping the events which arrived within an active *coincidence-gate*. The *idle-gate* and the *delayed-gate* are manually disabled in this method using a dip-switch. During the period when a trigger is issued, each event, including the trigger event, is shifted into a 16-wide shift register consisting of a 12-bit wide structure. The 12-bit data consists of a 4-bit detector identification number (i.e. a numerical number from 0 to 15) and an 8-bit copy of the *GateCounter* (which corresponds to the time elapsed between the trigger and the event in question). At the end of the *gate-width*, the 192-bit data stored in the shift register (i.e. 16-wide x 12-bit) along with the 32-bit *TriggerStamp* is pushed to a buffer. Subsequently an interrupt signal is issued to a subsystem which then reads the data, using which an *interval-time distribution*[1] is constructed (i.e. a variant of the Rossi-α distribution discussed in section 2.5.1 on page 34). This distribution is an array of 256 counters corresponding to the 8-bit *GateCounter* which is then incremented to represent the detection of the event. Since the *multiplicity register* is powered by a 200 MHz clock cycle, each counter represents the passing of 5 ns.

3.2.3 Implementation

The algorithm designed and constructed to run multiplicity analysis in this research was implemented using an Altera Cyclone V SoC 5CSEMA5F31C6 device [120]. The chip combines a FPGA fabric[2] (with up to 85 000 LEs (logic elements)) with a dual-core ARM Cortex-A9 MPCore processor [121] (referred to as the *subsystem* henceforth) surrounded by various sets of peripherals and a hardened memory controller. To reduce development time, Terasic DE1-SoC Development Kit (referred to as *DE1-SoC* henceforth) was used. The board is driven by the above mentioned Alter Cyclone V SoC and enables access to 6 *phase-locked loops (PLL)*,

[1] It corresponds to a series of tightly placed events (in time) that can be assumed to be correlated events from the same fission event.

[2] An FPGA fabric is made up of a two-dimensional array of uncommitted logic elements/blocks and a pool of interconnection resources of wire of various lengths and programmable switches to connect the logic blocks to the wire segments or one wire segment to another to form logic circuits.

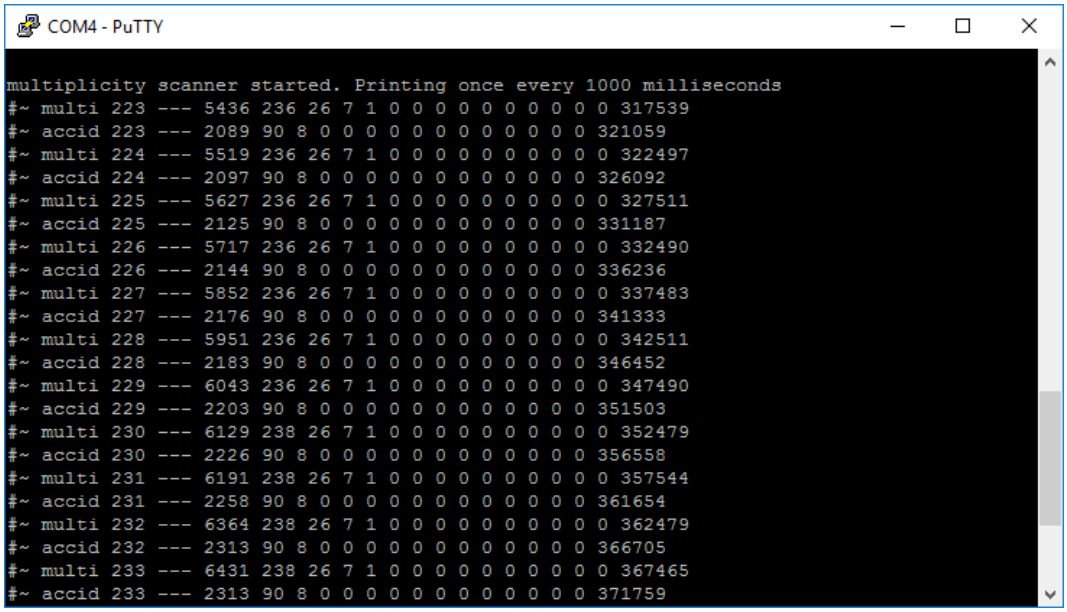

(a) Communicating with the multiplicity register using PuTTY

```
./base9 [-option] [-cnt] [-rst] [-shf] [-v]

PARAMETERS:
[base9]          Name of the executive file.
[-option]
    -p1 [val]    List all incoming events in list mode once
                 every [val] triggers.
    -p3 [val]    Construct the interval-time distribution
                 and print the distribution every [val] triggers.
    -w  [val]    Read and print the foreground and background
                 coincidence distribution every [val] millisecond.
    -r  [val]    Read and print the detector count rates every
                 [val] millisecond.
[-cnt]           When used in conjunction with -r, prints the total
                 counts per detector, instead of count rates.
[-rst]           Reset the device before starting the aquisition
[-shf]           Create the multiplicity histogram using the shift-
                 register algorithm, for validation purposes.
[-v]             Print results via USB-UART, otherwise data is
                 sent via the ethernet.
```

(b) Different available commands.

Figure 3.8 | Controlling the multiplicity register. (a) The FPGA can be connected to a remote computer using a UART port. Utilising any serial terminal emulator, i.e. PuTTY, it is able to control the acquisition and transfer of data. In the screenshot, the *foreground coincidence distribution* and the *background coincidence distribution* are reported once every user defined interval. **(b)** A list of the UNIX terminal commands that are used to acquire and transfer data from the *DE1-SoC* board onto a remote computer. The C program is able to list out the incoming triggers, the interval time distribution, the count rate or total counts. The script also allows for the computation of multiplicity histograms using the shift-register based algorithm.

universal serial bus (USB), *Universal Asynchronous Receiver/Transmitter (UART)* for serial communication, 10/100/1000 Ethernet for network connectivity, 10 dip-switches and 4 push-buttons for multiplicity parameter control, and two 40-pin 3.3V *general purpose input/output (GPIO)* for managing input/output of data signals [122].

The *DE1-SoC* is operated at 200 MHz using the PLL. The TTL outputs from the MFA are fed into the *DE1-SoC* which is flashed with firmware containing the algorithm described in sections 3.2.1 and 3.2.2. The size of the different *coincidence-gates* (i.e. *prompt-gate* and *delayed-gate*) in the algorithm is assigned using the 8 dip-switches as binary inputs. Thus the use of the 8-bit dip-switch leads to an effective range of 0 ns to 1275 ns for the *gate-width*. The remaining 2 dip-switches are used for selecting the Mode of operation (explained earlier in the section) and enabling/disabling the idle and delayed gate. The A9 core of the subsystem operates at 800 MHz and is connected to the FPGA fabric using a 100 MHz bus. The subsystem is running a UNIX distribution with *Lightweight X11 Desktop Environment (LXDE)* which can be accessed either by connecting a monitor, keyboard and mouse, or by connecting a standalone remote computer via UART. By using either of the two methods, a C program is executed from a UNIX console which can either read the two *coincidence distributions* periodically, or the constructed ITD. The results can either be printed on the console (in LXDE or over the UART) (as illustrated in figure 3.8(a)) or can be transmitted via Ethernet. The commands needed to extract the data are listed in figure 3.8(b).

3.2.4 Hardware interlink

Figure 3.9 illustrates a complete setup using the above-implemented instrumentation in conjunction with multiple fast neutron liquid scintillation detectors surrounding a sample source. The detectors' analogue signal and HT leads are connected to the MFA, which powers them and carries out PSD. The TTL outputs from the MFA, which use *Bayonet Neill-Concelman (BNC)* connection with 5V-TTL standard are level shifted to a 3.3 V standard using a daughter board, referred to as the *level-shifter*. This level shifting is required as the FPGA uses a 3.3 V standard. The outputs from the *level-shifter* are connected to the *DE1-SoC* board using a 40-pin GPIO connector. The *DE1-SoC*, which carries out the coincidence analysis, transmits the data either via UART or an RJ45 based 1G Ethernet connector. Close-up images of the *DE1-SoC* is provided in figure 3.10(a), while the *level-shifter* is shown in figure 3.10(b).

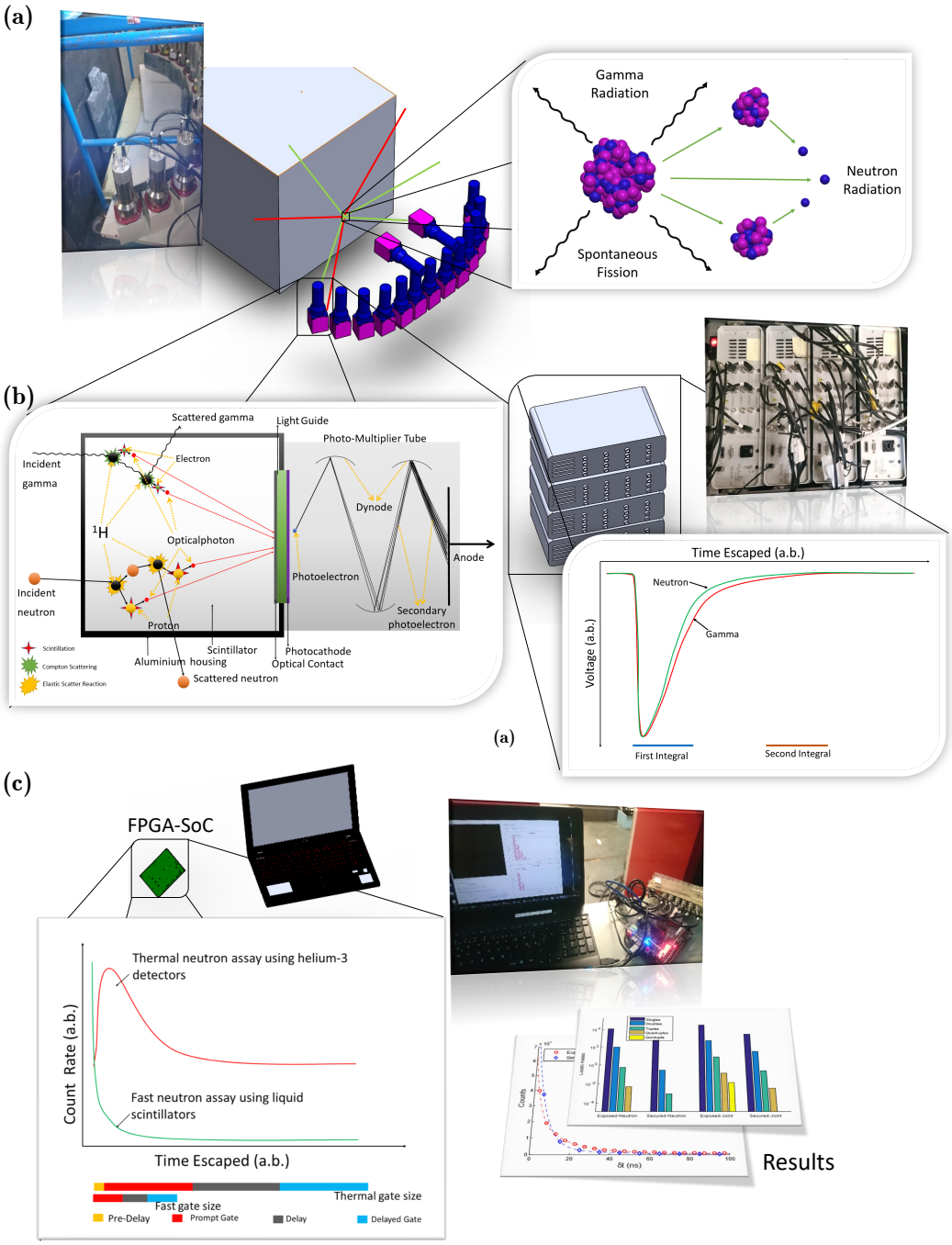

Figure 3.9 | Hardware interlink. (a) A ^{252}Cf nuclei in the source located at the edge of the water tank undergoes spontaneous fission yielding a burst of γ rays and fast neutrons correlated in time with the associated fission event. **(b)** These γ rays and neutrons are detected inside the detectors through Compton scattering and elastic scattering, respectively. The analogue signal is processed by the MFAs, where digitisation and pulse-shape discrimination is used to identify the particles as either γ rays or as neutrons. **(c.)** This information is then passed onto the *DE1-SoC*, where the *interval-time distribution* and neutron *coincidence distributions* are constructed using the appropriate algorithms.

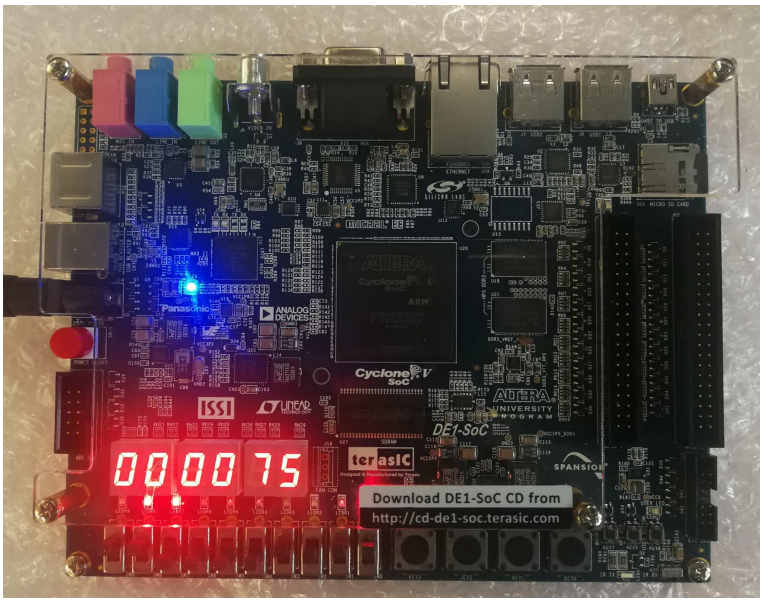

(a) Terasic DE1-SoC Development board.

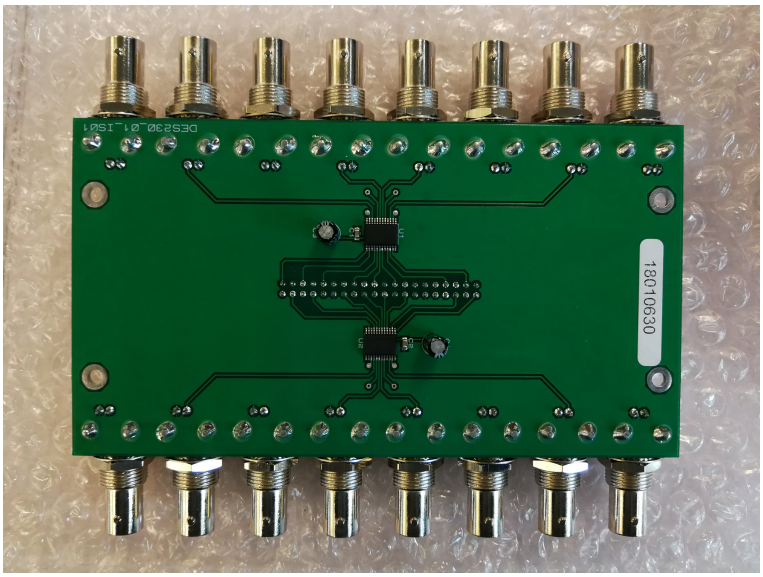

(b) Level-shifter board.

Figure 3.10 | Close-up of the DE1-SoC and the level-shifter. (a) The DE1-SoC development board which was used in the research is pictured. The six-digit 7-segment display shows the size of the *gate-width* in nanoseconds, which can be changed using the dipswitches located right below them. The push buttons can be used to reset the device manually. The 40-pin GPIO cable on the right-hand side of the board is used to input the TTL outputs from the MFA via the *level-shifter* daughter board. **(b)** Since the TTL drives on the MFA use a 5-V standard, while the DE1 board can only accept a maximum voltage of 3.3-V, the TTL outputs were level shifted using this custom *printed circuit board (PCB)*, which also routes the BNC connectors from the MFA to a 40-pin GPIO which the DE1 board supports.

3.2.5 Operational settings of the multiplicity register

Experiments can be conducted in four configurations: Conf-N, Conf-P, Conf-PF and Conf-J. These configurations are explained below, along with any special settings (i.e. Mode 1 or Mode 2) on the *multiplicity register*:

1. *Conf-N:* short for "neutron", in this mode the *coincidence distributions* and *interval-time distributions* are constructed using signals from neutron TTLs from all available detectors which are active. The *multiplicity register* is configured in Mode 1, unless stated otherwise, which means any available detectors may act as *trigger-events* and *satellite-events*. The *gate-width* was selected to be 25 ns when constructing the *coincidence distributions*.

2. *Conf-P:* in this case, P stands for "photon", and the *coincidence distributions* and *interval-time distributions* are constructed using signals from γ-ray TTLs from all available detectors which are active. The *multiplicity register* is configured in Mode 1, unless stated otherwise, which means any available detectors may act as *trigger-events* and *satellite-events*. The *gate-width* was selected to be 20 ns when determining the *coincidence distributions*.

3. *Conf-PF:* in this case, PF stands for "photon-flash", and the *coincidence distributions* and *interval-time distributions* are constructed using signals from both γ-ray and neutron TTLs. The *multiplicity register* is configured in Mode 2, where only 8 TTL inputs, originating from γ-ray TTLs in the MFA act as the *trigger event* for the *coincidence-gates*. The remaining 8 TTL inputs originate from the neutron TTL in the MFA as the source to the *satellite-events* (i.e. events which are recorded). The resulting distributions are photon-flash triggered neutron *interval-time distribution* and *coincidence distribution* and these are used to determine neutron spectroscopy from ^{252}Cf, assuming that the photon-flash is the starting point of the fission event.

4. *Conf-J:* in this case, J stands for "*joint*" events, where both γ rays and neutrons may act as *trigger-events* and *satellite-events*. Using 8 γ-ray TTLs and 8 neutron TTLs outputs from the MFA would essentially limit the number of effective event sensitive detectors for both γ rays and neutrons to 8 detectors each. Hence to avoid this, the PSD parameters in the MFA were altered such that all events are considered as neutrons and hence neutron TTL outputs from the MFA were connected to the *multiplicity register*. The *multiplicity register* is set to operate in Mode 1, so that any events are considered as *trigger-events* and *satellite-events* alike. The *gate-width* was selected to be 35 ns when determining the *coincidence distribution*.

3.3 Experimental setup

In this section, the experimental setups of all the experiments are detailed. There are four unique arrangements that were utilised to determine different parameters such as *interval-time distribution*, *coincidence distribution*, *neutron spectroscopy* and neutron *angular distribution*. The different radioactive samples that were used are detailed in section 3.3.1, while sections 3.3.2 through to 3.3.5 describe the different experimental arrangements.

3.3.1 Sources

Three sources, a 382.2 kBq cobalt-60 (^{60}Co) (15th Oct 2016), a 359.8 kBq ^{137}Cs (15th Oct 2016) and a 397 kBq ^{137}Cs (1st April 2009), were used to calibrate the energy response of the detectors, calibration certificates of the first two sources are included in appendix B.

The ^{252}Cf source used at Lancaster University with the *REFL15* setup yields approximately 10^7 fast, correlated neutrons from spontaneous fission in 4π per second (See appendix B.1). Three other bare ^{252}Cf sources were used with the bare setups, details of which are listed in table 3.1. The Cf-MAIN source is a standardised source contained in a capsule of height $\approx$ 10 mm and a diameter of $\approx$ 4 mm. The Cf-FC source was salvaged from an old fission chamber and was contained inside a sealed tube, while the last source was of unknown origin, but looked like a top-hat, and hence is referred to as the Cf252-TH. Additionally, four americium-lithium (AmLi) sources were used, each of which was stored within a cylindrical canister of height $\approx$ 6.5 cm and diameter $\approx$ 2.5 cm was constructed of 2.74 mm thick tungsten wall. The neutron emission rates of these sources are listed below in table 3.2.

Table 3.1 | Bare californium 252 sources. The neutron emission rates for the three bare ^{252}Cf sources along with their uncertainties are listed. The main ^{252}Cf source with (331541 $\pm$ 3381) n·s^{-1}is a standardised source with the value listed representing its activity on 27th February 2017. The Cf-FC was salvaged from an old fission chamber, while the Cf-TH was concealed in a top-hat shaped containment.

Source	***ID***	***Neutron Emission Rate***			***Comment***
		Value	*Std dev.*	*Units*	
^{252}Cf	Cf-MAIN	331541.1	3381.7	n·s^{-1}	27th Feb 2017, NIST cert.
^{252}Cf	Cf-FC[3]	94917.2	129.6	n·s^{-1}	ORNL estimate
^{252}Cf	Cf-TH[4]	26817.4	45.4	n·s^{-1}	ORNL estimate

In addition to the sources described above, further experiments were conducted using nine standard UOX canisters with radius 4 cm and height 8.9 cm each. Figure 3.11 shows an illustration of the canister's approximate construction. Five of the canisters contained 200 g of U_3O_2 powder with uranium-235 (^{235}U) enrichment of (0.3166 $\pm$ 0.0002)%, (0.7119 $\pm$ 0.005)%

[3]FC stands for Fission Chamber, as the source was salvaged from an old fission chamber
[4]TH stands for Top Hat, as the source looks like a top-hat. It was salvaged from old equipment.

Table 3.2 | Americium-lithium sources. The count rates of the four AmLi sources, which emit single uncorrelated sub-MeV neutrons due to the (α, n) reaction that takes places when the α particles emitted from the americium-241 (^{241}Am) isotope interact with the low-Z lithium isotope. These sources were used to carry out neutron multiplicity analysis and to stimulate *uranium oxide (UOX)* samples for multiplicity analysis using active interrogation methods.

Source	***ID***	***Neutron emission rate***			***Comment***
		Value	*Std. dev.*	*Units*	
AmLi	AMLI1	48860.5	3381.7	n·s^{-1}	
AmLi	AMLI2	49955.1	2770.6	n·s^{-1}	Mid May 2015,
AmLi	AMLI3	34833.8	5765.5	n·s^{-1}	ORNL estimate
AmLi	AMLI4	35012.9	5765.4	n·s^{-1}	

Table 3.3 | Composition of the U_3O_8 canisters. The mass of uranium content, mass content, atomic fraction and mass fraction of the ^{235}U content of the UOX canisters are listed based on their datasheet. This table includes an empty canister with identical composition with the exception of that having no uranium content (empty) which was used for measure the unadulterated AmLi component of the neutron flux.

Enrichment	***ID***	***Mass [g]***		***Fraction [%]***	
		U_3O_8 *mass*	^{235}U *mass*	^{235}U *Atom*	^{235}U *Mass*
Empty	000	Empty canister with no uranium content for background measurement			
0.31%	031	200.1 ± 0.2	0.5370 ± 0.0006	0.3205 ± 0.0002	0.3166 ± 0.0002
0.71%	071	200.1 ± 0.2	1.2184 ± 0.0015	0.7209 ± 0.0005	0.7119 ± 0.0005
1.94%	194	200.1 ± 0.2	3.2981 ± 0.0041	1.9664 ± 0.0014	1.9492 ± 0.0014
2.95%	295	200.1 ± 0.2	4.9878 ± 0.0062	2.9857 ± 0.0021	2.9492 ± 0.0021
4.46%	446	200.1 ± 0.2	7.5593 ± 0.0093	4.5168 ± 0.0032	4.4623 ± 0.0032
20.1%	201	229.99 ± 0.10	39.10 ± 0.04	20.31 ± 0.02	20.11 ± 0.02
52.5%	525	229.93 ± 0.10	101.72 ± 0.10	52.80 ± 0.04	52.49 ± 0.04
93.2%	932	230.04 ± 0.10	181.15 ± 0.12	93.23 ± 0.01	93.17 ± 0.01

wt, (1.9492 ± 0.0014)% wt, (2.9492 ± 0.0021)% wt and (4.4632 ± 0.0032)% wt., while the remaining three contained (229.99 ± 0.10) g of U_3O_2 with ^{235}U enrichment of (20.31 ± 0.02)% wt, (52.80 ± 0.04)% wt and (93.23 ± 0.01)% wt. The last canister, which is identical to its counterparts in dimensions, however has no uranium content present and hence was used to measure the neutron activity from the AmLi sources which were used for interrogating the UOX samples. This information is also summarised in table 3.3.

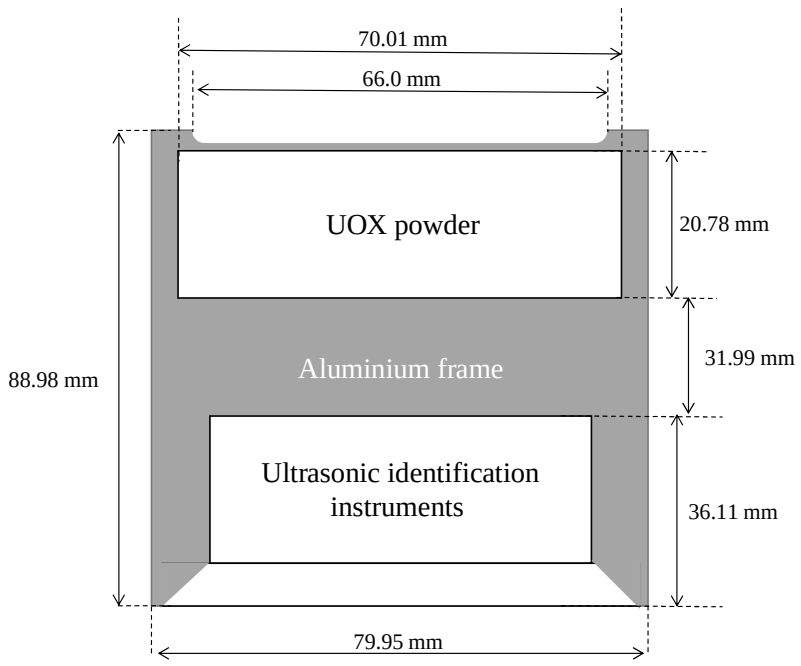

Figure 3.11 | Radioactive sources used in the experiments. Schematic illustration of the UOX canisters that were used in the experiments (not to scale). The cans were placed such that the filling containing the UOX powder was facing upwards.

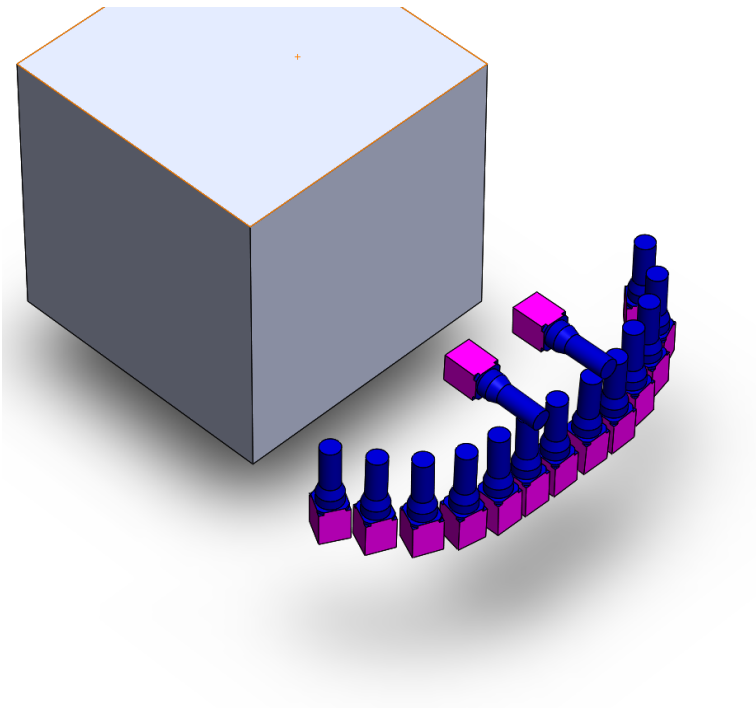

Figure 3.12 | Schematic of the reflective setup (REFL15). The ^{252}Cf source located at the centre of the water tank undergoes spontaneous fission yielding a burst of γ rays and fast neutrons correlated in time, angular position and energies. When placed at the centre of the tank, the neutrons are thermalised by the water from all directions, thereby severely limiting the extent to which neutrons can escape the water tank. This is referred to as the *secured* position. When in *exposed* state, the source is shifted toward the front face of the tank, reducing the volume of moderating water and allowing fast neutrons to escape the tank and interact with the array of 15 detectors. Diagram not to scale.

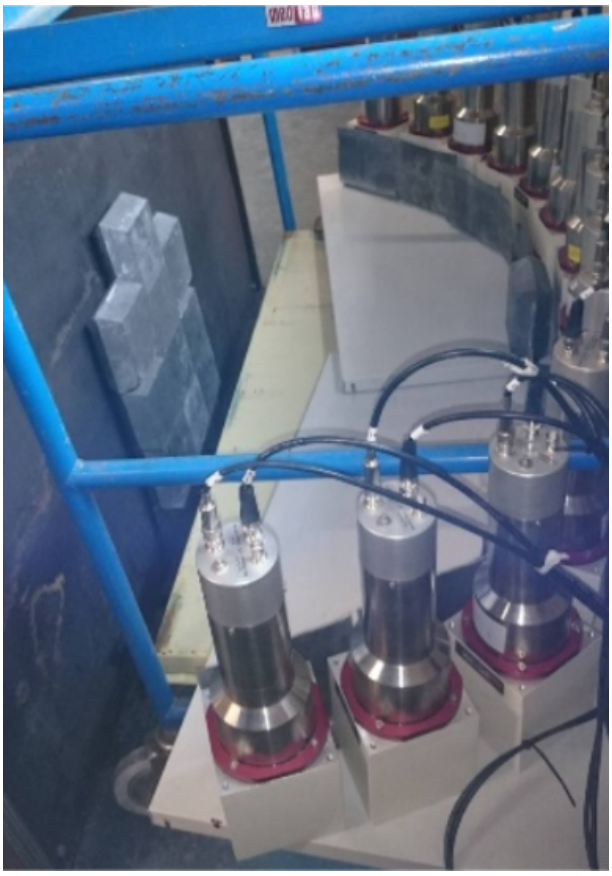

Figure 3.13 | Reflective setup. A photograph of the *REFL15* setup which shows the detectors being supported by a metal trolley.

3.3.2 Reflective arrangement with 15 detectors (REFL15)

In the neutron laboratory at Lancaster University (Lancaster, UK), a 75 MBq ^{252}Cf source is stored inside a light water bath. The water is contained in a 1 m × 1 m × 1 m fibre-glass tank, which is itself sealed inside a 1.5 m × 1.5 m × 1.5 m steel containment. The source is located in the water, 30 cm above the floor of the laboratory and configured in such a way that a pneumatic drive can move the source from the centre of the water volume (where it is stored when not in use, known as the *secured* position) to the periphery of the tank to yield radiation external to the tank for experimental purposes (known as the *exposed* position). Experiments were carried out with the source in both the *secured* and *exposed* positions, the results from these are labelled as *Secured* and *Exposed*. Therefore,

1. When in the *Exposed* mode, most of the correlated neutrons escape from the front face of the water tank.

2. In the *Secured* mode, the neutrons are thermalised in all 4π directions and hence only a very limited number of correlated neutrons can escape.

The 15 detectors were arranged in two rows along the face of the tank, as shown in figure 3.12 and figure 3.13. The ^{252}Cf is exposed to the detectors by bringing it towards the front face of the water tank. The detectors are positioned in an arc to cover the flux emitted from the front face of the water tank. The first row of detectors comprised of thirteen EJ-309 organic scintillation detectors (Scionix, Netherlands) was placed around the front face in an elliptical shape 40 cm above the laboratory floor, on top of a steel trolley. The smallest distance between the source in the tank and a detector in the ellipse was 0.4 m while the longest was 0.75 m to accommodate space constraints imposed by the structure of the laboratory walls. This tight elliptical setup had to be realised due to the limited clearance between the tank and the wall of the laboratory, which further promotes the reflective nature of the arrangement. Two additional detectors were placed in a second row at a distance of $\approx$ 1 m above the floor. In this arrangement, there was a gap of $\approx$ 2 cm between the thirteen detectors and a gap of 30 cm between the two detectors positioned in the top row.

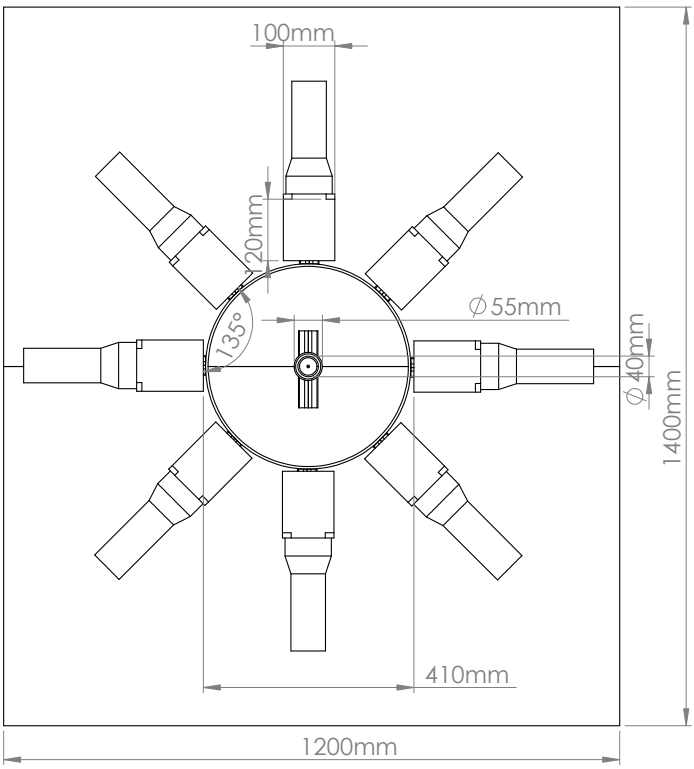

Figure 3.14 | Schematic of the 8-detector arrangement (BARE8). The distance from the source to the detector was 20.5 cm, while the angle between two adjacent detectors was 45˚when measured from the centre of the arrangement. Depending on the experimental needs, either a ^{252}Cf, or UOX and AmLi source were positioned at the centre. Additionally, a 0.4 cm thick cylindrical lead shielding of 20 cm radius was placed around the source to reduce the γ-ray flux.

3.3.3 Bare arrangement with 8 detectors (BARE8)

This arrangement was realised at the Oak Ridge National Laboratory (Tennessee, USA) and was paired with the different ^{252}Cf, AmLi and UOX sources as listed in section 3.3.1. Eight EJ-309 detectors were placed in a ring on top of an aluminium table 1 m above the floor with the sources positioned at the centre of the detectors. The distance from the source to the face of the detector was 20.5 cm for the eight-detector setup. This resulted in a corresponding angular separation of 45˚ between the detectors shown schematically in figure 3.14. Each of the detectors were placed on top of a 3.8 cm metal support to increase clearance between the table and the detectors. A thin lead shield of 0.4 cm thickness was placed between the detectors and the source to reduce the γ-ray flux when the neutron field was being measured. This sheet of lead, folded into a circle with a radius of 20 cm, was 0.4 cm thick and 20 cm high.

The ^{252}Cf source was lifted approximately 8.5 cm from the table to align it with the horizontal axis of the detectors using hollow aluminium supports, as shown in figure 3.15(a).

When using the UOX samples, which were described in section 3.3.1, the experiment did not

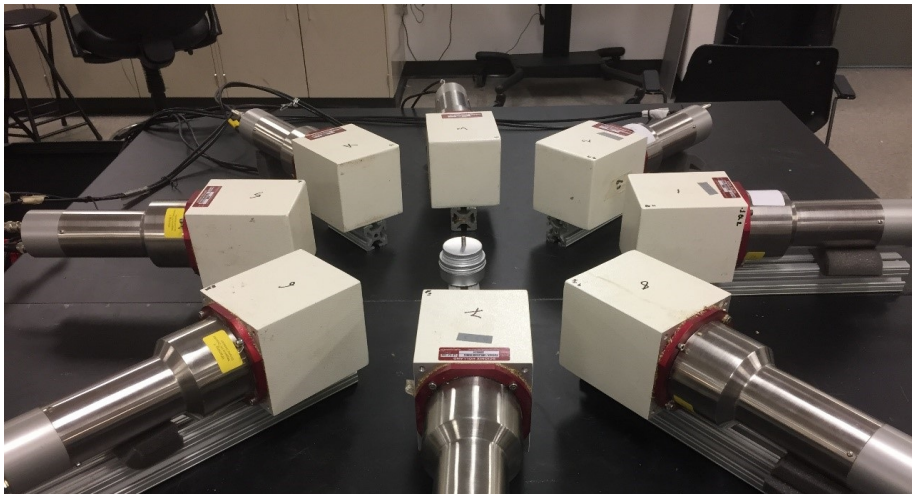

(a) BARE8 setup with ^{252}Cf source.

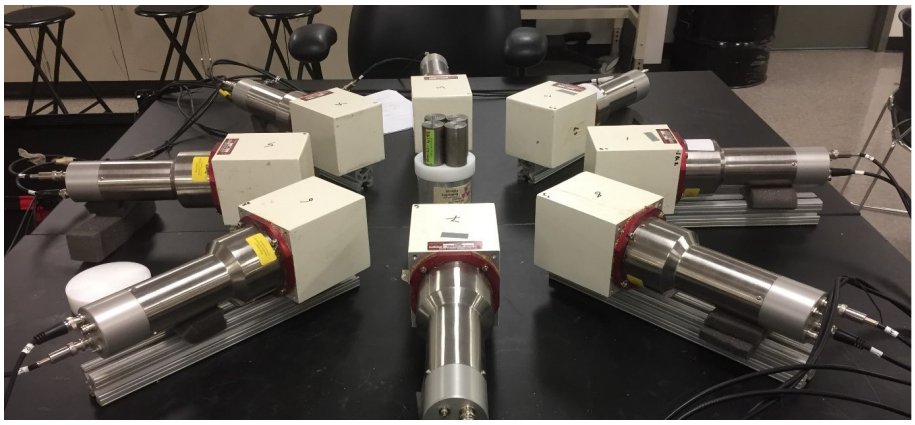

(b) BARE8 setup with UOX and AmLi sources.

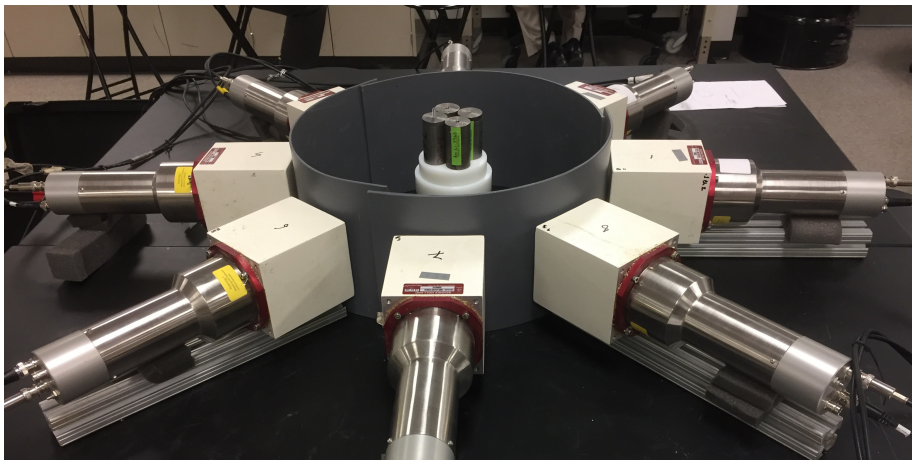

(c) Top view of the BARE8 setup with lead shielding.

Figure 3.15 | Examples of BARE8 Setup. Bare setup utilising **(a)** a ^{252}Cf and **(b)** UOX and AmLi setup. The lead shielding was removed for clarity of setup. **(c.)** Illustrates the arrangement with the lead shield.

require such support due to the construction of the canister in which the source was sealed, as can be observed in figures 3.15(b) and 3.15(c) (with and without lead shielding). These canisters were placed at the centre of the detector arrangements described above. Four AmLi sources, described in section 3.3.1, were placed on top of the UOX canister to provide the stimulating neutrons for inducing fission in the UOX sample. To thermalise the neutrons from the AmLi sources, depending on the experimental requirement, one or two polyethene disk(s) of 4.1 cm and 4.3 cm radius were placed between the UOX canister and the AmLi sources. One of the disks had a thickness of approximately 2 cm while the other had a thickness of approximately 1.75 cm. Hence the effective thickness of moderator was either approximately 2 cm or 3.75 cm.

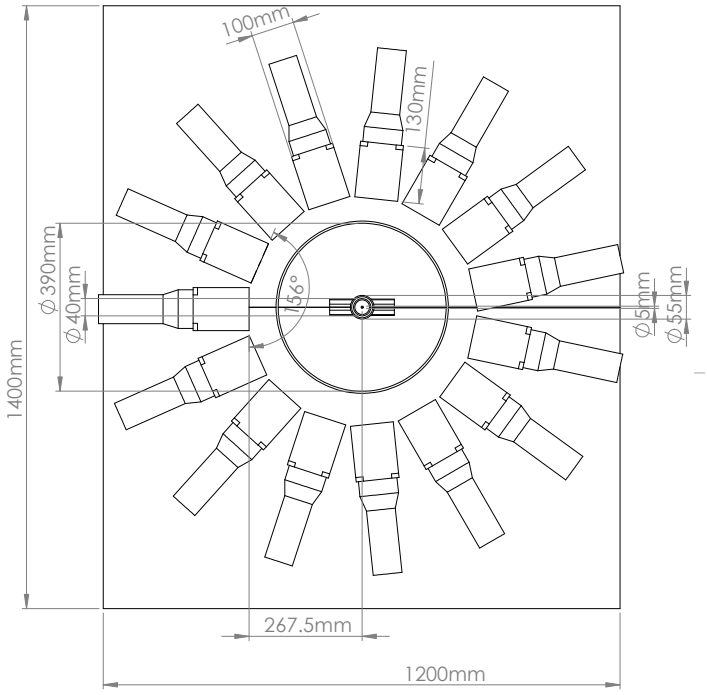

Figure 3.16 | Schematic of the 15-detector arrangement (BARE15). The distance from the source to the detector was 26.25 cm, while the angle between two adjacent detectors was 24° when measured from the centre of the arrangement. Depending on the experimental needs, ^{252}Cf, or UOX and AmLi sources were positioned at the centre. Additionally, a 0.4 cm thick cylindrical lead shielding of 20 cm radius was placed around the source to reduce the γ-ray flux.

3.3.4 Bare arrangement with 15 detectors (BARE15)

This arrangement, like the *BARE8*, was also realised at the Oak Ridge National Laboratory (Tennessee, USA) with different ^{252}Cf, AmLi and UOX sources. Fifteen EJ-309 detectors were placed in a ring on top of an aluminium table 1 m above the floor with the sources positioned at the centre of the detectors. The distance from the source to the face of the detector was 26.25 cm for the fifteen-detector setup. This resulted in a corresponding angular separation of 24° between the detectors as can be observed in figure 3.16. Each of the detectors were placed on top of a 3.8 cm metal support to increase clearance between the table and the detectors. Certain experiments utilised a thin lead shield of 0.4 cm thickness, which was placed between the detectors and the source to reduce the γ-ray flux when the neutron field was being measured. The lead shielding was shaped into a circle with a radius of 20 cm, was 0.4 cm thick and 20 cm high.

Like in the *BARE8* setup, when using ^{252}Cf, the source was lifted approximately 8.5 cm from the table to align it with the horizontal axis of the detectors using hollow aluminium supports. This setup was used to determine the Rossi-α distribution, as well as the *coincidence distributions*.

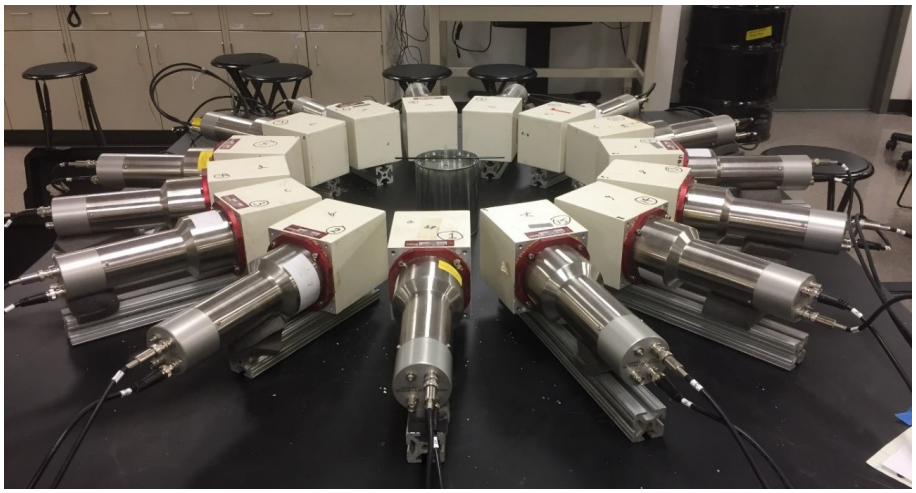

(a) Setup used for measuring neutron spectrum.

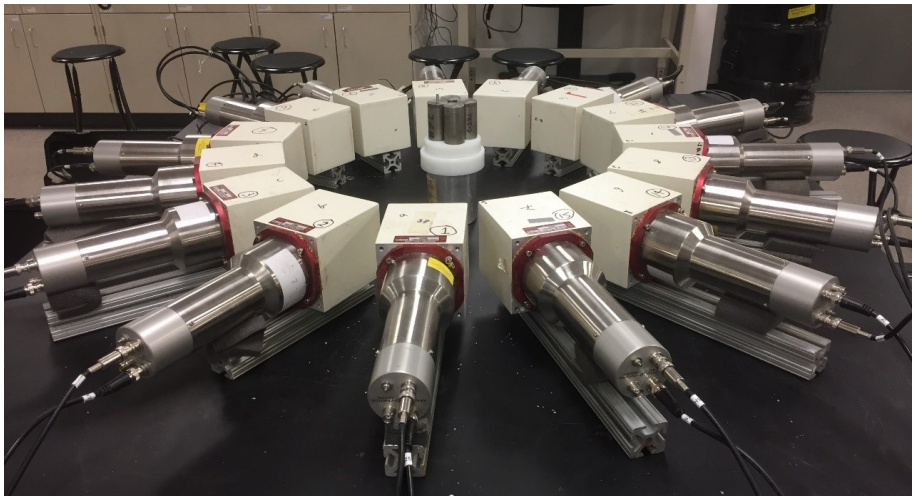

(b) Setup used for measuring UOX multiplicity.

Figure 3.17 | Examples of BARE15 Setup. Bare setup utilising **(a)** a ^{252}Cf source which was submerged into a water-filled cylinder of radius 5 cm and **(b)** UOX samples being irradiated with AmLi. The lead shielding was removed for clarity.

This setup was also used for the experimental determination of neutron spectrum from ^{252}Cf by placing the Cf252-MAIN source at the centre of the arrangement. To change the hardness of the spectrum, the source was submerged in water which was contained in three different cylinders of radius approximately 1 cm, 3 cm and 5 cm. Figure 3.17(a) illustrates the setup with a water-filled cylinder with a radius of 5 cm.

When using the UOX samples, which were described in section 3.3.1, the experiment did not require such support due to the construction of the canister in which the source was sealed. These canisters were placed at the centre of the detector arrangements described above. Four AmLi sources described in section 3.3.1 were placed on top of the UOX canister to provide the stimulating neutrons for inducing fission in the UOX sample. To thermalise the neutrons from the AmLi sources, depending on the experiment requirement, one or two polyethene disk(s) of

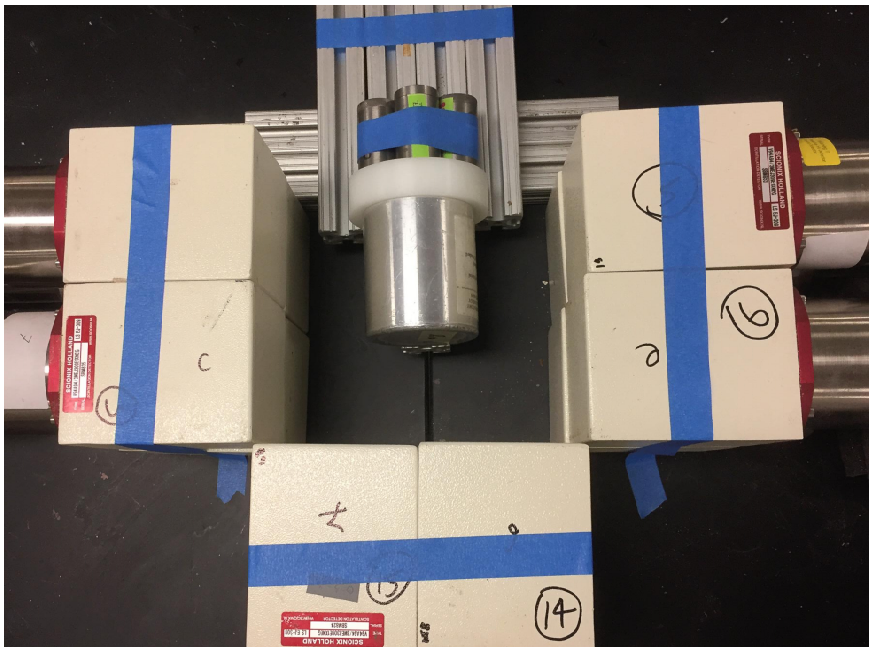

Figure 3.18 | A frontal picture of the 12-detector block arrangement (CASTLE12). (a) A frontal picture of the castle setup using three blocks of 2x2 scintillation detectors which were tightly placed to form a three-sided square shape of 20 cm length. A 2 cm polyethene block was placed between the UOX canister and the AmLi to encourage thermalisation of the neutron from AmLi to induce fission in the UOX sample. **(b)** Illustration of all the measurements of the arrangement.

4.1 cm and 4.3 cm radius were placed between the UOX canister and the AmLi sources. One of the disks had a thickness of 2 cm while the other had a thickness of 3.75 cm. The setup is illustrated in figure 3.17(b).

3.3.5 Castle arrangement with 12 detectors (CASTLE12)

The final arrangement realised at the Oak Ridge National Laboratory (Tennessee, USA) consists of twelve detectors in a castle formation and the UOX sources described in section 3.3.1. Three 2×2 stacks of closely-packed EJ-309 detectors were placed as three sides of a square arrangement with one open end, from where the sample is introduced. This is illustrated in figure 3.19. The arrangement was placed on top of the aluminium table 1 m above the floor. The UOX canister was placed horizontally (i.e. on its side) approximately 15 cm from the 2×2 detector stack exactly opposite to it, such that the UOX sample inside the canister is positioned approximately 20 cm from that face of four detectors. Additionally, the canister was lifted ≈ 3.8 cm from the table using aluminium supports. The four AmLi sources were also placed horizontally (i.e. on the longest axis) and were positioned such that they were approximately at the canister centre. To thermalise the neutrons from the AmLi sources, one polyethene disk of 4.3 cm radius and 2 cm thickness was placed between the UOX canister and the AmLi sources.

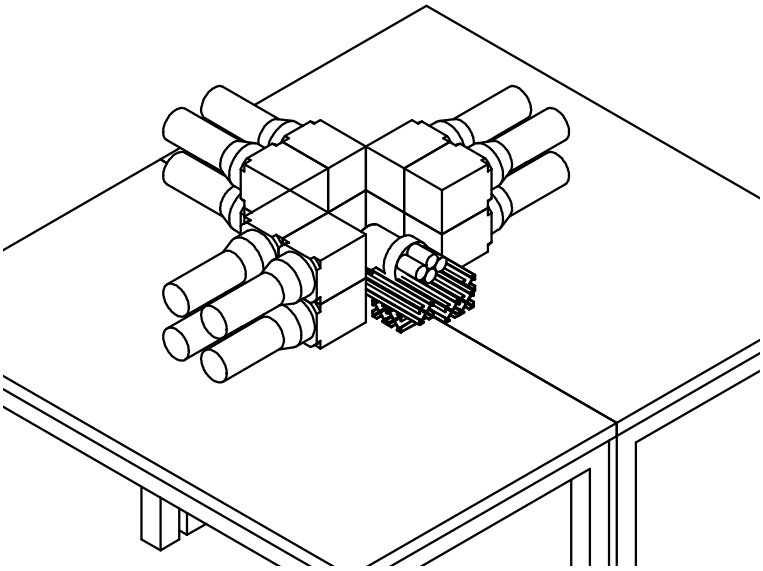

(a) Isometric schematic of the 12-detector CASTLE12 arrangement.

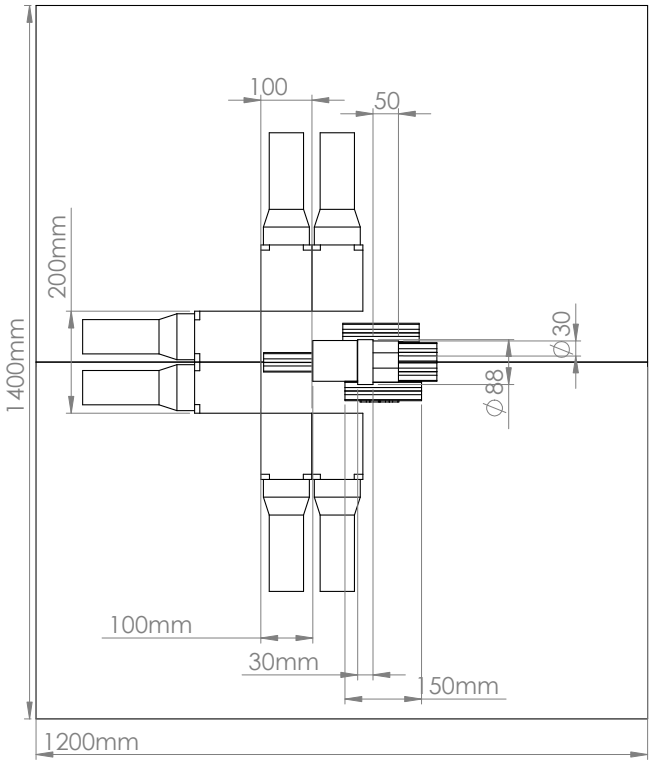

(b) Schematic of the 12-detector CASTLE12 arrangement.

Figure 3.19 | Schematic of the 12-detector block arrangement (CASTLE12). (a) Schematic of the castle setup using three blocks of 2x2 scintillation detectors which were tightly placed to form a three-sided square shape of 20 cm length. The source was placed such that the UOX sample inside the canisters was positioned approximately 20 cm from that face of the "inside" 2×2 stack. A 2 cm polyethene block was placed between the UOX canister and the AmLi to encourage thermalisation of the neutron from AmLi to induce fission in the UOX sample. **(b)** Illustration of all the dimensions of the arrangement.

3.4 Implementation of experiments

The different types of experiments were conducted with different analytical goals and were carried out utilising the various setups that are mentioned in section 3.3.2 through to section 3.3.5. A summary of the experiments are listed below:

1. *Interval-time distribution:* These experiments were conducted using both *REFL15* and *BARE15* setups by determining the *interval-time distribution*. The analysis was done for neutron-only signals, γ-only signals and also *joint* neutron-γ signals, i.e. the *multiplicity register* was configured such as to correspond to Conf-N, Conf-P and Conf-J, respectively, as described in section 3.2.5 on page 73.

2. *Neutron spectroscopy:* These experiments were carried out using ^{252}Cf source by utilising the *BARE15* setup. The multiplicity configuration was set as Conf-PF when determining the *interval-time distribution* making it akin to neutron spectrum.

3. *Angular correlation distributions:* These experiments were carried out using ^{252}Cf by utilising the *BARE15* setup in Conf-N to extract neutron angular correlation. This analysis was not done in real-time, but rather a list of correlated events were dumped using the "-p1 1" on the UNIX C script detailed in in figure 3.8(b), which was then post-processed using a C++ script (see appendix D.7).

4. *Passive coincidence distributions:* These experiments were carried out using ^{252}Cf, AmLi, ^{60}Co and ^{137}Cs using the *REFL15* and *BARE15* setups for neutron, γ-ray and *joint* neutron-γ signals, and hence the *multiplicity register* was configured such as to correspond to Conf-N, Conf-P and Conf-J, respectively, as described in section 3.2.5 on page 73.

5. *Active coincidence distributions:* These experiments were carried out using standardised UOX with AmLi as the stimulant. Only neutron signals were recorded using the *BARE8*, *BARE15* and *CASTLE12* setups with the *multiplicity register* configured to Conf-N.

3.5 Method of calibration

Calibration of the system was done in three distinct steps with the objective of firstly calibrating the individual detector response followed by the calibration of the total cumulative assay response. The first two steps were carried out to calibrate the energy response to incoming radiation and to properly discriminate between neutron and γ-ray events, respectively. However, despite a proper calibration of individual detectors, it was observed that the number of events being registered in individual detectors in a given assay varies in excess of 10% from detector to detector. Additionally, due to unequal source-to-detector distance of the elliptical detector arrangement in the REFL15 setup described in section 3.3.2, the detected number of events per second per detector was biased towards the detectors that were nearest to the source. To negate any effect on the *interval-time distributions* and *coincidence distributions* originating due to this bias, the final step involves an assay-wide calibration to ensure that the count rate on each channel was within 5% of each other.

The three system calibration steps performed are as follows:

1. *Energy calibration:* Firstly, a detector trigger threshold of 200 ADC bins[5] was assigned for all detectors. Next, from the MCA window (see figure 3.20(a)), the HT voltages of the detectors were altered to ensure that the Compton edge of the spectrum using a ^{137}Cs calibration source appeared at the same position in the x-axis. This ensures that responses from all detectors are energy calibrated and hence identical. The Compton edges for ^{137}Cs source (i.e. 478 keVee[6]) and the 200 keVee threshold were measured at approximately 1100 and 550 ADC channel, which results in a calibration curve of $y = 0.5x - 78$, where y is the calibrated light output in keVee and x is the ADC channel.

2. *Event type calibration:* This step of the calibration process involves the fine-tuning of the PSD parameters to ensure that proper discrimination of γ-ray and neutron events was carried out. This calibration was done using a ^{252}Cf source as it emits both neutron and γ-ray radiations. This is accomplished from the PSD window, as illustrated in figure 3.20(b).

3. *Detector count rate response:* The *multiplicity register* has an algorithm which determines the counter rate and total counts from individual detectors (see figure 3.20(c)) and, using this information, the detector's trigger threshold is altered to ensure that the count rates of individual detectors in the assay are to be approximately within 5% of each other when using a ^{252}Cf source.

[5]The difference between the two subsequent ADC samples must be more than 200 before an event can be registered.

[6]Light output in electron equivalent energy.

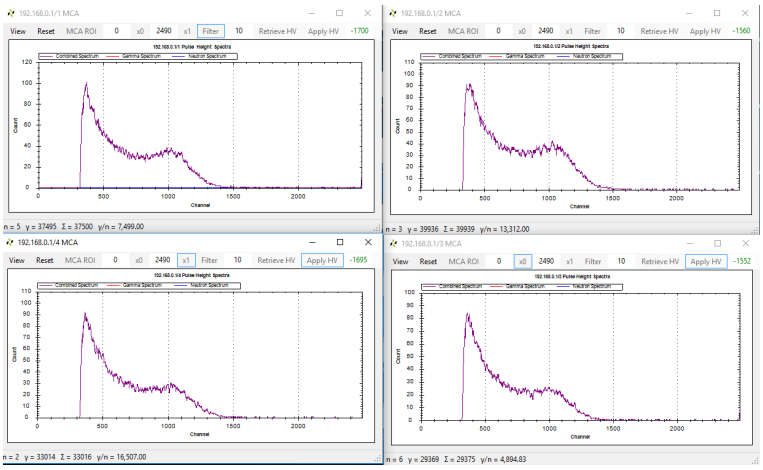

(a) HT supply calibration.

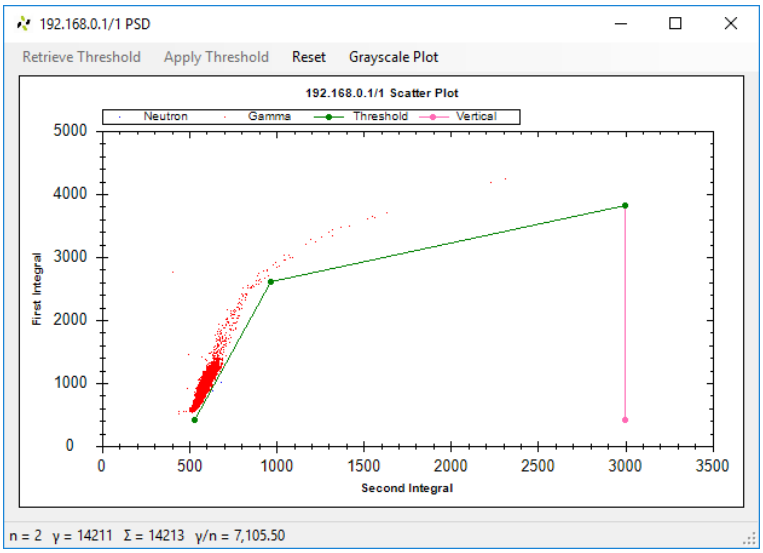

(b) PSD calibration.

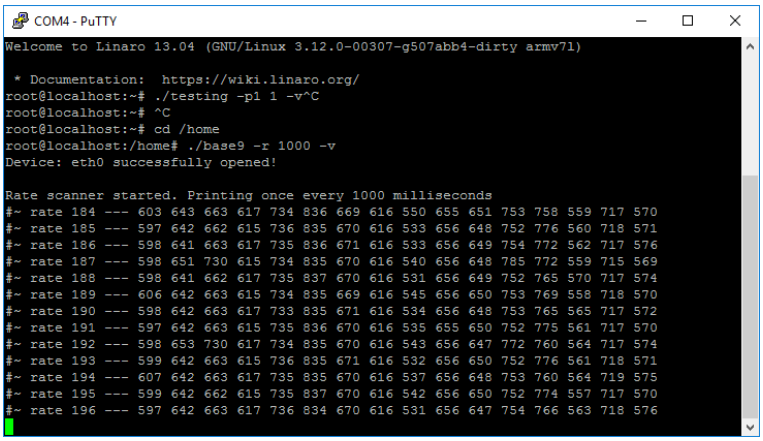

(c) Detector count-rate calibration.

Figure 3.20 | Calibration of instrumentation. Calibration was carried out in three steps: **(a)** The HT supply was configured such that the Compton edge for the 662 keV γ-ray line from ^{137}Cs was registered in the same ADC channel (i.e. x-axis) for all detectors. **(b)** the three-point line was configured in the PSD scatter plot such that the neutrons and gamma plumes are correctly separated. **(c)** the count rates for individual detectors were ensured to have approximately similar rates by altering the detector threshold from the MFA configuration window (see figure 3.4 on page 62).

3.6 Isotopic simulations

In this investigation, the evolution of isotopic composition of *spent nuclear fuel (SNF)* with time, and hence the correlated neutron emission rate arising from spontaneous fission and (α, n) reactions, is analysed to determine the presence of curium in both *mixed-oxide (MOX)* and UOX fuel. Given the current imperative to decarbonise global electricity supply networks and the key role that fission-based nuclear power is likely to play in this context in the near term, detailed knowledge of the critical dependencies in managing SNF is likely to remain an enduring global requirement. The objective of the analysis presented in this section is to quantify the evolution of the isotopic composition of curium in SNF with cooling-period, and hence to forecast its contribution towards correlated neutron emission arising from spontaneous fission and (α, n) reaction pathways in terms of the factorial moment distribution of the neutron number density for relevant isotopes. This will provide added context towards the reasoning behind the desire to use fast neutron assays for characterization of nuclear materials.

Two typical MOX fuels used in the *Pressurized Water Reactor (PWR)* and *Boiling Water Reactor (BWR)* in Beznau (Switzerland) and Dodewaard (The Netherlands) with approximately 6% plutonium content and natural oxides (i.e. 0.04% of oxygen-17 (^{17}O) and 0.20% of ^{18}O) have been modelled. For comparison, a UOX fuel of 4.2% enrichment was also considered from the Gösgen (Switzerland) PWR reactor. The initial composition of all the fuel types is provided in table 3.4 [123]. Other input parameters include the reactor operation conditions, namely that the reactors were operated at full power, with fully retracted control rods. Additionally, the BWR reactor was operated at 40 % void. The evolution of these isotopes should also depend strongly on the neutron spectrum which is used to deplete the fuel, i.e. whether it is hard or soft, as well as the position of the fuel pin in the reactor. This study aims to help understand the general dynamics of the process at hand in the context of specific isotopes.

These simulations were conducted using FISPIN [96], which is a fuel depletion code that calculates the changes in the numbers of atoms of the nuclides of various species and their activities (due to γ-ray, spontaneous fission or (α, n) activities) for periods of irradiation and cooling. The simulations were carried out at the *National Nuclear Laboratory (NNL)* at their Sellafield site, while the analysis was done at Lancaster University. The fuels were irradiated to burn-up of (10, 20, 35 and 55) GWd·MTU^{-1} (i.e. giga-watt day per metric tonne of uranium) using FISPIN in 10 equidistant time-steps. These burn-up levels were selected taking into consideration that most spent nuclear fuel awaiting disposal falls into these ranges. Once the desired burn-up was achieved in these FISPIN simulations, the fuel element was then cooled for 4750 days ($\approx$ 13 years) using the following time-steps: (10, 20, 30, 40, 50, 75, 100, 125, 150, 175, 200, 250, 300, 350, 400, 450, 500, 600, 700, 800, 900, 1000, 1200, 1400, 1600, 1800, 2000, 2250, 2500, 2750, 3000,

Table 3.4 | Composition of the fuel elements. The initial isotopic composition in terms of atomic number density and relative fraction of the mixed-oxide fuel element studied in this work [123].

Isotope	***PWR MOX (Beznau)***		***BWR MOX (Dodewaard)***		***PWR UOX (Gösgen)***	
	Density (atom/ MTU)	*Fraction*	*Density [atom/ MTU]*	*Fraction*	*Density [atom/ MTU]*	*Fraction*
^{16}O	5.05×10^{27}	6.639×10^{-01}	5.05×10^{27}	6.642×10^{-01}	5.05×10^{27}	6.642×10^{-01}
^{17}O	2.02×10^{24}	2.662×10^{-04}	2.02×10^{24}	2.663×10^{-04}	2.02×10^{24}	2.663×10^{-04}
^{18}O	1.01×10^{25}	1.331×10^{-03}	1.01×10^{25}	1.331×10^{-03}	1.01×10^{25}	1.331×10^{-03}
^{235}U	5.59×10^{24}	7.354×10^{-04}	5.73×10^{24}	7.531×10^{-04}	1.02×10^{26}	1.348×10^{-02}
^{238}U	2.39×10^{27}	3.136×10^{-01}	2.36×10^{27}	3.104×10^{-01}	2.43×10^{27}	3.193×10^{-01}
^{238}Pu	8.39×10^{23}	1.103×10^{-04}	2.28×10^{24}	3.004×10^{-04}	0	0
^{239}Pu	9.16×10^{25}	1.204×10^{-02}	1.00×10^{26}	1.317×10^{-02}	0	0
^{240}Pu	3.20×10^{25}	4.208×10^{-03}	3.77×10^{25}	4.958×10^{-03}	0	0
^{241}Pu	9.01×10^{24}	1.184×10^{-03}	1.42×10^{25}	1.864×10^{-03}	0	0
^{242}Pu	3.62×10^{24}	4.755×10^{-04}	7.27×10^{24}	9.560×10^{-04}	0	0
^{241}Am	1.26×10^{24}	1.655×10^{-04}	1.82×10^{24}	2.392×10^{-04}	0	0

3250, 3500, 3750, 4000, 4250, 4500 and 4750) days.

3.7 Monte Carlo simulations

When creating Monte Carlo simulation models for the stochastic study of the response of fast neutron detectors, there are two very important physical aspects of the assay that need to be preserved: (i) the correlation between the emitted particles from spontaneous and induced fission; and (ii) the non-linear behaviour of liquid scintillation detectors when exposed to neutron radiation as illustrated in figure 3.2 on page 60.

As explained in section 2.7.2 on page 50, for satisfactory event-by-event stochastic analysis of correlated particles that are emitted from materials under assessment, it is important to employ a nuclide-wise fission distribution, such as the models described in section 2.3.1 on page 27. Additionally, there are several approaches to solving the non-linear response of scintillation detectors, as described in section 2.7.3 on page 52, with the most common practice involving a post-processing script to convert the deposited energy to light output using an empirical formula [107].

In this research, Geant4 version 10.2.2 was used to simulate the different experimental setups as it has built-in physics models to simulate the optical processes that take place inside a scintillation detector. Additionally, it is possible to couple Geant4 with the latest C++ FREYA libraries (version 2.0.3) to model the correlated particles from fission of a variety of isotopes. The validity of Geant4 calculations in neutron transport has been shown to have comparable results to MCNPX in the past [124], whilst the light output model has also been widely studied and validated [111, 113].

3.7.1 Implementation

The Geant4 model is multi-thread ready[7] and was executed in the *High-End Cluster (HEC)* at the Lancaster University. When the Geant4 executable is launched, it requires certain parameters. These parameters define the different properties, i.e. type of geometry, particles, fission mode, seed to random number generators, etc., to carry out the simulations. Figure C.1 on page 222 lists these parameters along with their explanations. Different segments of the code were based on several examples provided with the Geant4 toolkit, as will be discussed further below.

The geometries of all the experiments are stored in the *DetectorConstructor* class which initialises the material components and the geometries by calling the "DefineMaterial()" and

[7] Able to utilize multiple processing core present in modern computers.

"Construct()" methods. Following the completion of this process, the physics models in PhysicsList.cpp are initialised (see appendix C.3, page 234). To take account of the corresponding transport physics, a custom physics list based on the Geant4 distributed QGSP BIC HP [125] was created. This included *G4HadronElasticProcess*, *G4ParticleHPElastic*, *G4NeutronInelasticProcess* and *G4ParticleHPInelastic* to model the scattering of different particles with materials, while the absorption reactions were modelled using the *G4HadronCaptureProcess*, *G4ParticleHPCapture*, *G4HadronFissionProcess* and *G4ParticleHPFission* models. These *high-precision (HP)* models were used in conjunction with the G4NDL4.5 neutron data library and thermal cross sections derived largely from the *Evaluated Nuclear Data Library (ENDF/B-VII)* [126]. The standard electromagnetic model of Geant4 was used for γ rays (see appendix C.3). These models were based on two examples provided with the Geant4 source code. The optical response from a scintillation detector was modelled with *G4OpticalPhysics* (see appendix C.3). Scintillation was done based on the particle type, i.e. electron or proton. The scintillation yield from electrons and protons are plotted in figure 3.2 on page 60 [118] (see appendix C.2, page 226). While literature measurements of the light yield functions for scintillators are typically very good and the only source of input data, these measurements are specific to the characteristics of the detector (i.e. geometry, volume, internal reflection, etc.), which can result in deviations from expectations if applied to a strongly differing case. This methodology also accommodates for amount of light being absorbed by taking into account the quantum efficiency of the PMT. A similar method was implemented in reference [111].

In the next stage, the particle generator is called by the simulator to sample a vertex of initial particle definitions such as energy, particle type, direction, etc. (see appendix C.4, page 238). Based on the user input (see figure C.1), the model is able to simulate a mono-energetic neutron or γ-ray source which may either be emitted along a mono-directional particle beam or into 4π. The code is also able to simulate ^{252}Cf, ^{60}Co and AmLi sources.

The ^{252}Cf source is modelled meticulously using the *Fission Reaction Event Yield Algorithm (FREYA)* model which is instantiated inside the *SponFis* class (see appendix C.4, page 238). The code is based on a worked example provided by the FREYA developers. Every vertex generated corresponds to individual fission events, and hence they contain multiple neutrons and γ rays that a given fission event emits. A second uncorrelated fission model is also implemented in the code using a special flag in the FREYA library to turn off all correlation. This uncorrelated model does not include the temporal or spatial correlation between the emitted particles, and only samples the neutron and photon energies from a normal distribution with means given in reference [127]. Using the "-mode" flag, as listed in figure C.1, it is possible to switch between the two fission models which are incorporated based on the FREYA library. Finally, in order to incorporate the CGMF and FIFRELIN fission models, binary dumps containing information of each emitted

particle in a fission tree is used to generate individual vertexes which are then simulated. The information includes particle energy and the directional momentum for approximately 0.5 and 15 million fission trees for the two models, respectively. These three fission models are switched using the "-cmod" flag.

Once the particle definitions are built, the Geant4 starts the simulation of the events. At the end of each step of the simulation (which may constitute a particle moving from position X to position Y, a nuclear reaction, destruction of the particle, generation of secondaries, etc.), all the relevant information on the interaction of neutrons, γ rays and optical photons are collected, provided that an interaction took place inside the scintillation detector. This is done using a method called "UserSteppingAction()" in the *SteppingAction* class in Geant4 (see appendix C.5 on page 242), which is called at the end of each step by the simulator to facilitate such user interaction. The information yielded includes (but is not limited to) energy deposited per collision, number of electrons, protons and *optical photons* generated along with the time, in nanoseconds, of interaction with respect to the time at which the fission tree was injected into the system. Such information can be used to determine the total energy deposited, the point in time when each detector crosses detection threshold, etc. The *TrackingAction* Class and the *TrackingInformation* class were used to track all the secondary particles that were produced, namely the γ rays from neutron capture and neutron inelastic scattering, which were flagged in order to record the *optical photons* produced from each primary and secondary particle. This information is stored into two classes, i.e. *RecordedParticle* and *RecordedEvent* (see appendix C.6 on page 249), where the former refers to the information of the generated particle and the latter corresponds to detectors which were triggered (see appendix C.5).

At the end of simulating each fission event, a method called "RecordEvent()" in the *Run* class (see appendix C.7, page 253) is called, which accumulates all the data that are collected by the *SteppingAction* class corresponding to that particular fission event and makes the required tables by calculating the *foreground coincidence distributions* and *background coincidence distributions*, and the subsequent *interval-time distributions* and *angular distributions*. Since the simulations are conducted in multi-threaded mode, all generated events (i.e. fission events) are simulated in different threads, with each having its own *Run* class. Hence, multiple different tables are generated which correspond to individual threads. After the completion of all histories, the *RunAction* class calls the "Merge()" method (see appendix C.7, page 253), which accumulates all the data processed by the different threads.

3.7.2 Output

At the end of the simulation, the *RunAction* class is then responsible for making the appropriate analysis and printing the results in an ASCII file. Two such files are produced:

1. *Correlated information:* this file contains different distributions which includes the neutron, γ-ray and joint *number distributions* and *angular distribution* of the source, the *foreground coincidence distributions* with and without *crosstalk* correction, time-of-flight of particles, *interval-time distribution* and detected event's *angular distributions* with and without crosstalk correction.

2. *Detector spectrum:* this file lists the energy spectrum of the source and the detected response. The latter is a summation of the response for all detectors.

3.7.3 Assumptions

Listed below are some of the properties of the scintillation detectors and geometries modelled, as well as any approximations made:

1. *Detectors:* the scintillation detectors used in this work are 100 mm $\times$ 100 mm $\times$ 100 mm cubes, which are only partially filled. However, no data were available as to the portion of the volume that was left empty. Therefore, it was assumed that 60% of the volume was filled with the liquid being positioned at the base of the detectors. Whilst the light yield of the scintillators due to electron excitation was obtained from the manufacturer's datasheet [116], the light yield function for proton's interaction for the specific detector was not available. As such, the light yield function was taken from previous works in reference [118], which used a 76 mm $\times$ 51 mm cylindrical EJ-309 detector.

2. *Detector threshold:* the detectors are setup such that 200 keVee is set as the threshold. Geant4 generates optical photons due to energy deposited by the incident particle. Then the chain of transport and detection occurs, resulting in a score (i.e. number of optical photons produced per detection) which requires "calibration". This "calibration" procedure is identical to what must be done during experimentation, where some voltage height or integrated voltage pulse area must be calibrated to reflect the energy deposited. This was done such that a γ ray depositing 1 keV in the model produces a light output of 1 keVee (see appendix C.5).

3. ^{252}*Cf sources:* All sources were approximated to be point sources. None of the simulations considered γ-ray production due to the decay of fission products that may have accumulated within the source, or the emission of γ rays due to non-fissioning decay of ^{252}Cf.

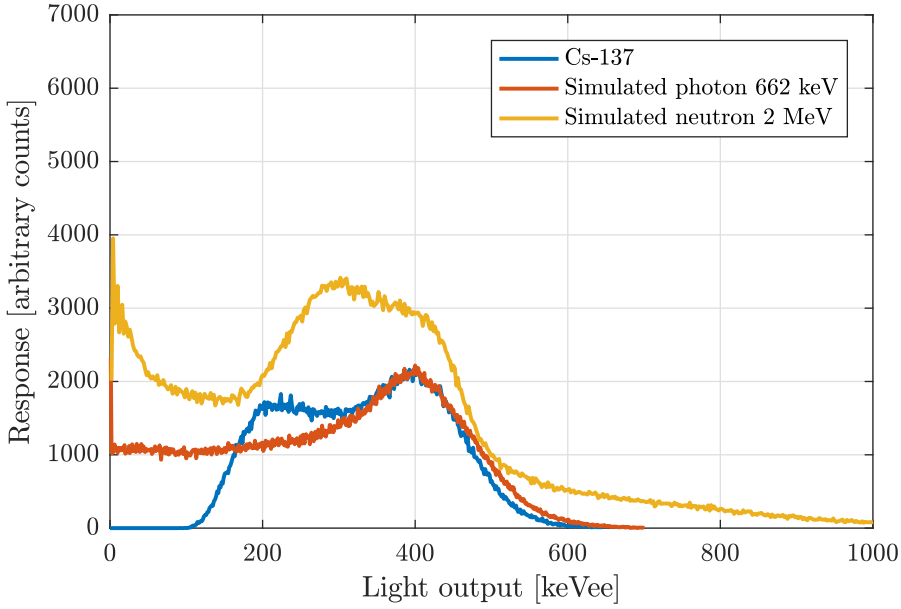

Figure 3.21 | Simulated spectra. The simulated liquid scintillator response to γ rays from a ^{137}Cs source and the simulated liquid scintillator response for 2 MeV mono-energetic neutrons. The experimentally obtained γ-ray response from ^{137}Cs that was recorded in this research is also included which shows good qualitative agreement with the simulated response.

4. AmLi sources: All sources were approximated to be point sources. Due to limited availability of data, the AmLi source was approximated to be a neutron only source having a uniform energy distribution between (0.3 and 1.3) MeV. The γ-ray emission was not modelled.

5. *REFL15:* the metal trolley on which the detectors are placed, as well as the detector cables, MFA and other small furniture were ignored in the model. Reasonable approximations were also made for the composition of the wall, floor, ceiling and the steel tank.

6. *BARE8 and BARE15*: the detector cables, MFA and other small furniture are ignored in the model. Reasonable approximations are also made for the composition of the wall, floor and ceiling.

3.7.4 Validation of Geant4 model

Figure 3.21 demonstrates the simulated detector responses to γ rays from a ^{137}Cs source and to a 2 MeV mono-energetic neutron source for validation. Qualitatively, the simulated γ spectrum closely matches the experimental data in the energy region beyond 300 keVee with the experimental response showing a slightly longer tail after 500 keVee. However, the experimental spectrum recorded higher responses in the low energy region, presumably due to electronic noise not accounted for in the simulation. While no comparison of mono-energetic neutron spectra was made, which would have been ideal for validation purposes, Hartwiga [111] has shown that a

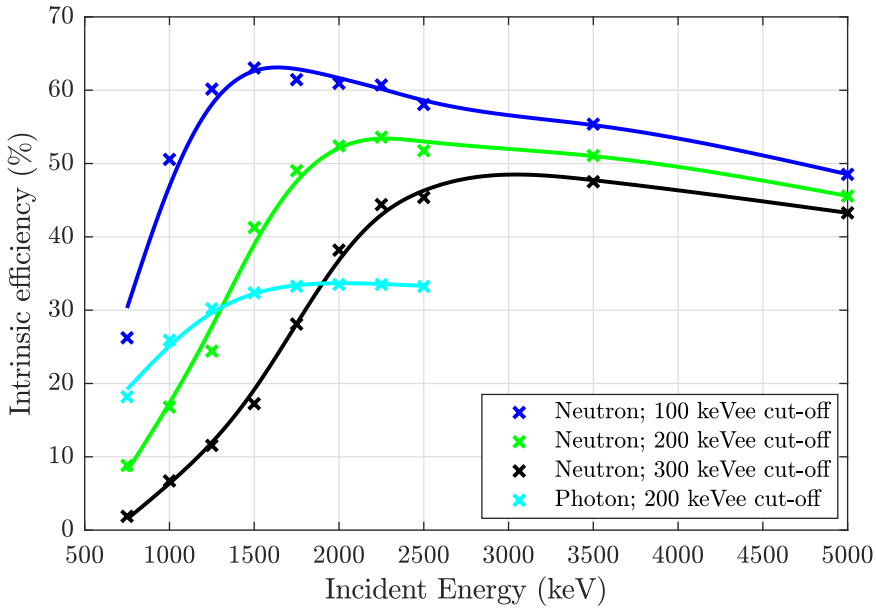

Figure 3.22 | Simulated neutron and γ ray efficiencies. The simulated neutron and γ ray efficiencies as computed by the Geant4 model using mono-energetic particle beams of (750, 1000, 1250, 1500, 1750, 2000, 2250, 2500, 3500 and 5000) MeV for different detector cut-offs.

Geant4 model of a similar configuration is effectively able to model neutron spectrum for a EJ-301 based detector (compared to NRESP7 [128]) whose light response due to neutron interaction has qualitatively similar trends compared to that of EJ-309 detectors. Compared to simulations conducted by Pino [117], the method implemented in this model produced similar, although not identical, pulse height spectrum, which could be due to the difference in geometric construction of the detectors (right-cylinder with 51 mm diameter and 51 mm thick cell) or imperfections in calibration. Additionally, the model developed in this work also had a longer tail, which is not seen in the reference [117]. Unfortunately, no experimental data are available to validate the neutron spectra.

Finally, using 1 million mono-energetic particle histories, the intrinsic neutron and γ-ray efficiencies of the detectors are presented in figure 3.22, which shows qualitatively similar findings to those illustrated by Pino *el. at.* [117], with the Geant4 model in this work yielding slightly higher efficiencies, due to the latter being expressed in terms of absolute efficiencies.

Chapter 4

Results

This chapter illustrates the results obtained from the experiments and simulations defined in Chapter 3. Section 4.1 focuses on the results from the FISPIN analysis of nuclear fuel to quantify the evolution of the isotopic composition of curium in *spent nuclear fuel (SNF)* with time, and hence forecast its contribution towards neutron emission arising from spontaneous fission and (α, n) reaction pathways in terms of their multiplicity. Section 4.2 outlines the *interval-time distributions* that were obtained using the *REFL15* and *BARE15* setups outlined in section 3.3. The results pertaining to neutron spectroscopy using the time-of-flight method are presented in section 4.3, while the measured *angular distributions* from californium-252 (^{252}Cf) are presented in section 4.4. Both sets of experiments were conducted using *BARE15* setup. Section 4.5.1 outlines the results from the coincidence counting using neutron (correlated and uncorrelated) and γ-ray sources, while section 4.5.2 presents the results from the *active fast neutron coincidence counting (AFNCC)* of standardised *uranium oxide (UOX)* canisters using americium-lithium (AmLi). Finally, to assert the different properties of *photon-breakthrough* and *crosstalk*, section 4.6 reports on some of the findings discovered during the course of carrying

out the *passive fast neutron coincidence counting (PFNCC)* experiments and the corresponding Geant4 simulations.

4.1 Correlated emission from spent nuclear fuel

In this section, results from the neutron activation analysis are presented to quantify the evolution of the isotopic composition for various plutonium and curium isotopes in SNF (i.e. both *mixed-oxide (MOX)* and UOX fuels used in modern *Boiling Water Reactor (BWR)* and *Pressurized Water Reactor (PWR)*) with cooling periods. The objective of this analysis is to forecast correlated neutron emission rates arising from the three depleted fuels due to the spontaneous fission and (α, n) reaction pathways originating from their constituent isotopes. The methodology followed in obtaining the results is detailed in section 3.6 on page 89. The isotopic data from FISPIN simulations (see section 3.6), namely the number densities of the actinides, and spontaneous fission and (α, n) activities that were extracted periodically, are presented in sections 4.1.1 and 4.1.2. Finally, the calculated correlated emission rates expressed in terms of their factorial moments are presented in section 4.1.3.

4.1.1 Isotopic composition

This section presents the evolution of the isotopic number densities of various plutonium and curium isotopes, and americium-241 (^{241}Am) with a cooling period using the raw number densities obtained from the FISPIN simulations. The number density signifies the number of atoms of an isotope present in the fuel element per metric tonne of uranium (MTU). The isotopic data were extracted periodically during the course of the depletion and cooling period simulations and were plotted using the Matlab script listed in appendix D.4.1 on page 265.

Figure 4.1 shows the evolution of major plutonium isotopes for the fuel pin that was depleted to (10, 20, 35 and 55) GWd·MTU^{-1} from the PWR-MOX, BWR-MOX and PWR-UOX configurations by plotting number densities of the various plutonium isotopes (i.e. plutonium-238 (^{238}Pu), ^{239}Pu, ^{240}Pu, ^{241}Pu and ^{242}Pu) as a function of time, expressed in days. The negative x-axis indicates the irradiation period when the fuel was inside a running reactor while the positive x-axis indicates the cooling period following removal from the reactor. The figure is arranged in sub-plots such that the plots in each column correspond to PWR-MOX, BWR-MOX and PWR-UOX fuel pins from left to right, respectively. Conversely, each row corresponds to the burn-up levels of (10, 20, 35 and 55) GWd·MTU^{-1} from top to bottom. The trends depicted in the plots also demonstrate the change in number densities during the irradiation period.

Finally, figure 4.2 illustrates the change in the number densities of ^{241}Am, ^{243}Am, curium-242 (^{242}Cm) and ^{244}Cm isotopes and is arranged in a configuration akin to that described for

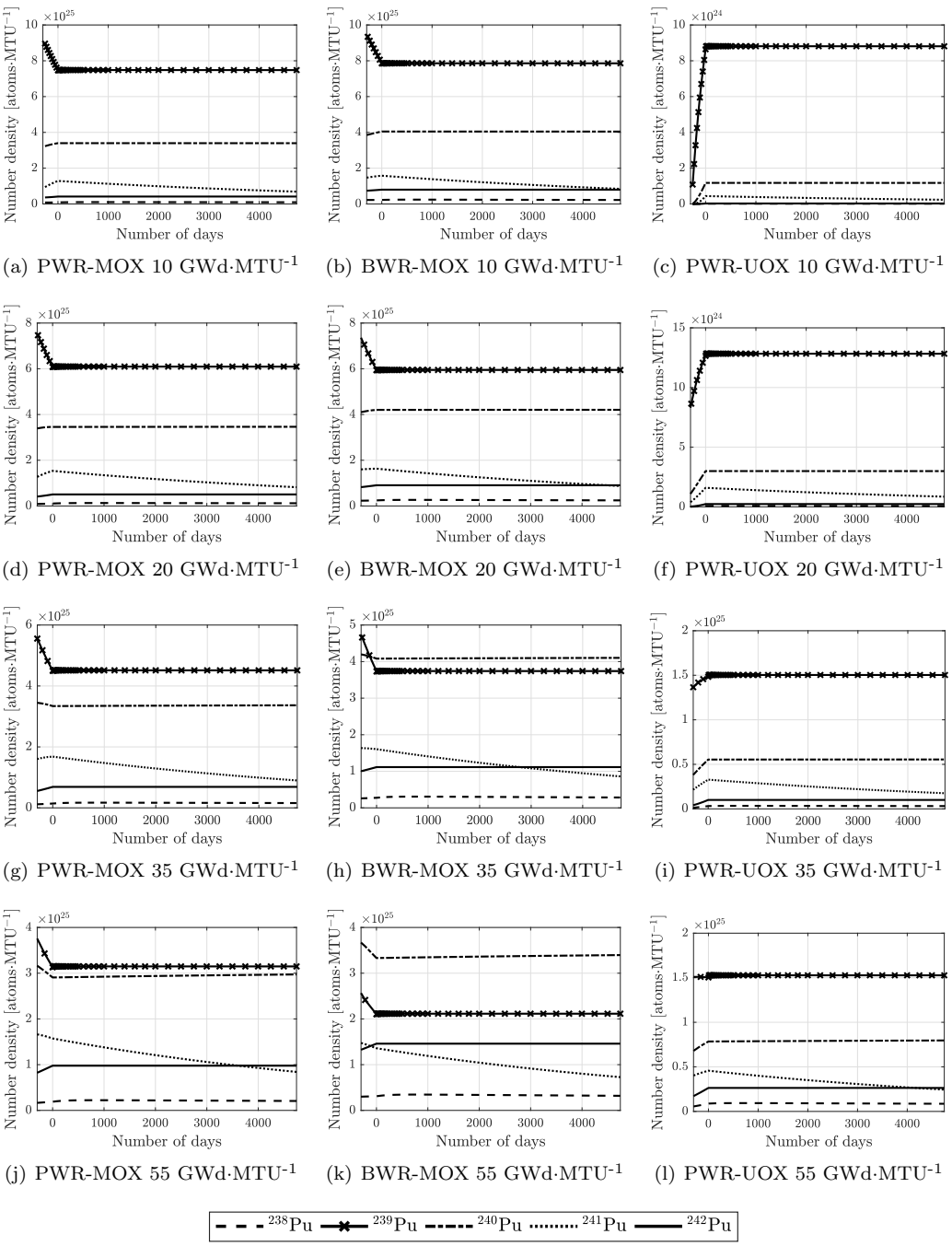

Figure 4.1 | The evolution of the isotopic number densities of plutonium isotopes. The evolution of the isotopic number densities of ^{238}Pu, ^{239}Pu, ^{240}Pu, ^{241}Pu and ^{242}Pu with time during the cooling period of the PWR-MOX, BWR-MOX and PWR-UOX fuel pins (first, second and third column, respectively) which have been irradiated to 10 GWd·MTU^{-1}, 20 GWd·MTU^{-1}, 35 GWd·MTU^{-1} and 55 GWd·MTU^{-1} (first, second, third and fourth row, respectively).

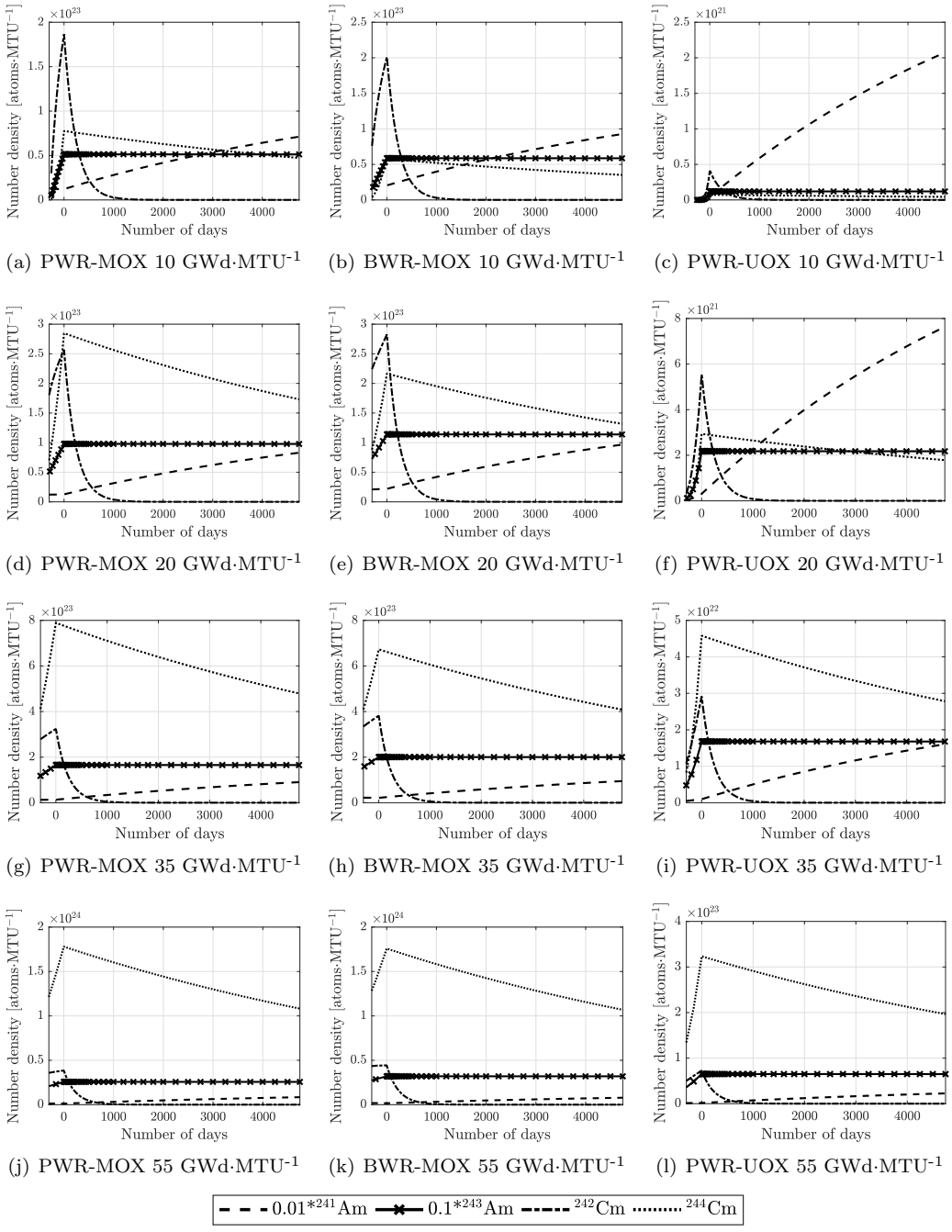

Figure 4.2 | The evolution of the isotopic number densities of non-plutonium heavy isotopes. The evolution of the isotopic number densities of ^{241}Am, ^{243}Am, ^{242}Cm and ^{244}Cm with time during the cooling period of a PWR-MOX, BWR-MOX and PWR-UOX (plots on the left-hand side, centre and right-hand side, respectively) fuel pin which has been irradiated to (10, 20, 35 and 55) GWd·MTU^{-1} (first, second, third and fourth row, respectively). The number densities of ^{241}Am and ^{243}Am were multiplied by a factor of 0.01 and 0.1, respectively, to improve visual perspective.

figure 4.1. As number densities for ^{241}Am were significantly higher compared to that of other isotopes for a few select cases of fuel types with low burn-up, these data were multiplied by a factor of 0.01.

4.1.2 Neutron activity

This section presents the data obtained from FISPIN regarding the change in the neutron activity due to spontaneous fission and (α, n) reactions from different plutonium and curium isotopes, and ^{241}Am for the three fuel types and their corresponding four different depletion cases. The figures presented in this section were constructed using the Matlab script listed in appendix D.4.1, which plots the relevant datasets that were obtained directly from the FISPIN simulations.

Figure 4.3 illustrates the evolution of spontaneous fission neutron activity with time produced by the variety of different plutonium isotopes in the three different fuel cases and their corresponding four different depletion histories. Similarly, figure 4.4 illustrates the spontaneous fission activity from ^{242}Cm and ^{244}Cm v.s. time. The rates of production of uncorrelated neutrons from (α, n) reactions on the ^{17}O and ^{18}O isotopes are demonstrated in figures 4.5 and 4.6, where the first figure refers to the dataset corresponding to the various plutonium isotopes, namely ^{238}Pu, ^{239}Pu, ^{240}Pu, ^{241}Pu and ^{242}Pu, and the second figure represents other major alpha sources, i.e. ^{242}Cm, ^{244}Cm and ^{241}Am.

All of the datasets included in the above mentioned figures are expressed in terms of neutron per second per MTU. Similar to the figures in section 4.1.1, these figures are also organised such that the plots in each column represent the PWR-MOX, BWR-MOX and PWR-UOX fuel pins from left to right, respectively, while the four rows represent the four different burn-up histories.

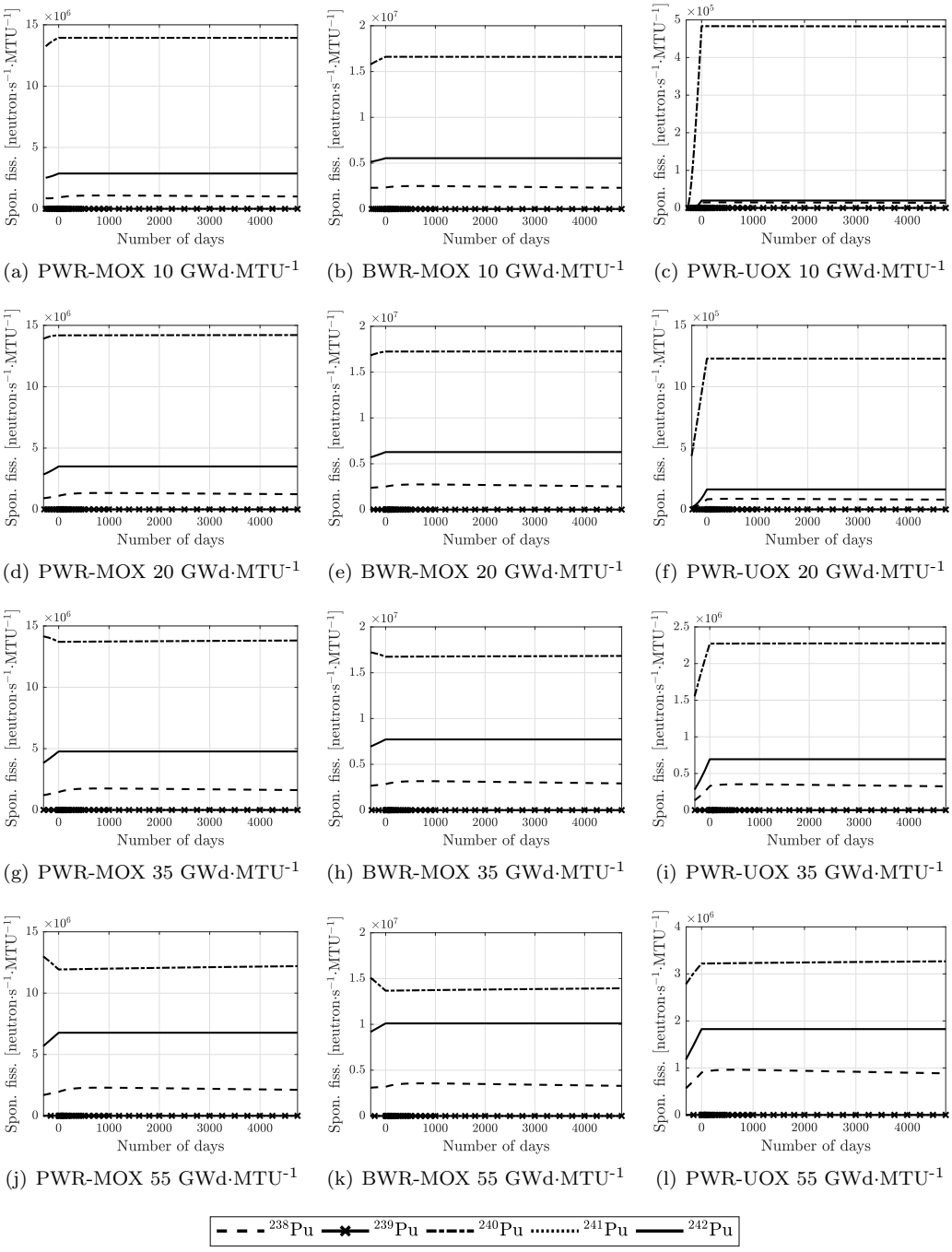

Figure 4.3 | The evolution of isotopic neutron activity with time due to spontaneous fission of various plutonium isotopes. The evolution of the isotopic neutron activity due to spontaneous fission of ^{238}Pu, ^{239}Pu, ^{240}Pu, ^{241}Pu and ^{242}Pu with time during the cooling period of a PWR-MOX, BWR-MOX and PWR-UOX (plots on the left-hand side, centre and right-hand side, respectively) fuel pin which has been irradiated to (10, 20, 35 and 55) GWd·MTU^{-1} (first, second, third and fourth row, respectively).

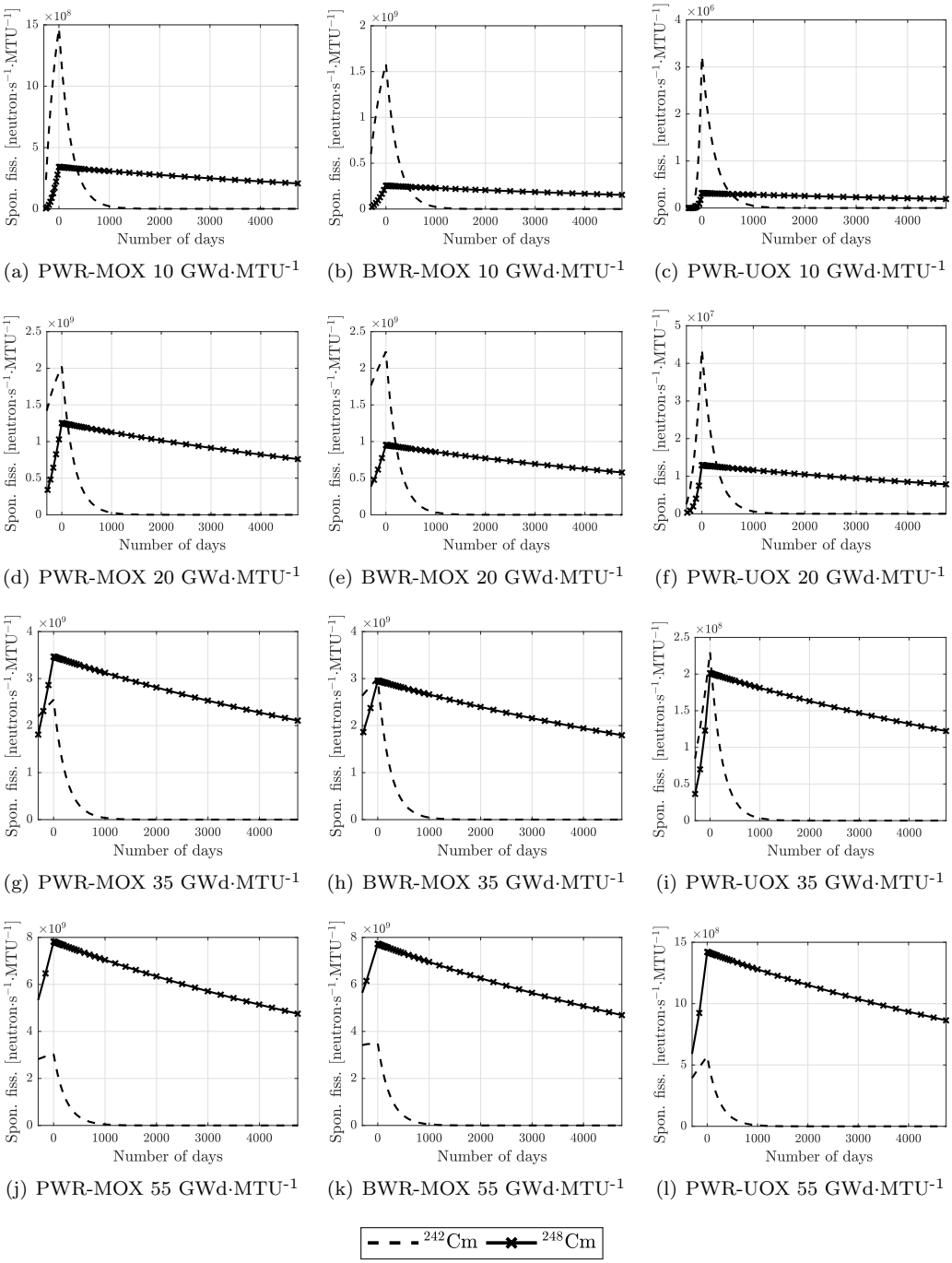

(a) PWR-MOX 10 GWd·MTU^{-1} (b) BWR-MOX 10 GWd·MTU^{-1} (c) PWR-UOX 10 GWd·MTU^{-1}

(d) PWR-MOX 20 GWd·MTU^{-1} (e) BWR-MOX 20 GWd·MTU^{-1} (f) PWR-UOX 20 GWd·MTU^{-1}

(g) PWR-MOX 35 GWd·MTU^{-1} (h) BWR-MOX 35 GWd·MTU^{-1} (i) PWR-UOX 35 GWd·MTU^{-1}

(j) PWR-MOX 55 GWd·MTU^{-1} (k) BWR-MOX 55 GWd·MTU^{-1} (l) PWR-UOX 55 GWd·MTU^{-1}

Figure 4.4 | The evolution of isotopic neutron activity with time due to spontaneous fission of various non-plutonium isotopes. The evolution of the isotopic neutron activity due to spontaneous fission of ^{242}Cm and ^{244}Cm with time during the cooling period of a PWR-MOX, BWR-MOX and PWR-UOX (plots on the left-hand side, centre and right-hand side, respectively) fuel pin which has been irradiated to (10, 20, 35 and 55) GWd·MTU^{-1} (first, second, third and fourth row, respectively).

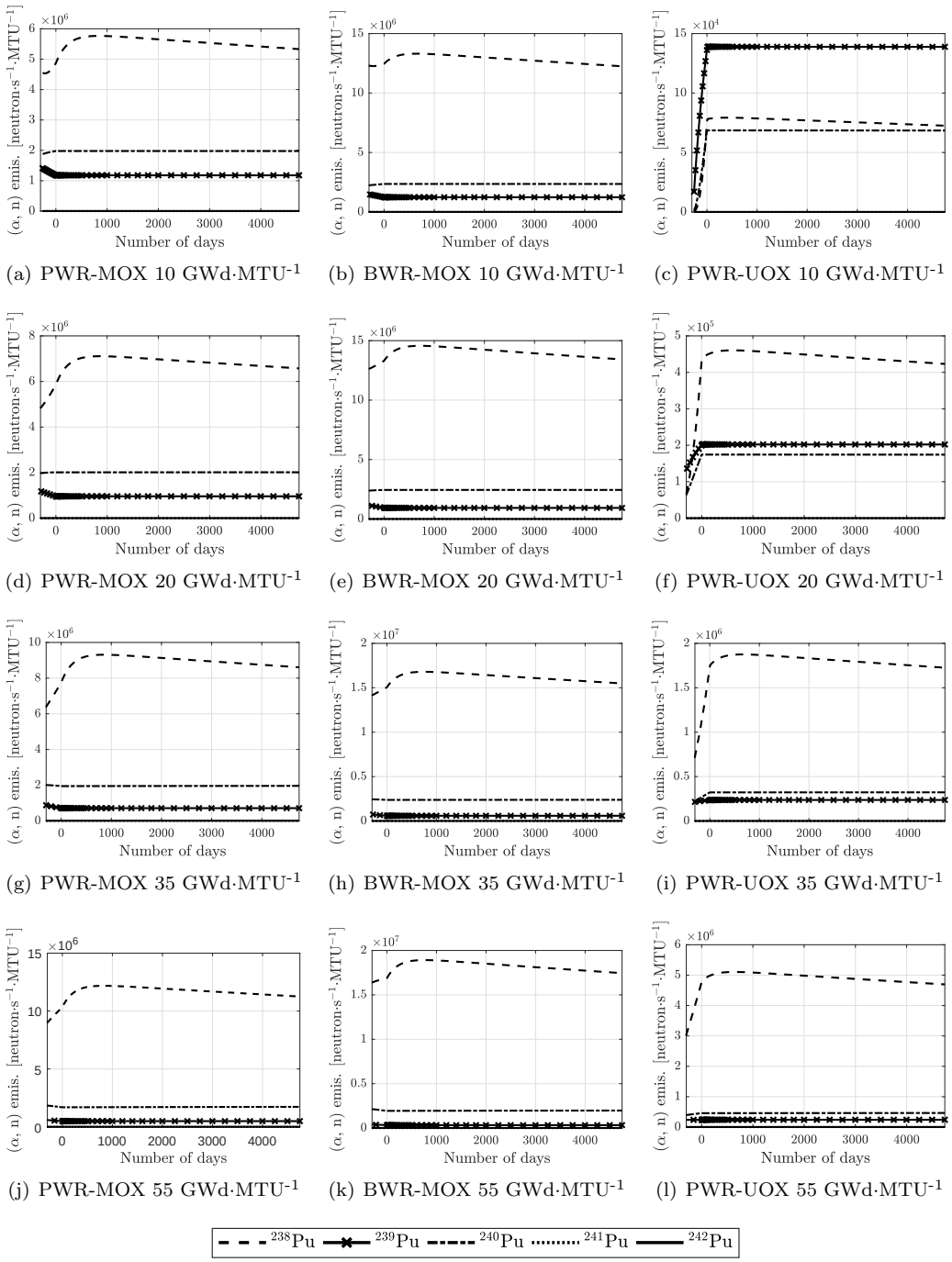

Figure 4.5 | The evolution of isotopic neutron activity with time due to (α, n) reactions of various plutonium isotopes. The evolution of the isotopic neutron activity due to (α, n) emission of ^{238}Pu, ^{239}Pu, ^{240}Pu, ^{241}Pu and ^{242}Pu with time during the cooling period of a PWR-MOX, BWR-MOX and PWR-UOX (plots on the left-hand side, centre and right-hand side, respectively) fuel pin which has been irradiated to (10, 20, 35 and 55) GWd·MTU^{-1} (first, second, third and fourth row, respectively).

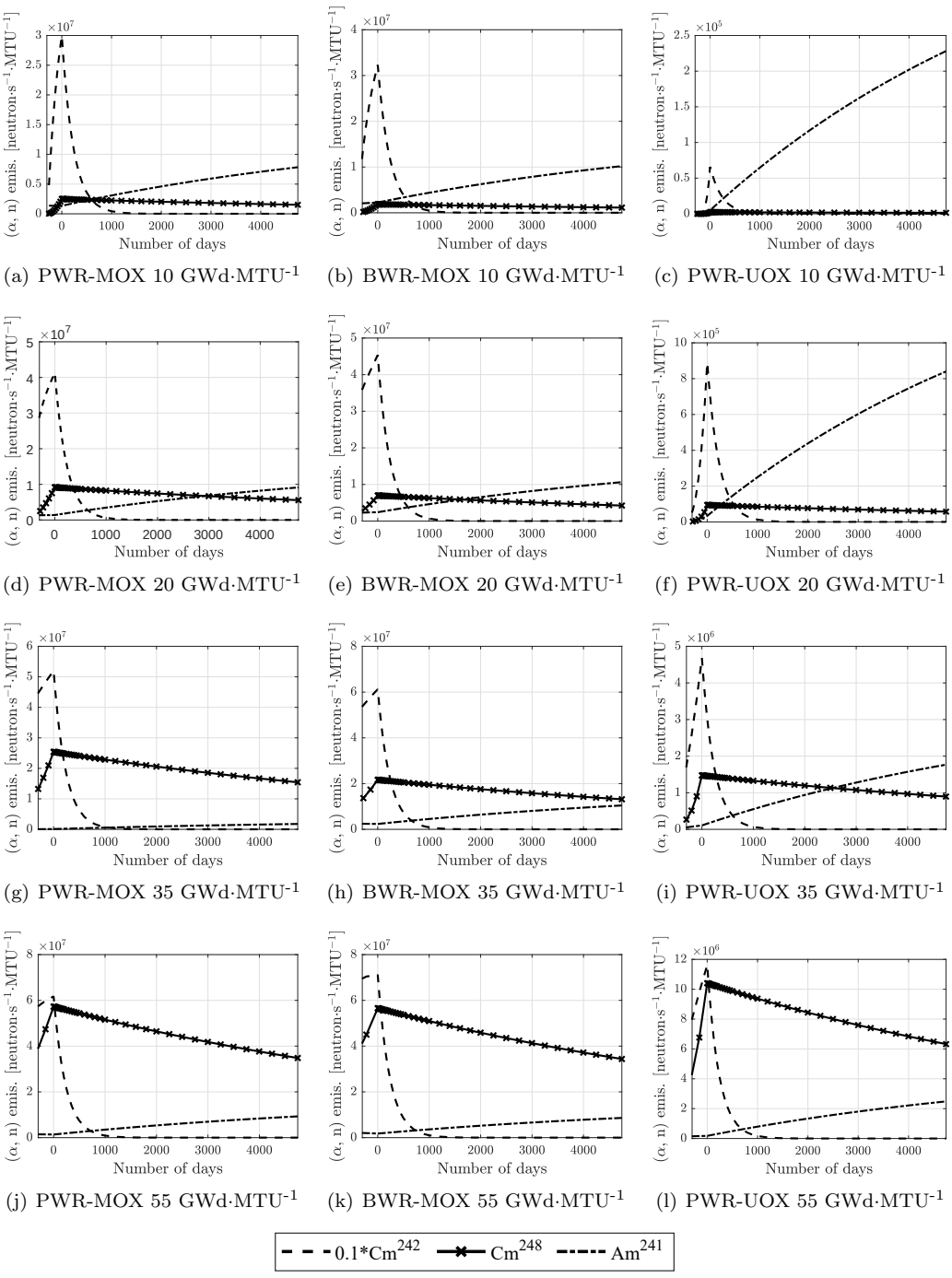

(a) PWR-MOX 10 GWd·MTU^{-1} (b) BWR-MOX 10 GWd·MTU^{-1} (c) PWR-UOX 10 GWd·MTU^{-1}

(d) PWR-MOX 20 GWd·MTU^{-1} (e) BWR-MOX 20 GWd·MTU^{-1} (f) PWR-UOX 20 GWd·MTU^{-1}

(g) PWR-MOX 35 GWd·MTU^{-1} (h) BWR-MOX 35 GWd·MTU^{-1} (i) PWR-UOX 35 GWd·MTU^{-1}

(j) PWR-MOX 55 GWd·MTU^{-1} (k) BWR-MOX 55 GWd·MTU^{-1} (l) PWR-UOX 55 GWd·MTU^{-1}

Figure 4.6 | The evolution of isotopic neutron activity with time due to (α, n) activity of various non-plutonium isotopes. The evolution of the isotopic neutron activity due to (α, n) emission of ^{241}Am, ^{242}Cm and ^{244}Cm with time during the cooling period of a PWR-MOX, BWR-MOX and PWR-UOX (plots on the left-hand side, centre and right-hand side, respectively) fuel pin which has been irradiated to (10, 20, 35 and 55) GWd·MTU^{-1} (first, second, third and fourth row, respectively). The activity of ^{242}Cm were multiplied by a factor of 0.1 to improve visual perspective.

The relative isotopic contribution to neutron emission

Figures 4.7 and 4.8 represent the relative neutron activity due to spontaneous fission and (α, n) emission, respectively, from the different actinides present in SNF, i.e. uranium, plutonium, americium and curium isotopes. The two figures are divided into three sub-plots, each corresponding to the three different fuel pins, i.e. PWR-MOX, BWR-MOX and PWR-UOX, respectively. Each sub-plot has 24 stack-bar plots divided into four groups representing the four burn-up cases, i.e. (10, 20, 35 and 55) GWd·MTU^{-1}, respectively. Further to this, each group has six stack-bars representing the relative isotopic activities following the 10-, 350-, 1000-, 2000-, 3000- and 4250-day cooling periods. The dataset for these plots were obtained by extracting the isotopic neutron activity rates for the two decay paths following the above mentioned cooling periods and dividing them by the total rate of neutron activity for the corresponding decay-paths. The Matlab script used for this processing is available in appendix D.4.2 on page 268.

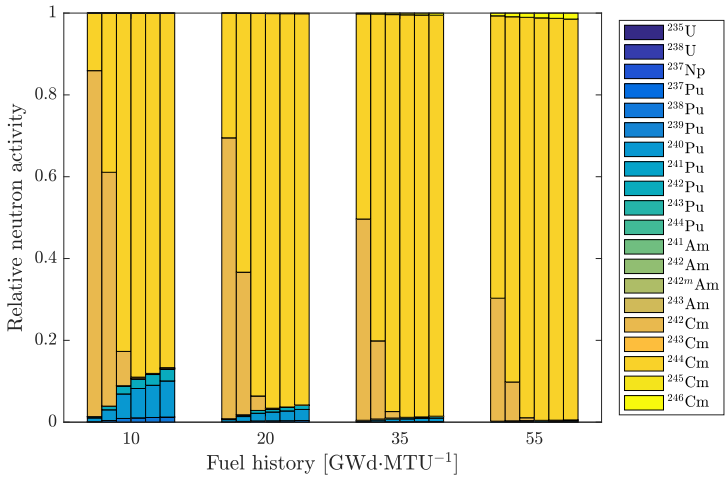

(a) PWR-MOX fuel pin.

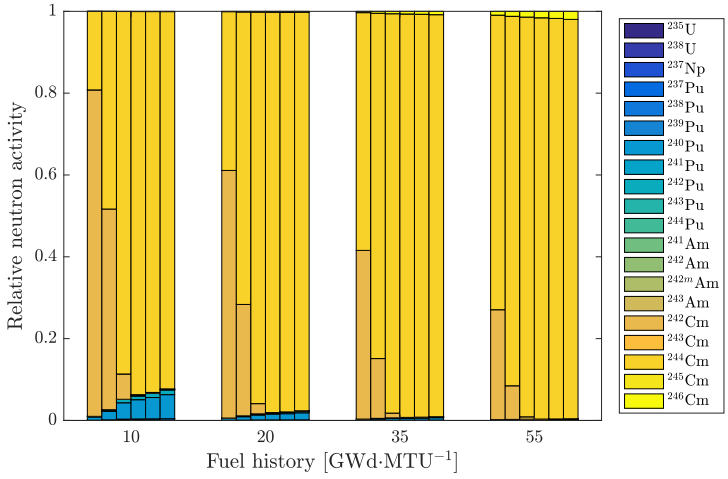

(b) BWR-MOX fuel pin.

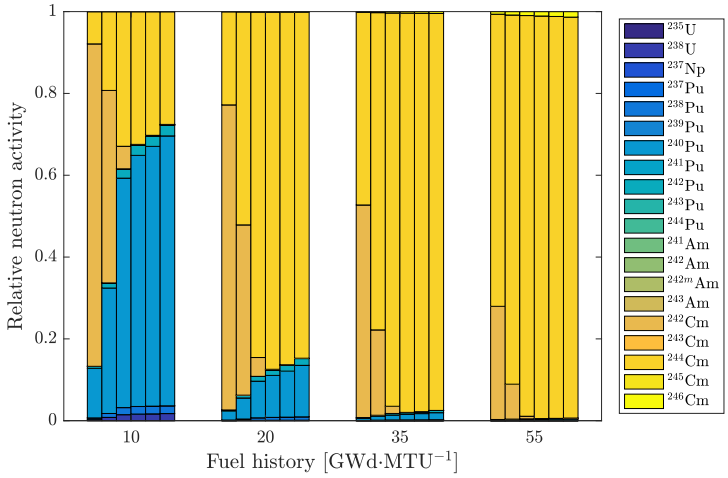

(c) PWR-UOX fuel pin.

Figure 4.7 | The relative neutron activity of the three cases due to spontaneous fission of major actinides. The relative contribution of different isotopes towards the spontaneous fission neutron flux after the irradiation of **(a)** PWR-MOX, **(b)** BWR-MOX and **(c)** PWR-UOX fuel pin. The four groups of stackbars represent the proportion of spontaneous fission neutron activity from different sources present in a fuel element irradiated to (10, 20, 35 and 55) GWd·MTU^{-1}. Each group contains six stackbars representing a 10-, 350-, 1000-, 2000-, 3000- and 4250-day cooling periods.

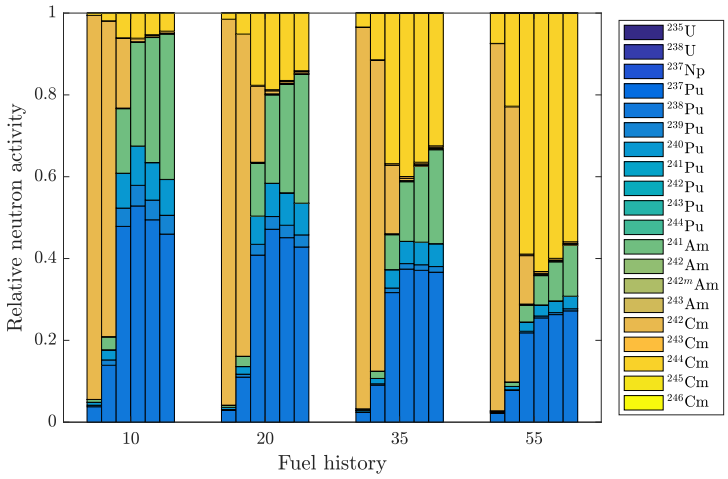

(a) PWR-MOX fuel pin.

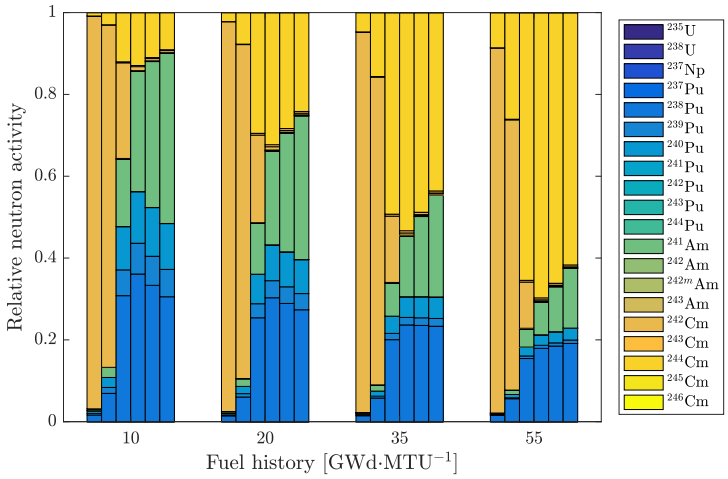

(b) BWR-MOX fuel pin.

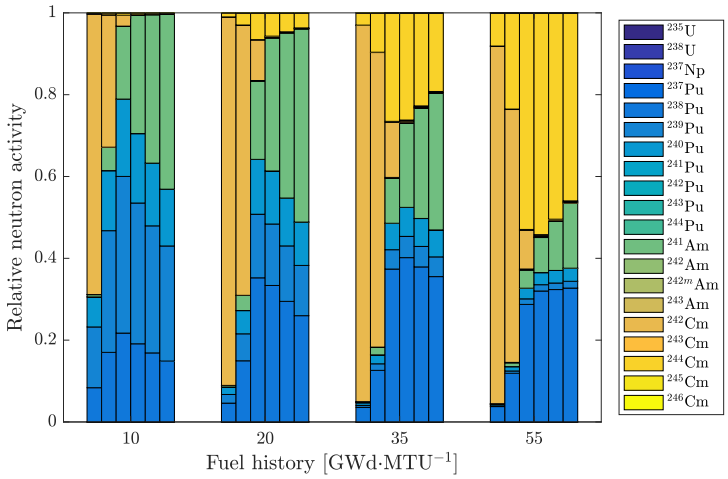

(c) PWR-UOX fuel pin.

Figure 4.8 | The relative neutron activity of the three cases due to (α, n) reactions due to major actinides. The relative contribution of different isotopes towards the (α, n) neutron contributions after the irradiation of **(a)** PWR-MOX, **(b)** BWR-MOX and **(c)** PWR-UOX fuel pin. The four groups of stackbars represent the proportion of (α, n) neutron activity from different sources present in a fuel element irradiated to 10, 20, 35 and 55 GWd·MTU^{-1}. The each group contains six stackbars representing a 10-, 350-, 1000-, 2000-, 3000- and 4250-day cooling periods.

4.1.3 Correlated neutron emission

An important, implicit aim of this study is to improve the current understanding of how the change in fuel composition affects the emission of correlated neutron emissions. In order to analyse this, the FISPIN simulated isotope-wise neutron emission datasets from spontaneous fission, presented in section 4.1.2, were divided by the average number of neutrons emitted per fission event for the corresponding isotopes. The resulting datasets therefore now reflect the isotope-wise spontaneous fission rates or the number of fission events taking place per second per MTU. These isotope-wise distributions were then multiplied by the number distribution corresponding to the probability of the different orders of correlated events that may be emitted following spontaneous fission, as demonstrated in table 2.2(a) on page 24. Finally, a summation of all related plutonium and curium isotope-wise number distributions was made, as well as the (α, n) emission rate datasets, using which the magnitude of the first eight factorial moments, commonly referred to as the singles, doubles, triples, quadruples, quintuples, sextuples, septuples, and octuples (i.e. ν_1, ν_2, etc), were computed. The mathematical expression for computing factorial moment is expressed in equation 2.49 on page 53 [15]. This analysis was made using the Matlab script in appendix D.4.3 on page 271.

Figure 4.9 illustrates the computed neutron multiplicity in terms of reduced factorial moments, as described above. Akin to previous figures, figure 4.9 is also organised such that the sub-figures in each column represent the PWR-MOX, BWR-MOX and PWR-UOX fuel pins from left to right, respectively, while the four rows represent the 10, 20, 35 and 55 GWd·MTU^{-1} burn-up histories.

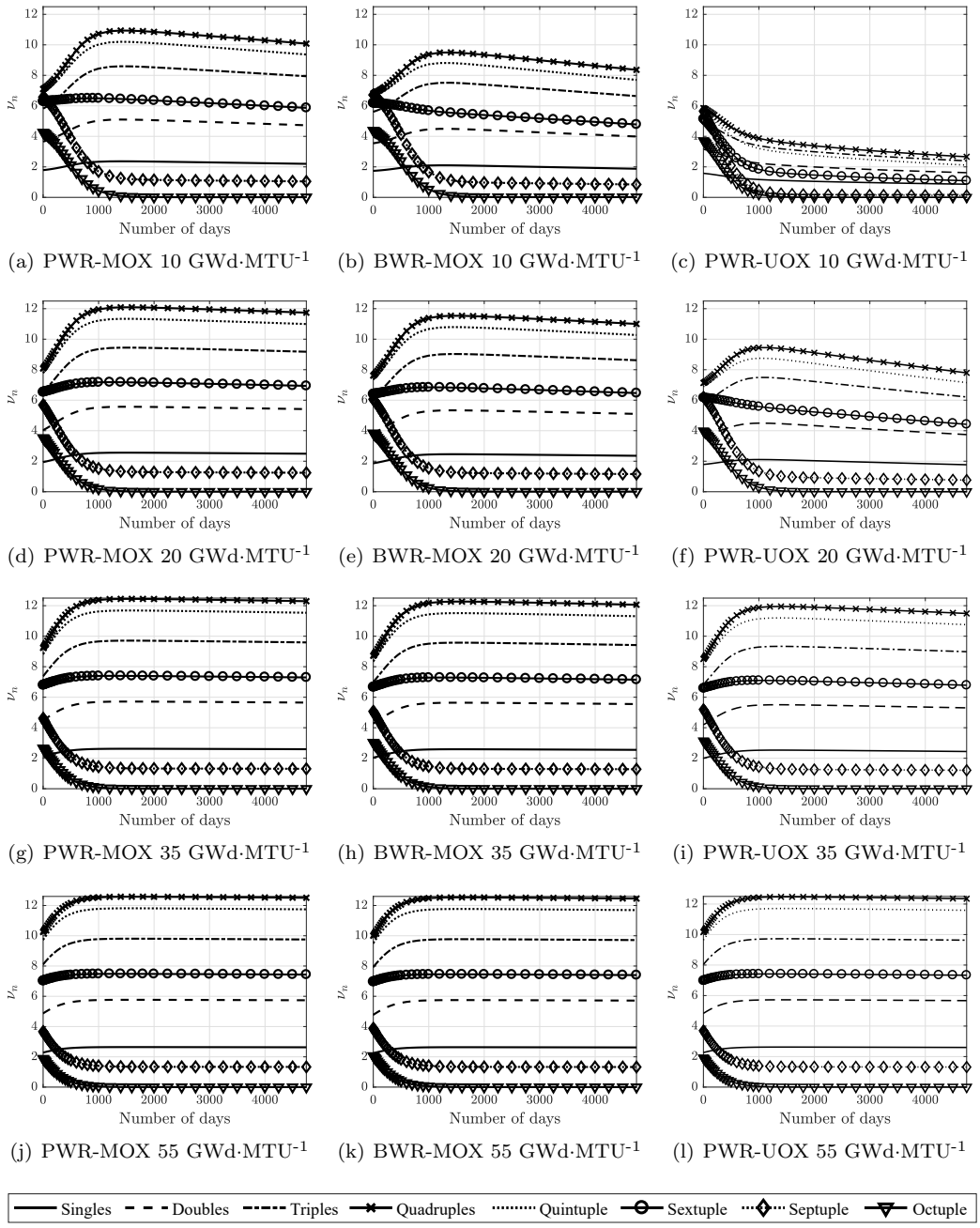

(a) PWR-MOX 10 GWd·MTU^{-1} (b) BWR-MOX 10 GWd·MTU^{-1} (c) PWR-UOX 10 GWd·MTU^{-1}

(d) PWR-MOX 20 GWd·MTU^{-1} (e) BWR-MOX 20 GWd·MTU^{-1} (f) PWR-UOX 20 GWd·MTU^{-1}

(g) PWR-MOX 35 GWd·MTU^{-1} (h) BWR-MOX 35 GWd·MTU^{-1} (i) PWR-UOX 35 GWd·MTU^{-1}

(j) PWR-MOX 55 GWd·MTU^{-1} (k) BWR-MOX 55 GWd·MTU^{-1} (l) PWR-UOX 55 GWd·MTU^{-1}

Figure 4.9 | Impact on neutron multiplicity due to the presence of various isotopes undergoing either or both spontaneous fission and (α, n) reactions. The evolution of the various orders of multiplicity illustrated using the factorial moments (i.e. singles, doubles, triples, etc.) with time during the cooling period of a PWR-MOX, BWR-MOX and PWR-UOX (plots on the left-hand side, centre and right-hand side, respectively) fuel pin which has been irradiated to (10, 20, 35 and 55) GWd·MTU^{-1} (first, second, third and fourth row, respectively).

4.2 Temporal correlation between particles emitted from spontaneous fission of ^{252}Cf

In these experiments, the correlated neutrons are acquired within a small time interval ΔT (comprised of many smaller bins of width δt) to determine the *non-Poissonian* properties of the temporal spread in the neutron activity arising from spontaneous fission (see section 2.3 on page 25 and section 2.5.1 on page 34 for further context). To summarise, this time interval, referred to as the *coincidence-gate*, is started when the first neutron is detected in the *event-train*. The time elapsed between that first neutron and any subsequent neutrons is plotted into an *interval-time distribution*, sometimes referred to as the Rossi-α distribution. These distributions reflect the intensity of neutron emission resulting from a nuclear process, e.g. spontaneous fission in this case, as a function of time elapsed since the first neutron was detected within the time interval of ΔT.

Experiments were carried out using arrangements defined in section 3.3 on page 74 where the prompt, correlated counts versus time for spontaneous fission of ^{252}Cf were measured in a *reflective* arrangement (i.e. *REFL15* setup in section 3.3.2 on page 77) using a water-filled tank to encourage neutron scattering in the arrangement; and also in a *bare* arrangement with minimum scatter from the environment (i.e. *BARE15* setup in section 3.3.4 on page 82). These measurements were based on the methodology depicted in figure 3.9, whereby the neutrons and γ rays are detected by an array of organic liquid scintillation detectors and the resulting electronic signals are processed in real-time and output to a real-time *multiplicity register*, which was used to build the corresponding *interval-time distribution* (see section 3.4 for further details). The 15 detectors were calibrated using a methodology detailed in section 3.5 on page 87.

For each of the two arrangements, distributions were obtained for neutron, photon and *joint* neutron-γ *event-trains*[1] by taking advantage of the different configurations options of the *multiplicity register* detailed in section 3.2.5 (i.e. Conf-N, Conf-P and Conf-J, respectively). In order to validate the experimentally obtained results, simulations were carried out using the Geant4 model described in section 3.7 on page 91 to reconstruct the neutron, γ-ray and joint *interval-time distributions* for both the reflective and the bare arrangements. For the reflective case, 160 million fission events were simulated. These simulations were executed in 16 batches with 10 million histories each having different initial seeds for the random number generator of the simulator. Similarly, for the bare case, 14 million fission events were simulated for the bare case, which were conducted in 7 batches of 2 million fission histories.

[1] The *joint* distribution was obtained when counts are recorded without discriminating neutrons from γ rays.

4.2.1 Reflective arrangement

The *interval-time distributions* data for the tank are given in figures 4.10(a), 4.10(b) and 4.10(c) for γ rays, neutrons, and the combination of γ rays and neutrons (i.e. the *joint* distribution), respectively. The plot includes the experimental data denoted by black crosses. The simulation results are implanted into the corresponding figures in two formats: (i) "Simulated data (binned)" represents the simulation data binned in accordance to the bin-sizes of the experimental data (red crosses), and (ii) "Simulated data" represents the simulation with a 1-ns bin-size for better resolution (magenta circles). Since these simulations are computationally heavy, requiring extensive processor time with 200 million fission history, not enough intensity was recorded in the simulated response, and hence the plots in figure 4.10 were normalized with the first data point from the respective distributions. The error bars, computed using the formulations described in section 2.8.2 on page 53, were omitted from the plots as they were too small to be clearly visible. The resolution of the measurements is limited to 5 ns using the instrumentation (with the first bin being 10 ns) but the responses may in fact be smaller.

For each of the distributions, the expected trend comprising a *single exponent* (equation 2.23 on page 34) has been applied to the data. The coefficients of the equation were determined using the Matlab® curve fitting toolbox [129] using the non-linear least squares method for each dataset and are listed in table 4.1 along with their reduced χ^2_v goodness-of-fit (see section 2.8.3 on page 54). An optimisation based on the Least Absolute Residuals (LAR)[2] yielded better consistency, particularly early in the distributions. The confidence bounds were determined using an estimated covariance matrix of the coefficient estimates [129] to reflect 1σ. The gate-width was computed using equation 4.1 on the basis that it is necessary to accommodate 99.7% of the counts, per 3σ. The Matlab script used to determine these parameters is included in appendix D.5 on page 275.

$$\textit{gate-width} = -\tau \times \ln(1 - 0.997) \tag{4.1}$$

The *single exponent* model reproduces the trend of the data for $\Delta T < 15$ ns satisfactorily but not the entire trend because an additional, more slowly-varying, time-dependent component is apparent, particularly for fast neutrons in the reflective arrangement. To better describe the distributions, equation 2.23 was empirically expanded as per equation 4.2, which now includes a short-term component (having a proportion of A and a detector die-away τ_s), a longer-term component (having a proportion of B and a decay constant τ_l) and a time-independent term.

$$P(t) = A\exp^{-t/\tau_s} + B\exp^{-t/\tau_l} + C \tag{4.2}$$

[2] "The LAR method finds a curve that minimizes the absolute difference of the residuals, rather than the squared differences. Therefore, extreme values have a lesser influence on the fit."

Table 4.1 | The coefficients for the reflected case as per the parameterisation of the single and double exponent model. (a) Fit parameters for the experimental data using the single exponent model. **(b)** The coefficients A, B and C of the double exponent model proposed in this work. The first table corresponds to the parameters for the experimental data, including the estimates for the short and long gate-widths have been made on the basis that it is necessary to accommodate 99.7% of the counts, per 3σ. The uncertainties were computed to reflect 1σ.

(a) Single exponent: $Ae^{-t/\tau} + C$

Coefficient/parameter type		***Neutrons***	**γ rays**	***Joint***
Components	*A [counts]*	10538 ± 857	56621 ± 3164	186281 ± 6098
	τ [ns]	10.42 ± 0.58	2.82 ± 0.08	4.58 ± 0.09
Accidentals	*C [counts]*	144 ± 8	125 ± 3	1233 ± 21
gate-width [ns]		60.6 ± 3.4	16.6 ± 0.4	26.6 ± 0.5
χ^2_v		26.62	3.61	20.24

(b) Double exponent: $Ae^{-t/\tau_s} + Be^{-t/\tau_l} + C$

		Experimental		
Coefficient/parameter type		***Neutrons***	**γ rays**	***Joint***
Short (prompt)	*A [counts]*	17536 ± 816	60663 ± 2754	279564 ± 4793
component	*τ_s [ns]*	4.24 ± 0.20	2.70 ± 0.06	3.16 ± 0.03
Long (scatter)	*B [counts]*	3013 ± 163	115 ± 20	5930 ± 131
component	*τ_l [ns]*	21.6 ± 0.6	53.8 ± 12.1	35.7 ± 0.6
Accidentals	*C [counts]*	134.1 ± 1.7	114.0 ± 3.2	1172.3 ± 6.8
Short gate-width [ns]		24.7 ± 1.2	15.7 ± 0.4	18.4 ± 0.2
Long gate-width [ns]		125.3 ± 3.5	312.5 ± 70.4	207.6 ± 3.8
χ^2_v		0.86	1.46	1.12

The magnitude of the coefficients A, B and C indicate the proportion of counts at time $\Delta T = 0$ of the respective components. The coefficients of equation 4.2 were determined using the Matlab® Curve Fitting Toolbox; while also listing the the short and long gate-widths necessary to accommodate 99.7% (3σ) of the events under the short and long components of the response. The short and long gate-widths were computed using equation 4.1 by utilising the Matlab script in appendix D.5 on page 275. The values of the coefficients for the two data sets are presented in table 4.1(b).

The two models, i.e. single and double exponent fits, are denoted by red and blue lines, respectively, in figures 4.10(a), 4.10(b) and 4.10(c) for the neutron, γ-ray and joint distributions; and were computed using the experimental data. The proportion of the three components, i.e. A, B and C, in the double exponential model is represented as per the corresponding shading: the short response (green), the long response (blue) and the time-independent response (red).

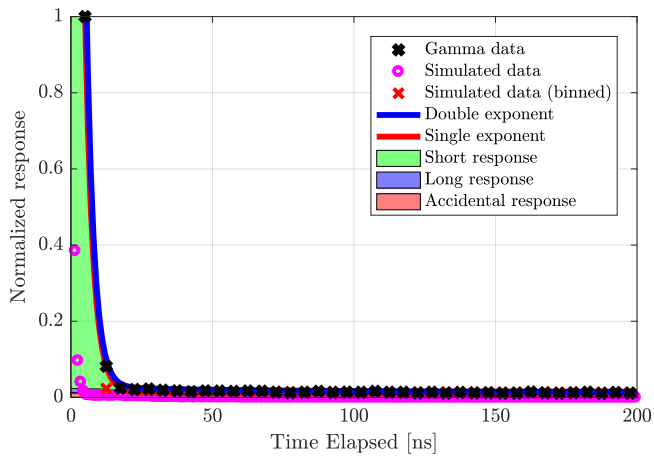

(a) γ-ray distribution.

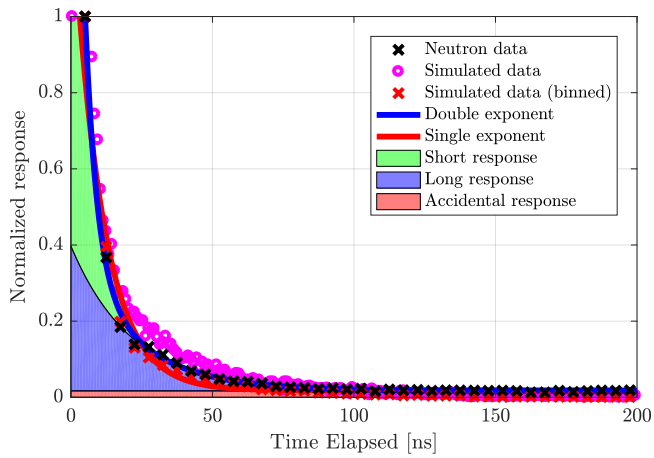

(b) Neutron distribution.

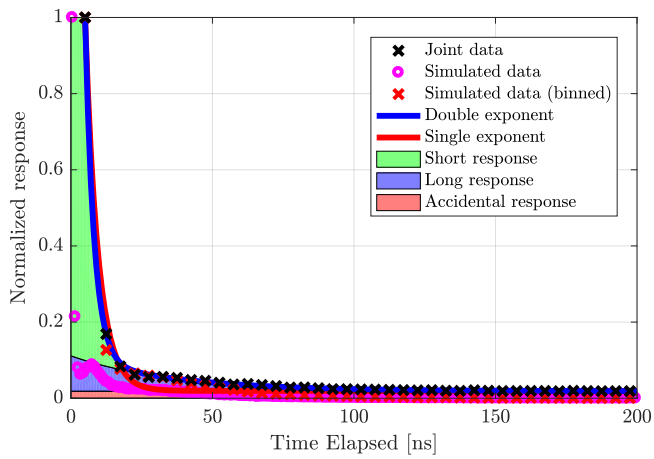

(c) Joint distribution.

Figure 4.10 | Interval time distribution for the detected radiation from ^{252}Cf source using the REFL15 arrangement. The *interval-time distributions* measured using the reflective arrangement comprising a comparison of experimental data (black cross) using detected signals, fits according to the three-term model reported in this work (blue line), and the single exponential model (red line) for the **(a.)** γ rays, **(b.)** neutron and **(c.)** joint cases. The distribution has been decomposed into the contributions from each term as per the corresponding shading; the short response (green), the long response (blue) and the time-independent response (red). Simulated data are also included for the three distributions with 1 ns (magenta crosses) and 5 ns bins (red circles).

Table 4.2 | The coefficients for the bare case as per the parameterisation of the single and double exponent model. (a) Fit parameters for the experimental data using the single exponent model. **(b)** The coefficients A, B and C of the double exponent model proposed in this work. The first table corresponds to the parameters for the experimental data, including the estimates for the short and long gate-widths have been made on the basis that it is necessary to accommodate 99.7% of the counts, per 3σ. The uncertainties were computed to reflect 1σ.

(a) Single exponent: $Ae^{-t/\tau} + C$

Coefficient/parameter type		***Neutrons***	**γ rays**	***Joint***
Components	*A [counts]*	141029 ± 3774	162171 ± 1331	130275 ± 1052
	τ [ns]	5.01 ± 0.07	4.30 ± 0.02	5.61 ± 0.03
Accidentals	*C [counts]*	135 ± 6	408 ± 3	351 ± 3
Gate-width [ns]		29.1 ± 0.4	25.0 ± 0.1	32.6 ± 0.2
χ^2_v		15.09	1.05	1.54

(b) Double exponent: $Ae^{-t/\tau_s} + Be^{-t/\tau_l} + C$

		Experimental		
Coefficient/parameter type		***Neutrons***	**γ rays**	***Joint***
Short (prompt)	*A [counts]*	147861 ± 1889	180667 ± 2883	131872 ± 1646
component	*τ_s [ns]*	4.78 ± 0.04	3.62 ± 0.10	5.52 ± 0.04
Long (scatter)	*B [counts]*	145 ± 24	9264 ± 2891	121 ± 25
component	*τ_l [ns]*	92.7 ± 31.0	9.1 ± 0.8	147.6 ± 133.3
Accidentals	*C [counts]*	106 ± 9	407 ± 3	311 ± 37
Short gate-width [ns]		27.7 ± 0.2	21.0 ± 0.6	32.1 ± 0.3
Long gate-width [ns]		538.7 ± 180.1	53.1 ± 4.8	857.2 ± 774.1
χ^2_v		2.85	1.16	3.23

4.2.2 Bare arrangement

To validate that the proposed extension to the Rossi-α model is indeed referring to the neutron that underwent geometric scatter, *BARE15* configuration was utilised with the main ^{252}Cf source, Cf252-MAIN, to determine the γ-ray, neutron and *joint* response. The data for the three cases are represented in the plots in figures 4.11(a), 4.11(b) and 4.11(c), while the coefficients of the fits for the two models discussed in the preceding section are provided in table 4.2, along with their corresponding χ^2_v values. The figures and the tables include all the different information that were presented for the reflective cases.

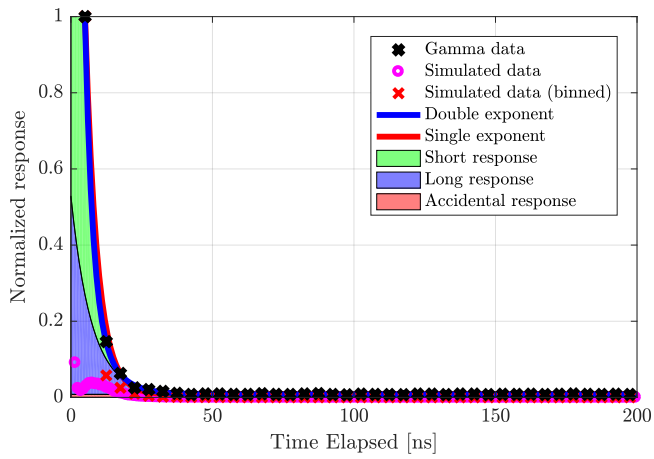

(a) γ-ray distribution.

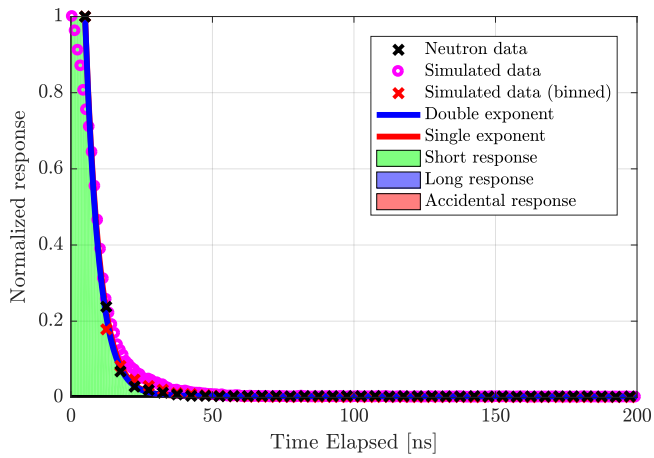

(b) Neutron distribution.

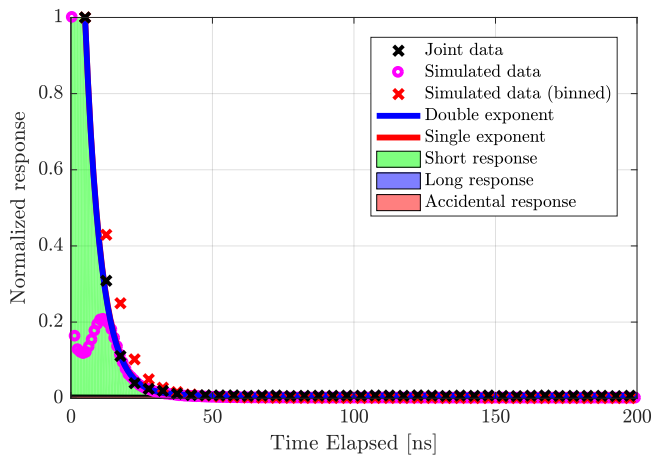

(c) Joint distribution.

Figure 4.11 | Interval time distribution for the detected radiation from ^{252}Cf source using the BARE15 arrangement. The *interval-time distributions* measured using the bare arrangement comprising a comparison of experimental data (black cross) using detected signals, fits according to the three-term model reported in this work (blue line), and the single exponential model (red line) for the **(a.)** γ rays, **(b.)** neutron and **(c.)** joint cases. The distribution has been decomposed into the contributions from each term as per the corresponding shading; the short response (green), the long response (blue) and the time-independent response (red). Simulated data are also included for the three distributions with 1 ns (magenta crosses) and 5 ns bins (red circles).

4.3 Neutron spectrum of ^{252}Cf

Briefly recapping some basic information already provided in section 2.3 on page 25, during spontaneous fission, multiple neutrons and photons are emitted with different energies, separated in the time domain by $< 10^{-13}$ seconds. The results of the experiment presented in this section were designed to attempt experimental determination of the neutron spectrum of ^{252}Cf by measuring the emission-to-detection time of each neutron under the assumptions that all neutrons and γ rays from a single fission event are emitted at the same time (i.e. despite the 10^{-13}-second spread), and that a photon travelling at the speed of light is instantly available for detection following its emission. While neither of the two assumptions are strictly valid, the resolution of the instruments (i.e. 5 ns) prevents such fine measurements to be made in any case. Under these assumptions, it is therefore possible to determine emission-to-detection time by equating it to be the same as the time escaped between a γ-ray event and subsequent neutron event. This γ-ray event is referred to as the photon-flash. To realise this, the *multiplicity register* was configured in the "Conf-PF" so that the *coincidence-gates* are only triggered upon the detection of a γ ray, while only the neutron events are considered as *satellite-events*, as described in section 3.2.5 on page 73. Therefore, the *interval-time distributions* produced by the *multiplicity register* correspond to a histogram illustration of the intensity of the time elapsed, ΔT, between the photon flash and the subsequently detected neutron. This ΔT was converted to energy using equation 2.6 on page 16 using a Matlab script (see appendix D.6 on page 280), where the distance between the source and the detector was 0.367 m (including the detector's thickness, i.e. $d = 0.2625$ m + 0.10 m = 0.3625 m). Once converted, each bin of the detected distribution was further divided by the width of the bin, in MeV, and experimental duration, in seconds, to ascertain the response per MeV per second.

The *BARE15* arrangement, detailed in section 3.3.4 on page 82, was used in the experiments with a ^{252}Cf source at the centre. In order to change the hardness of the spectrum, the experiment was repeated several times, with the source placed inside different water-filled cylinders of different radii (i.e. 1, 3 and 5) cm. The method of calibrating detectors is detailed in section 3.5 on page 87. Figure 3.17(a) on page 83 illustrates the setup with a water-filled cylinder of radius of 5 cm. The four experiments were conducted for (511, 652, 760 and 643) seconds, respectively.

Figure 4.12 illustrates the detected spectrum response per MeV per second for the different cases with the source placed in (i) no water, (ii) water-filled cylinder of 1 cm radius, (iii) water-filled cylinder of 3 cm radius and (iv) water-filled cylinder of 5 cm radius. The plots were fitted with a spline-smoothing fit, which uses a form of numerical fit where the interpolant is a type of piecewise polynomial, to guide the eye. The data points for the distributions for the different cases are marked in red, magenta, blue and black circles, respectively, while the corresponding

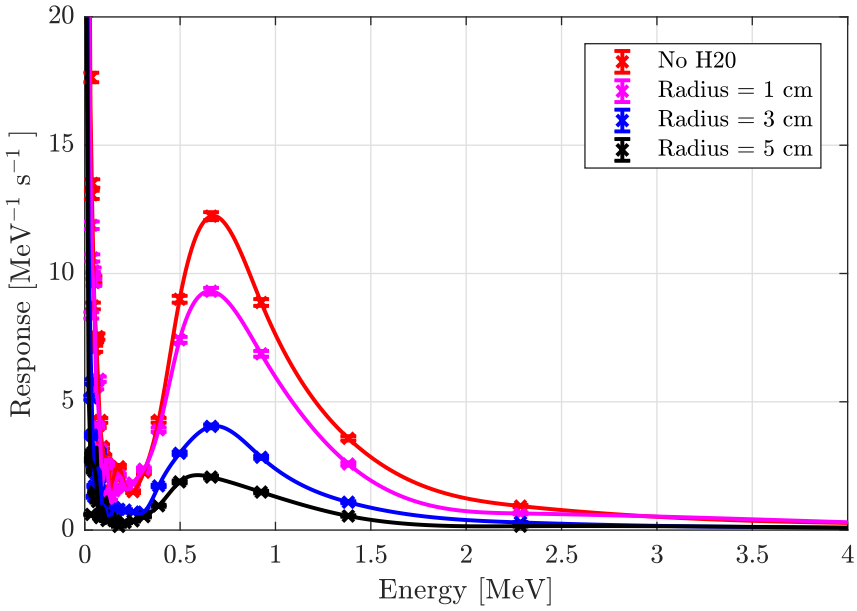

Figure 4.12 | Neutron spectrum of ^{252}Cf. Experimental neutron spectrum of the main ^{252}Cf using *BARE15* arrangement. The experiment was repeated four times with no water and a water-filled cylinder with radius 1 cm, 3 cm and 5 cm to forcefully change the hardness of the spectrum.

fits are shown with solid lines of the same colour. The error bars were computed using the formulations in section 2.8.2 on page 53.

4.4 Spatial correlation between neutrons emitted from spontaneous fission of ^{252}Cf

As an unstable nucleus of ^{252}Cf undergoes spontaneous fission, it usually splits up into two fragments (i.e. fission fragments), as mentioned in section 2.3 on page 25 in the *centre-of-mass frame of reference*. Each of these fragments is expelled from the other in the opposing direction (i.e. anisotropic in nature). As the two fragments are moving away from one another, they emit multiple neutrons (and γ rays). It is established that in more than 95% of the cases, this evaporation of neutrons takes place from fully accelerated fragments. These emitted neutrons carry their fission fragment's trajectory and hence they also have an anisotropic *angular distribution*, manifest in the intensity of particles resulting from a nuclear process, spontaneous fission in this case, as a function of angles relative to a specified direction. The results presented in this section are from experiments that were designed to determine the *angular distribution* of the neutrons emitted from such spontaneous fission.

With the apparatus available for the experiments, there was no practical way to experimentally determine the reference directions along which the two fragments from the scission process are ejected. Hence the *reference* point was determined by taking the position of the first detected neutron in an *event-train* and then determining the position of any subsequently detected correlated neutrons (i.e. within a *gate-width* of 25 ns) with respect to that reference. These subsequent events are referred to as the *second*, *third*, *fourth*, etc. particle (i.e. neutron or photon), i.e. each event in the event-train is labelled according to the 'order' or sequence in which it arrived at the detector. Once the position of the subsequent events were determined with respect to (w.r.t.) the *reference* event, they were tallied into separate spatial responses, which represent the total number of triggers detected in a specified direction. Each of these responses was normalised by dividing them by their respective peaks, as the responses had vastly different count rates due to decreasing probability of detecting higher-order coincidence events. Thus, each distribution consists of the normalised coincident fast neutron response as a function of the angle of the detector position relative to that of a *reference* detector, the latter being the detector that triggers the coincidence trigger window. This distribution is referred to as the *angular distribution*. The first neutron detected in the *event-train*, which was used as a *reference*, is not necessarily the first neutron that was emitted but rather the neutron with higher energy compared to other neutrons that were emitted in the same fission event as it reached the detector first; assuming that all neutrons travelled in a straight line before being detected.

The experiments were conducted using the *BARE15* setup, detailed in section 3.3.4 on page 82, with the *multiplicity register* in the Conf-N mode (see section 3.2.5 on page 73). The detectors were calibrated using a methodology detailed in section 3.5 on page 87. The exper-

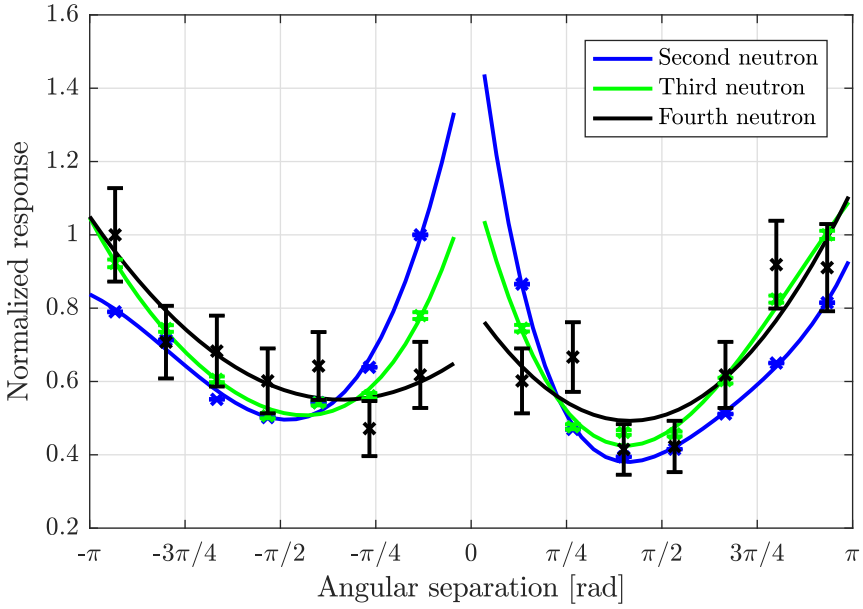

Figure 4.13 | Angular distribution of the neutrons emitted from the spontaneous fission of ^{252}Cf. Using the *BARE15* arrangement, the normalised coincident detected fast neutron response as a function of the angle of the detector position relative to that of a *reference* detector, the latter usually being the detector that triggers the coincidence trigger window, is presented.

iment was conducted overnight, which is approximately 17 hours. The correlated events, i.e. the *event-trains*, were dumped in list mode (see figure 3.8(b) on page 69) and post-processed using a C++ script to determine the neutron *angular distribution* of ^{252}Cf (see appendix D.7 on page 281).

Figure 4.13 illustrates the *angular distribution* of the detected correlated neutrons from the spontaneous fission of ^{252}Cf. The *angular distributions* were classified into three categories: (i) the *second* correlated neutron that was detected w.r.t. the *reference* neutron (blue crosses), (ii) the *third* correlated neutron that was detected w.r.t. the *reference* neutron (green crosses) and (iii) the *fourth* correlated neutron that was detected w.r.t. the *reference* neutron (black crosses). The fourteen data points of each distribution are illustrated by the "*" symbols with error bars which were computed using the formulations in section 2.8.2 on page 53. Each distribution was split in two halves, each representing either side of the *reference* detector which were fitted with individual two-term Fourier series (with the exception of the *fourth* neutron which needed a two-term polynomial function) using Matlab's Curve Fitting Toolbox to guide the eye and is plotted using solid lines of the corresponding colour. The discontinuity at 0 rad is a consequence of the dead-time of the *reference* detectors. The goodness-of-fit parameters for the different fits are listed in table 4.3.

The dataset of the *angular distributions* corresponding to the *Second*, *Third* and *Fourth*

Table 4.3 | Goodness-of-fit for angular distribution fits. Goodness-of-fit for the fits shown in figure 4.13 using *sum of squares due to error (SSE)*, *R-square* and *Root Mean Squared Error (RMSE)* techniques.

Neutron	***Type***	***SSE***	***R-Square***	***RMS***
Second-Left	Fourier-2 term	0.0042	0.9820	0.0652
Second-Right	Fourier-2 term	0.0011	0.9968	0.0330
Third-Left	Fourier-2 term	0.0034	0.9822	0.0585
Third-Right	Fourier-2 term	0.0056	0.9848	0.0749
Fourth-Left	Polynomial-2 term	0.0249	0.8422	0.0789
Fourth-Right	Polynomial-2 term	0.0639	0.7452	0.1264

neutron were further reconstructed with a restriction on the *gate-width* such that the constituents of the corresponding distributions may only contain events that are present within the first (10, 15 and 20) ns, respectively. These three distributions are presented using blue circles in figures 4.14(a), 4.14(b) and 4.14(c), respectively, along with the corresponding unrestricted distribution with a *gate-width* of 25 ns (red circles) for all cases for comparison. Each half of the three distributions were normalized to the data-point with the least magnitude. By restricting the size of the *gate-width*, the assay is modified such that it reduces scattered neutron events and also increases detector threshold.

Further to this, figure 4.14 also includes Geant4 simulation results using the *Fission Reaction Event Yield Algorithm (FREYA)* (light blue crosses), CGMF (orange crosses), FIFRELIN (yellow crosses) and the uncorrelated fission model (green crosses) described in section 3.7. The responses obtained from the four models are labelled as “FREYA”, “CGMF”, “FIFRELIN” and “Uncorrelated”, respectively. The FREYA and the uncorrelated fission models were also used to obtain *crosstalk* corrected distributions (cyan and magenta crosses, respectively), by constructing the responses which ignored all detections registered as a consequence of *crosstalk*. Thus, the *crosstalk* corrected distributions, labelled as “XT corrected” in the figures to distinguish them from the standard responses, show the impact of *crosstalk* on such experiments. All simulations constituted 50 million fission histories, which were executed in 5 batched of 10 million fission histories each. The seeds to the random number generator used by the physics models were randomly defined for each execution to avoid any unintended correlations between different runs. Since the binary files corresponding to the CGMF and FIFRELIN models did not contain the required number of histories, the datasets were therefore recycled; whereby all recycled fission events were rotated along the x-axis by a random angle to reduce possible correlation due to the recycle scheme, making sure that the seed to the random number generator used to determine the angle was different for each batch.

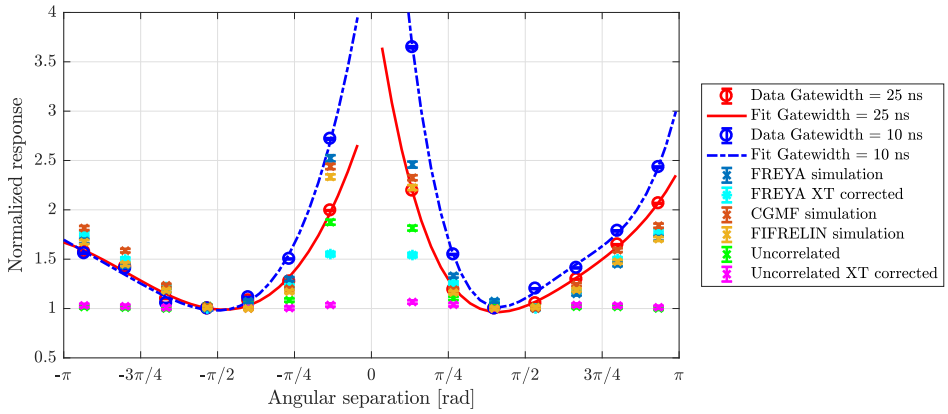

(a) Second neutron distribution.

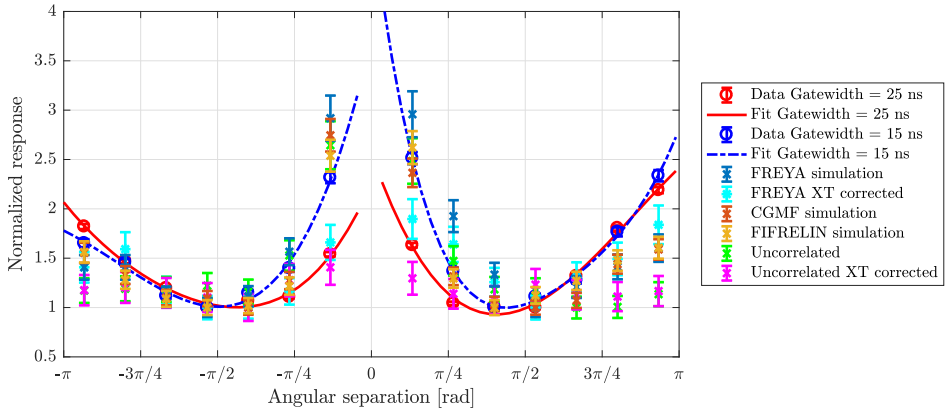

(b) Third neutron distribution.

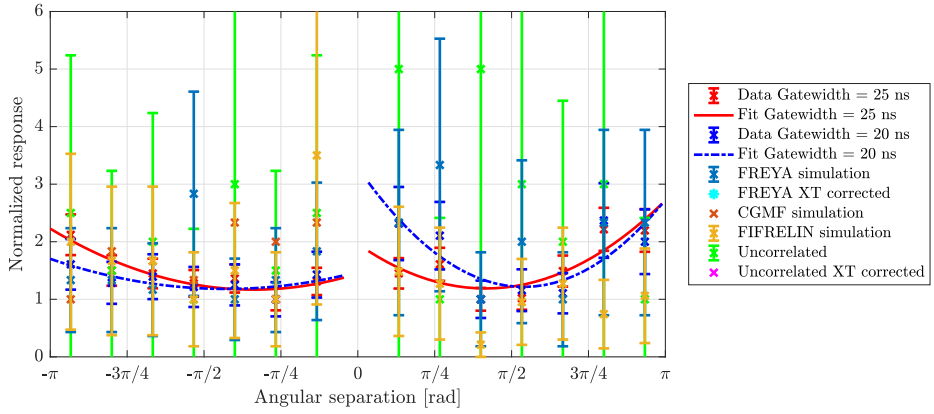

(c) Fourth neutron distribution.

Figure 4.14 | Comparison between restricted, unrestricted and simulated angular distributions. A comparison of angular distributions obtained using an unrestricted *gate-width* of 25 ns (red data points) and a restricted *gate-width* (blue data points) for the **(a)** *Second*, **(b)** *Third* and **(c)** *Fourth* events from ^{252}Cf. The experimental data are denoted by cross symbol while the corresponding fits by the solid lines. Geant4 simulation using FREYA, CGMF, FIFRELIN and uncorrelated fission model; two datasets for FREYA and uncorrelated are presented: with and without *crosstalk* correction.

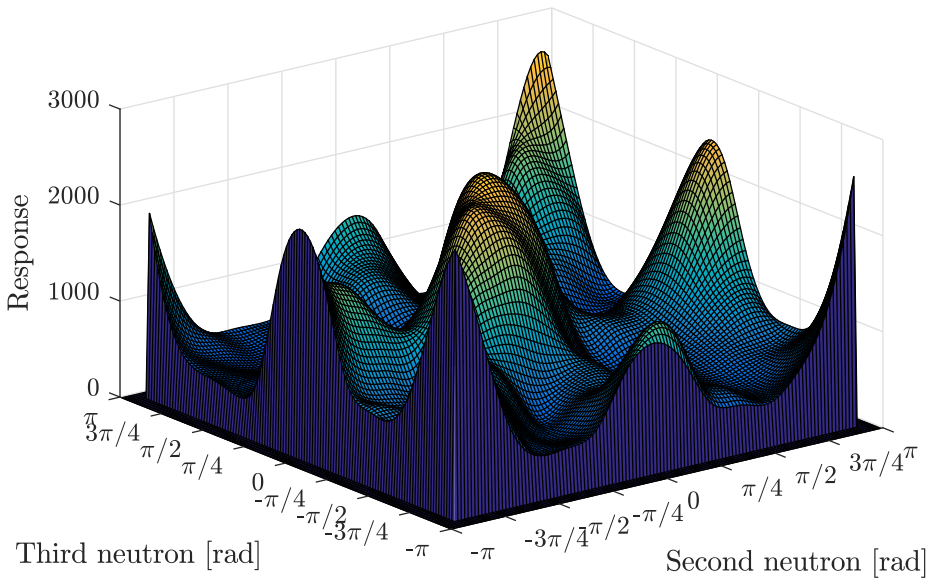

Figure 4.15 | Angular correlation between the second and *third* neutron in an event chain w.r.t. the first event. The intensity of the third neutron with neutron as a function of the angular disposition of the *first* and *second* event in the *event-train*. The x-axis and the y-axis of the plot correspond to the angular positions of the *second* and *third* neutrons, w.r.t. the *reference* neutron, respectively, while the z-axis represents the intensity of the response. The mesh-fineness of the surface plot was increased in post-process by using a split-smoothing based interpolation method.

The angular position of the *third* detected correlated neutron is not only correlated to the *reference* neutron, but also the *second* correlated neutron in the *event-train*. This relationship cannot be seen in the traditional 2-dimensional *angular distribution* demonstrated in figure 4.13. To illustrate this high-order angular correlation between the *first*, *second* and *third* neutron, a surface plot is constructed, as shown in figure 4.15, where the intensity of the surface plot corresponds to the displacement of the *third* neutron w.r.t. the *first* and *second* neutron. Here, the x-axis and the y-axis of the plot correspond to the angular positions of the *second* and *third* neutron, respectively, w.r.t. the *reference* neutrons, while the z-axis represents the intensity of the response. This response, computed using the C++ script mentioned earlier from the *event-trains* listed by the *multiplicity register*, was further post-processed using Matlab's spline-smoothing algorithm in order to increase the fineness of the plot and remove any discontinuity existing due to the dead-time related to the detectors where the first and second neutrons were triggered.

4.5 Analysis of the neutron and photon temporal correlation via coincidence counting

As already mentioned in 2.5, while the Rossi-α distributions illustrated in section 4.2 can be utilised to characterise unknown radioactive samples undergoing spontaneous and induced fission, historically, it is a common practice to produce multiplicity histograms instead by placing two *coincidence-gates* (i.e. *prompt-gate* and *delayed-gate*) producing a *reduced factorial moment distribution* of incoming neutron events. The two *coincidence-gates* correspond to two groups; (i) those from correlated and uncorrelated neutrons (i.e. *real events* and *accidental events*) and (ii) those from uncorrelated processes (i.e. *accidental events*) from different fission chains, (α, n) reactions, and random sources of background. Section 3.2.1 on page 65 describes a new method of extracting the same information by using a cluster-size based algorithm instead, using which all results presented here were obtained. In this section, several correlated and uncorrelated sources are examined to illustrate the difference in response. Section 4.5.1 shows the neutron, and γ-ray *coincidence distributions* obtained from PFNCC of ^{252}Cf, caesium-137 (^{137}Cs), and cobalt-60 (^{60}Co), whereas section 4.5.2 illustrates the neutron *coincidence distributions* from AFNCC of U_3O_8.

4.5.1 Passive coincidence counting

In this section, the *foreground coincidence distribution* and *background coincidence distribution* from the PFNCC of various samples are presented. These experiments can be grouped in three categories. The four sets of experiments in the first category are as follows:

1. *Cf252-BARE8:* The main ^{252}Cf (i.e. Cf252-MAIN) source was placed at the centre of the eight-detector arrangement (i.e. *BARE8*), measuring the *coincidence distributions* for neutron and γ-ray events. The durations of the experiments were 1202 and 244 seconds, respectively.

2. *Cf252-BARE15:* The main ^{252}Cf (i.e. Cf252-MAIN) source was placed at the centre of the fifteen-detector arrangement (i.e. *BARE15*), measuring the *coincidence distributions* for neutron and γ events. The durations of the experiments were 603 and 303 seconds, respectively.

3. *Co60-BARE15:* The ^{60}Co calibration source was placed at the centre of the fifteen-detector arrangement (i.e. *BARE15*), measuring the *coincidence distributions* for γ events. The duration of the experiment was 2775 seconds.

4. *Cs137-BARE15:* The ^{137}Cs calibration source was placed at the centre of the fifteen-detector arrangement (i.e. *BARE15*), measuring the *coincidence distributions* (or the lack

there of) for γ events. The duration of the experiment was 689 seconds.

The different arrangements of the detectors and the sources are detailed in section 3.3 on page 74. All the detectors were calibrated using a methodology detailed in section 3.5 on page 87. The *gate-width* of the *multiplicity register* was set to 25 ns and 20 ns for the neutron and photon sources, respectively, based on the results obtained in table 4.2(b) on page 115. For each distribution, the efficiencies of the *Totals* and the *multiplet ratios* (i.e. doublet-to-singlet and triplet-to-singlet ratios) were calculated. The former refers to the total number of events detected, whilst the latter refers to the sensitivity of the doublet and triplet events per singlet event. The *Totals* were computed using the expression in equation 4.3, where, f_x is the *foreground coincidence distribution* for the type of particle x.

$$\text{Totals} = \sum_{n=1}^{\infty} n f_x(n) \tag{4.3}$$

Figure 4.16(a) illustrates the *foreground coincidence distribution* and *background coincidence distribution* of four different sources clustered in four sets of bar plots i.e. (from left to right) Cf252-BARE8 (neutron), Cf252-BARE15 (neutron), Cs137-BARE15 and Co60-BARE15. Each of the bars in the four sets corresponds to the count rates in the different orders of the *foreground coincidence distribution* (i.e. singlets, doublets, triplets, etc.), while the *background coincidence distribution* is reflected by the superimposed red bars on top of the *foreground coincidence distribution* to which they belong. The first two distributions correspond to the neutron *coincidence distributions*, while the latter two are photon *coincidence distributions*. As the *multiplicity register* computes the *coincidence distributions* directly, a Matlab script, demonstrated in appendix D.8 on page 287 was used to make the plot as well as handling the compilation of the error bars based on the equations listed in section 2.8.2 on page 53. The efficiency of the *Totals* and the *multiplets* ratio along with their corresponding uncertainties are presented in tables 4.4(a) and 4.4(b), respectively. The photon *coincidence distributions* for the two ^{252}Cf cases are available in tables E.1(b) on page 299 and E.2(d) on page 300.

The second category of experiments used all of the three different ^{252}Cf sources (see 3.1 on page 74 for their strengths) that were available in conjunction with *BARE15* arrangement for carrying out the following three experiments to determine the neutron *coincidence distributions*:

1. *Cf252-TH:* The setup used the Cf252-TH source mentioned in section 3.3.1 on page 74 and the experiment was conducted for 953 seconds.

2. *Cf252-FC:* The setup used the Cf252-FC source mentioned in section 3.3.1 and the experiment was conducted for 743 seconds.

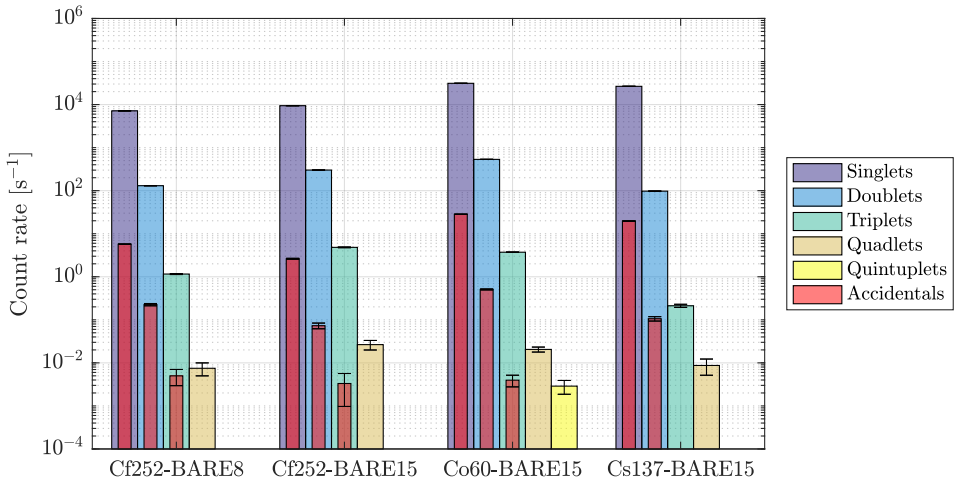

(a) Neutron and photon coincidence distributions from ^{252}Cf, ^{137}Cs and ^{60}Co.

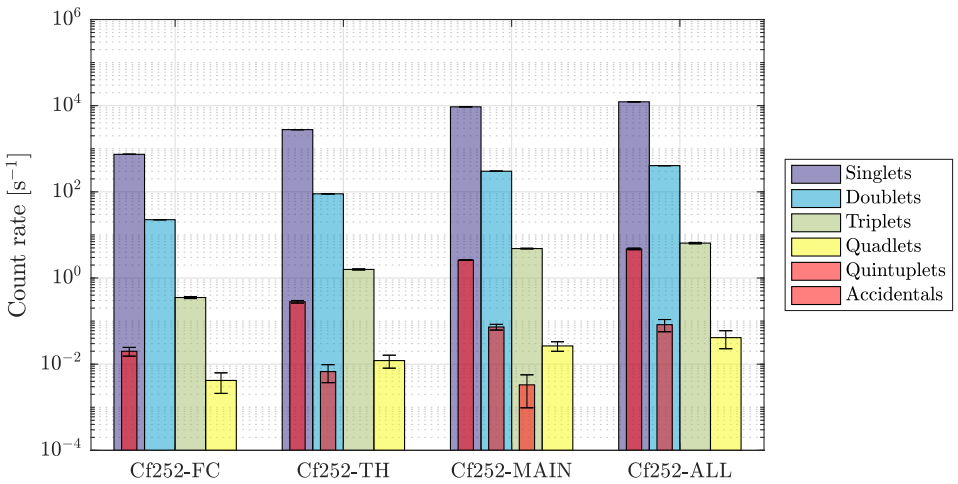

(b) Neutron coincidence distributions from ^{252}Cf of different strengths.

Figure 4.16 | Neutron and photon coincidence distributions from BARE8 and BARE15 arrangements. (a) The first two clusters of the bar plots are the neutron *coincidence distributions* of main ^{252}Cf source while using *BARE8* and *BARE15* arrangement, respectively. Higher *multiplet* is recorded when using the arrangement with larger detector count despite an increase in source-to-detector distance from 20.25 cm to 26.75 cm. The photon *coincidence distributions* of ^{137}Cs and ^{60}Co sources using *BARE15* arrangement are illustrated by the latter two clusters of bar plots, which demonstrate the increased *multiplets* when using ^{60}Co despite using the same arrangement and sources with the same activity. **(b)** The change in response of neutron *coincidence distributions* due to change in the strength of the ^{252}Cf source is illustrated. Higher *multiplet* is registered when using stronger source.

Table 4.4 | Total efficiency and multiplet ratios. Efficiency of **(a)** Totals and **(b)** doublets and triplets for the experimental data using the main ^{252}Cf, ^{60}Co and ^{137}Cs sources.

(a) Totals

Source	***Activity [pps]***	***Setups***	***Experiment***		***Simulation***	
			Totals [cps]	*Eff. [%]*	*Totals [cps]*	*Eff. [%]*
^{252}Cf	331541	BARE8	8051 ± 3	2.24 ± 0.03	7179 ± 88	2.17 ± 0.03
^{252}Cf	331541		10027 ± 4	3.02 ± 0.03	9185 ± 101	2.78 ± 0.04
^{60}Co	360490	BARE15	32273 ± 6	4.48 ± 0.02	18885 ± 16	2.62 ± 0.08
^{137}Cs	355850		26738 ± 3	7.51 ± 0.03	4106 ± 17	1.15 ± 0.04

(b) Multiplet

Source	***Activity [pps]***	***Setups***	***Experiment***		***Simulation***	
			Doublet-Singlet ratio ($\times 10^{-2}$)	*Triplet-Singlet ratio ($\times 10^{-4}$)*	*Doublet-Singlet ratio ($\times 10^{-2}$)*	*Triplet-Singlet ratio ($\times 10^{-4}$)*
^{252}Cf	331541	BARE8	1.910 ± 0.004	1.88 ± 0.04	3.18 ± 0.22	4.07 ± 2.47
^{252}Cf	331541		3.201 ± 0.008	5.12 ± 0.10	5.85 ± 0.27	13.42 ± 4.06
^{60}Co	360490	BARE15	1.710 ± 0.001	1.19 ± 0.01	1.74 ± 0.01	0.10 ± 0.01
^{137}Cs	355850		0.367 ± 0.001	0.080 ± 0.006	0.38 ± 0.03	0

3. *Cf252-ALL:* The setup combined all the three ^{252}Cf sources (i.e. Cf252-TH, Cf252-FC and Cf252-MAIN) mentioned in section 3.3.1 and the experiment was conducted for 743 seconds.

Figure 4.16(b) illustrates the neutron *coincidence distributions* of the four different ^{252}Cf sources that were available using the *BARE15* setup (i.e. from left to right; Cf252-TH, Cf252-FC, Cf252-MAIN and Cf252-ALL). The presentation of the data is consistent to that found in figure 4.16(a). Additionally, the *multiplet* ratios can be found in table E.5 on page 302 in appendix E.

The final category of experiments utilised the *REFL15* setup in both *exposed* and *secured* configuration to determine the neutron and *joint* coincidence events which are referred to as the Exposed-Neutron, Secured-Neutron, Exposed-Joint and Secured-Joint. Here, 'Exposed' refers to the cases with the source 'exposed' to the edge of the tank while 'Secured' refers to the case where the source is 'secured' at the centre of the tank to minimise correlated events from escaping (see section 3.3.2 on page 77). The experiments were conducted for (1800, 70535, 300 and 600) seconds, respectively. While the neutron *coincidence distribution* was determined using a *gate-width* of 25 ns, the *joint coincidence distribution* utilised a *gate-width* of 35 ns. The normalised factorial moments for each of the four *coincidence distributions* were computed using equation 2.50 on page 53. Prior to this computation, the distribution was corrected for the efficiency of the assay which was approximated to be 1.2% and 2.3% for neutron and joint radiation field, respectively, using the Geant4 simulations. These calculations were done in

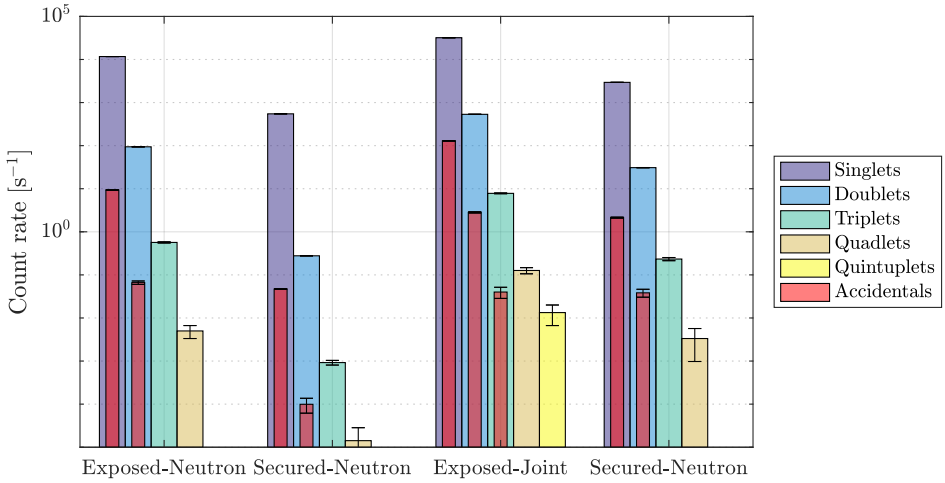

(a) Neutron coincidence distributions.

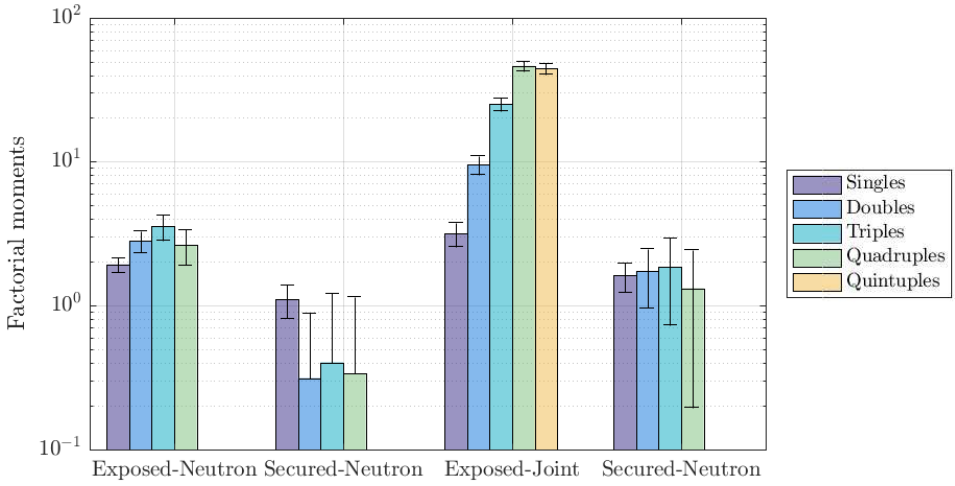

(b) Computed normalised factorial moment distribution.

Figure 4.17 | Coincidence and factorial moment distributions from REFL15 arrangements. The **(a)** *foreground coincidence distributions* and **(b)** normalised factorial moment distributions for the contrasting experiments using *REFL15* arrangement using both neutron and *joint* γ-ray & neutron signals for the source subject to reduced degree reflection and moderation (exposed) and central to the light water moderator (secured) subject to a prompt *gate-width* of 25 ns. A higher order of multiplicity for the exposed source is observed when compared to the secured source. Estimates of the accidentals rates are obtained with a *gate-width* delayed by 150 ns relative to the prompt gate.

Maltab command prompt.

Figure 4.17(a) illustrates the *coincidence distributions* that were obtained using the *REFL15* setup at Lancaster University. The presentation of the data is consistent to that found in figure 4.16(a). Finally, figure 4.17(b) illustrated the normalised factorial moments of the *coincidence distributions* obtained from the *REFL15* based experiments using the expression in equation 2.50 on page 53. The four different sets of bar plots from left to right correspond to those from figure 4.17(a).

4.5.2 Active coincidence counting

For a practical demonstration of an AFNCC assay for SNF measurements, nine standardised samples of UOX of the various enrichments, described in section 3.3.1 on page 74, were irradiated with the four AmLi sources using three detector arrangements: *BARE8*, *BARE15* and *CASTLE12* illustrated in sections 3.3.3, 3.3.4 and 3.3.5, respectively, starting page 79. A layer of polyethylene cylinder of approximately 4.3 cm radius was added between the UOX canister and the AmLi sources to moderate the neutrons from the AmLi source so that they are able to induce fission in the UOX canisters. The height of the polyethylene cylinder was 2 cm for all experiments, however the *BARE15* experiment was repeated with a second polyethylene cylinder, making the effective height 3.75 cm so as to quantify the impact of increased moderation. Using the Matlab script attached in appendix D.9 on page 289, the datasets were normalised to the distribution measured with an empty sample canister and with AmLi to remove any contribution from background and AmLi. This removes the coupling effect of the presence of AmLi and minimises the effect of *photon-breakthrough* as most of the registered activity comes from the AmLi source.

Tables E.6 and E.7 in appendix E.3 on page 303 provide the *coincidence distributions* obtained from the induced fission of the various samples of UOX, as well as the durations of the experiments. Further to this, figures 4.18(a) and 4.18(b) illustrate the trend in the relationships of the singlet and doublet count rates obtained from the experiment with uranium-235 (^{235}U) mass for the two assays. The two datasets are presented in the left and right y-axis, respectively, and are colour coded as blue and orange. The error bars for the datasets were computed based on the equations listed in section 2.8.2 on page 53. Figure 4.19 illustrates the effect of increased moderation for the *BARE15* arrangement by comparing the doublet count rates from the cases with 2 cm and 3.75 cm moderator, which are colour coded to be blue and black, respectively. Additionally, table E.8 tabulates all the raw *coincidence distributions* directly from the *multiplicity register* for the different enrichment cases. Finally, the *coincidence distributions* from the *CASTLE12* setup can be examined in table E.9. Figure 4.20, similar to figures 4.18(a) and

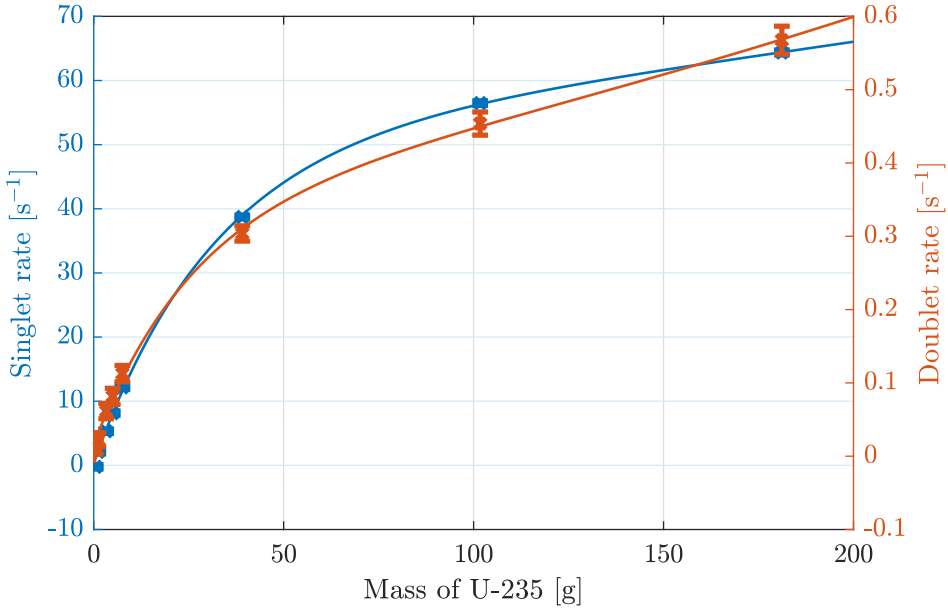

(a) BARE8: 8-detector bare arrangement.

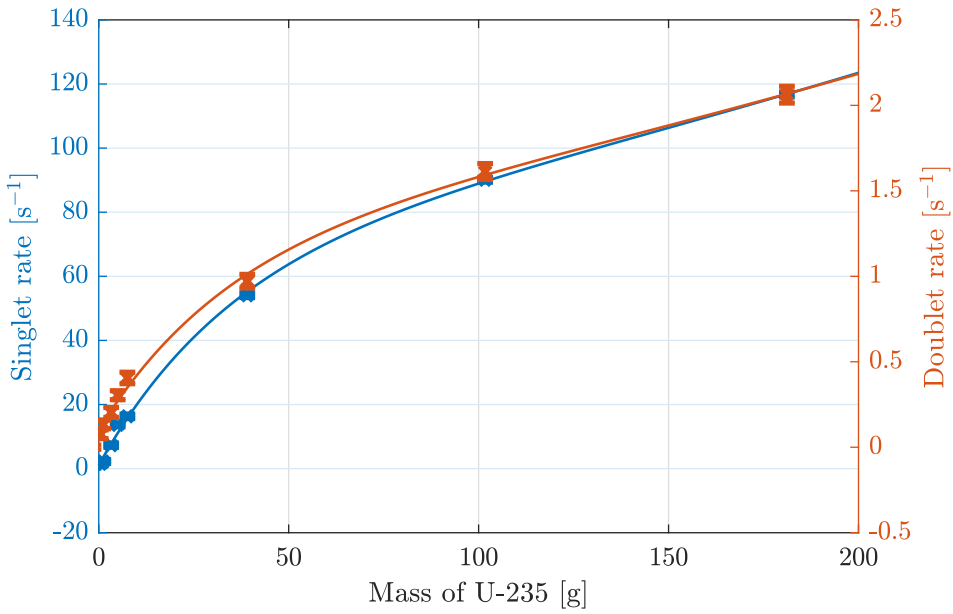

(b) BARE15: 15-detector bare arrangement.

Figure 4.18 | Active interrogation of UOX samples for BARE8 and BARE15 arrangements. The singles and the doublet count rates (per second) of the **(a)** *BARE8* and **(b)** *BARE15* arrangement using liquid scintillation detectors during the active interrogation of UOX. Both plots are approaching linearity in the low-enrichment region while a decreasing trend in fission rate is exhibited. A double exponent based fit is added to guide the eye.

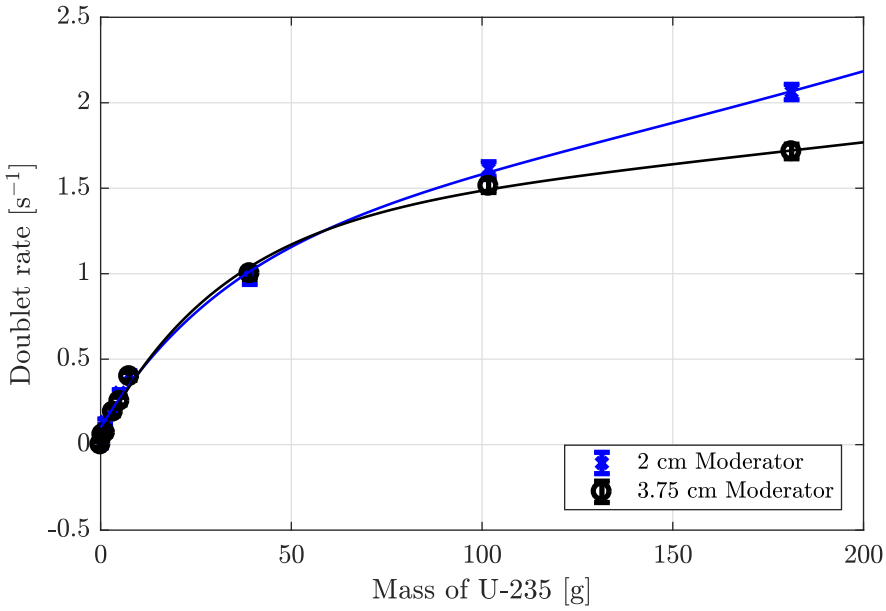

Figure 4.19 | Active interrogation of UOX samples for BARE15 arrangement using different levels of moderation. The doublet count rates (per second) of the *BARE15* arrangement using liquid scintillation detectors during the active interrogation of UOX using one of two cylindrical polyethylene blocks, each having the same radius of 5 cm, but with different heights; 2 cm or 3.75 cm. A double exponent based fit is added to guide the eye.

4.18(b), illustrates the relationships of the singlet and doublet count rates with ^{235}U mass for the *CASTLE12* assays.

The fits to all the figures demonstrated in this section are that of a double exponent. The coefficients of these fits along with goodness-of-fit are provided in table 4.5.

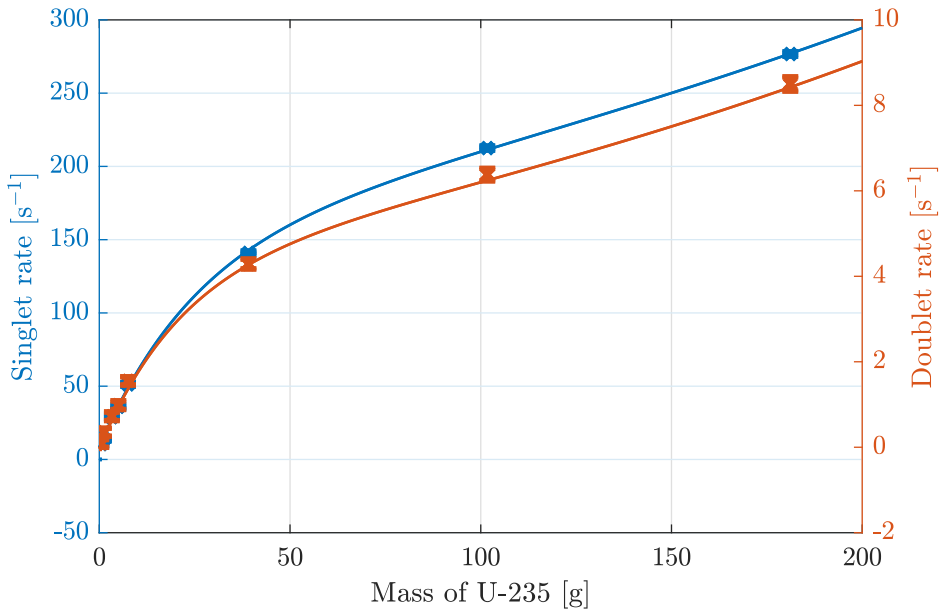

Figure 4.20 | Active interrogation of UOX samples for CASTLE12 arrangements. The singles and the doublet count rates (per second) of the *CASTLE12* arrangement using liquid scintillation detectors during the active interrogation of UOX samples. A double exponent based fit is added to guide the eye.

Table 4.5 | Coefficients and Goodness-of-fit for ANCC fits. List of all the coefficients from the double exponential equation and the corresponding goodness-of-fit (see section 2.8.3 on page 54) for the **(a)** singlet and **(b)** doublet fits shown in figures 4.18 to 4.20. The uncertainties of the various coefficients were determined using an estimated covariance matrix of the coefficient estimates by Matlab [129].

(a) Singlet fits

	Coefficients of $a * exp(b * x) + c * exp(d * x)$				***Goodness-of-fit***		
Type	*a*	*b*	*c*	*d*	*SSE*	*R-Square*	*RMS*
BARE8	50 ± 3	0.0014 ± 0.0003	-50 ± 3	-0.033 ± 0.003	1.88	0.999	0.68
BARE15 (2 cm)	70 ± 7	0.0029 ± 0.0005	-69 ± 6	-0.028 ± 0.005	11.1	0.999	1.66
BARE15 (3.75 cm)	57 ± 3	0.0031 ± 0.0004	-57 ± 3	-0.049 ± 0.009	13.4	0.999	1.82
CASTLE12	154 ± 5	0.0032 ± 0.0002	-145 ± 5	-0.039 ± 0.003	15.6	0.9998	1.97

(b) Doublet fits

	Coefficients of $a * exp(b * x) + c * exp(d * x)$				***Goodness-of-fit***		
Type	*a*	*b*	*c*	*d*	*SSE*	*R-Square*	*RMS*
BARE8	0.34 ± 0.02	0.0029 ± 0.0004	-0.33 ± 0.02	-0.04 ± 0.01	0.0003	0.999	0.009
BARE15 (2 cm)	1.23 ± 0.18	0.003 ± 0.001	-1.14 ± 0.17	-0.03 ± 0.01	0.009	0.998	0.046
BARE15 (3.75 cm)	1.33 ± 0.18	0.001 ± 0.001	-1.29 ± 0.17	-0.03 ± 0.01	0.007	0.998	0.041
CASTLE12	4.40 ± 0.16	0.003 ± 0.001	-4.34 ± 0.16	-0.05 ± 0.01	0.0269	0.999	0.082

4.6 Photon-breakthrough and crosstalk

As mentioned in sections 2.6.3 and 2.6.4 on page 48, scattered based detectors, such as those using the organic scintillation materials, are subject to two sources of event-based biases: *photon-breakthrough* and *crosstalk*. The results obtained from the investigation of the properties of these phenomena are provided in the following subsections, sections 4.6.1 and 4.6.2, respectively.

4.6.1 Photon-breakthrough

During the calibration process using ^{252}Cf, a list of the two integrals from the PGA technique was kept for all detectors for the mixed-field radiation emitted by the source. Using one such list corresponding to a randomly selected detector, figure 4.21 was constructed, which demonstrates a contour and a surface plot of the pulse shape discriminated outputs from a ^{252}Cf source, illustrating a considerable overlap of events in the low-energy region. Of the 15 detectors that were used during the experiments in *Oak Ridge National Laboratory (ORNL)*, table 4.6 illustrates the percentage of γ rays that were misclassified by the PSD technique employed by the *Mixed-Field Analysers (MFA)*, i.e. PGA. The data acquisition was made over 60 seconds using the main ^{252}Cf source. This was calculated by first constructing an intensity matrix of the first and second integrals using data obtained during calibration with ^{252}Cf. This matrix is identical to the dataset used to create figure 4.21. To account for the bend in the distribution seen in figure 4.21, the constructed matrix was then split into 13 smaller segments, which were fitted with either a single or a double Gaussian equation (depending on whether both neutron and γ plumes were present or not), and using the fit parameters, the total number of misclassified γ-ray events were identified. This calculation was done using a Matlab script, presented in appendix D.10.

Further to this, three experiments from section 4.5 were repeated a second time with minor changes to influence the γ-flux: (i) Cf252-MAIN source placed at the centre of the *BARE15* arrangement, (ii) active interrogation of the 20.1% enriched UOX sample in the *CASTLE12* arrangement and (iii) Cf252-MAIN source at the centre of the *BARE8* arrangement. These changes are listed below:

1. Cf252-MAIN source in the *BARE15* arrangement was placed inside a tungsten container of $\approx$ 2.5 mm thickness in the first experiment which would reduce the low energy γ-ray flux.

2. The 20% enriched UOX canister in the *CASTLE12* arrangement was interrogated with AmLi while being placed with several different γ-ray calibration sources that were available in the laboratory (see appendix B.4 on page 215) emitting γ rays of various energies at $\approx$ 2.15 MBq to drastically increase the γ-ray flux.

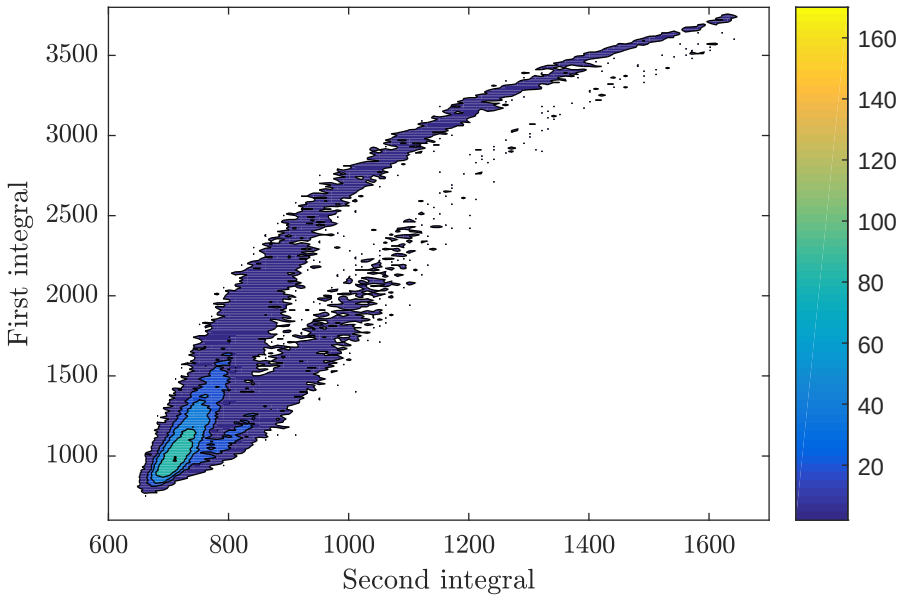

(a) Two-dimensional plot of first-versus-second integrals.

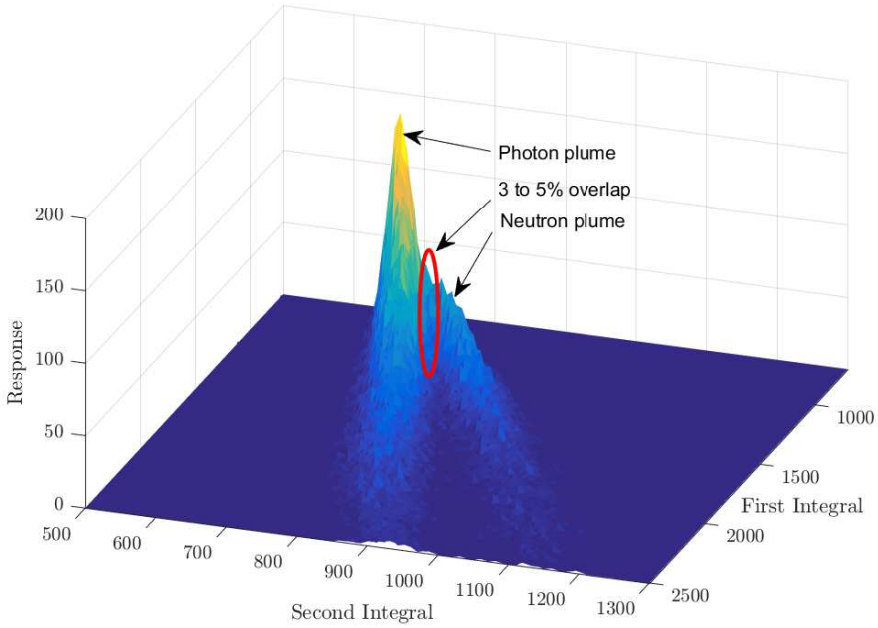

(b) Surface plot first and second integrals.

Figure 4.21 | Plots of first integral versus second integral used to depict the quality of pulse-shape discrimination and the extent of event misidentification. The *pulse shape discrimination (PSD)* plots using the *Pulse Gradient Analysis (PGA)* technique of a detector that was used in the experiments in this research showing the well-known degradation in discrimination between neutrons and photons in the low-energy region (low values of first- and second-integral) and much-improved discrimination in the high-energy region (high values); **(a)** Two-dimensional plot of first-versus-second integrals, and **(b)** surface plot derived with response as the third parameter.

Table 4.6 | Percentage of false neutrons. Demonstrates the percentage of γ-ray events that were incorrectly classified as neutrons.

MFA serial no.	***Channel***	***Total γ count***	***False neutron count***	***Percentage (%)***
4310	1	17342	759	4.38
	2	24581	1511	6.15
	3	21456	586	2.73
	4	28287	665	2.35
4311	1	30606	489	1.60
	2	26705	452	1.69
	3	28999	360	1.24
	4		Not connected	
4313	1	26761	2468	9.22
	2	25692	995	3.88
	3	23517	1117	4.75
	4	26004	697	2.68

3. The Cf252-MAIN source in the *BARE8* arrangement without the lead shielding to increase the γ-ray flux mentioned in section 3.3.

Table 4.7 presents the *Total* neutron count rates obtained for all three experiments showing the results both prior to the changes being implemented and also after the changes had been made. The *coincidence distributions* may be found in tables E.4, E.9(j) and E.2. For the second experiment, using the UOX canister, the AmLi contributions, per table E.9(i) on page 310, were removed prior to the calculation.

Table 4.7 | Totals rate for modified coincidence counting experiments. The *Total* neutron count rates for the modified experiments illustrating change in neutron counts.

	Case 1	***Case 2***	***Case 3***
Before	10 309	149	7 406
After	10 064	821	8 051

4.6.2 Detector crosstalk

As highlighted in section 2.6.4 on page 48, *crosstalk* occurs when a single neutron is first detected in one scintillator, then scattered to another scintillator leading to a second detection. Using data from the Geant4 simulations described in section 3.7 on page 91, figure 4.22 illustrates the probability of *crosstalk* events taking place for the fifteen-detector set-up, based on a 5 MeV mono-energetic neutron beam. Exponential fits were made using the datasets to guide the eye. The detectors were subjected to a variety of cut-off energies, i.e. (0, 100, 200 and 300) keVee. This simulation, along with others in this section, was conducted with 1 million particles from

a mono-energetic neutron or photon source. The particles were emitted from the centre of each arrangement with a fixed directional vector towards the top-most detector.

Based on the same Geant4 model, further simulations were conducted using mono-energetic neutrons of (1, 2 3.5 and 5.0) MeV with 200 keVee detector cut-off energy and no *gate-width*. Figure 4.23 shows the time that elapses between the primary detection and the detection of the *crosstalk* event between adjacent detectors. The y-axis denotes the number of particles detected per 1 million histories that were simulated.

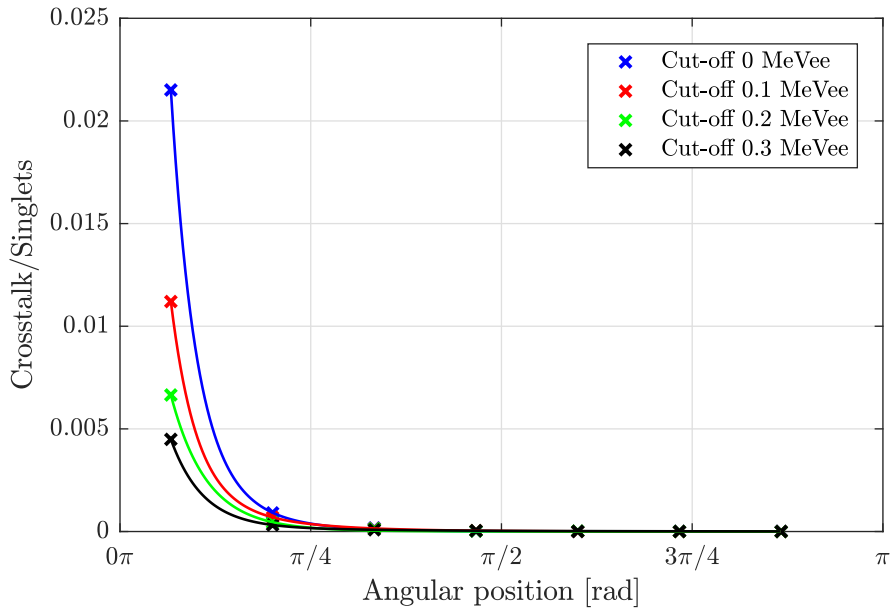

Figure 4.22 | Detector crosstalk probability. Detector *crosstalk* probability and corresponding spline-smoothing fit for 5 MeV neutrons for different cut-off energies (i.e. (0, 0.1, 0.2 and 0.3) MeVee) as a function of detector angle relative to the position of the detector triggered by the first event.

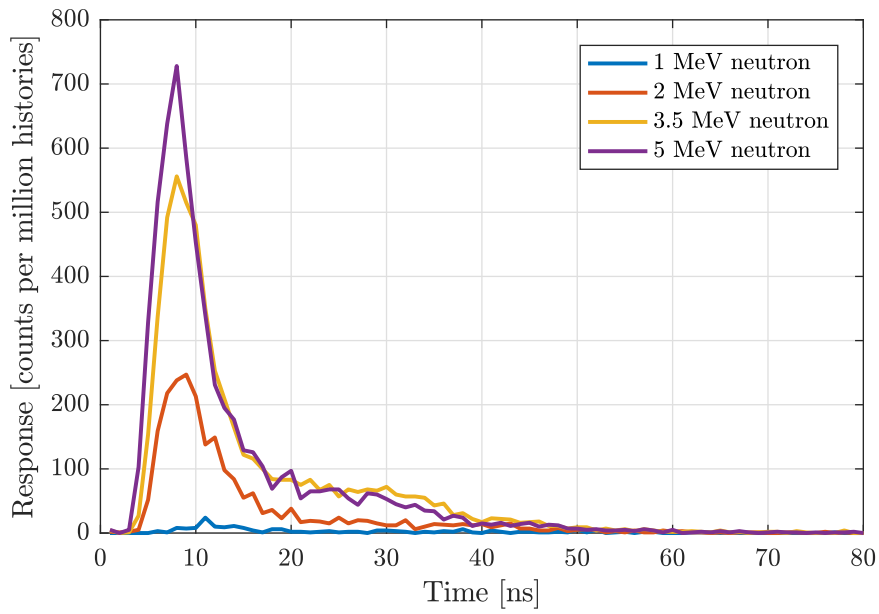

Figure 4.23 | The delay-between-crosstalk distribution. The delay-between-crosstalk (i.e. time escaped between initial event and the *crosstalk* event) distribution during *crosstalk* of (1.5, 2, 3.5 and 5.0) MeV neutrons between adjacent detectors.

Chapter 5

Discussion

This chapter discusses the experimental results presented in chapter 4 and compares them with some relevant prior-art. Similar to the results chapter, this chapter is split into six main sections. The first section discusses results from the FISPIN study of the evolution of correlated events from *spent nuclear fuel (SNF)*. The following section, section 5.2, discusses the different *interval-time distributions* presented in section 4.2 and validates the proposed extension of the Rossi-α model for empirical characterisation of the temporal distribution of radiation fields to quantise the effect of geometric scatter. Section 5.3 considers the results from the experiments aimed towards the determination of neutron spectrum from ^{252}Cf from fast scintillation detectors using the *time-of-flight (ToF)* method. Following this, the results presented in section 4.4 are investigated in section 5.4 showing evidence of the higher-order angular distribution between

correlated neutrons from the spontaneous fission of ^{252}Cf. Then in section 5.5, the results obtained by measuring different correlated, uncorrelated and stimulated sources using the proposed cluster-size based *passive fast neutron coincidence counting (PFNCC)* and *active fast neutron coincidence counting (AFNCC)* techniques are discussed. This discussion continues to the final section, section 5.6, where correction models to account for *photon-breakthrough* and *crosstalk* phenomena are introduced.

5.1 Correlated neutron emission from spent nuclear fuel

In this section, the results from neutron activation analysis in section 4.1, page 98, are discussed with the objective of forecasting the correlated neutron emission rates arising from depleted fuel due to the spontaneous fission and (α, n) reaction pathways for various plutonium and curium isotopes in SNF with a prolonged cooling period.

5.1.1 Evolution of isotopic composition

During the irradiation period, the actinides present in the fuel are transformed by radioactive decay, neutron capture, induced fission and spontaneous fission. The major decay pathways are illustrated in figure E.1 on page 298 along with their capture cross-sections, their decay paths and their half-lives. Some salient aspects of this scheme merit further explanation. For example, although the cross-section leading to the production of ^{237}U via double neutron absorption of ^{235}U is small, there is still a non-zero possibility of its occurrence. Whatever amount of ^{237}U is formed as a result, quickly transforms to ^{238}Pu (two β^- decays and one neutron absorption cycle later) and ^{239}Pu (two β^- decays and two neutron absorption cycles later) due to the short half-lives of 6.75, 7.12 and 2.35 days for ^{237}U, ^{238}Np and ^{239}Np, respectively. Additionally, the plutonium isotopes have high neutron absorption cross-sections, thereby resulting in a heavier plutonium inventory.

Since ^{241}Pu has a reasonably short half-life of 14.35 years relative to ^{241}Am, there is a steady build-up of ^{241}Am as a result of its decay. ^{241}Am again has a large cross-section for neutron absorption, thereby leading to the production of ^{242}Am. As a result of the short half-life of ^{242}Am, most of this is quickly converted to ^{242}Cm. This leads to the continuous production of ^{244}Cm via subsequent neutron capture reactions.

The datasets corresponding to the PWR-MOX fuel pin, illustrated in figures 4.1(a), 4.1(d), 4.1(g) and 4.1(j) on page 99 (as well as figures 4.1(b), 4.1(d), 4.1(h) and 4.1(k) corresponding to the BWR-MOX fuel pin) show similar trends in the isotopic composition of the plutonium isotopes for all four burn-up levels during the fuel irradiation periods. It can be observed that the higher burn-up cases (i.e. fuel pins at 55 GWd·MTU^{-1}) have lower concentrations of plutonium

isotopes as they have been burnt longer during the irradiation period. This decrease is less pronounced in the *Boiling Water Reactor (BWR)* for heavier plutonium isotopes (i.e. ^{242}Pu), as can be observed when comparing figures 4.1(j) and 4.1(k) to each other, due to the BWR reactor's operation in the void region, which results in a harder neutron spectrum, to encourage plutonium breeding. For the *uranium oxide (UOX)* fuel pins (i.e. figures 4.1(c), 4.1(f), 4.1(i) and 4.1(l)), as they start with zero plutonium content, only an increase in their concentration is evident with increased burn-up during the irradiation periods.

From the data in figure 4.1 it is clear that once the cooling period begins, the concentrations of ^{238}Pu, ^{239}Pu, ^{240}Pu and ^{242}Pu show very small change due to their long half-lives of (87.7, 2.41×10^4, 6.5×10^3 and 3.73×10^3) years, respectively, mostly undergoing α decay. However, there is a noticeable change in the concentration of ^{241}Pu as it decays to ^{241}Am via β^- decay with a relatively short half-life. Moreover, although it cannot be seen in these plots clearly, the number density of ^{238}Pu registers a very slight increase during the first ≈ 700 days of cooling as the ^{238}Np that is already built up in the reactor during the irradiation period decays to ^{238}Pu with a half-life of only 7.12 days.

For all cases, the trend in the initial concentrations of ^{241}Am, prior to the start of the cooling period, as illustrated in figure 4.2 on page 100, is similar to the corresponding trend of ^{241}Pu. During the cooling period, the concentration of ^{241}Am exhibits a steady increase, owing to the rather rapid decay of ^{241}Pu (compared to ^{241}Am) via β^- decay. Additionally, the concentration of ^{243}Am is higher in the fuel pin that was irradiated for longer, e.g. the 55 GWd·MTU^{-1}; the primary production path for ^{243}Am involves either two neutron absorptions on ^{241}Am or β^- decays of ^{243}Pu. Although ^{243}Am is also an α-particle emitter, its long half-life of 7370 years means that any change in its concentration cannot be discerned from the plots.

Finally, as also illustrated in figure 4.2, due to the very short half-life of ^{242}Cm (i.e. 162 days via a combination of α decay and spontaneous fission), there is a very rapid change in its concentration during the cooling period. This leads to essentially no ^{242}Cm isotope remaining in the fuel element after approximately 1200 days of cooling. Meanwhile, due to the relatively longer half-life of ^{244}Cm (18.1 years via α decay and spontaneous fission), only a steady decline in its concentration is observed. Moreover, comparing figure 4.2(c) (which represents 10 GWd·MTU^{-1} burn-up level) to figure 4.2(l) (which represents 55 GWd·MTU^{-1} burn-up level) reveals that because the fuel pin was irradiated for a longer period of time, the concentrations of both the curium isotopes are higher in the 55 GWd·MTU^{-1} fuel pin. Compared to *mixed-oxide (MOX)* fuel pins, the concentration of the curium is approximately 10 to 100-times lower in the UOX fuel pins. While doing this analysis, one has to keep in mind that curium isotopes suffer the consequences of the combination of an extensive cascade of decays and neutron activation steps in

which the uncertainties in capture cross-sections and decay pathways can be significant [130, 131]. The impact of such uncertainties was not investigated in this research.

5.1.2 Evolution of neutron activity

Number densities alone do not provide a complete basis on which to estimate the contribution of each isotope to the neutron activity from a given waste assay because each individual isotope has different yields associated to the spontaneous fission and (α, n) pathways. Thus spontaneous fission and (α, n) neutron emission rates from FISPIN were further analysed, the results of which are presented in section 4.1.2 on page 101 from the two different points-of-view; further to this, the isotope-wise relative neutron emission was also studied. This section provides an analysis of these results to highlight the major aspects of the evolution trends.

Spontaneous Fission

Figures 4.3(a) and 4.3(j) on page 102 illustrate the evolution of spontaneous fission neutron activity with time produced by the variety of different plutonium isotopes for the 10 GWd·MTU^{-1} and 55 GWd·MTU^{-1} PWR-MOX cases. As expected, the rate of neutron emission is fairly constant for all isotopes, except ^{238}Pu, throughout the entire cooling period because the number densities of the isotopes are also relatively constant during this time. However, due to the relative large spontaneous fission yield of ^{238}Pu (2590 n·s^{-1}·g^{-1}) (see table 2.1 [34]), the steady increase of ^{238}Pu inventory, as ^{238}Np decays into ^{238}Pu, is magnified resulting in a slow increase of ^{238}Pu induced spontaneous fission neutron emission rate in the first $\approx$ 700 days. Whilst only the even-even isotopes (i.e. ^{238}Pu, ^{240}Pu and ^{242}Pu) undergo spontaneous fission to an extent that is significant, ^{238}Pu and ^{242}Pu are responsible for a smaller contribution despite their shorter spontaneous fission half-lives of 4.77×10^{10} years and 6.84×10^{10} years (resulting in spontaneous fission yields of 2590 n·s^{-1}·g^{-1} and 1720 n·s^{-1}·g^{-1}, respectively) compared to 1.16×10^{11} years of ^{240}Pu (spontaneous fission yield of 1020 n·s^{-1}·g^{-1}) [34]. This is due to the significantly larger inventory of the latter isotope. The BWR-MOX and PWR-UOX fuel pins show very similar trends in line with their number densities, as illustrated in figures 4.3(b) and 4.3(k), and figures 4.3(c) and 4.3(l), respectively.

Figure 4.4 on page 103 illustrates the spontaneous fission activity in terms of neutrons per second per MTU from ^{242}Cm and ^{244}Cm v.s. time. Due to the short half-life of ^{242}Cm, its spontaneous fission activity diminishes rapidly with almost no trace remaining after 1200 days of cooling. Conversely, ^{244}Cm only experiences a slow decrease in its activity owing to its relatively longer half-life (i.e. 18.1 years as opposed to 162 days for ^{242}Cm), despite having a 100 times larger spontaneous fission branching ratio. Special notice must be made of the y-axes of the plots in figures 4.3 and 4.4, which suggest that the magnitudes of spontaneous fission activity for

the plutonium isotopes are, on average, a factor of 100 lower than the magnitude of the curium isotopes for the MOX fuel pins (for UOX fuel pins, this factor is 10) despite the plutonium being 100 times (1000 times for UOX fuel pins) more abundant (comparing figures 4.1 and 4.2). This dominance is due to the high yields of spontaneous fission and relatively shorter half-lives of the curium isotopes compared to the plutonium isotopes.

(α, n) reactions

Many of the actinides present in irradiated fuel decay by α-particle emission. When α decay occurs in a fuel matrix comprising material of low atomic number (such as oxygen, fluorine, etc.) there is a possibility that the α particle will collide with the nucleus of susceptible low-Z isotopes and release a neutron, as explained in section 2.2 on page 16. The rate of production of these uncorrelated neutrons for a given target isotope will depend on the yield of the α particles, their energies and the thresholds for such reactions. ^{17}O and ^{18}O are the primary isotopic targets susceptible to such reactions in the fuel pins that were considered in these simulations.

Since the energies of the emitted α particles from the ^{238}Pu, ^{239}Pu and ^{240}Pu isotopes are similar to each other (i.e. ^{238}Pu = 5.49 MeV, ^{239}Pu = 5.15 MeV and ^{240}Pu = 5.15 MeV), the magnitudes of their contributions are dictated primarily by their number densities (illustrated in figure 4.1 on page 99) and their corresponding α-particle yields (i.e. ^{238}Pu = 6.4×10^{11} $\alpha \cdot s^{-1} \cdot g^{-1}$, ^{239}Pu = 2.3×10^{9} $\alpha \cdot s^{-1} \cdot g^{-1}$ and ^{240}Pu = 8.4×10^{9} $\alpha \cdot s^{-1} \cdot g^{-1}$) [73]. Despite being the least abundant of the five plutonium isotopes considered in this study, ^{238}Pu makes by far the largest contribution, as can be observed in figure 4.5 on page 104, due to its larger α-particle yield and shorter half-life compared to other plutonium isotopes (see table 2.1). In fact, its yield is so strong that with even the slightest increase in the concentration of ^{238}Pu, due to the decay of ^{238}Np, the change in (α, n) emission rate of ^{238}Pu is amplified. The ^{241}Pu and ^{242}Pu isotopes have minimal footprints (i.e. ^{241}Pu = 9.4×10^{7} $\alpha \cdot s^{-1} \cdot g^{-1}$ and ^{242}Pu = 1.4×10^{8} $\alpha \cdot s^{-1} \cdot g^{-1}$) due to their lower α-particle energies (i.e. ^{241}Pu = 4.89 MeV and ^{242}Pu = 4.90 MeV).

While the number density of ^{241}Am grows considerably with time (as observed in figure 4.2 on page 100), this isotope has a half-life of 433.6 years, which is longer than the half-lives of ^{242}Cm and ^{244}Cm (163 days and 18.1 years, respectively). Therefore, the α yield of ^{241}Am (1.3×10^{11} $\alpha \cdot s^{-1} \cdot g^{-1}$) is considerably lower compared to those of ^{242}Cm and ^{244}Cm (1.2×10^{14} $\alpha \cdot s^{-1} \cdot g^{-1}$ and 3.0×10^{12} $\alpha \cdot s^{-1} \cdot g^{-1}$, respectively). As a result, figure 4.6 on page 105 demonstrates that the (α, n) emission for ^{241}Am is much smaller than that of the curium isotopes. Again, due to the short half-life of ^{242}Cm, the contribution to neutron activity by this isotope dissipates rapidly while ^{244}Cm only undergoes a small decrease during the same extended period.

The relative isotopic contribution to neutron emission

It is evident from figure 4.7 on page 107 that the curium isotopes dominate the neutron activity relative all other plutonium and uranium isotopes combined, primarily because their half-lives are short compared to the other isotopes present in the fuel pins. The fuel pins with higher burn-up contain larger inventories of curium, and hence almost all of the neutron flux arising from spontaneous fission activity is from the curium isotopes (approximately 99%, 99.4%, 99.6% and 99.8% for (10, 20, 35 and 55) GWd·MTU^{-1}, respectively, after the 10-day cooling period). However, as the ^{242}Cm inventory decays away quickly due to its short half-life, ^{244}Cm is left as the dominant isotope with there being no significant contribution of ^{242}Cm after a cooling period of 1000 days. Although, with time, the concentration of ^{244}Cm also starts to diminish, even after the 4250-day ($\approx$ 11.5 years) cooling, less than 2.4%, 0.8% and 0.5% of the spontaneous fission neutron flux is from the non-curium isotopes in the (20, 35 and 55) GWd·MTU^{-1} fuel pins. This contribution from the curium isotopes in the UOX fuel pins is significantly lower compared to that of the MOX fuel pins due to the limited curium inventory, especially for the cases with lower burn-up levels.

Figure 4.8 on page 108 illustrates the relative contribution of individual isotopes in the fuel pin towards the neutron flux yielded by (α, n) reactions. Due to the large α-particle yield and high energy of α particles from the two curium isotopes, the (α, n) emission is dominated by them for the first year for all four burn-up cases. Again, as depletion of the fuel continues (i.e. comparing across (10, 20, 35 and 55) GWd·MTU^{-1}), the relative contribution from the curium isotopes increases due to their larger abundance in the SNF. After 1000 days, the curium contents has reduced significantly allowing ^{238}Pu and ^{241}Am induced (α, n) emission to make up a significant proportion of the total (α, n) emission flux. With time, one will observe the growth in the ^{241}Am inventory evident by its increasing presence in the stack-bar plots for the 1000-, 3000- and 4250-day cooling periods.

5.1.3 Evolution of correlated neutron emission

Inspection of figure 4.9 on page 110 shows that the singles rate, which corresponds to the average number of neutrons emitted, for all cases at the start of the irradiation period is slightly lower than 2. This is despite the fact that all isotopes involved in consideration emit more than 2 neutrons per fission event [44]. This reduced magnitude is caused by the emission of uncorrelated neutrons from the (α, n) reactions taking place in the SNF.

It can be further observed in figure 4.9(a) that there is a steady increase in magnitude of the lower order ν_n (i.e. singles through to quintuples) during the first $\approx$ 700 days. Re-examining figures 4.1 and 4.2 demonstrates rapid changes in the inventories of the ^{242}Cm and

^{244}Cm isotopes. However, interestingly, both isotopes are actually decreasing in number density during the period in question, and hence the increasing magnitudes of the factorial moments, ν_n, inferred in figure 4.9(a) seem counter-intuitive. The explanation of this trend lies in the complex interplay between the spontaneous fission and (α, n) activity. The former gives rise to correlated neutrons, thereby increasing the magnitude of ν_n, while the latter gives rise to uncorrelated neutrons which decreases the magnitude of ν_n. Comparing the y-axis of the corresponding sub-figures in figures 4.4 and 4.5, it can be seen that the different plutonium isotopes have similar orders of magnitude for spontaneous fission and (α, n) activity. However, the ^{242}Cm and ^{244}Cm isotopes have a considerably stronger contribution from spontaneous fission compared to (α, n) activity (i.e. spontaneous fission activity is 2 orders of magnitude higher, see figures 4.4 and 4.6). The ^{242}Cm isotope has favourable contribution from (α, n) reactions compared to its spontaneous fission activity (only 1 order of magnitude lower). Hence, as the ^{242}Cm isotopes decay with a shorter half-life, so do the uncorrelated neutrons due to ^{242}Cm-derived (α, n) reactions. This gives the initial increase in the magnitude of the ν_n in the first $\approx$ 700 days of cooling period. Once most of the ^{242}Cm isotope has decayed, the trend in the magnitude of ν_n is dominated by the ^{244}Cm isotope since it is the major contributor towards the emitted neutron field, as shown in figure 4.7.

This premise was confirmed by a hypothetical study where the activity from spontaneous fission and (α, n) reaction from both curium isotopes were independently suppressed to zero to analyse the change in the trends. Additionally, this decreasing trend in ν_n is also coupled with the ^{241}Am growth which becomes more prominent as the ^{244}Cm isotope decays away. The higher orders of ν_n, i.e. septuple and octuple, are not affected by (α, n) reactions due to the formulation of the equation used to compute the factorial moments (see equation 2.49), and hence their trends follow the course dictated by the isotopic density of ^{244}Cm, which emits larger number of neutrons per fission event compared to the plutonium isotopes, see table 2.2(a) on page 24. As a consequence, the previously seen growth in neutron emission from the spontaneous fission and (α, n) reaction from ^{238}Pu isotope is not visible in figure 4.5.

With increased burn-up, as shown in figure 4.9(d), the initial increase in the magnitude of ν_n over the first 700 days of cooling, and the subsequent decrease, are less prominent. This is due to the more pronounced inventory of the curium isotopes, as observed when comparing the corresponding isotopic data presented in figures 4.2(a) and 4.2(d). For the cases of (35 and 55) GWd·MTU^{-1}in figures 4.9(g) and 4.9(j), the deviation in the lower orders of multiplicity after 700 days of cooling is almost undiscernible. This can again be attributed to the large inventory of ^{244}Cm which overpowers the (α, n) activity from the ^{241}Am isotope. Additionally, the magnitudes of the different orders of ν_n are consistently higher for fuels with a higher burn-up due to their larger curium inventories.

For the low burn-up UOX cases (i.e. 10 GWd·MTU^{-1} and 20 GWd·MTU^{-1}), the change in the magnitude of ν_n with cooling period is most prominent. This is due to the limited inventory of curium isotopes discussed earlier. The rate of change in the magnitude of ν_n can be observed for the burn-up level of 35 GWd·MTU^{-1}, though at a much subtler rate. However, there is almost no discernible change for the 55 GWd·MTU^{-1} case as the ^{242}Cm and ^{244}Cm isotopes saturate the neutron activity from the fuel pins.

5.1.4 Context and prior-art

There are two priorities associated with the long-term management and disposal of radioactive SNF. Firstly, to protect human health, and secondly, to protect the environment from deleterious effects of these materials [132]. There are several different classifications of such radioactive waste in existence spanning the possible extremes in terms of radiotoxicity and volume. To address these priorities in the context of the management of SNF and *high-level waste (HLW)*, accurate assessments of the projected radioactivity of these materials are essential because, without this information, estimates for the duration of the necessary confinement and robustness of the candidate disposal options cannot be made.

There are several techniques [133] that are applied in industry to verify SNF. However, most of the currently employed well-established techniques are tedious and introduce high levels of uncertainties. For example, standard α spectrometry may be used to determine the presence of ^{242}Cm and ^{244}Cm isotopes, which are α-particle emitters with energies of 6.1 MeV and 5.8 MeV, respectively. This is a slow laboratory-based process subject to high levels of uncertainties due to procedural errors or insufficient sampling or both. An alternative process of achieving these characterizations could be the use of depletion codes. However, this again will be limiting, this time by the quality of the burn-up history as an incomplete history will exacerbate uncertainties. In addition, there will be potential errors introduced by uncertainties in the nuclear data used in such codes.

Being a non-destructive method, γ-ray spectrometry would have been an ideal alternative characterization approach due to the distinctive 152.63 keV γ-ray line of ^{244}Cm. However, the use of this technique is also subject to several limitations, namely, (i) γ rays from several plutonium isotopes, as well as some fission products, have similar energies which can lead to contaminated readings; and (ii) high levels of attenuation for such low-energy γ rays will lead to large uncertainties due to the heterogeneous nature of the SNF and thus influence. Additionally, the heterogeneous nature of the test sample will also influence any measurements that are of interest.

A variety of analytical techniques have been developed [7, 8, 26] to measure the neutron

emission rates to ascertain the plutonium and uranium content in nuclear materials experimentally. Some of these methods rely on the detection of correlated neutrons emitted during the spontaneous fission of the different major actinides, either via passive or active means. Given the emission of spontaneous fission neutrons, which are correlated in the temporal domain, these techniques measure the deviation from the correlated characteristics of the correlated neutron field to determine the total mass of fissile materials. A common practice is to examine each SNF sample for the presence of plutonium, ^{242}Cm and ^{244}Cm [133] using thermal neutron detectors.

Previous studies [134, 135, 136, 137] have adopted various approaches to comprehensively identify those isotopes which may pose severe constraints on the projected life of consignment and the operation of pre-disposal neutron assay systems. For example, studies have been made showing the contribution of curium towards net multiplication [138] and neutron flux measurements [139, 140, 141, 142, 143] for verification of SNF. However, the specific role of curium with regards to correlated neutron emissions has remained relatively unexplored despite the relatively significant abundance of this element, along with americium, as one of the few long-lived components in almost all radioactive waste samples derived from SNF [144]. Results obtained in this research demonstrate that the concentration of ^{242}Cm and ^{244}Cm build-up inside a fuel pin during irradiation depends on the fuel burn-up level, quality of the neutron flux (i.e. hard or soft energy spectrum) and consequently the position of the fuel element in the reactor and reactor operational parameters. However, as can be seen from figure 4.2, even a trace amount (i.e. $<0.5\%$) of these two isotopes in the SNF will lead to significant neutron activities which will easily overwhelm the contribution to the total flux from the plutonium isotopes, as illustrated in figures 4.4 and 4.5. For safeguard techniques based on the assay of coincident neutrons from different plutonium isotopes, commonly referred to as the $^{240}\mathrm{Pu}_{\mathrm{eff}}$, this constitutes a severe obstacle for the measurement of plutonium effective mass in these materials. Blind assessment without accounting for the curium contribution would lead to a number of problems for the assessment of plutonium mass in spent fuel assay, including the incorrect estimation of plutonium mass and increased levels of statistical uncertainties [134, 145, 146]. Further to this, the presence of large quantities of high-energy α-particle emitters leads to an additional contribution to uncorrelated neutron flux, for example due to the presence of ^{17}O and ^{18}O in the oxides. The in-growth of ^{241}Am can be observed in figure 4.9 via the change in the magnitudes of the factorial moments for the fuel pins with low burn-up UOX fuel pins. Unless considered, these uncorrelated events will perturb estimated of $^{240}\mathrm{Pu}_{\mathrm{eff}}$, while at the same time, increasing uncertainty in related assessments.

Using a thermal neutron detector assay, it is possible to determine the doubles and triples distributions effectively [15]. However, higher-order multiplicity is generally not possible due to the large gate-widths and detector die-aways [26] of such assays which increase the uncertainties

in measurements due to contamination by uncorrelated events. By using fast neutron detectors it is possible to detect higher orders of coincidence with reduced accidentals [147]. This will possibly allow the determination of the evolution of the factorial moment arising due to the spontaneous fission emission from SNF with low burn-ups have a steady decay with increasing cooling period.

Additionally, there is a subtle, but nonetheless distinct, difference in the spontaneous fission multiplicity distribution between plutonium and curium isotopes, as shown in figure 2.8. Therefore, a method exploiting this feature might be a possible solution in order to determine the composition of SNF. Moreover, the in-growth of ^{241}Am and decay of curium isotopes, if identified successfully, may allow the age of the SNF to be determined. However, this is complicated in MOX fuel due to any increase in (α, n) emission from ^{241}Am being countered by the decrease in the inventory from ^{242}Cm and ^{244}Cm. To achieve the best results, one benefits from being able to detect higher-order multiplicities (i.e. higher than singles, doubles and triples), which is not feasible when using thermal neutron detectors due to their long die-aways. Fast neutron detectors using organic scintillants can be viable alternatives, however the complexities of these detectors (i.e. predominately chemical instability and sensitivity to γ rays) have prevented such systems from being mainstay of the industry [19, 148].

5.2 Temporal correlation between particles emitted from spontaneous fission of ^{252}Cf

The correlation with which radiation is emitted from a nuclear fission event, described in section 2.3 on page 25, enables fissile materials to be discerned from ones that are not. Significant delay beyond the time over which fission-derived radiation is evolved (i.e. less than 10^{-13} seconds) prior to detection is undesirable when carrying out such assessments as the neutron field becomes vulnerable to contaminant nuclear reactions that are not indicative of the fissile inventory. Section 4.2 on page 111 presents the *interval-time distributions* obtained for ^{252}Cf in this work which investigate this *non-Poissonian* property of the emitted mixed radiation field. Analysis of the results is based on the Rossi-α model, which describes the response of the *interval-time distributions* using the exponential equation, equation 2.23 on page 34, where the time dependent term describes the decay of correlated neutrons from a fission event in time, i.e. *real events*. Here, $\Delta T = 0$ s indicates the time at which the first neutron from the fission event is detected. The time independent term of the equation corresponds to the *accidental events*, i.e. uncorrelated processes such as those from different fission events, (α, n) reactions, and random sources of background. This section aims to discuss the findings from experiments conducted using the instrumentation described in section 3.2.2.

Experimentally-obtained *interval-time distributions*, with a resolution of 5 ns (except for the first bin, which is 10 ns long), are presented for two different arrangements, i.e. *REFL15* and *BARE15* respectively, described in section 3.3.2 and section 3.3.4. The first arrangement corresponds to a reflective arrangement, while the second relates to a bare arrangement.

5.2.1 Reflective arrangement

Results presented in figure 4.10 for the reflective cases reproduce the trend of the data for $\Delta T < 15$ ns that is described satisfactorily by the *single exponential* model presented in equation 2.23 on page 34, but not the entire trend because an additional, more slowly-varying, time-dependent component is apparent, particularly for fast neutrons in the reflective arrangement. This influence is consistent with the timescales of the scatter of fast neutrons from the water reflector, the geometry of the experimental set-up and the neutron energy spectrum of a range 15 ns $< \Delta T <$ 100 ns, (e.g. the transit time for a 750 keV neutron being scattered over a distance of 1 m, i.e. distance between source-floor-detector, is about 80 ns). To better describe the distributions, equation 2.23 was empirically expanded as per equation 4.2, where the two exponents correspond to a short and long time-dependent component. The duration of the short component is consistent with the proportion of the neutrons that travel directly from the source to the detectors following fission without undergoing an interaction and is independent of geo-

metric scatter, while the long component corresponds favourably with scattered events. Similar to the traditional single exponent model, the time-independent term reflects the events from the uncorrelated processes. This revised representation provides a significant improvement over the *single exponential* fit, as is evident from the χ_v^2 values in table 4.1, especially for the neutron case, where the scatter component is most significant and is particularly relevant for assessments in environment where scatter is appreciable.

A comparison of the short-response coefficients, τ_s in table 4.1(b) on page 113, indicates that γ rays have the shortest decay whilst neutrons have the longest and this is evident from figure 5.1. This figure contains three subplots in order to demonstrate one-on-one comparisons between the three different responses, i.e. neutron, γ ray and joint, that were obtained using the reflective arrangement. The narrower short-response of the γ-ray distribution is expected because of (i) dispersion in the transit time of the fission γ rays due to variance in the source-detector distance is small; the most significant influence being due to the detector volume to the order of ± 0.3 ns as depicted by the simulation results with 1 ns bins, and (ii) hysteresis in the electronics due to lack of a memory-mapped randomiser to allocate the correct timestamp when two or more events arrive in the same clock cycle (i.e. with the present implementation, the second event will be processed assuming that it arrived one cycle after the first event). However, the proportion of these mismapped events is expected to be relatively low, while having the largest impact on the γ-ray distribution. Additionally, the small number of neutron events discriminated erroneously as γ rays may also bias the short-response coefficients towards higher values, however, the proportion of such erroneous events can be assumed to be insignificant as the γ-ray field is much stronger than the neutron field. The short detector die-away, τ_s, for the γ-ray distribution is (2.70 ± 0.06) ns and requires a *coincidence-gate* (i.e. short gate-width in table 4.1(b) on page 113) of (15.7 ± 0.4) ns to account for 99.7% of the prompt, unscattered γ-ray distribution. The γ-ray distribution is very closely matched by the 5 ns-binned Geant4 simulations (depicted by the "red crosses" in figure 4.10(a) on page 114), however, with a finer time resolution, this response is much narrower, as depicted by the 1 ns-binned simulated response (depicted by the "magenta circles" in figure 4.10(a)). The classic *single exponential* model is able to predict the γ-ray distribution satisfactorily as γ rays are less susceptible to scattering as most of the material is low-Z in nature and therefore less scattering. The contribution of the long component of the γ-ray distribution is $\approx 0.18\%$ of the total counts at $\Delta T = 0$ ns. This long component of the γ-ray distribution is believed to be due to the 2.2 MeV γ rays released from neutron capture on hydrogen in the water reflector and in the hydrogen atom within the detector; these are correlated with fission but delayed as a result, and influenced by the dispersion of the neutron component. Since the long-response is small relative to the short-response, the τ_l and the long gate-width for γ rays contain relatively large errors and are observed at (53.8 ± 12.1) ns and (313 ± 70) ns,

respectively.

Compared to γ-ray distribution, the neutron distribution in figure 4.10(b) on page 114 illustrates greater values for die-away and short gate-width, (4.24 ± 0.20) ns and (24.7 ± 1.2) ns, respectively, to account for 99.7% of the prompt, unscattered neutrons, as can be seen in figure 5.1(a) and table 4.1(b). These values are well modelled by Geant4, considering the approximations made in its geometry. The computed detector die-away and short gate-width from the experimental data are quantitatively consistent with the dispersion of source-to-detector transit time, which is expected on the basis of the fission neutron spectrum and the dependence of the detector response on the incident energy. Adopting a relatively conservative detector energy threshold of 750 keV and an upper limit for the detected neutron energy of ≈ 4.9 MeV[1], yields an average transit time of less than 20 ns. The neutron distribution in figure 5.1(a), exhibits a significantly larger proportion of the long-response counts, B, which is $\approx 17\%$ of the short-response counts at $\Delta T = 0$ compared to $\approx 0.19\%$ for the γ-ray distribution. The associated τ_l and the long *gate-width* were recorded to be (21.6 ± 0.6) ns and (125 ± 4) ns, respectively. The main constituents of the long-response component are the neutrons which are scattered from the water reflector and the laboratory (e.g. floor, walls, etc.) before they trigger a response in a detector. Furthermore, it is believed that any *photon-breakthrough*, which is to be discussed later in this chapter, may be a contributing factor as any misclassified γ ray would arrive significantly before the subsequent neutron counts, thereby elongating the long die-away. Finally, the neutron distribution also consists of a larger proportion of *accidental events* compared to the γ-ray distribution, i.e. $\approx 0.76\%$ compared to $\approx 0.18\%$. As mentioned earlier, the single exponential model describes the experimental neutron data set poorly, as demonstrated by the fit parameters in table 4.1(a).

For the joint distribution, as listed in table 4.1(b), the τ_s and short gate-width are measured at (3.16 ± 0.02) ns and (18.4 ± 0.1) ns, respectively, consistent with the significantly stronger γ-ray emission of ^{252}Cf relative to neutron emission. Since the neutrons emitted from spontaneous fission traverse at a much slower speed compared to γ rays, their arrival is consistent with the shoulder that can be observed between 10 ns to 30 ns in the 1 ns-binned simulated data ("magenta circles") in figure 4.10(c) on page 114. However, the 5 ns time resolution of the experimental data prevents the detection of this granular trend. Again, it can be observed that the proportion of accidental counts for the joint distribution is higher compared to the γ-ray distribution, at $\approx 0.41\%$. Finally, comparing the neutron and joint distributions in figure 5.1(c), it can be observed that the accidental counts are roughly the same for both the distributions, while the joint distribution has a much narrower short-response.

[1]This is consistent with the limiting energy, beyond which the neutron population is less than 1% for a Watt spectrum with a mean energy of 2.13 MeV.

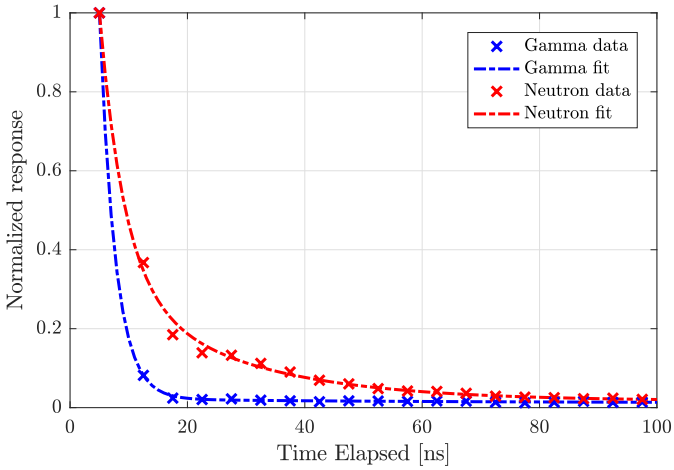

(a) γ-ray and neutron distribution.

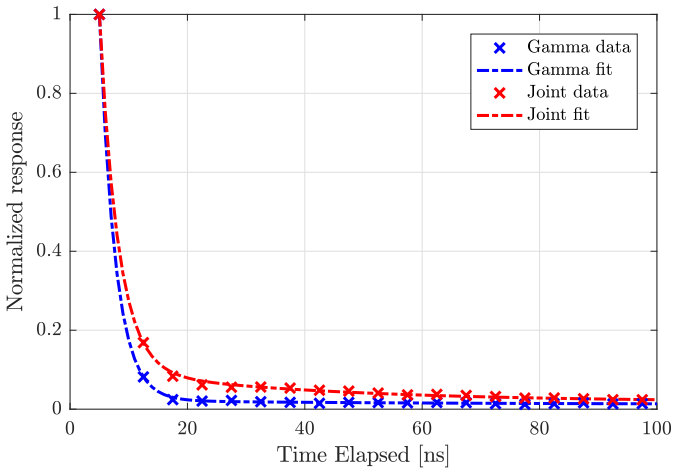

(b) γ-ray and joint distribution.

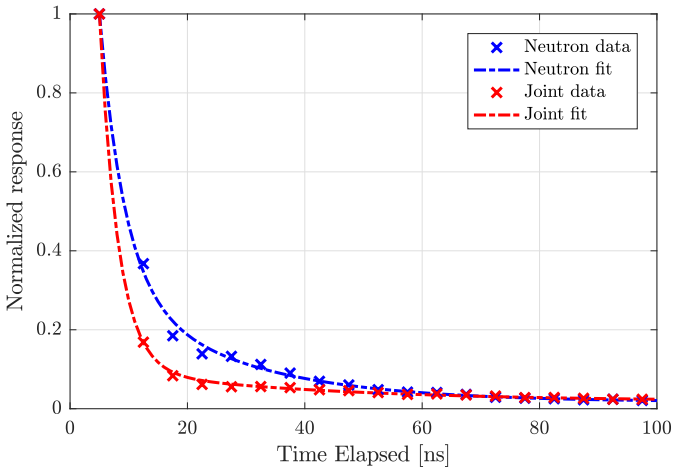

(c) Neutron and joint distribution.

Figure 5.1 | Comparison between the three interval-time distributions for the reflective arrangement. A comparison of *interval-time distributions* measured in this work based on **a.** γ-ray events and fast neutron events, **b.** γ-ray events and joint events, and **c.** fast neutron events and joint events from ^{252}Cf. The experimental data are denoted by crosses while the double exponent model by the broken lines. All distributions were normalised to the first entry from the experimental data set.

5.2.2 Bare arrangement

In order to validate the model without reflection, experiments were carried out using a bare arrangement with minimal geometric scatter. These results are presented in section 4.2.2 on page 115. As can be observed in figures 4.11(a), 4.11(b) and 4.11(c) on page 116, both the single and double exponential models performed satisfactorily, in line with expectation due to the low scatter geometric arrangement. Further to this, the three distributions obtained with the bare arrangements were compared to the corresponding distributions for reflective arrangements. These comparisons are illustrated in figure 5.2, where the red crosses and dashed-line correspond to the data points and fit for the bare case while the blue crosses and dashed-line corresponding to the reflective case. Figures 5.2(a), 5.2(b) and 5.2(c) reflect comparison for the γ, neutron and *joint* responses, respectively. Finally, similar to figure 5.1, figure 5.3 compares the three different distributions that were measured using the bare arrangement.

The γ-ray distribution for the bare arrangement is given in figure 4.11(a), while the corresponding comparison between the data obtained from the bare and reflective arrangement is provided in figure 5.2(a). The short detector die-away, τ_s, and the short gate-width components for the γ-ray distribution with the bare arrangement were measured to be (3.62 ± 0.10) ns and (21.0 ± 0.6) ns, respectively, as listed in table 4.2(b) on page 115. These values are approximately 25% wider compared to those for the reflective case (in table 4.1(b)). This is also evident when comparing the two distributions in figure 5.2(a). This is believed to be due to the lower intensity of the γ-ray field in the bare setups, consistent with the absence of γ rays produced via the neutron capture on the hydrogen atom present in water, and also due to increased correlated counts as the detectors now form a complete ring around the source. As a consequence, the ratio between the first two bins for the bare case is not as dominating as the reflective case, thereby leading to a wider gate-width. Again, it may be noticed that using instrumentation with much better time resolution would result in a narrower gate-width, as demonstrated by the 1 ns-binned simulation data ("magenta circles" in figure 4.11(a) on page 116). Moreover, instruments with better resolution would also reveal a shoulder between 10 ns and 25 ns, which is consistent with the 2.2 MeV γ rays emitted due to the capture of thermal neutrons within the hydrogen atoms present in the detector's active region. As this contribution was only present to a smaller proportion in the reflective case, it was not noticeable in that case. Since it is believed that these events primarily reside within the long component of the double exponential model, a consequence was the manifestation of a significantly larger proportion of long-response counts, at $\approx 5\%$ of the short-response counts at $\Delta T = 0$, when compared to the neutron or joint distributions with the bare arrangement.

For the neutron case, the short detector die-away and the short gate-width, recorded to be

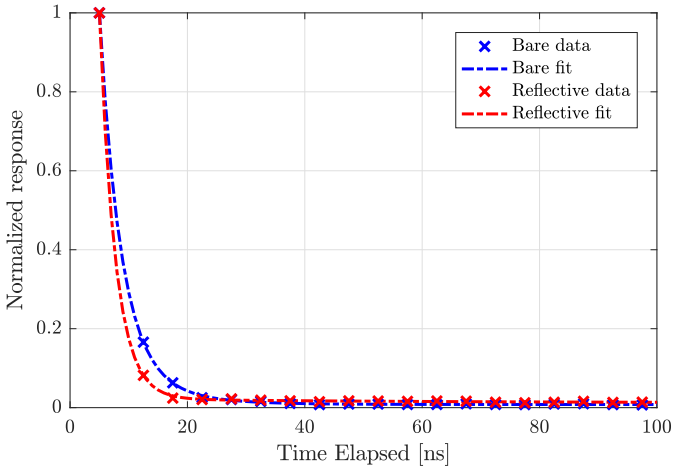

(a) γ-ray distribution.

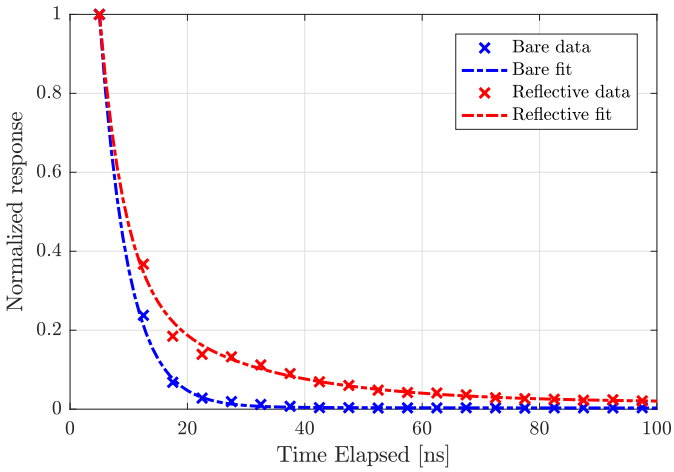

(b) Neutron distribution.

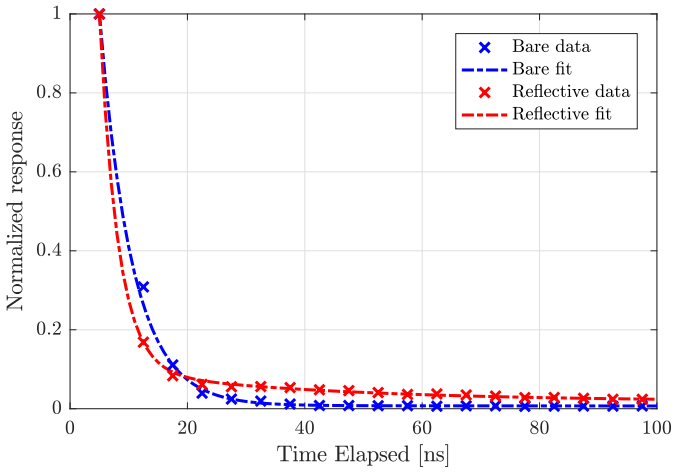

(c) Joint distribution.

Figure 5.2 | Comparison of the different interval-time distributions between the two arrangements. A comparison of *interval-time distributions* between the reflective and the bare arrangement measured in this work based on **(a)** γ-ray events, **(b)** fast neutron events, and **(c)** *joint* events from ^{252}Cf. The experimental data are denoted by crosses while the double exponential fits by the broken lines. All distributions were normalised to the first entry from the experimental dataset.

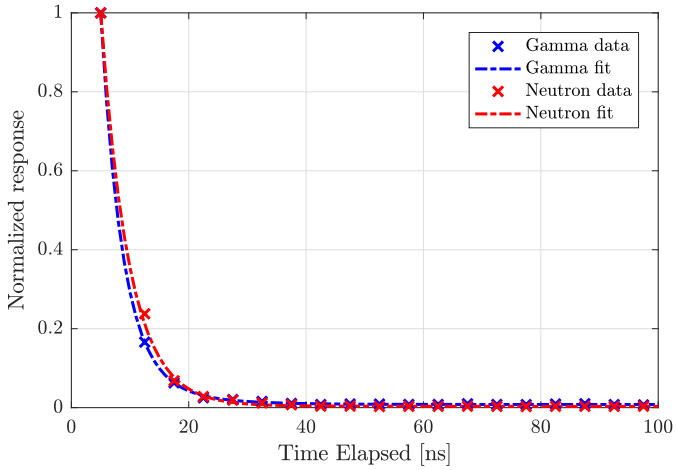

(a) γ-ray and neutron distribution.

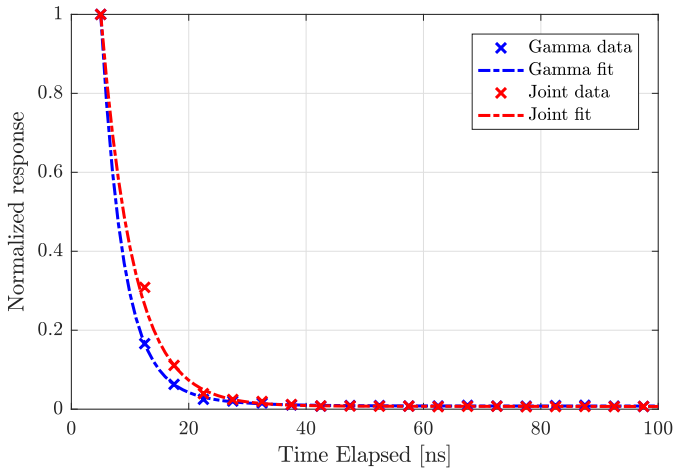

(b) γ-ray and joint distribution.

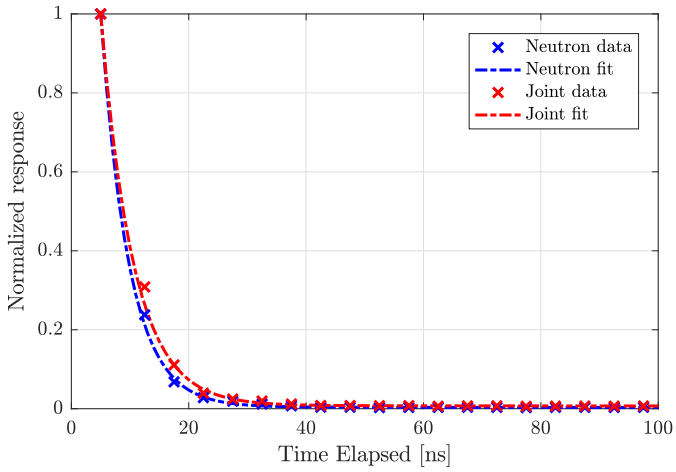

(c) Neutron and joint distribution.

Figure 5.3 | Comparison between the three interval-time distributions for the bare arrangement. A comparison of *interval-time distributions* measured in this work based on **a.** γ-ray events and fast neutron events, **b.** γ-ray events and joint events, and **c.** fast neutron events and joint events from ^{252}Cf from the *BARE15* setup. The experimental data are denoted by crosses while the double exponent model by the broken lines. All distributions were normalised to the first entry from the experimental data set.

(4.78 ± 0.04) ns and (27.7 ± 0.7) ns, respectively, are consistent with that of the reflective arrangement confirming that it is independent of scattering, as expected, having the characteristics of an intrinsic resolution coupled with hysteresis introduced by the electronics. The magnitude of the long component is very small for the bare arrangement compared to the reflective arrangement ($\approx 0.1\%$ as opposed to $\approx 18\%$), consistent with the reduced scatter, requiring a gate-width of (538 ± 180) ns. This massive disparity between the two cases can also be observed in figure 5.2(b) on page 154. Additionally, the proportion of *accidental events* was recorded at 0.07% for the bare arrangement compared to 0.76% for the reflective arrangement. This is again consistent with expectation due to the longer time it takes for neutrons to travel when scattered down to a lower energy band.

In the final case of joint distribution, demonstrated in figure 4.11(c), the neutron shoulder is more prominent for the bare case compared to the reflective case, as can be observed in the 1 ns-binned simulation data. This is because the neutrons are inherently faster in the bare arrangement due to the absence of the water-bath. Additionally, the reflective arrangement has a much larger γ-ray flux compared to the bare arrangement. These differences between the two arrangements, coupled with the shorter source-to-detector distances (i.e. ≈ 0.4 m to ≈ 0.75 m for the reflective arrangement compared to 0.2625 m for the bare arrangement), meant that the die-away for the bare case is not as steep as that of the reflective case, as can be observed in figure 5.2(c) on page 154. Additionally, as a consequence of the longer source-to-detector distance, the neutron signals appear earlier in the joint distribution for the bare case than they do for the reflective case; and subsequently get absorbed within the short die-away, thereby making the short die-away appear wider compared to that of the reflective case (i.e. 18 ns v.s. 32 ns).

Figure 5.3 compares the different cases using the bare arrangement. As with the reflective case, the γ-ray distribution has a steeper die-away compared to the neutron and joint distributions. However, the neutron distribution in this case has a narrower die-away compared to the joint, as can be seen in figure 5.3(c). This trend, which can also be observed from the short gate-widths in table 4.2(b) (i.e. 27 ns v.s. 32 ns), is due to both the lack of a moderating environment and shorter source-to-detector distance in the bare arrangement. As a consequence, the neutron signals appear earlier in the joint distribution for the bare case; and subsequently get absorbed within the short die-away, thereby making the short die-away appear wider.

5.2.3 Alternative techniques and prior-art

Traditional *interval-time distributions* or the Rossi-α distribution is constructed using a shift-register based algorithm discussed previously. In this method, every incoming event triggers a sweep to determine the time elapsed between the triggering event and any subsequent events, which themselves start another sweep. This is contrary to the algorithm proposed in this work, which only considers unique events to be able to issue a trigger to start a sweep for subsequent coincident events (i.e. the subsequent events do not trigger additional sweeps) and is more similar to techniques used in high energy particle physics. Analytically, this will imply that the shift-register based Rossi-α distribution will have a slightly steeper decay constant compared to the algorithm which was implemented as part of the *multiplicity register*.

There are several other analytical techniques to achieve this that have been explored in the past by Endelmann [149], whereby the technique would: (i) start a sweep on an incoming event and measure the difference in arrival time between the trigger and all preceding events over some interval; (ii) trigger on an incoming event and measure the time from the trigger to all subsequent events over a predefined interval, stop and wait for the next event after the sweep to start a new sweep; and (iii) trigger when a pair is detected within a short time gate and then log the time elapsed between subsequent pairs, i.e. time interval between pulse pairs. However, no implementations of these techniques were seen in the literature.

Another popular method involves analysing the frequency distribution, which represents the number of events that follow a triggered gate [150]. This analysis can be realised in one of two ways: (i) auto-correlation and (ii) cross-correlation. Auto-correlation represents correlation between events from an activated source and a detector, underlining the fluctuation of particles with time [150]. Cross-correlation comes from the correlation between a pair of detector events as a function of the time delay between the detectors. The time distribution of cross-correlated events show the detection time difference between all γ-ray and neutron pairs in a specified time window [151, 152, 153, 154]. Usually, no *pulse shape discrimination (PSD)* is carried out to distinguish between neutrons and γ rays. The latter method is similar to the implemented joint method in this work, with the exception that the proposed distribution not only represents pairs but also higher order coincidences.

Additionally, there is also evidence of more exotic forms of analysis, like the 3-dimensional Rossi-α distribution which constructs a surface plot to illustrate the correlation between not only the first two events, but also the third event in an *event-train* [155].

These distributions are challenging to obtain for fast neutrons due to the speed at which data acquisition systems are required to operate given the short time gap between events. However,

since the late-1990s, such temporal correlation between the emitted neutrons have been studied using the Nuclear Materials Identification System (NMIS) [24, 156]. These measurements were based on an analogue system and were limited to five detectors only. With the introduction of electronics capable of digitizing the analogue signals from the detectors, these measurements were repeated for plutonium and californium sources using the cross-correlation technique with a digitizer utilising 250 MHz 12-bit *analogue-to-digital converter (ADC)* with double data rate in the late 2000s [154, 157, 158, 159]. In these experiments, digitized pulse widths were collected in "oscilloscope" mode and by taking advantage of the 12 bit vertical resolution, the pulses were sometimes further analysed to improve the time resolution to 1 ns by interpolation techniques [154]; this resulted in further improved time resolution. Similar measurements were subsequently also carried out using MOX fuel [160]. While these experiments were conducted using EJ-309 scintillation detectors, recently a new array, NEUANCE, which utilises 21 stilbene scintillators was used to construct the auto-correlation distribution using 0.25 ns time resolution [27, 31]. Although not mentioned in the reference, this high resolution was possibly achieved by oversampling the 500 MHz ADC. However, no gate-width analysis was performed by any of the previously cited reference authors, as was done in this work. Although visually the distributions presented in this thesis look similar to those in the references, analytically, they do not provide the same information. This is because the cross-correlation method provides information between a pair of events, whereas, the proposed method in this work provides information between all orders of correlated events. Additionally, since the methods in the above cited references implemented offline PSD techniques, such analysis does not include electronic dead-time. Moreover, using offline techniques, although a less than ideal solution, allows careful selection of events that are to be considered; discarding events that do not meet certain criteria, e.g. pulse pile-up, pulse clipping, negative undershooting, etc. This is expected to be a source of deviation between the cited references and the work presented in this paper, as such filtering options were not available with the real-time PSD algorithm implemented by the *Mixed-Field Analysers (MFA)*.

Previous reports of fast neutron assays for the coincidence counting of nuclear materials have used *coincidence-gates* in the 40 ns to 100 ns range [24, 94, 161]. This is due, in part, to the limiting resolution of the available instrumentation, but also due to preconceptions regarding the width of the fast, fission neutron distribution. Widths of 100 ns offer dramatic reductions in accidentals rates achieved with ^{3}He-based detection systems and the change events per trigger. The results presented in this thesis imply that a significantly narrower gate-width can be determined using the double exponential model for use in fast-neutron coincidence assay; a gate-width of 25 ns is sufficient to account for 99.7% of the un-scattered correlated neutron events. Moreover, in this work it has been shown that all *interval-time distributions* associated with the

fast, un-scattered radiation emitted in nuclear fission are governed by an exponent term with a short time constant. As the source-to-detector distance is reduced to optimize the form factor and efficiency of detection systems, the width of the fast *interval-time distributions* will possibly fall. Similarly, using a digital system with even higher clock would also significantly reduce the gate-widths of the γ-ray distribution. Further to this, this parameter appears to be immune to the influence of scatter in the environment.

Based on the findings in reference [24], Mihalczo *el. at.* had previously postulated that the trend in the *interval-time distributions* contains discernible signatures of both directly transmitted and scattered neutrons, while only visually examining the detected response to conclude that it "contains at least two characteristic decays: a fast decay (before 50 ns) associated with the casting, and a slower decay that persists beyond 100 ns associated with the casting surrounded by moderator". Using the same system, the reflection component due to the concrete floor was asserted [162]. Since most of the references cited above used a bare arrangement, scatter was not a concern. However, when analysing nuclear waste drums, it is expected that there will be a considerable amount of heterogeneous medium, sometimes loaded with hydrogen-rich materials. Consequently, the potential exists for scatter-derived events in the range of 10 ns to 75 ns to be separated from un-scattered emissions. This heralds the possibility of removing this perturbation from fast-neutron fission detection systems at the point of detection via the application of a specified gate-width. It may reduce the requirement for independent experimental measurements or estimates via Monte-Carlo modelling of scatter and inter-detector *crosstalk*; both can be sources of uncertainty. Whilst the potential exists for sub-nanosecond levels of scrutiny to be exploited in real-time, this is beyond the processing capabilities of current instrumentation used in this research.

Although the contribution by accidentals is small ($< 1\%$) in these experiments, the magnitude of the scatter contribution is dependent on the nature of the assay. Significant influencing factors are likely to be the proximity of the source or nuclear material to hydrogenous scatterers and of the detectors to each other. A wide *prompt-gate*, as per current approaches, captures all of the radiation (neutrons) emitted by the fissile sample under scrutiny; while a short *prompt-gate* focuses the assay on those that escape without interaction. This research introduces a simple and effective means by which the fissile material assays might be characterized via the real-time detector array using fast *interval-time distributions*. It presents a more comprehensive picture of the temporal emission dynamics of radiation emitted in nuclear fission and also highlights a basis on which confirming the whereabouts of the world's nuclear stockpiles might be improved.

5.3 Neutron spectra

In this thesis, experimental results are presented in section 4.3 on page 117, which attempt to determine the neutron spectra of a ^{252}Cf source in various configurations. This was achieved by measuring the emission-to-detection time of each neutron under the assumption that all neutrons and γ rays from a single fission event are emitted at the same time. This section provides a discussion for the measurements presented in section 4.3.

The reconstructed spectrum for the "No water" case, i.e. bare ^{252}Cf using the *REFL15* arrangement, in figure 4.12 on page 118, peaks at approximately 650 keV (E_{max}). This value is marginally below 700 keV, which is the most probable energy at which a neutron may be emitted from the spontaneous fission of ^{252}Cf. The trend in the $E < 500$ keV region shows that the spectrum rapidly drops off during the region of 200 keV $< E <$ 490 keV, which is due to the detector cut-off energy as it lowers the sensitivity of the detectors gradually to zero [117]. Below the region of 120 keV, there is a spike in the spectrum which arises due to the presence of neutrons which were scattered in the environment (i.e. they have longer emission-to-detection time). This spike is further amplified by the increasingly smaller denominator due to a smaller energy bin.

The more interesting cases are the ones which place the ^{252}Cf source inside the water filled cylinders. In these cases, the detected spectra always peak at the same $\approx$ 662 keV but with different intensities. This implies that the change in the hardness of spectrum does not translate to a detectable shift in spectrum (i.e. the detected E_{max} value remains constant), as is confirmed by normalizing the different spectra, illustrated in figure 5.4. This occurs because the incident neutrons and the hydrogen atoms in the detector's active region, with which the neutrons undergo elastic scatter, have approximately the same mass. Hence, the lethargy per collision is very high, i.e. a head-on collision will essentially half the energy of the incident neutrons. Therefore, a neutron with energy of 1 MeV or less (which is the most probable energy region) will require one head-on collision to drop below the cut-off energy of the detector, essentially removing it from the system.

Another interesting observation is the location of the peak at 662 keV, where the neutron detection efficiency is very small and hence a peak in this location is unlikely. This is indeed the case as the peak prior to ascertaining the response in terms of "per MeV" was approximately located in the 1 MeV region.

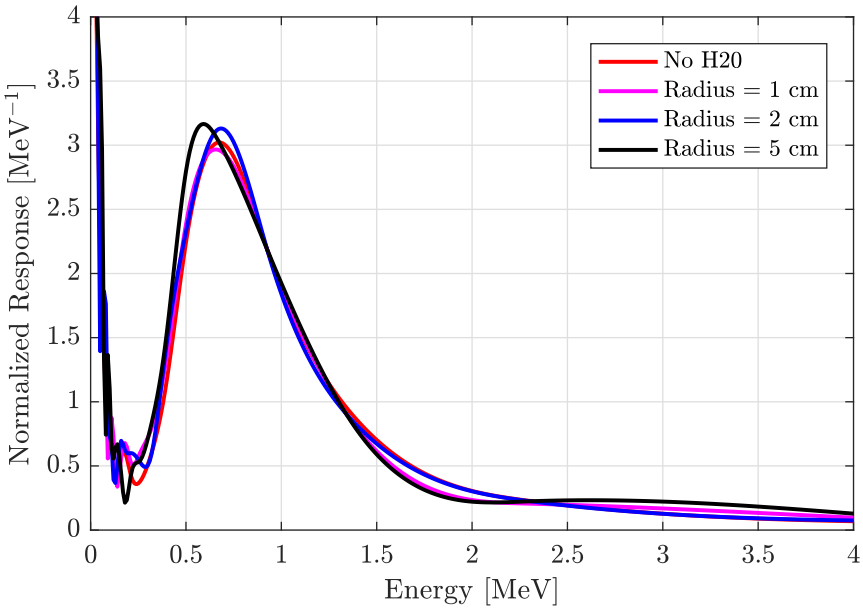

Figure 5.4 | Normalised neutron spectrum of ^{252}Cf. Normalised experimental neutron spectrum of the main ^{252}Cf using *BARE15* arrangement. The experiment was repeated four times with no water and a water filled cylinder with radii 1 cm, 3 cm and 5 cm to forcefully change the hardness of the spectrum. No change in lateral movement of the peak was noticed along the x-axis, however the amplitude of the peak diminished with increase in water volume.

5.3.1 Prior-art

Although there are methods of determining neutron spectrum without carrying out analysis of the temporal relationship between particles [163], using ToF to ascertain the velocity and hence the energy of neutrons is a proven and well-established technique since the discovery of neutrons in the 1930s [164]. Additionally, such techniques may also be used to experimentally determine different cross-sections of a target material for different neutron energies using a chopper [165, 166]. Due to their sensitivity to fast neutron and geometric scalability, scintillators have widely been the choice of sensor in recent years [153, 167]. The experiments conducted in this thesis have in fact been conducted by several researchers using EJ-301 and EJ-204 detector arrays for measuring the neutron spectra of neutrons emitted during the spontaneous fission of ^{252}Cf [168, 169]. Additionally, using a EJ-309 based array, the neutron spectrum from photofission and induced fission of ^{235}U was also measured [170]. The measurements were made using a methodology similar to that which was followed in this research, by tagging the γ-rays emitted from the fission events [171]. Compared to the data presented in this thesis, which shows a peak at 662 keV, the above cited literatures would suggest that this peak should appear at much higher energies (>1 MeV) [168] due to the associated detector cut-off energies. This could likely be due to *photon-breakthrough* or scatter from the floor, however, more analysis is needed before asserting it with confidence. Nonetheless, the novelty of this method lies in the real-time capability of the developed instrumentation to carry out the analysis. Once these distributions

are obtained, and should they fail to correctly determine the neutron spectra due some bias, they may also be used in conjunction with various unfolding techniques [172, 173] in order to reconstruct the incident energy distribution [174].

5.4 Spatial correlations between neutrons emitted from spontaneous fission of ^{252}Cf

The fission fragments expelled during spontaneous fission of ^{252}Cf accelerate away from each other in opposite directions (i.e. are anisotropic in nature). Since these fragments are neutron rich, they emit multiple neutron (and γ-ray) particles, which therefore carry forward the fission fragment's frame of reference, resulting in an anisotropic neutron spatial distribution (i.e. *angular distribution*). The *event-trains* obtained from the *multiplicity register* were analysed to obtain the angular distribution using ^{252}Cf, the results of which are presented in section 4.4 on page 119.

As can be observed in figure 4.13 on page 120, the Fourier and polynomial fits used in the plots have good agreement with the measured dataset, as shown in table 4.3 on page 121, with the *fourth* neutron response being the exception. The *second* neutron response is a dipolar *angular distribution*, i.e. shaped like a cosine curve, consistent with the two bodies accelerating away from one another in opposite directions. Careful observation of the *second* neutron response reveals that the distribution is biased towards one side (i.e. the crest at the centre of figure 4.13 or at 0 rad is of higher amplitude compared to the crests at $\pm\pi$ rad for the *second* neutron response). This trend manifests from the fact that the two fragments produced during spontaneous fission are seldom of similar mass, and hence one of the two fragments emits more neutrons than the other. This anisotropy can also be observed by measuring the angular separation of an emitted neutron relative to the angular momentum of the fission fragment (θ_{bl}), which may be parametrised by $1 + A \sin\theta_{bl}$ [175]. The experimental response is well reproduced by the Geant4 simulation, also using the *Fission Reaction Event Yield Algorithm (FREYA)*, CGMF, FIFRELIN fission models, as can be observed in figure 4.14(a), except for the neighbouring detector on the left-half of the response. The simulated response constructed using the FIFRELIN model was the closest to the experimental dataset, followed by CGMF and the FREYA model. However, the deviation between the models is quite small and manifests neat 0 rad and $\pm\pi$ rad.

The crests at $\pm 168^\circ$ (i.e. $\pm 42\pi/45$ rad) are approximately 80% of the peak at $\pm 24^\circ$ (i.e. $\pm 2\pi/15$ rad) in the distribution, which is contrary to what is seen in the raw *angular distribution*[2] obtained directly from the FREYA model, as presented in figure 2.9 on page 27 [176]. However, the "FREYA XT corrected" response, which does not contain any *crosstalk* events, suggests that the crests at $\pm 42\pi/45$ rad should in fact be higher than the corresponding crests at $\pm 2\pi/15$ rad. This also confirmed by the *crosstalk* corrected response from uncorrelated fission model, which is isotropic in nature, compared to the standard simulation (i.e. with *crosstalk*) using the uncorrelated fission model. The latter response shows increased activity near the *reference* detector (i.e. either side of 0 rad). Therefore, it can be asserted that neutron *crosstalk* plays

[2] Direct measurement of the angular separation between the neutron that are emitted, not the detector response.

a significant role in the distributions and is the cause of the contradiction seen between the measured distribution in figure 4.13 and the raw FREYA distribution in figure 2.9.

It can also be seen in the experimental results that when the *gate-width* is restricted to 10 ns for the *second* neutron response, the amplitudes of the crests at $\pm 42\pi/45$ rad are approximately 60% of those of the crests at $\pm 2\pi/15$ rad. The shallower anisotropy of the unrestricted response with a 25 ns *gate-width* is likely to be due to contamination of the neutron *event-train* by scattered events, since that phenomenon has no angular correlation. Such contamination is unlikely to happen when the *gate-width* is restricted as restricting the gate-width effectively discards these scattered events which have a longer source-to-detector traverse time. Of course the threshold is also relevant when trying to restrict influence of scattering, which will be demonstrated in coming sections.

The *angular distribution* of the *third* neutron has similar trends compared to the *second* neutron's response; however, the crest at 0 rad is much lower compared to that of the *second* neutron response at the same location. The crests at $-\pi$ and π rads are also higher compared to the crest at 0 rad, which is contrary to what was seen with the *second* neutron response. Again, the trough of the distribution is slightly biased towards the left-hand side. This is to be expected as any minor deviation observed in the first order response is likely to be amplified in the higher-order responses. The restricted experimental dataset is the closest match to the simulated dataset, but only for the left-hand side of the response. Finally, the deviation between the experimental and simulated observations is significantly increased compared to what was seen for the second neutron, as may be observed in figure 4.14(b).

Due to the limited number of quadruplets events with four correlated events, which are the constituents of the *fourth* neutron response, the *angular distribution* for the *fourth* neutron has the least intensity, and hence has the highest uncertainty compared to others, as can be observed in figures 4.13 and 4.14(c). However, it can be ascertained that the *angular distribution* of the *fourth* neutron response is such that the crest at 0 rad is lower compared to the crests at $\pm\pi$ rad. Comparing to the *second* and *third* neutron *angular distributions*, the centre crest is such that it diminishes in magnitude. This is attributed to the fact that when multiple neutrons are emitted (as implied by the detection of multiple correlated neutrons), it is likely that both fission fragments were involved in the emission of the neutrons; hence making the response more isotropic in nature. The simulation data provided for the *fourth* neutron has very large uncertainties due to limited registered events; longer simulations were not undertaken as the computational requirement was very high.

The angular displacement of the *third* neutron (w.r.t. the *reference* neutron) as a function of

the displacement of the *second* neutron (w.r.t. the *reference* neutron) is illustrated in figure 4.15 on page 123. The data was post-processed using Matlab's spline-smoothing algorithm to increase the fineness of the plot and remove any discontinuity existing due to the dead-time related to the detectors where the *reference* and *second* event were triggered. As per expectation, the trend outlined by this surface plot is dipolar in nature. Since triplet events are required to build such a 3-dimensional surface plot, the acquisition time needed to determine it is very long. Nonetheless, this distribution shows information regarding the spatial correlation that has not been seen before.

5.4.1 Alternative techniques and prior-art

Spatial correlations between particles that are emitted from the fission fragments following spontaneous or induced fission, due to the kinematics and rotation of the fragments has been investigated quite extensively, as discussed in section 2.3. The characteristics have been studied extensively by Bowman [177, 178], Skarsvåg [179] and Vorobyev [180] for ^{252}Cf spontaneous fission, and Fraser studied this for the induced fission of ^{233}U, ^{235}U and ^{239}Pu [181]. These measurements were made using multiple neutron and fission fragment detectors which allowed for measuring the angle between a detected neutron and the two fragments that are emitted during the fission process, thus measuring the average angle between the neutron and the fission fragments.

With the absence of apparatus to isolate the axis along which the fission fragments were accelerated, it is only possible to extract the density of spatial correlations by measuring the angle of separation between two correlated neutrons. This concept has been previously used by several researchers [59, 176, 179, 182, 183, 184, 185, 186] in conjunction with a ^{252}Cf source. The cited references also studied the impact of different detector thresholds on the measured *angular distribution*, and their results demonstrated that decreasing the threshold makes the *angular distributions* less anisotropic. Figure 5.5 shows the measured responses from the three references [183, 184, 185][3] for cases between 1 MeV and 1.5 MeV, which is notionally equivalent to 200 keVee according to the light output response functions measured by Enqvist [118] (i.e. consistent with the experiments conducted in this thesis). Each of these distributions was fitted with a two-term Fourier series, consistent with the analysis presented in section 4.4 on page 119. The figure also plots the *angular distribution* of the *Second* neutron which was measured in this thesis. In order to be consistent with the other distributions, the two halves of the unrestricted *angular distribution* presented in figure 4.14(a) were added together. The comparison shows good agreement between the results obtained in this work and those from reference [185] (green data points). The measurements made using the *multiplicity register* in this thesis show lower intensity

[3] Results presented by Vogt were from simulation using the FREYA model [184].

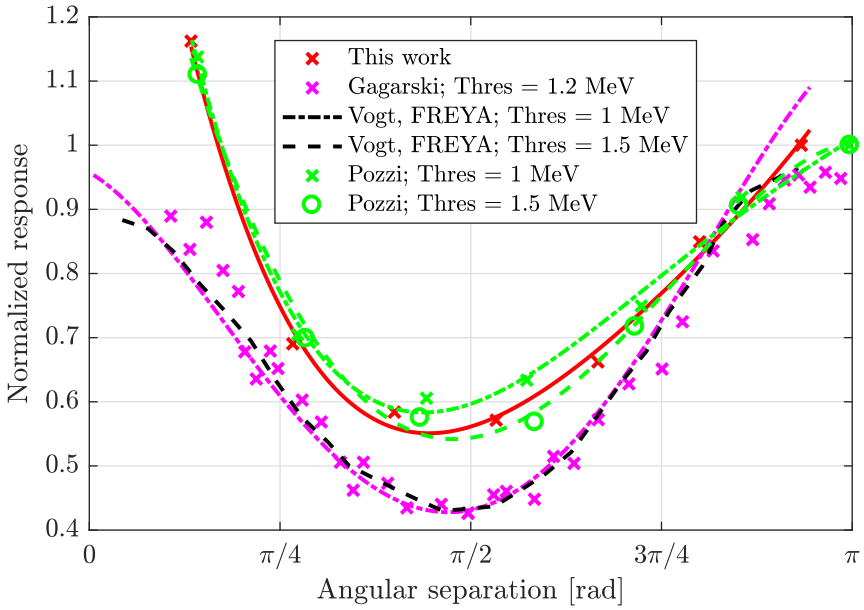

Figure 5.5 | Angular correlation between the *First* and *Second* neutron. A comparison of different experiments conducted with the objective of measuring the neutron-neutron separation from spontaneous fission of ^{252}Cf source. The data were collected from references [183, 184, 185]. The data points from each response was fitted with a two-term Fourier series, and were normalized to the experimental-data point which is nearest π rad since that is the point where *crosstalk* is expected to be the lowest.

between $3\pi/4$ and $\pi/4$ rad compared to the simulations using the FREYA model provided in reference [184] (black line and crosses) in the latter cases. Finally, there is also considerable disagreement between the results in this thesis and results presented in reference [183] (magenta and crosses), possibly due to the use of borated polyethylene which would reduce the *crosstalk* in the latter assay.

There are several other examples in which such a setup could be used, e.g. for measuring the neutron scattering angular distribution [187], for measuring the *angular distribution* from the spontaneous fission of plutonium isotopes [30, 188, 189], etc.

The novelty of this study compared to the above-mentioned research is three-fold. Firstly, it demonstrated the first evidence of spatial correlation across multi-order (triplets and quadruplets) correlated neutrons. This is very interesting as it shows the prospect of using high-order spatial correlation for characterization of nuclear materials. Secondly, it was demonstrated in figure 4.14 that having a relaxed *gate-width* illustrates the impact scattered neutrons have on such analysis. This is similar to having a higher detection threshold, however, with the latter approach, the assay will also be blind to low energy neutrons emitted during spontaneous fission. However, the latter approach has an added potential advantage of reducing *photon-breakthrough*. Finally, from figure 4.15 on page 123, the spatial correlation between the first three detected correlated

neutrons is demonstrated.

5.5 Analysis of the neutron and photon temporal correlation via coincidence counting

In this section the results of PFNCC and AFNCC analysis achieved with the cluster-size based algorithm are discussed by examining the results presented in section 4.5. Additionally, the cluster-size based algorithm is compared with the traditional analytical technique, i.e. the shift-register method, which has been adopted by some for use with fast neutron detectors.

5.5.1 Passive coincidence counting

When comparing the Cf252-BARE8 and Cf252-BARE15 neutron *coincidence distributions*, in figure 4.16(a) on page 126, and tables E.1(a) on page 299 and E.2(c) on page 300, it can be observed that the *BARE15* arrangement with seven additional detectors resulted in approximately 1.3 times higher count rate for the singlet, 2.3 times higher for the doublet, 4.2 times higher for triplet and 3.8 times higher for quadruplets events than the *BARE8* arrangement. The γ-ray *coincidence distributions* of the ^{137}Cs source (uncorrelated[4] source emitting a single γ ray per decay) and the ^{60}Co source (correlated source emitting two γ rays per decay) illustrate that the correlated ^{60}Co source registers higher *multiplets* despite being of approximately the same activity. This is as expected as ^{60}Co emits two correlated γ rays per decay.

The efficiency of the *Totals* and the multiplet ratios are presented in tables 4.4(a) and 4.4(b) on page 127, respectively. The first table shows the *Totals* efficiencies, for the *BARE8* and *BARE15* arrangements using Cf252-MAIN source, which are marginally higher compared to the Geant4 simulated efficiencies. One reason for this is attributed to *photon-breakthrough*; due to these misclassified events the experimental neutron count is higher compared to those computed by the simulations. This also results in the experimental data having lower multiplet efficiencies (the different *multiplets* to the singlet count rate, i.e. doublet-to-singlet, triplet-to-singlet and quadruplets-to-singlet ratios) compared to the simulated data, as demonstrated in table 4.4(b). From figure 4.16(a) and table 4.4(b), it can be observed easily by comparing the doublet-to-singlet and triplet-to-singlet ratios that despite emitting one or two γ ray(s), both experiments using ^{137}Cs and ^{60}Co register high orders of coincident events which cannot be accounted for by their rate of *accidental events*. This is believed to be due to detector *crosstalk*, and will be addressed in section 5.6 on page 174 in further detail.

In figure 4.16(b) on page 126, all the *multiplets* registered increased count rates with increase in mass, except for the quadruplets count rate of Cf252-ALL compared to Cf252-MAIN, which could be due to the short duration of the experiments and correspondingly low statistics. The

[4] When only a single radiation particle is emitted per decay.

different multiplet efficiencies (i.e. doublet-to-singlet, triplet-to-singlet and quadruplets-to-singlet ratios) however remain relatively constant at approximately 3.2×10^{-2}, 5.12×10^{-4} and 5.45×10^{-6}, respectively, for all four experiments (see table E.5 in appendix E on page 297). The Cf252-FC is an exception to this as it registered slightly lower ratios, possibly due to its age. The quadruplets-to-singlet ratio demonstrates the most fluctuation, due to having a higher probability of being affected by *accidental events*, *photon-breakthrough* and *crosstalk*. In all the experimental results demonstrated in figure 4.16, the accidental counts were consistently 1000 times lower in magnitude.

The *coincidence distributions* that were obtained using the ^{252}Cf source in the *REFL15* setup at Lancaster University demonstrated results consistent with expectations, with higher *multiplets* being registered when the correlated neutrons are able to escape the tank (i.e. when the source is placed at the edge of the tank for the cases marked "Exposed"). When joint neutron and γ-ray events are considered, the *multiplets* for both Exposed and Secured cases increase compared to both the neutron-only distributions as more correlated events are available when constructing the *coincidence distributions*. The normalised factorial moments of the *coincidence distributions*, as demonstrated by figure 4.17(b) on page 128, obtained from the *REFL15* arrangement are lower compared to expectation, appearing as if the assay is blind to a significant portion of the incident radiation field. For example, it is expected that the first three orders of factorial moment distribution for the Exposed-Neutron case will be notionally equal to 3.76, 11.96 and 31.78, which were computed from the probability distribution of ^{252}Cf in table 2.2 on page 24. However, as demonstrated by figure 4.17(b), this is not the case and a large deviation can be observed from the first moment onwards suggesting that, despite correcting for efficiency, a large portion of the neutrons are not being accounted for. As will be shown in section 4.6, the singlet bin of the *coincidence distributions* contains excess events which are leading to inconsistent results.

5.5.2 Active coincidence counting

For a practical demonstration of a SNF assay, measurements were made during the irradiation of nine standardised samples of UOX of the various enrichments described in section 3.3.1, with the same AmLi source using three detector arrangements; *BARE8*, *BARE15* and *CASTLE12* illustrated in sections 3.3.3, 3.3.4 and 3.3.5, respectively, starting at page 79. The results from this investigation may be found in section 4.5.2 on page 129.

Figures 4.18(a) and 4.18(b) on page 130 illustrate the trend in the relationships of the singlet and doublet counts with the mass of the ^{235}U content (i.e. enrichment) for the *BARE8* and *BARE15* assays. The results exhibit well-defined trends for the two rates in the low-enrichment region, i.e. ^{235}U mass < 20 g, which increase almost linearly. This, for the upper three samples in

Table 5.1 | Doublet-to-singlet ratios for the AFNCC cases. The values of the ratio between the doublet and singlet counts for the different UOX canisters after having the AmLi dominated background contribution removed. The trend in the ratios within the four cases is constant, however, the three out of four cases of depleted uranium shows negative ratios as the recorded singlet count for these responses were less than the response from the AmLi contribution when used with the empty canister.

	Doublet-to-Singlet Ratios			
Enrichment	*BARE8*	*BARE15 (2 cm)*	*BARE15 (3.75 cm)*	*CASTLE12*
0.31%	-0.0536	0.0498	-0.0803	0.0085
0.71%	0.0107	0.0601	0.0234	0.0252
1.92%	0.0116	0.0278	0.0208	0.0251
2.95%	0.0100	0.0223	0.0165	0.0274
4.46%	0.0093	0.0248	0.0224	0.0303
20.1%	0.0078	0.0180	0.0183	0.0304
52.5%	0.0080	0.0179	0.0192	0.0300
93.2%	0.0088	0.0177	0.0172	0.0307

terms of mass, i.e. mass > 30 g corresponding to ^{235}U enrichments of $20.31 \pm 0.02, 52.80 \pm 0.04$ and $93.23 \pm 0.01\%$ wt., becomes a decreasing trend. This is consistent with the higher thermal neutron absorption cross-section for ^{235}U compared to that of ^{238}U, which removes the thermal neutron from the assay prior to inducing fission. The effect of increased moderation is illustrated in figure 4.19 on page 131, for the *BARE15* arrangement, which shows that the case with the smaller thickness of the moderator yields slightly higher count rates as the increased polyethylene removes some of the neutrons due to absorption within itself. The results for the experiments using the *CASTLE12* arrangement in figure 4.20 on page 132 infer similar conclusions. Nonetheless, due to the compact nature of the detector placement, this case will unavoidably lead to higher rates of *crosstalk* as well.

Table 5.1 lists the doublet-to-singlet ratios for all the different arrangements, which shows a steady trend for all cases except for the depleted UOX samples (i.e. 0.31% enrichment). The depleted samples have negative ratios, which are unphysical, as the singlet counts for depleted uranium were very close to AmLi background and numerically had negative count rates for three out of the four experiments after AmLi counts were removed. However, the doublet count rates, as shown in figures 4.18(a), 4.18(b) and 4.20, were consistent with the presence of ^{235}U in the depleted sample despite having small magnitudes. The fit parameters provided in table 4.5(b) show that the *sum of squares due to error (SSE)* and *Root Mean Squared Error (RMSE)* values for the doublet response are close to zero indicating that there is small deviation of the response values from the fit. Therefore, the doublet relationship with the enrichment might be effectively used as calibration data for characterisation of unknown UOX samples. This demonstrates the effectiveness of using coincidence counting techniques compared to measuring uncorrelated

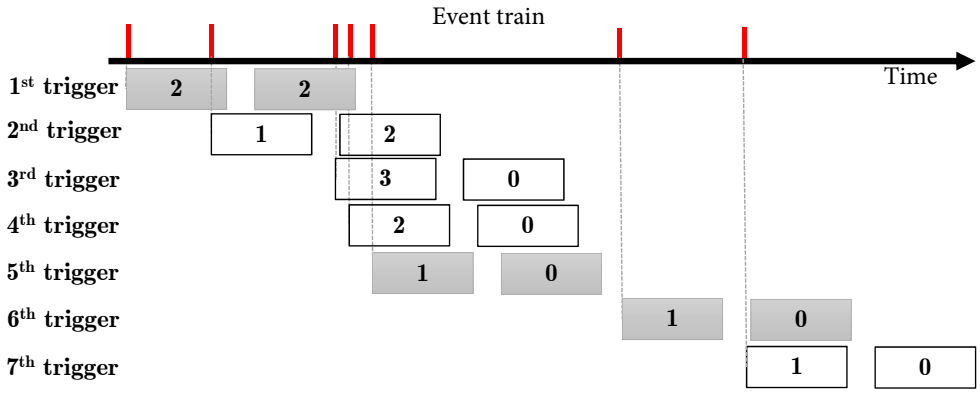

Figure 5.6 | Comparison between shift-register method and cluster-size based method. A common *event-train* being processed by the shift-register algorithm and the one-shot cluster-size based algorithm which are highlighted in grey. The shift-register based algorithm opens a *coincidence-gate* for every incoming event, i.e. 7 triggers are issued, thereby creating a distribution corresponding to the reduced factorial moment of the *event-train*. The proposed one-shot cluster-size algorithm only issues *coincidence-gates* for unique events, i.e. the 1st, 5th and 6st triggers highlighted in grey, thereby creating a distribution corresponding to the size of the incoming clusters.

intensity of the radiation field emitted during the fission process.

5.5.3 Alternative techniques and prior-art

The *passive neutron coincidence counting (PNCC)* and *active neutron coincidence counting (ANCC)* assays based on thermal neutron detectors tend to have large source-to-detector flight times, in the order of 32 to 300 microseconds, due to the time necessary for thermalisation which substantially increases the detector die-away. This prevents the use of one-shot coincidence algorithm [82], like the proposed cluster-size method, to be used with such thermal detectors; and as such, historically, the shift-register method, mentioned in section 2.5 on page 34, has been used with thermal detectors. Due to this reason, this approach has become a universally-accepted standard for fissile materials assay in nuclear safeguards. In the shift-register method, triggers are issued for every incoming event, starting a new *coincidence-gate* as illustrated in figure 5.6. This yields a *reduced factorial moment distribution* of incoming neutron events.

However, the limitation imposed by the long source-to-detector flight time is not valid for fast neutron assays. For example, using the MFA with liquid scintillators significantly reduces electronic dead-time, and these are capable of processing up to 3 million events per second. Moreover, because thermalisation is unnecessary, the source-to-detector ToF is very small ($\approx$ 20 ns as shown in section 5.2 on page 149). Despite this, in many different instances, the shift-register based technique has been adopted with fast neutron detectors as well; instead of a cluster-size method as proposed in section 3.2.1 on page 65. The resulting *foreground coincidence distribution*

and *background coincidence distribution* generated by this method are comprised of only the 1st, 5th and 6th triggers shown in figure 5.6, as this is when the trigger mechanism is sensitive to incoming events. This prevents the same neutron event from being counted multiple times and the resulting distribution corresponds to the size of the incoming neutron cluster in the *event-train*. This *coincidence distribution* can easily be converted to the *reduced factorial moment distribution* to apply existing analytical models (as discussed in section 2.5.1 on page 34) using equation 2.49, while having the benefit of being able to directly infer the *multiplets*, i.e. the size of the clusters or bursts, without the need to carry out further mathematical analysis. This allows for the implementation of easy-to-maintain correction models for physical phenomena, such as *photon-breakthrough* and *crosstalk*, as will be demonstrated in section 5.6.

The prospect of liquid scintillation detectors for neutron multiplicity counting is a well researched topic [19, 24, 190, 191]. There are several research papers that were published in the last decade using arrays of scintillation detectors (as a detector on its own or in conjunction with other types of detectors) coupled with high-speed digitizers to measure the correlated fields (i.e. neutron, γ-ray and mixed field) emitted during the spontaneous fission of ^{252}Cf [192, 193]. In all cases, the event-by-event coincidence analysis used the shift-register method. While the data accumulated in this research could potentially be converted to the corresponding *reduced factorial moment distributions*, a direct comparison between the assays is difficult due to differences in geometries, detector models, detector thresholds, etc. However, the trend in the data presented in this thesis is consistent with the literature; for example, based on reference [193], the doublet-to-singlet ratio for the case with 30 cm source-to-detector distance was computed to be ≈ 0.02 compared to ≈ 0.032 in the *BARE15* setup in this thesis. Similar measurements were carried out recently by a combination of inorganic and organic scintillation detectors using ^{252}Cf [159, 194], which also demonstrated similar trends. Additionally, several attempts were made towards characterisation of correlated particles emitted during the spontaneous fission of plutonium isotopes within fuel pallets [94, 157]. Recently, publications were made outlining a fast neutron counter which was used to characterise plutonium metal plates of various masses using eight EJ-309 and eight stilbene detectors [195, 196, 197]. These papers expand further on measurements by computing the effective mass of fissile material present in the samples that were examined.

Prior-art related to AFNCC is more scarce compared to PFNCC, possibly due to the complexity involved in such measurements due to the coupling between the radiation fields from the induced fission and the interrogator (e.g. AmBe). Recently, however there have been various publications related to induced fission of uranium samples when interrogated using an AmLi source [23, 198, 199]. While the first paper demonstrates the effect of *photon-breakthrough* and *crosstalk*, it is understood from personal correspondence with the authors of the second paper

that a more detailed publication based on the second paper is in preparation, which would analytically delink the coupling between the neutron fields emitted from the AmLi and uranium samples. Recent publications consider the measurement of correlated neutron coincidence due to photofission (i.e. photon induced fission) of ^{235}U [170] as well as the multiplicity of the prompt γ-ray field emitted during the neutron-induced fission of ^{239}Pu [200].

Arrays utilising scintillation detectors benefit from being able to detect both neutrons and γ rays, which consequently leads to more observables compared to the case of pure neutron multiplicity counting using ^{3}He [197, 201, 202]. While introducing some extra parameters (related to the γ-ray processes), such distributions could be leveraged to carry out sample characterisation.

The novelty of this section again lies in the real-time implementation of the algorithm, in conjunction with the MFA. Additionally, the cluster-size based algorithm, using which the *coincidence distributions* were determined, has not been investigated widely. Due to the reduced number of triggers, the count rates obtained from such techniques will be lower compared to those for the shift-register method for an identical source and geometry. As a result, to have the same level of confidence in the analysis based on measurements made using this cluster-size algorithm compared to the shift-register method, the experiments will need to be conducted for a longer duration. However, its versatility will be demonstrated in section 5.6 to build correction models in order to correct for biases that only exist in scatter-based detectors, i.e. *photon-breakthrough* and *crosstalk*.

5.6 Photon-breakthrough and Crosstalk

As mentioned in section 2.6.4 and 2.6.3 on page 47, scattered-based detectors, such as those comprising organic scintillation materials, are subject to two main disadvantages:

- The relatively high sensitivity to γ rays coupled with shortfalls in the event discrimination mechanism can lead to 3% to 5% of γ-ray events (depending on the pulse shape discrimination (PSD) algorithm being used) being misclassified as neutrons. This phenomenon is defined as *photon-breakthrough* in this thesis and can lead to a disproportionate impact on neutron count rates as the ratio between number of neutrons and γ rays emitted from either spontaneous or induced fission is typically in the order of 1:10.
- Due to the dependence on scatter-based nuclear reactions and partial energy deposition, a single neutron (or γ ray) has a non-zero probability of triggering multiple detectors and masquerading as a higher-order correlated multiplet event. This is referred to as *crosstalk* in this thesis.

If corrections are not made to compensate for these phenomena, then the numerical analysis conducted using the data acquired from a scatter-based detector assay may be undermined. The results obtained from the investigation of the properties of the above-mentioned phenomena are provided in section 4.6.1 on page 133 and section 4.6.2 on page 135, respectively. In this chapter, a discussion of these results is made in section 5.6.1. Additionally, a model for quantifying their contribution is also proposed, which therefore can be used as a correction model prior to any numerical analysis. Finally, section 5.6.2 validates the model from the PFNCC point-of-view based on the measurements made with a standardised ^{252}Cf source. As the accidental counts are very low when using fast neutron assay (as shown in previous sections), *accidental events* were ignored in all calculations.

5.6.1 Correction models

In this section, the results in Sections 4.6.1 and 4.6.2 are discussed following which, two correction models are proposed for the multiplicity algorithm discussed in section 3.2.1 on page 65 to address both *photon-breakthrough* and *crosstalk*. The coefficients for these models can be derived experimentally and through simulations.

Photon-breakthrough

The emission of γ rays is always associated with the emission of neutrons, and often the rate of γ-ray emission is significantly greater. Although, depending on the type of algorithm and the assigned detector threshold, only a small proportion of events might be misclassified by a

PSD technique, even a small degree of misclassification of γ-ray events can impact the neutron count significantly, as will be shown in this section. Low energy γ rays are most susceptible to such degradation in discrimination performance between neutrons and γ rays, as can be seen in figure 4.21 on page 134, which demonstrates a contour and a surface plot of the pulse shape discriminated outputs from a ^{252}Cf source, illustrating a considerable overlap of events in the low-energy region. Additionally, it is also possible for a high energy γ-ray to undergo a scatter reaction where it only deposited small amount of energy, thereby leading to the same erroneous detection. This is a common occurrence as the analogue signal induced by the low-energy particles do not have sufficient amplitude to provide enough resolution for the PSD technique to be applied effectively, thereby making this region the most prominent in leading to misclassified events. As can be observed from the data presented in table 4.6, 1% to 6% of all γ-ray events may be misclassified as neutrons.

Section 4.6.1 on page 133 reports on three test cases to investigate the effect of *photon-breakthrough*. Ideally, as a result of the modifications made to the reference experiments reported in section 4.5 on page 124, the γ-ray count rate is expected to change, while the neutron count rate is expected to remain similar as the experiments were designed to influence the γ-ray field only. The findings from the modified experiments however reflect that the neutron flux also changes, sometimes significantly. The results, which are listed in table 4.7 on page 135, can be summarised below, which illustrates the impact of such erroneous counts. If not corrected for, these erroneous counts may contribute towards misleading conclusions from critical measurements and increase the uncertainty of the measurements being made.

1. When the Cf252-MAIN source was placed in the tungsten container, the total neutron count rate dropped to 10064 cps compared to a count rate of 10,309 cps when the Cf252-MAIN source was open, which corresponds to a 2.37% change, as illustrated in Tables E.4 on page 301 and E.5(c) on page 302.

2. When the extra γ-ray sources were added to the *CASTLE12* arrangement, along with the 20.1% enriched UOX canister, the total neutron count rate jumped to 821 cps compared to a count rate of 149 cps in the standard run. This is an increase of more than 500%.

3. When the lead shielding was removed from the *BARE8* arrangement, the CF252-MAIN source recorded a 8.7% increase in count rate from 7406 cps to 8051 cps, as illustrated in table E.2 on page 300.

The effect of *photon-breakthrough* on the *coincidence distributions* can manifest in different ways, as has been considered in an analogous way to that which follows on the basis of what is observed in experimental measurements. For example, the singlet neutron bin might register

more counts due to the misidentification of γ rays. Additionally, in the event that a *photon-breakthrough* takes place in conjunction with actual neutron events, the doublet and triplet bins of the *coincidence distribution* will gain one more count, while the preceding multiplet will have effectively lost a count relative to the hypothetical scenario where breakthrough is zero. The model described in this research ignores the second category as, whilst not negligible, its probability is smaller than that of the first category. Hence, only the singlet bin in the distribution, $f'_x(1)$ of an event type x (i.e. neutron or photon), is corrected according to equation 5.1,

$$f'_x(1) = f_x(1) - B_x \sum_{l=1}^{\infty} f_{\bar{x}}(l) \tag{5.1}$$

where, $f'_{\bar{x}}(l)$ is the *coincidence distribution* corrected for *photon-breakthrough*, $\bar{x}$ is the event type complementary to x (in this case for γ-ray distribution as the correction is focused on neutron), l is the *multiplet* and B_x is the *particle breakthrough factor*. The B_x term is expressed as the ratio of the number of misclassified x events to the total number of $\bar{x}$ events detected, i.e. the *breakthrough factors* can be computed by tallying all the misidentified particles and expressing this quantity as a ratio of the total counts of that particle.

Crosstalk

As highlighted in section 2.6.4 on page 48, when *crosstalk* yields a second count due to scattering between detectors which, if occurring within the time window that is used to discriminate correlated neutrons, can be mistaken as being the second event of a correlated pair; hence a singlet might appear to be a doublet. Higher-order *crosstalk* events are plausible in the event of subsequent scatters that occur within the time gate. For clarity, one singlet manifesting as a doublet is referred to as *first-order crosstalk*, while a singlet appearing as a triplet is referred to as *second-order crosstalk*. If not corrected, potentially-significant errors can result from singlet events being misconstrued as correlated events in this way.

From the dependencies of the data presented in figures 4.22 on page 137, it can be concluded, in line with expectation, that the probability of *crosstalk* for between adjacent detectors is highest when the detectors involved in the event are nearest to one another with a small scattering angle relative to other scenarios. The contribution from cross-talk is negligible at angles greater than $\approx 45^{\circ}$. Additionally, from figure 4.23, it is evident that the neutron beams with higher kinetic energies exhibit higher *crosstalk* compared to the cases with lower kinetic energies. This is in line with expectation as neutrons with higher incident energies are expected to exit the first detector with enough kinetic energy to enable them to trigger a second detector. While most of the *crosstalk* takes place between 5 ns and 40 ns for all cases, it can be observed that the response for higher energy neutron, i.e. for 5 MeV mono-energetic neutron beam, start a few nanoseconds

prior to other cases. The same observation may also be made for the location of the peaks in the distributions with the responses peaking at (11, 9 and 8) ns for the (1, 2, 3.5 and 5) MeV cases, respectively. Hence, it is desirable to correct for the excess activity that arises due to *crosstalk*.

Based on this analysis, it is evident that a correction term for *crosstalk* is a complex function of the *geometry*, i.e. the solid angles subtended between source-to-detector and by detector-to-detector, *detector cut-off*, *coincidence gate-width* and, to a lesser extent, the *incident neutron energy*.

When a *crosstalk* event takes place, it can influence the *coincidence distributions* in two ways. From the perspective of a particular event chain; (i) the singlet bin loses one count (referred to as *updraft*) and (ii) the doublet (and potentially the higher-order bins) gain one count (referred to as *downdraft*). For clarity, one can also define the terms from the perspective of a given *multiplet* (i.e. a particular bin in the *coincidence distribution*, $f(k)$); *updraft* is when the given bin loses a count, and *downdraft* is when that bin gains a count. The extent to which this occurs reflects the order of *crosstalk*, i.e. whether the neutron scatters into one detector registering an event or two thus registering two further events. Additionally, a doublet may also appear as a triplet if one of the two neutrons comprising the true doublet is scattered and detected by other detectors within the gate. For simplicity, the case where both particles in a real doublet undergo *crosstalk* is ignored as this is generally considered highly improbable[5], as subsequent analysis will show.

Based on the assumptions described above, a correction model based on a truncated balance equation for each of the multiplets (i.e. f_x) follows, as expressed in equation 5.2,

$$f'_x(k) = f_x(k) \underbrace{\left(1 + \sum_{n=1}^{\infty} XT(n)\right)}_{\text{correction term for updraft}} - \underbrace{\sum_{m=k-n}^{\infty} \left(f_x(m) \sum_{l=1} XT(l)\right)}_{\text{correction term for downdraft}} \tag{5.2}$$

where $f'_x(k)$ is the kth multiplet distribution corrected for *crosstalk* and XT is the empirical, arrangement dependent *crosstalk-factor*; this is defined as the ratio of the number of *crosstalk* events to the total number of events detected as a function of order of *crosstalk*, l. The type of event, i.e. neutron or γ ray, is denoted by x, n is the order of multiplet (i.e. singlets, doublets, triplets, etc.) and $m = k - n$ where $m > 0$.

The distributions in table 5.2 illustrate the first-order *crosstalk-factor* from both experiments using these uncorrelated sources and dedicated simulations for both *BARE8* and *BARE15* arrangements. The simulations were conducted with 1 million particles in each case, representing mono-energetic neutron and γ-ray beams of (0.75, 1, 1.25, 1.5, 1.75, 2, 2.25, 2.5, 3.5 and 5) MeV, ^{252}Cf (neutron), AmLi (neutron) and ^{137}Cs (γ-ray) source. In this case an AmLi source was

[5]For example, the probability of *crosstalk* for a 2.5 MeV neutron in the fifteen-detector setup is estimated at only 0.18%, as shown in table 5.2.

Table 5.2 | Cross-talk factors for neutrons and γ rays in the BARE8 and BARE15 arrangements First-order *crosstalk-factors* for (0.75, 1, 1.25, 1.5, 1.75, 2, 2.25 and 2.5) MeV monoenergetic neutron and γ-ray beams as well as AmLi (neutron) and ^{137}Cs (γ-ray) sources. The values were calculated based on Geant4 simulation except where denoted 'exp.' The detector cut-off and *gate-width* were set at 200 keVee and 25 ns, respectively, for both the simulations and experiments.

Incident	***Neutrons***		***Photons***	
Energy (keV)	*BARE8*	*BARE15*	*BARE8*	*BARE15*
750	0.0000 ± 0.0000	0.0001 ± 0.0002	0.0011 ± 0.0001	0.0057 ± 0.0003
1000	0.0004 ± 0.0001	0.0008 ± 0.0002	0.0015 ± 0.0001	0.0075 ± 0.0003
1250	0.0009 ± 0.0001	0.0019 ± 0.0001	0.0022 ± 0.0001	0.0086 ± 0.0003
1500	0.0009 ± 0.0001	0.0022 ± 0.0001	0.0024 ± 0.0001	0.0091 ± 0.0003
1750	0.0011 ± 0.0001	0.0028 ± 0.0001	0.0026 ± 0.0001	0.0096 ± 0.0003
2000	0.0013 ± 0.0001	0.0038 ± 0.0001	0.0027 ± 0.0001	0.0100 ± 0.0003
2250	0.0015 ± 0.0001	0.0045 ± 0.0001	0.0029 ± 0.0001	0.0107 ± 0.0003
2500	0.0019 ± 0.0001	0.0055 ± 0.0001	0.0030 ± 0.0001	0.0108 ± 0.0003
3500	0.0034 ± 0.0001	0.0089 ± 0.0001	0.0038 ± 0.0001	0.0144 ± 0.0003
5000	0.0041 ± 0.0001	0.0115 ± 0.0002	0.0047 ± 0.0001	0.0166 ± 0.0003
AmLi	0.0007 ± 0.0001	0.0010 ± 0.0002	Not Examined	
AmLi (exp)	0.0008 ± 0.0001	0.0016 ± 0.0001		
^{252}Cf	0.0025 ± 0.0001	0.0072 ± 0.0001	Not Examined	
^{137}Cs (662 keV)	Not Applicable		0.0010 ± 0.0002	0.0038 ± 0.0003
^{137}Cs (exp)			Not Examined	0.00367 ± 0.00001

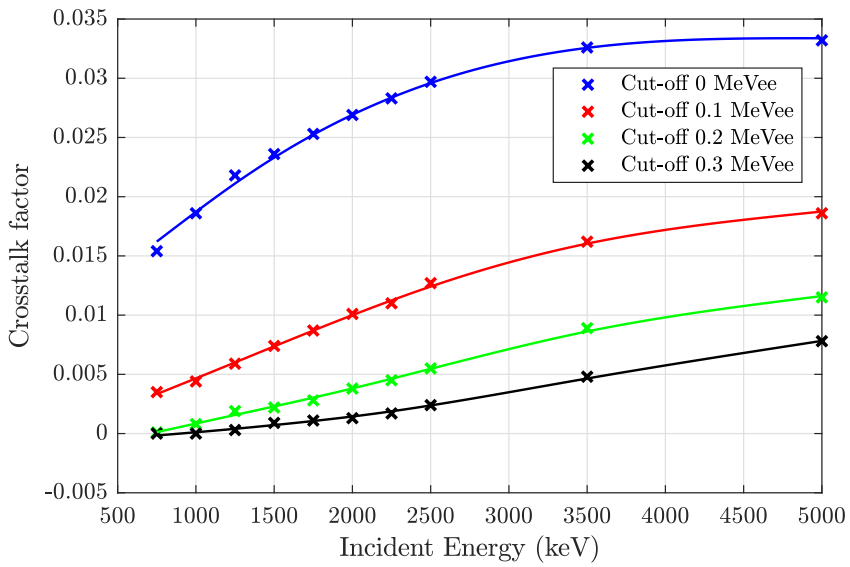

Figure 5.7 | Crosstalk factor. The relationship between first-order *crosstalk-factor*, as defined in equation 5.2, and initial incident energy of the neutron. The impact of different levels of detector cut-off is also illustrated. A quadratic fit is added to guide the eye. With increased detector cut-off, the magnitude of the *crosstalk-factor* increases but with a decreasing rate.

simulated as a neutron source with a uniform energy distribution between 0.3 and 1.3 MeV, whilst for the simulation of ^{252}Cf, its spectrum was obtained from the FREYA model but only generated one neutron per history with a fixed directional vector. The cut-off energy and *gate-width* was set at 200 keVee and 25 ns, respectively, in accordance with the experiment. Since the radiation emitted by AmLi and ^{137}Cs is not correlated, any pair of events recorded within the specified *gate-width* for these sources constitutes *crosstalk* and hence the *crosstalk-factor* can be determined from such measurements, not withstanding its dependency in cut-off energy. Further to this, figure 5.7 illustrates the trend in *crosstalk* factor as a function of neutron energy for different cut-off energies, i.e. (0, 100, 200 and 300) keVee, for the 15-detector arrangement.

Compared to the experimentally measured *crosstalk-factor* for the AmLi source, the simulated response is slightly lower, specially for the 15 detector arrangement, possibly due to the approximated implementation of its spectra that were made in the simulation model; however, the measured and computed *crosstalk-factor* using the ^{137}Cs source was well matched. The mono-energetic photon beams registered a near linear relationship between the computed *crosstalk-factors* and their incident energies. However, the neutron *crosstalk-factors* for different cut-off energies had differing trends compared to the respective detector cut-offs and incident energies. For example, the 0 keVee cut-off case registered a strongly non-linear response with a decreasing ratio between singlets and doublets. With increasing cut-offs, this non-linearity slowly reverses its bias; a subtly increasing relationship between the *crosstalk-factor* and the incident energies can be observed in figure 5.7. For the cases of 100 keVee, this relationship is linear for neutron beams below 3.5 MeV, after which the decreasing trend prevails. For the 200 keVee cut-off cases, there is an proportional relationship between the regions of 0.75 MeV and 3 MeV; whilst an proportional relationship can also be observed for the entire energy range for the case implementing 300 keVee cut-off.

5.6.2 Validation of the models

To validate the models described in the previous section, experimental results obtained using the main ^{252}Cf source (approximately 3.32×10^5 neutron per second) with the *BARE8* and *BARE15* arrangements were further studied. The validation was done using the *doubles gate-fraction* (f_d) for doubles in the analytical formulation proposed by Ensslin, as introduced in equation 2.34 on page 39 in section 2.5.1. Since liquid scintillators detect fast neutrons with a detector prompt die-away coefficient of typically ≈ 4.78 ns, as shown in table 4.2(b) on page 115, the f_d is very close to unity, i.e. 0.99, because the majority of the prompt neutrons are detected within the limit of the assigned gate (in this case 25 ns). Table 5.3 shows the details of the correction terms and the final f_d for the two experiments and the results of the corresponding simulations constituting 1 million fission histories, which correspond to only 11.13 seconds of

Table 5.3 | Detailed trends in coincidence distribution and doubles gate-fraction. The first three orders of the coincidence distributions (i.e. f_n) from the *BARE8* and *BARE15* arrangements with the main ^{252}Cf source were obtained from experiments and simulations. The *photon-breakthrough* and the *crosstalk* corrections were applied to obtain the 'Photon-corrected' and the 'Photon & XT-corrected' distributions, respectively. For each of these distributions, the *doubles gate-fraction* (f_d) was computed which demonstrates that upon application of the two correction models, the *doubles gate-fraction* approaches close to unity according to exceptions.

		BARE8 arrangement				**BARE15 arrangement**			
		Experiment		***Simulation***		***Experiment***		***Simulation***	
		Value	1cf_d	Value	f_d	*Value*	f_d	Value	f_d
Time [s]		1202		11.13		603		11.13	
Foreground distribution	$f_n(1)$	8584970 ± 2930	0.87± 0.01	76246 ± 276	1.02± 0.03	5674396 ± 2382	0.92± 0.01	94640 ± 307	1.12± 0.03
	$f_n(2)$	156696 ± 395		2428 ± 49		181625 ± 426		4417 ± 44	
	$f_n(3)$	1391 ± 37		31 ± 6		2907 ± 53		127 ± 11	
Foreground distribution (s^{-1})	$f_n(1)$	7142.7 ± 2.4		6471 ± 24		9410.3 ± 4.0		8367 ± 27	
	$f_n(2)$	130.0 ± 0.3		214.7 ± 4.4		301.2 ± 0.7		390.5 ± 5.8	
	$f_n(3)$	1.16 ± 0.03		2.74 ± 0.49		4.82 ± 0.09		11.23 ± 1.00	
Photon-corrected foreground distribution (s^{-1})	$f_n(1)$	5770 ± 16	1.20± 0.01	Not Applicable		7977 ± 17	1.21± 0.01	Not Applicable	
	$f_n(2)$	130.5 ± 0.3				301.2 ± 0.7			
	$f_n(3)$	1.16 ± 0.03				4.82 ± 0.09			
Photon- and XT-corrected foreground distribution (s^{-1})	$f_n(1)$	5785 ± 16	1.06± 0.01	6758 ± 92	0.95± 0.03	8034 ± 17	0.96 ± 0.01	8427.6 ± 21	0.96 ± 0.02
	$f_n(2)$	116.2 ± 0.5		226 ± 4		246.2 ± 1.2		333 ± 5	
	$f_n(3)$	0.82 ± 0.07		2.18 ± 0.51		2.72 ± 0.22		10.5 ± 1.03	

the experimental time. It presents the uncorrected *foreground coincidence distributions* and count rates, and distributions corrected for breakthrough and for *crosstalk*. At each stage of the analysis, this *coincidence distribution* was corrected for MFA dead-time[6] and was subsequently converted to the *reduced factorial moment distribution* by using equation 2.49 on page 53 and the effective f_d was computed accordingly using equations 2.35, 2.36, 2.37 and 2.34 on page 39. Prior to applying the correction factors, the effective f_d values of the *BARE8* and *BARE15* arrangements were (0.799 ± 0.004) and (0.88 ± 0.01), while the efficiencies of two assays are listed in table 4.4 on page 127, respectively. By way of illustration, these estimates were reached by determining i) the detection efficiency via the ratio of the total number of neutron events detected to the source neutron emission rate (the latter given in section 3) and ii), the foreground distribution doublet and triplet rates in table 5.3, corrected for the relative dead-time. The latter conjected that, by definition, for doublets a detector is busy with a neutron count and for triplets two detectors are busy with a neutron count each; the influence of the γ-ray field was incorporated by apportioning two busy detectors to photon events for each case to reflect the higher photon field intensity but reduced interaction probability by which photons might be detected. Values for the first, ν_{s1}, and second, ν_{s2}, factorial moments of the ^{252}Cf spontaneous fission distribution of 3.76 and 11.96 were used, respectively. Finally, the doubles count rate was then computed by determining the second factorial moment of the distribution. An excel file is included in the multimedia package to demonstrate the calculation flow.

First, *photon-breakthrough* was accounted for by considering a *photon-breakthrough* of 4% of γ-ray events with a standard deviation of 2% based on 11 detectors selected from those constituting the arrays, see table 4.6 on page 135. Since γ rays are not present in the simulations, and hence there is no *photon-breakthrough*, no data are included for these. The correction made to the singlet bin ($F_n(1)$) results in an increase in uncertainty from $\pm 0.03\%$ to $\pm 0.27\%$ for the *BARE8* arrangement and from $\pm 0.04\%$ to $\pm 0.21\%$ for the *BARE15* arrangement. At this stage, with the removal of the misidentified γ-ray contribution, the f_d for the two setups were 1.19 ± 0.01 and 1.20 ± 0.01, respectively. These results imply that the assay is registering more neutrons than it should from the ^{252}Cf source which is consistent with a contribution due to *crosstalk*, which in turn increases the multiplet order, as discussed earlier. These values are consistent with the results of the simulation, as both sets of data contain *crosstalk* neutrons. Also, the neutron singlet count is increased by (18 to 24)% due to *photon-breakthrough* which impacts the analysis, as illustrated by the change in f_d.

Finally, the *crosstalk-factor* was applied to correct the distribution for this effect, which results in a f_d of 1.06 ± 0.01 and 1.06 ± 0.01 for *BARE8* and *BARE15* cases. This suggests

[6]Dead-time was assumed to be such that for every detected neutron, *BARE8* and *BARE15* assay had two and three additional detectors that were busy processing γ-ray events, respectively. This arises from the 346-ns dead-time of the MFA, during which time it is insensitive to further incident radiation.

that, subsequent to the correction for *photon-breakthrough* and *crosstalk*, almost (95-99)% of all detected neutrons from spontaneous fission have been detected correctly in the assay. This is also confirmed by the simulations. The results demonstrate that even a small contribution due to *crosstalk* (<1%) can increase the *doubles gate-fraction* f_d significantly, i.e. by 20%, while the inflation seen in doublets and triplets is estimated to be at 8-12% and (30 to 40)%, respectively.

Upon application of the correction models, the experimental setup was found to have Totals efficiencies for the *BARE8* and *BARE15* setups of (1.98±0.03)% and (2.52±0.03)%, respectively, Geant4 recorded $(2.87 \pm 0.03)\%$ and $(2.77 \pm 0.03)\%$ for the two arrangements. This difference in the computed values of the efficiencies is perhaps due to the Geant4 simulations not taking account of the secondary γ-ray source from decay products; hence the Geant4 depiction of the detectors had a lower dead-time, despite an approximate dead-time analysis of the experimental data having been made. Compared to the post-correction efficiencies listed in table 4.4, the newly computed values are lower since erroneous counts have been removed from the distributions.

5.6.3 Alternative techniques and prior-art

The adverse effect of *photon-breakthrough* and *crosstalk* has been reported as early as the 1980s when the earliest fast-neutron multiplicity counters based on analogue pulse processing technique were implemented [19]. This highlighted the particular significance of correction models for these phenomena for the case of materials exhibiting high γ-ray and (α, n) yields (relative to fission neutrons) in reducing significant discrepancies in mass assessments that might arise otherwise. Based on the results presented in this thesis, the effect of *photon-breakthrough* and *crosstalk* on the doubles *gate-fraction* when using ^{252}Cf has been determined to be approximately 50% and 20%, respectively. Similarly, *photon-breakthrough* can lead to an erroneous increase of 20% in neutron counts whilst *crosstalk* has been found to be approximately 0.3%, 20% and 50% for the first-, second- and third-order coincidences (singlet, doublet and triplet counts), respectively, when using the ^{252}Cf source.

Whilst it is possible to configure the PSD algorithm to have very high detector cut-offs, in order to operate the detector array in a region where these phenomena are not a hindrance, such an approach is not ideal as it comes at the expense of reduced neutron counts, i.e. reduced neutron efficiency. This will reduce both *photon-breakthrough* and *crosstalk*. Perhaps others simply discard coincident events in adjacent detectors (usually by the acquisition firmware or in post-processing) on the basis that *crosstalk* is most likely to occur between neighbouring detectors [156, 203]; this is indeed implemented in some commercially-available systems by default. However, this is less than ideal as it might lead to an over-correction given the bimodal spatial correlation of particles emitted from fission events, discussed earlier in section 5.4, where a real correlation

in neighbouring detectors might be plausible.

Several attempts have been made to address these issues, both experimentally [204, 205, 206] and analytically [197, 207]. The characteristics of neutron *crosstalk* have been examined before [208] for ^{252}Cf, however the results were akin to the cosine distribution consistent with the angular distribution of the source rather than the isotropic distribution anticipated for *crosstalk*. The analytical methods suggested by Li *et al.* [207] and Shin *et al.* [197] address this problem in a complicated manner using a reduced factorial distribution from a shift register based algorithm.

This thesis has proposed and validated a new approach to derive the correlated event composition for the assessment of fissile substances based on the proposed cluster-size based coincidence algorithm. Methods by which the effects of *crosstalk* and photon breakthrough might be corrected have been discussed, based on an algorithm that relates the *crosstalk* of coincidence event data. In future, these proposed correction models, used with carefully constructed sensitivity coefficients, may enable bias in results due to *crosstalk* and *photon-breakthrough* to be minimized, as shown in this paper using the doubles *gate-fraction*. Moreover, compared to the alternative analytical *crosstalk* models based on the *reduced factorial moment distribution* [197, 207], the proposed method is straightforward and easy to compute. Due to the differing analytical process, no direct comparison between the three methods was possible. Unfortunately, as these models were developed after the AFNCC experiments were conducted at the *Oak Ridge National Laboratory (ORNL)*, the required data, namely the γ-ray *coincidence distributions*, needed to apply the models to the UOX data in section 4.5.2 on page 129 were not collected and so no analysis with these data was possible.

Chapter 6

Recommendations for future works

In this chapter recommendations for further work are made based on the results in this thesis. The chapter is divided into two sections, the first section concentrates on near-term recommendations specific to further research prospects that may be developed based on the outcomes. The second section of this chapter addresses some of the more general opportunities not only the field of nuclear safeguards, but also for a variety of applications that may benefit from some of the advances reported in this thesis.

6.1 Short term

The results presented in this thesis show that such fast scintillation detector based coincidence assays can complement traditional thermal neutron based assays. However, further research is needed to better understand the best approach towards realizing this goal.

The instrumentation developed in this research requires the use of two *field-programable gate array (FPGA)* based systems, one hosting the *pulse shape discrimination (PSD)* algorithm, the *Mixed-Field Analysers (MFA)*, and the other hosting the multiplicity algorithm. This current implementation can be complex due to trailing signal cables going from the MFA to the DE1 board. This complexity can be reduced by implementing the multiplicity algorithm directly into the PSD-based FPGA. This will require redesigning the *VHSIC Hardware Description Language (VHDL)* source code of the MFA to include the additional functionality, improving the commu-

nication protocol to transfer data from the MFA to the host computer. Attempts have been made to this end, and the coincidence counter (i.e. the part of the algorithm which computes the coincidence distributions) has already been implemented, along with the necessary communication protocols and *graphical user interface (GUI)*. However, the FPGA driving the MFA requires updating to be able to implement real-time determination of interval-time distributions. These can be exploited to construct the Rossi-α, angular and spectrum distributions using a single self-contained unit. Moreover, it may be desirable to have the functionality of the *crosstalk*, *photon-breakthrough* and possible pile-up correction model implemented as well.

The methodology used to determine the angular distributions presented in section 5.4 was not real-time, hence this could also be automated. Finally, the experiments that were conducted in this research utilised a 2-dimensional array; it is prudent to repeat the measurements with a 3-dimensional array and construct a 4π angular distribution. Such an excercise would help improve the underlining understanding of the fission process and further validate the fission models.

Obtaining the γ-ray spectrum using scatter based detectors, like liquid scintillators, is a very complex process, as only a portion of the incident energy of the incoming particle is deposited via Compton scattering, i.e. they do not undergo photoelectric absorption as they are low-Z material. There are various spectrum unfolding methods that can be exploited to solve the problem, however these are not real-time based solutions. It may be possible to determine the γ-ray spectrum using correlated particles, such as from ^{60}Co, to construct a spectrum in real time. It is recommended that research be carried out to investigate towards a proof-of-concept. Although Germanium based detectors can already achieve this without the added complexities, being able to determine photon spectrum using scintillation would be a nice development for mixed-field environments.

Additionally, when such systems are used for research purposes, it is recommended that any real-time instrumentation must be accompanied by the option of obtaining and storing raw detector pulses, in limited scope at the very least, as it allows researchers to investigate any anomalous results that may arise, especially when investigating *photon-breakthrough*. Although this would dramatically increase the engineering complexities in developing such a device, thereby making it an impractical solution for commercial deployment, both in terms of physical dimensions and cost, such a feature will reduce the troubleshooting time when developing new techniques or investigating unexpected measurements, and also provide further assurance when affirming conclusions. Further to this, the availability of raw data from large-scale physics experiments will ensure the possibility of retroactively analysing with new and improved algorithm to generate information which may potentially give rise to rapid development of such techniques without the need to conduct new experiments to enable proof-of-concept.

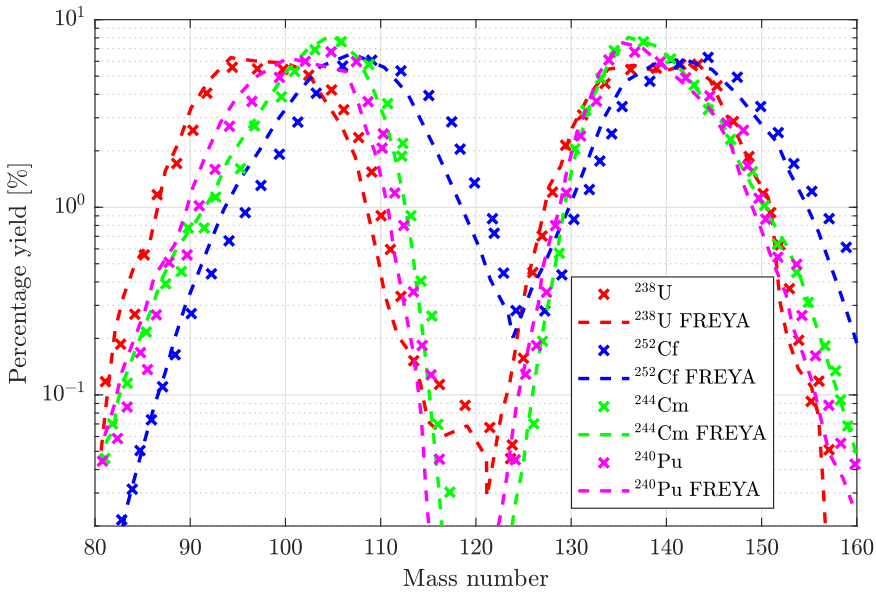

Figure 6.1 | Distribution of fission fragments from induced fission. The percentage yield of fission fragments from the spontaneous fission of ^{238}U, ^{240}Pu, ^{244}Cm and ^{252}Cf. The data points were obtained from reference [184] and therein.

Finally, the demonstrations provided in this thesis are made using single homogeneous sources. Further study should be undertaken to investigate how the assay would react to non-homogeneous samples (e.g. when a source is hidden in other materials, sample containing multiple sources, etc.).

6.2 Long term

Fast digitization of correlated neutrons is a field that is currently in its infancy and therefore has may different opportunities for applications. These include the neutron spectrometry of mixed-field environments and the temporal and spatial analysis of scattered radiations for imaging applications. Real-time instrumentation has significant advantages, including flexibility and the elimination of the need to post-process digitally-recorded signals. The prospect of implementing clever algorithm is vast and opens up opportunities to apply fast neutron detectors in applications that were previously impossible. Some of the opportunities are mentioned below.

1. *Nuclear material characterization:* The determination of higher-order coincidence is imperative to improve the understanding of the constituents of a sample of nuclear fuel with unknown composition. Figure 4.9 on page 110 shows the subtle deviations in the multiplicity number distribution which could give vital information for characterization [209]. Additionally, the fission fragment mass distribution is also indicative of different fissile materials, as illustrated in Figure 6.1, leading to an isotope-dependent angular distribution.

Using a spatial analysis, it should be possible in principle to characterize samples. A similar method has been recently attempted [189].

2. *Nuclear decommissioning:* The analysis of correlated events from irradiated waste materials and structures can lead to better classification of waste materials leading to monetary savings from not misclassifying low waste materials in the high waste stream.

3. *Nuclear imaging:* There are already several applications which use uncorrelated neutron counts to produce 2-dimensional and 3-dimensional tomographic analysis. These analyses can be further improved by taking advantage of temporal and spatial analysis to better image correlated sources. Similar kind of research has already been undertaken are are in preliminary stages of assessment [210].

Chapter 7

Conclusions

The challenges preventing the large-scale implementation of fast organic scintillation detectors towards measurement of correlated radiation are being overcome with time. The increasing availability of cheap, fast digital processors has opened new possibilities for the use of real-time complex, yet elegant, analytical techniques that enable organic scintillation detectors to characterise mixed-fields used for *passive fast neutron coincidence counting (PFNCC)* and *active fast neutron coincidence counting (AFNCC)* in the field of nuclear safeguards. This thesis reports on the development and implementation of a new, real-time algorithm, using organic liquid scintillation based fast neutron detectors, to investigate some of the basic properties, in the time and space domains, of the correlated radiation field emerging from spontaneous and induced fission. Using this technique, it was possible to observe some of the poorly understood aspects of the correlated and non-correlated radiation sources to further the knowledge in this field. The experiments conducted and reported here undoubtedly provide evidence that there is vast scope for the development of fast neutron assays using the advantages afforded by organic liquid scintillation detectors. In addition to the development of a simple, and inherently, fast technique for the analysis of correlated neutron and γ-ray events from fissile materials, the processing of these events in real-time has provided a simple and robust platform to acquire radiation field data quickly and easily without the need to post-process an unreasonably large unlimited number of events. The scope in this context is bound only by the ingenuity of the software engineer.

The development and implementation of a digital algorithm for the analysis of temporal and spatial correlation of the *non-Poissonian* radiation field from spontaneous and induced fission was detailed in section 3.2 on page 65. The versatility of this technique allows it to perform both interval-time and cluster-size based coincidence counting analysis using the same instrumentation. This technique was demonstratively verified using laboratory experiments and the merits of the

instrumentation were identified as follows:

1. The flexibility of the cluster-size based algorithm allows easy implementation of correction models for various phenomena.
2. The cluster-size based coincidence distribution may easily be converted to traditionally-used *reduced factorial moment distributions* for analytical purpose using the previously established methodologies.
3. A single device, with a very small footprint, can carry out all of the analysis making the system fairly portable. However, further simplification could be made if the algorithm is to be implemented in the MFAs directly, at the expense of limiting the number of input channels to four.
4. It does not require post-processing of multi-million detector responses in a tedious fashion but provides effective instant results with limited complexity.
5. It has the potential to be operated by operators with minimal skills.

The proposed technique was used to successfully investigate and compare the digital measurement of *interval-time distributions* from ^{252}Cf sources using two different kind of arrangements, i.e. the reflective and bare arrangements. Subsequently, based on this analysis, the standard single exponent-based Rossi-α model was expanded upon to quantify the impact of neutron scattering on such analysis. Results presented in section 4.2 demonstrate that the prompt neutron and γ-ray responses are approximately 25 ns and 20 ns wide, respectively. However, based on Geant4 simulations, the γ-ray responses would have a much narrower *gate-width* if the *analogue-to-digital converter (ADC)* system could sample at a high rate. While it is possible to use an oversampling technique to interpolate between ADC samples to achieve finer measurements in real-time, it is probably more elegant to use a device which is natively able to sample at a higher frequency. A device capable of providing TTL signals at 1 GHz could achieve this; however, such a device was not available during the course of the project.

Using the instrumentation techniques described, experiments were performed to quantify the energy spectra of neutron fields from a ^{252}Cf source in various arrangements, the results of which were presented in section 4.3. Unfortunately, the relatively high detector cut-off energy of organic scintillation detectors prevented the full characterization of the fission neutron spectrum. Nonetheless, such techniques could be used for analysing spectra involving high energy neutrons, such as those from fusion reactions.

Section 4.4 describes the determination and investigation of the multi-order neutron angular correlation between the neutrons which are emitted during the spontaneous fission of ^{252}Cf;

the first of this kind of analysis. Although the results met theoretical expectation, biases were observed possibly due to neutron scattering in the environment and in-between detectors, i.e. *crosstalk*. The former reduces the degree of isotropy of the angular distribution, whereas the latter is responsible for an increased isotropy at shallow angles. Additionally, this thesis proposes a 3-dimensional neutron angular distribution which not only demonstrates the correlation between the first two time-correlated neutrons, but also the third correlated neutron. Whilst this is a difficult measurement to make, with significantly lower detectable counts per second relative to the two-neutron assays, such distributions give a unique perspective about the angular correlation between the emitted fission particles.

This thesis further demonstrates the effectiveness of the proposed cluster-size based coincidence algorithm in both PFNCC and AFNCC scenarios using ^{252}Cf and *uranium oxide (UOX)* material fuel of different ^{235}U enrichment, as presented in section 4.5. The results show that correlated sources register higher-orders of coincidence and that the accidental events are negligible in comparison. Therefore, it reduces the duration over which the measurement has to be made, or conversely improves the inherent statistics of the data. This distribution can be analytically converted to the traditionally-used *reduced factorial moment distributions* in order to take advantage of the well-established mathematical model for analysis.

Historically, such mathematical analytical methods have been deployed using detector systems based on ^{3}He gas for the detection of time-correlated, thermalised neutrons, which increased the emission-to-detection time of emitted radiation particles (i.e. neutrons) by large margins; thereby, vastly complicating the temporal and spatial analysis of the radiation fields due to increased scattered events. While organic scintillators have been proven in the past to be viable alternatives to overcome these limitation, however, not only were the previous implementations not conducted in real-time, the analysis done with the measurements were based on models developed for thermal neutron assays, thereby not accounting for the differences between the detection physics of the two detector technologies. Two such differences in the detection techniques arise from the facts that organic scintillators are scatter-based detectors and are sensitive to both neutrons and γ rays. Hence, they are affected by detector *crosstalk* and *photon-breakthrough*, thereby leading to erroneous measurements. This thesis proposes two semi-empirical models to correct the measurements with the aim of removing the two biases. Based on the analysis of the various coincidence distributions, from experiment and simulation, as shown in section 5.6, the two geometry-specific models were demonstrated to be effective. These models are easy to maintain compared alternative approaches and take advantage flexible properties of a cluster-size based distribution.

The results obtained during the course of this research have led to four conference papers,

including two oral presentations at the IEEE Nuclear Science Symposium and the Symposium on Radiation Measurements and Applications, respectively. Additionally, two journal paper has been published related to the *crosstalk* and *photon-breakthrough* analysis from section 5.6.1 and the active measurements presented in section 4.5. A further two papers are in preparation based on the results from sections 4.1 and 4.2.

In summary this thesis has (i) developed and implemented a versatile digital algorithm for the real-time analysis of temporal and spatial correlated in a *non-Poissonian* radiation field from spontaneous and induced fission, (ii) demonstrated and investigated the *interval-time distribution* of the temporally correlated neutron and γ-ray fields from spontaneous fission, (iii) expanded the standard Rossi-α model for the quantification of neutron scatter in the environment on the interval time distribution, (iv) determined the energy spectrum of a neutron field, (v) provided first evidence of spatial correlation between higher-order coincident events from spontaneous fission of ^{252}Cf, (vi) demonstrated PFNCC and AFNCC techniques using a cluster-based algorithm and (vii) proposed and validated two semi-empirical correction models for *photon-breakthrough* and *crosstalk*. The instrumentation and techniques reported in this research, along with the associated findings, will help direct further interest towards advancements needed to realize the reliable application of organic scintillation detectors with pulse shape discriminators in the field of nuclear safeguards and non-proliferation verification.

Bibliography

[1] "Overview: Bulletin of the Atomic Scientists." `https://thebulletin.org/overview`, 2017. [Online; accessed 28-Dec-2017].

[2] D. D. Eisenhower, "Address Before the General Assembly of the United Nations on Peaceful Uses of Atomic Energy," in *United Nations*, December 8, 1953.

[3] $112^{\mathbf{th}}$ Congress; $2^{\mathbf{nd}}$ Session, "Nuclear Regulatory Legislation," Tech. Rep. NUGEG-0980 vol. 1, No. 10, United States Nuclear Regulatory Commission, September 2013.

[4] C. Eckerberg, "Plan 2016 - Costs from and including 2018 for the radioactive residual products from nuclear power," Tech. Rep. SKB TR-17-02, Swedish Nuclear Fuel and Waste Management Company, April 2017.

[5] H. A. Smith, "Chapter 7: The Measurement of Uranium Enrichment," in *Passive Nondestructive Assay of Nuclear Material* (D. Reilly, N. Ensslin, and H. A. Smith, Jr., eds.), Washington, DC 20555: Los Alamos National Laboratory, LA-UR-90-732, 1991.

[6] T. E. Sampson, "Chapter 8: Plutonium Isotopic Composition by Gamma-Ray Spectroscopy," in *Passive Nondestructive Assay of Nuclear Material* (D. Reilly, N. Ensslin, and H. A. Smith, Jr., eds.), Washington, DC 20555: Los Alamos National Laboratory, LA-UR-90-732, 1991.

[7] P. M. Rinard and G. E. Bosler, "Safeguarding LWR Spent Fuel with the Fork Detector," Tech. Rep. LA-11096-MS, Los Alamos National Laboratory, United States, 1988.

[8] G. Eccleston, H. O. Menlove, M. C. B. M. Abhold, and J. Pecos, "The underwater coincidence counter UWCC for plutonium measurements in mixed-oxide fuels," in *Proccesdings of the 39th Annual Meeting on Nuclear Materials Management*, July 26-30, 1998.

[9] E. Attas, J. Chen, and G. Young, "A cherenkov viewing device for used-fuel verification," *Nuclear Instruments and Methods in Physics Research Section A: Accelerators, Spectrometers, Detectors and Associated Equipment*, vol. 299, no. 1-3, pp. 88 – 93, 1990.

[10] J. L. Parker, "Chapter 6: Attenuation Correction Procedure," in *Passive Nondestructive Assay of Nuclear Material* (D. Reilly, N. Ensslin, and H. A. Smith, Jr., eds.), Washington, DC 20555: Los Alamos National Laboratory, LA-UR-90-732, 1991.

[11] J. D. Orndoff, "Prompt neutron periods of metal critical assemblies," *Nuclear Science and Engineering*, vol. 2, no. 4, pp. 450–460, 1957.

[12] F. de Hoffmann, "Intensity Fluctuations of a Neutron Chain Reaction," Tech. Rep. MDDC-382 (LADC-256), Los Alamos National Laboratory, United States, 1946.

[13] R. E. Uhrig, *Random Noise Techniques in Nuclear Reactor System.* Ronald Press, 1970.

[14] R. Feynman, F. D. Hoffmann, and R. Serber, "Dispersion of the neutron emission in U-235 fission," *Journal of Nuclear Energy*, vol. 3, no. 1, pp. 64 – IN10, 1956.

[15] N. Ensslin, W. C. Harker, M. S. Krick, D. G. Langner, M. M. Pickrell, and J. E. Stewart, "Application Guide to Neutron Multiplicity Counting," Tech. Rep. LA-13422-M, Los Alamos National Laboratory, United States, November 1998.

[16] A. C. Kaplan, V. Henzl, H. O. Menlove, M. T. Swinhoe, A. P. Belian, M. Flaska, and S. A. Pozzi, "Determination of total plutonium content in spent nuclear fuel assemblies with the differential die-away self-interrogation instrument," *Nuclear Instruments and Methods in Physics Research Section A: Accelerators, Spectrometers, Detectors and Associated Equipment*, vol. 764, pp. 347 – 351, 2014.

[17] A. J. Keller, "An Increasingly Rare Isotope," *Stanford University*, 2011.

[18] R. T. Kouzes, "The ^{3}He Supply Problem," Tech. Rep. PNNL-18388, Pacific Northwest National Laboratory, United States, 2009.

[19] J. R. Wachter, E. L. Adams, and N. Ensslin, "Prototype fast neutron counter for the assay of impure plutonium," in *INMM/ANS Conference on the Safeguards Facility Process Interface*, Nov 1987.

[20] M. D. Aspinall, *Real time digital assay of mixed radiation fields.* PhD thesis, Lancaster University, Lancaster, United Kingdom, 2008.

[21] M. Joyce, M. Aspinall, F. Cave, and A. Lavietes, "Real-Time, Digital Pulse-Shape Discrimination in Non-Hazardous Fast Liquid Scintillation Detectors: Prospects for Safety and Security," *Nuclear Science, IEEE Transactions on*, vol. 59, pp. 1245–1251, Aug 2012.

[22] CAEN, "How to make coincidences with CAEN Digitizers," Tech. Rep. GD2827, CAEN S.pA., Italy, 2017.

[23] J. S. Beaumont, T. H. Lee, M. Mayorov, C. Tintori, F. Rogo, B. Angelucci, and M. Corbo, "A fast-neutron coincidence collar using liquid scintillators for fresh fuel verification," *Journal of Radioanalytical and Nuclear Chemistry*, vol. 314, pp. 803–812, Nov 2017.

[24] J. Mihalczo, J. Mullens, J. Mattingly, and T. Valentine, "Physical description of nuclear materials identification system (NMIS) signatures," *Nuclear Instruments and Methods in Physics Research Section A: Accelerators, Spectrometers, Detectors and Associated Equipment*, vol. 450, no. 2, pp. 531 – 555, 2000.

[25] L. F. Nakae, G. F. Chapline, A. M. Glen, *et al.*, "The use of fast neutron detection for materials accountability," Tech. Rep. LLNL-CONF-64380, Lawrence Livermore National Laboratory, United States, September 2013.

[26] D. L. Chichester *et al.*, "MPACT Fast Neutron Multiplicity System Design Concepts," Tech. Rep. INL/EXT-12-27619, Los Alamos National Laboratory, United States, 2012.

[27] M. Jandel, G. Rusev, E. Bond, T. Bredeweg, M. Chadwick, A. Couture, *et al.*, "Prompt Fission Gamma-ray Studies at DANCE," *Physics Procedia*, vol. 59, pp. 101 – 106, 2014. GAMMA-2 Scientific Workshop on the Emission of Prompt Gamma-Rays in Fission and Related Topics.

[28] R. Haight, C. Wu, H. Lee, T. Taddeucci, B. Perdue, J. O'Donnell, *et al.*, "The lanl/llnl prompt fission neutron spectrum program at lansce and approach to uncertainties," *Nuclear Data Sheets*, vol. 123, pp. 130 – 134, 2015. Special Issue on International Workshop on Nuclear Data Covariances April 28 - May 1, 2014, Santa Fe, New Mexico, USA http://t2.lanl.gov/cw2014.

[29] Gomez, J.A., Devlin, M., Haight, R.C., O'Donnell, J.M., Lee, H.Y., Mosby, S.M., Taddeucci, T.N., *et al.*, "The 235U prompt fission neutron spectrum measured by the Chi-Nu project at LANSCE," *EPJ Web Conf.*, vol. 146, p. 04040, 2017.

[30] M. J. Marcath, T. H. Shin, S. D. Clarke, P. Peerani, and S. A. Pozzi, "Neutron angular distribution in plutonium-240 spontaneous fission," *Nuclear Instruments and Methods in Physics Research Section A: Accelerators, Spectrometers, Detectors and Associated Equipment*, vol. 830, pp. 163 – 169, 2016.

[31] M. Jandel, B. Baramsai, T. Bredeweg, A. Couture, A. Favalli, A. Hayes, *et al.*, "Correlated fission data measurements with dance and neuance," *Nuclear Instruments and Methods in Physics Research Section A: Accelerators, Spectrometers, Detectors and Associated Equipment*, vol. 882, pp. 105 – 113, 2018.

[32] B. D'Mellow, M. Aspinall, R. Mackin, M. Joyce, and A. Peyton, "Digital discrimination of neutrons and γ-rays in liquid scintillators using pulse gradient analysis," *Nuclear Instruments and Methods in Physics Research Section A: Accelerators, Spectrometers, Detectors and Associated Equipment*, vol. 578, no. 1, pp. 191 – 197, 2007.

[33] N. Soppera, M. Bossant, and E. Dupont, "JANIS 4: An Improved Version of the NEA Java-based Nuclear Data Information System," *Nuclear Data Sheets*, vol. 120, no. Supplement C, pp. 294 – 296, 2014.

[34] D. Reilly, "Chapter 1: The Orgin of Gamma Rays," in *Passive Nondestructive Assay of Nuclear Material* (D. Reilly, N. Ensslin, and H. A. Smith, Jr., eds.), Washington, DC 20555: Los Alamos National Laboratory, LA-UR-90-732, 1991.

[35] O. Litaize, D. Regnier, and O. Serot, "Prompt Fission Gamma-ray Spectra and Multiplicities for Various Fissioning Systems," *Physics Procedia*, vol. 59, no. Supplement C, pp. 89 – 94, 2014. GAMMA-2 Scientific Workshop on the Emission of Prompt Gamma-Rays in Fission and Related Topics.

[36] T. Wang, G. Li, *et al.*, "Correlations of neutron multiplicity and γ-ray multiplicity with fragment mass and total kinetic energy in spontaneous fission of ^{252}Cf," *Phys. Rev. C*, vol. 93, p. 014606, Jan 2016.

[37] S. J. Rose, F. Zeiser, J. N. Wilson, *et al.*, "Energy dependence of the prompt γ-ray emission from the (d,p)-induced fission of ^{234}U* and ^{240}Pu*," *Phys. Rev. C*, vol. 96, p. 014601, Jul 2017.

[38] I. Stetcua, P. Talou, and T. Kawano, "Prompt fission neutron and properties as a function of incident neutron energy," in *Proc. 5th International Workshop on Compound-Nuclear Reactions and Related Topics*, CNR*15, 21 June 2016.

[39] G. Nelson and D. Relly, "Chapter 2: Gamma-Ray Interaction with Matter," in *Passive Nondestructive Assay of Nuclear Material* (D. Reilly, N. Ensslin, and H. A. Smith, Jr., eds.), Washington, DC 20555: Los Alamos National Laboratory, LA-UR-90-732, 1991.

[40] G. Choppin, J.-O. Liljenzin, J. Rydberg, and C. Ekberg, "Chapter 8 - Detection and Measurement Techniques," in *Radiochemistry and Nuclear Chemistry*, pp. 192 – 238, Woburn: Butterworth-Heinemann, third ed., 2002.

[41] R. D. Evans, "Chapter 25: Attenuation and Absorption of Electromagnetic Radiation," in *The atomic nucleus*, McGraw Hill Book Company, 1955.

[42] N. Ensslin and D. Reilly, "Chapter 2: Gamma Rays Interactions with Matter," in *Passive Nondestructive Assay of Nuclear Material* (D. Reilly, N. Ensslin, and H. A. Smith, Jr., eds.), Washington, DC 20555: Los Alamos National Laboratory, LA-UR-90-732, 1991.

[43] J. R. Lamarsh, *Introduction to Nuclear Reactor Theory.* LaGrange Park, USA: American Nuclear Society, Inc., 2002.

[44] N. Ensslin, "Chapter 11: The Origin of Neutron Radiation," in *Passive Nondestructive Assay of Nuclear Material* (D. Reilly, N. Ensslin, and H. A. Smith, Jr., eds.), Washington, DC 20555: Los Alamos National Laboratory, LA-UR-90-732, 1991.

[45] N. Bohr and J. A. Wheeler, "The mechanism of nuclear fission," *Phys. Rev.*, vol. 56, pp. 426–450, Sep 1939.

[46] R. D. Evans, "Chapter 11: Model of Nuclie," in *The atomic nucleus*, McGraw Hill Book Company, 1955.

[47] G. Choppin, J.-O. Liljenzin, J. Rydberg, and C. Ekberg, "Chapter 11 - Nuclear Structure," in *Radiochemistry and Nuclear Chemistry*, pp. 299 – 333, Woburn: Butterworth-Heinemann, third ed., 2002.

[48] P. Talou, R. Vogt, J. Randrup, M. E. Rising, S. A. Pozzi, *et al.*, "Correlated prompt fission data in transport simulations," *The European Physical Journal A*, vol. 54, p. 9, Jan 2018.

[49] H. Navirian, "Measurement of the Properties of Liquid Scintillator Neutron Detectors at MAX-lab," Master's thesis, Lund University, 2005.

[50] B. C. Diven, H. C. Martin, R. F. Taschek, and J. Terrell, "Multiplicities of fission neutrons," *Phys. Rev.*, vol. 101, pp. 1012–1015, Feb 1956.

[51] I. Stetcu, P. Talou, T. Kawano, and M. Jandel, "Properties of prompt-fission γ rays," *Phys. Rev. C*, vol. 90, p. 024617, Aug 2014.

[52] Stetcu, Ionel, Talou, Patrick, and Kawano, Toshihiko, "Prompt fission neutron and energy," in *EPJ Web Conf.*, vol. 146, p. 04026, 2017.

[53] J. Verbeke, J. Randrup, and R. Vogt, "Fission Reaction Event Yield Algorithm, FREYA - For event-by-event simulation of fission," *Computer Physics Communications*, vol. 191, no. Supplement C, pp. 178 – 202, 2015.

[54] V. Dushin, F.-J. Hambsch, V. Jakovlev, *et al.*, "Facility for neutron multiplicity measurements in fission," *Nuclear Instruments and Methods in Physics Research Section A: Accelerators, Spectrometers, Detectors and Associated Equipment*, vol. 516, no. 2, pp. 539 – 553, 2004.

[55] R. Billnert, F.-J. Hambsch, A. Oberstedt, and S. Oberstedt, "New prompt spectral γ-ray data from the reaction ^{252}Cf(sf) and its implication on present evaluated nuclear data files," *Phys. Rev. C*, vol. 87, p. 024601, Feb 2013.

[56] H. W. Schmitt, J. H. Neiler, and F. J. Walter, "Fragment energy correlation measurements for ^{252}Cf spontaneous fission and ^{235}U thermal-neutron fission," *Phys. Rev.*, vol. 141, pp. 1146–1160, Jan 1966.

[57] J. Randrup and R. Vogt, "Refined treatment of angular momentum in the event-by-event fission model FREYA," *Phys. Rev. C*, vol. 89, p. 044601, Apr 2014.

[58] K. Skarsvåg, "Differential angular distribution of prompt gamma rays from spontaneous fission of ^{252}Cf," *Phys. Rev. C*, vol. 22, pp. 638–650, Aug 1980.

[59] Verbeke, Jérŏme M., Petit, Odile, Chebboubi, Abdelhazize, and Litaize, Olivier, "Correlated Production and Analog Transport of Fission Neutrons and Photons using Fission Models FREYA, FIFRELIN and the Monte Carlo Code TRIPOLI-4®.," *EPJ Web Conf.*, vol. 170, p. 01019, 2018.

[60] W. Hauser and H. Feshbach, "The inelastic scattering of neutrons," *Phys. Rev.*, vol. 87, pp. 366–373, Jul 1952.

[61] P. Talou, T. Kawano, and I. Stetc, "CGMF Documentation," Tech. Rep. LA-UR-99-4927, Los Alamos National Laboratory, United States, 2015.

[62] T. Kawano, P. Talou, M. B. Chadwick, and T. Watanabe, "Monte carlo simulation for particle and γ-ray emissions in statistical hauser-feshbach model," *Journal of Nuclear Science and Technology*, vol. 47, pp. 462–469, 2010.

[63] O. Litaize, O. Serot, and L. Berge, "Fission modelling with FIFRELIN," *The European Physical Journal A*, vol. 51, p. 177, Dec 2015.

[64] J. Verbeke, C. Hagmann, and D. Wright, "Simulation of Neutron and Gamma Ray Emission from Fission and Photofission - LLNL Fission Library 2.0.2.," Tech. Rep. UCRL-AR-228518-REV-1, Lawrence Livermore National Laboratory, United States, October 2016.

[65] J. Terrell, "Distributions of Fission Neutron Numbers," *Phys. Rev.*, vol. 108, pp. 783–789, Nov 1957.

[66] T. E. Valentine, "Evaluation of prompt fission gamma rays for use in simulating nuclear safeguard measurements," *Annals of Nuclear Energy*, vol. 28, no. 3, pp. 191 – 201, 2001.

[67] D. Cullen, "Sampling ENDL Watt Fission Spectra," Tech. Rep. UCRL-TR-203351, Lawrence Livermore National Laboratory, United States, 2004.

[68] H. A. Smith, Jr. and M. Lucas, "Chapter 3: Gamma-Ray Detectors," in *Passive Nondestructive Assay of Nuclear Material* (D. Reilly, N. Ensslin, and H. A. Smith, Jr., eds.), Washington, DC 20555: Los Alamos National Laboratory, LA-UR-90-732, 1991.

[69] G. F. Knoll, "Chapter 6 - Proportional Counters," in *Radiation Detection and Measurement*, New York, NY: John Wiley & Sons, Ltd, third ed., 1999.

[70] G. F. Knoll, "Chapter 7 - Gieger-Mueller Counters," in *Radiation Detection and Measurement*, New York, NY: John Wiley & Sons, Ltd, third ed., 1999.

[71] G. F. Knoll, "Chapter 11 - Semiconductor Diode Detectors," in *Radiation Detection and Measurement*, New York, NY: John Wiley & Sons, Ltd, third ed., 1999.

[72] G. F. Knoll, "Chapter 8: Scintillation Detector Principles," in *Radiation Detection and Measurement*, John Wiley & Sons, Inc., 1999.

[73] J. E. Stewart, "Chapter 13: Neutron Detectors," in *Passive Nondestructive Assay of Nuclear Material* (D. Reilly, N. Ensslin, and H. A. Smith, Jr., eds.), Washington, DC 20555: Los Alamos National Laboratory, LA-UR-90-732, 1991.

[74] M. Chadwick *et al.*, "ENDF/B-VII.1 Nuclear Data for Science and Technology: Cross Sections, Covariances, Fission Product Yields and Decay Data," *Nuclear Data Sheets*, vol. 112, no. 12, pp. 2887 – 2996, 2011. Special Issue on ENDF/B-VII.1 Library.

[75] A. Syntfeld, M. Moszynski, R. Arlt, M. Balcerzyk, *et al.*, "^{6}LiI(Eu) in neutron and γ-ray spectrometry-a highly sensitive thermal neutron detector," *IEEE Transactions on Nuclear Science*, vol. 52, pp. 3151–3156, Dec 2005.

[76] S. Guizhen, W. Yingmin, W. Xiufen, *et al.*, "The preparation and properties of cerium-activated lithium glass scintillators," *Journal of Non-Crystalline Solids*, vol. 80, no. 1, pp. 594 – 599, 1986.

[77] J. Iwanowska-Hanke, *The comparative studies of neutron detectors in the crisis of ^{3}He supply.* PhD thesis, National Centre for Nuclear Research, Poland, 2015.

[78] J. Birks, "Chapte 12 - Alkali Halide Crystal Scintillator and their Applications," in *The Theory and Practice of Scintillation Counting* (J. Birks, ed.), International Series of Monographs in Electronics and Instrumentation, pp. 470 – 540, Pergamon, 1964.

[79] A. Yamazaki, K. Watanabe, A. Uritani, *et al.*, "Neutron-gamma discrimination based on pulse shape discrimination in a Ce:LiCaAlF6 scintillator," *Nuclear Instruments and Methods in Physics Research Section A: Accelerators, Spectrometers, Detectors and Associated Equipment*, vol. 652, no. 1, pp. 435 – 438, 2011.

[80] L. Viererbl, V. Klupak, M. Vins, M. Koleska, J. Soltes, A. Yoshikawa, and M. Nikl, "LiCaAlF6 scintillators in neutron and gamma radiation fields," *International Journal of Modern Physics: Conference Series*, vol. 44, p. 1660234, 2016.

[81] M. Smith, T. Achtzehn, H. Andrews, E. Clifford, P. Forget, J. Glodo, R. Hawrami, H. Ing, P. O'Dougherty, K. Shah, U. Shirwadkar, L. Soundara-Pandian, and J. Tower, "Fast neutron measurements using cs2liycl6:ce (clyc) scintillator," *Nuclear Instruments and Methods in Physics Research Section A: Accelerators, Spectrometers, Detectors and Associated Equipment*, vol. 784, pp. 162 – 167, 2015. Symposium on Radiation Measurements and Applications 2014 (SORMA XV).

[82] N. Ensslin, "Chapter 16: Principles of Neutron Coincidence Counting," in *Passive Non-destructive Assay of Nuclear Material* (D. Reilly, N. Ensslin, and H. A. Smith, Jr., eds.), Washington, DC 20555: Los Alamos National Laboratory, LA-UR-90-732, 1991.

[83] I. Pázsit and L. Pál, "Chapter 11: Theory of Multiplicity in Nuclear Safeguards," in *Neutron Fluctuations* (I. Pázsit and L. PáL, eds.), pp. 294 – 311, Amsterdam: Elsevier, 2008.

[84] N. Ensslin, M. Evans, H. Menlove, and J. Swansen, "Neutron coincidence counters for plutonium measurements," *Nuclear Materials Management*, vol. 7, pp. 43–65, 1978.

[85] J. E. Stewart, S. C. Bourret, and A. Gorobets, "New Shift-Register electronics for improved precision of neutron coincidence and multiplicity assay of plutonium and uranium mass," Tech. Rep. LA-UR-99-4927, Los Alamos National Laboratory, United States, 1999.

[86] K. Bohnel, "The Effect of Multiplication on the Quantitative Determination of Spontaneously Fissioning Isotopes by Neutron Correlation Analysis," *Nuclear Science and Engineering*, vol. 90, no. 1, pp. 75–82, 1985.

[87] J. B. Birks, D. W. Fry, L. Costrell, and K. Kandiah, "Chapter 3: Scintillation Process in Organic Materials - I," in *The theory and practice of scintillation counting*, Elsevier Science, 1967.

[88] F. Brooks, "A scintillation counter with neutron and gamma-ray discriminators," *Nuclear Instruments and Methods*, vol. 4, no. 3, pp. 151 – 163, 1959.

[89] T. Alexander and F. Goulding, "An amplitude-insensitive system that distinguishes pulses of different shapes," *Nuclear Instruments and Methods*, vol. 13, no. Supplement C, pp. 244 – 246, 1961.

[90] C. Sosa, M. Flaska, and S. Pozzi, "Comparison of analog and digital pulse-shape-discrimination systems," *Nuclear Instruments and Methods in Physics Research Section A: Accelerators, Spectrometers, Detectors and Associated Equipment*, vol. 826, no. Supplement C, pp. 72 – 79, 2016.

[91] M. Aspinall, B. D'Mellow, R. Mackin, M. Joyce, *et al.*, "Verification of the digital discrimination of neutrons and γ rays using pulse gradient analysis by digital measurement of time of flight," *Nuclear Instruments and Methods in Physics Research Section A: Accelerators, Spectrometers, Detectors and Associated Equipment*, vol. 583, no. 2, pp. 432 – 438, 2007.

[92] M. Nakhostin and P. Walker, "Application of digital zero-crossing technique for neutron-gamma discrimination in liquid organic scintillation detectors," *Nuclear Instruments and Methods in Physics Research Section A: Accelerators, Spectrometers, Detectors and Associated Equipment*, vol. 621, no. 1, pp. 498 – 501, 2010.

[93] D. Chernikova, K. Axell, I. Pázsit, A. Nordlund, and R. Sarwar, "A direct method for evaluating the concentration of boric acid in a fuel pool using scintillation detectors for joint-multiplicity measurements," *Nuclear Instruments and Methods in Physics Research Section A: Accelerators, Spectrometers, Detectors and Associated Equipment*, vol. 714, no. Supplement C, pp. 90 – 97, 2013.

[94] M. Joyce, K. Gamage, M. Aspinall, F. Cave, and A. Lavietes, "Real-Time, Fast Neutron Coincidence Assay of Plutonium With a 4-Channel Multiplexed Analyzer and Organic Scintillators," *Nuclear Science, IEEE Transactions on*, vol. 61, pp. 1340–1348, June 2014.

[95] S. Pommë, F. Hardeman, P. Robouch, *et al.*, "Neutron activation analysis with k_0-standardisation : general formalism and procedure," Tech. Rep. BLG-700, SCK·CEN, Belgium, 1997.

[96] R. F. Burstall, "FISPIN- A computer code for nuclide inventory calculations," Tech. Rep. ND-R-328, The UK Atomic Energy Authority, 1979.

[97] OECD/NEA Data Bank, "The JEF-2.2 Nuclear Data Library," Tech. Rep. JEFF Report 17, ISBN 92-64-17686-1, Nuclear Energy Agency, 1979.

[98] D. R. Parker and R. W. Mills, "FISPIN10 Validation Review," Tech. Rep. RAT1972 Issue 02, The UK Nuclear Nuclear Laboratory, 2001.

[99] S. M. Connolly, "Repeat of the FISPIN10 Validation Review Using 172 Group Libraries," Tech. Rep. RAT3612 Issue 01, The UK Nuclear Nuclear Laboratory, 2003.

[100] G. I. Bell and S. Glasstone, *Nuclear Reactor Theory.* Van Nostrand Reinhold Company, 1970.

[101] X-5 Monte-Carlo-Team, "MCNP - a General Monte Carlo N-Particle Transport Code, version 5," Tech. Rep. LA-UR-03-1987, Los Alamos National Laboratory, United States, 2008.

[102] D. Cullen, "TART 2002: A Coupled Neutron-Photon 3-D, Combinatorial Geometry, Time Dependent Monte Carlo Transport Code," Tech. Rep. UCRL-ID-126455, Lawrence Livermore National Laboratory, United States, July 2003.

[103] S. Agostinelli, J. Allison, K. Amako, *et al.*, "Geant4-a simulation toolkit," *Nuclear Instruments and Methods in Physics Research Section A: Accelerators, Spectrometers, Detectors and Associated Equipment*, vol. 506, no. 3, pp. 250 – 303, 2003.

[104] S. A. Pozzi, E. Padovani, and M. Marseguerra, "MCNP-PoliMi: a Monte-Carlo code for correlation measurements," *Nuclear Instruments and Methods in Physics Research Section A: Accelerators, Spectrometers, Detectors and Associated Equipment*, vol. 513, no. 3, pp. 550 – 558, 2003.

[105] D. B. Pelowitz, J. W. Durkee, *et al.*, "MCNPX 2.7.0 extensions," Tech. Rep. LA-UR-11-229, Los Alamos National Laboratory, United States, April 1988.

[106] J. T. Goorley, M. R. James, *et al.*, "Initial Overview - MCNP6 version 1.0," Tech. Rep. LA-UR-13-22934, Los Alamos National Laboratory, United States, 2013.

[107] S. A. Pozzi, M. Flaska, A. Enqvist, and I. Pázsit, "Monte Carlo and analytical models of neutron detection with organic scintillation detectors," *Nuclear Instruments and Methods in Physics Research Section A: Accelerators, Spectrometers, Detectors and Associated Equipment*, vol. 582, no. 2, pp. 629 – 637, 2007.

[108] J. K. Dickens, "SCINFUL: A Monte Carlo Based Computer Program to Determine a Scintillator Full Energy Response to Neutron Detection for En Between 0.1 and 80 MeV: Program Development and Comparisons of Program Predictions with Experimental Data," Tech. Rep. ORNL-6463, Oak Ridge National Laboratory, United States, 1988.

[109] T. Novotny, "Photon spectrometry in mixed neutron-photon fields using NE 213 liquid scintillation detectors," Tech. Rep. PTB-N-28, Physikalisch-Technische Bundesanstalt, Braunschweig (Germany), 1997.

[110] I. Stetcua, P. Talou, and T. Kawano, "Response Function of a NE213 Liquid Saintillation Detector Simulated by EGS4/PRESTA Code for a Collimated γ-Ray Beam," in *Proc. 2nd International Workshop on EGS*, 8.-12. August 2000.

[111] Z. S. Hartwig and P. Gumplinger, "Simulating response functions and pulse shape discrimination for organic scintillation detectors with Geant4," *Nuclear Instruments and Methods in Physics Research Section A: Accelerators, Spectrometers, Detectors and Associated Equipment*, vol. 737, no. Supplement C, pp. 155 – 162, 2014.

[112] N. Ghal-Eh, M. Scott, R. Koohi-Fayegh, and M. Rahimi, "A photon transport model code for use in scintillation detectors," *Nuclear Instruments and Methods in Physics Research Section A: Accelerators, Spectrometers, Detectors and Associated Equipment*, vol. 516, no. 1, pp. 116 – 121, 2004.

[113] J. Nattress and I. Jovanovic, "Response and calibration of organic scintillators for gamma-ray spectroscopy up to 15-MeV range," *Nuclear Instruments and Methods in Physics Research Section A: Accelerators, Spectrometers, Detectors and Associated Equipment*, vol. 871, no. Supplement C, pp. 1 – 7, 2017.

[114] L. Lyons, *Statistics for Nuclear and Particle Physicists.* Cambridge University Press, 1986.

[115] A. Kaplan, M. Flaska, A. Enqvist, J. Dolan, and S. Pozzi, "EJ-309 pulse shape discrimination performance with a high gamma-ray-to-neutron ratio and low threshold," *Nuclear Instruments and Methods in Physics Research Section A: Accelerators, Spectrometers, Detectors and Associated Equipment*, vol. 729, no. Supplement C, pp. 463 – 468, 2013.

[116] "Eljen Technology - Organic Scintillators - EJ-301, EJ-309." `http://www.eljentechnology.com/products/liquid-scintillators/ej-301-ej-309`, 2016. [Online; accessed 30-September-2017].

[117] F. Pino, L. Stevanato, D. Cester, G. Nebbia, L. Sajo-Bohus, and G. Viesti, "The light output and the detection efficiency of the liquid scintillator EJ-309," *Applied Radiation and Isotopes*, vol. 89, no. Supplement C, pp. 79 – 84, 2014.

[118] A. Enqvist, C. C. Lawrence, B. M. Wieger, S. A. Pozzi, and T. N. Massey, "Neutron light output response and resolution functions in EJ-309 liquid scintillation detectors," *Nuclear Instruments and Methods in Physics Research Section A: Accelerators, Spectrometers, Detectors and Associated Equipment*, vol. 715, no. Supplement C, pp. 79 – 86, 2013.

[119] "16 Channel Mixed-Field Analyser Cluster." `http://hybridinstruments.com/products/mfax4.3c.html`, 2013. [Online; accessed 19-July-2017].

[120] Intel FPGA, *Cyclone V Device Datasheet*, December 2016.

[121] ARM, *Cortex-A9 Technical Reference Manual*, April 2010.

[122] Terasic, *DE1-SoC User Manual*, August 2015.

[123] R. T. Primm III, "ARIANE International Programme Final Report," Tech. Rep. ORNL/SUB/97-XSV750-1, Oak Ridge National Laboratory, United States, May 2003.

[124] R. Lemrani, M. Robinson, V. Kudryavtsev, M. D. Jesus, G. Gerbier, and N. Spooner, "Low-energy neutron propagation in mcnpx and geant4," *Nuclear Instruments and Methods in Physics Research Section A: Accelerators, Spectrometers, Detectors and Associated Equipment*, vol. 560, no. 2, pp. 454 – 459, 2006.

[125] "Reference Physics Lists." `http://geant4.web.cern.ch/geant4/support/proc_mod_catalog/physics_lists/referencePL.shtml`, 2013. [Online; accessed 19-July-2017].

[126] "Credit/citations for data files distributed with Geant4." `http://geant4.cern.ch/support/datafiles_origin.shtml`, 2015. [Online; accessed 19-July-2017].

[127] B. Beck, D. A. Brown, F. Daffin, J. Hedstrom, and R. Vogt, "Implementation of Energy-Dependent Q Values for Fission," Tech. Rep. UCRL-TR-234617, Lawrence Livermore National Laboratory, United States, 2007.

[128] G. Dietze and H. Klein, "NRESP4 and NEFF4 - Monte Carlo codes for the calculation of neutron response functions and detection efficiencies for NE 213 scintillation detectors," Tech. Rep. PTB-ND–22, Physikalisch-Technische Bundesanstalt, Braunschweig, Germany, 1982.

[129] MathWorks, *Curve Fitting Toolbox*, September 2017.

[130] G. Aliberti, G. Palmiotti, M. Salvatores, T. Kim, T. Taiwo, *et al.*, "Nuclear data sensitivity, uncertainty and target accuracy assessment for future nuclear systems," *Annals of Nuclear Energy*, vol. 33, no. 8, pp. 700 – 733, 2006.

[131] K. Shibata and T. Nakagawa, "Uncertainty Analyses of Neutron Cross Sections for Nitrogen-15, Lead-206,207,208, Bismuth-209, Plutonium-238, Americium-242m, and Curium-244 in JENDL-3.3," *Journal of Nuclear Science and Technology*, vol. 44, no. 1, pp. 1–9, 2007.

[132] N. Khelurkar, S. Shah, and H. Jeswani, "A review of radioactive waste management," in *2015 International Conference on Technologies for Sustainable Development (ICTSD)*, pp. 1–6, Feb 2015.

[133] P. Chard, T. W. Hutchinson, I. G. andTurner, A. Ross, and B. Greenhalgh, "Field examples of waste assay solutions for curium-contaminated wastes," in *ICEM'09/DECOM'09: 12th International Conference on Environmental Remediation and Radioactive Waste Management*, 10 - 11 October 2009.

[134] B. H. Armitage, P. M. J. Chard, *et al.*, "Limitations to accuracy in nda measurements of wastes for safeguards," in *Proccesdings of the 14th ESARDA Symposium on Safeguards & Nuclear Material Management*, 5-8 May 1992.

[135] P. Chard and S. Croft, "A database of $^{240}\mathrm{Pu}_{\mathrm{eff}}$ and $^{235}\mathrm{U}_{\mathrm{eff}}$ coefficients for various fertile and fissile isotopes," in *Proccesdings of the 19th ESARDA Symposium on Safeguards & Nuclear Material Management*, 13-15 May 1997.

[136] P. M. Rinard, G. E. Bosler, and J. R. Phillips, "Calculated Neutron Source Spectra from Selected Irradiated PWR Fuel Assemblies," Tech. Rep. LA-9125-MS, Oak Ridge National Laboratory, December 1981.

[137] G. E. Bosler, J. R. Phillips, W. B. Wilson, *et al.*, "Production of Actinide Isotopes in Simulated PWR Fuel and Their Influence on Inherent Neutron Emission," Tech. Rep. LA-9343, Oak Ridge National Laboratory, July 1982.

[138] J. G. Richard, M. L. Fensin, S. J. Tobin, *et al.*, "Characterization of the Neutron Source Term and Multiplicity of a Spent Fuel Assembly in Support of NDA Safeguards of Spent Nuclear Fuel," Tech. Rep. LA-UR-10-03927, Oak Ridge National Laboratory, May 1994.

[139] J. E. Stewart, K. Kaiada, J. K. Halbig, *et al.*, "Passive Neutron Assay of Irradiated Nuclear Fuels," Tech. Rep. LA-7645-MS, Oak Ridge National Laboratory, February 1979.

[140] N. Miura and H. O. Menlove, "The Use of Curium Neutrons to Verify Plutonium in Spent Fuel and Reprocessing Wastes," Tech. Rep. LA-12774-MS, Oak Ridge National Laboratory, May 1994.

[141] D. D. Cobb, J. R. Phillips, M. P. Baker, *et al.*, "Nondestructive Verification and Assay Systems for Spent Fuels," Tech. Rep. LA-9041 Vol. 2, Oak Ridge National Laboratory, April 1982.

[142] R. Weldon, M. Fensin, and H. Trellue, "Total neutron emission generation and characterization for a Next Generation Safeguards Initiative spent fuel library," *Progress in Nuclear Energy*, vol. 80, pp. 45 – 73, 2015.

[143] J. Debrue, C. D. Raedt, and G. Minsart, "Analysis of Neutron Emission on PWR Spent Fuel Assemblies for Burn-Up Assessment," *Reactor Dosimetry: Methods, Applications, and Standardization*, pp. 710–719, 1989.

[144] "Production of Minor Actinides in Thermal Nuclear Reactors and Nonproliferation," Tech. Rep. DE-AC01- 02NN40287, Analytical Center for Nonproliferation and the U.S. Department of Energy, United States.

[145] P. M. J. Chard, S. Croft, I. G. Hutchinson, T. W. Turner, A. Ross, and B. Greenhalgh, "Field examples of waste assay solutions for curium-contaminated wastes," in *ASME 2009 12th International Conference on Environmental Remediation and Radioactive Waste Management*, 10 - 11 October 2009.

[146] P. M. Rinard and H. O. Menlove, "Application of Curium Measurements for Safeguarding at Reprocessing Plants," Tech. Rep. LA-13134-MS, Oak Ridge National Laboratory, March 1996.

[147] R. Sarwar *et al.*, "Real-time determination of Rossi-α distribution, active fast neutron multiplicity, neutron angular distribution and neutron spectrum using organic liquid scintillators," in *2017 IEEE Nuclear Science Symposium and Medical Imaging Conference*, 21 - 28 October 2017.

[148] W. Geist, L. Carrillo, N. Ensslin, K. Ianakiev, D. Mayo, and M. Miller, "Evaluation of a fast neutron coincidence counter for the measurements of uranium samples," *Nuclear Instruments and Methods in Physics Research Section A: Accelerators, Spectrometers, Detectors and Associated Equipment*, vol. 470, no. 3, pp. 590 – 599, 2001.

[149] M. Endelmann, "New Rossi-α Measurement Methods," Tech. Rep. INR-4/68-15, Karlsruhe Nuclear Research Center, Germany, 1968.

[150] T.-A. A. Wellington, *Alternative Method for Determining Plutonium-240 Content.* PhD thesis, University of Tennessee, Knoxville, Tennessee, 2015.

[151] S. Pozzi, J. Mihalczo, P. Peerani, J. Loeschner, *et al.*, "Passive measurements on plutonium oxide samples," in *Proceedings of the Institute of Nuclear Materials Management, 46 Annual Meeting*, July 10-14, 2005.

[152] J. K. Mattingly, "Plutonium Attribute Estimation from Passive NMIS Measurements at VNIIEF," Tech. Rep. ORNL/TM-2002/20, Oak Ridge National Laboratory, Jan 2002.

[153] M. C. D. V. Jordan, P. L. Reeder *et al.*, "Methods and Instruments for Fast Neutron Detection," Tech. Rep. PNNL-15214, Pacific Northwest National Laboratory, United States, 2005.

[154] A. Enqvist, M. Flaska, and S. Pozzi, "Measurement and simulation of neutron/gamma-ray cross-correlation functions from spontaneous fission," *Nuclear Instruments and Methods in Physics Research Section A: Accelerators, Spectrometers, Detectors and Associated Equipment*, vol. 595, no. 2, pp. 426 – 430, 2008.

[155] M. Bruggeman, P. Baeten, W. D. Boeck, and R. Carchon, "Neutron coincidence counting based on time interval analysis with one- and two-dimensional rossi-alpha distributions: an application for passive neutron waste assay," *Nuclear Instruments and Methods in Physics Research Section A: Accelerators, Spectrometers, Detectors and Associated Equipment*, vol. 382, no. 3, pp. 511 – 518, 1996.

[156] S. A. Pozzi, R. B. Oberer, L. G. Chiang, J. K. Mattingly, and J. T. Mihalczo, "Higher-order statistics from nmis to measure neutron and gamma ray cross talk in plastic scintillators," *Nuclear Instruments and Methods in Physics Research Section A: Accelerators, Spectrometers, Detectors and Associated Equipment*, vol. 481, no. 1, pp. 739 – 748, 2002.

[157] S. Clarke, M. Flaska, S. Pozzi, and P. Peerani, "Neutron and gamma-ray cross-correlation measurements of plutonium oxide powder," *Nuclear Instruments and Methods in Physics Research Section A: Accelerators, Spectrometers, Detectors and Associated Equipment*, vol. 604, no. 3, pp. 618 – 623, 2009.

[158] M. Flaska, A. Enqvist, and S. A. Pozzi, "Measurement of fast neutron/gamma-ray cross-correlation functions with cf-252 and pu-be neutron sources," in *2009 IEEE Nuclear Science Symposium Conference Record (NSS/MIC)*, pp. 961–963, Oct 2009.

[159] Marcath, M.J., Shin, T.H., Fulvio, A. Di, Clarke, S.D., and Pozzi, S.A., "Correlations in prompt neutrons and gamma-rays from Cf-252 spontaneous fission," *EPJ Web Conf.*, vol. 146, p. 04038, 2017.

[160] E. C. Miller, J. L. Dolan, S. A. Pozzi, M. Flaska, S. D. Clarke, and P. Peerani, "Neutron and gamma-ray cross-correlation measurements of mox fuel using liquid scintillators," in *IEEE Nuclear Science Symposuim Medical Imaging Conference*, pp. 686–690, Oct 2010.

[161] A. Lavietes, R. Plenteda, N. Mascarenhas, L. M. Cronholm, M. Aspinall, M. Joyce, A. Tomanin, and P. Peerani, "Development of a liquid scintillator-based active interrogation system for leu fuel assemblies," in *2013 3rd International Conference on Advancements in Nuclear Instrumentation, Measurement Methods and their Applications (ANIMMA)*, pp. 1–4, June 2013.

[162] J. D. Edwards, J. K. Mattingly, and S. A. Pozzi, "Analysis of neutron reflection in correlation measurements," *Journal of Nuclear Materials Management*, vol. 32, no. 1, pp. 26–29, 2003.

[163] N. Jovančević, L. Daraban, S. Oberstedt, F. Hambsch, M. Hult, G. Lutter, and G. Marissens, "Measurement of the neutron spectrum using the activation method," *Physics Procedia*, vol. 59, pp. 154 – 159, 2014. GAMMA-2 Scientific Workshop on the Emission of Prompt Gamma-Rays in Fission and Related Topics.

[164] J. Chadwick, "The existence of a neutron," *Proceedings of the Royal Society of London A: Mathematical, Physical and Engineering Sciences*, vol. 136, no. 830, pp. 692–708, 1932.

[165] E. Fermi, J. Marshall, and L. Marshall, "A thermal neutron velocity selector and its application to the measurement of the cross section of boron," *Phys. Rev.*, vol. 72, pp. 193–196, Aug 1947.

[166] John R. D. Copley and Terrence J. Udovic, "Neutron Time-of-Flight Spectroscopy," *Journal of Research of the National Institute of Standards and Technology*, vol. 98, pp. 71–87, January-February 1993.

[167] J. W. Meadows, "^{252}Cf Fission Neutron Spectrum from 0.003 to 15.0 MeV," *Phys. Rev.*, vol. 157, pp. 1076–1082, May 1967.

[168] E. Blain, A. Daskalakis, R. C. Block, and Y. Danon, "Measurement of prompt fission neutron spectrum for spontaneous fission of ^{252}Cf using γ multiplicity tagging," *Phys. Rev. C*, vol. 95, p. 064615, Jun 2017.

[169] E. Blain, A. Daskalakis, R. C. Block, D. Barry, and Y. Danon, "A method to measure prompt fission neutron spectrum using gamma multiplicity tagging," *Nuclear Instruments and Methods in Physics Research Section A: Accelerators, Spectrometers, Detectors and Associated Equipment*, vol. 805, pp. 95 – 100, 2016. Special Issue in memory of Glenn F. Knoll.

[170] S. D. Clarke, B. M. Wieger, A. Enqvist, R. Vogt, J. Randrup, R. C. Haight, H. Y. Lee, B. A. Perdue, E. Kwan, C. Y. Wu, R. A. Henderson, and S. A. Pozzi, "Measurement of the energy and multiplicity distributions of neutrons from the photofission of ^{235}U," *Phys. Rev. C*, vol. 95, p. 064612, Jun 2017.

[171] F. D. Becchetti, M. Febbraro, R. Torres-Isea, M. Ojaruega, and L. Baum, "252Cf fission-neutron spectrum using a simplified time-of-flight setup: An advanced teaching laboratory experiment," *American Journal of Physics*, vol. 81, no. 2, pp. 112–119, 2013.

[172] M. Reginatto, "Overview of spectral unfolding techniques and uncertainty estimation," *Radiation Measurements*, vol. 45, no. 10, pp. 1323 – 1329, 2010.

[173] S. Itoh, "A fundamental study of neutron spectra unfolding based on the maximum likelihood method," *Nuclear Instruments and Methods in Physics Research Section A: Accelerators, Spectrometers, Detectors and Associated Equipment*, vol. 251, no. 1, pp. 144 – 155, 1986.

[174] "Neutron and gamma-ray energy reconstruction for characterization of special nuclear material," *Nuclear Engineering and Technology*, vol. 49, no. 6, pp. 1354 – 1357, 2017.

[175] Y. Kopatch, A. Chietera, L. Stuttgé, *et al.*, "Detailed Study of the Angular Correlations in the Prompt Neutron Emission in Spontaneous Fission of 252Cf," *Physics Procedia*, vol. 64, pp. 171 – 176, 2015. Scientific Workshop on Nuclear Fission Dynamics and the Emission of Prompt Neutrons and Gamma Rays, THEORY-3.

[176] R. Vogt and J. Randrup, "Neutron angular correlations in spontaneous and neutron-induced fission," *Phys. Rev. C*, vol. 90, p. 064623, Dec 2014.

[177] H. R. Bowman, S. G. Thompson, J. C. D. Milton, and W. J. Swiatecki, "Velocity and Angular Distributions of Prompt Neutrons from Spontaneous Fission of Cf^{252}," *Phys. Rev.*, vol. 126, pp. 2120–2136, Jun 1962.

[178] H. R. Bowman, J. C. D. Milton, S. G. Thompson, and W. J. Swiatecki, "Further Studies of the Prompt Neutrons from the Spontaneous Fission of Cf^{252}," *Phys. Rev.*, vol. 129, pp. 2133–2147, Mar 1963.

[179] K. Skarsvåg and K. Bergheim, "Energy and angular distributions of prompt neutrons from slow neutron fission of U235," *Nuclear Physics*, vol. 45, pp. 72 – 97, 1963.

[180] A. S. Vorobyev, O. A. Shcherbakov, A. M. Gagarski, G. A. Petrov, and G. V. Val'ski, "Experimental determination of the yield of "scission" neutrons from the spontaneous fission of 252cf," *Journal of Experimental and Theoretical Physics*, vol. 125, pp. 619–637, Oct 2017.

[181] J. S. Fraser, "The angular distribution of prompt neutrons emitted in fission," *Phys. Rev.*, vol. 88, pp. 536–541, Nov 1952.

[182] J. S. Pringle and F. D. Brooks, "Angular correlation of neutrons from spontaneous fission of ^{252}Cf," *Phys. Rev. Lett.*, vol. 35, pp. 1563–1566, Dec 1975.

[183] A. M. Gagarski, I. S. Guseva, V. E. Sokolov, G. V. Val'ski, G. A. Petrov, D. O. Krinitsin, D. V. Nikolaev, T. A. Zavarukhina, and V. I. Petrova, "Neutron-neutron angular correlations in spontaneous fission of 252cf," *Bulletin of the Russian Academy of Sciences: Physics*, vol. 72, pp. 773–777, Jun 2008.

[184] R. Vogt and J. Randrup, "Event-by-event study of neutron observables in spontaneous and thermal fission," *Phys. Rev. C*, vol. 84, p. 044621, Oct 2011.

[185] S. A. Pozzi, B. Wieger, A. Enqvist, S. D. Clarke, M. Flaska, M. Marcath, E. Larsen, R. C. Haight, and E. Padovani, "Correlated Neutron Emissions from 252Cf," *Nuclear Science and Engineering*, vol. 178, no. 2, pp. 250–260, 2014.

[186] J. Lestone, "Neutron-fragment and neutron-neutron correlations in low-energy fission," *Nuclear Data Sheets*, vol. 131, pp. 357 – 376, 2016. Special Issue on Nuclear Reaction Data.

[187] Pirovano, Elisa, Beyer, Roland, Junghans, Arnd, Nolte, Ralf, Nyman, Markus, and Plompen, Arjan, "Measurements of neutron scattering angular distributions with a new scintillator setup," *EPJ Web Conf.*, vol. 146, p. 11008, 2017.

[188] M. J. Marcath, T. H. Shin, S. D. Clarke, J. L. Dolan, M. Flaska, E. W. Larsen, S. A. Pozzi, and P. Peerani, "Plutonium metal spontaneous fission neutron cross-correlation measurements," in *2014 IEEE Nuclear Science Symposium and Medical Imaging Conference (NSS/MIC)*, pp. 1–3, Nov 2014.

[189] J. Mueller and J. Mattingly, "Using anisotropies in prompt fission neutron coincidences to assess the neutron multiplication of highly multiplying subcritical plutonium assemblies," *Nuclear Instruments and Methods in Physics Research Section A: Accelerators, Spectrometers, Detectors and Associated Equipment*, vol. 825, pp. 87 – 92, 2016.

[190] M. C. Browne, A. P. Belian, *et al.*, "Prototype Neutron-Capture Counter for Fast-Coincidence Assay of Plutonium in Residues," in *Proccesdings of the 31st ESARDA Symposium on Safeguards & Nuclear Material Management*, May 8-10,2001.

[191] K. Frame, W. Clay, T. Elmont, E. Esch, P. Karpius, D. MacArthur, E. McKigney, P. Santi, M. Smith, J. Thron, and R. Williams, "Development of a liquid scintillator neutron multiplicity counter (LSMC)," *Nuclear Instruments and Methods in Physics Research Section A: Accelerators, Spectrometers, Detectors and Associated Equipment*, vol. 579, no. 1, pp. 192 – 195, 2007. Proceedings of the 11th Symposium on Radiation Measurements and Applications.

[192] A. Enqvist, S. A. Pozzi, M. Flaska, and I. Pázsit, "Initial evaluation for a combined neutron and gamma ray multiplicity counter," *Nuclear Instruments and Methods in Physics Research Section A: Accelerators, Spectrometers, Detectors and Associated Equipment*, vol. 621, no. 1, pp. 493 – 497, 2010.

[193] A. Enqvist, K. J. Weinfurther, M. Flaska, and S. A. Pozzi, "Characterization of a mixed multiplicity counter based on liquid organic scintillators," *IEEE Transactions on Nuclear Science*, vol. 58, pp. 2413–2420, Oct 2011.

[194] M. J. Marcath, A. D. Fulvio, T. H. Shin, S. D. Clarke, E. W. Larsen, E. Padovani, R. C. Haight, and S. A. Pozzi, "Prompt neutron and gamma-ray correlations from cf-252 spontaneous fission," in *2015 IEEE Nuclear Science Symposium and Medical Imaging Conference (NSS/MIC)*, pp. 1–3, Oct 2015.

[195] A. D. Fulvio, T. Shin, T. Jordan, C. Sosa, M. Ruch, S. Clarke, D. Chichester, and S. Pozzi, "Passive assay of plutonium metal plates using a fast-neutron multiplicity counter," *Nuclear Instruments and Methods in Physics Research Section A: Accelerators, Spectrometers, Detectors and Associated Equipment*, vol. 855, pp. 92 – 101, 2017.

[196] T. Shin, M. Hua, A. D. Fulvio, and S. A. Pozzi, "Validation of the fast-neutron multiplicity expressions for fissile mass estimation," in *Institute of Nuclear Materials Management 58th Annual Meeting*, July 2017.

[197] T. H. Shin, M. Y. Hua, M. J. Marcath, D. L. Chichester, I. Pázsit, A. D. Fulvio, S. D. Clarke, and S. A. Pozzi, "Neutron Multiplicity Counting Moments for Fissile Mass Estimation in Scatter-Based Neutron Detection Systems," *Nuclear Science and Engineering*, vol. 188, no. 3, pp. 246–269, 2017.

[198] A. D. Fulvio, T. Shin, A. Basley, C. Swenson, C. Sosa, S. Clarke, J. Sanders, S. Watson, D. Chichester, and S. Pozzi, "Fast-neutron multiplicity counter for active measurements of uranium oxide certified material," *Nuclear Instruments and Methods in Physics Research Section A: Accelerators, Spectrometers, Detectors and Associated Equipment*, pp. –, 2018.

[199] T. Shin, A. D. Fulvio, S. D. Clarke, *et al.*, "Fast-neutron multiplicity counter for the detection of diversion scenarios," in *Institute of Nuclear Materials Management 58th Annual Meeting*, July 2017.

[200] J. L. Ullmann, E. M. Bond, T. A. Bredeweg, A. Couture, R. C. Haight, M. Jandel, T. Kawano, H. Y. Lee, J. M. O'Donnell, A. C. Hayes, I. Stetcu, T. N. Taddeucci, P. Talou, D. J. Vieira, J. B. Wilhelmy, J. A. Becker, A. Chyzh, J. Gostic, R. Henderson, E. Kwan, and C. Y. Wu, "Prompt γ-ray production in neutron-induced fission of ^{239}Pu," *Phys. Rev. C*, vol. 87, p. 044607, Apr 2013.

[201] S. Avdic, A. Enqvist, and I. Pázsit, "Unfolding sample parameters from neutron and gamma multiplicities using artificial neural networks.," pp. 21–29, 01 2009.

[202] A. Enqvist, I. Pázsit, and S. Avdic, "Sample characterization using both neutron and gamma multiplicities," *Nuclear Instruments and Methods in Physics Research Section A: Accelerators, Spectrometers, Detectors and Associated Equipment*, vol. 615, no. 1, pp. 62 – 69, 2010.

[203] B. Simony, C. Deyglun, B. Pérot, C. Carasco, N. Saurel, S. Colas, and J. Collot, "Cross-talk characterization in passive neutron coincidence counting of radioactive waste drums with plastic scintillators," *IEEE Transactions on Nuclear Science*, vol. 63, pp. 1513–1519, June 2016.

[204] J. Wang, A. Galonsky, J. Kruse, P. Zecher, F. Deák, . Horváth, A. Kiss, Z. Seres, K. Ieki, and Y. Iwata, "Neutron cross-talk in a multi-detector system," *Nuclear Instruments and Methods in Physics Research Section A: Accelerators, Spectrometers, Detectors and Associated Equipment*, vol. 397, no. 2, pp. 380 – 390, 1997.

[205] M. Cronqvist, B. Jonson, T. Nilsson, G. Nyman, K. Riisager, H. Roth, . Skeppstedt, O. Tengblad, and K. Wilhelmsen, "Experimental determination of cross-talk between neutron detectors," *Nuclear Instruments and Methods in Physics Research Section A: Accelerators, Spectrometers, Detectors and Associated Equipment*, vol. 317, no. 1, pp. 273 – 280, 1992.

[206] J. Harms, P. B. Rose, and A. Erickson, "Characterization of γ-Ray Cross Talk in Cherenkov-Based Detectors for Active Interrogation Imaging Applications," *IEEE Sensors Journal*, vol. 17, pp. 6707–6715, Oct 2017.

[207] S. Li, S. Qiu, Q. Zhang, Y. Huo, and H. Lin, "Fast-neutron multiplicity analysis based on liquid scintillation," *Applied Radiation and Isotopes*, vol. 110, pp. 53 – 58, 2016.

[208] T. H. Shin, M. J. Marcath, A. DiFulvio, S. D. Clarke, and S. A. Pozzi, "Neutron cross-talk characterization of liquid organic scintillators," in *2015 IEEE Nuclear Science Symposium and Medical Imaging Conference (NSS/MIC)*, pp. 1–4, Oct 2015.

[209] T. Wada, T. Asano, and N. Carjan, "Effects of the fission fragments on the angular distribution of scission particles," *Physics Procedia*, vol. 64, pp. 34 – 39, 2015. Scientific Workshop on Nuclear Fission Dynamics and the Emission of Prompt Neutrons and Gamma Rays, THEORY-3.

[210] M. Hamel, J. Polack, A. Poitrasson-Riviŕe, M. Flaska, S. Clarke, S. Pozzi, A. Tomanin, and P. Peerani, "Stochastic image reconstruction for a dual-particle imaging system," *Nuclear Instruments and Methods in Physics Research Section A: Accelerators, Spectrometers, Detectors and Associated Equipment*, vol. 810, pp. 120 – 131, 2016.

Appendix A

EJ-309 scintillation detectors

A.1 Technical datasheet

NEUTRON/GAMMA PSD LIQUID SCINTILLATOR EJ-301, EJ-309

EJ-301 exhibits excellent pulse shape discrimination (PSD) properties, particularly for fast neutron counting and spectrometry in the presence of gamma radiation. It is identical to the widely reported NE-213 and exhibits all of the properties of that scintillator.

EJ-309 has been developed as an alternate to the more commonly used low-flash point PSD liquid scintillators based on the solvent xylene. With a flash point of 144°C, it eliminates the fire hazard associated with low-flash point liquid scintillators. While EJ-309 provides slightly poorer PSD characteristics than that of EJ-301, EJ-309 possesses a number of chemical properties recommending it for use in environmentally difficult conditions. These properties include: high flash point, low vapor pressure, low chemical toxicity, and compatibility with cast acrylic plastics. EJ-309 is also available loaded with natural boron as EJ-309B.

PROPERTIES	EJ-301	EJ-309
Light Output (% Anthracene)	78	80
Scintillation Efficiency (photons/1 MeV e-)	12,000	12,300
Wavelength of Maximum Emission (nm)	425	424
Decay Time, Short Component (ns)	3.2	3.5
Mean Decay Times of First 3 Components (ns)	3.16 32.3 270	-
Bulk Light Attenuation Length (m)	2.5 - 3	> 1
Specific Gravity	0.874	0.959
Refractive Index	1.505	1.57
Flash Point (°C)	26	144
Boiling Point (°C at 1 atm)	141	290 - 300
Vapor Pressure (mm Hg, at 20°C)	-	0.002
H Atoms per cm³ ($\times 10^{22}$)	4.82	5.43
C Atoms per cm³ ($\times 10^{22}$)	3.98	4.35
Electrons per cm³ ($\times 10^{23}$)	2.27	3.16

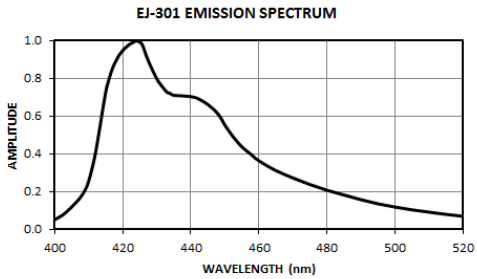

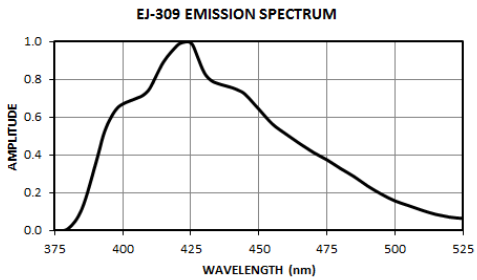

Revision Date: 02/11/2016

ELJEN TECHNOLOGY
1300 W. Broadway, Sweetwater, TX 79556
www.eljentechnology.com • eljen@eljentechnology.com
Toll Free (USA): (888)-800-8771 • Tel: (325)-235-4276 • Fax: (325) 235-0701

A.2 Photomultiplier tube

78 mm (3") photomultiplier
9821B series data sheet

ET Enterprises electron tubes

1 description

The 9821B is a 78mm (3″) diameter, end window photomultiplier with blue-green sensitive bialkali photocathode on a plano-concave window, and 12 BeCu dynodes of linear focused design for good linearity and timing.

2 applications

- high energy physics studies
- scintillation spectroscopy

3 features

- good SER
- high pulsed linearity
- fast time response

4 window characteristics

	9821B borosilicate
spectral range *(nm)	285 - 630
refractive index (n_d)	1.47
K (ppm)	300
Th (ppb)	550
U (ppb)	450

* wavelength range over which quantum efficiency exceeds 1 % of peak

5 typical spectral response curves

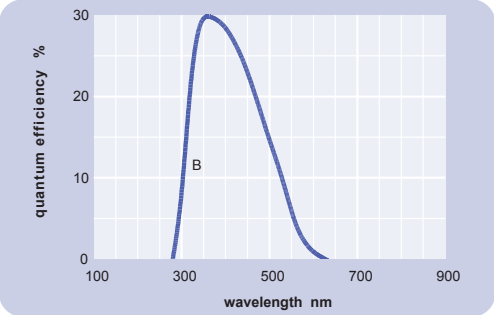

6 characteristics

	unit	min	typ	max
photocathode: bialkali				
active diameter	mm		67	
quantum efficiency at peak	%		30	
luminous sensitivity	µA/lm		75	
with CB filter		8	12	
with CR filter			2	
dynodes: 12LFBeCu				
anode sensitivity in divider B:				
nominal anode sensitivity	A/lm		500	
max. rated anode sensitivity	A/lm		2000	
overall V for nominal A/lm	V		2000	2600
overall V for max. rated A/lm	V		2250	
gain at nominal A/lm	x 10^6		7	
dark current at 20 °C:				
dc at nominal A/lm	nA		10	50
dc at max. rated A/lm	nA		40	
dark count	s^{-1}		500	
pulsed linearity (-5% deviation):				
divider A	mA		50	
divider B	mA		150	
pulse height resolution:				
single electron peak to valley	ratio		2	
rate effect (I_a for $\Delta g/g$=1%):	µA		1	
magnetic field sensitivity:				
the field for which the output decreases by 50 %				
most sensitive direction	T x 10^{-4}			
temperature coefficient:	% $°C^{-1}$		± 0.5	
timing:				
single electron rise time	ns		2.1	
single electron fwhm	ns		3.2	
single electron jitter (fwhm)	ns		2.2	
transit time	ns		42	
weight:	g		260	
maximum ratings:				
anode current	µA			100
cathode current	nA			200
gain	x 10^6			27
sensitivity	A/lm			2000
temperature	°C	-30		60
V (k-a)[1]	V			2900
V (k-d1)	V			600
V (d-d)[2]	V			450
ambient pressure (absolute)	kPa			202

[1] subject to not exceeding max. rated sensitivity [2] subject to not exceeding max rated V(k-a)

7 typical voltage gain characteristics

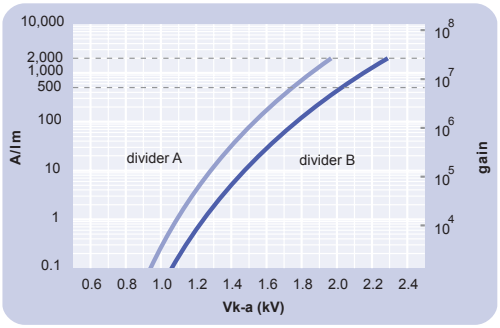

4944

8 voltage divider distribution

	k	d_1	d_2	d_9	d_{10}	d_{11}	d_{12}	a	
A	450V	R		R	R	R	R	R	Standard
B	450V	R		R	1.25R	1.5R	2R	3R	High Pulsed linearity

note: focus connected to d_1

Characteristics contained in this data sheet refer to divider B unless stated otherwise.

9 external dimensions mm

The drawings below show the 9821B in hardpin format and the 9821KB with the B20 cap fitted.

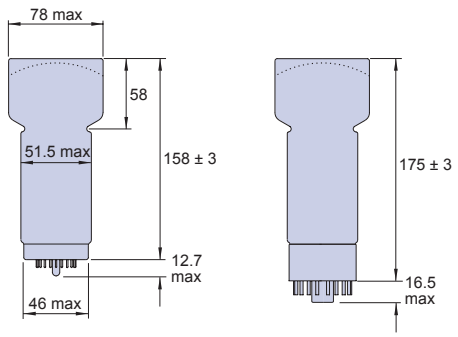

10 base configuration (viewed from below)

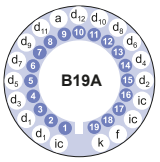

B19A hardpin base
(for 9821B)
'ic' indicates an internal connection

note: connect f to d_1

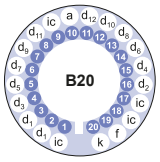

B20 cap
(for 9821KB)
'ic' indicates an internal connection

note: connect f to d_1

Our range of B19A sockets is available to suit the hardpin base. Our range of B20 sockets is available to suit the B20 cap. Both socket ranges include versions with or without a mounting flange, and versions with contacts for mounting directly onto printed circuit boards.

11 ordering information

The 9821B meets the specification given in this data sheet. You may order **variants** by adding a suffix to the type number. You may also order **options** by adding a suffix to the type number. You may order product with **specification options** by discussing your requirements with us. If your selection option is for one-off order, then the product will be referred to as 9816A. For a repeat order, ET Enterprises will give the product a two digit suffix after the letter B, for example B21. This identifies your specific requirement.

9821 ☐ ☐ ☐

base options
K capped

options
E electrostatic shielding see drawing below
M supplied with spectral response calibration

specification options
B as given in data sheet
A single order to selected specification
Bnn repeat order to selected specification

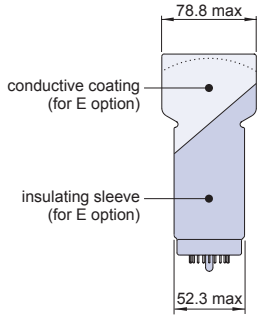

12 voltage dividers

The standard voltage dividers available for these pmts are tabulated below:

9821B	9821KB	k	d_1	d_2	d_8	d_9	d_{10}	d_{11}	d_{12}	a
C638P	C640P	3R	R	.....	R	R	R	R	R	
C638R	C640R	3R	R	.....	R	1.25R	1.5R	2R	3R	
C638S	C640S	450 V	R	.....	R	R	R	R	R	
C638T	C640T	450 V	R	.....	R	1.25R	1.5R	2R	3R	

R = 330 kΩ note: focus connected to d_1

*mumetal is a registered trademark of Magnetic Shield Corporation

ET Enterprises Limited
45 Riverside Way
Uxbridge UB8 2YF
United Kingdom
tel: +44 (0) 1895 200880
fax: +44 (0) 1895 270873
e-mail: sales@et-enterprises.com
web site: www.et-enterprises.com

ADIT Electron Tubes
300 Crane Street
Sweetwater TX 79556 USA
tel: (325) 235 1418
toll free: (800) 399 4557
fax: (325) 235 2872
e-mail: sales@electrontubes.com
web site: www.electrontubes.com

choose accessories for this pmt on our website

an ISO 9001 registered company

DS_ 9821B Issue 9 (23/01/12)

Appendix B

Nuclear Sources

B.1 Californium-252 (Lancaster) datasheet

Sources

Californium-252

Spontaneous Fission Neutron Sources

Nuclear Data

Californium-252 decays by α-emission and spontaneous fission emitting neutrons.

Half-life (α-decay):	2.73 years
Half-life (spontaneous fission):	85.5 years
Half-life (effective):	2.65 years
Neutron emission:	2.3×10^9n/sec per mg
Average neutron energy:	~2MeV
Equilibrium γ-exposure rate (from unshielded source):	1.6×10^2mR/h at 1m per mg ~Air kerma rate at 1m of 1.4mGy/h per mg
Neutron dose rate:	~2.3rem/h at 1m per mg ~23mSv/h at 1m per mg
Specific activity:	~20GBq/mg, ~536mCi/mg

Composition
Californium-252 is incorporated in ceramic material.

Encapsulation
The radioactive material is doubly-encapsulated in welded stainless steel capsules.

Nominal ^{252}Cf content	Nominal ^{252}Cf content activity	Nominal activity*	Emission n/sec*	Capsule	Code
0.01µg	0.2MBq	5µCi	0.023×10^6	X.1	CVN.101
0.1µg	2MBq	54µCi	0.23×10^6	X.1	CVN.1
0.5µg	10MBq	268µCi	1.15×10^6	X.1	CVN.2
1.0µg	20MBq	536µCi	2.3×10^6	X.1	CVN.3
2.0µg	40MBq	1.07mCi	4.6×10^6	X.1	CVN.4
5µg	100MBq	2.7mCi	1.15×10^7	X.1	CVN.5
10µg	200MBq	5.4mCi	2.3×10^7	X.1	CVN.6
20µg	400MBq	10.7mCi	4.6×10^7	X.1	CVN.7
50µg	1GBq	27mCi	1.15×10^8	X.1	CVN.10
100µg	2GBq	54mCi	2.3×10^8	X.1	CVN.11
200µg	4GBq	107mCi	4.6×10^8	X.1	CVN.12

*Tolerance -10, +20%

Recommended working life: 15 years

Quality Control
Wipe test A
Bubble test D
Immersion test L

Neutron emission measured against standard using BF_3/wax moderator system.

The test report includes a statement of the neutron emission.

Neutron spectrum

Americium 241/beryllium source made and measured at AEA Technology using a stilbene crystal and pulse shape discrimination.

Spectrum reproduced by courtesy of: LORCH, E.A. Int. J. Appl. Radiat. Isotopes, **24**, 588-9, 1973.

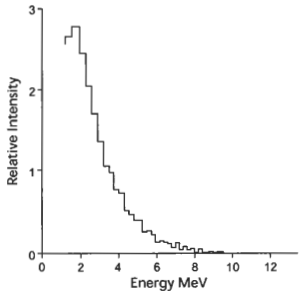

X.1

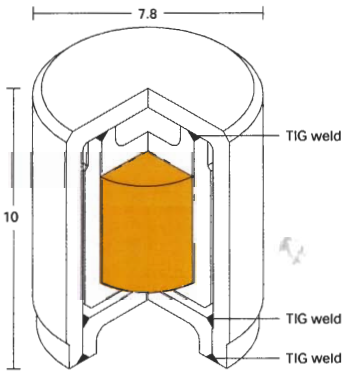

Safety performance testing

ANSI/ISO classification	IAEA special form	Model no.
C66545	GB/007/S-85	CVN.CY2

B15

United Kingdom: 329 Harwell, Didcot, OX11 0QJ, Tel: +44 1235 431267
United States: 40 North Avenue, Burlington, MA 01803, Tel: 781-272-2000
Germany: GmbH, Gieselweg 1, D-38110 Braunschweig, Tel: 0049 - (0) 5307 - 932113
Hong Kong: Suite 1208 12/F, Central Plaza, 18 Harbour Road, Wanchai, Tel: 00 852 2519 3966

AEA TECHNOLOGY QSA

B.2 Caesium-137 (ORNL) datasheet

Eckert & Ziegler
Isotope Products

24937 Avenue Tibbitts
Valencia, California 91355

Tel 661·309·1010
Fax 661·257·8303

CERTIFICATE OF CALIBRATION
GAMMA STANDARD SOURCE

Radionuclide:	Cs-137	**Customer:**	UT-BATTELLE LLC
Half-life:	30.17 ± 0.16 years	**P.O. No.:**	4000149401
Catalog No.:	GF-290-10D	**Reference Date:**	15-Oct-16 12:00 PST
Source No.:	1893-73-5	**Contained Radioactivity:**	9.725 µCi 359.8 kBq

Physical Description:

A. Capsule type: D (25.4 mm OD x 6.35 mm maximum THK)
B. Nature of active deposit: Evaporated metallic salt
C. Active diameter/volume: 5 mm
D. Backing: Epoxy
E. Cover: Acrylic

Radioimpurities:

Cs-134 = 0.0429% on 15-Oct-16

Method of Calibration:

This source was assayed using gamma ray spectrometry.

Peak energy used for integration: 661.7 keV
Branching ratio used: 0.851 gammas per decay

Uncertainty of Measurement:

A. Type A (random) uncertainty: ± 0.4 %
B. Type B (systematic) uncertainty: ± 3.0 %
C. Uncertainty in aliquot weighing: ± 0.0 %
D. Total uncertainty at the 99% confidence level: ± 3.0 %

Notes:

- See reverse side for leak test(s) performed on this source.
- EZIP participates in a NIST measurement assurance program to establish and maintain implicit traceability for a number of nuclides, based on the blind assay (and later NIST certification) of Standard Reference Materials (as in NRC Regulatory Guide 4.15).
- Nuclear data was taken from IAEA-TECDOC-619, 1991.
- This source has a recommended working life of 5 years.

Daniel James Van Dalsem — Quality Control

16-Sep-16 — Date

EZIP Ref. No.: 1893-73

ISO 9001 CERTIFIED

Medical Imaging Laboratory
24937 Avenue Tibbitts Valencia, California 91355

Industrial Gauging Laboratory
1800 North Keystone Street Burbank, California 91504

B.3 Cobalt-60 (ORNL) datasheet

Eckert & Ziegler
Isotope Products

24937 Avenue Tibbitts
Valencia, California 91355

Tel 661·309·1010
Fax 661·257·8303

CERTIFICATE OF CALIBRATION
GAMMA STANDARD SOURCE

Radionuclide:	Co-60	**Customer:**	UT-BATTELLE LLC
Half-life:	5.272 ± 0.001 years	**P.O. No.:**	4000149401
Catalog No.:	GF-290-10D	**Reference Date:**	15-Oct-16 12:00 PST
Source No.:	1893-73-4	**Contained Radioactivity:**	10.33 µCi 382.2 kBq

Physical Description:

A. Capsule type:	D (25.4 mm OD x 6.35 mm maximum THK)
B. Nature of active deposit:	Evaporated metallic salt
C. Active diameter/volume:	5 mm
D. Backing:	Epoxy
E. Cover:	Acrylic

Radioimpurities:

None detected

Method of Calibration:

This source was assayed using gamma ray spectrometry.

Peak energy used for integration:	1173, 1333 keV
Branching ratio used:	0.9986, 0.9998 gammas per decay

Uncertainty of Measurement:

A. Type A (random) uncertainty:	± 0.5 %
B. Type B (systematic) uncertainty:	± 3.0 %
C. Uncertainty in aliquot weighing:	± 0.0 %
D. Total uncertainty at the 99% confidence level:	± 3.0 %

Notes:

- See reverse side for leak test(s) performed on this source.
- EZIP participates in a NIST measurement assurance program to establish and maintain implicit traceability for a number of nuclides, based on the blind assay (and later NIST certification) of Standard Reference Materials (as in NRC Regulatory Guide 4.15).
- Nuclear data was taken from IAEA-TECDOC-619, 1991.
- This source has a recommended working life of 5 years.

Daniel James Van Dalsem — Quality Control

16-Sep-16 — Date

EZIP Ref. No.: 1893-73

ISO 9001 CERTIFIED

Medical Imaging Laboratory
24937 Avenue Tibbitts Valencia, California 91355

Industrial Gauging Laboratory
1800 North Keystone Street Burbank, California 91504

B.4 Other (ORNL) datasheet

Eckert & Ziegler
Isotope Products

24937 Avenue Tibbitts
Valencia, California 91355

Tel 661·309·1010
Fax 661·257·8303

CERTIFICATE OF CALIBRATION
GAMMA STANDARD SOURCE

Radionuclide:	Ba-133	**Customer:**	UT-BATTELLE LLC
Half-life:	3862 ± 15 days	**P.O. No.:**	4000149401
Catalog No.:	GF-290-10D	**Reference Date:**	15-Oct-16 12:00 PST
Source No.:	1893-73-1	**Contained Radioactivity:**	10.34 µCi 382.6 kBq

Physical Description:

A. Capsule type:	D (25.4 mm OD x 6.35 mm maximum THK)
B. Nature of active deposit:	Evaporated metallic salt
C. Active diameter/volume:	5 mm
D. Backing:	Epoxy
E. Cover:	Acrylic

Radioimpurities:

None detected

Method of Calibration:

This source was assayed using gamma ray spectrometry.

Peak energy used for integration:	302.9, 356.0 keV
Branching ratio used:	0.183, 0.619 gammas per decay

Uncertainty of Measurement:

A. Type A (random) uncertainty:	± 0.5 %
B. Type B (systematic) uncertainty:	± 3.0 %
C. Uncertainty in aliquot weighing:	± 0.0 %
D. Total uncertainty at the 99% confidence level:	± 3.0 %

Notes:

- See reverse side for leak test(s) performed on this source.
- EZIP participates in a NIST measurement assurance program to establish and maintain implicit traceability for a number of nuclides, based on the blind assay (and later NIST certification) of Standard Reference Materials (as in NRC Regulatory Guide 4.15).
- Nuclear data was taken from IAEA-TECDOC-619, 1991.
- This source has a recommended working life of 5 years.

Daniel James Charlson — Quality Control

16-Sep-16 — Date

EZIP Ref. No.: 1893-73

ISO 9001 CERTIFIED

Medical Imaging Laboratory
24937 Avenue Tibbitts Valencia, California 91355

Industrial Gauging Laboratory
1800 North Keystone Street Burbank, California 91504

4959

Eckert & Ziegler
Isotope Products

24937 Avenue Tibbitts
Valencia, California 91355

Tel 661·309·1010
Fax 661·257·8303

CERTIFICATE OF CALIBRATION
GAMMA STANDARD SOURCE

Radionuclide:	Cd-109	**Customer:**	UT-BATTELLE LLC
Half-life:	462.6 ± 0.7 days	**P.O. No.:**	4000149401
Catalog No.:	GF-290-10D	**Reference Date:**	15-Oct-16 12:00 PST
Source No.:	1893-73-2	**Contained Radioactivity:**	9.695 µCi 358.7 kBq

Physical Description:

A. Capsule type:	D (25.4 mm OD x 6.35 mm maximum THK)
B. Nature of active deposit:	Evaporated metallic salt
C. Active diameter/volume:	5 mm
D. Backing:	Epoxy
E. Cover:	Acrylic

Radioimpurities:

Cd-115m < 0.0001%; Zn-65 < 0.0001% on 15-Oct-16

Method of Calibration:

This source was assayed using gamma ray spectrometry.

Peak energy used for integration:	88.0 keV
Branching ratio used:	0.0363 gammas per decay

Uncertainty of Measurement:

A. Type A (random) uncertainty:	± 0.3 %
B. Type B (systematic) uncertainty:	± 3.0 %
C. Uncertainty in aliquot weighing:	± 0.0 %
D. Total uncertainty at the 99% confidence level:	± 3.0 %

Notes:

- See reverse side for leak test(s) performed on this source.
- EZIP participates in a NIST measurement assurance program to establish and maintain implicit traceability for a number of nuclides, based on the blind assay (and later NIST certification) of Standard Reference Materials (as in NRC Regulatory Guide 4.15).
- Nuclear data was taken from IAEA-TECDOC-619, 1991.
- This source has a recommended working life of 2.5 years.

Daniel James Van Da Osem — 16-Sep-16

Quality Control — Date — EZIP Ref. No.: 1893-73

ISO 9001 CERTIFIED

Medical Imaging Laboratory
24937 Avenue Tibbitts Valencia, California 91355

Industrial Gauging Laboratory
1800 North Keystone Street Burbank, California 91504

4960

Eckert & Ziegler
Isotope Products

24937 Avenue Tibbitts
Valencia, California 91355

Tel 661·309·1010
Fax 661·257·8303

CERTIFICATE OF CALIBRATION
GAMMA STANDARD SOURCE

Radionuclide:	Co-57	**Customer:**	UT-BATTELLE LLC
Half-life:	271.79 ± 0.09 days	**P.O. No.:**	4000149401
Catalog No.:	GF-290-10D	**Reference Date:**	15-Oct-16 12:00 PST
Source No.:	1893-73-3	**Contained Radioactivity:**	10.18 µCi 376.7 kBq

Physical Description:

A. Capsule type:	D (25.4 mm OD x 6.35 mm maximum THK)
B. Nature of active deposit:	Evaporated metallic salt
C. Active diameter/volume:	5 mm
D. Backing:	Epoxy
E. Cover:	Acrylic

Radioimpurities:

Co-56 = 0.0411%; Co-58 = 0.00906% on 15-Oct-16

Method of Calibration:

This source was assayed using gamma ray spectrometry.

Peak energy used for integration:	122.1, 136.5 keV
Branching ratio used:	0.8560, 0.1068 gammas per decay

Uncertainty of Measurement:

A. Type A (random) uncertainty:	± 0.4 %
B. Type B (systematic) uncertainty:	± 3.0 %
C. Uncertainty in aliquot weighing:	± 0.0 %
D. Total uncertainty at the 99% confidence level:	± 3.0 %

Notes:

- See reverse side for leak test(s) performed on this source.
- EZIP participates in a NIST measurement assurance program to establish and maintain implicit traceability for a number of nuclides, based on the blind assay (and later NIST certification) of Standard Reference Materials (as in NRC Regulatory Guide 4.15).
- Nuclear data was taken from IAEA-TECDOC-619, 1991.
- This source has a recommended working life of 18 months.

Daniel James Van Delsen — 16-Sep-16

Quality Control — Date

EZIP Ref. No.: 1893-73

ISO 9001 CERTIFIED

Medical Imaging Laboratory
24937 Avenue Tibbitts Valencia, California 91355

Industrial Gauging Laboratory
1800 North Keystone Street Burbank, California 91504

4961

Eckert & Ziegler
Isotope Products

24937 Avenue Tibbitts
Valencia, California 91355

Tel 661·309·1010
Fax 661·257·8303

CERTIFICATE OF CALIBRATION
GAMMA STANDARD SOURCE

Radionuclide:	Mn-54	**Customer:**	UT-BATTELLE LLC
Half-life:	312.3 ± 0.4 days	**P.O. No.:**	4000149401
Catalog No.:	GF-290-10D	**Reference Date:**	15-Oct-16 12:00 PST
Source No.:	1893-73-6	**Contained Radioactivity:**	9.892 µCi 366.0 kBq

Physical Description:

A. Capsule type:	D (25.4 mm OD x 6.35 mm maximum THK)
B. Nature of active deposit:	Evaporated metallic salt
C. Active diameter/volume:	5 mm
D. Backing:	Epoxy
E. Cover:	Acrylic

Radioimpurities:

None detected

Method of Calibration:

This source was assayed using gamma ray spectrometry.

Peak energy used for integration:	834.8 keV
Branching ratio used:	0.9998 gammas per decay

Uncertainty of Measurement:

A. Type A (random) uncertainty:	± 0.4 %
B. Type B (systematic) uncertainty:	± 3.0 %
C. Uncertainty in aliquot weighing:	± 0.0 %
D. Total uncertainty at the 99% confidence level:	± 3.0 %

Notes:

- See reverse side for leak test(s) performed on this source.
- EZIP participates in a NIST measurement assurance program to establish and maintain implicit traceability for a number of nuclides, based on the blind assay (and later NIST certification) of Standard Reference Materials (as in NRC Regulatory Guide 4.15).
- Nuclear data was taken from IAEA-TECDOC-619, 1991.
- This source has a recommended working life of 2 years.

Daniel James VanDelsen — Quality Control

16-Sep-16 — Date

EZIP Ref. No.: 1893-73

4962

Eckert & Ziegler
Isotope Products

24937 Avenue Tibbitts
Valencia, California 91355

Tel 661·309·1010
Fax 661·257·8303

CERTIFICATE OF CALIBRATION
GAMMA STANDARD SOURCE

Radionuclide:	Na-22	**Customer:**	UT-BATTELLE LLC
Half-life:	950.8 ± 0.9 days	**P.O. No.:**	4000149401
Catalog No.:	GF-290-10D	**Reference Date:**	15-Oct-16 12:00 PST
Source No.:	1893-73-7	**Contained Radioactivity:**	10.41 µCi 385.2 kBq

Physical Description:

A. Capsule type:	D (25.4 mm OD x 6.35 mm maximum THK)
B. Nature of active deposit:	Evaporated metallic salt
C. Active diameter/volume:	5 mm
D. Backing:	Epoxy
E. Cover:	Acrylic

Radioimpurities:

None detected

Method of Calibration:

This source was assayed using gamma ray spectrometry.

Peak energy used for integration:	1275 keV
Branching ratio used:	0.9994 gammas per decay

Uncertainty of Measurement:

A. Type A (random) uncertainty:	± 0.5 %
B. Type B (systematic) uncertainty:	± 3.0 %
C. Uncertainty in aliquot weighing:	± 0.0 %
D. Total uncertainty at the 99% confidence level:	± 3.0 %

Notes:

- See reverse side for leak test(s) performed on this source.
- EZIP participates in a NIST measurement assurance program to establish and maintain implicit traceability for a number of nuclides, based on the blind assay (and later NIST certification) of Standard Reference Materials (as in NRC Regulatory Guide 4.15).
- Nuclear data was taken from IAEA-TECDOC-619, 1991.
- This source has a recommended working life of 5 years.

Daniel James Van Dalsen — 16-Sep-16

Quality Control — **Date** — EZIP Ref. No.: 1893-73

ISO 9001 CERTIFIED

Medical Imaging Laboratory
24937 Avenue Tibbitts Valencia, California 91355

Industrial Gauging Laboratory
1800 North Keystone Street Burbank, California 91504

Appendix C

Geant4 Code

```
./OpNovice [-option] [-geometry_select] [-spectrum_select]  [-particle_select]

PARAMETERS:
[OpNovice]          Name of the executive file.
[-option]
    -m [file]    Passes the file name of the macro which contains
                 information on the number of histories to simulate.
                 If not included, the OpenGL GUI will be displayed
                 for geometry inspection.
    -r [val]     Sets the random number seed to [val] (optional).
    -t [val]     Sets the number of threads to be used (default = 1).
    -c [val]     Sets the threshold for the scintillation detectors
                 to [val] which is expressed in keV (default = 200 keV).
[-geometry_select]
    -assay       Selects the LSD mock-up assay.
    -lancs       Selects the REFL15 setup.
    -l           Selects the BARE15 setup.
    !!!!If neither -lancs or -l flag is not used, BARE8 is used.
    -w [val]     Selects the radius of water filled cylinder used in
                 neutron spectroscopy experiments. Only functional if
                 -assay and -lancs flags are not used.
[-spectrum_select]
    -mono        Sets the particle generator to use mono-energetic
                 particle beams with a directional vector of (0, 0, 1).
                 The energy is defined by the -n or -g flag.
    -AmLi        Sets the particle generator to use approximated AmLi
                 neutron particle.
    !!!!If neither [-spectrum_select] flag is used, FREYA generated Cf-252
    spectrum is used.
[-particle_select]
    -n [energy]  Selects neutron particles to be simulated. If -mono flag
                 has been declared, then the neutron energy is set assay
                 [energy] keV. Otherwise only neutrons from FREYA Cf-252
                 distribution is simulated.
    -g [energy]  Selects photon particles to be simulated. If -mono flag
                 has been declared, then the photon energy is set assay
                 [energy] keV. Otherwise only photons from FREYA Cf-252
                 distribution is simulated.
```

Figure C.1 | Geant4 simulator arguments. The Geant4 model was designed such that all the different major geometries (i.e. *BARE8*, *BARE15*, *REFL15* and scintillant based assay mock-up) and sources used in this research can be configured and executed from a single executable. The command-line arguments listed above can be used to switch between different options.

C.1 Main function

```
//
// ********************************************************************
// *                                                                  *
// * This  code  implementation is the based on the example provided  *
// * by the GEANT4 collaboration.                                     *
// * By using,  copying,  modifying or  distributing the software (or *
// * any work based  on the software)  you  agree  to acknowledge its *
// * use  in  resulting  scientific  publications,  and indicate your *
// * acceptance of all terms of the Geant4 Software license.          *
// ********************************************************************
/*
The Main fucntion of the Geant4 simulation model
Based on OpNovice example provided with the Geant4 toolket.
*/
//....oooOO0OOooo........oooOO0OOooo........oooOO0OOooo........oooOO0OOooo......
namespace {
  void PrintUsage() {
    G4cerr << " Usage: " << G4endl;
    G4cerr << " OpNovice [-m macro ] [-u UIsession] [-t nThreads] [-r seed] [-c cutoff] [-mono beam]"
           << G4endl;
    G4cerr << "   note: -t option is available only for multi-threaded mode."
           << G4endl;
  }
}

//....oooOO0OOooo........oooOO0OOooo........oooOO0OOooo........oooOO0OOooo......

int main(int argc,char** argv)
{
  // Evaluate arguments
  //
  if ( argc > 20 ) {
    PrintUsage();
    return 1;
  }
  SourceListing *SL;
  //SL = new SourceListing();
  G4String macro;
  G4String session;
#ifdef G4MULTITHREADED
  G4int nThreads = 0;
#endif

  G4long myseed = 345354;
  for ( G4int i=1; i<argc; i=i+2 )
  {
        if      ( G4String(argv[i]) == "-m" ) macro   = argv[i+1];
        else if ( G4String(argv[i]) == "-u" ) session = argv[i+1];
        else if ( G4String(argv[i]) == "-r" ) myseed  = atoi(argv[i+1]);
        else if (G4String(argv[i]) == "-c")
            RunAction::cutOu = atoi(argv[i + 1]);
        else if (G4String(argv[i]) == "-l")
        {
            DetectorConstruction::nb_cryst = 15;
            DetectorConstruction::ring_R1 = 26.25 * cm;
        }
        else if (G4String(argv[i]) == "-w")
        {
            DetectorConstruction::ring_W1 = atoi(argv[i+1])/10 * cm;
        }
        else if (G4String(argv[i]) == "-j")
        {
            PrimaryGeneratorAction::gamma = true;
            PrimaryGeneratorAction::neutron = true;
        }
        else if (G4String(argv[i]) == "-mono")
        {
            PrimaryGeneratorAction::mono = true;
            if ( atoi(argv[i + 1]) == 1 )
                PrimaryGeneratorAction::beam = true;
```

4974

```
71
72          }
73          else if (G4String(argv[i]) == "-AmLi")
74          {
75              PrimaryGeneratorAction::AmLi = true;
76              PrimaryGeneratorAction::neutron = true;
77              PrimaryGeneratorAction::energy = 4121;
78          }
79          else if (G4String(argv[i]) == "-cmod")
80          {
81              PrimaryGeneratorAction::sfif = true;
82              std::string s1(argv[i+1]);
83              SponFiss_FF::filename = s1;
84          }
85          else if (G4String(argv[i]) == "-Co")
86          {
87              PrimaryGeneratorAction::Co = true;
88              PrimaryGeneratorAction::neutron = false;
89              PrimaryGeneratorAction::gamma = true;
90              PrimaryGeneratorAction::name = "gamma";
91              PrimaryGeneratorAction::mono = false;
92              PrimaryGeneratorAction::beam = false;
93              PrimaryGeneratorAction::energy = 1121;
94          }
95          else if (G4String(argv[i]) == "-g")
96          {
97              PrimaryGeneratorAction::gamma = true;
98              PrimaryGeneratorAction::neutron = false;
99              PrimaryGeneratorAction::energy = atoi(argv[i + 1]);
100             PrimaryGeneratorAction::name = "gamma";
101
102         }
103         else if (G4String(argv[i]) == "-n")
104         {
105             PrimaryGeneratorAction::gamma = false;
106             PrimaryGeneratorAction::neutron = true;
107             PrimaryGeneratorAction::energy = atoi(argv[i + 1]);
108         }
109         else if (G4String(argv[i]) == "-mode")
110         {
111             PrimaryGeneratorAction::mode = atoi(argv[i + 1]);
112         }
113         else if (G4String(argv[i]) == "-gw")
114         {
115             SteppingAction::gwidth = atoi(argv[i + 1]);
116         }
117         else if (G4String(argv[i]) == "-lancs")
118         {
119             DetectorConstruction::lancs = true;
120         }
121
122 #ifdef G4MULTITHREADED
123         else if ( G4String(argv[i]) == "-t" ) {
124                     nThreads = G4UIcommand::ConvertToInt(argv[i+1]);
125         }
126 #endif
127         else {
128             std::cout << argv[i] << std::endl;
129             PrintUsage();
130             return 1;
131         }
132   }
133
134   // Choose the Random engine
135   //
136   G4Random::setTheEngine(new CLHEP::RanecuEngine);
137
138   // Construct the default run manager
139   //
140 #ifdef G4MULTITHREADED
141   G4MTRunManager * runManager = new G4MTRunManager;
```

4975

```
  if ( nThreads > 0 ) runManager->SetNumberOfThreads(nThreads);
#else
  G4RunManager * runManager = new G4RunManager;
#endif

  // Seed the random number generator manually
  G4Random::setTheSeed(myseed);
    DetectorConstruction* dDet = new DetectorConstruction();
  // Set mandatory initialization classes
  //
  // Detector construction
    runManager->SetUserInitialization(dDet);
  // Physics list
  runManager-> SetUserInitialization(new PhysicsList());
  // User action initialization
    runManager->SetUserInitialization(new ActionInitialization(dDet));

  // Initialize G4 kernel
  //
  runManager->Initialize();

#ifdef G4VIS_USE
  // Initialize visualization
  //
  G4VisManager* visManager = new G4VisExecutive;
  // G4VisExecutive can take a verbosity argument - see /vis/verbose guidance.
  // G4VisManager* visManager = new G4VisExecutive("Quiet");
  visManager->Initialize();
#endif

  // Get the pointer to the User Interface manager
  //
  G4UImanager* UImanager = G4UImanager::GetUIpointer();

  if ( macro.size() ) {
     // Batch mode
     G4String command = "/control/execute ";
     UImanager->ApplyCommand(command+macro);
  }
  else // Define UI session for interactive mode
  {
#ifdef G4UI_USE
     G4UIExecutive * ui = new G4UIExecutive(argc,argv,session);
#ifdef G4VIS_USE
     UImanager->ApplyCommand("/control/execute vis.mac");
#else
     UImanager->ApplyCommand("/control/execute OpNovice.in");
#endif
     if (ui->IsGUI())
        UImanager->ApplyCommand("/control/execute gui.mac");
     ui->SessionStart();
     delete ui;
#endif
  }

  // Job termination
  // Free the store: user actions, physics_list and detector_description are
  //                 owned and deleted by the run manager, so they should not
  //                 be deleted in the main() program !

#ifdef G4VIS_USE
  delete visManager;
#endif
  delete runManager;

  return 0;
}
```

C.2 Material constructor

```
/*
The DetectorConstruction class inherrits from the G4VUserDetectorConstruction
which lets the user assign the tpye and properties of geometry that is to be
simulated.
*/

////////////////////////////////////////////////////////////////////////////////
// DefineMaterials method who assigns all the material and detector
// materials
////////////////////////////////////////////////////////////////////////////////
void DetectorConstruction::DefineMaterials()
{
    G4NistManager* nist = G4NistManager::Instance();
    G4double a;  // atomic mass
    G4double z;  // atomic number

    G4int polyPMMA = 1;
    G4int nC_PMMA = 3 + 2 * polyPMMA;
    G4int nH_PMMA = 6 + 2 * polyPMMA;
    G4int polyeth = 1;
    G4int nC_eth = 2 * polyeth;
    G4int nH_eth = 4 * polyeth;
    //
    // ------------ Generate & Add Material Properties Table ------------
    //

    G4double wls_Energy[] =
    { 2.00 * eV, 2.87 * eV, 2.90 * eV, 3.47 * eV };
    const G4int wlsnum = sizeof(wls_Energy) / sizeof(G4double);

    G4double AbsFiber[] =
    { 9.00 * m, 9.00 * m, 0.1 * mm, 0.1 * mm };
    assert(sizeof(AbsFiber) == sizeof(wls_Energy));

//fiber
    G4double EmissionFib[] =
    { 1.0, 1.0, 0.0, 0.0 };
    assert(sizeof(EmissionFib) == sizeof(wls_Energy));
    G4double RefractiveIndexFiber[] =
    { 1.60, 1.60, 1.60, 1.60 };
    assert(sizeof(RefractiveIndexFiber) == sizeof(wls_Energy));
    ////////////////////////////////////////////////////////
//***Elements
    G4String symbol;
    G4double density;
    G4int Z, A, n_iso;


    fN = new G4Element(symbol = "N", symbol = "N", n_iso = 2);
    fiN = new G4Isotope(symbol = "N", Z = 7, A = 14);
    fN->AddIsotope(fiN, 99.6 * perCent);
    G4Isotope *fiN15 = new G4Isotope(symbol = "N", Z = 7, A = 15);
    fN->AddIsotope(fiN15, 99.6 * perCent);

    fO = new G4Element(symbol = "O", symbol = "O", n_iso = 3);
    fiO = new G4Isotope(symbol = "O", Z = 8, A = 16);
    G4Isotope *fiO17 = new G4Isotope(symbol = "O", Z = 8, A = 17);
    G4Isotope *fiO18 = new G4Isotope(symbol = "O", Z = 8, A = 18);
    fO->AddIsotope(fiO, 99.76 * perCent);
    fO->AddIsotope(fiO17, 0.04 * perCent);
    fO->AddIsotope(fiO18, 0.2 * perCent);

    fH = new G4Element(symbol = "H", symbol = "H", n_iso = 2);
    fiH = new G4Isotope(symbol = "H", Z = 1, A = 1);
    G4Isotope *fiH2 = new G4Isotope(symbol = "H", Z = 1, A = 2);
    fH->AddIsotope(fiH, 99.98 * perCent);
    fH->AddIsotope(fiH2, 0.02 * perCent);

    fC = new G4Element(symbol = "C", symbol = "C", n_iso = 2);
    fiC = new G4Isotope(symbol = "C", Z = 6, A = 12);
    G4Isotope *fiC2 = new G4Isotope(symbol = "C", Z = 6, A = 13);
```

4978

```
71      fC->AddIsotope(fiC, 98.9 * perCent);
72      fC->AddIsotope(fiC2, 1.1 * perCent);
73
74      fCa = new G4Element(symbol = "Ca", symbol = "Ca", n_iso = 6);
75      fiCa = new G4Isotope(symbol = "Ca", Z = 20, A = 40);
76      G4Isotope *fiCa2 = new G4Isotope(symbol = "Ca", Z = 20, A = 42);
77      G4Isotope *fiCa3 = new G4Isotope(symbol = "Ca", Z = 20, A = 43);
78      G4Isotope *fiCa4 = new G4Isotope(symbol = "Ca", Z = 20, A = 44);
79      G4Isotope *fiCa5 = new G4Isotope(symbol = "Ca", Z = 20, A = 46);
80      G4Isotope *fiCa6 = new G4Isotope(symbol = "Ca", Z = 20, A = 48);
81      fCa->AddIsotope(fiCa, 96.941 * perCent);
82      fCa->AddIsotope(fiCa2, .647 * perCent);
83      fCa->AddIsotope(fiCa3, .135 * perCent);
84      fCa->AddIsotope(fiCa4, 2.086 * perCent);
85      fCa->AddIsotope(fiCa5, .004 * perCent);
86      fCa->AddIsotope(fiCa6, .187 * perCent);
87
88      fS = new G4Element(symbol = "S", symbol = "S", n_iso = 4);
89      fiS = new G4Isotope(symbol = "S", Z = 16, A = 32);
90      G4Isotope *fiS2 = new G4Isotope(symbol = "S", Z = 16, A = 33);
91      G4Isotope *fiS3 = new G4Isotope(symbol = "S", Z = 16, A = 34);
92      G4Isotope *fiS4 = new G4Isotope(symbol = "S", Z = 16, A = 36);
93      fS->AddIsotope(fiS, 94.99 * perCent);
94      fS->AddIsotope(fiS2, .75 * perCent);
95      fS->AddIsotope(fiS3, 4.25 * perCent);
96      fS->AddIsotope(fiS4, .01 * perCent);
97
98      fLi = new G4Element(symbol = "L", symbol = "Li", n_iso = 2);
99      fiLi = new G4Isotope(symbol = "Li", Z = 3, A = 6);
100     G4Isotope *fiLi2 = new G4Isotope(symbol = "Li", Z = 3, A = 7);
101     fLi->AddIsotope(fiLi, 7.59 * perCent);
102     fLi->AddIsotope(fiLi2, 92.41 * perCent);
103
104     fAm = new G4Element("Am", "Am", z = 92., a = 241 * g / mole);
105
106
107     fiU233 = new G4Isotope(symbol = "U", Z = 92, A = 234);
108     fiU235 = new G4Isotope(symbol = "U", Z = 92, A = 235);
109     fiU236 = new G4Isotope(symbol = "U", Z = 92, A = 236);
110     fiU238 = new G4Isotope(symbol = "U", Z = 92, A = 238);
111     fU = new G4Element(symbol = "U", symbol = "U", n_iso = 4);
112     fU->AddIsotope(fiU233, .149 * perCent);
113     fU->AddIsotope(fiU235, U235p * perCent);
114     fU->AddIsotope(fiU236, .197 * perCent);
115     fU->AddIsotope(fiU238, (100 - .149 - .197 - U235p) * perCent);
116     fUOx = new G4Material("UOx", density = 12.69 * g / cm3, 2);
117     fUOx->AddElement(fU, 84.5 * perCent);
118     fUOx->AddElement(fO, 15.5 * perCent);
119
120     // cross section for Z > 92 has restrictions, which prevents its
121     // use in public clusters
122     Z = 92; //94;
123     fiPu238 = new G4Isotope(symbol = "Pu", Z, A);// = 238);
124     fiPu239 = new G4Isotope(symbol = "Pu", Z, A);// = 239);
125     fiPu240 = new G4Isotope(symbol = "Pu", Z, A);// = 240);
126     fiPu241 = new G4Isotope(symbol = "Pu", Z, A);// = 241);
127     fiPu242 = new G4Isotope(symbol = "Pu", Z, A);// = 242);
128     fPu = new G4Element(symbol = "U", symbol = "U", n_iso = 5);
129     fPu->AddIsotope(fiPu238, .149 * perCent);
130     fPu->AddIsotope(fiPu239, U235p * perCent);
131     fPu->AddIsotope(fiPu240, .197 * perCent);
132     fPu->AddIsotope(fiPu241, (100 - .149 - .197 - U235p) * perCent);
133     fPu->AddIsotope(fiPu242, .2 * perCent);
134
135     Z = 92; //94;
136     fiCm242 = new G4Isotope(symbol = "Cm", Z, A);// = 242);
137     fiCm244 = new G4Isotope(symbol = "Cm", Z, A);// = 244);
138     fiCm248 = new G4Isotope(symbol = "Cm", Z, A);// = 248);
139     fiCm246 = new G4Isotope(symbol = "Cm", Z, A);// = 246);
140     fCm = new G4Element(symbol = "Cm", symbol = "Cm", n_iso = 4);
141     fCm->AddIsotope(fiCm242, 22 * perCent);
```

4979

```
142        fCm->AddIsotope(fiCm244, 70 * perCent);
143        fCm->AddIsotope(fiCm246, 5 * perCent);
144        fCm->AddIsotope(fiCm248, 3 * perCent);
145
146        fPu_src = new G4Material("POx", density = 12.69 * g / cm3, 3);
147        fPu_src->AddElement(fPu, 80.0 * perCent);
148        fPu_src->AddElement(fCm, 4.5 * perCent);
149        fPu_src->AddElement(fO, 15.5 * perCent);
150
151        fiCf249 = new G4Isotope(symbol = "Cf", Z, A);// = 249);
152        fiCf250 = new G4Isotope(symbol = "Cf", Z, A);// = 250);
153        fiCf251 = new G4Isotope(symbol = "Cf", Z, A);// = 251);
154        fiCf252 = new G4Isotope(symbol = "Cf", Z, A);// = 252);
155        fiCf254 = new G4Isotope(symbol = "Cf", Z, A);// = 254);
156        fiCf256 = new G4Isotope(symbol = "Cf", Z, A);// = 254);
157        fCf = new G4Element(symbol = "Cf", symbol = "Cf", n_iso = 6);
158        fCf->AddIsotope(fiCf249, 3.411 * perCent);
159        fCf->AddIsotope(fiCf250, 8.702 * perCent);
160        fCf->AddIsotope(fiCf251, 2.6 * perCent);
161        fCf->AddIsotope(fiCf252, 85.273 * perCent);
162        fCf->AddIsotope(fiCf254, .004 * perCent);
163        fCf->AddIsotope(fiCf256, .01 * perCent);
164
165        fCf_src = new G4Material("Cf-252", density = 12.69 * g / cm3, 2);
166        fCf_src->AddElement(fCf, 96.625 * perCent);
167        fCf_src->AddElement(fCm, (100 - 96.625) * perCent);
168
169
170        fAmLi = new G4Material("AmLi", density = 12 * g / cm3, 2);
171        fAmLi->AddElement(fAm, 1);
172        fAmLi->AddElement(fLi, 3);
173        //***Materials
174        //Aluminum
175        fAl = new G4Material("Al", z = 13., a = 26.98 * g / mole,
176                density = 2.7 * g / cm3);
177        //Vacuum
178        fVacuum = new G4Material("Vacuum", z = 1., a = 1.01 * g / mole, density =
179                universe_mean_density, kStateGas, 0.1 * kelvin, 1.e-19 * pascal);
180        //Steel
181        fSteel = nist->FindOrBuildMaterial("G4_STAINLESS-STEEL");
182        //concrete
183        fConcrete = nist->FindOrBuildMaterial("G4_CONCRETE");
184        //plaster
185        fplaster = new G4Material("Plaster", density = 0.85 * g / cm3, 3);
186        fplaster->AddElement(fO, 4);
187        fplaster->AddElement(fCa, 1);
188        fplaster->AddElement(fS, 1);
189        //source
190        // wood
191        fWood = new G4Material("Wood", density = 0.90 * g / cm3, 4);
192        fWood->AddElement(fC, 50 * perCent);
193        fWood->AddElement(fO, 42 * perCent);
194        fWood->AddElement(fH, 7 * perCent);
195        fWood->AddElement(fN, 1 * perCent);
196        // lead
197        fLead = nist->FindOrBuildMaterial("G4_LEAD_OXIDE");
198
199        //water
200        fwater = new G4Material("Water_ts", 1.000 * g / cm3, 2, kStateLiquid,
201                300 * kelvin, 150 * bar);
202        fwater->AddElement(fO, 1);
203        G4Element* H = new G4Element("TS_H_of_Water", "H", 1., 1.0079 * g / mole);
204        fwater->AddElement(H, 2);
205        fwater->GetIonisation()->SetMeanExcitationEnergy(78.0 * eV);
206
207        //HE3
208        G4Isotope* He3 = new G4Isotope("He3", z = 2, 3, a = 235.01 * g / mole);
209        G4Element * eHe3 = new G4Element("He3Det", "He3", 1);
210        eHe3->AddIsotope(He3, 100. * perCent);
211        fHe3 = new G4Material("Plaster", density = 0.0495 * kg / m3, 1);
212        fHe3->AddElement(eHe3, 1);
```

4980

```
213        fCd = nist->FindOrBuildMaterial("G4_Cd");
214        fPb = nist->FindOrBuildMaterial("G4_Pb");
215        //Pyrex
216        fPyrex = nist->FindOrBuildMaterial("G4_Pyrex_Glass");
217        fPyrex->GetIonisation()->SetBirksConstant(0.126 * mm / MeV);
218        fPyrex->SetMaterialPropertiesTable(matH2O);
219        //Glass
220        fGlass = new G4Material("Glass", density = 1.032 * g / cm3, 2);
221        fGlass->AddElement(fC, 91.533 * perCent);
222        fGlass->AddElement(fH, 8.467 * perCent);
223        fGlass->GetIonisation()->SetBirksConstant(0.126 * mm / MeV);
224        fGlass->SetMaterialPropertiesTable(matH2O);
225        //Pstyrene
226        fPstyrene = nist->FindOrBuildMaterial("G4_POLYSTYRENE");
227        fPstyrene->GetIonisation()->SetBirksConstant(0.126 * mm / MeV);
228        fPstyrene->SetMaterialPropertiesTable(matH2O);
229        //Double cladding(flourinated polyethylene)
230        fPethylene2 = new G4Material("Pethylene2", density = 1400 * kg / m3, 2);
231        fPethylene2->AddElement(fH, nH_eth);
232        fPethylene2->AddElement(fC, nC_eth);
233        G4double RefractiveIndexPethylene2[] =
234        { 1.42, 1.42, 1.42, 1.42 };
235        assert(sizeof(RefractiveIndexPethylene2) == sizeof(wls_Energy));
236        G4MaterialPropertiesTable* Pethylene2Properties =
237                new G4MaterialPropertiesTable();
238        Pethylene2Properties->AddProperty("RINDEX", wls_Energy,
239                RefractiveIndexPethylene2, wlsnum);
240        Pethylene2Properties->AddProperty("ABSLENGTH", wls_Energy, AbsFiber,
241                wlsnum);
242        fPethylene2->SetMaterialPropertiesTable(Pethylene2Properties);
243        //Cladding(polyethylene)
244        fPethylene1 = new G4Material("Pethylene1", density = 1200 * kg / m3, 2);
245        fPethylene1->AddElement(fH, nH_eth);
246        fPethylene1->AddElement(fC, nC_eth);
247        G4double RefractiveIndexPethylene1[] =
248        { 1.49, 1.49, 1.49, 1.49 };
249        assert(sizeof(RefractiveIndexPethylene1) == sizeof(wls_Energy));
250        G4MaterialPropertiesTable* Pethylene1Properties =
251                new G4MaterialPropertiesTable();
252        Pethylene1Properties->AddProperty("RINDEX", wls_Energy,
253                RefractiveIndexPethylene1, wlsnum);
254        Pethylene1Properties->AddProperty("ABSLENGTH", wls_Energy, AbsFiber,
255                wlsnum);
256        fPethylene1->SetMaterialPropertiesTable(Pethylene1Properties);
257        //Air
258        fAir = nist->FindOrBuildMaterial("G4_AIR");
259
260        // photocathod + scintillator
261        fPMMA = new G4Material("PMMA", density = 1190 * kg / m3, 3);
262        fPMMA->AddElement(fH, 52);
263        fPMMA->AddElement(fC, 43);
264        fPMMA->AddElement(fO, 18);
265
266        fscintillator = new G4Material("Scintillator",
267                density = 0.964  * g / cm3, 2,  kStateLiquid);
268        fscintillator->AddElement(fH, 5);
269        fscintillator->AddElement(fC, 4);
270
271        fPyrex->GetIonisation()->SetBirksConstant(0.126 * mm / MeV);
272
273        G4double scintillator_Energy[] =
274                { 3.2204 * eV, 3.0996 * eV, 2.9876 * eV, 2.9173 * eV, 2.8700 * eV,
275                 2.8114* eV, 2.3616 * eV };
276        const G4int scintillatornum = sizeof(scintillator_Energy)
277                / sizeof(G4double);
278
279        G4double SCY_Energy[201] =
280                {0.01000*MeV, 0.1000*MeV, 0.2000*MeV, 0.3000*MeV, 0.4000*MeV, ...
281                0.5000*MeV, 0.6000*MeV, 0.7000*MeV, 0.8000*MeV, 0.9000*MeV, ...
282                1*MeV, 1.100*MeV, 1.200*MeV, 1.300*MeV, 1.400*MeV, 1.500*MeV, ...
283                1.600*MeV, 1.700*MeV, 1.800*MeV, 1.900*MeV, 2*MeV, 2.100*MeV,...
```

4981

```
            2.200*MeV, 2.300*MeV, 2.400*MeV,2.500*MeV, 2.600*MeV, 2.700*MeV, ...
            2.800*MeV, 2.900*MeV, 3*MeV, 3.100*MeV, 3.200*MeV, 3.300*MeV, ...
            3.400*MeV, 3.500*MeV, 3.600*MeV, 3.700*MeV, 3.800*MeV, 3.900*MeV, ...
            4*MeV, 4.100*MeV, 4.200*MeV, 4.300*MeV, 4.400*MeV, 4.500*MeV, ...
            4.600*MeV, 4.700*MeV, 4.800*MeV, 4.900*MeV, 5*MeV, 5.100*MeV, ...
            5.200*MeV, 5.300*MeV, 5.400*MeV, 5.500*MeV, 5.600*MeV, 5.700*MeV, ...
            5.800*MeV, 5.900*MeV, 6*MeV, 6.100*MeV, 6.200*MeV, 6.300*MeV, ...
            6.400*MeV, 6.500*MeV, 6.600*MeV, 6.700*MeV, 6.800*MeV, 6.900*MeV, ...
            7*MeV, 7.100*MeV, 7.200*MeV, 7.300*MeV, 7.400*MeV, 7.500*MeV, ...
            7.600*MeV, 7.700*MeV, 7.800*MeV, 7.900*MeV, 8*MeV, 8.100*MeV, ...
            8.200*MeV, 8.300*MeV, 8.400*MeV, 8.500*MeV, 8.600*MeV, 8.700*MeV, ...
            8.800*MeV, 8.900*MeV, 9*MeV, 9.100*MeV, 9.200*MeV, 9.300*MeV, ...
            9.400*MeV, 9.500*MeV, 9.600*MeV, 9.700*MeV, 9.800*MeV, 9.900*MeV, ...
            10*MeV, 10.10*MeV, 10.20*MeV, 10.30*MeV, 10.40*MeV, 10.50*MeV, ...
            10.60*MeV, 10.70*MeV, 10.80*MeV, 10.90*MeV, 11*MeV, 11.10*MeV, ...
            11.20*MeV, 11.30*MeV, 11.40*MeV, 11.50*MeV, 11.60*MeV, 11.70*MeV, ...
            11.80*MeV, 11.90*MeV, 12*MeV, 12.10*MeV, 12.20*MeV, 12.30*MeV, ...
            12.40*MeV, 12.50*MeV, 12.60*MeV, 12.70*MeV, 12.80*MeV, 12.90*MeV, ...
            13*MeV, 13.10*MeV, 13.20*MeV, 13.30*MeV, 13.40*MeV, 13.50*MeV, ...
            13.60*MeV, 13.70*MeV, 13.80*MeV, 13.90*MeV, 14*MeV, 14.10*MeV, ...
            14.20*MeV, 14.30*MeV, 14.40*MeV, 14.50*MeV, 14.60*MeV, 14.70*MeV, ...
            14.80*MeV, 14.90*MeV, 15*MeV, 15.10*MeV, 15.20*MeV, 15.30*MeV, ...
            15.40*MeV, 15.50*MeV, 15.60*MeV, 15.70*MeV, 15.80*MeV, 15.90*MeV, ...
            16*MeV, 16.10*MeV, 16.20*MeV, 16.30*MeV, 16.40*MeV, 16.50*MeV, ...
            16.60*MeV, 16.70*MeV, 16.80*MeV, 16.90*MeV, 17*MeV, 17.10*MeV, ...
            17.20*MeV, 17.30*MeV, 17.40*MeV, 17.50*MeV, 17.60*MeV, 17.70*MeV, ...
            17.80*MeV, 17.90*MeV, 18*MeV, 18.10*MeV, 18.20*MeV, 18.30*MeV, ...
            18.40*MeV, 18.50*MeV, 18.60*MeV, 18.70*MeV, 18.80*MeV, 18.90*MeV, ...
            19*MeV, 19.10*MeV, 19.20*MeV, 19.30*MeV, 19.40*MeV, 19.50*MeV, ...
            19.60*MeV, 19.70*MeV, 19.80*MeV, 19.90*MeV, 20 *MeV};

    G4double SCY_Electron[201] = { 123, 1230, 2460, 3690.000, 4920, 6150, ...
            7380.000, 8610, 9840, 11070, 12300, 13530.00, 14760.00, 15990, ...
            17220, 18450, 19680, 20910.00, 22140, 23370, 24600, 25830, 27060, ...
            28290.00, 29520.00, 30750, 31980, 33210, 34440, 35670.00, 36900, ...
            38130, 39360, 40590, 41820.00, 43050, 44280, 45510, 46740, 47970.00,...
            49200, 50430.00, 51660, 52890, 54120.00, 55350, 56580.00, 57810, ...
            59040.00, 60270.00, 61500, 62730.00, 63960, 65190.00, 66420, 67650, ...
            68880, 70110, 71340.00, 72570, 73800, 75030, 76260, 77490.00, ...
            78720, 79950, 81180, 82410, 83640.00, 84870, 86100, 87330, 88560, ...
            89790.00, 91020, 92250, 93480, 94710, 95940.00, 97170, 98400, ...
            99630, 100860.0, 102090.0, 103320, 104550, 105780, 107010.0, ...
            108240.0, 109470, 110700, 111930, 113160.0, 114390.0, 115620, ...
            116850, 118080.0, 119310.0, 120540.0, 121770, 123000, 124230, ...
            125460.0, 126690.0, 127920.0, 129150, 130380, 131610, 132840, ...
            134070, 135300, 136530, 137760, 138990, 140220, 141450, 142680, ...
            143910, 145140, 146370, 147600, 148830, 150060, 151290, 152520.0, ...
            153750, 154980, 156210, 157440, 158670.0, 159900, 161130, 162360, ...
            163590, 164820.0, 166050, 167280, 168510, 169740, 170970.0, 172200, ...
            173430, 174660, 175890, 177120.0, 178350, 179580, 180810, 182040, ...
            183270.0, 184500, 185730, 186960, 188190, 189420.0, 190650, ...
            191880, 193110, 194340, 195570.0, 196800, 198030.0, 199260, 200490, ...
            201720.0, 202950, 204180.0, 205410, 206640, 207870.0, 209100, ...
            210330.0, 211560, 212790, 214020.0, 215250, 216480.0, 217710, ...
            218940, 220170.0, 221400, 222630.0, 223860, 225090, 226320.0, ...
            227550, 228780.0, 230010, 231240, 232470.0, 233700, 234930.0, ...
            236160, 237390, 238620.0, 239850, 241080.0, 242310, 243540, ...
            244770.0, 246000 };
    G4double SCY_Proton[201] = { 4.55700250495120, 58.2718603538135, ...
            144.245466277281, 257.110173580758, 396.079060189878, ...
            560.388231958463, 749.296148795582, 962.082970512382, ...
            1198.04992181157, 1456.51867585940, 1736.83075589639, ...
            2038.34695435885, 2360.44676899881, 2702.52785550500, ...
            3064.00549614188, 3444.31208393803, 3842.89662196899, ...
            4259.22423729255, 4692.77570910807, 5143.04701072333, ...
            5609.54886492490, 6091.80631235992, 6589.35829254840, ...
            7101.75723715646, 7628.56867517177, ...
            8169.37084963287, 8723.75434557418, 9291.32172885864, ...
            9871.68719557923, 10464.4762317202, 11069.3252827778, ...
            11685.8814330487, 12313.8020943040, 12952.7547035729, ...
            13602.4164297713, 14262.4738889143, 14932.6228676632, ...
```

4982

```
355                 15612.5680549620, 16302.0227815277, ...
356                 17000.7087669635, 17708.3558742720, 18424.7018715531, ...
357                 19149.4922006745, 19882.4797527122, 20623.4246499620, ...
358                 21372.0940343304, 22128.2618619176, 22891.7087036116, ...
359                 23662.2215515183, 24439.5936310549, ...
360                 25223.6242185431, 26014.1184641396, 26810.8872199485, ...
361                 27613.7468731633, 28422.5191840923, 29237.0311289233, ...
362                 30057.1147470900, 30882.6069931048, 31713.3495927271, ...
363                 32549.1889033415, 33389.9757784206, 34235.5654359550, ...
364                 35085.8173307332, 35940.5950303589, 36799.7660948961, ...
365                 37663.2019600374, 38530.7778236897, 39402.3725358796, ...
366                 40277.8684918803, 41157.1515284664, 42040.1108232038, ...
367                 42926.6387966873, 43816.6310176390, 44709.9861107837, ...
368                 45606.6056674201, 46506.3941586093, ...
369                 47409.2588509032, 48315.1097245396, 49223.8593940304, ...
370                 50135.4230310745, 51049.7182897258, 51966.6652337514, ...
371                 52886.1862661157, 53808.2060605272, 54732.6514949899, ...
372                 55659.4515872976, 56588.5374324169, 57519.8421417026, ...
373                 58453.3007838910, 59388.8503278209, ...
374                 60326.4295868300, 61265.9791647792, 62207.4414036557, ...
375                 63150.7603327097, 64095.8816190799, 65042.7525198630, ...
376                 65991.3218355865, 66941.5398650431, 67893.3583614461, ...
377                 68846.7304898684, 69801.6107859273, 70757.9551156769, ...
378                 71715.7206366763, 72674.8657601950, 73635.3501145255, ...
379                 74597.1345093695, 75560.1809012655, 76524.4523600290, ...
380                 77489.9130361739, 78456.5281292883, ...
381                 79424.2638573346, 80393.0874268487, 81362.9670040114, ...
382                 82333.8716865654, 83305.7714765555, 84278.6372538648, ...
383                 85252.4407505272, 86227.1545257903, 87202.7519419080, ...
384                 88179.2071406427, 89156.4950204536, 90134.5912143536, ...
385                 91113.4720684138, 92093.1146208971, 93073.4965820024, ...
386                 94054.5963142013, 95036.3928131508, 96018.8656891640, ...
387                 97001.9951492235, 97985.7619795204, 98970.1475285051, ...
388                 99955.1336904338, 100940.702889396, 101926.838063811, ...
389                 102913.522651376, 103900.740574453, 104888.476225893, ...
390                 105876.714455260, 106865.440555471, 107854.640249821, ...
391                 108844.299679387, 109834.405390805, 110824.944324400, ...
392                 111815.903802666, 112807.271519083, 113799.035527259, ...
393                 114791.184230395, 115783.706371051, 116776.591021216, ...
394                 117769.827572670, 118763.405727624, 119757.315489636, ...
395                 120751.547154793, 121746.091303149, 122740.938790419, ...
396                 123736.080739908, 124731.508534683, 125727.213809971, ...
397                 126723.188445780, 127719.424559734, 128715.914500124, ...
398                 129712.650839152, 130709.626366385, 131706.834082388, ...
399                 132704.267192554, 133701.919101110, 134699.783405293, ...
400                 135697.853889711, 136696.124520850, 137694.589441760, ...
401                 138693.242966883, 139692.079577039, 140691.093914558, ...
402                 141690.280778552, 142689.635120330, 143689.152038941, ...
403                 144688.826776852, 145688.654715751, 146688.631372473, ...
404                 147688.752395046, 148689.013558850, 149689.410762892, ...
405                 150689.940026186, 151690.597484246, 152691.379385669, ...
406                 153692.282088835, 154693.302058686, 155694.435863615, ...
407                 156695.680172431, 157697.031751429, 158698.487461529, ...
408                 159700.044255513, 160701.699175334, 161703.449349508, ...
409                 162705.291990578, 163707.224392659, 164709.243929050, ...
410                 165711.348049912, 166713.534280027, 167715.800216608, 168718.143527181 };
411
412         G4double scintillator_SCINT[] =
413         { 0.1, 0.65, 0.75, 1.0, 0.8, 0.7, 0.1 };
414         assert(sizeof(scintillator_SCINT) == sizeof(scintillator_Energy));
415         G4double scintillator_RIND[] =
416         { 1.59, 1.58, 1.58, 1.57, 1.56, 1.55, 1.54 };
417         assert(sizeof(scintillator_RIND) == sizeof(scintillator_Energy));
418         G4double scintillator_ABSL[] =
419         { 35. * cm, 35. * cm, 35. * cm, 35. * cm, 35. * cm, 35. * cm, 35. * cm };
420         assert(sizeof(scintillator_ABSL) == sizeof(scintillator_Energy));
421         fScintillator_mt = new G4MaterialPropertiesTable();
422         fScintillator_mt->AddProperty("FASTCOMPONENT", scintillator_Energy,
423                 scintillator_SCINT, scintillatornum);
424         fScintillator_mt->AddProperty("SLOWCOMPONENT", scintillator_Energy,
425                 scintillator_SCINT, scintillatornum);
```

4983

```
    fScintillator_mt->AddProperty("RINDEX", scintillator_Energy,
            scintillator_RIND, scintillatornum);
    fScintillator_mt->AddProperty("ABSLENGTH", scintillator_Energy,
            scintillator_ABSL, scintillatornum);
    fScintillator_mt->AddProperty("ELECTRONSCINTILLATIONYIELD", SCY_Energy,
            SCY_Electron, 200);
    fScintillator_mt->AddProperty("PROTONSCINTILLATIONYIELD", SCY_Energy,
            SCY_Proton, 200);
    fScintillator_mt->AddConstProperty("RESOLUTIONSCALE", 1.0);
    fScintillator_mt->AddConstProperty("FASTTIMECONSTANT", 3.5 * ns);
    fScintillator_mt->AddConstProperty("SLOWTIMECONSTANT", 32. * ns);
    fScintillator_mt->AddConstProperty("YIELDRATIO", .8);
    fscintillator->SetMaterialPropertiesTable(fScintillator_mt);

    cryst_mat = nist->FindOrBuildMaterial("G4_POLYSTYRENE");
    G4double rIndexPstyrene[] =
    { 1.5, 1.5, 1.5, 1.5 };
    assert(sizeof(rIndexPstyrene) == sizeof(wls_Energy));
    G4double absorption1[] =
    { 2. * cm, 2. * cm, 2. * cm, 2. * cm };
    assert(sizeof(absorption1) == sizeof(wls_Energy));
    G4double scintilFast[] =
    { 0.00, 0.00, 1.00, 1.00 };
    assert(sizeof(scintilFast) == sizeof(wls_Energy));
    fcryst_mat = new G4MaterialPropertiesTable();
    fcryst_mat->AddProperty("RINDEX", wls_Energy, rIndexPstyrene, wlsnum);
    fcryst_mat->AddProperty("ABSLENGTH", wls_Energy, absorption1, wlsnum);
    fcryst_mat->AddProperty("FASTCOMPONENT", wls_Energy, scintilFast, wlsnum);
    cryst_mat->SetMaterialPropertiesTable(fcryst_mat);
    //fPMMA->SetMaterialPropertiesTable(fcryst_mat);
    G4cout << *(G4Material::GetMaterialTable()) << G4endl;

}

//....oooOOOOOooo........oooOOOOOooo........oooOOOOOooo........oooOOOOOooo......

G4VPhysicalVolume* DetectorConstruction::Construct()
{
    G4Box* expHall_box = new G4Box("World", fExpHall_x / 2, fExpHall_y / 2,
            fExpHall_z / 2);

    G4LogicalVolume* expHall_log = new G4LogicalVolume(expHall_box, fAir,
            "World", 0, 0, 0);

    G4VPhysicalVolume* expHall_phys = new G4PVPlacement(0, G4ThreeVector(),
            expHall_log, "World", 0, false, 0, fCheckOverlaps);

    //expHall_log->SetVisAttributes(visAttHide);
    //Room

    //He3 assay
    //DefineChamber(expHall_log);

    if (!lancs) DefineORNL(expHall_log, 15);
    else DefineLANCS(expHall_log);

    //source_position = G4ThreeVector(0 * cm, 0 * cm, 0*cm);
    G4cout << "EJ309 created" << G4endl;
    fPBox = expHall_phys;
    return expHall_phys;
}

void DetectorConstruction::SurfaceProperties(G4LogicalVolume *fHousing_log2,
        G4LogicalVolume *fPhotocath_log)
{
    G4double ephoton[] =
    { 2. * eV, 3.47 * eV };
    const G4int num = sizeof(ephoton) / sizeof(G4double);

    //**Scintillator housing properties
    G4double reflectivity[] =
```

4984

```
497         { 1.35, 1.40 };
498         assert(sizeof(reflectivity) == sizeof(ephoton));
499         G4double efficiency[] =
500         { 0.0, 0.0 };
501         assert(sizeof(efficiency) == sizeof(ephoton));
502         G4MaterialPropertiesTable* scintHsngPT = new G4MaterialPropertiesTable();
503         scintHsngPT->AddProperty("REFLECTIVITY", ephoton, reflectivity, num);
504         scintHsngPT->AddProperty("EFFICIENCY", ephoton, efficiency, num);
505         G4OpticalSurface* OpScintHousingSurface = new G4OpticalSurface(
506                 "HousingSurface", unified, polished, dielectric_metal);
507         OpScintHousingSurface->SetMaterialPropertiesTable(scintHsngPT);
508
509
510         //**Photocathode surface properties
511         G4double photocath_EFF[] =
512         { .25, .25 }; //Enables 'detection' of photons
513         assert(sizeof(photocath_EFF) == sizeof(ephoton));
514         G4double photocath_ReR[] =
515         { 1.92, 1.92 };
516         assert(sizeof(photocath_ReR) == sizeof(ephoton));
517         G4double photocath_ImR[] =
518         { 1.69, 1.69 };
519         assert(sizeof(photocath_ImR) == sizeof(ephoton));
520         G4MaterialPropertiesTable* photocath_mt = new G4MaterialPropertiesTable();
521         photocath_mt->AddProperty("EFFICIENCY", ephoton, photocath_EFF, num);
522         photocath_mt->AddProperty("REALRINDEX", ephoton, photocath_ReR, num);
523         photocath_mt->AddProperty("IMAGINARYRINDEX", ephoton, photocath_ImR, num);
524         G4OpticalSurface* photocath_opsurf = new G4OpticalSurface(
525                 "photocath_opsurf", glisur, polished, dielectric_metal);
526         photocath_opsurf->SetMaterialPropertiesTable(photocath_mt);
527
528         //**Create logical skin surfaces
529         new G4LogicalSkinSurface("ScintSurface", fHousing_log2,
530                 OpScintHousingSurface);
531         new G4LogicalSkinSurface("photocath_surf", fPhotocath_log,
532                 photocath_opsurf);
533     }
534
535
536
```

C.3 Physics list

```

/*
Main constructor of the PhysicsList class, which assigns of the physics model
*/

////////////////////////////////////////////////////////////////////////////////
// PhysicsList Class which acts as wrapper to the FREYA fission library
// It samples constructor which initilizes and loads all the different
// libraries needed for the simulation
////////////////////////////////////////////////////////////////////////////////
PhysicsList::PhysicsList()
:G4VModularPhysicsList()
{
    G4int verb = 0;
    SetVerboseLevel(verb);

  //add new units
  //
    new G4UnitDefinition("millielectronVolt", "meV", "Energy", 1.e-3 * eV);
    new G4UnitDefinition( "mm2/g",  "mm2/g", "Surface/Mass", mm2/g);
    new G4UnitDefinition("um2/mg", "um2/mg", "Surface/Mass", um * um / mg);

    // Neutron Physics
    RegisterPhysics(new NeutronHPphysics("neutronHP"));

    //RegisterPhysics(new HadronElasticPhysicsHP(verb));

    RegisterPhysics(new G4HadronPhysicsQGSP_BIC_HP(verb));

    // Ion Physics
    RegisterPhysics(new G4IonPhysics(verb));
    ////RegisterPhysics( new G4IonINCLXXPhysics(verb));

    // stopping Particles
    RegisterPhysics(new G4StoppingPhysics(verb));

    // Gamma-Nuclear Physics
    // EM physics
    RegisterPhysics(new ElectromagneticPhysics());

    // Decay
    //RegisterPhysics(new G4DecayPhysics());

    // Radioactive decay
    //RegisterPhysics(new G4RadioactiveDecayPhysics());

    defaultCutValue = 1.0 * mm;

    // EM Physics
    RegisterPhysics(new EMPhysics("standard EM"));

    // Muon Physics
    RegisterPhysics(new MuonPhysics("muon"));

    // Optical Physics
    G4OpticalPhysics* opticalPhysics = new G4OpticalPhysics();
    RegisterPhysics(opticalPhysics);

    opticalPhysics->SetWLSTimeProfile("delta");
    opticalPhysics->SetScintillationByParticleType(true);
    opticalPhysics->SetScintillationYieldFactor(.5);
    opticalPhysics->SetScintillationExcitationRatio(0.0);

    opticalPhysics->SetTrackSecondariesFirst(kCerenkov, true);
    opticalPhysics->SetTrackSecondariesFirst(kScintillation, true);



}

void PhysicsList::ConstructParticle()
```

4987

```
{
    G4BosonConstructor pBosonConstructor;
    pBosonConstructor.ConstructParticle();

    G4LeptonConstructor pLeptonConstructor;
    pLeptonConstructor.ConstructParticle();

    G4MesonConstructor pMesonConstructor;
    pMesonConstructor.ConstructParticle();

    G4BaryonConstructor pBaryonConstructor;
    pBaryonConstructor.ConstructParticle();

    G4IonConstructor pIonConstructor;
    pIonConstructor.ConstructParticle();

    G4ShortLivedConstructor pShortLivedConstructor;
    pShortLivedConstructor.ConstructParticle();

}



////////////////////////////////////////////////////////////////////////////
//ConstructProcess method of the NeutronHPphysics class, which
//assigns the neutron model
////////////////////////////////////////////////////////////////////////////
void NeutronHPphysics::ConstructProcess()
{
    G4ParticleDefinition* neutron = G4Neutron::Neutron();
    G4ProcessManager* pManager = neutron->GetProcessManager();

    // delete all neutron processes if already registered
    //
    G4ProcessTable* processTable = G4ProcessTable::GetProcessTable();
    G4VProcess* process = 0;
    process = processTable->FindProcess("hadElastic", neutron);
    if (process)
        pManager->RemoveProcess(process);
    //
    process = processTable->FindProcess("neutronInelastic", neutron);
    if (process)
        pManager->RemoveProcess(process);
    //
    process = processTable->FindProcess("nCapture", neutron);
    if (process)
        pManager->RemoveProcess(process);
    //
    process = processTable->FindProcess("nFission", neutron);
    if (process)
        pManager->RemoveProcess(process);

    // (re) create process: elastic
    //
    G4HadronElasticProcess* process1 = new G4HadronElasticProcess();
    pManager->AddDiscreteProcess(process1);
    //
    // model1a
    G4ParticleHPElastic* model1a = new G4ParticleHPElastic();
    process1->RegisterMe(model1a);
    process1->AddDataSet(new G4ParticleHPElasticData());
    //
    // model1b
    if (fThermal)
    {
        model1a->SetMinEnergy(4 * eV);
        G4ParticleHPThermalScattering* model1b =
                new G4ParticleHPThermalScattering();
        process1->RegisterMe(model1b);
        process1->AddDataSet(new G4ParticleHPThermalScatteringData());
    }
```

4988

```
143
144       // (re) create process: inelastic
145       //
146       G4NeutronInelasticProcess* process2 = new G4NeutronInelasticProcess();
147       pManager->AddDiscreteProcess(process2);
148       //
149       // cross section data set
150       G4ParticleHPInelasticData* dataSet2 = new G4ParticleHPInelasticData();
151       process2->AddDataSet(dataSet2);
152       //
153       // models
154       G4ParticleHPInelastic* model2 = new G4ParticleHPInelastic();
155       process2->RegisterMe(model2);
156
157     // (re) create process: nCapture
158       //
159       G4HadronCaptureProcess* process3 = new G4HadronCaptureProcess();
160       pManager->AddDiscreteProcess(process3);
161       //
162       // cross section data set
163       G4ParticleHPCaptureData* dataSet3 = new G4ParticleHPCaptureData();
164       process3->AddDataSet(dataSet3);
165       //
166       // models
167       G4ParticleHPCapture* model3 = new G4ParticleHPCapture();
168       process3->RegisterMe(model3);
169
170       // (re) create process: nFission
171       //
172       G4HadronFissionProcess* process4 = new G4HadronFissionProcess();
173       pManager->AddDiscreteProcess(process4);
174       //
175       // cross section data set
176       G4ParticleHPFissionData* dataSet4 = new G4ParticleHPFissionData();
177       process4->AddDataSet(dataSet4);
178       //
179       // models
180       G4ParticleHPFission* model4 = new G4ParticleHPFission();
181       process4->RegisterMe(model4);
182   }
183
184   ////////////////////////////////////////////////////////////////////////////////
185   //ConstructProcess method of the ElectromagneticPhysics class, which
186   //assigns the EM model
187   ////////////////////////////////////////////////////////////////////////////////
188   void ElectromagneticPhysics::ConstructProcess()
189   {
190     G4PhysicsListHelper* ph = G4PhysicsListHelper::GetPhysicsListHelper();
191
192     // Add standard EM Processes
193     //
194       //auto particleIterator = GetParticleIterator();
195       aParticleIterator->reset();
196       while ((*aParticleIterator)())
197       {
198           G4ParticleDefinition* particle = aParticleIterator->value();
199       G4String particleName = particle->GetParticleName();
200
201       if (particleName == "gamma") {
202
203         ph->RegisterProcess(new G4PhotoElectricEffect, particle);
204               ph->RegisterProcess(new G4ComptonScattering, particle);
205               ph->RegisterProcess(new G4GammaConversion, particle);
206
207       } else if (particleName == "e-") {
208
209         ph->RegisterProcess(new G4eMultipleScattering(), particle);
210               ph->RegisterProcess(new G4eIonisation, particle);
211               ph->RegisterProcess(new G4eBremsstrahlung(), particle);
212
213       } else if (particleName == "e+") {
```

4989

```
214
215         ph->RegisterProcess(new G4eMultipleScattering(), particle);
216               ph->RegisterProcess(new G4eIonisation, particle);
217               ph->RegisterProcess(new G4eBremsstrahlung(), particle);
218               ph->RegisterProcess(new G4eplusAnnihilation(), particle);
219
220           }
221           else if (particleName == "mu+" ||
222                  particleName == "mu-"    ) {
223
224         ph->RegisterProcess(new G4MuMultipleScattering(), particle);
225               ph->RegisterProcess(new G4MuIonisation, particle);
226               ph->RegisterProcess(new G4MuBremsstrahlung(), particle);
227               ph->RegisterProcess(new G4MuPairProduction(), particle);
228
229       } else if( particleName == "proton" ||
230                  particleName == "pi-" ||
231                  particleName == "pi+"    ) {
232
233               ph->RegisterProcess(new G4hMultipleScattering(), particle);
234               ph->RegisterProcess(new G4hIonisation, particle);
235
236           }
237           else if (particleName == "alpha" ||
238                  particleName == "He3"    ) {
239
240         ph->RegisterProcess(new G4hMultipleScattering(), particle);
241               ph->RegisterProcess(new G4ionIonisation, particle);
242               ph->RegisterProcess(new G4NuclearStopping(), particle);
243
244       } else if( particleName == "GenericIon" ) {
245
246         ph->RegisterProcess(new G4hMultipleScattering(), particle);
247         G4ionIonisation* ionIoni = new G4ionIonisation();
248         ionIoni->SetEmModel(new G4IonParametrisedLossModel());
249               ph->RegisterProcess(ionIoni, particle);
250               ph->RegisterProcess(new G4NuclearStopping(), particle);
251
252       } else if ((!particle->IsShortLived()) &&
253                  (particle->GetPDGCharge() != 0.0)
254                   &&
255                  (particle->GetParticleName() != "chargedgeantino")) {
256
257         //all others charged particles except geantino
258         ph->RegisterProcess(new G4hMultipleScattering(), particle);
259               ph->RegisterProcess(new G4hIonisation(), particle);
260       }
261     }
262   }
```

C.4 Particle constructor

```

/*
The PrimaryGeneratorAction class inherrits from the G4VUserPrimaryGeneratorAction
which lets the user assign the tpye and properties of particles that are to beam
generated. The constructor is called once, while the GeneratePrimaries() method is
called once every new particle is needed.
*/

int PrimaryGeneratorAction::energy = 500;
double PrimaryGeneratorAction::decay_time = 0;
G4String PrimaryGeneratorAction::name = "neutron";

////////////////////////////////////////////////////////////////////////////////
// constructor to the PrimaryGeneratorAction class which initializes some
// parameters including initialization of the SponFiss which is a wrapper
// from the FREYA fission library
////////////////////////////////////////////////////////////////////////////////
PrimaryGeneratorAction::PrimaryGeneratorAction()
:G4VUserPrimaryGeneratorAction(), fParticleGun(0)
{
    // initialize particlegun (produces particles)
    fParticleGun = new G4ParticleGun(1);
    fParticleGun->SetParticleDefinition(
            G4ParticleTable::GetParticleTable()->FindParticle(name));
    fParticleGun->SetParticleEnergy(energy * keV);
    fParticleGun->SetParticlePosition(DetectorConstruction::source_position);
    fParticleGun->SetParticleTime(0.0 * ns);
    fParticleGun->SetParticleMomentumDirection(G4ThreeVector(1., 0., 0.));

    // Specify isotopic composition and fission rates in fissions/sec
    time = 0; // set to 0 initially
    G4ThreeVector* center = &DetectorConstruction::source_position;

    //initialize SponFiss class which is a wrapper from the FREYA library
    posDist = new G4SPSPosDistribution();
    posDist->SetPosDisType("Volume");
    posDist->SetPosDisShape("Sphere");
    posDist->SetCentreCoords(*center);
    posDist->SetRadius(radius);
    iso = new SponFiss(98252, posDist);
}


PrimaryGeneratorAction::~PrimaryGeneratorAction()
{
    delete fParticleGun;
    delete posDist;
    delete iso;
}

////////////////////////////////////////////////////////////////////////////////
// The GeneratePrimaries is called once every cycle and based in the
// particle flags, generates nuclear particles for simulation
////////////////////////////////////////////////////////////////////////////////
void PrimaryGeneratorAction::GeneratePrimaries(G4Event* anEvent)
{
    //create amono energetic source
    if (mono)
    {
       fParticleGun->SetParticleEnergy(energy * keV);
        if (!beam)
        {
            G4ThreeVector direction;
            direction.setRThetaPhi(1.0, std::acos(G4UniformRand() * 2 - 1),
                         (G4UniformRand() * 2 - 1) * 180 * deg);
            fParticleGun->SetParticleMomentumDirection(direction);
        }
        fParticleGun->GeneratePrimaryVertex(anEvent);
    }
    else if (Co)
    {
```

4992

```
72          fParticleGun->SetParticleEnergy(1121 * keV);
73          G4ThreeVector direction;
74          direction.setRThetaPhi(1.0, std::acos(G4UniformRand() * 2 - 1),
75                          (G4UniformRand() * 2 - 1) * 180 * deg);
76          fParticleGun->SetParticleMomentumDirection(direction);
77          fParticleGun->GeneratePrimaryVertex(anEvent);
78
79          fParticleGun->SetParticleEnergy(1333 * keV);
80          direction.setRThetaPhi(1.0, std::acos(G4UniformRand() * 2 - 1),
81                          (G4UniformRand() * 2 - 1) * 180 * deg);
82          fParticleGun->SetParticleMomentumDirection(direction);
83          fParticleGun->GeneratePrimaryVertex(anEvent);
84      }
85      else if(AmLi)
86      {
87          fParticleGun->SetParticleEnergy((G4UniformRand()+.3 ) * MeV);
88          /*G4ThreeVector direction;
89          direction.setRThetaPhi(1.0, std::acos(G4UniformRand() * 2 - 1),
90                          (G4UniformRand() * 2 - 1) * 180 * deg);
91          fParticleGun->SetParticleMomentumDirection(direction);*/
92          fParticleGun->GeneratePrimaryVertex(anEvent);
93      }
94      else if(sfif)
95      {
96
97          G4MUTEXLOCK(&aMutex);
98          static SponFiss_FF *fif = new SponFiss_FF(posDist);
99          fif->GeneratePrimaryVertex(anEvent);
100         G4MUTEXUNLOCK(&aMutex);
101     }
102     else
103     {
104
105         decay_time += 1 / 331000;
106         G4MUTEXLOCK(&aMutex);
107         iso->GeneratePrimaryVertex(anEvent, decay_time * ns, mode);
108         G4MUTEXUNLOCK(&aMutex);
109     }
110
111 }
112
113 ////////////////////////////////////////////////////////////////////////////////
114 // SponFiss Class which acts as wrapper to the FREYA fission library
115 // It samples the FREYA distributions and produces multiple particles according
116 // to the specifications
117 ////////////////////////////////////////////////////////////////////////////////
118
119 void SponFiss::GeneratePrimaryVertex(G4Event* anEvent, G4double time)
120 {
121     // Generate a spontaneous fission using the fission library and emit
122     // the neutrons and gamma-rays
123
124     fissionEvent* fe = new fissionEvent(isotope, 0, -1., 0., 0);
125     fe->setCf252Option(2, 0);
126     fe->setCorrelationOption(0);
127     if (3 == fe->getCorrelationOption())
128     {
129         int err_len = 1000;
130         char* error_message = new char[err_len];
131         fe->getFREYAerrors(&err_len, error_message);
132         if (err_len>1)
133         {
134             G4ExceptionDescription ed;
135             ed << "Call to new fissionEvent("
136             << "isotope=" << isotope << ", "
137             << "time=" << time << ", "
138             << "nubar=-1." << ", "
139             << "eng=0." << ", "
140             << "0) failed with error message from FREYA: "
141             << G4endl
142             << error_message;
```

4993

```
            delete [] error_message;
            G4Exception("G4FissionLibrary_new::SampleMult", "freya001",
            FatalException,
                    ed);
        }
        delete [] error_message;
    }
    G4int nPrompt, gPrompt;
    nPrompt = fe->getNeutronNu();
    gPrompt = fe->getPhotonNu();

    if (verbosityLevel > 1)
    {
        G4cout << " nPrompt: " << nPrompt << G4endl << " gPrompt: " << gPrompt
        << G4endl;
    }

    // Position
    G4ThreeVector sampled_particle_position = DetectorConstruction::source_position;

    // create a new vertex
    G4PrimaryVertex* vertex = new G4PrimaryVertex(sampled_particle_position,
            0.);

    G4double mom, momx, momy, momz, eng;

    if (verbosityLevel >= 2)
        G4cout << "Creating primaries and assigning to vertex" << G4endl;

    G4DynamicParticle* it;
    // Build neutrons
    if (PrimaryGeneratorAction::neutron)
    for (G4int i = 0; i < nPrompt; i++)
    {
        it = new G4DynamicParticle();
        it->SetDefinition(neutron_definition);
            eng = fe->getNeutronEnergy(i);
        if (eng > 19.9)                     // cap energy
            eng = 19;
        it->SetKineticEnergy(eng);
        mom = it->GetTotalMomentum();

        momx = mom * fe->getNeutronDircosu(i);
        momy = mom * fe->getNeutronDircosv(i);
        momz = mom * fe->getNeutronDircosw(i);

        G4PrimaryParticle* particle = new G4PrimaryParticle(neutron_definition,
                momx, momy, momz, eng * MeV);
        //particle->SetMomentum(1.,0.,0.);
        particle->SetMass(neutron_definition->GetPDGMass());
        particle->SetCharge(neutron_definition->GetPDGCharge());
        particle->SetPolarization(particle_polarization.x(),
                particle_polarization.y(), particle_polarization.z());


        if (verbosityLevel > 1)
        {
            G4cout << "Particle name: "
                    << particle->GetG4code()->GetParticleName() << G4endl;
            G4cout << "     Momentum: " << particle->GetMomentum() << G4endl;
            G4cout << "     Position: " << vertex->GetPosition() << G4endl;
        }

        if (fe->getNeutronAge(i) != -1)
            particle->SetProperTime(fe->getNeutronAge(i) * ns);
        else
            particle->SetProperTime(0 * ns);

        vertex->SetPrimary(particle);
        delete it;
    }
```

4994

```
213
214
215     // Build gammas
216     if (PrimaryGeneratorAction::gamma)
217     for (G4int i = 0; i < gPrompt; i++)
218     {
219         it = new G4DynamicParticle();
220         it->SetDefinition(photon_definition);
221         eng = fe->getPhotonEnergy(i);
222             if (eng > 19.9)                 //cap energy
223                 eng = 19;
224         it->SetKineticEnergy(eng);
225         mom = it->GetTotalMomentum();
226
227         momx = mom * fe->getPhotonDircosu(i);
228         momy = mom * fe->getPhotonDircosv(i);
229         momz = mom * fe->getPhotonDircosw(i);
230
231         G4PrimaryParticle* particle = new G4PrimaryParticle(photon_definition,
232                 momx, momy, momz, eng * MeV);
233         particle->SetMass(photon_definition->GetPDGMass());
234         particle->SetCharge(photon_definition->GetPDGCharge());
235         particle->SetPolarization(particle_polarization.x(),
236                 particle_polarization.y(), particle_polarization.z());
237
238         if (verbosityLevel > 1)
239         {
240             G4cout << "Particle name: "
241                     << particle->GetG4code()->GetParticleName() << G4endl;
242             G4cout << "     Momentum: " << particle->GetMomentum() << G4endl;
243             G4cout << "     Position: " << vertex->GetPosition() << G4endl;
244         }
245
246         if (fe->getPhotonAge(i) != -1)
247             particle->SetProperTime(fe->getPhotonAge(i) * ns);
248         else
249             particle->SetProperTime(0 * ns);
250         vertex->SetPrimary(particle);
251         delete it;
252     }
253     delete fe;
254     vertex->SetT0(time);
255
256     anEvent->AddPrimaryVertex(vertex);
257     if (verbosityLevel > 1)
258         G4cout << " Primary Vetex generated !" << G4endl;
259 }
260
```

C.5 Track and step analyser

```
/*
Code clock from the SteppingAction class. The SteppingAction() is constructed
at the begining of each event, and the UserSteppingAction() method is called
at the end of each step. This method was utilized to extract information regarding
incident particle
*/
////////////////////////////////////////////////////////////////////////////////
// SteppingAction consttructor which resets the class variables
////////////////////////////////////////////////////////////////////////////////

SteppingAction::SteppingAction(G4String fn, TrackingAction* TrAct) :
        G4UserSteppingAction(), fTrackingAction(TrAct)
{
    filename = fn;
    fgInstance = this;
    fout.open("SteppingAction", std::ios::out | std::ios::trunc);
}

////////////////////////////////////////////////////////////////////////////////
// SteppingAction Reset method
////////////////////////////////////////////////////////////////////////////////
void SteppingAction::Reset()
{
    //release particle buffers
    for (int i = 0; i < 2; i++)
        if (rParticle[i].size() > 0)
        {
            for (int j = 0; j < rParticle[i].size(); j++)
            {
                if (rParticle[i].at(j) != NULL)
                    delete rParticle[i].at(j);
                rParticle[i].at(j) = NULL;
            }
            rParticle[i].clear();
        }
    //release event buffers
    if (rEvent.size() > 0)
    {
        for (int j = 0; j < rEvent.size(); j++)
        {
            rEvent.at(j)->delete_class();
            if (rEvent.at(j) != NULL)
                delete rEvent.at(j);
            rEvent.at(j) = NULL;
        }
        rEvent.clear();
    }
    crEvent = NULL;
    crParticle = NULL;
    _cnnt = 0; _cnnt2 = -1; _eng_l = 1; _tm_l = 1000000;
    return;
}
////////////////////////////////////////////////////////////////////////////////
// SteppingAction StackParticle method used to identifying parent particles
// and assiging unit id to each of them.
////////////////////////////////////////////////////////////////////////////////
void SteppingAction::StackParticle(const G4Step* step, const G4StepPoint * point)
{
    G4Track* track = step->GetTrack();
    if ((_eng_l !=  step->GetPreStepPoint()->GetKineticEnergy())
            && ( _cnnt2 != track->GetTrackID()))
        {
            TrackInformation* trackInfo
                = (TrackInformation*)(track->GetUserInformation());
            _cnnt++;

            _cnnt2 = track->GetTrackID() ;
            _tm_l = step->GetTrack()->GetGlobalTime();
            ParticleName = track->GetDynamicParticle()->
                        GetParticleDefinition()->GetParticleName();
            _eng_l =  point->GetKineticEnergy();
```

4997

```
72              crParticle = new RecodedParticle(_cnnt, ParticleName, _eng_l,
73                              track->GetGlobalTime(),point->GetMomentumDirection () );
74              trackInfo->fID = _cnnt;
75              if (track->GetParentID() == 0) trackInfo->fParentType = ParticleName;
76              track->SetUserInformation(trackInfo);
77
78              rParticle[ParticleName == "neutron" ? 1 : 0].push_back(crParticle);
79          }
80  }
81  ////////////////////////////////////////////////////////////////////////////
82  // SteppingAction UserSteppingAction method called at the end of each Step by
83  // Geant4, which includes the code for collecting relavent information.
84  ////////////////////////////////////////////////////////////////////////////
85  void SteppingAction::UserSteppingAction(const G4Step* step)
86  {
87
88      const G4StepPoint* endPoint = step->GetPostStepPoint();
89      const G4VProcess* process = endPoint->GetProcessDefinedStep();
90      Run* run =
91              static_cast<Run*>(G4RunManager::GetRunManager()->GetNonConstCurrentRun());
92      run->CountProcesses(process);
93
94      //
95      // collect information on the first particle
96      if (step->GetTrack()->GetTrackID() == 1)
97      {
98              G4double ekin = endPoint->GetKineticEnergy();
99              G4double trackl = step->GetTrack()->GetTrackLength();
100             G4double time = step->GetTrack()->GetLocalTime();
101             fTrackingAction->UpdateTrackInfo(ekin, trackl, time);
102             G4AnalysisManager::Instance()->FillH1(7, ekin);
103     }
104     G4Track* track = step->GetTrack();
105
106
107     // collect information on the particles generated and populate the buffers
108     TrackInformation* trackInfo
109             = (TrackInformation*)(track->GetUserInformation());
110     if ((track->GetParentID() == 0) )
111     {
112         StackParticle(step, step->GetPreStepPoint());
113
114     }
115     else if (trackInfo->GetTrackingStatus() > 0)
116     {
117
118         if ((
            track->GetDynamicParticle()->GetParticleDefinition()->GetParticleName() ==
            "gamma" ) && _eng_l != track->GetParentID())
119             {
120             StackParticle(step, step->GetPreStepPoint());
121             _eng_l = track->GetParentID();
122
123         }
124     }
125     ParticleName = track->GetDynamicParticle()->
126                         GetParticleDefinition()->GetParticleName();
127
128     //only process if inside scintillator volume
129     if (step->GetTrack()->GetVolume()->GetName() != "Scintillator")
130         return;
131
132
133     // Change to correct parent particle for tracking
134     if (trackInfo->fID > _cnnt+1)
135         return;
136     else if (trackInfo->fID != crParticle->particleid)
137     {
138         RecodedParticle* tmp = NULL;
139
140         for (int j = 0; j < 2; j++)
```

4998

```
141         {
142             int sz = rParticle[j].size();
143             int found = -1;
144             for (int i = 0; i < sz; i++)
145             {
146                 if (rParticle[j].at(i)->particleid == trackInfo->fID) {
147                     found = i;
148                     break;
149                 }
150             }
151             if (found != -1){
152                 tmp = rParticle[j].at(found);
153                 break;
154             }
155         }
156         if (tmp != NULL )
157             crParticle=tmp;
158         else
159             return;
160     }
161
162
163     // initialize the boarder process function.
164     static G4ThreadLocal G4OpBoundaryProcess *boundary = NULL;
165     if (!boundary)
166     {
167         G4ProcessManager* pm =
168                 step->GetTrack()->GetDefinition()->GetProcessManager();
169         G4int nprocesses = pm->GetProcessListLength();
170         G4ProcessVector* pv = pm->GetProcessList();
171         G4int i;
172         for (i = 0; i < nprocesses; i++)
173         {
174             if ((*pv)[i]->GetProcessName() == "OpBoundary")
175             {
176                 boundary = (G4OpBoundaryProcess*) (*pv)[i];
177                 break;
178             }
179         }
180     }
181
182     // collect information on the detectors in which the simulation is taking place
183     int idx_det = step->GetTrack()->GetVolume()->GetCopyNo();
184     if ((crEvent == NULL)  || (crEvent->detectorID != idx_det))
185     {
186         int sz = rEvent.size();
187         int found = -1;
188         for (int i = 0; i < sz; i++)
189         {
190             if (rEvent.at(i)->detectorID == idx_det) {
191                 found = i;
192                 break;
193             }
194         }
195         if (found != -1)
196             crEvent = rEvent.at(found);
197         else{
198             crEvent = new RecodedEvent(idx_det, crParticle,
                step->GetTrack()->GetGlobalTime()) ;
199             rEvent.push_back(crEvent);
200         }
201     }
202
203     // check if particle is new in the detector
204     crEvent->CheckPart(crParticle);
205
206
207     // for optical photons, detect the boundary absorption os the particles and
        count them
208     if (track->GetDynamicParticle()->GetParticleDefinition()->GetParticleName()
209             == "opticalphoton")
```

4999

```
210         {
211             G4OpBoundaryProcessStatus boundaryStatus = boundary->GetStatus();
212             if (step->GetPostStepPoint()->GetStepStatus() == fGeomBoundary)
213             {
214                 double idx = 0;
215                 if (boundaryStatus == Detection)
216                 {
217
218                     crEvent->recordProduction(0,
                        step->GetPreStepPoint()->GetTotalEnergy()*425.4885 ,
219                                 step->GetPostStepPoint()->GetGlobalTime());
220                 }
221             }
222             return;
223         }
224
225         // identify compton and elastic scattering of photons and neutrons, respectively.
226         if (ParticleName == "neutron" || ParticleName == "gamma")
227         {
228             if (step->GetPostStepPoint()->GetProcessDefinedStep()->GetProcessName()
229                     == "compt")
230             {
231                 G4double deng = step->GetPreStepPoint()->GetTotalEnergy()
232                                 - step->GetPostStepPoint()->GetTotalEnergy();
233                 crEvent->recordReaction(0, deng,
                    step->GetPostStepPoint()->GetGlobalTime(),
234                                 step->GetPreStepPoint()->GetTotalEnergy());
235
236             }
237             if (step->GetPostStepPoint()->GetProcessDefinedStep()->GetProcessName()
238                     == "hadElastic")
239             {
240                 G4double deng = step->GetPreStepPoint()->GetKineticEnergy()
241                                 - step->GetPostStepPoint()->GetKineticEnergy();
242                 crEvent->recordReaction(1, deng,
                    step->GetPostStepPoint()->GetGlobalTime(),
243                                 step->GetPreStepPoint()->GetKineticEnergy());
244             }
245         }
246         if (ParticleName == "e-")
247         {
248             if (step->GetPostStepPoint()->GetProcessDefinedStep()->GetProcessName()
249                     == "eIoni")
250             {
251                 G4double deng = step->GetPreStepPoint()->GetKineticEnergy()
252                                 - step->GetPostStepPoint()->GetKineticEnergy();
253                 crEvent->recordReaction(2, deng);
254             }
255         }
256         if (ParticleName == "proton")
257         {
258             if (step->GetPostStepPoint()->GetProcessDefinedStep()->GetProcessName()
259                     == "hIoni")
260             {
261                 G4double deng = step->GetPreStepPoint()->GetKineticEnergy()
262                                 - step->GetPostStepPoint()->GetKineticEnergy();
263                 crEvent->recordReaction(3, deng);
264
265             }
266         }
267
268         // track secondary particles
269         const std::vector<const G4Track*>* secondaries =
270                 step->GetSecondaryInCurrentStep();
271         if (secondaries->size() > 0)
272         {
273             for (unsigned int i = 0; i < secondaries->size(); ++i)
274             {
275                 if (secondaries->at(i)->GetParentID() > 0)
276                 {
277                     if (secondaries->at(i)->GetDynamicParticle()->GetParticleDefinition()
```

5000

```
                        == G4OpticalPhoton::OpticalPhotonDefinition())
                {
                    if (secondaries->at(i)->GetCreatorProcess()->GetProcessName()
                            == "Scintillation")
                    {

                        crEvent->recordProduction(1,step->GetPostStepPoint()->GetGloba
                        lTime(), secondaries->at(i)->GetKineticEnergy());
                    }
                    if (secondaries->at(i)->GetCreatorProcess()->GetProcessName()
                            == "Cerenkov")
                    {
                        crEvent->recordProduction(5,
                        secondaries->at(i)->GetKineticEnergy());
                    }
                }
                else if
                (secondaries->at(i)->GetDynamicParticle()->GetParticleDefinition()->Ge
                tParticleName()
                        == "neutron" && ParticleName != "neutron"
                        &&
                        track->GetDynamicParticle()->GetParticleDefinition()->GetParti
                        cleName()
                                != "proton")
                {
                    crEvent->recordProduction(3,
                    secondaries->at(i)->GetKineticEnergy());
                }
                else if
                (secondaries->at(i)->GetDynamicParticle()->GetParticleDefinition()->Ge
                tParticleName()
                        == "proton" && ParticleName != "proton"
                        &&
                        track->GetDynamicParticle()->GetParticleDefinition()->GetParti
                        cleName()
                                != "proton")
                {
                    crEvent->recordProduction(2,
                    secondaries->at(i)->GetKineticEnergy());
                }
                else if
                (secondaries->at(i)->GetDynamicParticle()->GetParticleDefinition()->Ge
                tParticleName()
                        == "e-" && ParticleName != "e-"
                        &&
                        track->GetDynamicParticle()->GetParticleDefinition()->GetParti
                        cleName()
                                != "e-")
                {
                    crEvent->recordProduction(4,
                    secondaries->at(i)->GetKineticEnergy());
                }
                else if
                (secondaries->at(i)->GetDynamicParticle()->GetParticleDefinition()->Ge
                tParticleName()
                                                == "gamma" )
                {

                }

            }
        }
    }

}
```

5001

```
329 ////////////////////////////////////////////////////////////////////////////
330 // TrackingAction PostUserTrackingAction which is called by Geant4 at the end
331 // of each Track. Using this method, Tracking information class is added to
332 // each new secondary particle and assigns an ID value to identify which
333 // particle generated the secondary particles.
334 ////////////////////////////////////////////////////////////////////////////
335
336 void TrackingAction::PostUserTrackingAction(const G4Track* track)
337 {
338
339     G4TrackVector* secondaries = fpTrackingManager->GimmeSecondaries();
340     if(secondaries)
341     {
342         TrackInformation* info =
343             (TrackInformation*)(track->GetUserInformation());
344         size_t nSeco = secondaries->size();
345
346         G4String name = track->GetDynamicParticle()->
347                         GetParticleDefinition()->GetParticleName();
348
349         if(nSeco>0)
350         {
351             for(size_t i=0;i<nSeco;i++)
352             {
353                 name = (*secondaries)[i]->GetDynamicParticle()->
354                             GetParticleDefinition()->GetParticleName();
355
356                 TrackInformation* infoNew = new TrackInformation(info);
357                 // copy parent id from the particle id of the parent
358                 infoNew->fParentID = info->fID;
359                 infoNew->fID = info->fID;
360                 // copy parent particle type, i.e. neutron or gamma
361                 infoNew->fParentType = info->fParentType;
362
363                 (*secondaries)[i]->SetUserInformation(infoNew);
364             }
365         }
366     }
367     // collect variuos information on the track
368     Trajectory* trajectory = (Trajectory*) fpTrackingManager->GimmeTrajectory();
369
370     trajectory->SetDrawTrajectory(true);
371     G4int trackID = track->GetTrackID();
372     if (trackID > 1)
373         return;
374
375     Run* run =
376             static_cast<Run*>(G4RunManager::GetRunManager()->GetNonConstCurrentRun());
377     run->SumTrackLength(fNbStep1, fNbStep2, fTrackLen1, fTrackLen2, fTime1,
378             fTime2);
379
380 }
381
382
383
384 ////////////////////////////////////////////////////////////////////////////
385 // StackingAction ClassifyNewTrack method which is called by Geant4 at the end
386 // everytime a new primary or secondary particle is pushed into the simulation
387 // Stack. This method was used assign priority of the simulation and identify
388 // particles which needs to be classified/treated as a parent particle (e.g.
389 // gamma rays emitted from neutron capture or inelastic scattering)
390 ////////////////////////////////////////////////////////////////////////////
391 G4ClassificationOfNewTrack StackingAction::ClassifyNewTrack(const G4Track* aTrack)
392 {
393     //keep primary particle and tracking information
394     if (aTrack->GetParentID() == 0)
395     {
396         TrackInformation* trackInfo;
397         trackInfo = new TrackInformation(aTrack);
398         trackInfo->SetTrackingStatus(1);
399         trackInfo->fParentID = 0;
```

5002

```
        G4Track* theTrack = (G4Track*)aTrack;
        theTrack->SetUserInformation(trackInfo);
        return fUrgent;
    }

    //count particles generated
    G4String name = aTrack->GetDefinition()->GetParticleName();
    G4double energy = aTrack->GetKineticEnergy();
    Run* run =
            static_cast<Run*>(G4RunManager::GetRunManager()->GetNonConstCurrentRun());
    run->ParticleCount(name, energy);

    //count opticalphoton particles
    if (aTrack->GetDefinition() == G4OpticalPhoton::OpticalPhotonDefinition())
    { // particle is optical photon
        if (aTrack->GetParentID() > 0)
        { // particle is secondary
            if (aTrack->GetCreatorProcess()->GetProcessName()
                    == "Scintillation")
                fScintillationCounter++;
            if (aTrack->GetCreatorProcess()->GetProcessName() == "Cerenkov")
                fCerenkovCounter++;
            // move to waiting stack, to be simulated after all gamma/neutrons
            // have be completed.
            return fWaiting;
        }
    }

    //if the secondary particle is a gamma particle
    if (aTrack->GetDefinition()->GetParticleName() == "gamma")
    {
        if (aTrack->GetParentID() > 0)
        { // particle is secondary
            // kill particle if less than 10 keV
            if (aTrack->GetKineticEnergy()/keV < 10)
                return fKill;
            // if gamma was generated from neutron capture
            else if (aTrack->GetCreatorProcess()->GetProcessName()
                    == "nCapture")
            {
                G4Track* theTrack = (G4Track*)aTrack;
                TrackInformation* trackInfo
                = (TrackInformation*)(aTrack->GetUserInformation());
                trackInfo->SetTrackingStatus(1);
                theTrack->SetUserInformation(trackInfo);
                return fUrgent;
            }
            else
            {   // other reactions, i.e. inelastic scattering, eBram, etc.
                G4Track* theTrack = (G4Track*)aTrack;
                TrackInformation* trackInfo
                = (TrackInformation*)(aTrack->GetUserInformation());
                trackInfo->SetTrackingStatus(2);
                theTrack->SetUserInformation(trackInfo);
                return fUrgent;
            }
        }
    }
    //kill particle if energy is more than 20 MeV.
    if (energy*MeV > 20*MeV) return fKill;

    return fUrgent;
}
```

C.6 Particle and event analyser

```
enum ptype { PMT = 0, optical = 1, proton = 2, neutron = 3, electron = 4, Cerenkov = 5, holder = 6 };
enum rtype { compt = 0, hadElastic = 1, eIoni = 2, hIoni = 3, alpha = 4 };

/*
Storage class for each tracked particles (i.e. parents and secondary gammas)
*/
class RecodedParticle{
    public:
    RecodedParticle(int pid, std::string nm, G4double eng, G4double tm, G4ThreeVector dir){
        particleid = pid; name = nm;
        direction = dir;
        IncidentEnergy = eng; Time = tm;
    }
    std::string Pout(int j)
    {
        G4cout << "Particle No " << particleid << G4endl;
        G4cout << "    Particle Type " << name << G4endl;
        G4cout << "    IncidentEnergy " << IncidentEnergy/MeV << G4endl;
        G4cout << "    EntryEnergy " << EntryEnergy/MeV << G4endl;
        G4cout << "    Time " << Time << G4endl;
        G4cout << "    Direction " << direction << G4endl;
    }

    int particleid = -1;
    std::string name = "";
    G4ThreeVector direction;
    G4double IncidentEnergy = 0;
    G4double EntryEnergy = 0;
    G4double Time = 0;
    bool del = true;
};

/*
Storage class for each detector which had some sort of energy deposited
*/
class RecodedEvent
{
  public:
    // constructor for RecodedEvent class
    RecodedEvent(int det, RecodedParticle* nue, G4double time)
    {
        detectorID = det;
        particledef.push_back(*nue);
        masterTime = time;
        triggermap = new std::map<G4double, G4double>[100];
        for (int i = 0; i < 7; i++)
        {
            intervaltimeEnergy[i] = (G4double *) calloc(10000, sizeof(G4double));
            intervaltimeCounter[i] = (G4int *) calloc(10000, sizeof(G4int));
        }

        for (int i = 0; i < 100; i++)
          for (int j = 0; j < 7; j++)
            {
                firstDepo[i][j] = -1;
                firstInteraction[i][j] = -1;
            }
        for (int i = 0; i < 100 ; i++)
            triggermap[i].clear();
    };

    // remove memory allocations
    void delete_class()
    {
        for (int i = 0; i < 100 ; i++)
            triggermap[i].clear();
        delete [] triggermap;
        for (int i = 0; i < 7; i++)
```

5005

```
        {
            if (intervaltimeEnergy[i] != NULL)
                free(intervaltimeEnergy[i]);
            if (intervaltimeCounter[i] != NULL)
                free(intervaltimeCounter[i]);
        }
    }

    // collected data
    std::map<G4double, G4double> *triggermap;   // map storing energy deposited with time
    int detectorID = -1;                        // detector identification no
    std::vector<RecodedParticle> particledef;   // vector containing all the particle
                                                // that entered the detector
    RecodedParticle* ptr_particledef = NULL;    // pointer to the dominant particle
    G4double masterTime = -1;                   // time when the first particle enetered
    G4double triggerTime = -1;                  // time when the detector threshold was crossed
    std::string name = "";                      // particle type
    G4double firstDepo[100][7];                 // time when the first energy was deposited
                                                // by each particle
    G4double firstInteraction[100][7];          // time when the compton/elastic scattering
                                                // reaction too place by each particle
    G4double reacCounter[100][5] = {{0}};       // number of time each type of reaction took place
    G4double reacEnergy[100][5] = {{0}};        // energy deposited by each type of reaction
    G4double depoCounter[100][7] = {{0}};       // number of optical photon absorbed
    G4double depoEnergy[100][7] = {{0}};        // energy scalar for the deposited optical photons
    G4double *intervaltimeEnergy[7] = {NULL};   // detector response with time.
    G4int *intervaltimeCounter[7] = {NULL} ;    // detector response with time.
    G4int idp = 0, idn = 0, idx = 0;
    G4int pCount = 0;

    ////////////////////////////////////////////////////////////////////////////////
    // Check if particle is valid
    ////////////////////////////////////////////////////////////////////////////////
    bool IsValid()
    {
        ParticleType();
        if (name == "neutron"
            && reacEnergy[idx][1]/keV < 1*depoEnergy[idx][0]/keV)
                return false;

        if (name == "neutron"
            && ptr_particledef->EntryEnergy/keV < reacEnergy[idx][1]/keV)
                return false;

        return true;
    }

    ////////////////////////////////////////////////////////////////////////////////
    // Identify dominating particle
    ////////////////////////////////////////////////////////////////////////////////
    int ParticleType ()
    {
        G4double engp = 0, engn = 0;
        if (ptr_particledef != NULL) return idx;
        for (int i = 0; i < particledef.size(); i++)
        {
            if (reacEnergy[i][0] > engp) {engp = reacEnergy[i][0]; idp = i;}
            if (reacEnergy[i][1] > engn) {engn = reacEnergy[i][1]; idn = i;}

        }
        if (engp > engn*2) {ptr_particledef = &particledef.at(idp);  idx = idp;}
        else { ptr_particledef = &particledef.at(idn); idx = idn;}

```

5006

```
        name = ptr_particledef->name;
        return idx;

    }

    ////////////////////////////////////////////////////////////////////////////
    // Calculate time when detector crossed the threshold
    ////////////////////////////////////////////////////////////////////////////
    G4double GetTriggerTime(G4double cutoff)
    {
        if (!IsValid()) return -1;
        triggerTime = -1;
        if (depoEnergy[idx][0]/keV < cutoff) return triggerTime;

        if (triggermap[idx].size() < 1 ) return triggerTime;
        std::map<G4double, G4double>::iterator it = triggermap[idx].begin();
        for (; it != triggermap[idx].end(); it++)
            if (it->second/keV > cutoff) {
                triggerTime =  it->first;
                break;
            }
         return triggerTime;

    };


    ////////////////////////////////////////////////////////////////////////////
    // Check if the particle has previously been in this detector, if not, append it
    ////////////////////////////////////////////////////////////////////////////
    bool CheckPart(RecodedParticle* crParticle)
    {
        if (particledef.size() > 95) return false;
        for (int i = 0; i < particledef.size(); i++)
        {
            pCount=i;
            if (particledef.at(i).particleid == crParticle->particleid) return true;
        }
        particledef.push_back(*crParticle);
        pCount=particledef.size()-1;
        return false;
    }
    ////////////////////////////////////////////////////////////////////////////
    // record light output
    ////////////////////////////////////////////////////////////////////////////
    void recordProduction(int _idx, G4double eng, G4double time = 0)
    {
        if (_idx < 2){
            int id = 0;
            if (firstDepo[pCount][_idx] == -1)
                firstDepo[pCount][_idx] = time;
            else
                id = (int) (time  * 10 - firstDepo[pCount][_idx] * 10);
            if (id > -1 && id < 10000){
                intervaltimeCounter[_idx][id]++;
                intervaltimeEnergy[_idx][id] += eng;
            }
        }

        depoEnergy[pCount][_idx] += eng;
        depoCounter[pCount][_idx]++;

        if (_idx == 0)
            triggermap[pCount][time] = depoEnergy[pCount][_idx];
    }
    ////////////////////////////////////////////////////////////////////////////
    // record reaction information
    ////////////////////////////////////////////////////////////////////////////
    void recordReaction(int _idx, G4double eng, G4double time = 0, G4double eng2 = 0)
    {

        reacEnergy[pCount][_idx] += eng;
```

5007

```
        reacCounter[pCount][_idx]++;

        if (_idx < 2){
            if (firstInteraction[pCount][_idx] == -1)
            {
                firstInteraction[pCount][_idx] = time;
                particledef.at(pCount).EntryEnergy = eng2;
            }
        }

    }
    ////////////////////////////////////////////////////////////////////////////////
    // Print information
    ////////////////////////////////////////////////////////////////////////////////
    void Print()
    {
        ParticleType();
        if (depoEnergy[idx][PMT] == 0) return;

        G4cout << " \\\\\\\\\\\\\\ " << G4endl;
        G4cout << "Det No " << detectorID << G4endl;
        G4cout << "    masterTime " << G4BestUnit(masterTime, "Time") << G4endl;
        G4cout << "Number of Particle" << particledef.size() << G4endl;
        for (int i = 0; i < particledef.size(); i++)
        {
            G4cout << " ---------------- " << G4endl;
            G4cout << "    Particle No " << particledef.at(i).particleid << (idx == i ? " Accepted " : " ")
                   << particledef.at(i).name << G4endl;
            G4cout << "    Particle I Energy " << G4BestUnit(particledef.at(i).IncidentEnergy, "Energy") << G4endl;
            G4cout << "    Particle E Energy " << G4BestUnit(particledef.at(i).EntryEnergy, "Energy") << G4endl;
            G4cout << "    firstDepo[i][0] " << G4BestUnit(firstDepo[i][0], "Time") << G4endl;
            G4cout << "    firstDepo[i][1] " << G4BestUnit(firstDepo[i][1], "Time") << G4endl;
            G4cout << "    depoEnergy[i][0] " << G4BestUnit(depoEnergy[i][0], "Energy") << G4endl;
            G4cout << "    depoEnergy[i][1] " << G4BestUnit(depoEnergy[i][1], "Energy") << G4endl;
            G4cout << "    firstInteraction[i][0] " << G4BestUnit(firstInteraction[i][0], "Time") << G4endl;
            G4cout << "    firstInteraction[i][1] " << G4BestUnit(firstInteraction[i][1], "Time") << G4endl;
            G4cout << "    reacEnergy[i][0] " << G4BestUnit(reacEnergy[i][0], "Energy") << G4endl;
            G4cout << "    reacEnergy[i][1] " << G4BestUnit(reacEnergy[i][1], "Energy") << G4endl;
            G4cout << " ---------------- " << G4endl;
        }
        G4cout << " \\\\\\\\\\\\\\ " << G4endl;

    }

};
```

C.7 Table constructors

```
/*
The Run is a worker class for a given thread, which is responsible for for calling
the RecordEvent() method to collect all information regarding the simulation of
a particle. It is called once for every particle generated in the ParticleAction
class i.e. once for every fission event. Since it is thread specific class, there
will be one instance of this class for every thread.
*/
////////////////////////////////////////////////////////////////////////////////
// RecordEvent method is called at the end of every event, and it
// collects all the information extracted by the SteppingAction class
// and creates the respective event. Since every thread has its own
// class, the tables will be unique for each thread
////////////////////////////////////////////////////////////////////////////////

void Run::RecordEvent(const G4Event* evt)
{
    gEventNumber++;

    if (gEventNumber % 1000 == 0)
        G4cout << "NPS: " << gEventNumber << " Neutron: " << multi_detected[1][1]
                    << " " << multi_detected[1][2] << " " << multi_detected[1][3] <<
                    G4endl;

    SteppingAction* SA = SteppingAction::Instance();
    // collect source information.
    std::vector<RecodedParticle*>* nContainer = SA->GetRecodedNeutrons();
    std::vector<RecodedParticle*>* pContainer = SA->GetRecodedPhotons();
    /*G4cout << "====================" << G4endl;
    G4cout << "Event = " <<  gEventNumber << G4endl;
    G4cout << "number of neutron = " <<  nContainer->size() << G4endl;
    G4cout << "number of  photon = " <<  pContainer->size() << G4endl;*/
    int cnt_g = 0, cnt_n = 0;
    for (int i = 0; i < nContainer->size(); i++)
    {
        //nContainer->at(i)->Pout(i);
        if ((nContainer->at(i)->IncidentEnergy/keV) < 9555)
            spec_theroy[1][(int)(nContainer->at(i)->IncidentEnergy/keV/2)]++;
        cnt_n++;

    }
    for (int i = 0; i < pContainer->size(); i++)
    {
        //pContainer->at(i)->Pout(i);
        if ((pContainer->at(i)->IncidentEnergy/keV) < 9555)
            spec_theroy[0][(int)(pContainer->at(i)->IncidentEnergy/keV/2)]++;
        cnt_g++;
    }
    if (cnt_g < 33) multi_theroy[0][cnt_g]++;
    if (cnt_n < 33) multi_theroy[1][cnt_n]++;
    if (cnt_g+cnt_n < 33) multi_theroy[2][cnt_g+cnt_n]++;

    std::vector<RecodedEvent*>* eContainer = SA->GetRecodedEvents();

    std::vector<RecodedEvent*> dPhotons;
    std::vector<RecodedEvent*> dNeutrons;
    std::vector<RecodedEvent*> dJoint;
    int idpn = 0;
    // collect detector responses
    if (eContainer->size()>0){

        for (int i = 0; i < eContainer->size(); i++)
        {
            RecodedEvent* tmp = eContainer->at(i);
            int detID = 0;
            //tmp->Print();
            idpn = tmp->ParticleType();
            if ((tmp->depoEnergy[idpn][PMT] == 0) && (tmp->reacEnergy[idpn][PMT] >
            0)) continue;
            int fPartType = (tmp->name == "neutron" ? 1 : 0);
            if ((tmp->depoEnergy[idpn][PMT] == 0) && (tmp->depoEnergy[idpn][PMT] >
```

5010

```
                tmp->reacEnergy[idpn][fPartType])) continue;
                if (!tmp->IsValid()) continue;


                if (fPartType == 1) dNeutrons.push_back(tmp);
                else dPhotons.push_back(tmp);
                dJoint.push_back(tmp);

                if ((tmp->particledef.at(0).IncidentEnergy/keV) < 9555)
                    fIncidentEnergy[fPartType][(int)
                    (tmp->ptr_particledef->IncidentEnergy/keV/2)]++;
                if ((tmp->particledef.at(0).EntryEnergy/keV) < 9555)
                    fEntryEnergy[fPartType][(int)
                    (tmp->ptr_particledef->EntryEnergy/keV/2)]++;


                    if (tmp->reacEnergy[idpn][fPartType]/keV < 9555)
                        fParticleDeposit[fPartType ][(int)
                        (tmp->reacEnergy[idpn][fPartType]/keV/2)]++;


                if (tmp->reacEnergy[idpn][2]/keV < 9555)
                    fElectronDeposited[fPartType][(int)
                    (tmp->reacEnergy[idpn][2]/keV/2)]++;

                if (tmp->depoEnergy[idpn][electron]/keV < 9555)
                    fElectronProduced[fPartType][(int)
                    (tmp->depoEnergy[idpn][electron]/keV/2)]++;

                if (tmp->depoEnergy[idpn][proton]/keV > 0 &&
                tmp->depoEnergy[idpn][proton]/keV < 9555)
                    fProtonProduced[fPartType][(int)
                    (tmp->depoEnergy[idpn][proton]/keV/2)]++;

                if (tmp->reacEnergy[idpn][hIoni]/keV > 0 &&
                tmp->reacEnergy[idpn][hIoni]/keV < 9555)
                    fProtonDeposited[fPartType][(int)
                    (tmp->reacEnergy[idpn][hIoni]/keV/2)]++;

                if (tmp->depoEnergy[idpn][optical]/keV > 0 &&
                tmp->depoEnergy[idpn][optical]/keV < 9555)
                    fOphotonProduced[fPartType][(int)
                    (tmp->depoEnergy[idpn][optical]/keV/2)]++;
                if (tmp->depoEnergy[idpn][Cerenkov]/keV > 0 &&
                tmp->depoEnergy[idpn][Cerenkov]/keV < 9555)
                    fCerenkovProduced[fPartType][(int)
                    (tmp->depoEnergy[idpn][Cerenkov]/keV/2)]++;

                if (tmp->depoEnergy[idpn][PMT]/keV > 0 &&
                tmp->depoEnergy[idpn][PMT]/keV  < 9555)
                    fOphotonDeposited[fPartType][(int) (tmp->depoEnergy[idpn][PMT]/keV
                    /2)]++;


                fEventRegistered[detID]++;
                fEventNumber++;
            }
        }

        // append detectors which were triggered into a container
        std::map<double, entry> stNeutron;
        std::map<double, entry> stJoint;
        for (int i = 0; i < dNeutrons.size(); i++)// neutrons
        {
            double t = dNeutrons.at(i)->GetTriggerTime(RunAction::cutOu)/ns;
            if (t < 0) continue;
            entry tmp_;
            tmp_.didx = dNeutrons.at(i)->detectorID;
            tmp_.pid = dNeutrons.at(i)->particledef.at(0).particleid;
            stNeutron[t] = tmp_;
            stJoint[t] = tmp_;
```

5011

```
            if (t < 500)
                if (i > 0 || PrimaryGeneratorAction::mono )
                n_spec[(int)t]++;

        }

        std::map<double, entry> stPhoton; // photons
        for (int i = 0; i < dPhotons.size(); i++)
        {
            double t = dPhotons.at(i)->GetTriggerTime(RunAction::cutOu)/ns;
            if (t < 0) continue;
            entry tmp_;
            tmp_.didx = dPhotons.at(i)->detectorID;
            tmp_.pid = dPhotons.at(i)->particledef.at(0).particleid;
            stPhoton[t] = tmp_;
            stJoint[t] = tmp_;
        }

        int multi_n = 0, multi_g = 0, multi_j = 0;
        int multi_nxc = 0, multi_gxc = 0, multi_jxc = 0;
        std::vector<int> angular, ang, an;
        std::vector<int> angularcx;

        // analyze coincodence
        if ((stNeutron.size() > 0))
            if (stNeutron.size() == 1) {multi_n++;multi_nxc++;}
            else
                ProcessCoincidence(stNeutron, angular, angularcx, multi_n, multi_nxc,
                rossi_[1], rossi_cx[1]);

        if ((stPhoton.size() > 0))
            if (stPhoton.size() == 1) {multi_g++;multi_gxc++;}
            else
                ProcessCoincidence(stPhoton, ang, an, multi_g, multi_gxc, rossi_[0],
                rossi_cx[0]);
        an.clear(); ang.clear();
        if ((stJoint.size() > 0) )
            if (stJoint.size() == 1) {multi_j++;multi_jxc++;}
            else
                ProcessCoincidence(stJoint, ang, an, multi_j, multi_jxc, rossi_[2],
                rossi_cx[2]);

        // increment coincidence distributions
        multi_detected[1][multi_n]++;
        multi_detected[0][multi_g]++;
        multi_detected[2][multi_j]++;
        multi_detectedcx[1][multi_nxc]++;
        multi_detectedcx[0][multi_gxc]++;
        multi_detectedcx[2][multi_jxc]++;


        // increment angular distributions
        if (angular.size() > 1)
        {
            int base = angular.at(0)+1;
            int shift = 8 - base;
            int v = 0;
            for (int i = 1; i < angular.size(); i++)
            {
                int val = angular.at(i) + shift + 1;
                if (val < 1 ) val += 15;
                else if (val > 15) val -= 15;

                angular_plot[0][val]++;
                angular_plot[i][val]++;
                if (i == 1) v = val;
                else if (i == 2) angular_contour[v][val]++;
            }
        }
        if (angularcx.size() > 1)
```

5012

```
    {
        int base = angularcx.at(0)+1;
        int shift = 8 - base;
        int v = 0;
        for (int i = 1; i < angularcx.size(); i++)
        {
            int val = angularcx.at(i) + shift + 1;
            if (val < 1 ) val += 15;
            else if (val > 15) val -= 15;

            angular_plotcx[0][val]++;
            angular_plotcx[i][val]++;
            if (i == 1) v = val;
            else if (i == 2) angular_contourcx[v][val]++;
        }
    }


    SteppingAction::Instance()->Reset();

    G4Run::RecordEvent(evt);
}
////////////////////////////////////////////////////////////////////////////////
// Method to constrct the coincidence distributions, including interval time
// distributions and angular distribution
////////////////////////////////////////////////////////////////////////////////
void Run::ProcessCoincidence(std::map<double, entry> storage, std::vector<int>& angular,
                std::vector<int>& angularcx, int &multi, int &multi_cx, int* rossi, int* rossicx)
{
    std::map<double, entry>::iterator it = storage.begin();
    double tim = -1;
    bool cx_map[64] = {false};
    for (; it != storage.end(); it++)
    {
        entry en = it->second;
        int deltaT = (int)(it->first - tim);
        if (tim == -1)
        {
            tim = it->first;
            multi++;
            multi_cx++;
            angular.push_back(en.didx);
            angularcx.push_back(en.didx);
            cx_map[en.pid] = true;
        }
        else if (deltaT  < SteppingAction::gwidth)
        {
            multi++;
            angular.push_back(en.didx);
            rossi[deltaT]++;
            if (!cx_map[en.pid]) {
                multi_cx++;
                angularcx.push_back(en.didx);
                rossicx[deltaT]++;
            }
            else
                _time[en.didx][deltaT]++;
            cx_map[en.pid] = true;
        }
        else if(deltaT < 500)
        {
            rossi[deltaT]++;
            if (!cx_map[en.pid]) {
                rossicx[deltaT]++;
            }
            else
                _time[en.didx][deltaT]++;
            cx_map[en.pid] = true;
        }
```

5013

```
    }
};
////////////////////////////////////////////////////////////////////////////////
// Since every thread has its own class, the tables will be unique
// for each thread. Hence at the end of the simulation, the Merge() method
// is called to collect all the tables into one master table.
////////////////////////////////////////////////////////////////////////////////
void Run::Merge(const G4Run* run)
{
    const Run* localRun = static_cast<const Run*>(run);

    //primary particle info
    //
    fParticle = localRun->fParticle;
    fEkin = localRun->fEkin;

    // accumulate sums
    //
    fNbStep1 += localRun->fNbStep1;
    fNbStep2 += localRun->fNbStep2;
    fTrackLen1 += localRun->fTrackLen1;
    fTrackLen2 += localRun->fTrackLen2;
    fTime1 += localRun->fTime1;
    fTime2 += localRun->fTime2;

    //map: processes count
    std::map<G4String, G4int>::const_iterator itp;
    for (itp = localRun->fProcCounter.begin();
            itp != localRun->fProcCounter.end(); ++itp)
    {

        G4String procName = itp->first;
        G4int localCount = itp->second;
        if (fProcCounter.find(procName) == fProcCounter.end())
        {
            fProcCounter[procName] = localCount;
        }
        else
        {
            fProcCounter[procName] += localCount;
        }
    }

    std::map<G4String, ParticleData>::const_iterator itn;
    for (itn = localRun->fParticleDataMap.begin();
            itn != localRun->fParticleDataMap.end(); ++itn)
    {

        G4String name = itn->first;
        const ParticleData& localData = itn->second;
        if (fParticleDataMap.find(name) == fParticleDataMap.end())
        {
            fParticleDataMap[name] = ParticleData(localData.fCount,
                    localData.fEmean, localData.fEmin, localData.fEmax);
        }
        else
        {
            ParticleData& data = fParticleDataMap[name];
            data.fCount += localData.fCount;
            data.fEmean += localData.fEmean;
            G4double emin = localData.fEmin;
            if (emin < data.fEmin)
                data.fEmin = emin;
            G4double emax = localData.fEmax;
            if (emax > data.fEmax)
                data.fEmax = emax;
        }
    }

    gEventNumber += localRun->gEventNumber;
    G4cout << "local event count = " << localRun->gEventNumber << " "
```

5014

```
            << "global event count = " << gEventNumber << G4endl;

    for (uint k = 0; k <  2; k++)
        for (uint i = 0; i < 5000; i++)
        {
            fLightResponse[k][i] += localRun->fLightResponse[k][i];
            fLightHistogram[k][i] += localRun->fLightHistogram[k][i];
            fPMTResponse[k][i] += localRun->fPMTResponse[k][i];
            fPMTHistogram[k][i] += localRun->fPMTHistogram[k][i];
            fIncidentEnergy[k][i] += localRun->fIncidentEnergy[k][i];
            fParticleDeposit[k][i] += localRun->fParticleDeposit[k][i];
            fElectronDeposited[k][i] += localRun->fElectronDeposited[k][i];
            fElectronProduced[k][i] += localRun->fElectronProduced[k][i];
            fProtonProduced[k][i] += localRun->fProtonProduced[k][i];
            fProtonDeposited[k][i] += localRun->fProtonDeposited[k][i];
            fOphotonProduced[k][i] += localRun->fOphotonProduced[k][i];
            fCerenkovProduced[k][i] += localRun->fCerenkovProduced[k][i];
            fOphotonDeposited[k][i] += localRun->fOphotonDeposited[k][i];
            fEntryEnergy[k][i] += localRun->fEntryEnergy[k][i];



        }
    for (int i = 0; i < 3; i++)
        for (int k = 0; k < 500; k++)
        {
            rossi_[i][k] += localRun->rossi_[i][k];
            rossi_cx[i][k] += localRun->rossi_cx[i][k];
        }
    for (int k = 0; k < 500; k++)
        n_spec[k] += localRun->n_spec[k];

    for (int i = 0; i < DETECTOR_COUNT; i++)
        for (int k = 0; k < 500; k++)
            _time[i][k] += localRun->_time[i][k];

    for (uint i = 0; i < 5000; i++)
    {
        spec_theroy[0][i] += localRun->spec_theroy[0][i];
        spec_theroy[1][i] += localRun->spec_theroy[1][i];
    }

    for (int ii = 0; ii < 20; ii++)
    {
        fEventRegistered[ii] += localRun->fEventRegistered[ii];
    }

    for(int i  = 0; i  < 16; i ++)
    for(int ii = 0; ii < 16; ii++)
    {
        angular_plot[i][ii] += localRun->angular_plot[i][ii];
        angular_contour[i][ii] += localRun->angular_contour[i][ii];
        angular_plotcx[i][ii] += localRun->angular_plotcx[i][ii];
        angular_contourcx[i][ii] += localRun->angular_contourcx[i][ii];
    }

    for (int ii = 0; ii < 32; ii++)
    {
        multi_theroy[0][ii] += localRun->multi_theroy[0][ii];
        multi_theroy[1][ii] += localRun->multi_theroy[1][ii];
        multi_theroy[2][ii] += localRun->multi_theroy[2][ii];
        multi_detected[0][ii] += localRun->multi_detected[0][ii];
        multi_detected[1][ii] += localRun->multi_detected[1][ii];
        multi_detected[2][ii] += localRun->multi_detected[2][ii];
        multi_detectedcx[0][ii] += localRun->multi_detectedcx[0][ii];
        multi_detectedcx[1][ii] += localRun->multi_detectedcx[1][ii];
        multi_detectedcx[2][ii] += localRun->multi_detectedcx[2][ii];
    }

    G4Run::Merge(run);
}
```

Appendix D

Analytical scripts

D.1 Extracting number distribution from FREYA

```
/*
C++ Script for extracting number distribution of varous isotopes
from FREYA Library. Based on example script provided by the
publisher
*/
#define iterations 3000000
#define nbins 50

#include <stdio.h>
#include "fissionEvent.h"

void init(void);
FILE* openfile(char* name);
void output(int* hist);
/*
Main function
*/
int main(int argc,char** argv) {
   bool spontaneous_fission=true;
   bool gamma = false;
   int isotope = 98252;
   double energy_MeV = 2.1;
   double nubar = 2.523670;
   double time = 0.;

   //get isotope ID and gamma flaf from argument list
   isotope   = atoi(argv[2]);
   if (argc == 4 ) gamma = true;

   //initialize
   printf("Isotope=%d Particle=%s\n", isotope, gamma ? "Gamma" : "Neutron");
   int maxerrorlength=10000;
   char errors[maxerrorlength];

   int hist[nbins];
   for (int i=0; i<nbins; i++) hist[i] = 0.;

   init();
   //iterate to build up history
   for (int i=0; i<iterations; i++) {
       //call FREYA library
      fissionEvent* fe = new fissionEvent(isotope, time, nubar, energy_MeV, (spontaneous_fission)?0:1);
      int errorlength=maxerrorlength;
      fe->getFREYAerrors(&errorlength, &errors[0]);
      //error check
      if (errorlength>1) {
         printf("%s\n",errors);
         exit(1);
      }
      //create distribution
      int npart = 0;
      if (!gamma)
        npart = fe->getNeutronNu();
      else if (gamma)
        npart = fe->getPhotonNu();
      else
          continue;
      hist[npart]++;
      delete fe;
   }
   output(hist);
}

void init(void) {
   unsigned short int s[3] = {1234, 5678, 9012};
```

5033

```
66      int i;
67      seed48(s);
68      fissionEvent::setCorrelationOption(3);
69      return;
70   }
71
72   /*
73   Open file
74   */
75   FILE* openfile(char* name) {
76      FILE* fp = fopen(name, "w");
77      if (fp == (FILE *) 0) fprintf(stderr, "Could not open %s for writing", name);
78      return fp;
79   }
80   /*
81   Print output to file
82   */
83   void output(int* hist) {
84      char filename [1024];
85      sprintf(filename, "nu_dist.res");
86      FILE* fp = openfile(filename);
87
88      unsigned int sum=0;
89      for (int i=0; i<nbins; i++) sum += hist[i];
90      for (int i=0; i<nbins; i++) fprintf(fp, "%d : %10.8f\n", i, 1.*hist[i]/sum);
91
92      for (int i=0; i<nbins; i++)
93        printf("nu[%d]=%g\n", i, 1.*hist[i]/sum);
94
95      double nu_bar=0;
96      for (int i=1; i<nbins; i++) nu_bar += 1.*i*hist[i]/sum;
97      printf("nu_bar=%g\n", nu_bar);
98      double nu_2=0;
99      for (int i=2; i<nbins; i++) nu_2 += 0.5*i*(i-1)*hist[i]/sum;
100     printf("nu2=%g\n", nu_2);
101     double nu_3=0;
102     for (int i=3; i<nbins; i++) nu_3 += 1./6*i*(i-1)*(i-2)*hist[i]/sum;
103     printf("nu3=%g\n", nu_3);
104     double nu_4=0;
105     for (int i=4; i<nbins; i++) nu_4 += 1./6/4*i*(i-1)*(i-2)*hist[i]/sum;
106     printf("nu4=%g\n", nu_4);
107     double nu_5=0;
108     for (int i=5; i<nbins; i++) nu_5 += 1./6/4/5*i*(i-1)*(i-2)*hist[i]/sum;
109     printf("nu5=%g\n", nu_5);
110
111     printf("D2=%g\n", nu_2/nu_bar);
112     printf("D3=%g\n", nu_3/nu_bar);
113     printf("D4=%g\n", nu_4/nu_bar);
114     printf("D5=%g\n", nu_5/nu_bar);
115
116     fclose(fp);
117     return;
118  }
119
120
```

D.2 Extracting angular correlation distribution from FREYA

```
/*
C++ Script to extract angular distribution from FREYA library
Based on example code provided by the publisher.
*/

#define iterations 300000
#define nbins 100

#include <stdio.h>
#include "fissionEvent.h"

void init(void);
FILE* openfile(char* name);
void output(int* hist);

/*
Main function
*/
int main() {
   bool spontfiss=false;
   int isotope = 98252;
   double energy_MeV = 2.;
   double nubar = 3.163;
   double time = 0.;

   int maxerrorlength=10000;
   char errors[maxerrorlength];

   int hist[nbins];
   for (int i=0; i<nbins; i++) hist[i] = 0.;

   init();
   for (int i=0; i<iterations; i++) {
      fissionEvent* fe = new fissionEvent(isotope, time, nubar, energy_MeV, (spontfiss)?0:1);
      int errorlength=maxerrorlength;
      fe->getFREYAerrors(&errorlength, &errors[0]);
      if (errorlength>1) {
         printf("%s\n",errors);
         exit(1);
      }
      int nneutrons = fe->getNeutronNu();
      for(int n1=0; n1<nneutrons; n1++) {
         double u1 = fe->getNeutronDircosu(n1), v1 = fe->getNeutronDircosv(n1), w1 = fe->getNeutronDircosw(n1);
         for(int n2=n1+1; n2<nneutrons; n2++) {
            double u2 = fe->getNeutronDircosu(n2), v2 = fe->getNeutronDircosv(n2), w2 = fe->getNeutronDircosw(n2);
            double scalar_product = u1*u2+v1*v2+w1*w2;

            int bin_index = (int) (nbins*(scalar_product+1)/2);
            hist[bin_index]++;
         }
      }
      delete fe;
   }
   output(hist);
}

/*
Initialize seed for random number generator
*/
void init(void) {
   unsigned short int s[3] = {1234, 5678, 9012};
   int i;
   seed48(s);
```

5036

```
   fissionEvent::setCorrelationOption(3);
   return;
}

/*
    Open output file
*/
FILE* openfile(char* name) {
   FILE* fp = fopen(name, "w");
   if (fp == (FILE *) 0) fprintf(stderr, "Could not open %s for writing", name);
   return fp;
}
/*
    Print output file
*/
void output(int* hist) {
   char filename [1024];
   sprintf(filename, "angular_correlation.res");
   FILE* fp = openfile(filename);

   unsigned int sum=0;
   for (int i=0; i<nbins; i++) sum += hist[i];
   for (int i=0; i<nbins; i++) fprintf(fp, "%e - %e : %e\n", -1+2.*i/nbins, -1+2.*(i+1)/nbins, 1.*hist[i]/sum);

   fclose(fp);
   return;
}
```

D.3 Factorial Moment

```
function [ output uncer ] = factorial_moment( input, uncertainty, range )
%FACTORIAL_MOMENT Summary of this function goes here
%   Detailed explanation goes here
%   input = Number distribution
%   uncertainty = Uncertainties in number
%   range = number of historams, for chain calculation
output = input;
uncer = uncertainty;
temp = input;
temp_p = (sum((((uncertainty).^.5).*temp)')./sum(temp')).^2;
temp_p2=uncertainty;
for (rng=1:range)
    temp (rng, :) = temp (rng, :)./sum(temp (rng, :));
    temp_p2(rng, 3:7)=temp_p2(rng, 3:7)+temp_p(rng);
    for (order=1:9)
        for (loop = 1:9)
            multiply_f=loop-order;
            if (multiply_f < 0) multiply_f = 0; end
            temp (rng, loop) = multiply_f * temp (rng, loop);
            temp_p2 (rng, loop+2) = multiply_f *  temp_p2 (rng, loop+2);
        end
        uncer (rng, order+2) = sum(temp_p2 (rng, 3:7));
        output (rng, order) = sum(temp (rng, :));
    end
end
```

D.4 Number density analysis

D.4.1 Number density and neutron activity

```
% Matlab script to post process all data
% naming convention:
%   first three characters = reactor type i.e. PWR or BWR
%   next three characters  = fuel type i.e. MOX or UOX
%   next two numbers       = burnup level i.e. 10, 20, 35 and 55
%   last two number        = data type i.e. 0 for number density
%                                9 for spontaneous fission activity
%                               10 for (alpha, n) activity
% The first coloum of the variables is the time of irradiation
% subsequent coloums corresponds to different isotopes
% i.e. 'Pu^{238}', 'Pu^{239}', 'Pu^{240}', 'Pu^{241}','Pu^{242}',
% 'Am^{241}' , Cm^{242}', 'Cm^{248}'
% corresponds to [37:41 47 57 59]


% correct the negative axis to signify irradiation
% replace PWRMOX with other combination.
PWRMOX55_10(2:11,1)=PWRMOX55_10(2:11,1)-PWRMOX55_10(11,1);
PWRMOX35_10(2:11,1)=PWRMOX35_10(2:11,1)-PWRMOX35_10(11,1);
PWRMOX20_10(2:11,1)=PWRMOX20_10(2:11,1)-PWRMOX20_10(11,1);
PWRMOX10_10(2:11,1)=PWRMOX10_10(2:11,1)-PWRMOX10_10(11,1);

PWRMOX55_9(2:11,1)=PWRMOX55_9(2:11,1)-PWRMOX55_9(11,1);
PWRMOX35_9(2:11,1)=PWRMOX35_9(2:11,1)-PWRMOX35_9(11,1);
PWRMOX20_9(2:11,1)=PWRMOX20_9(2:11,1)-PWRMOX20_9(11,1);
PWRMOX10_9(2:11,1)=PWRMOX10_9(2:11,1)-PWRMOX10_9(11,1);

PWRMOX55_0(2:11,1)=PWRMOX55_0(2:11,1)-PWRMOX55_0(11,1);
PWRMOX35_0(2:11,1)=PWRMOX35_0(2:11,1)-PWRMOX35_0(11,1);
PWRMOX20_0(2:11,1)=PWRMOX20_0(2:11,1)-PWRMOX20_0(11,1);
PWRMOX10_0(2:11,1)=PWRMOX10_0(2:11,1)-PWRMOX10_0(11,1);

%% Ploting number density of 20 GWd/MTU samples
% replace "0_" with spontanoeus fission and (alpha, n) emission data.
% replace PWRMOX with other combination.
figH = figure(1)
set(figH,'Position',[1 1 339.4 245.6]);
plot(PWRUOX20_0(2:end,1),PWRUOX20_0(2:end,37)*6.022E23,'--k','LineWidth',1.5)
hold on
plot(PWRUOX20_0(2:end,1),PWRUOX20_0(2:end,38)*6.022E23,'x-k','LineWidth',1.5)
plot(PWRUOX20_0(2:end,1),PWRUOX20_0(2:end,39)*6.022E23,'-.k','LineWidth',1.5)
plot(PWRUOX20_0(2:end,1),PWRUOX20_0(2:end,40)*6.022E23,':k','LineWidth',1.5)
plot(PWRUOX20_0(2:end,1),PWRUOX20_0(2:end,41)*6.022E23,'k','LineWidth',1.5)
xlim([-300 max(PWRUOX20_0(2:end,1)) ] )
xlabel ('Number of Days', 'FontSize', 12)
ylabel ('Number Density (atoms/MTU)', 'FontSize', 12)
title ('PWR-UOX Fuel-20GWd/MTU', 'FontSize', 10)
hold off
grid on

%% Ploting number density of Pu isotopes for the 35 GWd/MTU samples
% replace "0_" with spontanoeus fission and (alpha, n) emission data.
% replace PWRMOX with other combination.
figH = figure(4)
set(figH,'Position',[1 1 339.4 245.6]);
plot(PWRUOX35_0(2:end,1),PWRUOX35_0(2:end,37)*6.022E23,'--k','LineWidth',1.5)
hold on
plot(PWRUOX35_0(2:end,1),PWRUOX35_0(2:end,38)*6.022E23,'x-k','LineWidth',1.5)
plot(PWRUOX35_0(2:end,1),PWRUOX35_0(2:end,39)*6.022E23,'-.k','LineWidth',1.5)
plot(PWRUOX35_0(2:end,1),PWRUOX35_0(2:end,40)*6.022E23,':k','LineWidth',1.5)
plot(PWRUOX35_0(2:end,1),PWRUOX35_0(2:end,41)*6.022E23,'k','LineWidth',1.5)
xlim([-300 max(PWRUOX20_0(2:end,1)) ] )
xlabel ('Number of Days', 'FontSize', 12)
ylabel ('Number Density (atoms/MTU)', 'FontSize', 12)
title ('PWR-UOX Fuel-35GWd/MTU', 'FontSize', 10)
hold off
```

5042

```
grid on

%% Ploting number density of  Pu isotopes for the 55 GWd/MTU samples
% replace "0_" with spontanoeus fission and (alpha, n) emission data.
% replace PWRMOX with other combination.
figH = figure(7)
set(figH,'Position',[1 1 339.4 245.6]);
plot(PWRUOX55_0(2:end,1),PWRUOX55_0(2:end,37)*6.022E23,'--k','LineWidth',1.5)
hold on
plot(PWRUOX55_0(2:end,1),PWRUOX55_0(2:end,38)*6.022E23,'x-k','LineWidth',1.5)
plot(PWRUOX55_0(2:end,1),PWRUOX55_0(2:end,39)*6.022E23,'-.k','LineWidth',1.5)
plot(PWRUOX55_0(2:end,1),PWRUOX55_0(2:end,40)*6.022E23,':k','LineWidth',1.5)
plot(PWRUOX55_0(2:end,1),PWRUOX55_0(2:end,41)*6.022E23,'k','LineWidth',1.5)
xlim([-300 max(PWRUOX20_0(2:end,1)) ] )
xlabel ('Number of Days', 'FontSize', 12)
ylabel ('Number Density (atoms/MTU)', 'FontSize', 12)
title ('PWR-UOX Fuel-55GWd/MTU', 'FontSize', 10)
hold off
grid on


%% Ploting number density of  Pu isotopes for the 10 GWd/MTU samples
% replace "0_" with spontanoeus fission and (alpha, n) emission data.
% replace PWRMOX with other combination.
figH = figure(10)
set(figH,'Position',[1 1 339.4 245.6]);
plot(PWRUOX10_0(2:end,1),PWRUOX10_0(2:end,37)*6.022E23,'--k','LineWidth',1.5)
hold on
plot(PWRUOX10_0(2:end,1),PWRUOX10_0(2:end,38)*6.022E23,'x-k','LineWidth',1.5)
plot(PWRUOX10_0(2:end,1),PWRUOX10_0(2:end,39)*6.022E23,'-.k','LineWidth',1.5)
plot(PWRUOX10_0(2:end,1),PWRUOX10_0(2:end,40)*6.022E23,':k','LineWidth',1.5)
plot(PWRUOX10_0(2:end,1),PWRUOX10_0(2:end,41)*6.022E23,'k','LineWidth',1.5)
xlim([-300 max(PWRUOX10_0(2:end,1)) ] )
xlabel ('Number of Days', 'FontSize', 12)
ylabel ('Number Density (atoms/MTU)', 'FontSize', 12)
title ('PWR-UOX Fuel-10GWd/MTU', 'FontSize', 10)
hold off
grid on

%% Ploting number density Am and Cm isotopes for the 20 GWd/MTU samples% replace
%"0_" with spontanoeus fission and (alpha, n) emission data.
% replace PWRMOX with other combination.
figH = figure(1)
set(figH,'Position',[1 1 339.4 245.6]);
plot(PWRUOX20_0(2:end,1),PWRUOX20_0(2:end,47)*6.022E21,'--k','LineWidth',1.5)
hold on
plot(PWRUOX20_0(2:end,1),PWRUOX20_0(2:end,50)*6.022E22,'x-k','LineWidth',1.5)
plot(PWRUOX20_0(2:end,1),PWRUOX20_0(2:end,57)*6.022E23,'-.k','LineWidth',1.5)
plot(PWRUOX20_0(2:end,1),PWRUOX20_0(2:end,59)*6.022E23,':k','LineWidth',1.5)
xlim([-300 max(PWRUOX20_0(2:end,1)) ] )
xlabel ('Number of Days', 'FontSize', 12)
ylabel ('Number Density (atoms/MTU)', 'FontSize', 12)
title ('PWR-UOX Fuel-20GWd/MTU', 'FontSize', 10)
grid on
hold off

%% Ploting number density Am and Cm isotopes for the 35 GWd/MTU samples
% replace "0_" with spontanoeus fission and (alpha, n) emission data.
% replace PWRMOX with other combination.
figH = figure(4)
set(figH,'Position',[1 1 339.4 245.6]);
plot(PWRUOX35_0(2:end,1),PWRUOX35_0(2:end,47)*6.022E21,'--k','LineWidth',1.5)
hold on
plot(PWRUOX35_0(2:end,1),PWRUOX35_0(2:end,50)*6.022E22,'x-k','LineWidth',1.5)
plot(PWRUOX35_0(2:end,1),PWRUOX35_0(2:end,57)*6.022E23,'-.k','LineWidth',1.5)
plot(PWRUOX35_0(2:end,1),PWRUOX35_0(2:end,59)*6.022E23,':k','LineWidth',1.5)
```

5043

```
xlim([-300 max(PWRUOX20_0(2:end,1)) ] )
xlabel ('Number of Days', 'FontSize', 12)
ylabel ('Number Density (atoms/MTU)', 'FontSize', 12)
title ('PWR-UOX Fuel-35GWd/MTU', 'FontSize', 10)
grid on
hold off

%% Ploting number density Am and Cm isotopes for the 55 GWd/MTU samples
% replace "0_" with spontanoeus fission and (alpha, n) emission data.
% replace PWRMOX with other combination.
figH = figure(7)
set(figH,'Position',[1 1 339.4 245.6]);
plot(PWRUOX55_0(2:end,1),PWRUOX55_0(2:end,47)*6.022E21,'--k','LineWidth',1.5)
hold on
plot(PWRUOX55_0(2:end,1),PWRUOX55_0(2:end,50)*6.022E22,'x-k','LineWidth',1.5)
plot(PWRUOX55_0(2:end,1),PWRUOX55_0(2:end,57)*6.022E23,'-.k','LineWidth',1.5)
plot(PWRUOX55_0(2:end,1),PWRUOX55_0(2:end,59)*6.022E23,':k','LineWidth',1.5)
xlim([-300 max(PWRUOX20_0(2:end,1)) ] )
% legend('0.01*Am^{241}', '0.1*Am^{243}', 'Cm^{242}', 'Cm^{244}')
xlabel ('Number of Days', 'FontSize', 12)
ylabel ('Number Density (atoms/MTU)', 'FontSize', 12)
title ('PWR-UOX Fuel-55GWd/MTU', 'FontSize', 10)
grid on
hold off

%% Ploting number density Am and Cm isotopes for the 10 GWd/MTU samples
% replace "0_" with spontanoeus fission and (alpha, n) emission data.
% replace PWRMOX with other combination.
figH = figure(10)
set(figH,'Position',[1 1 339.4 245.6]);
plot(PWRUOX10_0(2:end,1),PWRUOX10_0(2:end,47)*6.022E21,'--k','LineWidth',1.5)
hold on
plot(PWRUOX10_0(2:end,1),PWRUOX10_0(2:end,50)*6.022E22,'x-k','LineWidth',1.5)
plot(PWRUOX10_0(2:end,1),PWRUOX10_0(2:end,57)*6.022E23,'-.k','LineWidth',1.5)
plot(PWRUOX10_0(2:end,1),PWRUOX10_0(2:end,59)*6.022E23,':k','LineWidth',1.5)
xlim([-300 max(PWRUOX10_0(2:end,1)) ] )
% legend('0.01*Am^{241}', '0.1*Am^{243}', 'Cm^{242}', 'Cm^{244}')
xlabel ('Number of Days', 'FontSize', 12)
ylabel ('Number Density (atoms/MTU)', 'FontSize', 12)
title ('PWR-UOX Fuel-10GWd/MTU', 'FontSize', 10)
grid on
hold off
```

D.4.2 Relative neutron activity

```
% Matlab script to post process all data
% naming convention:
%   first three characters = reactor type i.e. PWR or BWR
%   next three characters  = fuel type i.e. MOX or UOX
%   next two numbers       = burnup level i.e. 10, 20, 35 and 55
%   last two number        = data type i.e. 0 for number density
%                                 9 for spontaneous fission activity
%                                10 for (alpha, n) activity
% The first coloum of the variables is the time of irradiation
% subsequent coloums corresponds to different isotopes
% i.e. 'Pu^{238}', 'Pu^{239}', 'Pu^{240}', 'Pu^{241}','Pu^{242}',
% 'Am^{241}' , Cm^{242}', 'Cm^{248}'
% corresponds to [37:41 47 57 59]


% correct the negative axis to signify irradiation
% replace PWRMOX with other combination.


%% Calculate and plot relative activity
clear ratio_iso
BWRMOX_A(:,:,1) = BWRMOX10_10(:,[1 20 24 29 35 37 38 39 40 41 42 43 47 48 49 50 57 58 59 60 61]);
BWRMOX_A(:,:,2) = BWRMOX20_10(:,[1 20 24 29 35 37 38 39 40 41 42 43 47 48 49 50 57 58 59 60 61]);
BWRMOX_A(:,:,3) = BWRMOX35_10(:,[1 20 24 29 35 37 38 39 40 41 42 43 47 48 49 50 57 58 59 60 61]);
BWRMOX_A(:,:,4) = BWRMOX55_10(:,[1 20 24 29 35 37 38 39 40 41 42 43 47 48 49 50 57 58 59 60 61]);

PWRMOX_A(:,:,1) = PWRMOX10_10(:,[1 20 24 29 35 37 38 39 40 41 42 43 47 48 49 50 57 58 59 60 61]);
PWRMOX_A(:,:,2) = PWRMOX20_10(:,[1 20 24 29 35 37 38 39 40 41 42 43 47 48 49 50 57 58 59 60 61]);
PWRMOX_A(:,:,3) = PWRMOX35_10(:,[1 20 24 29 35 37 38 39 40 41 42 43 47 48 49 50 57 58 59 60 61]);
PWRMOX_A(:,:,4) = PWRMOX55_10(:,[1 20 24 29 35 37 38 39 40 41 42 43 47 48 49 50 57 58 59 60 61]);

PWRUOX_A(:,:,1) = PWRUOX10_10(:,[1 20 24 29 35 37 38 39 40 41 42 43 47 48 49 50 57 58 59 60 61]);
PWRUOX_A(:,:,2) = PWRUOX20_10(:,[1 20 24 29 35 37 38 39 40 41 42 43 47 48 49 50 57 58 59 60 61]);
PWRUOX_A(:,:,3) = PWRUOX35_10(:,[1 20 24 29 35 37 38 39 40 41 42 43 47 48 49 50 57 58 59 60 61]);
PWRUOX_A(:,:,4) = PWRUOX55_10(:,[1 20 24 29 35 37 38 39 40 41 42 43 47 48 49 50 57 58 59 60 61]);

BWRMOX_S(:,:,1) = BWRMOX10_9(:,[1 20 24 29 35 37 38 39 40 41 42 43 47 48 49 50 57 58 59 60 61]);
BWRMOX_S(:,:,2) = BWRMOX20_9(:,[1 20 24 29 35 37 38 39 40 41 42 43 47 48 49 50 57 58 59 60 61]);
BWRMOX_S(:,:,3) = BWRMOX35_9(:,[1 20 24 29 35 37 38 39 40 41 42 43 47 48 49 50 57 58 59 60 61]);
BWRMOX_S(:,:,4) = BWRMOX55_9(:,[1 20 24 29 35 37 38 39 40 41 42 43 47 48 49 50 57 58 59 60 61]);

PWRMOX_S(:,:,1) = PWRMOX10_9(:,[1 20 24 29 35 37 38 39 40 41 42 43 47 48 49 50 57 58 59 60 61]);
PWRMOX_S(:,:,2) = PWRMOX20_9(:,[1 20 24 29 35 37 38 39 40 41 42 43 47 48 49 50 57 58 59 60 61]);
PWRMOX_S(:,:,3) = PWRMOX35_9(:,[1 20 24 29 35 37 38 39 40 41 42 43 47 48 49 50 57 58 59 60 61]);
PWRMOX_S(:,:,4) = PWRMOX55_9(:,[1 20 24 29 35 37 38 39 40 41 42 43 47 48 49 50 57 58 59 60 61]);
```

5046

```
PWRUOX_S(:,:,1) = PWRUOX10_9(:,[1 20 24 29 35 37 38 39 40 41 42 43 47 48 49 50 57 58 59 60 61]);
PWRUOX_S(:,:,2) = PWRUOX20_9(:,[1 20 24 29 35 37 38 39 40 41 42 43 47 48 49 50 57 58 59 60 61]);
PWRUOX_S(:,:,3) = PWRUOX35_9(:,[1 20 24 29 35 37 38 39 40 41 42 43 47 48 49 50 57 58 59 60 61]);
PWRUOX_S(:,:,4) = PWRUOX55_9(:,[1 20 24 29 35 37 38 39 40 41 42 43 47 48 49 50 57 58 59 60 61]);

NumStacksPerGroup = 6;
NumGroupsPerAxis = 4;
NumStackElements = 20;
%      stackData is a 3D matrix (i.e., stackData(i, j, k) => (burnup, cooling time, ratios))

groupLabels = { '10 GWd/MTU'; '20 GWd/MTU'; '35 GWd/MTU'; '55 GWd/MTU'; };

for I = 1:4
    stackData(I,1,1:20)=BWRMOX_A(12, 2:21, I)./sum(BWRMOX_A(12, 2:21, I));
    stackData(I,2,1:20)=BWRMOX_A(25, 2:21, I)./sum(BWRMOX_A(25, 2:21, I));
    stackData(I,3,1:20)=BWRMOX_A(33, 2:21, I)./sum(BWRMOX_A(33, 2:21, I));
    stackData(I,4,1:20)=BWRMOX_A(38, 2:21, I)./sum(BWRMOX_A(38, 2:21, I));
    stackData(I,5,1:20)=BWRMOX_A(42, 2:21, I)./sum(BWRMOX_A(42, 2:21, I));
    stackData(I,6,1:20)=BWRMOX_A(47, 2:21, I)./sum(BWRMOX_A(47, 2:21, I));
end

plotBarStackGroups(stackData, groupLabels, 25);
ylabel('Relative neutron activity (neutrons/sec/MTU)', 'FontSize', 12);%, 'FontWeight', 'bold');
xlabel('Fuel history', 'FontSize', 12)
legend('U235','U238','Np237','Pu237','Pu238','Pu239','Pu240',...
    'Pu241','Pu242','Pu243','Pu244', 'Am241', 'Am242', 'Am242m',...
    'Am243','Cm242','Cm243','Cm244','Cm245','Cm246', 'Location','EastOutside');
ylim([0 1])
clear stackData Y internalPosCount i h groupDrawPos groupBins ;

for I = 1:4
    stackData(I,1,1:20)=BWRMOX_S(12, 2:21, I)./sum(BWRMOX_S(12, 2:21, I));
    stackData(I,2,1:20)=BWRMOX_S(25, 2:21, I)./sum(BWRMOX_S(25, 2:21, I));
    stackData(I,3,1:20)=BWRMOX_S(33, 2:21, I)./sum(BWRMOX_S(33, 2:21, I));
    stackData(I,4,1:20)=BWRMOX_S(38, 2:21, I)./sum(BWRMOX_S(38, 2:21, I));
    stackData(I,5,1:20)=BWRMOX_S(42, 2:21, I)./sum(BWRMOX_S(42, 2:21, I));
    stackData(I,6,1:20)=BWRMOX_S(47, 2:21, I)./sum(BWRMOX_S(47, 2:21, I));
end

plotBarStackGroups(stackData, groupLabels, 25);
ylabel('Relative neutron activity (neutrons/sec/MTU)', 'FontSize', 12);%, 'FontWeight', 'bold');
xlabel('Fuel history', 'FontSize', 12)
legend('U235','U238','Np237','Pu237','Pu238','Pu239','Pu240',...
    'Pu241','Pu242','Pu243','Pu244', 'Am241', 'Am242', 'Am242m',...
    'Am243','Cm242','Cm243','Cm244','Cm245','Cm246', 'Location','EastOutside');
ylim([0 1])

for I = 1:4
    stackData(I,1,1:20)=PWRMOX_A(12, 2:21, I)./sum(PWRMOX_A(12, 2:21, I));
    stackData(I,2,1:20)=PWRMOX_A(25, 2:21, I)./sum(PWRMOX_A(25, 2:21, I));
    stackData(I,3,1:20)=PWRMOX_A(33, 2:21, I)./sum(PWRMOX_A(33, 2:21, I));
    stackData(I,4,1:20)=PWRMOX_A(38, 2:21, I)./sum(PWRMOX_A(38, 2:21, I));
    stackData(I,5,1:20)=PWRMOX_A(42, 2:21, I)./sum(PWRMOX_A(42, 2:21, I));
    stackData(I,6,1:20)=PWRMOX_A(47, 2:21, I)./sum(PWRMOX_A(47, 2:21, I));
end

plotBarStackGroups(stackData, groupLabels, 25);
ylabel('Relative neutron activity (neutrons/sec/MTU)', 'FontSize', 12);%, 'FontWeight', 'bold');
```

5047

```
xlabel('Fuel history', 'FontSize', 12)
legend('U235','U238','Np237','Pu237','Pu238','Pu239','Pu240',...
    'Pu241','Pu242','Pu243','Pu244', 'Am241', 'Am242', 'Am242m',...
    'Am243','Cm242','Cm243','Cm244','Cm245','Cm246', 'Location','EastOutside');
ylim([0 1])

clear stackData Y internalPosCount i h groupDrawPos groupBins ;
for I = 1:4
    stackData(I,1,1:20)=PWRMOX_S(12, 2:21, I)./sum(PWRMOX_S(12, 2:21, I));
    stackData(I,2,1:20)=PWRMOX_S(25, 2:21, I)./sum(PWRMOX_S(25, 2:21, I));
    stackData(I,3,1:20)=PWRMOX_S(33, 2:21, I)./sum(PWRMOX_S(33, 2:21, I));
    stackData(I,4,1:20)=PWRMOX_S(38, 2:21, I)./sum(PWRMOX_S(38, 2:21, I));
    stackData(I,5,1:20)=PWRMOX_S(42, 2:21, I)./sum(PWRMOX_S(42, 2:21, I));
    stackData(I,6,1:20)=PWRMOX_S(47, 2:21, I)./sum(PWRMOX_S(47, 2:21, I));
end
plotBarStackGroups(stackData, groupLabels, 25);
ylabel('Relative neutron activity (neutrons/sec/MTU)', 'FontSize', 12);%,
'FontWeight', 'bold');
xlabel('Fuel history', 'FontSize', 12)
legend('U235','U238','Np237','Pu237','Pu238','Pu239','Pu240',...
    'Pu241','Pu242','Pu243','Pu244', 'Am241', 'Am242', 'Am242m',...
    'Am243','Cm242','Cm243','Cm244','Cm245','Cm246', 'Location','EastOutside');
ylim([0 1])

for I = 1:4
    stackData(I,1,1:20)=PWRUOX_A(12, 2:21, I)./sum(PWRUOX_A(12, 2:21, I));
    stackData(I,2,1:20)=PWRUOX_A(25, 2:21, I)./sum(PWRUOX_A(25, 2:21, I));
    stackData(I,3,1:20)=PWRUOX_A(33, 2:21, I)./sum(PWRUOX_A(33, 2:21, I));
    stackData(I,4,1:20)=PWRUOX_A(38, 2:21, I)./sum(PWRUOX_A(38, 2:21, I));
    stackData(I,5,1:20)=PWRUOX_A(42, 2:21, I)./sum(PWRUOX_A(42, 2:21, I));
    stackData(I,6,1:20)=PWRUOX_A(47, 2:21, I)./sum(PWRUOX_A(47, 2:21, I));
end
plotBarStackGroups(stackData, groupLabels, 25);
ylabel('Relative neutron activity (neutrons/sec/MTU)', 'FontSize', 12);%,
'FontWeight', 'bold');
xlabel('Fuel history', 'FontSize', 12)
legend('U235','U238','Np237','Pu237','Pu238','Pu239','Pu240',...
    'Pu241','Pu242','Pu243','Pu244', 'Am241', 'Am242', 'Am242m',...
    'Am243','Cm242','Cm243','Cm244','Cm245','Cm246', 'Location','EastOutside');
ylim([0 1])

clear stackData Y internalPosCount i h groupDrawPos groupBins ;
for I = 1:4
    stackData(I,1,1:20)=PWRUOX_S(12, 2:21, I)./sum(PWRUOX_S(12, 2:21, I));
    stackData(I,2,1:20)=PWRUOX_S(25, 2:21, I)./sum(PWRUOX_S(25, 2:21, I));
    stackData(I,3,1:20)=PWRUOX_S(33, 2:21, I)./sum(PWRUOX_S(33, 2:21, I));
    stackData(I,4,1:20)=PWRUOX_S(38, 2:21, I)./sum(PWRUOX_S(38, 2:21, I));
    stackData(I,5,1:20)=PWRUOX_S(42, 2:21, I)./sum(PWRUOX_S(42, 2:21, I));
    stackData(I,6,1:20)=PWRUOX_S(47, 2:21, I)./sum(PWRUOX_S(47, 2:21, I));
end

plotBarStackGroups(stackData, groupLabels, 25);
ylabel('Relative neutron activity (neutrons/sec/MTU)', 'FontSize', 12);%,
'FontWeight', 'bold');
xlabel('Fuel history', 'FontSize', 12)
legend('U235','U238','Np237','Pu237','Pu238','Pu239','Pu240',...
    'Pu241','Pu242','Pu243','Pu244', 'Am241', 'Am242', 'Am242m',...
    'Am243','Cm242','Cm243','Cm244','Cm245','Cm246', 'Location','EastOutside');
ylim([0 1])
```

D.4.3 Factorial moment analysis

```
% Matlab script to post process all data
% naming convention:
%   first three characters = reactor type i.e. PWR or BWR
%   next three characters  = fuel type i.e. MOX or UOX
%   next two numbers       = burnup level i.e. 10, 20, 35 and 55
%   last two number        = data type i.e. 0 for number density
%                                 9 for spontaneous fission activity
%                                10 for (alpha, n) activity
% The first coloum of the variables is the time of irradiation
% subsequent coloums corresponds to different isotopes
% i.e. 'Pu^{238}', 'Pu^{239}', 'Pu^{240}', 'Pu^{241}','Pu^{242}',
% 'Am^{241}' , Cm^{242}', 'Cm^{248}'
% corresponds to [37:41 47 57 59]


% correct the negative axis to signify irradiation
% replace PWRMOX with other combination.

%% calculate and plot multipliicty information
%% Sort data
% alpha, n activity
alphan_PWR_UOX(:,:,1) = PWRUOX10_10(2:end,[37:41 47 57 59]);
alphan_PWR_MOX(:,:,1) = PWRMOX10_10(2:end,[37:41 47 57 59]);
alphan_BWR_MOX(:,:,1) = BWRMOX10_10(2:end,[37:41 47 57 59]);
alphan_PWR_UOX(:,:,2) = PWRUOX20_10(2:end,[37:41 47 57 59]);
alphan_PWR_MOX(:,:,2) = PWRMOX20_10(2:end,[37:41 47 57 59]);
alphan_BWR_MOX(:,:,2) = BWRMOX20_10(2:end,[37:41 47 57 59]);
alphan_PWR_UOX(:,:,3) = PWRUOX35_10(2:end,[37:41 47 57 59]);
alphan_PWR_MOX(:,:,3) = PWRMOX35_10(2:end,[37:41 47 57 59]);
alphan_BWR_MOX(:,:,3) = BWRMOX35_10(2:end,[37:41 47 57 59]);
alphan_PWR_UOX(:,:,4) = PWRUOX55_10(2:end,[37:41 47 57 59]);
alphan_PWR_MOX(:,:,4) = PWRMOX55_10(2:end,[37:41 47 57 59]);
alphan_BWR_MOX(:,:,4) = BWRMOX55_10(2:end,[37:41 47 57 59]);

% spontaneous fission activity
mean_nu = [2.21 2.879 2.154 inf 2.149 inf 2.54  2.72 ];
 % pu238  pu239 pu240 pu241 pu242   am241 cm242 cm244
sf_PWR_UOX(:,:,1) = PWRUOX10_9(2:end,[37:41 47 57 59])./mean_nu;
sf_PWR_MOX(:,:,1) = PWRMOX10_9(2:end,[37:41 47 57 59])./mean_nu;
sf_BWR_MOX(:,:,1) = BWRMOX10_9(2:end,[37:41 47 57 59])./mean_nu;
sf_PWR_UOX(:,:,2) = PWRUOX20_9(2:end,[37:41 47 57 59])./mean_nu;
sf_PWR_MOX(:,:,2) = PWRMOX20_9(2:end,[37:41 47 57 59])./mean_nu;
sf_BWR_MOX(:,:,2) = BWRMOX20_9(2:end,[37:41 47 57 59])./mean_nu;
sf_PWR_UOX(:,:,3) = PWRUOX35_9(2:end,[37:41 47 57 59])./mean_nu;
sf_PWR_MOX(:,:,3) = PWRMOX35_9(2:end,[37:41 47 57 59])./mean_nu;
sf_BWR_MOX(:,:,3) = BWRMOX35_9(2:end,[37:41 47 57 59])./mean_nu;
sf_PWR_UOX(:,:,4) = PWRUOX55_9(2:end,[37:41 47 57 59])./mean_nu;
sf_PWR_MOX(:,:,4) = PWRMOX55_9(2:end,[37:41 47 57 59])./mean_nu;
sf_BWR_MOX(:,:,4) = BWRMOX55_9(2:end,[37:41 47 57 59])./mean_nu;

%% obtain isitope wise correlated activity
for i = 1:4
   for k = 1:8
       for l = 1:9
          Number_Distribution_PWR_MOX(:,k,l,i) =  sf_PWR_MOX(:,k,i)*nu_dist(k,l) ;
          Number_Distribution_BWR_MOX(:,k,l,i) =  sf_BWR_MOX(:,k,i)*nu_dist(k,l) ;
          Number_Distribution_PWR_UOX(:,k,l,i) =  sf_PWR_UOX(:,k,i)*nu_dist(k,l) ;
       end
   end
end

%% sum all correlated activity from fission
for i = 1:4
       for l = 1:9
          TotalNumberDistribution_PWR_MOX(:,1,l,i) =  sum(Number_Distribution_PWR_MOX
          (:,:,l,i)')';
```

5050

```
            TotalNumberDistribution_BWR_MOX(:,1,l,i) =   sum(Number_Distribution_BWR_MOX(:,:,l,i)')';
            TotalNumberDistribution_PWR_UOX(:,1,l,i) = sum(Number_Distribution_PWR_UOX(:,:,l,i)')';

            TotalNumberDistribution_PWR_MOX(:,2,l,i) =  sum(Number_Distribution_PWR_MOX(:,1:5,l,i)')';
            TotalNumberDistribution_BWR_MOX(:,2,l,i) =   sum(Number_Distribution_BWR_MOX(:,1:5,l,i)')';
            TotalNumberDistribution_PWR_UOX(:,2,l,i) = sum(Number_Distribution_PWR_UOX(:,1:5,l,i)')';

            TotalNumberDistribution_PWR_MOX(:,3,l,i) =  sum(Number_Distribution_PWR_MOX(:,6:8,l,i)')';
            TotalNumberDistribution_BWR_MOX(:,3,l,i) =   sum(Number_Distribution_BWR_MOX(:,6:8,l,i)')';
            TotalNumberDistribution_PWR_UOX(:,3,l,i) = sum(Number_Distribution_PWR_UOX(:,6:8,l,i)')';
        end
end

%% calculate factorial moment distrubution of spontanous fission activity only
tmp = [];
for i = 1:4
for k = 1:3
        for l = 1:48
            tmp= [];
            for m = 1:9
                tmp(m) =TotalNumberDistribution_PWR_MOX(l,k,m,i);
            end
           multi_PWR_MOX(l, :, k, i) = factorial_moment(tmp, 1);


            tmp= [];
            for m = 1:9
                tmp(m) =TotalNumberDistribution_BWR_MOX(l,k,m,i);
            end
           multi_BWR_MOX(l, :, k, i) = factorial_moment(tmp, 1);


            tmp= [];
            for m = 1:9
                tmp(m) =TotalNumberDistribution_PWR_UOX(l,k,m,i);
            end
           multi_PWR_UOX(l, :, k, i) = factorial_moment(tmp, 1);
        end
end
end

%% calculate factorial moment distrubution of spontanous fission activity + (alpha, n) emission
for i = 1:4 %% add (alpha, n) activity
    TotalNumberDistribution_PWR_MOX(:,1,1,i) = TotalNumberDistribution_PWR_MOX(:,1,1,i) + sum(alphan_PWR_MOX(:,:,i)')';
    TotalNumberDistribution_BWR_MOX(:,1,1,i) = TotalNumberDistribution_BWR_MOX(:,1,1,i) + sum(alphan_BWR_MOX(:,:,i)')';
    TotalNumberDistribution_PWR_UOX(:,1,1,i) = TotalNumberDistribution_PWR_UOX(:,1,1,i) + sum(alphan_PWR_UOX(:,:,i)')';
end

%% calculate factorial moment distrubution of spontanous fission activity + (alpha, n) emission
% CombinedFactorialMoment_PWR_UOX(time, order, type = total, burnup)
tmp = [];
for i = 1:4
for k = 1
```

5051

```
        for l = 1:48
            tmp= [];
            for m = 1:9
                 tmp(m) =TotalNumberDistribution_PWR_MOX(l,k,m,i);
            end
           CombinedFactorialMoment_PWR_MOX(l, :, k, i) = factorial_moment(tmp, 1);


            tmp= [];
            for m = 1:9
                 tmp(m) =TotalNumberDistribution_BWR_MOX(l,k,m,i);
            end
           CombinedFactorialMoment_BWR_MOX(l, :, k, i) = factorial_moment(tmp, 1);


            tmp= [];
            for m = 1:9
                 tmp(m) =TotalNumberDistribution_PWR_UOX(l,k,m,i);
            end
           CombinedFactorialMoment_PWR_UOX(l, :, k, i) = factorial_moment(tmp, 1);
        end
end
end

%% Plot for PWR_MOX for different burnup cases. change PWR and MOX flag for other
% fuel types and reactor types
close all
figH = figure(1)
set(figH,'Position',[1 1 339.4 251.6]);
time_axis = PWRMOX10_0(2:end,1);
plot(time_axis, CombinedFactorialMoment_PWR_MOX(:,1,1,1), '-k','Linewidth', 1.5)
hold on
grid on
plot(time_axis, CombinedFactorialMoment_PWR_MOX(:,2,1,1), '--k','Linewidth', 1.5)
plot(time_axis, CombinedFactorialMoment_PWR_MOX(:,3,1,1), '-.k','Linewidth', 1.5)
plot(time_axis, CombinedFactorialMoment_PWR_MOX(:,4,1,1), '-xk','Linewidth', 1.5)
plot(time_axis, CombinedFactorialMoment_PWR_MOX(:,5,1,1), ':k','Linewidth', 1.5)
plot(time_axis, CombinedFactorialMoment_PWR_MOX(:,6,1,1), '-ok','Linewidth', 1.5)
plot(time_axis, CombinedFactorialMoment_PWR_MOX(:,7,1,1), ':dk','Linewidth', 1.5)
plot(time_axis, CombinedFactorialMoment_PWR_MOX(:,8,1,1), '-vk','Linewidth', 1.5)
ylabel('\nu_n', 'FontSize', 12)
xlim([0 max(PWRMOX10_0(2:end,1)) ] )
xlabel ('Number of Days', 'FontSize', 12)
ylim([0 12.5 ] )
%title('PWR MOX 10')

figH = figure(2)
set(figH,'Position',[1 1 339.4 251.6]);
time_axis = PWRMOX20_0(2:end,1);
plot(time_axis, CombinedFactorialMoment_PWR_MOX(:,1,1,2), '-k','Linewidth', 1.5)
hold on
grid on
plot(time_axis, CombinedFactorialMoment_PWR_MOX(:,2,1,2), '--k','Linewidth', 1.5)
plot(time_axis, CombinedFactorialMoment_PWR_MOX(:,3,1,2), '-.k','Linewidth', 1.5)
plot(time_axis, CombinedFactorialMoment_PWR_MOX(:,4,1,2), '-xk','Linewidth', 1.5)
plot(time_axis, CombinedFactorialMoment_PWR_MOX(:,5,1,2), ':k','Linewidth', 1.5)
plot(time_axis, CombinedFactorialMoment_PWR_MOX(:,6,1,2), '-ok','Linewidth', 1.5)
plot(time_axis, CombinedFactorialMoment_PWR_MOX(:,7,1,2), ':dk','Linewidth', 1.5)
plot(time_axis, CombinedFactorialMoment_PWR_MOX(:,8,1,2), '-vk','Linewidth', 1.5)
ylabel('\nu_n', 'FontSize', 12)
xlim([0 max(PWRMOX10_0(2:end,1)) ] )
xlabel ('Number of Days', 'FontSize', 12)
ylim([0 12.5 ] )
%title('PWR MOX 20')

figH = figure(3)
```

5052

```
time_axis = PWRMOX35_0(2:end,1);
set(figH,'Position',[1 1 339.4 251.6]);
plot(time_axis, CombinedFactorialMoment_PWR_MOX(:,1,1,3), '-k','Linewidth', 1.5)
hold on
grid on
plot(time_axis, CombinedFactorialMoment_PWR_MOX(:,2,1,3), '--k','Linewidth', 1.5)
plot(time_axis, CombinedFactorialMoment_PWR_MOX(:,3,1,3), '-.k','Linewidth', 1.5)
plot(time_axis, CombinedFactorialMoment_PWR_MOX(:,4,1,3), '-xk','Linewidth', 1.5)
plot(time_axis, CombinedFactorialMoment_PWR_MOX(:,5,1,3), ':k','Linewidth', 1.5)
plot(time_axis, CombinedFactorialMoment_PWR_MOX(:,6,1,3), '-ok','Linewidth', 1.5)
plot(time_axis, CombinedFactorialMoment_PWR_MOX(:,7,1,3), ':dk','Linewidth', 1.5)
plot(time_axis, CombinedFactorialMoment_PWR_MOX(:,8,1,3), '-vk','Linewidth', 1.5)
ylabel('\nu_n', 'FontSize', 12)
xlim([0 max(PWRMOX10_0(2:end,1)) ] )
xlabel ('Number of Days', 'FontSize', 12)
ylim([0 12.5 ] )
%title('PWR MOX 35')

figH = figure(4)
time_axis = PWRMOX55_0(2:end,1);
set(figH,'Position',[1 1 339.4 251.6]);
plot(time_axis, CombinedFactorialMoment_PWR_MOX(:,1,1,4), '-k','Linewidth', 1.5)
hold on
grid on
plot(time_axis, CombinedFactorialMoment_PWR_MOX(:,2,1,4), '--k','Linewidth', 1.5)
plot(time_axis, CombinedFactorialMoment_PWR_MOX(:,3,1,4), '-.k','Linewidth', 1.5)
plot(time_axis, CombinedFactorialMoment_PWR_MOX(:,4,1,4), '-xk','Linewidth', 1.5)
plot(time_axis, CombinedFactorialMoment_PWR_MOX(:,5,1,4), ':k','Linewidth', 1.5)
plot(time_axis, CombinedFactorialMoment_PWR_MOX(:,6,1,4), '-ok','Linewidth', 1.5)
plot(time_axis, CombinedFactorialMoment_PWR_MOX(:,7,1,4), ':dk','Linewidth', 1.5)
plot(time_axis, CombinedFactorialMoment_PWR_MOX(:,8,1,4), '-vk','Linewidth', 1.5)
ylabel('\nu_n', 'FontSize', 12)
xlim([0 max(PWRMOX10_0(2:end,1)) ] )
ylim([0 12.6 ] )
xlabel ('Number of Days', 'FontSize', 12)
%title('PWR MOX 55')

legend ('Singles', 'Doubles', 'Triples', 'Quadruples', 'Quintuple', 'Sextuple',
'Septuple', 'Octuple')
```

D.5 Interval time analysis

```
% finding fits for interval time distributions
% repeat script with data sets, and initial estimate for different cases

%%%%%%%%%%%%%%%%%%%%%%%%%%%%%%%%%%%%
%% LANCASTER
%%%%%%%%%%%%%%%%%%%%%%%%%%%%%%%%%%%%
load('Lanc_data_complete3.mat')

%% Fit: 'untitled fit 1'.
ii = 62;
[xGamma, yGamma] = prepareCurveData( data(1:ii,1), (data(1:ii,2)));%/(sum((data(1:ii,2))-e(2))));
[xJoint, yJoint] = prepareCurveData( data(1:ii,1), (data(1:ii,3)));%-e(3))/(sum((data(1:ii,3))-e(3))));
[xNeutron, yNeutron] = prepareCurveData( data(1:ii,1), (data(1:ii,4)));
[xSim, ySim] = prepareCurveData( data(1:ii,1), (data(1:ii,5)));%/(sum(data(1:ii,5)-e(5))));
[xSim, ySimG] = prepareCurveData( data(1:ii,1), (data(1:ii,6)));%/(sum(data(1:ii,5)-e(5))));
[xSim, ySimJ] = prepareCurveData( data(1:ii,1), (data(1:ii,7)));%/(sum(data(1:ii,5)-e(5))));

sqroot=((data).^.5)./data;
sqsum=(sum(data).^.5)./sum(data);

qt_x=xGamma;
qt_y=[yGamma yJoint yNeutron yNeutron ySim]';

for i = 2:5
    uncertain(:,i) = (data(:,i)./sum(data(:,i))).*(( sqroot(:,i).^2 + sqsum(1,i)^2).^0.5);
end

ft = fittype( 'a*exp(-x/b)+c*exp(-x/d)+e', 'independent', 'x', 'dependent', 'y' );
opts = fitoptions( 'Method', 'NonlinearLeastSquares' );
opts.DiffMinChange = 1e-8;
opts.Display = 'Off';
opts.Robust = 'LAR';
opts.MaxIter = 400;
opts.TolFun = 1e-06;
opts.TolX = 1e-06;


opts.Weights = 1./yGamma;
opts.StartPoint = [38459 1.7900 119 47 115];
[fitresultG, gofGAMMA, infoG] = fit( xGamma, yGamma, ft, opts );
gofGAMMA.sse
-log(0.003)*fitresultG.b

opts.Weights = 1./yJoint;
opts.StartPoint = [12885 3.08 2317 21.9 133];
[fitresultJ, gofJoint, infoJ] = fit( xJoint, yJoint, ft, opts );
gofJoint.sse
-log(0.003)*fitresultJ.b


opts.Weights = 1./yNeutron;
opts.StartPoint = [189659 2.11 5211 36.6 1155];
[fitresultN, gofNEUTRON, infoN] = fit( xNeutron, yNeutron, ft, opts );
gofNEUTRON.sse
gofSIM= gofNEUTRON;
fitresultS= fitresultN;
-log(0.003)*fitresultN.b


%% old
%% old model
ft = fittype( 'a*exp(-x/b)+c', 'independent', 'x', 'dependent', 'y' );
opts = fitoptions( 'Method', 'NonlinearLeastSquares' );
opts.DiffMinChange = 1e-12;
opts.Display = 'Off';
```

5055

```
opts.Robust = 'LAR';
opts.MaxIter = 4000;
opts.TolFun = 1e-09;
opts.TolX = 1e-09;


opts.Weights = 1./yGamma;
opts.StartPoint = [38459 1.7000 115];
[fitresultG_old, gofGAMMA_old, infoG] = fit( xGamma, yGamma, ft, opts );
fitresultG_old
gofGAMMA_old.sse/57

opts.Weights =  1./yJoint;
opts.Robust = 'Off';
opts.StartPoint = [1.054e+04 10.42 144.2];
[fitresultJ_old, gofJoint_old, infoJ] = fit( xJoint, yJoint, ft, opts );
fitresultJ_old
gofJoint_old.sse/57
opts.Robust = 'LAR';

opts.Weights = 1./yNeutron;
opts.StartPoint = [100000 10  1000];
[fitresultN_old, gofNEUTRON_old, infoN] = fit( xNeutron, yNeutron, ft, opts );
fitresultN_old
gofNEUTRON_old.sse/57
%%%%%%%%%%%%%%%%%%%%%%%%%%%%%%%%%%%%
%% ORNL
%%%%%%%%%%%%%%%%%%%%%%%%%%%%%%%%%%%%
load('ORNL_data_complete5.mat')

%% Fit: 'untitled fit 1'.
ii = 62;
[xGamma, yGamma] = prepareCurveData( data(1:ii,1), (data(1:ii,2)));%/(sum((data(1:ii,2))-e(2))));
[xJoint, yJoint] = prepareCurveData( data(1:ii,1), (data(1:ii,3)));%-e(3))/(sum((data(1:ii,3))-e(3))));
[xNeutron, yNeutron] = prepareCurveData( data(1:ii,1), (data(1:ii,4)));
[xSim, ySim] = prepareCurveData( data(1:ii,1), (data(1:ii,5)));%/(sum(data(1:ii,5)-e(5))));
[xSim, ySimG] = prepareCurveData( data(1:ii,1), (data(1:ii,6)));%/(sum(data(1:ii,5)-e(5))));
[xSim, ySimJ] = prepareCurveData( data(1:ii,1), (data(1:ii,7)));%/(sum(data(1:ii,5)-e(5))));

%load('lancaster_exp_dec_final.mat', 'xGamma', 'xJoint', 'xNeutron', 'xSim')
ft = fittype( 'a*exp(-x/b)+c*exp(-x/d)+e', 'independent', 'x', 'dependent', 'y' );
opts = fitoptions( 'Method', 'NonlinearLeastSquares' );
opts.DiffMinChange = 1e-12;
opts.Display = 'Off';
opts.Robust = 'LAR';
opts.MaxIter = 4000;
opts.TolFun = 1e-09;
opts.TolX = 1e-09;


opts.Weights = 1./yGamma;
opts.StartPoint = [205433 1.5 17501 7 407];
[fitresultG, gofGAMMA, infoG] = fit( xGamma, yGamma, ft, opts );
fitresultG
gofGAMMA.sse/57
-log(0.003)*fitresultG.b

%neutron okay
opts.Weights = 1./yJoint;
opts.StartPoint = [107037 5.20 3906 15 127.3];
[fitresultJ, gofJoint, infoG] = fit( xGamma, yJoint, ft, opts );
fitresultJ
gofJoint.sse/57
-log(0.003)*fitresultJ.b

opts.Weights = 1./yNeutron;
```

5056

```
opts.StartPoint = [100000 5 1000 100 0.0971];
[fitresultN, gofNEUTRON, infoN] = fit( xNeutron, yNeutron, ft, opts );
fitresultN
gofNEUTRON.sse/57
-log(0.003)*fitresultN.b



%% old model
ft = fittype( 'a*exp(-x/b)+c', 'independent', 'x', 'dependent', 'y' );
opts = fitoptions( 'Method', 'NonlinearLeastSquares' );
opts.DiffMinChange = 1e-12;
opts.Display = 'Off';
opts.Robust = 'LAR';
opts.MaxIter = 4000;
opts.TolFun = 1e-09;
opts.TolX = 1e-09;


opts.Weights = 1./yGamma;
opts.StartPoint = [203238 1.5010 173];
[fitresultG_old, gofGAMMA_old, infoG] = fit( xGamma, yGamma, ft, opts );
fitresultG_old
gofGAMMA_old.sse/57
-log(0.003)*fitresultG_old.b

opts.Weights = 1./yJoint;
opts.StartPoint = [107015 3.183595  390];
[fitresultJ_old, gofJoint_old, infoJ] = fit( xJoint, yJoint, ft, opts );
fitresultJ_old
gofJoint_old.sse/57
-log(0.003)*fitresultJ_old.b

opts.Weights = 1./yNeutron;
opts.StartPoint = [92521 3.8595 365];
[fitresultN_old, gofNEUTRON_old, infoN] = fit( xNeutron, yNeutron, ft, opts );
fitresultN_old
gofNEUTRON_old.sse/57
-log(0.003)*fitresultN_old.b
```

Plot

```
%%
%%Plots
%%

figure(1) % neutron
T = [repmat(fitresultJ.e/yJoint(1),1,301)'
((fitresultJ.c*(exp(-1*[0:1:300]./fitresultJ.d)))/yJoint(1))'...
                ((fitresultJ.a*(exp(-1*[0:1:300]./fitresultJ.b)))/yJoint(1))' ];
a1 = area(0:1:300,T);
hold on
p2 = plot (.5:1:200, geant4_full(1:end,1)/max(geant4_full(1,1)), 'om', 'linewidth',
2, 'MarkerSize', 4);
p3 = plot (0:1:300, fitresultJ_old(0:300)/yJoint(1), '-r', 'linewidth', 3);
p4 = plot (0:1:300, fitresultJ(0:300)/yJoint(1), '-b', 'linewidth', 3);
p5 = plot (xSim, ySim/max(ySim), 'xr', 'linewidth', 2, 'MarkerSize', 7);
p1 = plot (xNeutron, yJoint/yJoint(1), 'xk', 'linewidth', 2, 'MarkerSize', 7);
a1(1).FaceColor = [1 0 0];
a1(2).FaceColor = [0 0 1];
a1(3).FaceColor = [0 1 0];
hold off
alpha(0.5)
ylim([0 1])
xlim([0 200])
xlabel ('Time Elapsed [ns]', 'Interpreter','latex')
ylabel ('Normalized response', 'Interpreter','latex');
set(gca,'TickLabelInterpreter','latex')
set(gcf, 'Position', [200, 100, 500, 325])
set(legend([p1 p2 p5 p4 p3 a1(3) a1(2) a1(1)], {'Neutron data', 'Simulated data',
'Simulated data (binned)', 'Double exponent',...
    'Single exponent', 'Short response', 'Long response', 'Accidental response'}) ,
    'Interpreter','latex');
grid on
figure(2)  % Gamma
T = [repmat(fitresultG.e/yGamma(1),1,301)'
((fitresultG.c*(exp(-1*[0:1:300]./fitresultG.d)))/yGamma(1))'...
                ((fitresultG.a*(exp(-1*[0:1:300]./fitresultG.b)))/yGamma(1))' ]
a1 = area(0:1:300,T);
hold on
p2 = plot (.5:1:200, geant4_full(1:end,2)/geant4_full(1,2)*2, 'om', 'linewidth', 2,
'MarkerSize', 4);
p3 = plot (0:1:300, fitresultG_old(0:300)/yGamma(1), '-r', 'linewidth', 3);
p4 = plot (0:1:300, fitresultG(0:300)/yJoint(1), '-b', 'linewidth', 3);
p5 = plot (xSim, ySimG/max(ySimG)+yGamma(50)/yGamma(1), 'xr', 'linewidth', 2,
'MarkerSize', 7);
p1 = plot (xNeutron, yGamma/yGamma(1),  'xk', 'linewidth', 3, 'MarkerSize', 7);
a1(1).FaceColor = [1 0 0];
a1(2).FaceColor = [0 0 1];
a1(3).FaceColor = [0 1 0];
hold off
alpha(0.5)
ylim([0 1])
xlim([0 200])
xlabel ('Time Elapsed [ns]', 'Interpreter','latex')
ylabel ('Normalized response', 'Interpreter','latex');
set(gca,'TickLabelInterpreter','latex')
set(gcf, 'Position', [200, 100, 500, 325])
set(legend([p1 p2 p5 p4 p3 a1(3) a1(2) a1(1)], {'Gamma data', 'Simulated data',
'Simulated data (binned)', 'Double exponent',...
    'Single exponent', 'Short response', 'Long response', 'Accidental response'}) ,
    'Interpreter','latex');
grid on

figure(3) % Joint
T = [repmat(fitresultN.e/yNeutron(1),1,301)'
((fitresultN.c*(exp(-1*[0:1:300]./fitresultN.d)))/yNeutron(1))'...
                ((fitresultN.a*(exp(-1*[0:1:300]./fitresultN.b)))/yNeutron(1))' ]
a1 = area(0:1:300,T);
hold on
p2 = plot (.5:1:200, geant4_full(1:end,3)/geant4_full(1,3), 'om', 'linewidth', 2,
'MarkerSize', 4);
p3 = plot (0:1:300, fitresultN_old(0:300)/yNeutron(1), '-r', 'linewidth', 3);
```

5059

```
p4 = plot (0:1:300, fitresultN(0:300)/yNeutron(1), '-b', 'linewidth', 3);
p5 = plot (xSim, ySimJ/max(ySimJ), 'xr', 'linewidth', 2, 'MarkerSize', 7);
p1 = plot (xNeutron, yNeutron/yNeutron(1), 'xk', 'linewidth', 2, 'MarkerSize', 7);
a1(1).FaceColor = [1 0 0];
a1(2).FaceColor = [0 0 1];
a1(3).FaceColor = [0 1 0];
hold off
alpha(0.5)
ylim([0 1])
xlim([0 200])
xlabel ('Time Elapsed [ns]', 'Interpreter','latex')
ylabel ('Normalized response', 'Interpreter','latex');
set(gca,'TickLabelInterpreter','latex')
set(gcf, 'Position', [200, 100, 500, 325])
set(legend([p1 p2 p5 p4 p3  a1(3) a1(2) a1(1)], {'Joint data', 'Simulated data', 'Simulated data (binned)', 'Double exponent',...
    'Single exponent', 'Short response', 'Long response', 'Accidental response'}) , 'Interpreter','latex');
grid on

figure(4) % Ratio Neutron vs Joint
p2 = plot (0:1:300, fitresultJ(0:300)/yJoint(1), '-.b', 'linewidth', 1.5);
hold on
p4 = plot (0:1:300, fitresultN(0:300)/yNeutron(1), '-.r', 'linewidth', 1.5);
p1 = plot (xNeutron, yJoint/yJoint(1), 'xb', 'linewidth', 1.5, 'MarkerSize', 7);
p3 = plot (xNeutron, yNeutron/yNeutron(1), 'xr', 'linewidth', 1.5, 'MarkerSize', 7);
set(legend([p1  p2 p3 p4], {'Neutron data', 'Neutron fit',...
    'Joint data', 'Joint fit'}) , 'Interpreter','latex');
xlabel ('Time Elapsed [ns]', 'Interpreter','latex')
ylabel ('Normalized response', 'Interpreter','latex');
set(gca,'TickLabelInterpreter','latex')
set(gcf, 'Position', [200, 100, 500, 325])
ylim([0 1])
xlim([0 100])
grid on
hold off

figure(5) % Ratio Neutron vs Gamma
p2 = plot (0:1:300, fitresultG(0:300)/yGamma(1), '-.b', 'linewidth', 1.5);
hold on
p4 = plot (0:1:300, fitresultN(0:300)/yNeutron(1), '-.r', 'linewidth', 1.5);
p1 = plot (xNeutron, yGamma/yGamma(1), 'xb', 'linewidth', 1.5, 'MarkerSize', 7);
p3 = plot (xNeutron, yNeutron/yNeutron(1), 'xr', 'linewidth', 1.5, 'MarkerSize', 7);
set(legend([p1  p2 p3 p4], {'Gamma data', 'Gamma fit',...
    'Joint data', 'Joint fit'}) , 'Interpreter','latex');
xlabel ('Time Elapsed [ns]', 'Interpreter','latex')
ylabel ('Normalized response', 'Interpreter','latex');
set(gca,'TickLabelInterpreter','latex')
set(gcf, 'Position', [200, 100, 500, 325])
ylim([0 1])
xlim([0 100])
grid on
hold off

figure(6) % Ratio Gamma vs Joint
p2 = plot (0:1:300, fitresultG(0:300)/yGamma(1), '-.b', 'linewidth', 1.5);
hold on
p4 = plot (0:1:300, fitresultJ(0:300)/yJoint(1), '-.r', 'linewidth', 1.5);
p1 = plot (xNeutron, yGamma/yGamma(1), 'xb', 'linewidth', 1.5, 'MarkerSize', 7);
p3 = plot (xNeutron, yJoint/yJoint(1), 'xr', 'linewidth', 1.5, 'MarkerSize', 7);
set(legend([p1  p2 p3 p4], {'Gamma data', 'Gamma fit',...
    'Neutron data', 'Neutron fit'}) , 'Interpreter','latex');
xlabel ('Time Elapsed [ns]', 'Interpreter','latex')
ylabel ('Normalized response', 'Interpreter','latex');
set(gca,'TickLabelInterpreter','latex')
set(gcf, 'Position', [200, 100, 500, 325])
ylim([0 1])
xlim([0 100])
grid on
hold off
```

D.6 Spectrum analysis

```
%% ORNL 26.75 cm radius Experiments
distance = .3625;
load('data_sept28.mat', 'exp_ornl')
for i = 1:size(exp_ornl)
    exp_ornl(i,2) = 0.5*1.66*(10^-27) * (distance/(exp_ornl(i,1)/1000000000))^2 * 6242000000000;
end

figure(3) % normalized distribution
w0 = fit_spec(exp_ornl(3:50,2), exp_ornl(3:50,3)./(exp_ornl(2:49,2)-exp_ornl(3:50,2))/511);
w1 = fit_spec(exp_ornl(3:50,2), exp_ornl(3:50,4)./(exp_ornl(2:49,2)-exp_ornl(3:50,2))/562);
w2 = fit_spec(exp_ornl(3:50,2), exp_ornl(3:50,5)./(exp_ornl(2:49,2)-exp_ornl(3:50,2))/760);
w3  = fit_spec(exp_ornl(3:50,2), exp_ornl(3:50,6)./(exp_ornl(2:49,2)-exp_ornl(3:50,2))/643);
errorbar(exp_ornl(3:30,2),1/511*exp_ornl(3:30,3)./(exp_ornl(2:29,2)-exp_ornl(3:30,2)), 1/511*(exp_ornl(3:30,3)./(exp_ornl(2:29,2)-exp_ornl(3:30,2))).^0.5,'xr', 'LineWidth', 1.5)
hold on
errorbar(exp_ornl(3:30,2),1/562*exp_ornl(3:30,4)./(exp_ornl(2:29,2)-exp_ornl(3:30,2)), 1/562*(exp_ornl(3:30,4)./(exp_ornl(2:29,2)-exp_ornl(3:30,2))).^0.5,'xm', 'LineWidth', 1.5)
errorbar(exp_ornl(3:30,2),1/760*exp_ornl(3:30,5)./(exp_ornl(2:29,2)-exp_ornl(3:30,2)), 1/760*(exp_ornl(3:30,5)./(exp_ornl(2:29,2)-exp_ornl(3:30,2))).^0.5,'xb', 'LineWidth', 1.5)
errorbar(exp_ornl(3:30,2),1/643*exp_ornl(3:30,6)./(exp_ornl(2:29,2)-exp_ornl(3:30,2)), 1/643*(exp_ornl(3:30,6)./(exp_ornl(2:29,2)-exp_ornl(3:30,2))).^0.5,'xk', 'LineWidth', 1.5)
plot (0.01:.01:6, w0(0.01:.01:6), '-r', 'LineWidth', 1.5)
plot (0.01:.01:6, w1(0.01:.01:6), '-m', 'LineWidth', 1.5)
plot (0.01:.01:6, w2(0.01:.01:6), '-b', 'LineWidth', 1.5)
plot (0.01:.01:6, w3(0.01:.01:6), '-k', 'LineWidth', 1.5)
hold off
grid on
xlim([0 4])
 set(legend('No H20','Radius = 1 cm','Radius = 3 cm','Radius = 5 cm'), 'Interpreter','latex')
xlabel('Energy [MeV]', 'Interpreter','latex')
ylabel('Response [MeV$^{-1}$ s$^{-1}$ ]', 'Interpreter','latex')
set(gca,'TickLabelInterpreter','latex')
set(gcf, 'Position', [200, 100, 500, 325])

ylim([0 10000/500])

figure(4) % actual distribution distribution
plot(exp_ornl(3:50,2),exp_ornl(3:50,3:end)./(exp_ornl(2:49,2)-exp_ornl(3:50,2))./max(exp_ornl(3:50,3:end)), 'LineWidth', 1.5)
plot (0.01:.01:6, w0(0.01:.01:6)./max(exp_ornl(3:50,3))*511, '-r', 'LineWidth', 1.5)
hold on
plot (0.01:.01:6, w1(0.01:.01:6)./max(exp_ornl(3:50,4))*562, '-m', 'LineWidth', 1.5)
plot (0.01:.01:6, w2(0.01:.01:6)./max(exp_ornl(3:50,5))*760, '-b', 'LineWidth', 1.5)
plot (0.01:.01:6, w3(0.01:.01:6)./max(exp_ornl(3:50,6))*643, '-k', 'LineWidth', 1.5)
ylim([0 7])
xlim([0 4])
grid on
 set(legend('No H20','Radius = 1 cm','Radius = 2 cm','Radius = 5 cm'), 'Interpreter','latex')
 xlabel('Energy [MeV]', 'Interpreter','latex')
 ylabel('Normalized Response [MeV$^{-1}$]', 'Interpreter','latex')
set(gca,'TickLabelInterpreter','latex')
set(gcf, 'Position', [200, 100, 500, 325])
```

D.7 Spatial analysis

```
// Angular.cpp : Defines the entry point for the console application.
//

//include mendatory header files
#include "stdafx.h"
#include <iostream>
#include <fstream>
#include <string>
#include <sstream>
#include <iterator>
#include <vector>

using namespace std;

/*
Cast the detectors ids in sequence of the detector arrangements
*/
//int cast[16] = { 6, 7, 14, 12, 10, 4, 16, 2, 3, 13, 15, 1, 9, 5, 8, 11 };
int cast[16] = { 3,4,1,2,10,9,16,11,14,13,15,12,8,6,7,5 };

int main()
{
    /*Define histograms
      hist[x][y] = angular dist for individual neutrons in the event train
          x = order of coincidence
          y = detector position

      hist3[x][y] = angular contour dist w.r.t. first and second neutron
          x = first order of coincidence
          y = second detector position
    */
    int hist[16][16] = { { 0 } };
    int hist3[16][16] = { { 0 } };

    //Open list fine containing all event trains
    fstream myfile;
    myfile.open("neutron-ang", ios::in);
    string line;


    int cnt = 0;                            // Count number of event train
    if (myfile.is_open())
    {
        //While data exists in file
        while (getline(myfile, line))
        {
            cnt++;

            // Status update
            if (cnt % 100000 == 0) cout << "\n processed " << cnt;

            //Parse data
            std::istringstream buf(line);
            std::istream_iterator<std::string> beg(buf), end;
            std::vector<std::string> tokens(beg, end);

            if (tokens.size() > 6)          // if valid entry found
            {
                int multi = stoi(tokens.at(1));
                if (multi > 2)              //If coincidence event found
                {

                    //Remove dead detector, id 6
                    if (stoi(tokens.at(tokens.size() - 2)) == 6) continue;

                    //For the first event
```

5064

```
                    //Cast detector position
                    int base = cast[stoi(tokens.at(tokens.size() - 2))];

                    //Find shift factor for the reference position
                    int shift = 8 - base;

                    int v = 0;
                    //For subsequent events
                    for (int i = 2; i < multi + 1; i++)
                    {
                        int val = cast[stoi(tokens.at(tokens.size() - 2 * i))];
                        if (val == 16) continue;

                        //Find position w.r.t. reference
                        val += shift;
                        if (val < 1) val += 15;
                        else if (val > 15) val -= 15;

                        //Build particle wise angular distribution
                        hist[0][val]++;
                        hist[i - 1][val]++;

                        //Build contour distribution
                        if (i == 2)
                            v = val;
                        if (i == 3)
                            hist3[v][val]++;
                    }
                }
            }
        }
        myfile.close();

        //Print outputs
        cout << "\n totals ==>";
        for (int i = 0; i < 16; i++)
            cout << hist[0][i] << "\t";
        cout << "\n singlets ==>";
        for (int i = 0; i < 16; i++)
            cout << hist[1][i] << "\t";
        cout << "\n couplets ==>";
        for (int i = 0; i < 16; i++)
            cout << hist[2][i] << "\t";
        cout << "\n triplets ==>";
        for (int i = 0; i < 16; i++)
            cout << hist[3][i] << "\t";
        cout << "\n quarts ==>";
        for (int i = 0; i < 16; i++)
            cout << hist[4][i] << "\t";
        cout << "\n pentlets ==>";
        for (int i = 0; i < 16; i++)
            cout << hist[5][i] << "\t";
        cout << "\n\n contour ==>\n";
        for (int i = 0; i < 16; i++)
        {
            for (int j = 0; j < 16; j++)
                cout << hist3[i][j] << " ";
            cout << "\n";
        }
    }
    std::cin.get();
    return 0;
}

```

Plots

```
%% angular.m    Matlab scripts for ploting the spatial distributions
%%%%%%%%%%%%%%%%%%%%%%%%%%%%%%%%%%%%%%%%%%%%%%%%%%%%%%%%%%%%%
%% Plot contour distribution
[xx yy] = meshgrid(0:0.05:2*pi);
h = surf(xx,yy, interp2(x,x,tripple,xx,yy,'spline',0))
ylim([0 2*pi])
xlim([0 2*pi])
zlabel('Response')
ylabel('Angle of the third neutron [rad]')
ylabel('Third neutron [rad]')
xlabel('Second neutron Angle [rad]')
xlabel('Second neutron [rad]')
xticks([0    pi/4    pi/2 3*pi/4 pi 5*pi/4 3*pi/2 7*pi/4 2*pi])
xticklabels({'-\pi','-3\pi/4', '-\pi/4','-\pi/4','0','\pi/4','\pi/3','-3\pi/4','\pi'})
yticks([0    pi/4    pi/2 3*pi/4 pi 5*pi/4 3*pi/2 7*pi/4 2*pi])
yticklabels({'-\pi','-3\pi/4', '-\pi/4','-\pi/4','0','\pi/4','\pi/3','-3\pi/4','\pi'})

%%%%%%%%%%%%%%%%%%%%%%%%%%%%%%%%%%%%%%%%%%%%%%%%%%%%%%%%%%%%%
%% Plot angular distribution
i = 1; [fm1 fm2] = left_fit(x,(neutron_ang(i,:))/max(neutron_ang(i,:)),0);
h1= plot(0:.1:3,(fm1(0:.1:3))', 'r', 'Linewidth', 1.5); hold on
plot(3.25:.1:2*pi,(fm2(3.25:.1:2*pi))', 'r', 'Linewidth', 1.5);
i = 2; [fm1 fm2] = left_fit(x,(neutron_ang(i,:))/max(neutron_ang(i,:)),0);
h2= plot(0:.1:3,(fm1(0:.1:3))', 'b', 'Linewidth', 1.5);
plot(3.25:.1:2*pi,(fm2(3.25:.1:2*pi))', 'b', 'Linewidth', 1.5);
i = 3; [fm1 fm2] = left_fit(x,(neutron_ang(i,:))/max(neutron_ang(i,:)),0);
h3= plot(0:.1:3,(fm1(0:.1:3))', 'g', 'Linewidth', 1.5);
plot(3.25:.1:2*pi,(fm2(3.25:.1:2*pi))', 'g', 'Linewidth', 1.5);
i = 4; [fm1 fm2] = left_fit(x,(neutron_ang(i,:))/max(neutron_ang(i,:)),1);
h4= plot(0:.1:3,(fm1(0:.1:3))', 'k', 'Linewidth', 1.5);
plot(3.25:.1:2*pi,(fm2(3.25:.1:2*pi))', 'k', 'Linewidth', 1.5);
set(legend ([h1, h2, h3, h4], 'Totals', 'Second neutron', 'Third neutron', 'Fourth neutron'), 'Interpreter','latex')
i = 1;errorbar(x(1:14), (neutron_ang(i,1:14))/max(neutron_ang(i,1:14)), (neutron_ang(i,1:14))/max(neutron_ang(i,1:14)).*...
             (1./neutron_ang(i,1:14) + 1./max(neutron_ang(i,1:14))).^0.5, 'xr', 'Linewidth', 1.5)
i = 2; errorbar(x(1:14), (neutron_ang(i,1:14))/max(neutron_ang(i,1:14)), (neutron_ang(i,1:14))/max(neutron_ang(i,1:14)).*...
             (1./neutron_ang(i,1:14) + 1./max(neutron_ang(i,1:14))).^0.5, 'xb', 'Linewidth', 1.5)
i = 3;errorbar(x(1:14), (neutron_ang(i,1:14))/max(neutron_ang(i,1:14)), (neutron_ang(i,1:14))/max(neutron_ang(i,1:14)).*...
             (1./neutron_ang(i,1:14) + 1./max(neutron_ang(i,1:14))).^0.5, 'xg', 'Linewidth', 1.5)
i = 4;errorbar(x(1:14), (neutron_ang(i,1:14))/max(neutron_ang(i,1:14)), (neutron_ang(i,1:14))/max(neutron_ang(i,1:14)).*...
             (1./neutron_ang(i,1:14) + 1./max(neutron_ang(i,1:14))).^0.5, 'xk', 'Linewidth', 1.5)
xlabel ('Angular separation [rad]', 'Interpreter','latex')
ylabel ('Normalized response', 'Interpreter','latex')
xticks([0    pi/4    pi/2 3*pi/4 pi 5*pi/4 3*pi/2 7*pi/4 2*pi])
xticklabels({'-$\pi$','-3$\pi$/4','-$\pi$/2','-$\pi$/4','0','$\pi$/4','$\pi$/2','3$\pi/$4','$\pi$'})
grid on
set(gca,'TickLabelInterpreter','latex')
set(gcf, 'Position', [200, 100, 500, 325])
xlim([0 2*pi])

%%%%%%%%%%%%%%%%%%%%%%%%%%%%%%%%%%%%%%%%%%%%%%%%%%%%%%%%%%%%%
%% Comparision with simulation
figure(1)
% unrestricted data
i = 2; [fm1 fm2] = left_fit(x,(neutron_ang(i,:))/max(neutron_ang(i,:)),0);
h1= plot(0:.1:3,(fm1(0:.1:3))', 'r', 'Linewidth', 1.5); hold on
plot(3.25:.1:2*pi,(fm2(3.25:.1:2*pi))', 'r', 'Linewidth', 1.5);
he1 = errorbar(x(1:14), (neutron_ang(i,1:14))/max(neutron_ang(i,1:14)), (neutron_ang(i,1:14))/max(neutron_ang(i,1:14)).*...
             (1./neutron_ang(i,1:14) + 1./max(neutron_ang(i,1:14))).^0.5, 'xr', 'Linewidth', 1.5)
% restricted data
```

5067

```
he2 = errorbar(x(1:14), (neutron_ang_limited(i,1:14))/max(neutron_ang_limited(i,1:14))/.36*.5, ((neutron_ang_limited(i,1:14))/max(neutron_ang_limited(i,1:14)).*...
            (1./neutron_ang_limited(i,1:14) + 1./max(neutron_ang_limited(i,1:14))).^0.5)/.36*.5, 'xb', 'Linewidth', 1.5)
[fm1 fm2] = left_fit(x,(neutron_ang_limited(i,:))/max(neutron_ang_limited(i,:))/.36*.5,0);
h2= plot(0:.1:3,(fm1(0:.1:3))', '-.b', 'Linewidth', 1.5);
plot(3.25:.1:2*pi,(fm2(3.25:.1:2*pi))', '-.b', 'Linewidth', 1.5);
% Freya
hs1 = errorbar(x(1:14), [((neutron_ang_sim(i,1:7))/max(neutron_ang_sim(i,1:7))/.4*.5) (neutron_ang_sim(i,8:14))/max(neutron_ang_sim(i,8:14))], (neutron_ang_sim(i,1:14))/max(neutron_ang_sim(i,1:14)).*...
            (1./neutron_ang_sim(i,1:14) + 1./max(neutron_ang_sim(i,1:14))).^0.5, 'xk', 'Linewidth', 1.5)
[fm1 fm2] = left_fit(x,(neutron_ang_sim(i,:))/max(neutron_ang_sim(i,:)),0);
% Freya CX
hs2 = errorbar(x(1:14), [((neutron_ang_sim_CX(i,1:7))/max(neutron_ang_sim_CX(i,1:7))/.4*.5) (neutron_ang_sim_CX(i,8:14))/max(neutron_ang_sim_CX(i,8:14))]/.7*.5, (neutron_ang_sim_CX(i,1:14))/max(neutron_ang_sim_CX(i,1:14)).*...
            (1./neutron_ang_sim_CX(i,1:14) + 1./max(neutron_ang_sim_CX(i,1:14))).^0.5, '*c', 'Linewidth', 1.5)
[fm1 fm2] = left_fit(x,(neutron_ang_sim_CX(i,:))/max(neutron_ang_sim_CX(i,:))/.7*.5,0);
% Uncorrelated
i = 2; hu0 = errorbar(x(1:14), [((neutron_ang_sim2(i,1:14))/max(neutron_ang_sim2(i,1:14)))]*.66, (neutron_ang_sim2(i,1:14))/max(neutron_ang_sim2(i,1:14)).*...
            (1./neutron_ang_sim2(i,1:14) + 1./max(neutron_ang_sim2(i,1:14))).^0.5, 'xg', 'Linewidth', 1.5)
% Uncorrelated CX
i = 2; hu1 = errorbar(x(1:14), [((neutron_ang_sim_CX2(i,1:14))/max(neutron_ang_sim_CX2(i,1:14)))]*.66, (neutron_ang_sim_CX2(i,1:14))/max(neutron_ang_sim_CX2(i,1:14)).*...
            (1./neutron_ang_sim_CX2(i,1:14) + 1./max(neutron_ang_sim_CX2(i,1:14))).^0.5, 'xm', 'Linewidth', 1.5)
set(legend ([he1, h1, he2, h2, hs1, hs2, hu0, hu1], 'Data Gatewidth = 25 ns', 'Fit Gatewidth = 25 ns', ...
        'Data Gatewidth = 10 ns', 'Fit Gatewidth = 10 ns', 'Freya Simulation', ...%'Freya Simulation Fit',...
        'Freya XT corrected', ...%'Freya XT corrected Fit',
        'Uncorrelated', ...
        'Uncorrelated XT corrected'), 'Interpreter','latex')
xlabel ('Angular separation [rad]', 'Interpreter','latex')
ylabel ('Normalized response', 'Interpreter','latex')
xticks([0    pi/4    pi/2 3*pi/4 pi 5*pi/4 3*pi/2 7*pi/4 2*pi])
xticklabels({'-$\pi$','-3$\pi$/4', '-$\pi$/2','-$\pi$/4','0','$\pi$/4','$\pi$/2','3$\pi/$4','$\pi$'})
grid on
set(gca,'TickLabelInterpreter','latex')
set(gcf, 'Position', [200, 100, 600, 325])
xlim([0 2*pi])

figure(2)
i = 3; [fm1 fm2] = left_fit(x,(neutron_ang(i,:))/max(neutron_ang(i,:)),0);
h1= plot(0:.1:3,(fm1(0:.1:3))', 'r', 'Linewidth', 1.5); hold on
plot(3.25:.1:2*pi,(fm2(3.25:.1:2*pi))', 'r', 'Linewidth', 1.5);
he1 = errorbar(x(1:14), (neutron_ang(i,1:14))/max(neutron_ang(i,1:14)), (neutron_ang(i,1:14))/max(neutron_ang(i,1:14)).*...
            (1./neutron_ang(i,1:14) + 1./max(neutron_ang(i,1:14))).^0.5, 'xr', 'Linewidth', 1.5)
%
he2 = errorbar(x(1:14), (neutron_ang_limited(i,1:14))/max(neutron_ang_limited(i,1:14))/.44*.5, ((neutron_ang_limited(i,1:14))/max(neutron_ang_limited(i,1:14)).*...
            (1./neutron_ang_limited(i,1:14) + 1./max(neutron_ang_limited(i,1:14))).^0.5), 'xb', 'Linewidth', 1.5)
[fm1 fm2] = left_fit(x,(neutron_ang_limited(i,:))/max(neutron_ang_limited(i,:))/.44*.5,0);
```

```
h2= plot(0:.1:3,(fm1(0:.1:3))', '-.b', 'Linewidth', 1.5);
plot(3.25:.1:2*pi,(fm2(3.25:.1:2*pi))', '-.b', 'Linewidth', 1.5);
% Freya
hs1 = errorbar(x(1:14), [((neutron_ang_sim(i,1:7))/max(neutron_ang_sim(i,1:7)))
(neutron_ang_sim(i,8:14))/max(neutron_ang_sim(i,8:14))]/.35*.5,
(neutron_ang_sim(i,1:14))/max(neutron_ang_sim(i,1:14)).*...
            (1./neutron_ang_sim(i,1:14) + 1./max(neutron_ang_sim(i,1:14))).^0.5,
            'xk', 'Linewidth', 1.5)
[fm1 fm2] = left_fit(x,(neutron_ang_sim(i,:))/max(neutron_ang_sim(i,:)),0);
% Freya CX
hs2 = errorbar(x(1:14),
[((neutron_ang_sim_CX(i,1:7))/max(neutron_ang_sim_CX(i,1:7))/.4*.5)
(neutron_ang_sim_CX(i,8:14))/max(neutron_ang_sim_CX(i,8:14))]/.7*.5,
(neutron_ang_sim_CX(i,1:14))/max(neutron_ang_sim_CX(i,1:14)).*...
            (1./neutron_ang_sim_CX(i,1:14) +
            1./max(neutron_ang_sim_CX(i,1:14))).^0.5, '*c', 'Linewidth', 1.5)
[fm1 fm2] =
left_fit(x,(neutron_ang_sim_CX(i,:))/max(neutron_ang_sim_CX(i,:))/.7*.5,0);
%Uncorrealated
i = 3; hu0 = errorbar(x(1:14),
[((neutron_ang_sim2(i,1:14))/max(neutron_ang_sim2(i,1:14)))]*.66,
(neutron_ang_sim2(i,1:14))/max(neutron_ang_sim2(i,1:14)).*...
            (1./neutron_ang_sim2(i,1:14) + 1./max(neutron_ang_sim2(i,1:14))).^0.5,
            'xg', 'Linewidth', 1.5)
% Uncorrelated CX
hu1 = errorbar(x(1:14),
[((neutron_ang_sim_CX2(i,1:14))/max(neutron_ang_sim_CX2(i,1:14)))]*.66,
(neutron_ang_sim_CX2(i,1:14))/max(neutron_ang_sim_CX2(i,1:14)).*...
            (1./neutron_ang_sim_CX2(i,1:14) +
            1./max(neutron_ang_sim_CX2(i,1:14))).^0.5, 'xm', 'Linewidth', 1.5)
set(legend ([he1, h1, he2, h2, hs1, hs2, hu0, hu1], 'Data Gatewidth = 25 ns', 'Fit
Gatewidth = 25 ns', ...
        'Data Gatewidth = 10 ns', 'Fit Gatewidth = 10 ns', 'Freya Simulation',
        ...%'Freya Simulation Fit',...
        'Freya XT corrected', ...%'Freya XT corrected Fit',
        'Uncorrelated', ...
        'Uncorrelated XT corrected'), 'Interpreter','latex')
xlabel ('Angular separation [rad]', 'Interpreter','latex')
ylabel ('Normalized response', 'Interpreter','latex')
xticks([0    pi/4    pi/2 3*pi/4 pi 5*pi/4 3*pi/2 7*pi/4 2*pi])
xticklabels({'-$\pi$','-3$\pi$/4',
'-$\pi$/2','-$\pi$/4','0','$\pi$/4','$\pi$/2','3$\pi/$4','$\pi$'})
grid on
set(gca,'TickLabelInterpreter','latex')
set(gcf, 'Position', [200, 100, 600, 325])
xlim([0 2*pi])
ylim([0.2 2])

figure(3)
i = 4; [fm1 fm2] = left_fit(x,(neutron_ang(i,:))/max(neutron_ang(i,:)),1);
h1= plot(0:.1:3,(fm1(0:.1:3))', 'r', 'Linewidth', 1.5);; hold on
plot(3.25:.1:2*pi,(fm2(3.25:.1:2*pi))', 'r', 'Linewidth', 1.5);
he1 = errorbar(x(1:14), (neutron_ang(i,1:14))/max(neutron_ang(i,1:14)),
(neutron_ang(i,1:14))/max(neutron_ang(i,1:14)).*...
            (1./neutron_ang(i,1:14) + 1./max(neutron_ang(i,1:14))).^0.5, 'xr',
            'Linewidth', 1.5)
[fm1 fm2] = left_fit(x,(neutron_ang_limited(i,:)),0);
h2= plot(0:.1:3,(fitted0(0:.1:3))'/max(neutron_ang_limited(i,:)), '-.b',
'Linewidth', 1.5);
plot(3.25:.1:2*pi,(fitted4(3.25:.1:2*pi))'/max(neutron_ang_limited(i,:)), '-.b',
'Linewidth', 1.5);
he2 = errorbar(x(1:14),
(neutron_ang_limited(i,1:14))/max(neutron_ang_limited(i,1:14)),
(neutron_ang_limited(i,1:14))/max(neutron_ang_limited(i,1:14)).*...
            (1./neutron_ang_limited(i,1:14) +
            1./max(neutron_ang_limited(i,1:14))).^0.5, 'xb', 'Linewidth', 1.5)
set(legend ([he1, h1, he2, h2], 'Data Gatewidth = 25 ns', 'Fit Gatewidth = 25 ns', ...
        'Data Gatewidth = 10 ns', 'Fit Gatewidth = 10 ns'), 'Interpreter','latex')
xlabel ('Angular separation [rad]', 'Interpreter','latex')
ylabel ('Normalized response', 'Interpreter','latex')
xticks([0    pi/4    pi/2 3*pi/4 pi 5*pi/4 3*pi/2 7*pi/4 2*pi])
```

```
xticklabels({'-$\pi$','-3$\pi$/4',
'-$\pi$/2','-$\pi$/4','0','$\pi$/4','$\pi$/2','3$\pi/$4','$\pi$'})
grid on
set(gca,'TickLabelInterpreter','latex')
set(gcf, 'Position', [200, 100, 600, 325])
xlim([0 2*pi])
ylim([0.2 1.6])

%%%%%%%%%%%%%%%%%%%%%%%%%%%%%%%%%%%%%%%%%%%%%%%%%%%%%%%%%%%%%
%% Comparision with Literature
figure (4)
[fm1 fm2] = left_fit([fliplr(24:24:180) fliplr(24:24:180)]/180*pi,(
[(neutron_ang(2,1:7)+fliplr(neutron_ang(2,8:14)))
neutron_ang(2,1:7)])/max([(neutron_ang(2,1:7)+fliplr(neutron_ang(2,8:14)))
neutron_ang(2,1:7)]),0)
h1 = plot(fliplr(24:24:180)/180*pi,(neutron_ang(2,1:7)+fliplr(neutron_ang(2,8:14)))...
    ./max(neutron_ang(2,1:7)+fliplr(neutron_ang(2,8:14))), 'xr', 'Linewidth', 1.5)
hold on
plot(fliplr(24:1:170)/180*pi,fm1(fliplr(24:1:170)/180*pi), '-r', 'Linewidth', 1.5)

[fm1 fm2] = left_fit((Gal(:,1))/180*pi,Gal(:,2)/(Gal(30,2)),3)
h2 = plot((Gal(:,1))/180*pi,Gal(:,2)/(Gal(30,2)), 'xm', 'Linewidth', 1.5)
plot((1:1:170)/180*pi,fm1(fliplr(1:1:170)/180*pi), '-.m', 'Linewidth', 1.5)
h3 = plot((vogt(:,3))/180*pi,vogt(:,4)/(vogt(23,4)), '-.k', 'Linewidth', 1.5)
h4 = plot((vogt(:,1))/180*pi,vogt(:,6)/(vogt(25,6)), '--k', 'Linewidth', 1.5)
h5 = plot(sarah(:,1)/180*pi,sarah(1:7,4)/max(sarah(1:7,4)), 'xg', 'Linewidth', 1.5)
[fm1 fm2] = left_fit(sarah(:,1)/180*pi, sarah(1:7,4)/max(sarah(1:7,4)),3)
plot(fliplr(24:1:180)/180*pi,fm1(fliplr(24:1:180)/180*pi), '-.g', 'Linewidth', 1.5)
h6 = plot(sarah(:,3)/180*pi,sarah(1:7,6)/max(sarah(1:7,6)), 'og', 'Linewidth', 1.5)
[fm1 fm2] = left_fit(sarah(:,3)/180*pi, sarah(1:7,6)/max(sarah(1:7,6)),3)
plot(fliplr(24:1:180)/180*pi,fm1(fliplr(24:1:180)/180*pi), '--g', 'Linewidth', 1.5)
xlabel ('Angular separation [rad]', 'Interpreter','latex')
ylabel ('Normalized response', 'Interpreter','latex')
xticks([0    pi/4    pi/2 3*pi/4 pi 5*pi/4 3*pi/2 7*pi/4 2*pi])
xticklabels({'0','$\pi$/4','$\pi$/3','3$\pi/$4','$\pi$'})
grid on
set(gca,'TickLabelInterpreter','latex')
set(gcf, 'Position', [200, 100, 500, 325])
set(legend ([h1, h2, h3, h4, h5, h6], 'This work', 'Gagarski; Thres = 1.2 MeV',
'Vogt, FREYA; Thres = 1 MeV', 'Vogt, FREYA; Thres = 1.5 MeV', 'Pozzi; Thres = 1
MeV', 'Pozzi; Thres = 1.5 MeV'), 'Interpreter','latex')
xlim([0 pi])

%%%%%%%%%%%%%%%%%%%%%%%%%%%%%%%%%%%%%%%%%%%%%%%%%%%%%%%%%%%%%
%% fragments
load('frag.mat')
plot(fragments(:,1), fragments(:,2), 'xr', 'Linewidth', 1.5)
hold on
plot(fragments(:,3), fragments(:,4), '--r', 'Linewidth', 1.5)
plot(fragments(:,5), fragments(:,6), 'xb', 'Linewidth', 1.5)
plot(fragments(:,7), fragments(:,8), '--b', 'Linewidth', 1.5)
plot(fragments(:,9), fragments(:,10), 'xg', 'Linewidth', 1.5)
plot(fragments(:,11), fragments(:,12), '--g', 'Linewidth', 1.5)
plot(fragments(:,13), fragments(:,14), 'xm', 'Linewidth', 1.5)
plot(fragments(:,15), fragments(:,16), '--m', 'Linewidth', 1.5)

set(legend ( '$^{238}$U', '$^{238}$U FREYA', '$^{252}$Cf', '$^{252}$Cf FREYA'...
    , '$^{244}$Cm', '$^{244}$Cm FREYA', '$^{240}$Pu', '$^{240}$Pu FREYA'),
    'Interpreter','latex')
grid on
set(gca, 'YScale', 'log')
xlim([80 160])
ylim([0.02 10])
xlabel ('Mass number', 'Interpreter','latex')
ylabel ('Percentage yield [\%]', 'Interpreter','latex')
set(gca,'TickLabelInterpreter','latex')
set(gcf, 'Position', [200, 100, 500, 325])
```

D.8 Passive coincidence counting analysis

```
%%
%%calculate uncertainties and plot data
%%

%% Cf-252/Co/Cs
figure (1)
w2 = 1;
yval= cdist_1;
yval(1,:) = yval(1,:)./time_1(1);
yval(2,:) = yval(2,:)./time_1(2);
yval(3,:) = yval(3,:)./time_1(3);
yval(4,:) = yval(4,:)./time_1(4);
handles.barc = bar(1:4,yval,w2)
hold on
w2 = .5;
yval= adist_1;
yval(1,:) = yval(1,:)./time_1(1);
yval(2,:) = yval(2,:)./time_1(2);
yval(3,:) = yval(3,:)./time_1(3);
yval(4,:) = yval(4,:)./time_1(4);
handles.bara = bar(1:4,yval,w2,'FaceColor',[1 0 0]);
set(gca, 'YScale', 'log')
errorbars_bar(handles.barc, cdist_1, time_1)
errorbars_bar(handles.bara, adist_1, time_1)
alpha(0.5)

ylabel ('Count rate [s$^{-1}$]', 'Interpreter','latex');
set(gca,'TickLabelInterpreter','latex')
set(gcf, 'Position', [200, 100, 650, 325])
set(legend('Singlets', 'Doublets', 'Triplets', 'Quadlets', 'Quintuplets',
'Accidentals'), 'Location', 'eastoutside', 'Interpreter','latex');
ax = gca;
ax.XTick = [1 2 3 4];
ax.XTickLabels = {'Cf252-BARE8','Cf252-BARE15','Co60-BARE145','Cs137-BARE15'};
grid on


%% Cf252
figure (2)
w2 = 1;
yval= cdist_2;
yval(1,:) = yval(1,:)./time_2(1);
yval(2,:) = yval(2,:)./time_2(2);
yval(3,:) = yval(3,:)./time_2(3);
yval(4,:) = yval(4,:)./time_2(4);
handles.barc = bar(1:4,yval,w2)
hold on
w2 = .5;
yval= adist_2;
yval(1,:) = yval(1,:)./time_2(1);
yval(2,:) = yval(2,:)./time_2(2);
yval(3,:) = yval(3,:)./time_2(3);
yval(4,:) = yval(4,:)./time_2(4);
handles.bara = bar(1:4,yval,w2,'FaceColor',[1 0 0]);
set(gca, 'YScale', 'log')
errorbars_bar(handles.barc, cdist_2, time_2)
errorbars_bar(handles.bara, adist_2, time_2)
alpha(0.5)

ylabel ('Count rate [s$^{-1}$]', 'Interpreter','latex');
set(gca,'TickLabelInterpreter','latex')
set(gcf, 'Position', [200, 100, 650, 325])
set(legend('Singlets', 'Doublets', 'Triplets', 'Quadlets', 'Quintuplets',
'Accidentals'), 'Location', 'eastoutside', 'Interpreter','latex');
ax = gca;
ax.XTick = [1 2 3 4];
ax.XTickLabels = {'Cf252-FC','Cf252-TH','Cf252-MAIN','Cf252-ALL'};
grid on

%% lancs
figure (3)
```

5072

```
w2 = 1;
yval= cdist_3;
yval(1,:) = yval(1,:)./time_3(1);
yval(2,:) = yval(2,:)./time_3(2);
yval(3,:) = yval(3,:)./time_3(3);
yval(4,:) = yval(4,:)./time_3(4);
handles.barc = bar(1:4,yval,w2)
hold on
w2 = .5;
yval= adist_3;
yval(1,:) = yval(1,:)./time_3(1);
yval(2,:) = yval(2,:)./time_3(2);
yval(3,:) = yval(3,:)./time_3(3);
yval(4,:) = yval(4,:)./time_3(4);
handles.bara = bar(1:4,yval,w2,'FaceColor',[1 0 0]);
set(gca, 'YScale', 'log')
errorbars_bar(handles.barc, cdist_3, time_3)
errorbars_bar(handles.bara, adist_3, time_3)
alpha(0.5)
ylim([0.00001 100000])

ylabel ('Count rate [s$^{-1}$]', 'Interpreter','latex');
set(gca,'TickLabelInterpreter','latex')
set(gcf, 'Position', [200, 100, 650, 325])
set(legend('Singlets', 'Doublets', 'Triplets', 'Quadlets', 'Quintuplets',
'Accidentals'), 'Location', 'eastoutside', 'Interpreter','latex');
ax = gca;
ax.XTick = [1 2 3 4];
ax.XTickLabels =
{'Exposed-Neutron','Secured-Neutron','Exposed-Joint','Secured-Neutron'};
grid on

%% moment lancs
figure (4)
w2 = 1;
yval= [[0, 0, 0, 0]' cdist_3];
sval =  sum(cdist_3');
uval= [[0, 0, 0, 0]' ((cdist_3).^0.5)];
eff = [0.012 0.012 0.023 0.023];
for i = 2:6
 for j = 1:4
     uval(j,i) = (((uval(j,i)/yval(j,i))^2 + (sum(yval(j,2:6).^0.5)/sval(j)).^2)) *
     yval(j,i)/(eff(j)^i);
     yval(j,i) = yval(j,i)/(eff(j)^i);
     if (isnan(uval(j,i)))
         uval(j,i) = 0;
     end
 end
end
pval = factorial_moment(yval,4);
evalu = factorial_moment(yval+uval,4);
evall = factorial_moment(yval-uval,4);
eval = evalu-evall;
handles.barc = bar(1:4,pval,w2)
hold on
errorbars_bar2(handles.barc, eval, [1 1 1 1],pval)
alpha(0.5)
set(gca, 'YScale', 'log')
ylim([0.1 100])

ylabel ('Factorial moments', 'Interpreter','latex');
set(gca,'TickLabelInterpreter','latex')
set(gcf, 'Position', [200, 100, 650, 325])
set(legend('Singles', 'Doubles', 'Triples', 'Quadruples'), 'Location',
'eastoutside', 'Interpreter','latex');
ax = gca;
ax.XTick = [1 2 3 4];
ax.XTickLabels =
{'Exposed-Neutron','Secured-Neutron','Exposed-Joint','Secured-Neutron'};
grid on
```

D.9 Active coincidence counting analysis

```
%%Matlab script to process and plot UOX induced coincidence distribution
%% load variables
load('sanity.mat')
load('raw_data.mat')
AmLe(:,1)=[];
AmLiBack(:,1)=[];
x_axis(:,1) = [];

%% remane variables
AmLi_hs=(AmLe);
U8x1_hs=(U8x1_fore);
U15x1_1_hs=(U15x1_fore1);
U15x1_2_hs=(U15x1_fore2);
Block_1_hs=(block_fore);
clearvars  AmLe AmLiBack U8x1_fore  U15x1_Back1 U8x1_back U15x1_fore1 Ga
clearvars  U15x1_fore2 U15x1_Back2 U8x1_fore U8x1_back block_back block_fore

%% convert to rates
AmLi_hs_rate= AmLi_hs./AmLi_hs(:,1); AmLi_hs_rate (:,1)=[];
U8x1_hs_rate= U8x1_hs./U8x1_hs(:,1); U8x1_hs_rate (:,1)=[];
U15x1_1_hs_rate= U15x1_1_hs./U15x1_1_hs(:,1); U15x1_1_hs_rate (:,1)=[];
U15x1_2_hs_rate= U15x1_2_hs./U15x1_2_hs(:,1); U15x1_2_hs_rate (:,1)=[];
Block_1_hs_rate= Block_1_hs./Block_1_hs(:,1); Block_1_hs_rate (:,1)=[];
clearvars Block_1_hs U8x1_2_hs  U15x1_2_hs U15x1_1_hs U8x1_hs AmLi_hs

%% Load uncertainty
load('uncir.mat')
clearvars  U15x1_unc1M U15x1_unc2M U8x1_uncM  U15x1_Back1 block_uncM U15x1_fore1

%% plots UOX data
figure(1) %% Eight Detector Arrangement
subplot (1,3,1)
title('Eight Detector Arrangement')
xlabel('Mass of U-235 (g)');
yyaxis left
f=fit_rates2(x_axis, U8x1_hs_rate(:,1)- U8x1_hs_rate(1,1));
errorbar(x_axis, U8x1_hs_rate(:,1) - U8x1_hs_rate(1,1),...
        ((U8x1_unc(:,2).*U8x1_hs_rate(:,1)).^2 + ...
        (U8x1_unc(1,2).*U8x1_hs_rate(1,1)).^2).^0.5, ...
        'x', 'LineWidth', 2); hold on;
plot(0:.1:200, f(0:.1:200), 'LineWidth', 1);
ylabel('Singlet rate (sps)')
yyaxis right
ylabel('Couplet rate (cps)')
f=fit_rates2(x_axis, U8x1_hs_rate(:,2)- U8x1_hs_rate(1,2));
errorbar(x_axis, U8x1_hs_rate(:,2)- U8x1_hs_rate(1,2), ...
        ((U8x1_unc(:,3).*U8x1_hs_rate(:,2)).^2 + ...
        (U8x1_unc(1,3).*U8x1_hs_rate(1,2)).^2).^0.5, ...
        'x', 'LineWidth', 2); hold on;
plot(0:.1:200, f(0:.1:200), 'LineWidth', 1);
grid on

figure(2) %% Fifteen Detector Arrangement
title('Fifteen Detector Arrangement')
xlabel('Mass of U-235 (g)');
yyaxis left
f=fit_rates2(x_axis, U15x1_1_hs_rate(:,1)-  U15x1_1_hs_rate(1,1));
f2=fit_rates2(x_axis, U15x1_2_hs_rate(:,1) -  U15x1_2_hs_rate(1,1));
errorbar(x_axis, U15x1_1_hs_rate(:,1)-U15x1_1_hs_rate(1,1), ...
```

5075

```
        ((U15x1_unc1(:,2).*U15x1_1_hs_rate(:,1)).^2 + ...
        (U15x1_unc1(1,2).*U15x1_1_hs_rate(1,1)).^2).^0.5, ...
        'x', 'LineWidth', 2); hold on;
plot(0:.1:200, f(0:.1:200), 'LineWidth', 1);
ylabel('Singlet rate (sps)')
yyaxis right
ylabel('Couplet rate (cps)')

f=fit_rats(x_axis, U15x1_1_hs_rate(:,2) - U15x1_1_hs_rate(1,2));
f2=fit_rats(x_axis, U15x1_2_hs_rate(:,2) - U15x1_2_hs_rate(2,2));
errorbar(x_axis, U15x1_1_hs_rate(:,2) - U15x1_1_hs_rate(1,2), ...
        ((U15x1_unc1(:,3).*U15x1_1_hs_rate(:,2)).^2 + ...
        (U15x1_unc1(1,3).*U15x1_1_hs_rate(1,2)).^2).^0.5, ...
        'x', 'LineWidth', 2); hold on;
plot(0:.1:200, f(0:.1:200), 'LineWidth', 1);
grid on
%legend ('Light Moderation', 'Heavy Moderation')

figure(3) %% Block Detector Arrangement
title('Block Arrangement')
xlabel('Mass of U-235 (g)');
yyaxis left
f=fit_rats(x_axis, Block_1_hs_rate(:,1) - Block_1_hs_rate(1,1));
errorbar(x_axis, Block_1_hs_rate(:,1) - Block_1_hs_rate(1,1), ...
        ((Block_1_hs_rate(:,1).*block_unc(:,2)).^2 + ...
        (Block_1_hs_rate(1,1).*block_unc(1,2)).^2).^.5, ...
        'x', 'LineWidth', 2); hold on;
plot(0:.1:200, f(0:.1:200), 'LineWidth', 1);
ylabel('Singlet rate (sps)')
yyaxis right
ylabel('Couplet rate (cps)')
f=fit_rats(x_axis, Block_1_hs_rate(:,2) - Block_1_hs_rate(2,2));
errorbar(x_axis, Block_1_hs_rate(:,2) - Block_1_hs_rate(1,2) , ...
        ((Block_1_hs_rate(:,2).*block_unc(:,3)).^2 + ...
        (Block_1_hs_rate(1,2).*block_unc(1,3)).^2).^.5, ...
        'x', 'LineWidth', 2); hold on;
plot(0:.1:200, f(0:.1:200), 'LineWidth', 1);
grid on

%% Plot different  moderation level
figure(1)
errorbar(x_axis, U15x1_1_hs_rate(:,2)- U15x1_1_hs_rate(1,2), ...
        U15x1_1_hs_rate(:,2).*U15x1_unc1(:,3), 'bx', 'LineWidth', 2); hold on;
errorbar(x_axis, U15x1_2_hs_rate(:,2) - U15x1_2_hs_rate(1,2), ...
        U15x1_2_hs_rate(:,2).*U15x1_unc2(:,3), 'ko', 'LineWidth', 2);
grid on
f1=fit_rats(x_axis, U8x1_hs_rate(:,2) - U8x1_hs_rate(1,2));
f2=fit_rats(x_axis, U15x1_1_hs_rate(:,2)- U15x1_1_hs_rate(1,2));
f3=fit_rats(x_axis, U15x1_2_hs_rate(:,2)- U15x1_2_hs_rate(1,2));

plot(0:.1:200, f2(0:.1:200), 'b','LineWidth', 1);
plot(0:.1:200, f3(0:.1:200), 'k','LineWidth', 1);
ylabel('Couplet rate (cps)')
xlabel('Mass of U-235 (g)');
legend ('2 cm Moderator', '3.75 cm Moderator')

%% function to find fit_rats
function [fitresult, gof] = fit_rates2(x_axis, y)
%fit_rates2(X_AXIS,Y)
```

5076

```
%  Data for 'untitled fit 1' fit:
%      X Input : x_axis
%      Y Output: y
%  Output:
%      fitresult : a fit object representing the fit.
%      gof : structure with goodness-of fit info.


[xData, yData, weights] = prepareCurveData( x_axis, y, abs(1./y) );

% Set up fittype and options.
ft = fittype( 'exp2' );
opts = fitoptions( 'Method', 'NonlinearLeastSquares' );
opts.Display = 'Off';
opts.StartPoint = [61.381333967166 0.000341207570440311 -62.6115434709868 -
0.0202447272697837];
opts.Weights = weights;
% Fit model to data.
[fitresult, gof] = fit( xData, yData, ft );
```

D.10 PSD analysis

```
%% Create PSD plots and table

%% make matrix
mesh_psd=zeros(400,400,12);
i = 0;

for j = 1:3
    if j == 1
        psd_temp = psd4310;
    elseif j == 2
        psd_temp = psd4311;
    else
        psd_temp = psd4313;
    end
    sz = size(psd_temp);
    t=zeros(4);
    for i = 1:sz(1)
        mesh_psd(int16(psd_temp(i,4)/10), int16(psd_temp(i,3)/10), (4*(j-1))+psd_temp(i,1)) ...
            = mesh_psd(int16(psd_temp(i,4)/10),int16(psd_temp(i,3)/10), (4*(j-1))+psd_temp(i,1)) + 1;
         t(psd_temp(i,1),1)=  t(psd_temp(i,1),1) +1;
    end
    disp(t)
end
totals = sum(mesh_psd,3);

%% make plot
contourf(1:10:4000,1:10:4000, mesh_psd(:,:,9)',[2 20 40 80 160 170])
xlim([600 1700])
ylim([600 3800])
ylabel ('First integral', 'Interpreter','latex')
xlabel ('Second integral', 'Interpreter','latex');
colorbar
set(gca,'TickLabelInterpreter','latex')
set(gcf, 'Position', [200, 100, 500, 325])

%% make table
for k = 1:12
[ft1 gf1] = createFitsGauss(1:400, sum(mesh_psd(:,80:85,k)'),1);
[ft2 gf2] = createFitsGauss(1:400, sum(mesh_psd(:,86:90,k)'),1);
[ft3 gf3] = createFitsGauss(1:400, sum(mesh_psd(:,91:95,k)'),1);
[ft4 gf4] = createFitsGauss(1:400, sum(mesh_psd(:,96:100,k)'),1);
[ft5 gf5] = createFitsGauss(1:400, sum(mesh_psd(:,101:105,k)'),2);
[ft6 gf6] = createFitsGauss(1:400, sum(mesh_psd(:,106:110,k)'),2);
[ft7 gf7] = createFitsGauss(1:400, sum(mesh_psd(:,111:115,k)'),2);
[ft8 gf8] = createFitsGauss(1:400, sum(mesh_psd(:,116:120,k)'),2);
[ft9 gf9] = createFitsGauss(1:400, sum(mesh_psd(:,121:125,k)'),2);
[ft10 gf10] = createFitsGauss(1:400, sum(mesh_psd(:,126:130,k)'),2);
[ft11 gf11] = createFitsGauss(1:400, sum(mesh_psd(:,131:150,k)'),2);
[ft12 gf12] = createFitsGauss(1:400, sum(mesh_psd(:,150:end,k)'),2);


if(k > 4)
    xlimi = [72 72.5 73 74 75 76 77 78 79 80 80 ];
else
    xlimi = [76 76.5 77 78 76 77 77 78 79 80 80 ];
end
i = 1
```

5079

```
ft= ft1;
a1 =  ft.a1; b1 =  ft.b1; c1 =  ft.c1;
sum_n = sum(a1*exp(-(([xlimi(i):400]-b1)/c1).^2))
sum_t =  sum(a1*exp(-(([1:400]-b1)/c1).^2))

i = 2
ft= ft2;
a1 =  ft.a1; b1 =  ft.b1; c1 =  ft.c1;
sum_n = sum_n + sum(a1*exp(-(([xlimi(i):400]-b1)/c1).^2))
sum_t = sum_t + sum(a1*exp(-(([1:400]-b1)/c1).^2))

i = 3
ft= ft3;
   a1 =  ft.a1; b1 =  ft.b1; c1 =  ft.c1;
sum_n = sum_n + sum(a1*exp(-(([xlimi(i):400]-b1)/c1).^2))
sum_t = sum_t + sum(a1*exp(-(([1:400]-b1)/c1).^2))

i = 4
ft= ft4;
   a1 =  ft.a1; b1 =  ft.b1; c1 =  ft.c1;
sum_n = sum_n + sum(a1*exp(-(([xlimi(i):400]-b1)/c1).^2))
sum_t = sum_t + sum(a1*exp(-(([1:400]-b1)/c1).^2))

i = 5
ft= ft5;
if (ft.a1 >  ft.a2)
   a1 =  ft.a1; b1 =  ft.b1; c1 =  ft.c1;
else
   a1 =  ft.a2; b1 =  ft.b2; c1 =  ft.c2;
end
sum_n = sum_n + sum(a1*exp(-(([xlimi(i):400]-b1)/c1).^2))
sum_t = sum_t + sum(a1*exp(-(([1:400]-b1)/c1).^2))

i = 6
ft= ft6;
if (ft.a1 >  ft.a2)
   a1 =  ft.a1; b1 =  ft.b1; c1 =  ft.c1;
else
   a1 =  ft.a2; b1 =  ft.b2; c1 =  ft.c2;
end
sum_n = sum_n + sum(a1*exp(-(([xlimi(i):400]-b1)/c1).^2))
sum_t = sum_t + sum(a1*exp(-(([1:400]-b1)/c1).^2))

i = 7
ft= ft7;
if (ft.a1 >  ft.a2)
   a1 =  ft.a1; b1 =  ft.b1; c1 =  ft.c1;
else
   a1 =  ft.a2; b1 =  ft.b2; c1 =  ft.c2;
end
sum_n = sum_n + sum(a1*exp(-(([xlimi(i):400]-b1)/c1).^2))
sum_t = sum_t + sum(a1*exp(-(([1:400]-b1)/c1).^2))

i = 8; ft= ft8;
if (ft.a1 >  ft.a2)
   a1 =  ft.a1; b1 =  ft.b1; c1 =  ft.c1;
else
   a1 =  ft.a2; b1 =  ft.b2; c1 =  ft.c2;
end
```

5080

```
sum_n = sum_n + sum(a1*exp(-(([xlimi(i):400]-b1)/c1).^2))
sum_t = sum_t + sum(a1*exp(-(([1:400]-b1)/c1).^2))

i = 9
ft= ft9;
if (ft.a1 >  ft.a2)
   a1 =  ft.a1; b1 =  ft.b1; c1 =  ft.c1;
else
   a1 =  ft.a2; b1 =  ft.b2; c1 =  ft.c2;
end
sum_n = sum_n + sum(a1*exp(-(([xlimi(i):400]-b1)/c1).^2))
sum_t = sum_t + sum(a1*exp(-(([1:400]-b1)/c1).^2))

i = 10
ft= ft10;
if (ft.a1 >  ft.a2)
   a1 =  ft.a1; b1 =  ft.b1; c1 =  ft.c1;
else
   a1 =  ft.a2; b1 =  ft.b2; c1 =  ft.c2;
end
sum_n = sum_n + sum(a1*exp(-(([xlimi(i):400]-b1)/c1).^2))
sum_t = sum_t + sum(a1*exp(-(([1:400]-b1)/c1).^2))

list_n(k) = sum_n;
list_t(k) = sum_t;
sum_n/sum_t
end

list_n([8]) = [];
list_t([8]) = [];
ratio = list_n./list_t
mean = sum(ratio)/11
std(ratio)
%%%%%%%%%%%%%%%%%%%%%%%%%%%%%%%%%%%%%%%%%%%%%%%%%%%%%%%%%%%%%%%%
%% Function to create fit'.
%%
function [fitresult, gof] = createFitsGauss(x1, y1,type)

%% x1, y1: plot data
%% type: select between 1 or 2 gaussian terms
[xData, yData] = prepareCurveData( x1, y1 );

% Set up fittype and options.
if type == 2
ft = fittype( 'gauss2' );
else
    ft = fittype( 'gauss1' );
end
opts = fitoptions( 'Method', 'NonlinearLeastSquares' );
opts.Display = 'Off';
opts.Lower = [-Inf -Inf 0 -Inf -Inf 0];
if type == 2
opts.StartPoint = [2402 69 1.57385159632041 235.858062481828 68 2.68804564072266];
else
opts.StartPoint = [2402 69 1.57385159632041 ];
end

% Fit model to data.
[fitresult, gof] = fit( xData, yData, ft, opts );
```

D.11 Crosstalk analysis

```
%% Make plots
figure (1)
xx= 2*pi/15:2*pi/15:28*pi/15;
plot(xx(8:end), cx_dist2(1,2:end)./cx_dist2(1,1), 'xb','Linewidth', 1.5)
hold on
plot(xx(8:end), cx_dist2(2,2:end)./cx_dist2(2,1), 'xr','Linewidth', 1.5)
plot(xx(8:end), cx_dist2(3,2:end)./cx_dist2(3,1), 'xg','Linewidth', 1.5)
plot(xx(8:end), cx_dist2(4,2:end)./cx_dist2(4,1), 'xk','Linewidth', 1.5)
plot((xx(8):.01:xx(end))', fittedmodel1((xx(8):.01:xx(end))),'b','Linewidth', 1.)
plot((xx(8):.01:xx(end))', fittedmodel2((xx(8):.01:xx(end))),'r','Linewidth', 1.)
plot((xx(8):.01:xx(end))', fittedmodel3((xx(8):.01:xx(end))),'g','Linewidth', 1.)
plot((xx(8):.01:xx(end))', fittedmodel4((xx(8):.01:xx(end))),'k','Linewidth', 1.)
ylabel ('Response [counts per million]', 'Interpreter','latex')
grid on
set(legend('Cut-off 0 MeVee','Cut-off 0.1 MeVee', 'Cut-off 0.2 MeVee', 'Cut-off 0.3 MeVee'), 'Interpreter','latex')
ylabel ('Crosstalk/Singlets', 'Interpreter','latex')
xlabel ('Angular position [rad]', 'Interpreter','latex')
xlim ([pi 2*pi])
xticks([0 .25*pi 1*pi/2 .75*pi pi 1.25*pi 3*pi/2 1.75*pi 2*pi])
xticklabels({'0$\pi$','$\pi/$4','$\pi/$2','3$\pi$/4', '0$\pi$','$\pi/$4','$\pi/$2','3$\pi$/4', '$\pi$'})
set(gca,'TickLabelInterpreter','latex')
set(gcf, 'Position', [200, 100, 500, 325])


figure (2)
plot(cx_tof(:,1:4), 'Linewidth', 1.5)
ylabel ('Response  [counts per million histories]', 'Interpreter','latex')
set(legend('1 MeV neutron', '2 MeV neutron', '3.5 MeV neutron', '5 MeV neutron'), 'Interpreter','latex')
xlabel ('Time [ns]','Interpreter','latex')
xlim([0 80])
grid on
set(gca,'TickLabelInterpreter','latex')
set(gcf, 'Position', [200, 100, 500, 325])


figure (3)
plot([750 1000 1250 1500 1750 2000 2250 2500 3500 5000],ratio_sim(:,1), 'bx','LineWidth', 1.5)
hold on
plot([750 1000 1250 1500 1750 2000 2250 2500 3500 5000],ratio_sim(:,2), 'rx','LineWidth', 1.5)
plot([750 1000 1250 1500 1750 2000 2250 2500 3500 5000],ratio_sim(:,3), 'gx','LineWidth', 1.5)
plot([750 1000 1250 1500 1750 2000 2250 2500 3500 5000],ratio_sim(:,4), 'kx','LineWidth', 1.5)
hold on;
plot([750:1:5000],fittedmodel_1(750:1:5000),'b','LineWidth', 1.)
plot([750:1:5000],fittedmodel_2(750:1:5000), 'r','LineWidth', 1.)
plot([750:1:5000],fittedmodel_3(750:1:5000), 'g','LineWidth', 1.)
plot([750:1:5000],fittedmodel_4(750:1:5000), 'k','LineWidth', 1.)
set(legend('Cut-off 0 MeVee','Cut-off 0.1 MeVee', 'Cut-off 0.2 MeVee', 'Cut-off 0.3 MeVee'), 'Interpreter','latex')
grid on
xlim([750 5000])
ylabel ('Crosstalk factor', 'Interpreter','latex')
xlabel ('Incident Energy (keV)', 'Interpreter','latex')
set(gca,'TickLabelInterpreter','latex')
set(gcf, 'Position', [200, 100, 500, 325])
```

Appendix E

Additional Data

E.1 Number density analysis

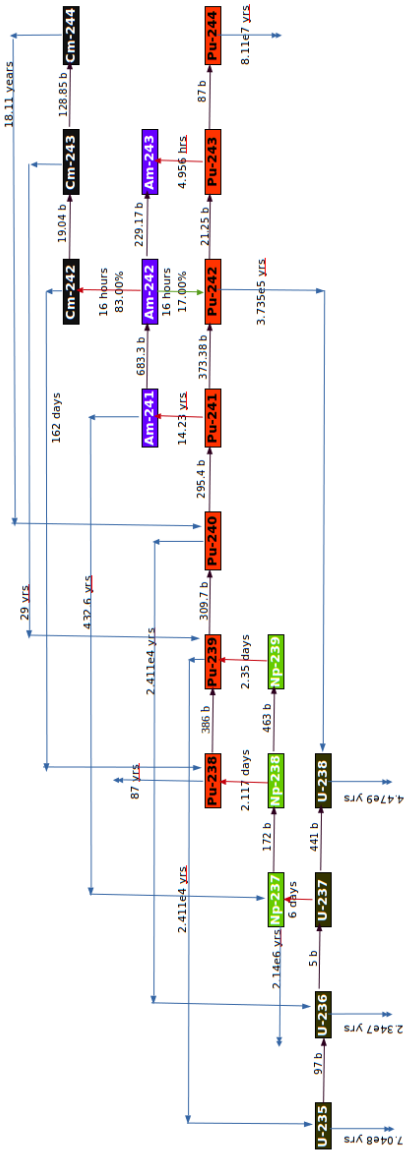

Figure E.1 | Decay and activation path-way. The isotopic depletion and decay scheme of the actinide isotopes relevant to this research, including neutron capture reactions (black arrows), α-decays (blue arrows), β^+ decays (green arrows) and β^- decays (red arrows) for isotopes with half-lives less than 10^6 year.

E.2 Passive coincidence counting analysis

Table E.1 | Coincidence distributions for the BARE15 setups.

(a) Neutron coincidence distribution with lead shielding

Date	27-Feb 2017							
Time [s]	603							
	Counts				***Count Rates [s^{-1}]***			
Distribution	*Singlet*	*Doublet*	*Triplet*	*Quadlet*	*Singlet*	*Doublet*	*Triplet*	*Quadlet*
Foreground	5674396	181625	2907	16	9410	301	4.8	0.027
Background	1578	44	2	0	2.61	0.03	0.0005	0
Ratio to *Singlet* $\times 10^{-4}$	—	320	5.12	0.028		—		

(b) γ coincidence distribution with lead shielding

Date	27-Feb 2017							
Time [s]	303							
	Counts				***Count Rates [s^{-1}]***			
Distribution	*Singlet*	*Doublet*	*Triplet*	*Quadlet*	*Singlet*	*Doublet*	*Triplet*	*Quadlet*
Foreground	9655988	382568	12342	236	31867	1262	40	0.779
Background	9710	339	10	1	32	0.03	0.0012	0
Ratio to *Singlet* $\times 10^{-4}$	—	396	12.7	0.244		—		

Table E.2 | Coincidence distributions for the BARE8 setups.

(a) Neutron coincidence distribution with no lead shielding

Date	21-Feb 2017							
Time [s]	1202							
	Counts				***Count Rates [s^{-1}]***			
Distribution	*Singlet*	*Doublet*	*Triplet*	*Quadlet*	*Singlet*	*Doublet*	*Triplet*	*Quadlet*
Foreground	9316331	177903	1755	7	7750	148	1.4	0.0058
Background	1900	53	0	0	1.58	0.045	0	0
Ratio to *Singlet* $\times 10^{-4}$	—	190	1.88	0.0075		—		

(b) γ coincidence distribution with no lead shielding

Date	21-Feb 2017							
Time [s]	182							
	Counts				***Count Rates [s^{-1}]***			
Distribution	*Singlet*	*Doublet*	*Triplet*	*Quadlet*	*Singlet*	*Doublet*	*Triplet*	*Quadlet*
Foreground	6712354	211873	5160	69	36881	1164	28.4	0.379
Background	6870	271	6	0	37.7	1.49	0.033	0
Ratio to *Singlet* $\times 10^{-4}$	—	315	7.68	0.103		—		

(c) Neutron coincidence distribution with lead shielding

Date	22-Feb 2017							
Time [s]	1202							
	Counts				***Count Rates [s^{-1}]***			
Distribution	*Singlet*	*Doublet*	*Triplet*	*Quadlet*	*Singlet*	*Doublet*	*Triplet*	*Quadlet*
Foreground	8584970	156696	1391	9	7142	130	1.2	0.0075
Background	6870	271	6	0	1.58	0.045	0	0
Ratio to *Singlet* $\times 10^{-4}$	—	190	1.88	0.0075		—		

(d) γ coincidence distribution with lead shielding

Date	22-Feb 2017							
Time [s]	244							
	Counts				***Count Rates [s^{-1}]***			
Distribution	*Singlet*	*Doublet*	*Triplet*	*Quadlet*	*Singlet*	*Doublet*	*Triplet*	*Quadlet*
Foreground	8032341	162939	2978	26	32919	667	12.2	0.107
Background	5936	217	5	0	24.3	0.89	0.020	0
Ratio to *Singlet* $\times 10^{-4}$	—	203	3.71	0.032		—		

Table E.3 | Coincidence distributions for the BARE15 setups for γ-ray sources.

(a) γ coincidence distribution with lead shielding for ^{60}Co

Date	27-Feb 2017							
Time [s]	2775							
	Counts				***Count Rates [s^{-1}]***			
Distribution	*Singlet*	*Doublet*	*Triplet*	*Quadlet*	*Singlet*	*Doublet*	*Triplet*	*Quadlet*
Foreground	86568025	1480006	10321	57	31195	533	3.7	0.027
Background	78592	1408	11	0	28.3	0.50	0.003	0
Ratio to *Singlet* $\times 10^{-4}$	—	170	1.19	0.006		—		

(b) γ coincidence distribution with lead shielding for ^{137}Cs

Date	27-Feb 2017							
Time [s]	689							
	Counts				***Count Rates [s^{-1}]***			
Distribution	*Singlet*	*Doublet*	*Triplet*	*Quadlet*	*Singlet*	*Doublet*	*Triplet*	*Quadlet*
Foreground	18287789	67156	146	6	26542	97	0.211	0.008
Background	13556	73	0	0	19.6	0.10	0	0
Ratio to *Singlet* $\times 10^{-4}$	—	36	0.080	0.00.		—		

Table E.4 | Coincidence distributions for the BARE15 setup with the main ^{252}Cf source inside a tungsten capsule.

Date	1-March 2017							
Time [s]	191							
	Counts				***Count Rates [s^{-1}]***			
Distribution	*Singlet*	*Doublet*	*Triplet*	*Quadlet*	*Singlet*	*Doublet*	*Triplet*	*Quadlet*
Foreground	1803761	57799	1004	6	9443	302	5.26	0.034
Background	492	9	1	0	2.57	0.05	0	0.005
Ratio to *Singlet* $\times 10^{-4}$	—	320	5.57	0.033		—		

Table E.5 | Coincidence distributions for the BARE15 setup with various ^{252}Cf sources.

(a) Neutron coincidence distribution with lead shielding for Cf252-FC source

Date	1-March 2017							
Time [s]	953							
	Counts				***Count Rates [s^{-1}]***			
Distribution	*Singlet*	*Doublet*	*Triplet*	*Quadlet*	*Singlet*	*Doublet*	*Triplet*	*Quadlet*
Foreground	708876	21521	336	4	743	22	0.35	0.004
Background	19	0	0	0	0.019	0	0	0
Ratio to *Singlet* $\times 10^{-4}$	—	303	4.73	0.06		—		

(b) Neutron coincidence distribution with no lead shielding for Cf252-TH source

Date	1-March 2017							
Time [s]	743							
	Counts				***Count Rates [s^{-1}]***			
Distribution	*Singlet*	*Doublet*	*Triplet*	*Quadlet*	*Singlet*	*Doublet*	*Triplet*	*Quadlet*
Foreground	2064635	66942	1176	69	2778	90	1.58	0.012
Background	209	5	0	0	0.28	1.49	0.007	0
Ratio to *Singlet* $\times 10^{-4}$	—	324	5.69	0.044		—		

(c) Neutron coincidence distribution with lead shielding for Cf252-MAIN source

Date	1-March 2017							
Time [s]	95							
	Counts				***Count Rates [s^{-1}]***			
Distribution	*Singlet*	*Doublet*	*Triplet*	*Quadlet*	*Singlet*	*Doublet*	*Triplet*	*Quadlet*
Foreground	917252	30268	520	5	9655	318	5.47	0.053
Background	262	9	0	0	2.75	0.09	0	0
Ratio to *Singlet* $\times 10^{-4}$	—	329	5.67	0.055		—		

(d) Neutron coincidence distribution with lead shielding for Cf252-All source

Date	1-March 2017							
Time [s]	121							
	Counts				***Count Rates [s^{-1}]***			
Distribution	*Singlet*	*Doublet*	*Triplet*	*Quadlet*	*Singlet*	*Doublet*	*Triplet*	*Quadlet*
Foreground	1489729	49151	782	5	12311	406	6.46	0.041
Background	573	10	0	0	4.74	0.083	0	0
Ratio to *Singlet* $\times 10^{-4}$	—	329	5.24	0.033		—		

E.3 Active coincidence counting analysis

Table E.6 | Coincidence distributions for the BARE8 setup with various UOX samples.

(a) Neutron coincidence distribution with lead shielding for 93% enriched UOX

Date	22-Feb 2017					
Time [s]	2107					
	Counts			***Count Rates[s^{-1}]***		
Distribution	*Singlet*	*Doublet*	*Triplet*	*Singlet*	*Doublet*	*Triplet*
Foreground	418671	1418	13	198	0.673	0.006
Background	2	1	0	0.001	0.000	0.000

(b) Neutron coincidence distribution with no lead shielding for 52% enriched UOX

Date	22-Feb 2017					
Time [s]	2718					
	Counts			***Count Rates[s^{-1}]***		
Distribution	*Singlet*	*Doublet*	*Triplet*	*Singlet*	*Doublet*	*Triplet*
Foreground	518626	1520	6	190.812	0.559	0.002
Background	6	0	0	0.002	0.000	0.000

(c) Neutron coincidence distribution with lead shielding for 21% enriched UOX

Date	22-Feb 2017					
Time [s]	3935					
	Counts			***Count Rates[s^{-1}]***		
Distribution	*Singlet*	*Doublet*	*Triplet*	*Singlet*	*Doublet*	*Triplet*
Foreground	683825	1624	6	173.780	0.413	0.002
Background	4	0	0	0.001	0.000	0.000

(d) Neutron coincidence distribution with lead shielding for 4% enriched UOX

Date	24-Feb 2017					
Time [s]	2732					
	Counts			***Count Rates[s^{-1}]***		
Distribution	*Singlet*	*Doublet*	*Triplet*	*Singlet*	*Doublet*	*Triplet*
Foreground	400237	596	3	146.500	0.218	0.001
Background	1	0	0	0.000	0.000	0.000

(e) Neutron coincidence distribution with lead shielding for 3% enriched UOX

Date		24-Feb 2017				
Time [s]		2400				
	Counts			***Count Rates[s^{-1}]***		
Distribution	*Singlet*	*Doublet*	*Triplet*	*Singlet*	*Doublet*	*Triplet*
Foreground	341930	449	0	142.471	0.187	0.000
Background	1	0	0	0.000	0.000	0.000

(f) Neutron coincidence distribution with no lead shielding for 2% enriched UOX

Date		24-Feb 2017				
Time [s]		2538				
	Counts			***Count Rates[s^{-1}]***		
Distribution	*Singlet*	*Doublet*	*Triplet*	*Singlet*	*Doublet*	*Triplet*
Foreground	354448	424	0	139.656	0.167	0.000
Background	0	0	0	0.000	0.000	0.000

(g) Neutron coincidence distribution with lead shielding for natural UOX

Date		24-Feb 2017				
Time [s]		2763				
	Counts			***Count Rates[s^{-1}]***		
Distribution	*Singlet*	*Doublet*	*Triplet*	*Singlet*	*Doublet*	*Triplet*
Foreground	377003	354	2	136.447	0.128	0.001
Background	4	0	0	0.001	0.000	0.000

(h) Neutron coincidence distribution with lead shielding for depleted UOX

Date		24-Feb 2017				
Time [s]		2410				
	Counts			***Count Rates[s^{-1}]***		
Distribution	*Singlet*	*Doublet*	*Triplet*	*Singlet*	*Doublet*	*Triplet*
Foreground	323193	284	0	134.105	0.118	0.000
Background	3	0	0	0.001	0.000	0.000

(i) Neutron coincidence distribution with lead shielding for empty UOX

Date		24-Feb 2017				
Time [s]		2408				
	Counts			***Count Rates[s^{-1}]***		
Distribution	*Singlet*	*Doublet*	*Triplet*	*Singlet*	*Doublet*	*Triplet*
Foreground	323480	254	1	134.336	0.105	0.000
Background	1	0	0	0.000	0.000	0.000

Table E.7 | Coincidence distributions for the BARE15 setup with various UOX samples with 2 cm moderator.

(a) Neutron coincidence distribution with lead shielding for 93% enriched UOX

Date	28-Feb 2017					
Time [s]	1268					
	Counts			***Count Rates[s^{-1}]***		
Distribution	*Singlet*	*Doublet*	*Triplet*	*Singlet*	*Doublet*	*Triplet*
Foreground	525413	3253	21	414.364	2.565	0.017
Background	15	0	0	0.012	0.000	0.000

(b) Neutron coincidence distribution with no lead shielding for 52% enriched UOX

Date	28-Feb 2017					
Time [s]	1202					
	Counts			***Count Rates[s^{-1}]***		
Distribution	*Singlet*	*Doublet*	*Triplet*	*Singlet*	*Doublet*	*Triplet*
Foreground	466085	2543	19	387.758	2.116	0.016
Background	5	0	0	0.004	0.000	0.000

(c) Neutron coincidence distribution with lead shielding for 21% enriched UOX

Date	28-Feb 2017					
Time [s]	1197					
	Counts			***Count Rates[s^{-1}]***		
Distribution	*Singlet*	*Doublet*	*Triplet*	*Singlet*	*Doublet*	*Triplet*
Foreground	402912	1804	10	336.602	1.507	0.008
Background	5	0	0	0.004	0.000	0.000

(d) Neutron coincidence distribution with lead shielding for 4% enriched UOX

Date	28-Feb 2017					
Time [s]	1239					
	Counts			***Count Rates[s^{-1}]***		
Distribution	*Singlet*	*Doublet*	*Triplet*	*Singlet*	*Doublet*	*Triplet*
Foreground	388969	1125	3	313.938	0.908	0.002
Background	2	0	0	0.002	0.000	0.000

(e) Neutron coincidence distribution with lead shielding for 3% enriched UOX

Date		28-Feb 2017				
Time [s]		2757				
	Counts			***Count Rates[s^{-1}]***		
Distribution	*Singlet*	*Doublet*	*Triplet*	*Singlet*	*Doublet*	*Triplet*
Foreground	858182	2225	10	311.274	0.807	0.004
Background	9	0	0	0.003	0.000	0.000

(f) Neutron coincidence distribution with no lead shielding for 2% enriched UOX

Date		28-Feb 2017				
Time [s]		1540				
	Counts			***Count Rates[s^{-1}]***		
Distribution	*Singlet*	*Doublet*	*Triplet*	*Singlet*	*Doublet*	*Triplet*
Foreground	469611	1088	2	304.942	0.706	0.001
Background	5	0	0	0.003	0.000	0.000

(g) Neutron coincidence distribution with lead shielding for natural UOX

Date		28-Feb 2017				
Time [s]		2432				
	Counts			***Count Rates[s^{-1}]***		
Distribution	*Singlet*	*Doublet*	*Triplet*	*Singlet*	*Doublet*	*Triplet*
Foreground	729240	1548	4	299.852	0.637	0.002
Background	3	0	0	0.001	0.000	0.000

(h) Neutron coincidence distribution with lead shielding for depleted UOX

Date		28-Feb 2017				
Time [s]		2236				
	Counts			***Count Rates[s^{-1}]***		
Distribution	*Singlet*	*Doublet*	*Triplet*	*Singlet*	*Doublet*	*Triplet*
Foreground	668904	1294	1	299.152	0.579	0.000
Background	7	0	0	0.003	0.000	0.000

(i) Neutron coincidence distribution with lead shielding for empty UOX

Date		28-Feb 2017				
Time [s]		1289				
	Counts			***Count Rates[s^{-1}]***		
Distribution	*Singlet*	*Doublet*	*Triplet*	*Singlet*	*Doublet*	*Triplet*
Foreground	383638	648	0	297.625	0.503	0.000
Background	3	0	0	0.002	0.000	0.000

Table E.8 | Coincidence distributions for the BARE15 setup with various UOX samples with 2 cm moderator.

(a) Neutron coincidence distribution with lead shielding for 93% enriched UOX

Date	28-Feb 2017					
Time [s]	1220					
	Counts			***Count Rates[s^{-1}]***		
Distribution	*Singlet*	*Doublet*	*Triplet*	*Singlet*	*Doublet*	*Triplet*
Foreground	465473	2709	37	381.535	2.220	0.030
Background	8	0	0	0.007	0.000	0.000

(b) Neutron coincidence distribution with no lead shielding for 52% enriched UOX

Date	28-Feb 2017					
Time [s]	1403					
	Counts			***Count Rates[s^{-1}]***		
Distribution	*Singlet*	*Doublet*	*Triplet*	*Singlet*	*Doublet*	*Triplet*
Foreground	506023	2832	28	360.672	2.019	0.020
Background	3	0	0	0.002	0.000	0.000

(c) Neutron coincidence distribution with lead shielding for 21% enriched UOX

Date	28-Feb 2017					
Time [s]	1242					
	Counts			***Count Rates[s^{-1}]***		
Distribution	*Singlet*	*Doublet*	*Triplet*	*Singlet*	*Doublet*	*Triplet*
Foreground	436830	1831	17	351.715	1.474	0.014
Background	2	0	0	0.002	0.000	0.000

(d) Neutron coincidence distribution with lead shielding for 4% enriched UOX

Date	28-Feb 2017					
Time [s]	1618					
	Counts			***Count Rates[s^{-1}]***		
Distribution	*Singlet*	*Doublet*	*Triplet*	*Singlet*	*Doublet*	*Triplet*
Foreground	485118	1464	1	299.826	0.905	0.001
Background	2	0	0	0.001	0.000	0.000

(e) Neutron coincidence distribution with lead shielding for 3% enriched UOX

Date		28-Feb 2017				
Time [s]		1468				
	Counts			***Count Rates[s^{-1}]***		
Distribution	*Singlet*	*Doublet*	*Triplet*	*Singlet*	*Doublet*	*Triplet*
Foreground	436606	1116	3	297.416	0.760	0.002
Background	4	0	0	0.003	0.000	0.000

(f) Neutron coincidence distribution with no lead shielding for 2% enriched UOX

Date		28-Feb 2017				
Time [s]		1443				
	Counts			***Count Rates[s^{-1}]***		
Distribution	*Singlet*	*Doublet*	*Triplet*	*Singlet*	*Doublet*	*Triplet*
Foreground	420209	1006	1	291.205	0.697	0.001
Background	7	0	0	0.005	0.000	0.000

(g) Neutron coincidence distribution with lead shielding for natural UOX

Date		28-Feb 2017				
Time [s]		1708				
	Counts			***Count Rates[s^{-1}]***		
Distribution	*Singlet*	*Doublet*	*Triplet*	*Singlet*	*Doublet*	*Triplet*
Foreground	486640	981	5	284.918	0.574	0.003
Background	1	0	0	0.001	0.000	0.000

(h) Neutron coincidence distribution with lead shielding for depleted UOX

Date		28-Feb 2017				
Time [s]		1784				
	Counts			***Count Rates[s^{-1}]***		
Distribution	*Singlet*	*Doublet*	*Triplet*	*Singlet*	*Doublet*	*Triplet*
Foreground	501737	1006	4	281.243	0.564	0.002
Background	3	0	0	0.002	0.000	0.000

(i) Neutron coincidence distribution with lead shielding for empty UOX

Date		28-Feb 2017				
Time [s]		1998				
	Counts			***Count Rates[s^{-1}]***		
Distribution	*Singlet*	*Doublet*	*Triplet*	*Singlet*	*Doublet*	*Triplet*
Foreground	563376	1010	3	281.970	0.506	0.002
Background	7	0	0	0.004	0.000	0.000

Table E.9 | Coincidence distributions for the CASTLE12 setup with various UOX samples.

(a) Neutron coincidence distribution with lead shielding for 93% enriched UOX

Date		1-March 2017				
Time [s]		447				
		Counts		Count Rates [s^{-1}]		
Distribution	*Singlet*	*Doublet*	*Triplet*	*Singlet*	*Doublet*	*Triplet*
Foreground	282728	4695	81	629	10	0.180
Background	9	0	0	0.020	0	0

(b) Neutron coincidence distribution with no lead shielding for 52% enriched UOX

Date		1-March 2017				
Time [s]		489				
		Counts		Count Rates [s^{-1}]		
Distribution	*Singlet*	*Doublet*	*Triplet*	*Singlet*	*Doublet*	*Triplet*
Foreground	276521	4076	64	565	8.3	0.131
Background	7	0	0	0.014	0.000	0.000

(c) Neutron coincidence distribution with lead shielding for 21% enriched UOX

Date		1-March 2017				
Time [s]		674				
		Counts		Count Rates [s^{-1}]		
Distribution	*Singlet*	*Doublet*	*Triplet*	*Singlet*	*Doublet*	*Triplet*
Foreground	332916	4208	54	493	6.243	0.080
Background	3	0	0	0.004	0.000	0.000

(d) Neutron coincidence distribution with lead shielding for 4% enriched UOX

Date		1-March 2017				
Time [s]		674				
		Counts		Count Rates [s^{-1}]		
Distribution	*Singlet*	*Doublet*	*Triplet*	*Singlet*	*Doublet*	*Triplet*
Foreground	272434	2365	21	404	3.509	0.031
Background	9	0	0	0.013	0.000	0.000

(e) Neutron coincidence distribution with lead shielding for 3% enriched UOX

Date		1-March 2017				
Time [s]		473				
		Counts		Count Rates [s^{-1}]		
Distribution	*Singlet*	*Doublet*	*Triplet*	*Singlet*	*Doublet*	*Triplet*
Foreground	183954	1391	8	388	2.941	0.017
Background	2	0	0	0.004	0.000	0.000

(f) Neutron coincidence distribution with no lead shielding for 2% enriched UOX

Date		1-March 2017				
Time [s]		445				
		Counts		Count Rates [s^{-1}]		
Distribution	*Singlet*	*Doublet*	*Triplet*	*Singlet*	*Doublet*	*Triplet*
Foreground	169906	1193	4	381	2.681	0.009
Background	0	0	0	0.000	0.000	0.000

(g) Neutron coincidence distribution with lead shielding for natural UOX

Date		1-March 2017				
Time [s]		494				
		Counts		Count Rates [s^{-1}]		
Distribution	*Singlet*	*Doublet*	*Triplet*	*Singlet*	*Doublet*	*Triplet*
Foreground	181255	1140	10	366	2.308	0.020
Background	2	0	0	0.004	0.000	0.000

(h) Neutron coincidence distribution with lead shielding for depleted UOX

Date		1-March 2017				
Time [s]		494				
		Counts		Count Rates [s^{-1}]		
Distribution	*Singlet*	*Doublet*	*Triplet*	*Singlet*	*Doublet*	*Triplet*
Foreground	179534	1010	3	363	2.045	0.006
Background	2	0	0	0.004	0.000	0.000

(i) Neutron coincidence distribution with lead shielding for empty UOX

Date		1-March 2017				
Time [s]		476				
		Counts		Count Rates [s^{-1}]		
Distribution	*Singlet*	*Doublet*	*Triplet*	*Singlet*	*Doublet*	*Triplet*
Foreground	168015	931	7	352.973	1.956	0.015
Background	0	0	0	0.000	0.000	0.000

(j) Neutron coincidence distribution with lead shielding for 20% enriched UOX with various calibration sources

Date		1-March 2017				
Time [s]		137				
		Counts		Count Rates [s^{-1}]		
Distribution	*Singlet*	*Doublet*	*Triplet*	*Singlet*	*Doublet*	*Triplet*
Foreground	159492	929	14	1164	6.781	0.102
Background	4	0	0	0.029	0.000	0.000